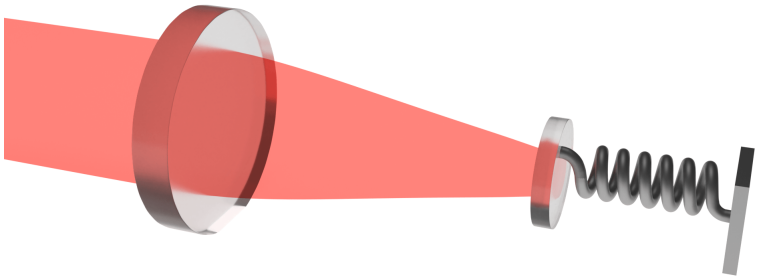
Nonlinear Cavity Quantum Optomechanics:
from Quantum Measurement to Quantum State Engineering



Jack Clarke

Imperial College London

Department of Physics

Supervisor: Michael R. Vanner

Thesis submitted in partial fulfilment of the requirements for the degree of

Doctor of Philosophy in Physics

September 2024

Declarations

I declare that the content of this thesis is my own work, completed whilst a candidate for the degree of Doctor of Philosophy in Physics at Imperial College London. The results presented have been obtained by myself or in close collaboration with colleagues whom I have directly acknowledged where appropriate. To the best of my knowledge, I have referenced work completed by others where appropriate.

Jack Clarke
Buxton and London, September 2024

The copyright of this thesis rests with the author. Unless otherwise indicated, its contents are licensed under a Creative Commons Attribution-Non Commercial 4.0 International Licence (CC BY-NC). Under this licence, you may copy and redistribute the material in any medium or format. You may also create and distribute modified versions of the work. This is on the condition that: you credit the author and do not use it, or any derivative works, for a commercial purpose. When reusing or sharing this work, ensure you make the licence terms clear to others by naming the licence and linking to the licence text. Where a work has been adapted, you should indicate that the work has been changed and describe those changes. Please seek permission from the copyright holder for uses of this work that are not included in this licence or permitted under UK Copyright Law.

Abstract

In a nutshell, a cavity optomechanical system consists of a mechanical oscillator inside an optical cavity. Cavity optomechanics studies the interplay between the light-matter radiation-pressure interaction and the change in the cavity frequency induced by mechanical motion. By leveraging the tools of quantum optics and quantum measurement, cavity quantum optomechanics enables the engineering of nonclassical quantum states of bulk matter.

In this thesis, I present protocols for engineering such nonclassical quantum states in Part II. First, I introduce a scheme to 'grow' a quantum kitten state of a mechanical oscillator into a macroscopic Schrödinger cat state using a series of nonlinear pulsed optomechanical interactions. Next, I detail our proposed schemes to generate and verify entanglement between two mechanical oscillators. Moving on from pulsed optomechanics, I describe the theory behind an experiment that achieved multi-phonon subtraction from a mechanical oscillator in a continuously driven Brillouin optomechanical system. In the final chapter of Part II, I provide a theoretical preview of an experiment that investigates the behaviour of the mechanical oscillator when no light is detected at the output.

In Part III, I introduce a new framework for nonlinear cavity quantum optomechanics that incorporates the intrinsic nonlinearity of the radiation-pressure interaction, the nonlinearity from the cavity enhancement, and higher-order mechanical position terms in the expansion of the cavity frequency. I then propose a scheme for measuring mechanical position using general-dyne detection, applicable to pulsed and continuous measurements. This predicts a new regime of operation, the "stochastic Gaussian" regime. Finally, I discuss a protocol for deterministic mechanical squeezing that utilizes the cavity response.

Acknowledgements

Dedicated to Stanley Frederick Clarke

Firstly, I would like to thank my supervisor Michael who I've known since I started my MPhys project in Oxford. It's been a pleasure working with you Michael and I'm looking forward to doing more physics together in the future. For interesting scientific discussions during my PhD, I would like to thank Georg, Kiran, Lydia, Sofia, Paulo, Giada, Ewold, Andreas, John, Lars, Evan, Benjamin, Edward, Almut, Pascal, Kyle, and everyone on level 12 of EEE. I'd like to acknowledge all my friends and family who've supported me over the course of my PhD. In particular, thanks to my brother Adam and to the best dog in the world: Rufus! I'd also like to thank my wonderful partner Harnaam for all her love and support and for being so kind and caring. Finally, I'd like to thank my parents and grandparents for being constantly supportive despite having absolutely no idea what I am doing.

Preface

List of publications

[1]: J. Clarke and M. R. Vanner, *Growing Macroscopic Superposition States via Cavity Quantum Optomechanics*, Quantum Science and Technology **4**, 014003, (2019).

[2]: J. Clarke, P. Sahium, K. E. Khosla, I. Pikovski, M. S. Kim, and M. R. Vanner, *Generating Mechanical and Optomechanical Entanglement via Pulsed Interaction and Measurement*, New Journal of Physics **22**, 063001 (2020).

[3]: P. Neveu, J. Clarke, M. R. Vanner, and E. Verhagen, *Preparation and Verification of Two-Mode Mechanical Entanglement through Pulsed Optomechanical Measurements*, New Journal of Physics **23**, 023026 (2021).

[4]: G. Enzian, L. Freisem, J. J. Price, A. Ø. Svela, J. Clarke, B. Shajilal, J. Janousek, B. C. Buchler, P. K. Lam, and M. R. Vanner, *Non-Gaussian Mechanical Motion via Single and Multiphonon Subtraction from a Thermal State*, Physical Review Letters **127**, 243601 (2021).

[5]: L. A. Kanari-Naish, J. Clarke, M. R. Vanner, and E. A. Laird, *Can the Displacemon Device Test Objective Collapse Models?*, AVS Quantum Science **3**, 045603 (2021).

[6]: L. A. Kanari-Naish, J. Clarke, S. Qvarfort, and M. R. Vanner, *Two-mode Schrödinger-cat States with Nonlinear Optomechanics: Generation and Verification of Non-Gaussian Mechanical Entanglement*, Quantum Science and Technology **7**, 035012, (2022).

[7]: J. Clarke, P. Neveu, K. E. Khosla, E. Verhagen, and M. R. Vanner, *Cavity Quantum Optomechanical Nonlinearities and Position Measurement beyond the Breakdown of the Linearized Approximation*, Physical Review Letters **131**, 053601 (2023).

[8]: J. Clarke, E. A. Cryer-Jenkins, A. Gupta, K. D. Major, J. Zhang, G. En-

zian, M. Szczykulska, A. C. Leung, H. Rathee, A. Ø Svela, A. K. C. Tan, A. Beige, K. Mølmer, and M. R. Vanner, *Theoretical Framework for Enhancing or Enabling Cooling of a Mechanical Resonator via the anti-Stokes or Stokes Interaction and Zero-Photon Detection*, Physical Review A **111**, 023516 (2025).

[9]: E. A. Cryer-Jenkins, K. D. Major, J. Clarke, G. Enzian, M. Szczykulska, J. Zhang, A. Gupta, A. C. Leung, H. Rathee, A. Ø Svela, A. K. C. Tan, A. Beige, K. Mølmer, and M. R. Vanner, *Enhanced Laser Cooling of a Mechanical Resonator via Zero-Photon Detection*, Physical Review Letters **134**, 073601 (2025).

[10]: L. A. Kanari-Naish, J. Clarke, S. Qvarfort, and M. R. Vanner, *Optimizing confidence in negative-partial-transpose-based entanglement criteria*, arXiv:2502.19624 (2025).

[11] J. Clarke, *Nonlinear cavity quantum optomechanics in the unresolved-sideband regime*, in Quantum Sensing, Imaging, and Precision Metrology III (SPIE, 2025) 13392, 147.

Manuscripts in preparation

[12]: P. Neveu, J. Clarke, M. R. Vanner, and E. Verhagen, *Deterministic Mechanical Squeezing With Strong Optical Pulses*, (In preparation).

[13] J. Clarke, P. Neveu, E. Verhagen, and M. R. Vanner, *Deterministic Mechanical Wigner Negativity via Nonlinear Cavity Quantum Optomechanics in the Unresolved-Sideband Regime*, (In preparation).

Initials of co-authors

J.C.	Jack Clarke
M.R.V.	Michael Vanner
P.S.	Paulo Sahium
K.E.K.	Kiran Khosla
I.P.	Igor Pikovski
M.S.K.	Myungshik Kim
P.N.	Pascal Neveu
E.V.	Ewold Verhagen
G.E.	Georg Enzian
L.F.	Lars Freisem
J.J.P.	John Price
A.Ø.S.	Andreas Svela
L.K.N.	Lydia Kanari-Naish
S.Q.	Sofia Qvarfort
E.A.L.	Edward Laird
E.C.J.	Evan Cryer-Jenkins
K.D.M.	Kyle Major

Outline of this thesis

This thesis is comprised of three distinct parts, which I shall briefly summarize in turn below. The target audience ranges from Masters students to active professional researchers. For convenience, in Fig. 1 I present a flow diagram for how one might navigate this thesis depending on their interests and experience.

In Part I, I review the theory that this thesis builds upon. Readers familiar with these concepts may wish to skip the corresponding sections within this part. In Chapters 1 and 2 I discuss some basic quantum mechanics and useful quantum optics theory. Here, I take the opportunity to establish the conventions used throughout this thesis. Readers familiar with quantum optics may therefore turn to Chapters 1 and 2 when they inevitably ask "what convention is being used here?" Chapter 3 reviews a selection of techniques in open quantum systems, which are used in the quantum state engineering and measurement protocols of this thesis. Many of the protocols I introduce pertain to Gaussian quantum states and so in Chapter 4 I present a tour of Gaussian continuous variable quantum mechanics. Generalized and continuous quantum measurement are vital ingredients in many of the protocols I introduce and so in Chapter 5 an overview of quantum measurement theory is provided. Finally, in Chapter 6 I provide a theoretical overview of the field of cavity quantum optomechanics, which is the field that the work presented in this thesis belongs to.

Part II details the quantum state engineering component of this thesis. Refs [1] to [6] of the publications listed in the "*List of publications*" fit into this category. I endeavour to motivate each work separately at the start of each chapter to allow the reader to navigate this thesis as they wish. In Chapter 7 the work of Ref. [1] is discussed, which details a multistep protocol to 'grow'

a mechanical superposition state towards the macroscopic scale. In particular, it is shown how one can grow a quantum cat from a quantum kitten. Then in Chapter 8, I discuss the works of Refs [2], [3], and [6], which detail protocols for generating and verifying entanglement between two mechanical oscillators. Focus is placed on [2], which also details how pulsed optomechanics can be used to verify optical-mechanical entanglement. Next, I then take a slight detour to the neighbouring field of Brillouin optomechanics in Chapter 9. It is shown how much of the underlying physics discussed in Chapter 6 applies here too, which allows one to delve into the theory behind the multi-phonon subtraction experiment of Ref. [4]. Finally in Chapter 10, I provide an introduction to a theoretical framework that explores how, strangely enough, subtracting zero phonons from a mechanical state can have interesting consequences.

In Part III, a major result of this PhD thesis is presented, namely a new framework of nonlinear cavity quantum optomechanics. Hence, I dedicate an entire part of this thesis to this framework, which expands on the work of Ref. [7]. In Chapter 11 I derive a whole class of unitaries to describe nonlinear cavity quantum optomechanics for an adiabatic cavity, which include the physics of arbitrary nonlinear couplings of the mechanical position to the photon number operator and various levels of enhancement from the cavity. Moving on to Chapter 12, a new position measurement scheme in the nonlinear regime is proposed. Specifically, optical general-dyne detection is employed to derive a measurement operator and a stochastic master equation, which describe pulsed and continuous position measurements, respectively. Then in Chapters 13 and 14 I specialize to the case of a linear coupling of mechanical position to the photon number operator, which allows focus to be placed on the nonlinear contribution to the system dynamics from the inherent nonlinearity of the radiation-pressure force and the enhancement of the interaction from the cavity. Chapter 13 details how pulsed back-action evading measurements can be performed in nonlinear optomechanics, allowing for a description that goes far beyond the point where the linearized theory breaks down. In Chapter 14, it is shown how our general nonlinear framework of continuous position measurement predicts a new regime: the *stochastic Gaussian* regime, which unlike the linear theory can describe optical rotations throughout the full cavity phase response. Finally, in Chapter 15 I discuss the theory behind the deterministic mechanical squeezing experiment of Ref. [12] and show how it agrees with the results from the previous chapters. An outlook towards quantum squeezing using this method is also provided.

As an aside, in Appendix D, I discuss how objective collapse models, which underpin the work of Ref. [5], may be understood from a quantum-measurement-theory perspective. These phenomenological models are equivalent to a standard description of a quantum system with measurement channels that are fundamentally inaccessible. In Ref. [5], we studied how an aluminium mechanical resonator may be used to test objective collapse models within the "displacemon" electromechanical device [14]. Although this work does not fit into the above outline, the discussion in Appendix D has been included so this thesis includes all the work carried out during my PhD.

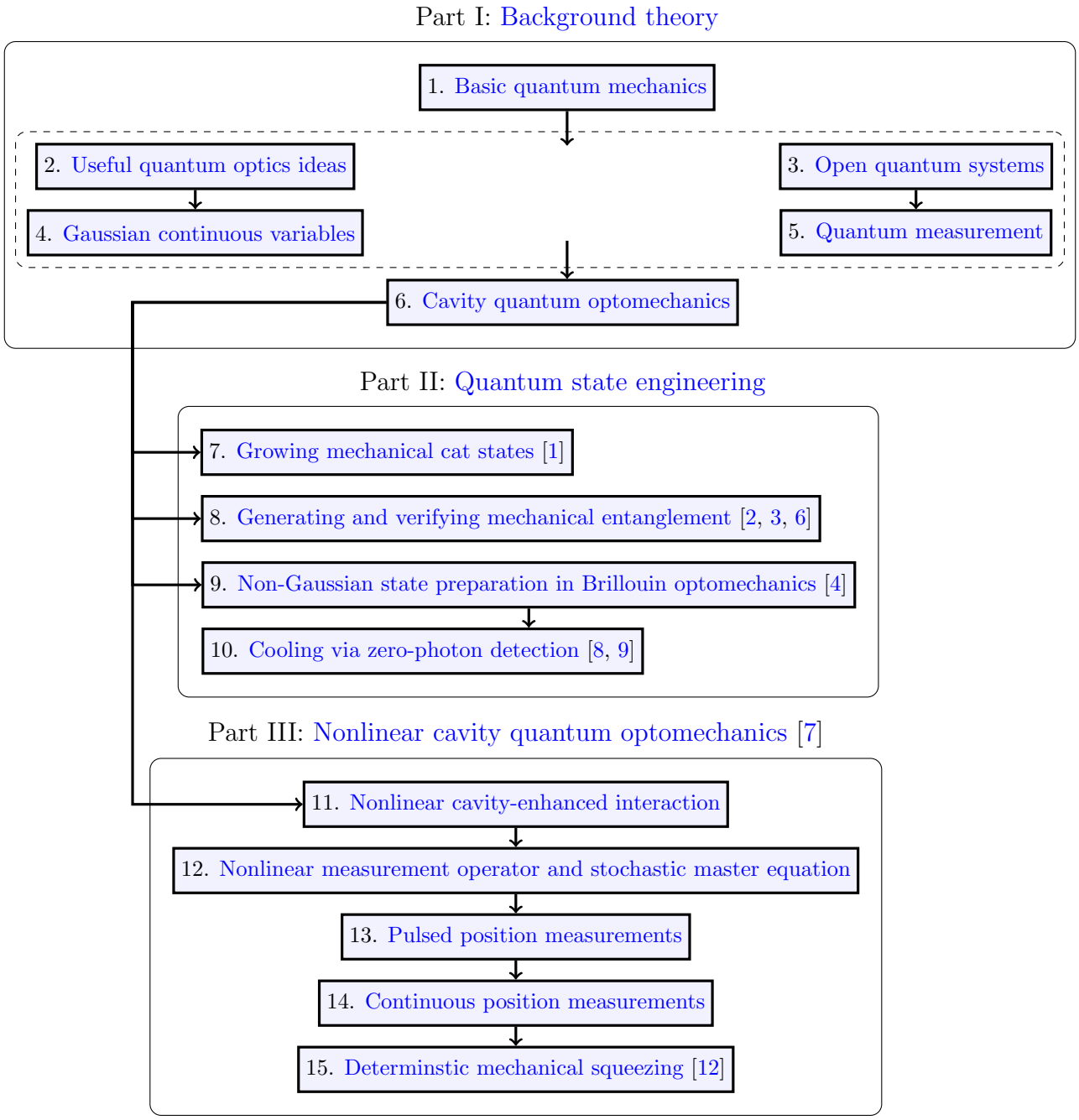


Figure 1: **How to read this thesis.** If you are beginning research in this area, start at Chapter 1 and then follow the arrows. For those familiar with quantum optics, open quantum systems, Gaussian continuous variable quantum mechanics, and quantum measurement theory start at Chapter 6. From Chapter 6, one can follow the arrows and go to either Chapter 7, 8, or 9, which may be all read independently from one another. Alternatively, one may go from Chapter 6 to Chapter 11 and start the journey through nonlinear cavity quantum optomechanics in the adiabatic regime.

Contents

I Background theory **1**

1 Basic quantum mechanics **2**

2 Useful quantum optics ideas **5**
2.1 The quantum harmonic oscillator and number states 5
2.2 Quadrature states of light and mechanics 6
2.3 Coherent states and the displacement operator 7
2.4 Other single mode states 8
2.5 Two mode states and entanglement 8
2.6 The beamsplitter 9
2.7 Characteristic functions and operator ordering 11
2.8 Quasiprobability distributions 12
2.8.1 Wigner distribution 12
2.8.2 Husimi Q function 14
2.8.3 Sudarshan-Glauber P function 14
2.8.4 s-parametrized Wigner function 15

3 Open quantum systems **17**
3.1 Markovianity 17
3.2 Quantum Lindblad master equations 18
3.2.1 Quantum optics master equation 18
3.2.2 Quantum Brownian motion and decoherence 19
3.2.3 Connection between the quantum optics master equation and quantum Brownian motion 21
3.3 Heisenberg-Langevin equations and input-output theory 24
3.3.1 Input noise correlation functions 26
3.3.2 Quantum optics Heisenberg-Langevin equation 27
3.3.3 Quantum Brownian motion Heisenberg-Langevin equation 29

4 Continuous-variable Gaussian quantum optics **31**
4.1 General formalism 31
4.2 Single mode symplectic transformations 33
4.3 Two mode symplectic transformations 33
4.4 Measurements and trace 34

4.5 Open system dynamics . . . 35
4.6 Gaussian entanglement . . . 36
4.6.1 Non-Gaussian entanglement . . . 36

5 Quantum measurement **38**
5.1 Generalized quantum measurements . . . 38
5.2 Continuous weak measurements . . . 40

6 Cavity quantum optomechanics **43**
6.1 The optomechanical Hamiltonian . . . 44
6.1.1 Quadratic coupling to position and beyond . . . 45
6.2 Regimes of optomechanics . . . 46
6.2.1 The strong coupling and ultra-strong coupling regimes . . . 46
6.2.2 The large optomechanical phase shift regime . . . 48
6.2.3 The sideband-resolution parameter: cooling, heating, and measurements . . . 48
6.3 Linearized cavity optomechanics and when it applies . . . 51
6.3.1 Validity of the linearization procedure and beyond . . . 51
6.3.2 Pulsed optomechanics . . . 54
6.3.3 Continuously driven optomechanics . . . 63
6.4 Nonlinear optomechanics . . . 67
6.4.1 The nonlinear pulsed unitaries . . . 67
6.4.2 Continuous nonlinear position measurements . . . 69

II Quantum state engineering **73**

7 Growing mechanical cat states **74**
7.1 Towards macroscopic quantum states . . . 75
7.1.1 The multi-port protocol . . . 77
7.2 The multistep protocol . . . 78
7.2.1 Schrödinger cat states . . . 78
7.2.2 The setup and overview . . . 79
7.2.3 Mathematical details and choice of phase in the multistep process . . . 80
7.3 Open system dynamics and heralding probability . . . 84
7.3.1 Heralding probability and optical loss . . . 84
7.3.2 Experimental considerations . . . 89
7.3.3 Scaling of the heralding probability with step number . . . 91
7.3.4 Mechanical decoherence . . . 93
7.4 Quantifying the cats . . . 95
7.4.1 Non-classicality . . . 95
7.4.2 Macroscopicity . . . 96
7.5 Results . . . 100
7.5.1 Cats versus kittens . . . 100
7.5.2 Experimental parameters . . . 102

7.5.3 The non-classicality and macroscopicity . . . 104
7.5.4 Effect of optical loss . . . 108
7.6 Optimizing the pulse shape . . . 110
7.6.1 Pulse shape in the original work . . . 110
7.6.2 Optimization with long pulses . . . 110
7.7 Detector timing with long pulses . . . 115
7.7.1 Time dependence of μ . . . 115
7.7.2 Detector timing . . . 116
7.8 Conclusion and outlook . . . 118

8 Generating and verifying mechanical entanglement 120
8.1 Entanglement in optomechanics . . . 121
8.1.1 Linearized pulsed optomechanics for generating and verifying entanglement . . . 123
8.1.2 Experimental realization and future work . . . 123
8.2 Pulsed optomechanics, Gaussian operations, and optical-mechanical entanglement . . . 124
8.2.1 The optomechanical interaction and Gaussian continuous variable quantum mechanics . . . 124
8.2.2 Mechanical precooling . . . 125
8.2.3 Optomechanical entanglement . . . 126
8.2.4 Experimental parameters . . . 127
8.3 Optical-mechanical entanglement in pulsed optomechanics . . . 129
8.3.1 Optical-mechanical entanglement generation . . . 129
8.3.2 Optical-mechanical entanglement verification . . . 130
8.3.3 Optical squeezing and non-monotonic behaviour . . . 133
8.3.4 Conservative approaches to entanglement estimation . . . 136
8.4 Mechanical-mechanical entanglement in pulsed optomechanics . . . 137
8.4.1 Interferometric scheme . . . 137
8.4.2 Non-interferometric scheme . . . 142
8.5 Comparison between the entanglement protocols . . . 147
8.6 Summary of the entanglement protocols . . . 150
8.7 Further entanglement works . . . 151
8.7.1 Entangling modes of the same resonator . . . 151
8.7.2 Two-mode mechanical cat states . . . 152
8.8 Conclusion and outlook . . . 154

9 Non-Gaussian state preparation via multi-phonon subtraction and addition in Brillouin optomechanics 156
9.1 Addition, subtraction, and quantum state tomography in bosonic systems . . . 157
9.1.1 Addition and subtraction operations in optical systems . . . 157
9.1.2 Quantum state tomography . . . 158
9.1.3 Looking ahead to Brillouin optomechanical systems . . . 158
9.1.4 Brillouin optomechanics with whispering gallery microresonators . . . 159

9.1.5 Experimental protocol and simplified setup 162
9.1.6 Multiphonon subtraction and addition to a thermal state: density operator, phonon number statistics, quasiprobability distributions, and moments 164
9.1.7 Probability distributions 170
9.1.8 The measured marginals and the s-parametrized Wigner function 171
9.1.9 The heterodyne signal as a function of time for verification 176
9.1.10 Experimental Results 178
9.1.11 Conclusion and outlook 180

10 Cooling via zero-photon detection **182**
10.0.1 Zero-photon detection in quantum optics 182
10.0.2 The optomechanical beamsplitter unitary 184
10.0.3 n-click detection without open-system dynamics 186
10.0.4 Zero-photon detection with optical loss 193
10.0.5 Conclusion and outlook 197

III Nonlinear cavity quantum optomechanics **198**

11 The nonlinear cavity-enhanced optomechanical interaction **199**
11.1 Linear coupling to position 200
11.1.1 Pulsed interaction 201
11.1.2 Continuous infinitesimal unitary 205
11.1.3 Dimensionless input and output operators 208
11.1.4 The cavity free limit 208
11.2 Arbitrary nonlinear position coupling 209
11.2.1 The expanded optomechanical Hamiltonian 210
11.2.2 Pulsed interaction 210
11.2.3 Continuous infinitesimal unitary 213
11.2.4 The cavity free limit 213
11.3 Summary of all the optomechanical unitaries 214
11.4 Conclusion and outlook 216

12 The nonlinear measurement operator and stochastic master equation for position measurement **217**
12.1 The need for a theory of nonlinear position measurement 218
12.2 General-dyne detection scheme 219
12.3 Measurement operator 220
12.4 Stochastic master equation 220
12.4.1 Infinitesimal measurement operator in rotating frame . . 221
12.4.2 A general continuous homodyne measurement 221
12.4.3 SME in the rotating frame 223
12.4.4 SME in the lab frame 224
12.5 Conclusion and outlook 226

13 Pulsed position measurements **227**
13.1 Pulsed measurement map . . . 228
13.1.1 Kraus map and heralding probability . . . 228
13.1.2 The output optical state . . . 228
13.1.3 Mechanical state tomography from the output light . . . 231
13.2 Gaussian approximation to pulsed measurement . . . 232
13.2.1 General-dyne coordinates . . . 232
13.2.2 Gaussian approximation to the filtering function F and its validity . . . 233
13.2.3 The output mechanical position probability and the heralding probability for a (z, δ) outcome . . . 236
13.3 Optical loss . . . 237
13.4 Results . . . 240
13.4.1 Range of $\mu\sigma$ and the Gaussian approximation . . . 240
13.4.2 Measuring only the phase quadrature . . . 242
13.5 Conclusion and outlook . . . 243

14 Continuous position measurements **245**
14.1 Measurement records . . . 246
14.2 Agreement with cavity-free and linearized optomechanics . . . 246
14.2.1 Cavity-free continuous measurements . . . 247
14.2.2 Standard linearized continuous measurements . . . 247
14.3 The stochastic Gaussian regime . . . 249
14.3.1 Derivation and mathematics . . . 250
14.3.2 Connection to classical estimation theory . . . 254
14.3.3 Origin of the asymmetry in the general-dyne distribution: the stochastic momentum kick term . . . 254
14.3.4 Drive locking via a Butterworth filter . . . 255
14.4 Results . . . 258
14.4.1 Solving the SDEs . . . 258
14.4.2 Figures of merit: The minimum squeezing variance V_{min} and the effective thermal occupation $\bar{n}_{\mathrm{eff}}$ . . . 258
14.4.3 Zero detuning . . . 260
14.4.4 Drive locking . . . 260
14.5 Conclusion and outlook . . . 263

15 Deterministic mechanical squeezing **265**
15.1 Mechanical squeezing in optomechanics . . . 265
15.2 An exact analysis . . . 266
15.3 Gaussian approximation to deterministic squeezing . . . 269
15.3.1 Quantum noise contributions . . . 270
15.3.2 Matrix transformation . . . 271
15.3.3 The squeezing factor . . . 272
15.3.4 Agreement with the exact analysis . . . 273
15.3.5 Finite mechanical evolution . . . 274
15.4 The two pulse sequence . . . 276

15.4.1 Results . . . 278
15.5 Is optical squeezing possible? . . . 283
15.5.1 The Wigner function with detuning . . . 283
15.6 Conclusions and outlook . . . 287

A Useful formulae in quantum optics 289

B Fourier transforms 291

C Useful sums and integrals 292

D Objective collapse models 294
D.1 Continuous spontaneous localization . . . 295
D.1.1 CSL collapse rate of an extended body . . . 296
D.2 Diósi-Penrose collapse . . . 298
D.2.1 Collapse time of an extended body . . . 299

E An adiabatic cavity 301
E.1 Relation between the input and cavity amplitudes in linear optomechanics . . . 301
E.2 The linearized measurement rate . . . 301
E.3 Adiabatic elimination outside the unresolved sideband regime . . . 302

F Details on growing mechanical cats 303
F.1 δ of the Schrödinger cat state . . . 303
F.2 Arbitrary input pulse . . . 305

G Details on generating and verifying mechanical entanglement 307
G.1 Verification procedure and inverse maps . . . 307
G.1.1 Outline of the verification procedure . . . 307
G.1.2 Including optical loss in σ_{VER} . . . 308
G.2 Single mode Gaussian state of fixed purity in a phase-insensitive decoherence channel . . . 309
G.3 Avoiding non-monotonic behaviour . . . 310
G.4 Kraus operator approach . . . 311
G.4.1 Optical-mechanical and the precooling stage . . . 311
G.4.2 Interferometric mechanical entanglement . . . 313
G.4.3 Non-interferometric mechanical entanglement . . . 316
G.5 The functions J_a, J_b, and J_c . . . 317

H Proof of Kraus map completeness 318

I Full Gaussian approximation to the pulsed position measurement 319
I.1 Polar decomposition and cavity coordinates . . . 320
I.2 Full covariance matrix transformation in Gaussian approximation 321

J Details on continuous position measurement **325**
J.1 Linearized continuous position measurements: Riccati equations 325
J.2 Gallery of results for the stochastic Gaussian regime simulations 326

Bibliography **330**

Part I

Background theory

Chapter 1

Basic quantum mechanics

Here, some of the core principles of quantum mechanics are briefly reviewed, which may be useful for readers less familiar with quantum theory.

The object $|\psi\rangle$, which is normalized according to $\langle\psi|\psi\rangle = 1$, is a vector in a complex vector space and represents the pure state of a quantum mechanical system. In the Schrödinger picture, the coherent evolution of the pure quantum state $|\psi\rangle$ is governed by the Schrödinger equation

$$\mathrm{i}\hbar\frac{\mathrm{d}\,|\psi(t)\rangle}{\mathrm{d}t} = H\,|\psi(t)\rangle\,, \tag{1.1}$$

where H is the Hamiltonian, which is the Hermitian linear operator that corresponds to the total energy of the system. Linear operators act on state vectors to produce another quantum state vector, which may not be normalized, and preserve vector addition and scalar multiplication operations. Hermitian linear operators correspond to physical observables of the system. The unitary operator $U(t)$ time evolves states according to $|\psi(t)\rangle = U(t)\,|\psi(0)\rangle$. Inserting this relation into Eq. (1.1) gives the Schrödinger equation for the time-evolution operator

$$\frac{\mathrm{d}}{\mathrm{d}t}U(t) = -\frac{\mathrm{i}}{\hbar}HU(t) \tag{1.2}$$

with solution $U(t) = \mathrm{e}^{-\mathrm{i}Ht/\hbar}$ for a time-independent Hamiltonian and solution $U(t) = \mathcal{T}\exp\left[-\frac{\mathrm{i}}{\hbar}\int_0^t H(t')\mathrm{d}t'\right]$ for a time-dependent Hamiltonian[1].

The superposition principle of quantum mechanics states that if $|\phi\rangle$ represents another possible state of the system, then $c_1\,|\psi\rangle + c_2\,|\phi\rangle$ is also a valid quantum state, with $|c_1|^2 + |c_2|^2 = 1$. More generally, for a discrete system, a pure quantum state may be written as a linear combination of basis vectors $\{|n\rangle\}$

$$|\psi\rangle = \sum_{n=0}^{N} c_n\,|n\rangle\,, \tag{1.3}$$

[1] Here, $\mathcal{T}$ denotes the time-ordering operation—see Appendix A.

with $\langle n|m\rangle = \delta_{n,m}$. While $\{|n\rangle\}$ represents any set of orthonormal basis vectors, I will typically take the set $\{|n\rangle\}$ to represent the number basis, i.e. eigenstates of the number operator n. Whereas for a continuous variable system, a general state may be written as

$$|\psi\rangle = \int_{-\infty}^{\infty} \psi(X)\,|X\rangle\,\mathrm{d}X \tag{1.4}$$

with $\langle X|X'\rangle = \delta(X - X')$. For a pure state, the superposition of states $\{|X\rangle\}$ is apparent for $\psi(X) \neq \delta(X)$. In this thesis, I will typically consider continuous variable states along one spatial dimension. Therefore, $|X\rangle$ will usually be taken to be an eigenstate of the one-dimensional position operator X and so in this case $\psi(X)$ represents the position wavefunction.

When the system is in a pure state $|\psi\rangle$, the expectation value of a Hermitian observable A is given by $\langle A\rangle = \langle\psi|\,A\,|\psi\rangle = \mathrm{tr}\,(A\,|\psi\rangle\,\langle\psi|)$. This quantity represents the average over all possible real measurement outcomes when observable A is measured. If there is a classical uncertainty as to which pure state the system was initially prepared in, then the expectation value can be calculated as a weighted sum over the ensemble of pure states $\{|\psi_n\rangle\}$

$$\langle A\rangle = \sum_n p_n\,\langle\psi_n|\,A\,|\psi_n\rangle = \sum_n p_n\,\mathrm{tr}\,(A\,|\psi_n\rangle\,\langle\psi_n|) = \mathrm{tr}\,(A\rho)\,, \tag{1.5}$$

where p_n is the classical probability to be in the pure state $|\psi_n\rangle$. Here, the density operator ρ has been identified as the classical mixture over the pure quantum states

$$\rho = \sum_n p_n\,|\psi_n\rangle\,\langle\psi_n|\,, \tag{1.6}$$

which represents a mixed state of a quantum system. Note that the mixed state ρ is still normalized such that $\mathrm{tr}\,(\rho) = 1$, obeys $\rho = \rho^\dagger$, and has real eigenvalues that are greater than or equal to zero.

The individual measurement results that comprise the expectation value $\langle A\rangle$ of the Hermitian observable A correspond to the real eigenvalues of A: $A\,|a\rangle = a\,|A\rangle$. A measurement which projects the quantum state into one of the eigenstates $|a\rangle$ via the projective operator $P_a = |a\rangle\,\langle a|$ is known as a *von-Neumann* measurement and is described by

$$\rho_a = \frac{P_a \rho P_a}{\mathcal{P}_a}, \tag{1.7}$$

where the probability for ρ to be in state $|a\rangle$ is $\mathcal{P}_a = \mathrm{tr}\left(\rho(P_a^2)\right) = \mathrm{tr}\,(\rho P_a) = \langle a|\,\rho\,|a\rangle$ and acts to normalize the state ρ_a after the measurement has taken place. This is the Born rule of quantum mechanics, which states that after a measurement the wavefunction collapses non-deterministically into one of the eigenstates $|a\rangle$ with probability $\mathcal{P}_a$.

Using Eqs (1.1) and (1.6), the deterministic coherent evolution of a mixed state in the Schrödinger picture is given by the von-Neumann equation

$$\dot{\rho}(t) \quad = \quad -\frac{\mathrm{i}}{\hbar}[H, \rho(t)]. \tag{1.8}$$

Moreover, in the Schrödinger picture, observables do not evolve in time and the density operator carries the time dependence of the quantum evolution. An equivalent formulation of quantum mechanics is given by the Heisenberg picture where the state vector does not evolve in time but observables evolve according to the Heisenberg equation of motion

$$\dot{A}(t) = \frac{\mathrm{i}}{\hbar}[H_{\mathrm{H}}, A(t)] + \left(\frac{\partial A}{\partial t}\right)(t), \tag{1.9}$$

where H_{H} is the Hamiltonian in the Heisenberg picture and the last term is typically zero unless A is explicitly time-dependent in the Schrödinger picture. Here, $\partial A/\partial t$ is the derivative of the initial Schrödinger operator A and not the Heisenberg operator $A(t)$. To connect the two pictures[2], the time-evolution unitary operator $U(t)$ may be used, which evolves states according to $\rho(t) = U(t)\rho U^{\dagger}(t)$ in the Schrödinger picture, and operators according to $A(t) = U^{\dagger}(t)AU(t)$ in the Heisenberg picture[3], and relates the Schrödinger Hamiltonian H to the Heisenberg Hamiltonian H_{H} via $H_{\mathrm{H}} = U^{\dagger}(t)HU(t)$.

[2] To show equivalence between the two pictures Eq. (1.2) is useful.

[3] Note this relation implies $\left(\frac{\partial A}{\partial t}\right)(t) = U^{\dagger}(t)\frac{\partial A}{\partial t}U(t)$ in Eq. (1.9).

Chapter 2

Useful quantum optics ideas

This chapter summarizes the core quantum optics concepts, which are most useful for this thesis. These concepts are explained in much greater detail in Refs [15, 16, 17, 18, 19] . A collection of useful formulae in quantum optics, used extensively throughout the work presented in this thesis, is given in Appendix A.

2.1 The quantum harmonic oscillator and number states

A quantum single-mode bosonic field—such as single mode of an electromagnetic field or a single vibrational mode of a mechanical oscillator—is described by a field operator a, whose expectation value is proportional to the field amplitude. The field operators obey the fundamental Bosonic commutation relation $[a, a^\dagger] = 1$, while the Hamiltonian of a single mode quantum harmonic oscillator of frequency ω is $H = \hbar\omega\left(a^\dagger a + \frac{1}{2}\right)$. The Hermitian number operator[1] is $\hat{n} = a^\dagger a$ with eigenvalue equation $\hat{n}\,|n\rangle = n\,|n\rangle$. The eigenvalue n is the number of particles, in this case bosons, associated with the number state (Fock state) $|n\rangle$. As $\hat{n}$ is Hermitian its eigenstates are chosen to form an orthonormal basis $\langle n|m\rangle = \delta_{n,m}$. The action of the field operator on the number states is deduced by

$$\begin{aligned} \hat{n}\,(a\,|n\rangle) &= a^\dagger a a\,|n\rangle = \left(aa^\dagger a - a\right)|n\rangle && (2.1)\\ &= (n-1)\,(a\,|n\rangle)\,, && (2.2) \end{aligned}$$

which implies that the state $a\,|n\rangle$ is a number state with $(n-1)$ bosons, i.e. $a\,|n\rangle \propto |n-1\rangle$. Normalizing gives

$$a\,|n\rangle = \sqrt{n}\,|n-1\rangle \tag{2.3}$$

[1] Throughout this thesis, hats will normally be missing from operators. However, in cases where confusion may arise, such as the eigenvalues sharing the same symbol as the operator, hats are used for clarity—as is the case here for the number operator.

and repeating the calculation for the state $a^\dagger |n\rangle$ gives

$$a^\dagger |n\rangle = \sqrt{n+1}\,|n+1\rangle\,. \tag{2.4}$$

This leads the field operator a being referred to as the annihilation operator and its Hermitian conjugate $a^\dagger$ as the creation operator, as the annihilation operators annihilate a boson from the state, while creation operators create a boson. Repeated application of the creation operator on the zero boson state $|0\rangle$ gives the useful property

$$|n\rangle = \frac{a^{\dagger n}}{\sqrt{n!}}\,|0\rangle\,. \tag{2.5}$$

The zero boson (ground or vacuum) state has the property $\hat{n}\,|0\rangle = a^\dagger a\,|0\rangle = 0$, which has two distinct solutions: (i) $a^\dagger a\,|0\rangle = 0$ *and* $a\,|0\rangle = 0$, (ii) $a^\dagger a\,|0\rangle = 0$ *but* $a\,|0\rangle \neq 0$. However, for the state to be normalizable, one must use solution (i) where $a\,|0\rangle = 0$ to define the zero boson state [18]. The energy eigenvalue of $|0\rangle$ is $\frac{1}{2}\hbar\omega$, which represents the zero point energy of a mode. Zero point fluctuations are important for understanding many fundamental phenomena in quantum physics such as the Casimir force, the Lamb shift, and the quantum mechanics of beamsplitters.

The number operator is the generator of rotations. Defining the rotation unitary to be $U(\theta) = \mathrm{e}^{-\mathrm{i}\theta\hat{n}}$, the Heisenberg transformation is $U^\dagger(\theta) a U(\theta) = a\mathrm{e}^{-\mathrm{i}\theta}$. Note that the free quantum harmonic oscillator Hamiltonian also generates rotations with $\theta = \omega t$.

2.2 Quadrature states of light and mechanics

The two dimensionless conjugate quadratures are defined as $X = \left(a + a^\dagger\right)/\sqrt{2}$ and $P = -\mathrm{i}\left(a - a^\dagger\right)/\sqrt{2}$, which obey the same canonical commutation $[X, P] = \mathrm{i}$ as the position and momentum operators, and therefore also have continuous eigenvalue spectra[2]. The conjugate quadratures allow the harmonic oscillator Hamiltonian to be written as $H = \frac{1}{2}\hbar\omega\left(X^2 + P^2\right)$. The eigenstates of X and P form orthogonal bases, $\langle X|X'\rangle = \delta(X - X')$ and $\langle P|P'\rangle = \delta(P - P')$, are related via Fourier transform, but are both non-normalizable. However, they are a useful mathematical tool for representing continuous variable quantum states. Furthermore, note that as X and P obey the same commutation relations of position and momentum, X is the generator of P translations and vice versa. Namely,

$$\mathrm{e}^{-\mathrm{i}X_\alpha P}\,|X\rangle = |X + X_\alpha\rangle\,, \tag{2.6}$$

$$\mathrm{e}^{\mathrm{i}P_\alpha X}\,|P\rangle = |P + P_\alpha\rangle\,, \tag{2.7}$$

[2]However, finite or periodic boundary conditions on X imply quantization of the eigenvalues of P, e.g. the pedagogic quantum particle in a box problem.

where X_α and P_α are real numbers. Eq. (2.6) follows from[3]

$$\hat{X}\mathrm{e}^{-\mathrm{i}X_\alpha\hat{P}}\left|X\right\rangle = \mathrm{e}^{-\mathrm{i}\hat{P}X_\alpha}\left(\hat{X}+\mathrm{i}X_\alpha[P,X]\right)\left|X\right\rangle \tag{2.8}$$

$$= \mathrm{e}^{-\mathrm{i}X_\alpha\hat{P}}\left(X+X_\alpha\right)\left|X\right\rangle, \tag{2.9}$$

where in the second line the Hadamard lemma from Appendix A was used, and Eq. (2.7) follows similarly.

I will now detail the convention used throughout this thesis, which discriminates between modes of the electromagnetic field, light, and vibrational harmonic modes in massive systems, mechanics. For light the amplitude quadrature is $X_{\mathrm{L}} = \left(a+a^\dagger\right)/\sqrt{2}$ and the phase quadrature is $P_{\mathrm{L}} = -\mathrm{i}\left(a-a^\dagger\right)/\sqrt{2}$, with field operator a. Thus, X_{L} and P_{L} are the real and imaginary parts of the field operator a. For mechanics the position quadrature is $X_{\mathrm{M}} = \left(b+b^\dagger\right)/\sqrt{2}$ and the momentum quadrature is $P_{\mathrm{M}} = -\mathrm{i}\left(b-b^\dagger\right)/\sqrt{2}$, with field operator b. Introducing the zero point fluctuations $x_0 = \sqrt{\hbar/m\omega_{\mathrm{M}}}$, $p_0 = \sqrt{\hbar m\omega_{\mathrm{M}}}$, allows one to write the mechanical quadratures in dimension-full units $x = x_0X_{\mathrm{M}}$ and $p = p_0P_{\mathrm{M}}$, for a mechanical oscillator of mass m and frequency ω_{M}. Thus, X_{M} and P_{M} are the dimensionless position and momentum quadratures. Note that some authors will define the dimensionless quadratures and the zero point fluctuations differently. Regardless of convention, the width of the quantum ground state should be $\Delta x = \sqrt{\hbar/2m\omega_{\mathrm{M}}}$ as this corresponds to a real physical distance all experiments must agree on for a given mass and frequency.

2.3 Coherent states and the displacement operator

A coherent state can be generated by displacing the zero boson state along the X and P axes $\left|\alpha\right\rangle = D(\alpha)\left|0\right\rangle$. Here and throughout $\left|0\right\rangle$ refers to the zero boson state and *not* the quadrature state at zero position or momentum. The displacement operator is given by

$$D(\alpha) = \mathrm{e}^{iP_\alpha X-\mathrm{i}X_\alpha P} \tag{2.10}$$

$$= \mathrm{e}^{\alpha a^\dagger-\alpha^* a}, \tag{2.11}$$

where $\alpha = (X_\alpha+\mathrm{i}P_\alpha)/\sqrt{2}$. Hence, the displacement operator acts to translate the zero boson state X_α along the X axis and P_α along the P axis.

The Zassenhaus formula from Appendix A can be used to rewrite the displacement operator as

$$D(\alpha) = \mathrm{e}^{-|\alpha|^2/2}\mathrm{e}^{\alpha a^\dagger}\mathrm{e}^{-\alpha^* a} \tag{2.12}$$

[3]To avoid confusion between the operator and its eigenvalue, hats have been temporarily used here: the position operator is represented by $\hat{X}$ and the eigenvalue is X, i.e. $\hat{X}\left|X\right\rangle = X\left|X\right\rangle$.

The exponentials can then be expanded and using $a|0\rangle = 0$ and Eq. (2.5) gives

$$|\alpha\rangle = \mathrm{e}^{-|\alpha|^2/2} \sum_{n=0}^{\infty} \frac{\alpha^n}{\sqrt{n!}} |n\rangle \tag{2.13}$$

From Eq. (2.13) it follows that the coherent state $|\alpha\rangle$ is an eigenstate of the annihilation operator $a|\alpha\rangle = \alpha|\alpha\rangle$. From Eq. (2.13), one can also show that

$$\langle\beta|\alpha\rangle = \mathrm{e}^{-\frac{1}{2}|\alpha|^2 - \frac{1}{2}|\beta|^2 + \beta^*\alpha}. \tag{2.14}$$

2.4 Other single mode states

Other typical single mode states include squeezed states and thermal states. The squeezed state is given by

$$|\zeta, \alpha\rangle = D(\alpha)S(\zeta)|0\rangle, \tag{2.15}$$

$$S(\zeta) = \mathrm{e}^{\frac{1}{2}(\zeta^* a^2 - \zeta a^{\dagger 2})}, \tag{2.16}$$

where $\zeta \in \mathbb{C}$. Meanwhile, thermal states may be written as

$$\rho_{\bar{n}} = \frac{1}{1+\bar{n}} \sum_{m=0}^{\infty} \left(\frac{\bar{n}}{1+\bar{n}}\right)^m |m\rangle\langle m|, \tag{2.17}$$

where the mean thermal occupation is $\bar{n} = \mathrm{tr}(\hat{n}\rho_{\bar{n}})$, which obeys Bose-Einstein statistics

$$\bar{n} = \frac{1}{\mathrm{e}^{\hbar\omega/k_{\mathrm{B}}T} - 1}. \tag{2.18}$$

Here, ω is the frequency of the single mode thermal state and T is the effective temperature.

2.5 Two mode states and entanglement

A system of two field modes is described by two field operators a_1 and a_2, which obey $[a_i, a_j^\dagger] = \delta_{i,j}$. The pure state of two independent field modes, in states $|\phi\rangle_1$ and $|\varphi\rangle_2$, respectively, is given by the tensor product between the two complex vector spaces $|\Phi\rangle_{12} = |\phi\rangle_1 \otimes |\varphi\rangle_2$—I will usually abbreviate $|\phi\rangle_1 \otimes |\varphi\rangle_2 = |\phi\rangle_1 |\varphi\rangle_2$. Here, $|\Phi\rangle_{12}$ is an example of a two-mode pure *separable* state. More generally, a two-mode pure state may be written as

$$|\Phi\rangle_{12} = \sum_{n,m} c_{nm} |n\rangle_1 |m\rangle_2, \tag{2.19}$$

where $\{|n\rangle_1\}$ and $\{|m\rangle_2\}$ are basis states of modes 1 and 2, and $c_{nm} \in \mathbb{C}$. If $|\Phi\rangle_{12}$ *cannot* be brought into the form of a separable state $|\Phi\rangle_{12} = |\phi\rangle_1 |\varphi\rangle_2$, then

$|\Phi\rangle_{12}$ is an *entangled state*. This definition can be extended to mixed states by considering a separable mixed state as a classical ensemble over pure separable states. A mixed separable state is then given by $\rho_{12} = \sum_i p_i \rho_i^1 \otimes \rho_i^2$, where the p_i are elements of a classical probability distribution, and states which cannot be written in this form are mixed entangled states. Importantly, entanglement allows for correlations between objects that can be much stronger than is allowed by classical physics [20, 21].

Expectation values of two mode operators A_{12} are calculated as $\langle A_{12}\rangle = \mathrm{tr}\left(\rho_{12} A_{12}\right)$. While single mode operators A_1 are calculated via

$$\begin{aligned} \langle A_1\rangle &= \mathrm{tr}\left(\rho_{12} A_1 \otimes \mathbb{1}\right) \\ &= \mathrm{tr}_1\left[\mathrm{tr}_2\left(\rho_{12} A_1 \otimes \mathbb{1}\right)\right] \\ &= \mathrm{tr}_1\left[\mathrm{tr}_2\left(\rho_{12}\right) A_1\right] \\ &= \mathrm{tr}_1\left(\rho_1 A_1\right), \end{aligned} \tag{2.20}$$

where $\mathrm{tr}(O_{12}) = \mathrm{tr}_1(\mathrm{tr}_2(O_{12})) = \mathrm{tr}_2(\mathrm{tr}_1(O_{12}))$ was used and the *reduced state* of mode 1 is defined via the *partial trace* over mode two $\rho_1 = \mathrm{tr}_2\left(\rho_{12}\right)$.

An example of a two mode state, commonly discussed in quantum optics, is the two-mode squeezed vacuum state $|\Psi\rangle$, which may be generated by applying the two-mode squeezing operator $S_{12}(\zeta) = \exp\left(\zeta a_1 a_2 - \zeta^* a_1^\dagger a_2^\dagger\right)$ on a product of zero boson states $|\Psi\rangle = S_{12}(\zeta)\,|0\rangle_1\,|0\rangle_2$, where $\zeta = r\mathrm{e}^{\mathrm{i}\phi}$. By writing $|\Psi\rangle$ in the number basis [16],

$$|\Psi\rangle = \frac{1}{\cosh r}\sum_{n=0}^{\infty}(-1)^n\left(\mathrm{e}^{\mathrm{i}\phi}\tanh r\right)^n |n\rangle_1\,|n\rangle_2 \tag{2.21}$$

one can see that the two-mode squeezed state is entangled in the number basis by inspection.

2.6 The beamsplitter

The most common two-mode operation utilized in this thesis will be the beamsplitter operation. In Part II and III beamsplitter operations between modes of light are implemented in almost every protocol discussed, while in Chapters 9 and 10 light-mechanics beamsplitter type interactions are discussed.

The transformation of a lossless beamsplitter is a linear transformation of the input field operators, a_1 and a_2, to the output field operators, a_1' and a_2':

$$\begin{pmatrix} a_1' \\ a_2' \end{pmatrix} = \underline{\underline{B}} \begin{pmatrix} a_1 \\ a_2 \end{pmatrix}, \tag{2.22}$$

$$\underline{\underline{B}} = \begin{pmatrix} B_{11} & B_{12} \\ B_{21} & B_{22} \end{pmatrix}, \tag{2.23}$$

where $\underline{\underline{B}}$ is a matrix. As a lossless beamsplitter conserves photon number and

preserves the canonical commutation relations, one has the relations

$$|B_{11}|^2 + |B_{12}|^2 = |B_{21}|^2 + |B_{22}|^2 = 1, \tag{2.24}$$

$$B_{11}B_{21}^* + B_{12}B_{22}^* = 0, \tag{2.25}$$

and it is seen that $\underline{\underline{B}}$ is, of course, a unitary matrix. The most general unitary $\underline{\underline{B}}$ is [18]

$$\underline{\underline{B}} = \mathrm{e}^{\mathrm{i}\Lambda/2} \begin{pmatrix} \cos(\Theta/2)\mathrm{e}^{\mathrm{i}(\Psi+\Phi)/2} & \sin(\Theta/2)\mathrm{e}^{\mathrm{i}(\Psi-\Phi)/2} \\ -\sin(\Theta/2)\mathrm{e}^{-\mathrm{i}(\Psi-\Phi)/2} & \cos(\Theta/2)\mathrm{e}^{-\mathrm{i}(\Psi+\Phi)/2} \end{pmatrix}. \tag{2.26}$$

Introducing

$$\varphi_T = (\Psi + \Phi)/2, \tag{2.27}$$

$$\varphi_R = (\Psi - \Phi)/2, \tag{2.28}$$

$$t = \mathrm{e}^{\mathrm{i}\varphi_T} \cos\Theta/2, \tag{2.29}$$

$$r = \mathrm{e}^{\mathrm{i}\varphi_R} \sin\Theta/2, \tag{2.30}$$

one can rewrite Eq. (2.26) as

$$\underline{\underline{B}} = \mathrm{e}^{\mathrm{i}\Lambda/2} \begin{pmatrix} t & r \\ -r^* & t^* \end{pmatrix}. \tag{2.31}$$

Here, t and r are the beamsplitter transmission and reflection coefficients, respectively, which satisfy $|t|^2+|r|^2 = 1$. Eq. (2.22) may be written as a Heisenberg transformation

$$\begin{pmatrix} a_1' \\ a_2' \end{pmatrix} = U^\dagger \begin{pmatrix} a_1 \\ a_2 \end{pmatrix} U, \tag{2.32}$$

where the unitary U, which corresponds to $\underline{\underline{B}}$, is [22]

$$U = \mathrm{e}^{\mathrm{i}\Lambda L_0}\mathrm{e}^{\mathrm{i}\Psi L_3}\mathrm{e}^{\mathrm{i}\Theta L_2}\mathrm{e}^{\mathrm{i}\Phi L_3}, \tag{2.33}$$

and the Jordan-Schwinger operators are

$$L_0 = \frac{1}{2}\left(a_1^\dagger a_1 + a_2^\dagger a_2\right), \tag{2.34}$$

$$L_1 = \frac{1}{2}\left(a_1^\dagger a_2 + a_2^\dagger a_1\right), \tag{2.35}$$

$$L_2 = \frac{\mathrm{i}}{2}\left(a_2^\dagger a_1 - a_1^\dagger a_2\right), \tag{2.36}$$

$$L_3 = \frac{1}{2}\left(a_1^\dagger a_1 - a_2^\dagger a_2\right), \tag{2.37}$$

which obey $[L_i, L_j] = \mathrm{i}\epsilon_{ijk}L_k$ and $L^2 = L_0(L_0+1) = L_1^2 + L_2^2 + L_3^2$. Using Ref. [23], the operator U can be recast into another convenient form

$$U = \mathrm{e}^{\mathrm{i}\Lambda L_0} t^{\hat{n}_1} \mathrm{e}^{-r^* a_2^\dagger a_1} \mathrm{e}^{r a_1^\dagger a_2} t^{-\hat{n}_2}. \tag{2.38}$$

2.7 Characteristic functions and operator ordering

The *characteristic function* χ provides an equivalent description of a quantum state as the density matrix ρ. This point will be discussed shortly, but first we need to define the most commonly used characteristic functions in quantum optics. For a single-mode quantum state, the normally-ordered, symmetrically-ordered, and anti-normally-ordered characteristic functions are defined by:

$$\text{Normal order:} \quad \chi(\lambda;+1) = \text{tr}\left(\rho e^{\lambda a^\dagger} e^{-\lambda^* a}\right), \tag{2.39}$$

$$\text{Symmetric order:} \quad \chi(\lambda;0) = \text{tr}\left(\rho e^{\lambda a^\dagger - \lambda^* a}\right), \tag{2.40}$$

$$\text{Anti-normal order:} \quad \chi(\lambda;-1) = \text{tr}\left(\rho e^{-\lambda^* a} e^{\lambda a^\dagger}\right), \tag{2.41}$$

with $\lambda \in \mathbb{C}$. Normal order[4] refers to any product of creation and annihilation operators where all creation operators are written on the left, $\{a^{\dagger m} a^n\}_1 = a^{\dagger m} a^n$. Anti-normal order is when the annihilation operators are written on the left, $\{a^{\dagger m} a^n\}_{-1} = a^m a^{\dagger n}$. Whereas, symmetric-ordering $\{a^{\dagger m} a^n\}_0$ refers to an average of all possible orderings of the field operators. For example, $\{a^{\dagger 2} a\}_0 = \frac{1}{3}(a^{\dagger 2} a + a a^{\dagger 2} + a^\dagger a a^\dagger)$. Interestingly, the symmetrically-ordered characteristic function is equal to the expectation value of the displacement operator $D(\lambda) = e^{\lambda a^\dagger - \lambda^* a}$. Using the Zassenhaus formula from Appendix A, one therefore has the relation $\chi(\lambda;+1) = e^{|\lambda|^2/2}\chi(\lambda;0) = e^{|\lambda|^2}\chi(\lambda;-1)$.

Why does a characteristic function provide a complete description of the quantum state ρ? It is because they can be used to calculate the expectation values of any system operator. For example, all normally-ordered expectation values of a single-mode state can be calculated via

$$\left\langle a^{\dagger m} a^n \right\rangle = \frac{\partial^{m+n}}{\partial(\lambda)^m \partial(-\lambda)^{*n}} \, \chi(\lambda;+1)|_{\lambda=0}, \tag{2.42}$$

and *any* system operator can be written as a combination of normally-ordered field operators [15]. Likewise, the characteristic functions $\chi(\lambda;0)$ and $\chi(\lambda;-1)$ can be used to compute symmetrically-ordered expectation values

$$\left\langle \{a^{\dagger m} a^n\}_0 \right\rangle = \frac{\partial^{m+n}}{\partial(\lambda)^m \partial(-\lambda)^{*n}} \, \chi(\lambda;0)|_{\lambda=0}, \tag{2.43}$$

and anti-normally-ordered expectation values

$$\left\langle a^m a^{\dagger n} \right\rangle = \frac{\partial^{m+n}}{\partial(-\lambda)^{*m} \partial\lambda^n} \, \chi(\lambda;-1)|_{\lambda=0}. \tag{2.44}$$

[4] The normal ordering of an operator A is written by $: A :$ and is computed by repeated application of the bosonic commutation relation $[a, a^\dagger] = 1$.

2.8 Quasiprobability distributions

The Fourier transforms of characteristic functions are called a *quasiprobability distributions*, which also provides a complete description of quantum states. Quasiprobability distributions are a commonly used to visualize quantum states.

2.8.1 Wigner distribution

The Wigner distribution may be defined via a 2D Fourier transform of the symmetrically-ordered characteristic function $\chi(\lambda;0)$

$$\begin{aligned} W(\alpha) &= \frac{1}{\pi^2}\int \mathrm{e}^{\alpha\lambda^*-\alpha^*\lambda}\chi(\lambda;0)\mathrm{d}^2\lambda \\ &= \frac{1}{\pi^2}\int \mathrm{e}^{\alpha\lambda^*-\alpha^*\lambda}\,\mathrm{tr}\left[\rho D(\lambda)\right]\mathrm{d}^2\lambda, \end{aligned} \tag{2.45}$$

where $\alpha\in\mathbb{C}$. Depending on the specific state ρ under consideration, there may be more convenient forms of the Wigner function compared to Eq. (2.45). For example, one may wish to write the Wigner function explicitly in terms of the X and P quadratures defined by $\alpha=(X+\mathrm{i}P)/\sqrt{2}$. In which case, if the trace in Eq.(2.45) is taken in the X-quadrature basis we arrive at

$$W(X,P) = \frac{1}{2\pi}\int \mathrm{e}^{\mathrm{i}Pu}\left\langle X-\frac{u}{2}\right|\rho\left|X+\frac{u}{2}\right\rangle \mathrm{d}u. \tag{2.46}$$

To derive Eq. (2.46)[5], Eq. (2.6) and the Fourier relation for the Dirac-delta function from Appendix B was used. Instead, if the trace in Eq. (2.45) is taken in the P-quadrature basis and Eq. (2.7) is used, we find that

$$W(X,P) = \frac{1}{2\pi}\int \mathrm{e}^{\mathrm{i}Xu}\left\langle P+\frac{u}{2}\right|\rho\left|P-\frac{u}{2}\right\rangle \mathrm{d}u. \tag{2.47}$$

The Wigner function has the unique property that integration along a quadrature axis yields a probability marginal. For example, the X and P probability marginals are

$$\mathrm{pr}(X) = \langle X|\,\rho\,|X\rangle = \int W(X,P)\mathrm{d}P, \tag{2.48}$$

$$\mathrm{pr}(P) = \langle P|\,\rho\,|P\rangle = \int W(X,P)\mathrm{d}X. \tag{2.49}$$

Here, the Fourier relation for the Dirac-delta function was once again used. This property of $W(X,P)$ is also true of a joint classical probability distribution that belongs to the phase space of X and P. However, to appreciate why $W(X,P)$ is referred to as a *quasi*-probability phase-space distribution, it is instructive to look at the Wigner function of a Schrödinger cat state.

[5] Eq. (2.46) was first derived by Eugene Wigner [24] in 1932.

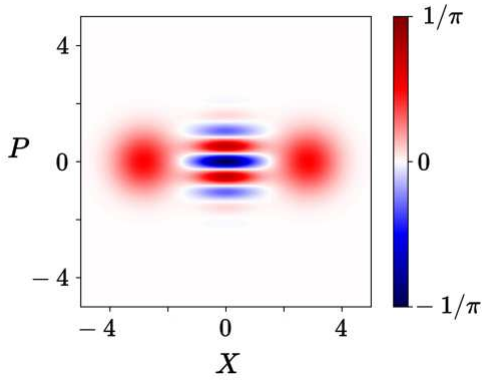


Figure 2.1: **Wigner function of a Schrödinger cat state.** The Wigner function $W(X,P)$ of the cat state $|\psi\rangle \propto |\beta\rangle - |-\beta\rangle$ is plotted with $\beta = 2$. The population components are centred at $X = \pm\sqrt{2}\beta$, with quantum interference between the population components around $X = 0$.

In quantum optics, a Schrödinger cat state is defined as a superposition of two coherent states. For concreteness, consider the specific case of the odd-Schrödinger cat state, defined about the origin of phase space

$$|\psi\rangle = \mathcal{N}\left(|\beta\rangle - |-\beta\rangle\right), \tag{2.50}$$

Here, $\mathcal{N}$ is the normalization and $\beta = X_\beta/\sqrt{2} \in \mathbb{R}$ for simplicity. Using Eq. (2.46) the Wigner function of the odd-cat state is given by

$$\begin{aligned} W(X,P) &= \frac{\mathcal{N}}{\pi}\Big[\mathrm{e}^{-(X-X_\beta)^2-P^2} + \mathrm{e}^{-(X+X_\beta)^2-P^2} \\ &\quad -2\cos(2X_\beta P)\mathrm{e}^{-X^2-P^2}\Big]. \end{aligned} \tag{2.51}$$

The first two Gaussian terms in the square brackets of Eq. (2.51) correspond to the population components: i.e. the contributions from $|\beta\rangle\langle\beta|$ and $|-\beta\rangle\langle-\beta|$ in the density matrix. While the last term corresponds to quantum interference between $|\beta\rangle$ and $|-\beta\rangle$, i.e. the terms $|\beta\rangle\langle-\beta|$ and $|-\beta\rangle\langle\beta|$ in the density matrix. Fig. 2.1 demonstrates the key differences between a classical- and a quantum quasi-probability distribution. Namely, the quasiprobability distribution (i) can be negative due to quantum interference between different superposition components, and (ii) the population terms have a finite width even for pure states; a consequence of the Heisenberg uncertainty relation between X and P. Furthermore, in general, the Wigner distribution is a bounded function: $-1/\pi \leq W(X,P) \leq 1/\pi$ [18].

2.8.2 Husimi Q function

Similar to the definition of the Wigner distribution, the Husimi Q function[6] is defined via a 2D Fourier transform of the anti-normally-ordered characteristic function $\chi(\lambda;-1)$

$$Q(\alpha) = \frac{1}{\pi^2}\int \mathrm{e}^{\alpha\lambda^*-\alpha^*\lambda}\chi(\lambda;-1)\mathrm{d}^2\lambda. \tag{2.52}$$

Taking the trace in Eq. (2.41) in the coherent basis we have

$$\begin{aligned}\chi(\lambda;-1) &= \frac{1}{\pi}\int \langle\alpha|\,\mathrm{e}^{\lambda a^\dagger}\rho\mathrm{e}^{-\lambda^* a}\,|\alpha\rangle\,\mathrm{d}^2\alpha \\ &= \frac{1}{\pi}\int \mathrm{e}^{-\alpha\lambda^*+\alpha^*\lambda}\,\langle\alpha|\,\rho\,|\alpha\rangle\,\mathrm{d}^2\alpha,\end{aligned} \tag{2.53}$$

Alternatively, the inverse Fourier transform of Eq. (2.52) may be used to write $\chi(\lambda;-1)$ as

$$\chi(\lambda;-1) = \int \mathrm{e}^{-\alpha\lambda^*+\alpha^*\lambda}Q(\alpha)\mathrm{d}^2\alpha. \tag{2.54}$$

The two forms of $\chi(\lambda;-1)$ in Eqs (2.53) and (2.54) are only equal if

$$Q(\alpha) = \frac{1}{\pi}\,\langle\alpha|\,\rho\,|\alpha\rangle\,. \tag{2.55}$$

Hence, it may be seen that the Q function is always positive $Q(\alpha)\geq 0$.

In Section 2.7, we saw how $\chi(\lambda;-1)$ was useful in calculating anti-normally-ordered expectation values via Eq. (2.44). Likewise, the Q function can also be used to calculate such expectation values. Combining Eqs (2.44) and(2.54) gives

$$\left\langle a^m a^{\dagger n}\right\rangle = \int Q(\alpha)\alpha^m\alpha^{*n}\mathrm{d}^2\alpha. \tag{2.56}$$

2.8.3 Sudarshan-Glauber P function

The Sudarshan-Glauber P function may be defined via the 2D Fourier transform of the normally-ordered characteristic function

$$P(\alpha) = \frac{1}{\pi^2}\int \mathrm{e}^{\alpha\lambda^*-\alpha^*\lambda}\chi(\lambda;+1)\mathrm{d}^2\lambda, \tag{2.57}$$

with the inverse transformation being

$$\chi(\lambda;+1) = \int \mathrm{e}^{-\alpha\lambda^*+\alpha^*\lambda}P(\alpha)\mathrm{d}^2\alpha. \tag{2.58}$$

[6] Named after Kôdi Husimi who introduced the function in 1940 [25].

However, the P function was originally introduced, by George Sudarshan [26] and Roy Glauber [27] in 1963, by expanding the density matrix ρ in the over-complete coherent-state basis

$$\rho = \int P(\alpha) \left|\alpha\right\rangle \left\langle\alpha\right| \mathrm{d}^2\alpha. \tag{2.59}$$

By inserting this form of the P function into the definition of $\chi(\lambda;+1)$ in Eq. (2.41), it may be seen that the form introduced by Sudarshan and Glauber recovers the inverse Fourier transform in Eq. (2.58). Like the Wigner distribution, the P function is not guaranteed to be positive and can even by be singular, involving the Dirac-delta function, or highly singular, involving derivatives of the Dirac-delta function. For example, Eq. (2.59) implies that the P function of a coherent state $|\beta\rangle$ is $P(\alpha) = \delta^2(\alpha - \beta)$.

In Section 2.7, it was shown that $\chi(\lambda;+1)$ is useful in calculating normally-ordered expectation values. Further, the P function can also be used to calculate such expectation values. Combining Eqs (2.42) and(2.58) gives

$$\left\langle a^{\dagger m} a^n \right\rangle \quad = \quad \int P(\alpha) \alpha^{*m} \alpha^n \mathrm{d}^2\alpha. \tag{2.60}$$

2.8.4 s-parametrized Wigner function

The relation between the characteristic functions from Section 2.7 $\chi(\lambda;+1) = \mathrm{e}^{|\lambda|^2/2}\chi(\lambda;0)$ and $\chi(\lambda;-1) = \mathrm{e}^{-|\lambda|^2/2}\chi(\lambda;0)$, suggest that a continuous family of *s-parametrized characteristic functions* can be defined via

$$\chi(\lambda;s) = \chi(\lambda;0)\mathrm{e}^{s|\lambda|^2/2}. \tag{2.61}$$

Every $\chi(\lambda;s)$ therefore defines an *s-parametrized Wigner function* [28]

$$W(\alpha;s) \quad = \quad \frac{1}{\pi^2} \int \mathrm{e}^{\alpha\lambda^* - \alpha^*\lambda} \chi(\lambda;s) \mathrm{d}^2\lambda. \tag{2.62}$$

Eq. (2.61) implies $\chi(\lambda;s) = \chi(\lambda;+1)\mathrm{e}^{-(1-s)|\lambda|^2/2}$. Then taking the inverse Fourier transform of this relation, using the convolution theorem from Appendix B, and taking $\alpha = (X + \mathrm{i}P)/\sqrt{2}$, one has

$$W(X,P;s) = \frac{1}{\pi(1-s)} \int\int P(X',P') \mathrm{e}^{-\frac{(X-X')^2+(P-P')^2}{1-s}} \mathrm{d}X' \mathrm{d}P'. \tag{2.63}$$

Hence, we see that the Wigner and the Husimi-Q function are related to the P-function via a 2D convolution with a Gaussian. For example, the P, W, and Q functions of the same thermal state $\rho_{\bar{n}}$ are given by

$$P(X,P) \quad = \quad \frac{1}{2\pi\bar{n}} \exp\left(-\frac{X^2+P^2}{2\bar{n}}\right), \tag{2.64}$$

$$W(X,P) \quad = \quad \frac{1}{2\pi(\bar{n}+\frac{1}{2})} \exp\left(-\frac{X^2+P^2}{2(\bar{n}+\frac{1}{2})}\right), \tag{2.65}$$

$$Q(X,P) \quad = \quad \frac{1}{2\pi(\bar{n}+1)} \exp\left(-\frac{X^2+P^2}{2(\bar{n}+1)}\right), \tag{2.66}$$

which demonstrates the progressive Gaussian smoothing from P to W to Q.

Chapter 3

Open quantum systems

In quantum mechanics, the coherent evolution of a closed system is given by the von-Neumann in Eq. (1.8). Open system dynamics describe the effective evolution of one part of interest of a total quantum system. All other parts of the system are usually referred to as the *environment*. Mathematically, open system dynamics are derived by tracing out the environmental modes of the total quantum system. From an operational point of view, open system dynamics describe some modification to the von-Neumann evolution due to the environment in a way that accurately models the physics, but ideally does not vastly increase the complexity of the problem at hand.

3.1 Markovianity

In general the evolution of a quantum state ρ is given by some causal completely-positive-trace-preserving (CPTP) map $\rho(t) = \mathcal{M}\left[\rho(t'), t' < t\right]$, where the state of the system at the next time step in the evolution $t \to t + \mathrm{d}t$ depends on the entire state up until time t. Hence, to evolve the state, one must store not only the initial conditions but the entire history of the state as well.

One simplification is to restrict the map $\mathcal{M}$ to a time-local mapping $\dot{\rho}(t) = \mathcal{L}\rho(t)$ described by a time-local superoperator $\mathcal{L}(t)$ [29]. In this case, the state of the system at time $t + \mathrm{d}t$ does not depend on the entire history of the state but only on the state of the system $\rho(t)$ and the specific form of the time-dependent superoperator $\mathcal{L}(t)$ at time t.

More commonly in quantum optics, and open-system dynamics more generally, a further assumption is made that the operator $\mathcal{L}(t)$ is time-independent, which leads to Markovian evolution. Markovianity is a property of a system's evolution, whereby the state of the system at time $t + \mathrm{d}t$ only depends on the state at time t and not it's entire history. This property significantly reduces the complexity and memory requirements of numerical simulations of open system dynamics.

3.2 Quantum Lindblad master equations

The most general deterministic Markovian evolution of the quantum state ρ is given by the Lindblad master equation [30]

$$\dot{\rho}(t) = -\frac{\mathrm{i}}{\hbar}[H, \rho(t)] + \sum_n \mathcal{D}[c_n]\rho(t), \tag{3.1}$$

where the dissipation superoperator is defined by $\mathcal{D}[O]\rho = O\rho O^\dagger - \frac{1}{2}\{O^\dagger O, \rho\}$ and $\{c_n\}$ are the Lindblad or *jump* operators of the system. Note that H may not only represent the bare Hamiltonian the system of interest but also include terms that describe a shift in energy levels due to interactions with the environment. Such terms are typically dubbed *Lamb shift* terms, owing to the famous shift in the energy levels of Hydrogen due to interactions with the vacuum environment, first measured by Willis Lamb and Robert Retherford in 1947 [31]. Furthermore, the Lindblad master equation implies that the expectation value of an arbitrary operator $A(t)$ evolves according to

$$\left\langle \dot{A}(t) \right\rangle = \frac{\mathrm{i}}{\hbar}\left\langle [H, A(t)] \right\rangle + \sum_n \left\langle c_n^\dagger A(t) c_n \right\rangle - \frac{1}{2}\left\langle \{c_n^\dagger c_n, A(t)\} \right\rangle. \tag{3.2}$$

The key assumptions that go into a microscopic derivation of the Lindblad master equation are (i) the Born approximation and (ii) the Markov approximation [32]. The Born approximation assumes a weak coupling between the system and the environment. Namely, if the total Hamiltonian of the system and environment is $H_{\mathrm{TOT}} = H_{\mathrm{S}} + H_{\mathrm{E}} + \beta H_{\mathrm{INT}}$, where β is some small coupling term, then a microscopic derivation of the Lindblad master equation proceeds by performing a perturbative expansion in β. Furthermore, the Markov approximation assumes that the state of the environment and the system of interest remains approximately separable for all time: $\rho_{\mathrm{TOT}}(t) \simeq \rho_{\mathrm{S}}(t) \otimes \rho_{\mathrm{E}}(t)$. For this to be true the timescale of the system-environment correlations τ_{INT} must be much less than the characteristic timescale of the system's evolution τ_{S}. Note the assumption $\tau_{\mathrm{INT}} \ll \tau_{\mathrm{S}}$ is consistent with the assumption of a weak system-environment coupling $\beta \ll 1$. Hence, the Born and Markov approximations are sometimes referred to collectively as the Born-Markov approximation.

3.2.1 Quantum optics master equation

The most commonly used master equation in quantum optics, and indeed this thesis, is the quantum optics master equation:

$$\dot{\rho}(t) = -\frac{\mathrm{i}}{\hbar}[H, \rho(t)] + 2\kappa(\bar{N}+1)\mathcal{D}[a]\rho(t) + 2\kappa\bar{N}\mathcal{D}[a^\dagger]\rho(t), \tag{3.3}$$

where κ is the amplitude decay rate and $\bar{N}$ is the Bose-Einstein occupation number of the environment. The $\mathcal{D}[a]$ Lindblad superoperator represents emission of bosons into the environment, which leads to damping, while $\mathcal{D}[a^\dagger]$ describes

absorption of bosons from the environment, which leads to heating. The asymmetry between these two processes is due to spontaneous emission of bosons into the environment, which is present even at $\bar{N} = 0$ and cannot be explained with only classical electromagnetism [1]. Using Eq. (3.2), one may show that if the Hamiltonian is a function of the number operator $H = f(a^\dagger a)$, Eq. (3.3) has a steady state $\langle a^\dagger a \rangle = \bar{N}$. Hence, the quantum optics master equation predicts that a quantum harmonic oscillator reaches thermal equilibrium with its thermal environment.

When a represents the field mode of an optical cavity, one may set $\bar{N} = 0$ as optical frequencies $\sim 10^{14} - 10^{16}$ Hz imply $\hbar\omega \gg k_{\mathrm{B}}T$, even at temperatures well above room temperature. If a represents a microwave field mode, at frequencies $\sim 10^8 - 10^{12}$ Hz, or an optomechanical oscillator $\sim 1 - 10^{10}$ Hz then taking $\bar{N} = 0$ is generally not valid.

3.2.2 Quantum Brownian motion and decoherence

Mechanical interactions with the environment may be accounted for with a Lindblad dissipator of the form $L = \sqrt{\lambda} X_{\mathrm{M}} + \mathrm{i}\sqrt{\nu} P_{\mathrm{M}}$, where λ and ν are positive real constants. The constants are typically chosen so that in the limit of a high temperature environment $T \to \infty$ the resulting master equation matches the Caldeira–Leggett model of quantum Brownian motion [36]. In this case, a possible choice of λ and ν is $\lambda = 4\gamma k_{\mathrm{B}}T/\hbar\omega_{\mathrm{M}}$ and $\nu = \hbar\omega_{\mathrm{M}}\gamma/4k_{\mathrm{B}}T$ [37, 38], where γ is the mechanical decay rate. Importantly, the Caldeira–Leggett model is a widely-used and very successful model of Brownian motion as it accurately reproduces the classical Fokker-Planck equation in the limit $\hbar \to 0$ and $T \to \infty$ [39].

However, one can make a slightly different choice of λ and ν as in Ref. [40]. This choice also agrees with classical Brownian motion in the limit $\hbar \to 0$ and $T \to \infty$, is applicable in the low-temperature limit, and, as we will show below, agrees with the quantum optics master equation in a rotating wave approximation. This choice is motivated by the fact that the quantum optics master equation and quantum motion Brownian are often used interchangeably in modelling a range of mechanical-oscillator experiments—see Section 3.2.3 for more discussion and to see the mathematical connection between these two models. Hence, in this thesis the choice of λ and ν is $\lambda = 4\gamma\left(\bar{N} + 1/2\right)$ and $\nu = \gamma/4\left(\bar{N} + 1/2\right)$, where $\bar{N}$ is again the Bose-Einstein occupation number of the environment. Explicitly, the free Hamiltonian H and the Lindblad dissipator

[1] Stochastic electrodyanmics is a classical theory, which accounts for vacuum fluctuations by letting the classical electromagnetic field also contain a stochastic part [33, 34]. Such a theory may be able to describe the asymmetry in absorption and emission and has been used to explain other phenomena, such as optomechanical sideband asymmetry, without relying on quantum theory [35]

$L = \sqrt{4\gamma\left(\bar{N}+1/2\right)}X_{\rm M} + {\rm i}\sqrt{\gamma/4\left(\bar{N}+1/2\right)}P_{\rm M}$ generate the master equation

$$\begin{aligned}\dot{\rho}(t) &= -\frac{\rm i}{\hbar}[H - \hbar\gamma X_{\rm M}P_{\rm M}, \rho(t)] - {\rm i}\gamma[X_{\rm M}, \{P_{\rm M}, \rho(t)\}] \\ &\quad -D_X[X_{\rm M}, [X_{\rm M}, \rho(t)]] - D_P[P_{\rm M}, [P_{\rm M}, \rho(t)]],\end{aligned} \tag{3.4}$$

where $D_X = \lambda^2/2 = 2\gamma\left(\bar{N}+1/2\right)$, $D_P = \nu^2/2 = \gamma/8\left(\bar{N}+1/2\right)$, and note $\lambda\nu = \gamma$. The Hamiltonian is renormalized by the frictional force of Brownian motion, the first non-unitary term describes momentum damping, the double commutator in $X_{\rm M}$ leads to momentum diffusion, while the double commutator in $P_{\rm M}$ predicts spatial diffusion [41]. Spatial diffusion is not predicted by classical quantum Brownian motion as, in a classical model, Brownian motion is due to random stochastic momentum kicks on the mechanical mode from particles in the environment. However, Markovian models of quantum Brownian motion which do not predict spatial diffusion, such as the Caldeira–Leggett model [42], *cannot* be brought into Lindblad form and hence may violate positivity of the density matrix.

In the high temperature limit $k_{\rm B}T \gg \hbar\omega_{\rm M}$, as $\bar{N} \to k_{\rm B}T/\hbar\omega_{\rm M}$ one recovers $D_X \to 2\gamma k_{\rm B}T/\hbar\omega_{\rm M}$, $D_P \to \hbar\gamma\omega_{\rm M}/8k_{\rm B}T$, which agrees with previous models of quantum Brownian motion described by the choice $\lambda = 4\gamma k_{\rm B}T/\hbar\omega_{\rm M}$ and $\nu = \hbar\omega_{\rm M}\gamma/4k_{\rm B}T$ [37]. Also, in this high temperature limit $\bar{N} \gg 1$, the spatial diffusion term is negligible, which agrees with the Caldeira–Leggett model. Moreover, as $D_P \propto \hbar$ in the high temperature limit, as $\hbar \to 0$ this term vanishes and classical Brownian motion is recovered.

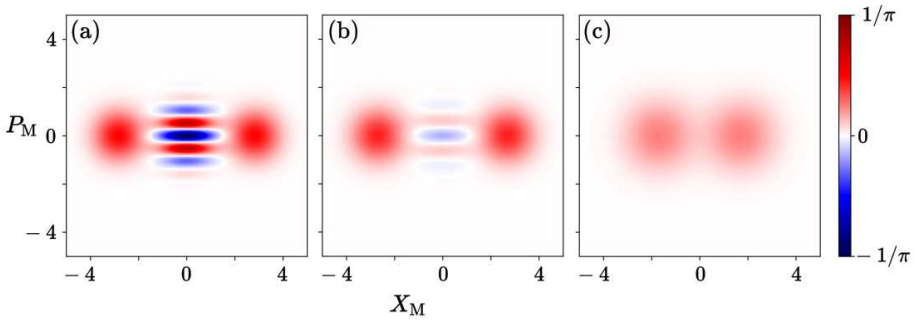


Figure 3.1: **Initial Schrödinger cat state undergoing quantum Brownian motion.** (a) An initial mechanical cat state $|\psi\rangle \propto |\beta\rangle - |-\beta\rangle$, which then undergoes harmonic evolution and quantum Brownian motion with $\beta = 2$, $\omega_{\rm M} = 100\,{\rm Hz}$, $\gamma = 0.1\,{\rm Hz}$, and $\bar{N} = 5$. (b) State after 2 periods shows significant loss of quantum coherence. (c) State after 20 periods shows amplitude damping. This demonstrates that the timescale of decoherence is much less than that of classical damping.

Decoherence is the progressive loss of quantum coherence that occurs due

to interactions with the environment. For a spatial superposition of size ΔX, the rate associated with decoherence in the quadrature bases is given by $D_{\text{TH}} = D_X \Delta X^2$, whereas the rate associated with the damping of the superposition components is γ [41]. Fig. 3.1 demonstrates the difference between the timescales of decoherence and damping. Namely, that $D_{\text{TH}} \gg \gamma$ even at relatively small thermal occupations.

3.2.3 Connection between the quantum optics master equation and quantum Brownian motion

The quantum optics master equation and quantum Brownian motion are often used interchangeably when the decoherence of a mechanical oscillator is being modelled. To see this connection between the quantum optics master equation and quantum Brownian motion, the rotating wave approximation (RWA) can be used on Eq. (3.4). Supposing a free Hamiltonian of a quantum harmonic oscillator $H = \hbar\omega_{\text{M}} b^\dagger b$, moving to a rotating frame via the unitary $U_{\text{F}} = \mathrm{e}^{-\mathrm{i}\omega_{\text{M}} b^\dagger b t}$ transforms the Hamiltonian according to

$$H \to U_{\text{F}}^\dagger H U_{\text{F}} + \mathrm{i}\hbar \dot{U}_{\text{F}} U_{\text{F}} = 0$$

and the mechanical field operators according to $b \to U_{\text{F}}^\dagger b U_{\text{F}} = b\mathrm{e}^{-\mathrm{i}\omega_{\text{M}} t}$, which is most easily proved using the Hadamard lemma in Appendix A. Moving to the rotating frame and using the RWA, the friction and damping terms from Eq. (3.4) transform according to

$$\begin{aligned} -\mathrm{i}\gamma[X_{\text{M}} P_{\text{M}}, \rho] \quad - \quad & \mathrm{i}\gamma[X_{\text{M}}, \{P_{\text{M}}, \rho\}] = \gamma\left(\mathrm{i}P_{\text{M}}\rho X_{\text{M}} - \mathrm{i}X_{\text{M}}\rho P_{\text{M}} + \rho\right) \\ & \to \gamma\left[\frac{1}{2}(b\mathrm{e}^{-\mathrm{i}\omega_{\text{M}} t} - b^\dagger \mathrm{e}^{\mathrm{i}\omega_{\text{M}} t}\rho(b\mathrm{e}^{-\mathrm{i}\omega_{\text{M}} t} + b^\dagger \mathrm{e}^{\mathrm{i}\omega_{\text{M}} t})\right. \\ & \left. -\frac{1}{2}(b\mathrm{e}^{-\mathrm{i}\omega_{\text{M}} t} + b^\dagger \mathrm{e}^{\mathrm{i}\omega_{\text{M}} t}\rho(b\mathrm{e}^{-\mathrm{i}\omega_{\text{M}} t} - b^\dagger \mathrm{e}^{\mathrm{i}\omega_{\text{M}} t}) + \rho\right] \\ & \approx \gamma\mathcal{D}[b]\rho - \gamma\mathcal{D}[b^\dagger]\rho, \end{aligned} \tag{3.5}$$

the double commutator in X_{M} transforms as

$$\begin{aligned} -D_X[X_{\text{M}}, [X_{\text{M}}, \rho]] \quad & \to -D_X \frac{1}{2}\left[(b\mathrm{e}^{-\mathrm{i}\omega_{\text{M}} t} + b^\dagger \mathrm{e}^{\mathrm{i}\omega_{\text{M}} t})^2\rho + \rho(b\mathrm{e}^{-\mathrm{i}\omega_{\text{M}} t} + b^\dagger \mathrm{e}^{\mathrm{i}\omega_{\text{M}} t})^2\right. \\ & \left. -2(b\mathrm{e}^{-\mathrm{i}\omega_{\text{M}} t} + b^\dagger \mathrm{e}^{\mathrm{i}\omega_{\text{M}} t})\rho(b\mathrm{e}^{-\mathrm{i}\omega_{\text{M}} t} + b^\dagger \mathrm{e}^{\mathrm{i}\omega_{\text{M}} t})\right] \\ & \approx D_X\mathcal{D}[b]\rho + D_X\mathcal{D}[b^\dagger]\rho, \end{aligned} \tag{3.6}$$

and the double commutator in $P_{\rm M}$ transforms as

$$\begin{aligned} -D_P[P_{\rm M},[P_{\rm M},\rho]] \quad &\to D_P\frac{1}{2}\Big[(b\mathrm{e}^{-\mathrm{i}\omega_{\rm M}t}-b^\dagger\mathrm{e}^{\mathrm{i}\omega_{\rm M}t})^2\rho+\rho(b\mathrm{e}^{-\mathrm{i}\omega_{\rm M}t}-b^\dagger\mathrm{e}^{\mathrm{i}\omega_{\rm M}t})^2 \\ &\quad -2(b\mathrm{e}^{-\mathrm{i}\omega_{\rm M}t}-b^\dagger\mathrm{e}^{\mathrm{i}\omega_{\rm M}t})\rho(b\mathrm{e}^{-\mathrm{i}\omega_{\rm M}t}-b^\dagger\mathrm{e}^{\mathrm{i}\omega_{\rm M}t})\Big] \\ &\approx D_P\mathcal{D}[b]\rho+D_P\mathcal{D}[b^\dagger]\rho, \end{aligned} \tag{3.7}$$

Here, the RWA and the phase invariance of the dissipation superoperator was used in the last line. More precisely, the RWA involves neglecting the fast rotating components in Eqs (3.5), (3.6), and (3.7) at $\pm 2\omega_{\rm M}$. This is valid for mechanical oscillators with quality factors $Q = \omega_{\rm M}/\gamma \gg 1$ as illustrated in Fig. 3.2. Terms which oscillate at large frequencies may be neglected if the characteristic decay time γ is comparatively small, i.e. $Q = \omega_{\rm M}/\gamma \gg 1$. This is because, when the equation of motion is integrated, envelope functions will multiply these quickly oscillating terms with a characteristic timescale of $1/\gamma$. When the quantum Brownian motion is solved to obtained $\rho(t)$, these quickly oscillating terms will integrate to zero within this slowly varying envelope.

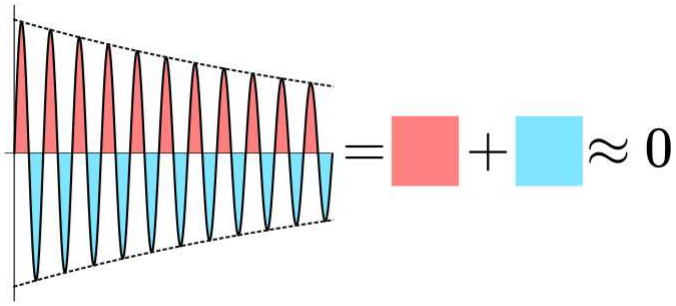


Figure 3.2: **Visualizing the rotating wave approximation in the time domain.** An envelope decays slowly over a timescale $1/\gamma$. Within the envelope, the function oscillates rapidly at frequency $\omega_{\rm M} \gg \gamma$. The integral over the entire function may be subdivided into a positive area (red) and a negative area (blue). Providing $\omega_{\rm M} \gg \gamma$ these two contributions approximately cancel.

Transforming back to the lab frame, the quantum Brownian motion master equation in the rotating wave approximation is

$$\dot{\rho}(t) \quad = \quad -\frac{\mathrm{i}}{\hbar}[H,\rho(t)]+2\gamma(\bar{N}_Q+1)\mathcal{D}[b]\rho(t)+2\gamma\bar{N}_Q\mathcal{D}[b^\dagger]\rho(t), \tag{3.8}$$

where

$$\bar{N}_Q = \bar{N}+\frac{1}{16(\bar{N}+1/2)}. \tag{3.9}$$

In the high temperature limit, $\bar{N}_Q \approx \bar{N}$, relabelling $b \to a$ and $\gamma \to \kappa$, Eq. (3.8) is exactly equal to the quantum optics master equation of Eq. (3.3), including the $+1$ from spontaneous emission. To summarize, at $Q \gg 1$ and $\bar{N} \gg 1$, the quantum optics master equation and quantum Brownian motion predict very similar descriptions of open-system dynamics.

Interestingly, at $\bar{N} = 0$, $\bar{N}_Q = 1/8 \neq 0$, which originates from the definition of the momentum diffusion term chosen above. However, the quantum Brownian models used more widely in the literature [37, 39] are not well defined at $\bar{N} = 0$. Namely, choosing $\lambda = 4\gamma k_{\mathrm{B}} T/\hbar\omega_{\mathrm{M}}$ and $\nu = \hbar\omega_{\mathrm{M}}\gamma/4k_{\mathrm{B}}T$ gives

$$\begin{aligned} \dot{\rho} &= -\frac{\mathrm{i}}{\hbar}[H,\rho] + 2\gamma(\bar{N} + 1/2 - 1/16\bar{N})\mathcal{D}[b]\rho \\ &+ 2\gamma(\bar{N} - 1/2 + 1/16\bar{N})\mathcal{D}[b^\dagger]\rho, \end{aligned} \tag{3.10}$$

where now $\bar{N}$ is given by $k_{\mathrm{B}}T/\hbar\omega_{\mathrm{M}}$. Compared to Eq. (3.8), Eq. (3.10) does not agree as well with the quantum optics master equation. This is because defining an effective thermal occupation for Eq. (3.10), as in Eq. (3.8), gives $\bar{N}'_Q = \bar{N} + 1/16\bar{N} - 1/2$, which is not well defined at $\bar{N} = 0$. Therefore, the choice of λ and ν used in this thesis, which gives agreement with classical Brownian motion *and* the quantum optics master equation for high temperatures, allows a quantum Brownian motion model to be used in the limit $\bar{N} \to 0$.

A caveat

Implicit in the application of the RWA is the assumption that the master equation is being solved over more than one mechanical period. From Fig. 3.2, it is seen that the RWA requires that $\rho(t)$ is solved over multiple mechanical periods such that the positive and negative contributions from the integral approximately cancel. Clearly, the RWA is not applicable if one is interested in open system dynamics that occur on a timescale that is shorter than a mechanical period $\lesssim 1/\omega_{\mathrm{M}}$. When studying open system dynamics over such short timescales, it is not appropriate to use the quantum optics master equation and quantum Brownian motion interchangeably.

However, despite how the information is presented in this thesis—quantum optics master equation for light and quantum Brownian motion for mechanical systems—there is a lack of experimental evidence[2] to suggest which master equation more accurately models a given quantum experiment's open system dynamics for high-frequency mechanical oscillators. Therefore, it is often the case that the quantum optics master equation is employed to study open system dynamics in mechanical systems[3]. Importantly, both master equations are first order in field operators and so respect the spirit of open system dynamics, as laid out at the start of this chapter: they describe some modification that accurately models the physics, but ideally does not vastly increase the complexity of the problem at hand.

[2] To the best of the author's knowledge.
[3] Indeed, this is done in Refs [2] and [3].

3.3 Heisenberg-Langevin equations and input-output theory

In Ref. [43], Collett and Gardiner derived the *input-output* formalism for damped quantum systems. This formalism is complementary to the Lindblad equation approach to open quantum systems, but works in the Heisenberg picture instead of the Schrödinger picture. The modified Heisenberg equations that input-output theory produces are known as *Heisenberg-Langevin* equations, which take into account environmental interactions through non-unitary terms in the equations of motion. First, I will review input-output theory for a general quantum system, before specializing to an optical cavity and a mechanical oscillator, which realize complementary descriptions of the quantum optics master equation and quantum Brownian motion, respectively.

Let the total Hamiltonian of the system of interest and its environment be

$$H_{\mathrm{TOT}} = H + H_{\mathrm{E}} + H_{\mathrm{INT}}, \tag{3.11}$$

$$H_{\mathrm{E}} = \int \hbar\omega b^{\dagger}(\omega)b(\omega)\mathrm{d}\omega, \tag{3.12}$$

$$H_{\mathrm{INT}} = \int \hbar g(\omega)\left[b^{\dagger}(\omega)a + a^{\dagger}b(\omega)\right]\mathrm{d}\omega. \tag{3.13}$$

Here, H is the Hamiltonian describing the system of interest and a is the field operator of this system. The environment is modelled as a bath of quantum harmonic oscillators with a continuous frequency spectrum. Here, the bath bosonic commutation relations are $[b(\omega), b^{\dagger}(\omega')] = \delta(\omega - \omega')$. To avoid an overly complicated description, the interaction term H_{INT} is taken to be as simple as possible. Therefore, H_{INT} describes linear couplings between the field mode a and each bath mode $b(\omega)$ with a real coupling rate $g(\omega)$ for each frequency[4]. Inserting, $b(\omega)$ and H_{TOT} into the Heisenberg equation of motion, the forward and backward time solutions may be derived:

$$b(\omega,t) = \mathrm{e}^{-\mathrm{i}\omega(t-t_0)}b(\omega,t_0) - \mathrm{i}g(\omega)\int_{t_0}^{t}\mathrm{e}^{-\mathrm{i}\omega(t-t')}a(t')\mathrm{d}t', \tag{3.14}$$

$$= \mathrm{e}^{-\mathrm{i}\omega(t-t_1)}b(\omega,t_1) + \mathrm{i}g(\omega)\int_{t}^{t_1}\mathrm{e}^{-\mathrm{i}\omega(t-t')}a(t')\mathrm{d}t', \tag{3.15}$$

valid for $t > t_0$ and $t < t_1$, respectively. While the Heisenberg equation of motion for an arbitrary operator O of the system of interest is

$$\dot{O} = \frac{\mathrm{i}}{\hbar}[H, O(t)] + \mathrm{i}\int \mathrm{d}\omega g(\omega)\left\{b^{\dagger}(\omega,t)[a,O] + [a^{\dagger},O]b(\omega,t)\right\}. \tag{3.16}$$

[4]This type of beamsplitter coupling $b^{\dagger}a + b^{\dagger}$ is typically assumed for optical systems and is equivalent to $(a + a^{\dagger})(b + b^{\dagger})$ after a rotating wave approximation has been made.

The input $a_{\rm in}$ and $a_{\rm out}$ output modes are defined as

$$a_{\rm in}(t) = -\frac{\mathrm{i}}{\sqrt{2\pi}}\int \mathrm{e}^{-\mathrm{i}\omega(t-t_0)}b(\omega,t_0)\mathrm{d}\omega, \tag{3.17}$$

$$a_{\rm out}(t) = \frac{\mathrm{i}}{\sqrt{2\pi}}\int \mathrm{e}^{-\mathrm{i}\omega(t-t_1)}b(\omega,t_1)\mathrm{d}\omega \tag{3.18}$$

for later convenience. Note that these definitions imply $[a_{\rm in}(t),a_{\rm in}^\dagger(t')]=\delta(t-t')$, $[a_{\rm out}(t),a_{\rm out}^\dagger(t')]=\delta(t-t')$, and that they are operators of the environmental mode. Furthermore, $a_{\rm in}$ and $a_{\rm out}$ have units of $\mathrm{s}^{-1/2}$. Therefore, the quantities $a_{\rm in}^\dagger a_{\rm in}(t)$ and $a_{\rm out}^\dagger a_{\rm out}(t)$ are the number operators *per second* of the input and output modes. Notice how $a_{\rm in}$ depends on the environmental modes at some initial time $t_0<t$, while $a_{\rm out}$ depends on the environmental modes at some final time $t_1>t$. Hence, $a_{\rm in}(t)$ may be interpreted as the input field, which describes the effect of interaction between the system's field mode $a(t)$ and its environment at early times. While $a_{\rm out}(t)$ is the output field, which describes the effect of the system-environment interactions at later times.

To proceed, the approximation that the coupling rates are frequency-independent $g(\omega)=\sqrt{\kappa/\pi}$ is made. Collett and Gardiner refer to this approximation as the *first Markov approximation* as it leads to a Heisenberg-Langevin equation which is Markovian, as we will soon see. Inserting the forward time solution for $b(\omega,t)$ into Eq. (3.16), then gives

$$\begin{aligned}\dot{O} &= \frac{\mathrm{i}}{\hbar}[H,O(t)]\\ &+\mathrm{i}\sqrt{\frac{\kappa}{\pi}}\int \mathrm{d}\omega\left\{\mathrm{e}^{\mathrm{i}\omega(t-t_0)}b^\dagger(\omega,t_0)[a,O]+[a^\dagger,O]\mathrm{e}^{-\mathrm{i}\omega(t-t_0)}b(\omega,t_0)\right\}\\ &+\frac{\kappa}{\pi}\int \mathrm{d}\omega\int_{t_0}^{t}\mathrm{d}t'\left\{\mathrm{e}^{\mathrm{i}\omega(t-t')}a^\dagger(t')[a,O]+[a^\dagger,O]\mathrm{e}^{-\mathrm{i}\omega(t-t')}a(t')\right\}.\end{aligned} \tag{3.19}$$

The definition of $a_{\rm in}$ from Eq. (3.17) can be inserted in the second term of Eq. (3.19). Furthermore, the expressions

$$\frac{1}{2\pi}\int_{-\infty}^{\infty}\mathrm{d}\omega\mathrm{e}^{\pm\mathrm{i}\omega(t-t')} = \delta(t-t'), \tag{3.20}$$

$$\int_{t_0}^{t}\mathrm{d}t' f(t')\delta(t-t') = \frac{1}{2}f(t), \tag{3.21}$$

can be used to simplify[5] the final term Eq. (3.19). Note that Eq. (3.20) assumes integration over the frequency range $\omega\in(-\infty,+\infty)$, which is typically a good approximation provided one is interested in problems involving high frequencies far from zero. Eq. (3.19) then gives the forward-in-time Heisenberg-Langevin

[5] The factor of 1/2 in Eq. (3.21) appears as t is the upper limit of the integration, which may be appreciated by considering the Dirac delta as the limit of some suitable test function—such as an infinitely narrow double-sided exponential.

equation for an arbitrary system operator O

$$\begin{aligned}\dot{O} &= \frac{\mathrm{i}}{\hbar}[H, O(t)] - \sqrt{2\kappa}\left\{a_{\mathrm{in}}^{\dagger}(t)[a, O] + [a^{\dagger}, O]a_{\mathrm{in}}(t)\right\} \\ &\quad +\kappa\left\{a^{\dagger}(t)[a, O] + [a^{\dagger}, O]a(t)\right\}, \end{aligned} \tag{3.22}$$

which is clearly Markovian as the right hand side only depends on time t.

Instead, if the backward time solution for $b(\omega, t)$ is inserted into Eq. (3.16), one arrives at the backward-in-time Heisenberg-Langevin equation

$$\begin{aligned}\dot{O} &= \frac{\mathrm{i}}{\hbar}[H, O(t)] + \sqrt{2\kappa}\left\{a_{\mathrm{out}}^{\dagger}(t)[a, O] + [a^{\dagger}, O]a_{\mathrm{out}}(t)\right\} \\ &\quad -\kappa\left\{a^{\dagger}(t)[a, O] + [a^{\dagger}, O]a(t)\right\}. \end{aligned} \tag{3.23}$$

To derive a relation between a, a_{in}, and a_{out}, Eq. (3.22) is subtracted from Eq. (3.23), which gives

$$0 = [a^{\dagger}, O]\left\{a_{\mathrm{out}}(t) + a_{\mathrm{in}}(t) - \sqrt{2\kappa}a(t)\right\} + \mathrm{h.c.} \tag{3.24}$$

This condition must be true for any system operator O, as the term in the curly brackets represents a boundary condition between the environment a_{in} and a_{out} and the particular system operator a with which the environment interacts. In general, $[a^{\dagger}, O] \neq 0$, and therefore, the input-output boundary condition is

$$a_{\mathrm{out}}(t) = \sqrt{2\kappa}a(t) - a_{\mathrm{in}}(t). \tag{3.25}$$

3.3.1 Input noise correlation functions

Important in many calculations are the correlation functions between the input mode operators. If the environmental input mode is in a thermal state with frequency $\bar{N}$, then the relevant correlations may be computed from Eq. (3.17):

$$\left\langle a_{\mathrm{in}}^{\dagger}(t)a_{\mathrm{in}}(t')\right\rangle = \bar{N}\delta(t - t'), \tag{3.26}$$

$$\left\langle a_{\mathrm{in}}(t)a_{\mathrm{in}}(t')^{\dagger}\right\rangle = (\bar{N} + 1)\delta(t - t'), \tag{3.27}$$

$$\left\langle a_{\mathrm{in}}(t)a_{\mathrm{in}}(t')\right\rangle = 0. \tag{3.28}$$

$$\tag{3.29}$$

For example the $\langle a_{\mathrm{in}}(t)a_{\mathrm{in}}(t')\rangle$ is calculated from Eq. (3.17) via

$$\begin{aligned}\left\langle a_{\mathrm{in}}^{\dagger}(t)a_{\mathrm{in}}(t')\right\rangle &= \frac{1}{2\pi}\int \mathrm{d}\omega_1 \int \mathrm{d}\omega_2 \mathrm{e}^{\mathrm{i}\omega_1(t-t_0)}\mathrm{e}^{-\mathrm{i}\omega_2(t'-t_0)}\left\langle b^{\dagger}(\omega_1, t_0)b(\omega_2, t_0)\right\rangle \\ &= \frac{1}{2\pi}\int \mathrm{d}\omega_1 \int \mathrm{d}\omega_2 \mathrm{e}^{\mathrm{i}\omega_1(t-t_0)}\mathrm{e}^{-\mathrm{i}\omega_2(t'-t_0)}\bar{N}\delta(\omega_1 - \omega_2) \\ &= \frac{\bar{N}}{2\pi}\int \mathrm{d}\omega \mathrm{e}^{\mathrm{i}\omega(t-t')} \\ &= \bar{N}\delta(t - t'). \end{aligned}$$

These two-point correlation functions between the the input mode operators are delta correlated. Without this result, the Heisenberg-Langevin equations would not be Markovian as the bath and the system would become correlated over some finite timescale.

However, a question arises: What frequency should $\bar{N}$ be taken at? From Section 2.4, we know that $\bar{N}$ is a function of frequency and our environment is comprised of quantum harmonic oscillators with a continuous range of frequencies. The *quantum-optics approximation* tells us we should take $\bar{N}$ to be calculated at the harmonic frequency of the system's field mode a [44]. The quantum-optics approximation is valid for high quality factor oscillators so that there is a only small range of relevant bath frequencies about the harmonic frequency. Note that the quantum optics approximation was made in the above example for $\left\langle a_{\text{in}}^{\dagger}(t)a_{\text{in}}(t')\right\rangle$ when $\bar{N}$ was pulled out of the integral. Furthermore, the quantum-optics approximation isn't necessary for optical systems as $\bar{N}=0$, and the only non-zero two-point correlation function is $\left\langle a_{\text{in}}(t)a_{\text{in}}(t')^{\dagger}\right\rangle = \delta(t-t')$ for an optical vacuum environment.

3.3.2 Quantum optics Heisenberg-Langevin equation

In the forward-in-time Heisenberg equation [Eq. (3.22)], taking $O=a$ gives

$$\dot{a}(t) = \frac{\mathrm{i}}{\hbar}[H,a(t)] - \kappa a(t) + \sqrt{2\kappa}a_{\text{in}}(t). \tag{3.30}$$

Here, a may be interpreted as the field mode of an optical cavity as in Fig. 3.3. In this case, a_{in} and a_{out} represent the field entering and leaving the cavity. As previously stated a_{in} and a_{out} have units of $\mathrm{s}^{-1/2}$, so the input and output photon number operators may be defined as

$$n_{\text{in}} = \int \mathrm{d}t a_{\text{in}}^{\dagger}a_{\text{in}}(t), \tag{3.31}$$

$$n_{\text{out}} = \int \mathrm{d}t a_{\text{out}}^{\dagger}a_{\text{out}}(t). \tag{3.32}$$

Note that if H preserves the photon number, one has $n_{\text{in}}=n_{\text{out}}$ as in Ref. [7].

In the input-output formalism, the Heisenberg-Langevin equation explicitly includes an operator for the input mode. However, Eq.(3.30) gives rise to the same dynamics as the quantum optics master equation (3.3) for the field operator a—even though the master equation does not include an input operator. The equivalence between the two formalisms[6] can be checked by using the adjoint master equation for $\langle a(t)\rangle$ in Eq. (3.2) and using $\mathrm{tr}\left(a\mathcal{D}[a]\rho\right) = -\kappa\langle a\rangle/2$ and $\mathrm{tr}\left(a\mathcal{D}[a^{\dagger}]\rho\right) = +\kappa\langle a\rangle/2$.

[6] Eq. (3.2) is an extremely useful way to check which convention an author is using, i.e. is an author taking κ to be an intensity or amplitude quantity?

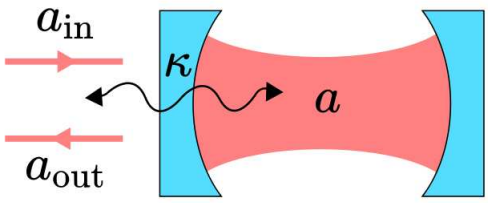


Figure 3.3: **Input-output formalism for a one-sided optical cavity.** The cavity mode a couples to the input a_{in} and output a_{out} modes. Here, the cavity linewidth κ, determined by the reflectivity of the input-output mirror, is equal to the amplitude decay rate of the cavity mode.

External versus intrinsic loss

Eq. (3.30) describes the ideal situation where all the light entering the cavity is transmitted into a single output mode a_{out}, which the experimenter may collect and then send towards the next part of their experiment. In practice there will always be intrinsic cavity losses, due to optical imperfections of the cavity. Such imperfections include scattering of light out of the optical cavity and absorption losses by the cavity mirrors.

To model these intrinsic cavity losses, another independent set of environmental modes $c(\omega)$ may be introduced that also linearly couple to the cavity field mode a. Here, these modes $c(\omega)$ are referred to as the *intrinsic modes* as they represent intrinsic losses, while the original environmental modes $b(\omega)$ are now referred to as *external modes* as they represent an external coupling to the cavity mode. Therefore, the total system Hamiltonian is

$$H_{\text{TOT}} = H + H_{\text{E}}^{\text{ex}} + H_{\text{INT}}^{\text{ex}} + H_{\text{E}}^{\text{i}} + H_{\text{INT}}^{\text{i}}, \tag{3.33}$$

$$H_{\text{E}}^{\text{ex}} = \int \hbar\omega b^\dagger(\omega)b(\omega)\mathrm{d}\omega, \tag{3.34}$$

$$H_{\text{INT}}^{\text{ex}} = \int \hbar g_{\text{ex}}(\omega)\left[b^\dagger(\omega)a + a^\dagger b(\omega)\right]\mathrm{d}\omega, \tag{3.35}$$

$$H_{\text{E}}^{\text{i}} = \int \hbar\omega c^\dagger(\omega)c(\omega)\mathrm{d}\omega, \tag{3.36}$$

$$H_{\text{INT}}^{\text{i}} = \int \hbar g_{\text{i}}(\omega)\left[c^\dagger(\omega)a + a^\dagger c(\omega)\right]\mathrm{d}\omega. \tag{3.37}$$

Repeating the same steps as above and taking $g_{\text{ex}} = \sqrt{\kappa_{\text{ex}}/\pi}$ and $g_{\text{i}} = \sqrt{\kappa_{\text{i}}/\pi}$ gives

$$\dot{a}(t) = \frac{\mathrm{i}}{\hbar}[H, a(t)] - (\kappa_{\text{ex}} + \kappa_{\text{i}})a(t) + \sqrt{2\kappa_{\text{ex}}}a_{\text{in}}^{\text{ex}}(t) + \sqrt{2\kappa_{\text{i}}}a_{\text{in}}^{\text{i}}(t). \tag{3.38}$$

Here, the external input-output modes are defined as above, while $a_{\text{in}}^{\text{i}}(t)$ is defined with $b(\omega, t_0)$ replaced by $c(\omega, t_0)$ in Eq. (3.17). In principle, the intrinsic

input-output modes also obey a boundary condition similar to Eq. (3.25), but as these models are typically assumed to be inaccessible, this boundary condition is less useful in practice. When $\kappa_{\rm ex} \gg \kappa_{\rm i}$, the cavity is said to be *overcoupled* and most of the input light is transmitted back into the external output mode. When $\kappa_{\rm ex} = \kappa_{\rm i}$, the cavity is *critically coupled*[7] as on average all the input power is lost within the cavity when it is driven on resonance. This can be shown by considering the input-output relation for $a_{\rm in}^{\rm ex}(t)$ [45]. While, a cavity with $\kappa_{\rm ex} \ll \kappa_{\rm i}$ is said to be *undercoupled*.

Beamsplitter model for loss

Alternatively to Eq. (3.38), intrinsic cavity losses and detection inefficiencies may be taken into account with a beamsplitter model for loss [18]—see Fig. 3.4. In this model, the output of the cavity is sent towards one input of a fictitious beamsplitter and the other beamsplitter input is assumed to be vacuum. A trace operation is then performed over one of the beamsplitter output modes. The advantage of this strategy is that one can derive a unitary transformation between the input and output modes from Eq. (3.30)–as in Ref. [7]—and then treat non-unitary losses separately.

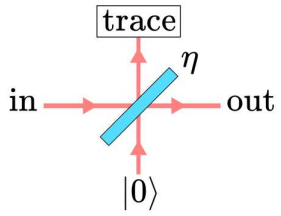


Figure 3.4: **The beamsplitter model for optical loss.** The input optical mode labelled "in" interacts with the optical vacuum $|0\rangle$ on a beamsplitter, which has a transmission coefficient $\sqrt{\eta}$. One of the output ports is lost to the optical environment, which is described by a trace operation, while the other output mode labelled "out" has suffered optical loss.

3.3.3 Quantum Brownian motion Heisenberg-Langevin equation

In the derivation of the Heisenberg-Langevin equations presented in the previous two sections, I assumed a beamsplitter type coupling between the system and its environment—see Eq. (3.13). For a Heisenberg-Langevin equation that describes quantum Brownian motion for mechanical systems, one should instead

[7] Taking inspiration from electronic systems, this is also sometimes referred to as an impedance matched cavity.

assume an X-X quadrature type coupling between the mechanical mode and its environment:

$$H_{\text{INT}} = \int \hbar g(\omega) X_{\text{M}} X_{\text{E}}(\omega) \mathrm{d}\omega, \tag{3.39}$$

where $X_{\text{E}}(\omega)$ are the environmental position operators at each frequency. From Section 2.2, we know that the position operator is the generator of momentum translations. Hence, it is expected that this type of X-X coupling to produce an input noise operator that effects only the momentum quadrature of the mechanical mode. However, the derivation of the quantum Brownian motion Heisenberg-Langevin equation is a lot more involved than the derivation of the quantum optics Heisenberg-Langevin equation. This is because the form of H_{INT} leads to an asymmetry between the X_{M} and P_{M} quadratures, which makes the Heisenberg equations generated by H_{TOT} more complicated to solve. Refs [32] and [44] detail the derivation of the following Heisenberg-Langevin equations:

$$\dot{X}_{\text{M}}(t) = \frac{\mathrm{i}}{\hbar}[H, X_{\text{M}}(t)], \tag{3.40}$$

$$\dot{P}_{\text{M}}(t) = \frac{\mathrm{i}}{\hbar}[H, P_{\text{M}}(t)] - \gamma P_{\text{M}}(t) + \sqrt{2\gamma} P_{\text{in}}(t). \tag{3.41}$$

As before, there exists an input-output relation for the input noise operator $P_{\text{in}}(t)$ and the corresponding output operator, but in practice this output mode is inaccessible so the input-output relation is not typically useful. In addition to the first Markov approximation, which assumes $g(\omega) \propto \sqrt{\gamma}$, a further Markov approximation must be made on the two-point correlation function so that it is delta-correlated. Ref. [44] details this approximation, which requires $Q/\bar{N} \gg 1$, and leads to

$$\langle P_{\text{in}}(t) P_{\text{in}}(t') \rangle = \left(\bar{N} + \frac{1}{2} \right) \delta(t - t'). \tag{3.42}$$

The quantity $Q/\bar{N} \gg 1$ is an important parameter in mechanical systems as its inverse $\bar{N}/Q$ is proportional to the number of thermal quanta added from the bath to the oscillator over one mechanical cycle.

Chapter 4

Continuous-variable Gaussian quantum optics

Gaussian states are the set of states which have Gaussian Wigner functions and are ubiquitous in quantum optics. Indeed, vacuum states, coherent states, squeezed states, and thermal states discussed in Chapter 2 are all examples of Gaussian states. These Gaussian states are central to many optical and mechanical systems and provide a useful mathematical description of quantum sensing protocols involving squeezed states [46], quantum state engineering of entangled states [2, 3], and ground state cooling in mechanical systems [45]. Moreover, Gaussian states are important for quantum computing with continuous-variable optical systems [47]. I shall briefly discuss the formalism of continuous-variable Gaussian quantum optics, while Ref. [48] provides further details. The formalism presented in this chapter underpins the proposals of Refs [2] and [3], is used in the derivation of the *Stochastic Gaussian regime* introduced in Ref. [7], and is utilized in the deterministic squeezing protocol of Ref. [12].

4.1 General formalism

An n-mode Gaussian state may be fully characterized by the first and second moments of its quadrature vector $\mathbf{r} = (X_1, P_1, X_2, P_2, \ldots, X_n, P_n)^{\mathrm{T}}$. The first moments are given by $\langle \mathbf{r} \rangle$, while the second moments correspond to elements of the covariance matrix σ, which are given by

$$\sigma_{i,j} = \frac{1}{2}\langle X_i X_j + X_j X_i \rangle - \langle X_i \rangle \langle X_j \rangle. \tag{4.1}$$

Note that $\dim(\mathbf{r}) = 2n$ implies $\dim(\sigma) = 2n \times 2n$. Furthermore, the canonical commutation relations between the quadrature operators can be written as $[\mathbf{r}, \mathbf{r}^{\mathrm{T}}] = \mathrm{i}\Omega$, where the symplectic form Ω is given by

$$\Omega = \bigoplus_{i=1}^{n} \begin{pmatrix} 0 & 1 \\ -1 & 0 \end{pmatrix}, \tag{4.2}$$

where $\oplus$ represents the tensor sum. Explicitly, the general Wigner function of an n-mode Gaussian state is then

$$W_G(\mathbf{r}) = \frac{1}{(2\pi)^n\sqrt{\det(\sigma)}}\exp\left\{-\frac{1}{2}(\mathbf{r}-\langle\mathbf{r}\rangle)^{\mathrm{T}}\sigma^{-1}(\mathbf{r}-\langle\mathbf{r}\rangle)\right\}, \tag{4.3}$$

which is properly normalized such that

$$\int_{-\infty}^{+\infty} \mathrm{d}^{2n}r\; W_G(\mathbf{r}) = 1. \tag{4.4}$$

Here, the multidimensional Gaussian integral from Appendix C is useful[1].

In this thesis, I will be interested in a bipartition of the n modes. For example, the situation where the n modes are separated into one group of m modes and another group of $n-m$ modes will often arise. In this case, the block matrix form of the covariance matrix will be useful:

$$\sigma = \begin{pmatrix} A & C \\ C^{\mathrm{T}} & B \end{pmatrix}, \tag{4.5}$$

where $\dim(A) = 2m \times 2m$, $\dim(B) = 2(n-m)\times 2(n-m)$, and $\dim(C) = 2(n-m)\times 2m$. In the block matrix form, A and B correspond to the covariance matrices of the m and $n-m$ modes, respectively, while the off-diagonal block C represents the correlations between all the modes on each side of the bipartition. If $C = 0$ then σ may be written as the tensor sum of the covariance matrices A and B: $\sigma = A \oplus B$. For $n = 2$, the Gaussian state with covariance matrix $\sigma = A \oplus B$ is a separable state[2].

If the n-mode Hamiltonian contains terms which are either linear or quadratic in the quadrature operators, the unitary U_{G} it generates will transform Gaussian states into other Gaussian states [47]. One can show that in the Heisenberg picture, the transformation of the quadrature vector takes the simple form [48]

$$U_{\mathrm{G}}^{\dagger}\mathbf{r}U_{\mathrm{G}} = S\mathbf{r} + \mathbf{d}. \tag{4.6}$$

Here, $\mathbf{d}$ is a real vector with $\dim(\mathbf{d}) = 2n$, while S belongs to the real symplectic group $S \in Sp(2n,\mathbb{R})$ defined by

$$S\Omega S^{\mathrm{T}} = \Omega. \tag{4.7}$$

Furthermore, as the covariance matrix is invariant under linear transformations, Eq. (4.6) implies it transforms according to $\sigma \to S\sigma S^{\mathrm{T}}$. A necessary and sufficient condition for the covariance matrix σ to be a bona fide covariance matrix and thus represent a Gaussian state is given by the uncertainty relation

[1] One must also use that for an invertible matrix such as σ, $\det(\sigma\sigma^{-1}) = \det(\mathbb{1}) = 1$ implies $\det(\sigma^{-1}) = 1/\det(\sigma)$

[2] Notice how the tensor product description of separable states in Hilbert space from Chapter 2, now corresponds to the tensor sum in this phase-space formulation of quantum mechanics.

$\sigma + \mathrm{i}\Omega/2 \geq 0$ [49]. Eq. (4.7) therefore implies that the symplectic transform S preserves the Gaussian character of the quantum state.

To summarize, all unitary transformations from one Gaussian state to another can be described by

$$\langle \mathbf{r} \rangle \rightarrow S \langle \mathbf{r} \rangle + \mathbf{d}, \tag{4.8}$$

$$\sigma \rightarrow S \sigma S^{\mathrm{T}}. \tag{4.9}$$

4.2 Single mode symplectic transformations

Here, I review the single mode symplectic transformations utilized in this thesis. Consider a single mode described by the quadrature vector $\mathbf{r} = (X, P)^{\mathrm{T}}$.

Rotation

The unitary $U(\theta) = \mathrm{e}^{-\mathrm{i}\theta\hat{n}}$ from Chapter 2 corresponds to a rotation by an angle θ in phase space, and has the symplectic matrix

$$S_{\mathrm{ROT}}(\theta) = \begin{pmatrix} \cos\theta & \sin\theta \\ -\sin\theta & \cos\theta \end{pmatrix}. \tag{4.10}$$

Single mode squeezer

From Chapter 2, the squeezing operation is described by the unitary operator $S(\zeta) = \mathrm{e}^{\frac{\zeta}{2}[(a^\dagger)^2 - a^2]}$. For $\zeta = r \in \mathbb{R}$, the corresponding symplectic matrix is given by

$$S_{\mathrm{SQ}}(r) = \begin{pmatrix} \mathrm{e}^{r} & 0 \\ 0 & \mathrm{e}^{-r} \end{pmatrix}. \tag{4.11}$$

A general squeezing operation with $\zeta \in \mathbb{C}$ can be described as a combination of a squeezing operation with $\zeta = r \in \mathbb{R}$ and single mode rotation operations [50].

4.3 Two mode symplectic transformations

In this section, I specialize to two modes: $\mathbf{r} \rightarrow \mathbf{X}$, where $\mathbf{X} = (\mathbf{X}_1, \mathbf{X}_2)^{\mathrm{T}} = (X_1, P_1, X_2, P_2)^{\mathrm{T}}$, and review the two-mode transformations used in this thesis.

Beamsplitter

The unitary operation $\exp\{\mathrm{i}\alpha\cos\beta(a_1^\dagger a_2 - a_1 a_2^\dagger) + \mathrm{i}\alpha\sin\beta(a_1^\dagger a_2 + a_1 a_2^\dagger)\}$ comprises a beamsplitter operation and corresponds to the symplectic transformation

$$S_{\mathrm{BS}}(\alpha, \beta) = \begin{pmatrix} \cos\alpha & 0 & \sin\alpha\cos\beta & -\sin\alpha\sin\beta \\ 0 & \cos\alpha & \sin\alpha\sin\beta & \sin\alpha\cos\beta \\ -\sin\alpha\cos\beta & -\sin\alpha\sin\beta & \cos\alpha & 0 \\ \sin\alpha\sin\beta & -\sin\alpha\cos\beta & 0 & \cos\alpha \end{pmatrix}. \tag{4.12}$$

Comparison with Eq. (2.31) implies that $S_{\text{BS}}(\alpha,\beta)$ is a beamsplitter with $\Lambda = 0$, $t = \cos\alpha$, and $r = \sin\alpha\cos\beta + \mathrm{i}\sin\alpha\sin\beta$. Therefore, the most general beamsplitter operation may be achieved through a combination of S_{BS} and tensor sums of local rotations $S_{\text{ROT}}(\theta_1) \oplus S_{\text{ROT}}(\theta_2)$.

Linearized-pulsed optomechanical interaction

A pulsed linear optomechanical interaction[3] is described by $\mathrm{e}^{\mathrm{i}\chi X_1 X_2}$ and corresponds to the symplectic transformation

$$S_{\text{OM}} = \begin{pmatrix} 1 & 0 & 0 & 0 \\ 0 & 1 & \chi & 0 \\ 0 & 0 & 1 & 0 \\ \chi & 0 & 0 & 1 \end{pmatrix}, \tag{4.13}$$

where $\chi \in \mathbb{R}$. Using the results of Chapter 2, this transformation may be seen by recognizing $\mathrm{e}^{\mathrm{i}\chi X_1 X_2}$ is an X_2 dependent displacement on mode 1 along the P_1 quadrature, i.e.

$$X_1 \rightarrow X_1, \tag{4.14}$$
$$P_1 \rightarrow P_1 + \chi X_2, \tag{4.15}$$

and vice versa for mode 2:

$$X_2 \rightarrow X_2, \tag{4.16}$$
$$P_2 \rightarrow P_2 + \chi X_1. \tag{4.17}$$

4.4 Measurements and trace

In this section, I again focus on two modes, while the generalization to n modes may be found in Ref. [50]. In the Schrödinger picture, a general Gaussian measurement is described by a measurement operator Υ_{G} via $\rho \rightarrow \Upsilon_{\text{G}}\rho\Upsilon_{\text{G}}^\dagger / \operatorname{tr}\left(\Upsilon_{\text{G}}^\dagger\Upsilon_{\text{G}}\rho\right)$, see Chapter 5. Meanwhile, in terms of the first-moments vector $\langle\mathbf{X}\rangle$ and the covariance matrix of Eq. (4.5), a Gaussian measurement on mode 1 is described by the mapping[4]

$$\langle\mathbf{X_2}\rangle \rightarrow \langle\mathbf{X_2}\rangle + C^{\text{T}}(A+\sigma_{\text{meas}})^{-1}(\langle\mathbf{X}_{\text{meas}}\rangle - \langle\mathbf{X_1}\rangle), \tag{4.18}$$
$$B \rightarrow B - C^{\text{T}}(A+\sigma_{\text{meas}})^{-1}C, \tag{4.19}$$

and a similar expression exists for a measurement on mode 2. Here, $\langle\mathbf{X}_{\text{meas}}\rangle$ is the measurement outcome and σ_{meas} describes the Gaussian measurement [51]. In the limit of a projection onto an infinitely squeezed Gaussian state, which constitutes a homodyne measurement, the term $(A+\sigma_{\text{meas}})^{-1}$ becomes $(\Pi_\varphi A \Pi_\varphi)^{\text{MP}}$.

[3] The pulsed linear optomechanical unitary is introduced in Chapter 6.

[4] See Ref. [50] for a neat derivation of this measurement map via the characteristic function.

Here, MP refers to the Moore-Penrose pseudo-inverse [52] and Π_φ is the projection operator onto the $X_1(\varphi) = X_1 \cos\varphi + P_1 \sin\varphi$ quadrature

$$\Pi_\varphi = \begin{pmatrix} \cos^2\varphi & \cos\varphi\sin\varphi \\ \cos\varphi\sin\varphi & \sin^2\varphi \end{pmatrix}. \tag{4.20}$$

The measurement operator corresponding to Π_φ is given by $|X_1(\varphi)\rangle\langle X_1(\varphi)|$, with $\int_{-\infty}^{+\infty} \mathrm{d}X_1(\varphi)\, |X_1(\varphi)\rangle\langle X_1(\varphi)| = \mathbb{1}$.

Meanwhile, the partial trace operation is particularly simple in the formalism presented here, namely tracing out one mode 1 gives [48]

$$\langle \mathbf{X} \rangle \to \langle X_2 \rangle, \tag{4.21}$$

$$\sigma \to B, \tag{4.22}$$

and a similar mapping exists for tracing out mode 2.

4.5 Open system dynamics

The quantum optics master equation from Chapter 3 preserves the Gaussian character of the initial state as the coupling between the system and bath field operators is quadratic. For this form of open-system dynamics, Ref. [53] shows that, for an initial Gaussian n-mode state, the first moments vector $\langle \mathbf{r} \rangle$ and covariance matrix σ transform according to

$$\langle \mathbf{r} \rangle \to G^{1/2} \langle \mathbf{r} \rangle, \tag{4.23}$$

$$\sigma \to G^{1/2} \sigma G^{1/2} + (\mathbb{1} - G)\sigma_{\text{env}}, \tag{4.24}$$

$$G = \bigoplus_{i=1}^{n} \mathrm{e}^{-2\kappa_i t}, \tag{4.25}$$

$$\sigma_{\text{env}} = \bigoplus_{i=1}^{n} \left(\bar{N}_i + \frac{1}{2}\right) \mathbb{1}_2. \tag{4.26}$$

Here, κ_i and $\bar{N}_i$ are the amplitude decay rates and environmental thermal occupations[5] of each mode, respectively, while t is the time over which the master equation is propagated. Note that in Ref. [2], the matrix $G = \mathrm{e}^{-\gamma t}$ is used to model interactions of a mechanical mode with the environment and hence γ is an intensity decay rate.

One may also consider modelling optical loss through the beamsplitter model for loss from Chapter 3. A beamsplitter symplectic matrix S_{BS} with real transmission coefficient $t = \sqrt{\eta}$ is used to model the interaction between the initial state and the optical vacuum environment. A trace operation is then used to describe loss of information to the optical environment. Following the formalism detailed in the previous sections, one find that this loss is also modelled by Eqs (4.23) and (4.24) but with $G = \eta\mathbb{1}_2$ and $\sigma_{\text{env}} = \frac{1}{2}\mathbb{1}$.

[5] The covariance matrix of a thermal state is given by $\sigma_{\text{TH}} = \left(\bar{N} + \frac{1}{2}\right)\mathbb{1}_2$.

4.6 Gaussian entanglement

A necessary condition for a state to be separable is the positivity of the partial transpose, i.e. when the transpose operation is carried out on one mode of a multi-mode system, the eigenvalues of the resulting density matrix all remain greater than or equal to zero. This condition is known as the PPT criterion [54, 55]. For Gaussian states of $1 \oplus 1$ and $1 \oplus n$ modes, the PPT criterion is also a necessary *and* sufficient condition for entanglement [56, 57]. To measure entanglement in bipartite systems, the *logarithmic negativity* $E_{\mathcal{N}}(\sigma)$ is often used, which measures the extent to which the positivity of the density operator is violated after the partial transpose operation. The logarithmic negativity is a genuine entanglement monotone for low-dimensional discrete variable systems [58, 59] and for bipartite continuous variable Gaussian states [60].

In this thesis, I will focus on entanglement between two modes. Therefore, for a two-mode system, the partial transposition operation leads to a covariance matrix with eigenvalues given by

$$\tilde{\nu}_{\pm} = \sqrt{\frac{\tilde{\Delta} \pm \sqrt{\tilde{\Delta}^2 - 4 \det \sigma}}{2}} \tag{4.27}$$

where $\tilde{\Delta} = \det A + \det B - 2 \det C$. In terms of the lowest eigenvalue $\tilde{\nu}_-$, the violation of the PPT criterion is equivalent to Simon's necessary and sufficient condition for $1 \oplus 1$ Gaussian states to be entangled: $\tilde{\nu}_- < 1/2$ [56]. The logarithmic negativity of the two-mode state with covariance matrix σ is then calculated as

$$E_{\mathcal{N}}(\sigma) = \max\{0, -\log_2(2\tilde{\nu}_-)\}. \tag{4.28}$$

The logarithmic negativity therefore completely characterizes and measures the entanglement of a two-mode Gaussian state.

4.6.1 Non-Gaussian entanglement

For non-Gaussian states, the PPT criterion is a necessary condition for separability. Therefore, violation of the PPT criterion is only a sufficient condition for a non-Gaussian state to be entangled, but this violation will not capture all non-Gaussian entanglement. Moreover, Simon's condition $\tilde{\nu}_- < 1/2$ is a sufficient condition for non-Gaussian entanglement, but in practice it is not always useful because only a small class of non-Gaussian entangled states may be detected. Importantly, Simon's condition is designed for Gaussian states, whose description is completely characterized by their first and second moments, and hence Simon's condition may be derived solely from the covariance matrix of the quantum state. And so the detection of non-Gaussian entangled states—whose description necessitates the inclusion of higher order quadrature moments—through the violation of the PPT criterion can be made more encompassing by designing entanglement criteria involving third, and even higher, order quadrature moments. In Ref. [61], Shchukin and Vogel designed such negative-partial-transpose (NPT) based criteria for detecting entanglement. One example NPT

criteria is given by the negativity of the determinant

$$S_{\text{III}} = \begin{vmatrix} 1 & \left\langle a_2^\dagger \right\rangle & \left\langle a_1 a_2^\dagger \right\rangle \\ \langle a_2 \rangle & \left\langle a_2^\dagger a_2 \right\rangle & \left\langle a_1 a_2^\dagger a_2 \right\rangle \\ \left\langle a_1^\dagger a_2 \right\rangle & \left\langle a_1^\dagger a_2^\dagger a_2 \right\rangle & \left\langle a_1^\dagger a_1 a_2^\dagger a_2 \right\rangle \end{vmatrix}, \tag{4.29}$$

which, along with Simon's condition, was utilized in Ref. [6] to investigate entanglement in two-mode mechanical Schrödinger cat states. In Ref. [10], we develop of framework to select optimal NPT criteria by determining their confidence levels. Our statistical framework utilizes a Lagrange mutliplier method to find the optimal allocation of measurements in the presence of environmental noise and a finite number of measurements.

Chapter 5

Quantum measurement

Projective measurements were described in Chapter 1. These describe the projection of a quantum state onto an eigenstate of a Hermitian operator via Eq (1.7). However, this thesis also considers general measurements on quantum systems, which I briefly review below. I then discuss the *stochastic master equation* description of continuous quantum measurements, which is an extension of the Lindblad master equation subject to continuous monitoring of a set of system observables. These concepts are explained in much greater detail in Refs [62] and [63].

5.1 Generalized quantum measurements

The set of operators $\{\Upsilon_n\}$ that obey

$$\sum_n \Upsilon_n^\dagger \Upsilon_n = \mathbb{1}, \tag{5.1}$$

correspond to a possible generalized measurement on a quantum system. Each Υ_n is referred to as a *measurement operator*[1]. Furthermore, each discrete label n corresponds a different possible outcome. If the measurement outcomes are instead described by a continuous variable, say X, Eq. (5.1) becomes

$$\int \Upsilon^\dagger(X)\Upsilon(X)\mathrm{d}X = \mathbb{1}. \tag{5.2}$$

Note that it may be more convenient to label the measurement operators with multiple indices or variables[2], i.e. $\Upsilon_{n,m,\ldots}$ or $\Upsilon(X_1, X_2, \ldots)$.

When the outcome n is recorded by an experimenter, the initial quantum

[1] Measurement operators are sometimes called Kraus operators after Karl Kraus who derived generalized quantum measurements in the more general context of CPTP maps [64].

[2] The example given shortly below is such a case.

state ρ changes via a generalized quantum measurement:

$$\rho_n = \frac{\Upsilon_n \rho \Upsilon_n^\dagger}{\mathcal{P}_n}, \tag{5.3}$$

$$\mathcal{P}_n = \mathrm{tr}\left(\Upsilon^\dagger \Upsilon \rho\right). \tag{5.4}$$

As with a projective measurement, $\mathcal{P}_n$ is the heralding probability for the particular outcome n, which normalizes the output state ρ_n. Furthermore, the $\mathcal{P}_n$ sum to unity, $\sum_n \mathcal{P}_n = 1$. As before, Υ_n is replaced with $\Upsilon(X)$ to describe a measurement with a continuous outcome. Below, an example of constructing a *general-dyne* measurement operator is given.

Example of a measurement operator's construction

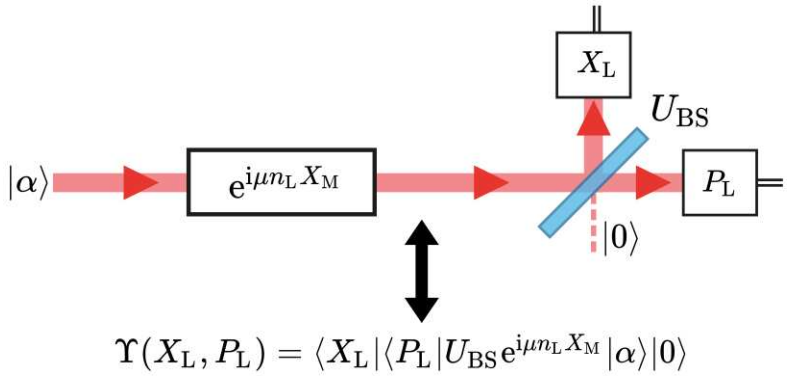


Figure 5.1: **Constructing a measurement operator.** Here, the optical mode, initially in the state $|\alpha\rangle$, interacts with a mechanical mode via the unitary $e^{i\mu n_\mathrm{L} X_\mathrm{M}}$. The output optical mode, and a vacuum mode, then impinge on a beamsplitter described by U_BS, with real transmission coefficient ζ. Amplitude (X_L) and phase (P_L) homodyne measurements are then made on the output modes. The measurement operator $\Upsilon(X_\mathrm{L}, P_\mathrm{L})$, which acts on the mechanical subspace, is constructed by sandwiching the total unitary between the input optical states and the quadrature states corresponding to the homodyne outcomes.

Consider an optical mode in the initial state $|\alpha\rangle$. The optical mode enters a cavity and interacts with a mechanical mode. After the light exits the cavity, the interaction may be described by the nonlinear pulsed cavity unitary interaction[3] $e^{i\mu n_\mathrm{L} X_\mathrm{M}}$—see Chapter 6. The output light is then sent towards a

[3] Note that $e^{i\mu n_\mathrm{L} X_\mathrm{M}}$ describes a cavity-free nonlinear optomechanical interaction. Ref. [7], which is described in Part III, includes the cavity-enhanced optomechanical interaction in the derivation of its position measurement operator.

general-dyne detector, comprised of a beamsplitter[4] with: real transmission coefficient ζ, vacuum on one input, an X_{L} amplitude homodyne detector at one output, and a P_{L} phase homodyne detector at the other. In this way, the output light is projected onto a general Gaussian state [65, 66]. Fig. 5.1, illustrates the construction of the measurement operator. When the pair of homodyne detectors record a particular (X_{L}, P_{L}) outcome, the measurement operator is

$$\begin{aligned}\Upsilon(X_{\text{L}}, P_{\text{L}}) &= \langle X_{\text{L}}| \langle P_{\text{L}}| U_{\text{BS}} \mathrm{e}^{\mathrm{i}\mu n_{\text{L}} X_{\text{M}}} |\alpha\rangle |0\rangle \qquad (5.5)\\ = \;& \frac{1}{\sqrt{\pi}} \exp\Big[-\frac{1}{2}\Big(X_{\text{L}} - \sqrt{1-\zeta^2} X_\alpha \cos\mu X_{\text{M}}\Big)^2 \\ & -\frac{1}{2}\left(P_{\text{L}} - \zeta X_\alpha \sin\mu X_{\text{M}}\right)^2 - \mathrm{i}\zeta X_\alpha P_{\text{L}} \cos\mu X_{\text{M}} \\ & +\mathrm{i}\sqrt{1-\zeta^2} X_\alpha X_{\text{L}} \sin\mu X_{\text{M}} - \frac{\mathrm{i}}{2}(1-2\zeta^2) X_\alpha^2 \cos\mu X_{\text{M}} \sin\mu X_{\text{M}}\Big].\end{aligned}$$

Here, the formula for the overlap between a rotated quadrature state and a coherent state from Appendix A was used and $\alpha = X_\alpha/\sqrt{2} \in \mathbb{R}$ was chosen. Note that X_{L} and P_{L} are being used to label the outcomes of measurements and so are real variables in this context. Furthermore, the measurement operator describes a bona fide general quantum measurement as

$$\iint_{-\infty}^{\infty} \Upsilon^\dagger(X_{\text{L}}, P_{\text{L}}) \Upsilon(X_{\text{L}}, P_{\text{L}}) \mathrm{d}X_{\text{L}} \mathrm{d}P_{\text{L}} = \mathbb{1}. \qquad (5.6)$$

5.2 Continuous weak measurements

In a continuous weak measurement, the quantum state of a system is continuously monitored and, unlike a projective measurement, the state of the system dynamically evolves even during the measurement process [67, 68]. The state's evolution is neatly described by a stochastic master equation (SME), which I will now describe.

An *output channel* is a channel through which the system of interest couples to—and exchanges information with—an external system. An output channel can either be unmonitored—a dissipation channel—or monitored with some efficiency—a measurement channel. For a total of n output channels, the Markovian SMEs considered in this thesis are of the form [69, 70]

$$\mathrm{d}\rho \;=\; -\frac{\mathrm{i}}{\hbar}[H,\rho]\mathrm{d}t + \sum_n \left(\mathcal{D}[c_n]\rho \mathrm{d}t + \sqrt{\eta_n}\mathcal{H}[c_n]\rho \mathrm{d}W_n\right), \qquad (5.7)$$

where the measurement superoperator is defined by $\mathcal{H}[O]\rho = O\rho + \rho O^\dagger - \left\langle O + O^\dagger \right\rangle \rho$, and the operators c_n are collectively referred to as *output operators*. Here, η_n are the quantum efficiencies and $\mathrm{d}W_n$ are the Wiener increments for

[4] Note that completely general general-dyne detection uses the most general beamsplitter transformation from Chapter 2. However, we take $t = \zeta \in \mathbb{R}$ so that comparison with Ref. [7] is easier.

the n^{th} output channel. Owing to the measurement superoperators, Eq. (5.7) includes the terms $\langle c_n + c_n^\dagger \rangle \rho = \text{tr}\left((c_n + c_n^\dagger)\rho\right)\rho$ and so the quantum evolution of the system is nonlinear in ρ. For output channels that correspond to dissipation, $\eta_n = 0$, c_n represent the Lindblad operators of Eq. (3.1). While for output operators that correspond to measurement, $0 < \eta_n \leq 1$, one may interpret $\mathcal{H}[c_n]\rho \text{d}W_n$ as terms that weakly localize the state continuously and the associated terms $\mathcal{D}[c_n]\rho \text{d}t$ represent the quantum back action of these continuous measurements.

The SME for a continuous Gaussian position measurement is derived in Ref. [71]. In Ref. [7], a similar derivation is followed to arrive at the SME for continuous position measurement in nonlinear cavity quantum optomechanics. This derivation is presented in Part III of this thesis.

Wiener increments and stochasticity

The Wiener increments are Gaussian random variables with zero mean and variance dt. Hence, they obey (i) the Itô rule[5] $\text{d}W_n \text{d}W_m = \delta_{n,m}\text{d}t$ and (ii) $\mathbb{E}[\text{d}W_n] = 0$. Here, $\mathbb{E}$ represents the stochastic average. More precisely, as the SME is propagated forwards in time over a time step dt, the terms dW_n will take a random value according to the Gaussian statistics described by conditions (i) and (ii), above. Over the states evolution, the particular set of values dW_n take are referred to as the *measurement trajectory*. Every measurement trajectory generally implies a different state evolution. This property is why the SME is stochastic. Let $O(t)$ be some quantum operator, whose time evolution is of key interest. Its quantum expectation value is given by $\langle O(t) \rangle$. If the evolution of the quantum state of the system is described by a SME, $\langle O(t) \rangle$ will vary from run to run of the experiment. The stochastic average of $\langle O(t) \rangle$ can be approximated by averaging over many runs of the experiment and is denoted by $\mathbb{E}\left(\langle O(t) \rangle\right)$.

The measurement record

In an experiment, an observer will record a string of outcomes at the output of a measurement channel via a measurement device. This string of outcomes is referred to as the *measurement record*, which depends on the specific measurement trajectory that the SME realizes. In practice, it will take a finite amount of time τ for the measurement device to produce a measurement outcome. For example, a semiconductor based photodiode will take a finite amount of type to convert the input optical signal into an electrical current. Here, τ is the integration time of the detector and its inverse $1/\tau$ is the measurement bandwidth.

Mathematically, the measurement record is defined over the infinitesimal

[5] Named after Kiyosi Itô, who invented a type of stochastic calculus called Itô calculus. This thesis uses this form of stochastic calculus rather than the other popular type in physics: Stratonovich calculus.

timestep $\mathrm{d}t$ [62],

$$\mathrm{d}y_n = \frac{1}{\sqrt{8k_n}} \left\langle c_n + c_n^\dagger \right\rangle \mathrm{d}t + \frac{\mathrm{d}W_n}{\sqrt{8\eta k_n}}. \tag{5.8}$$

Here, k_n is the measurement rate, which determines the rate of information transferred about c_n across the measurement channel[6].

[6]Note that the measurement record contains information about the Hermitian observable $c_n + c_n^\dagger$. This respects the formalism of Chapter 1, namely that the outcomes of measurements correspond to the eigenvalues of Hermitian observables.

Chapter 6

Cavity quantum optomechanics

Optomechanics is the study of the interactions between field modes of light and field modes of mechanical oscillation. In this context, the main light-matter interaction this thesis focuses on is the *radiation-pressure* interaction. Radiation pressure[1] occurs when incident light reflects off a mechanical object: the light exerts pressure on the mechanical object due to transfer of momentum between the light and the mechanical object. An optomechanical system can be placed in a cavity to enhance the light-matter interaction, leading to the field of cavity optomechanics.

The theory of cavity optomechanics underpins a vast range of physical systems, including ultra cold atoms in a cavity [74, 75], superconducting LC circuits [76, 77], suspended membranes and nanowires in a cavity [78, 79], vibrating photonic crystal nanobeams [80, 81], nanomechanical oscillators evanescently coupled to whispering gallery mode resonators [82, 83], and the LIGO gravitational wave detectors in large scale interferometers [84, 85]. Furthermore, optomechanical platforms offer a wide ranges of applications [86, 87] including: weak force sensing [88, 89], optical-to-microwave transducers [90, 91], quantum state engineering [92, 93, 94], and tests of fundamental physics [95, 96]. In this chapter, I will begin by discussing the basic physics of cavity quantum optomechanics, before describing the different regimes of operation.

[1] It's often stated in the optomechanics literature (and on the "Radiation pressure" page of Wikipedia) that Kepler was the first to postulate the existence of a radiation-pressure force in his *De cometis libelli tres* (1619) to explain why comet tails are not tangent to their trajectory. However, Kepler attributed this phenomena to the Sun heating material from the comet, which was then blown away by a 'solar breeze' (not to be confused with the more modern concept of solar wind). I could not find any indication that he believed that this force was due momentum transfer from the Sun's *light* itself. Hooke presented more refined arguments for the explanation of comet tails in his *Cometa* (1678) [72]. However, Maxwell was the first to recognize that light can carry momentum and therefore exert pressure on a surface in the 1860s [73].

6.1 The optomechanical Hamiltonian

The Hamiltonian of cavity quantum optomechanics was rigorously derived by Law in Ref. [97]. However, to help see the physics, one may consider a Fabry-Pérot cavity as the phenomenological model of cavity quantum optomechanics to motivate the optomechanical Hamiltonian—see Fig. 6.1. In this model, a small moveable mechanical oscillator replaces one of the end mirrors of the Fabry-Pérot cavity.

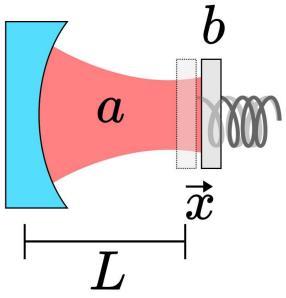


Figure 6.1: **A Fabry-Pérot as the phenomenological model of cavity quantum optomechanics.** The cavity mode a interacts with the mechanical mode b via radiation pressure. The mechanical object is displaced from its zero position by a distance x. Further, L is the length about which the operator x is defined, typically taken to be the equilibrium length of the cavity. The cavity mode modulates the position of the mirror x via a radiation-pressure force, which depends on the photon number, while the position of the mirror influences the phase of the cavity mode. Hence, to first order in position, this interaction is described by an interaction Hamiltonian $H_{\text{INT}} \propto a^\dagger a x$.

For a single cavity mode and single mechanical mode, the optomechanical Hamiltonian is given by [98, 99]

$$H = \hbar\omega_{\text{C}}(x)a^\dagger a + \hbar\omega_{\text{M}}b^\dagger b. \tag{6.1}$$

Here, ω_{M} is the angular frequency of the mechanical mode and the cavity frequency $\omega_{\text{C}}(x)$ is a function of the mechanical position operator x. This is because the cavity frequency is a function of the cavity length and therefore the mirror position[2], which depends upon the intensity of light in the cavity. For a given position, the length of the cavity is given by $L + x$, where L is the cavity length at zero mechanical position.

[2] When the cavity frequency $\omega_{\text{C}}(x)$ depends on the mechanical position, this is referred to as *dispersive optomechanics*. Another paradigm of optomechanics is *dissipative optomechanics*, where instead the cavity decay rate κ depends on the position x [100, 101]. However, in this thesis I will focus on the dispersive regime.

Practically speaking, the round trip time of a photon inside the cavity $2(L+x)/c$ will always be much shorter than the mechanical period of oscillation $2\pi/\omega_{\rm M}$, for any value of the operator x such that $\omega_{\rm M} \ll \pi c/(L+x)$ always holds [102]. In this case the cavity frequency will follow the mechanical position adiabatically[3], hence the time-independent relation is $\omega_{\rm C}(x) = \pi cn/(L+x)$. Here, $n \in \mathbb{Z}$ is the cavity mode number[4].

For the Fabry-Pérot, $\omega_{\rm C}(x)$ can be expanded in position when the spread of oscillator positions Δx satisfies $\Delta x/L < 1$. Hence, $\omega_{\rm C}(x)$ is

$$\omega_{\rm C}(x) = \frac{\pi cn}{L+x} = \frac{\pi cn}{L}\left(1 - \frac{x}{L} + \ldots\right) \tag{6.2}$$

The optomechanical Hamiltonian is therefore given by

$$\boxed{\begin{aligned} H &= \hbar\omega_{\rm C} a^\dagger a + \hbar\omega_{\rm M} b^\dagger b - \hbar g_0 a^\dagger a(b+b^\dagger) \\ &= H_0 + H_{\rm INT}, \\ H_0 &= \hbar\omega_{\rm C} a^\dagger a + \hbar\omega_{\rm M} b^\dagger b, \\ H_{\rm INT} &= -\hbar g_0 a^\dagger a(b+b^\dagger), \end{aligned}} \tag{6.3}$$

to linear order in x. Here, $\omega_{\rm C} = \omega_{\rm C}(0)$ and for the Fabry-Pérot $g_0 = \omega_{\rm C} x_0/(\sqrt{2}L)$ is the *optomechanical coupling rate*, which is the change in the cavity frequency when the mechanics is displaced by the width of the quantum ground state $\Delta x = x_0/\sqrt{2}$. For a general optomechanical system, the same optomechanical Hamiltonian as Eq. (6.3) will hold but with $g_0 = -x_0 \frac{\partial\omega_{\rm C}(x)}{\partial x}|_{x=0}/\sqrt{2}$.

6.1.1 Quadratic coupling to position and beyond

Instead, if the cavity frequency is expanded to second order, one has

$$\omega_{\rm C}(x) = \frac{\pi cn}{L+x} \approx \frac{\pi cn}{L}\left(1 - \frac{x}{L} + \frac{x^2}{L^2}\right), \tag{6.4}$$

which leads to an interaction Hamiltonian of the form

$$H_{\rm INT} \quad = \quad -\hbar a^\dagger a\left[g_0^{(1)}(b+b^\dagger) + g_0^{(2)}(b+b^\dagger)^2\right]. \tag{6.5}$$

Here, g_0 has been replaced by $g_0^{(1)}$ for clarity, while $g_0^{(2)}$ is the *second-order optomechanical coupling rate*. The second order term in x is crucial in explaining the physics of certain optomechanical systems. These include membrane-in-the-middle systems [104, 105], which achieve $g_0^{(1)} = 0$ by placing the membrane at a

[3] Note that same adiabatic condition $\omega_{\rm M} \ll \pi c/(L+x)$ is equivalent to the cavity mode spacing $\Delta\omega_{\rm C} = \pi c/(L+x)$ (free spectral range) being much greater than the mechanical frequency $\omega_{\rm M}$. Hence, the condition $\omega_{\rm M} \ll \pi c/(L+x)$ also implies that the optomechanical scattering of photons into neighbouring optical modes is negligible and the single optical mode analysis is valid [103].

[4] Not to be confused with the group velocity refractive index; one may divide the speed of light c by the group index to generalize the derivation presented here.

point in the cavity where $\frac{\partial\omega_{\rm C}(x)}{\partial x}|_{x=0} = 0$, and systems where both the first and second order coupling terms are appreciable [106, 107].

For the case of the Fabry-Pérot system, $g_0^{(1)} = \omega_{\rm C}x_0/(\sqrt{2}L)$ and $g_0^{(2)} = \omega_{\rm C}x_0^2/(2L^2)$. This thesis will often be concerned with mechanical oscillators which are well described by quantum physics at low temperatures, hence we may consider a range of mechanical oscillations $\Delta X \sim 1$. The ratio of the first and second order coupling terms is then $g_0^{(2)}/g_0^{(1)} = x_0/(\sqrt{2}L)$. Therefore, the condition for Eq. (6.3) to be an accurate description is $x_0/(\sqrt{2}L) = g_0/\omega_{\rm C} \ll 1$, which is easily met in many systems.

More generally, the condition for the second order coupling to be small is $g_0^{(2)}\Delta X/g_0^{(1)} \ll 1$. For a mechanical oscillator in a thermal state[5], $\Delta X_{\rm M} \sim \sqrt{\bar{n}}$ and so the condition is now $g_0^{(2)}\sqrt{\bar{n}}/g_0^{(1)} \ll 1$. For mechanical oscillators in large thermal states and for specific systems where $g_0^{(2)} \lesssim g_0^{(1)}$, the condition $g_0^{(2)}\sqrt{\bar{n}}/g_0^{(1)} \ll 1$ may now be not so easily met. Indeed, in Ref. [108], which operated near room temperature, a value of $g_0^{(2)}\sqrt{\bar{n}}/g_0^{(1)} \sim 2\times10^{-4}$ was achieved, which was already sufficient to observe differences from Eq. (6.3) in the optical spring effect[6].

Due to the wide number of different platforms and parameters to play with in optomechanics [109], it is therefore important to study the physics of both Eq. (6.3) and (6.5), as there will be many experiments where one description is valid and the other is not. Therefore, in Part III a theoretical framework that is capable of describing any arbitrary coupling to position is developed, which may include linear couplings, quadratic couplings, and beyond.

6.2 Regimes of optomechanics

6.2.1 The strong coupling and ultra-strong coupling regimes

The optomechanical single-photon *strong coupling regime*[7] is defined by $g_0 > \{\kappa, \gamma\}$ [110, 111]. In this regime, the rate of the nonlinear optomechanical interaction dominates over both the optical and mechanical decay rates, allowing for the preparation of non-Gaussian quantum states of light and mechanics in the steady state [44]. Theoretically, single-photon strong coupling has garnered much interest, while experimental systems with higher and higher ratios of g_0/κ and g_0/γ are being realized [112, 113, 114]. Furthermore, the *single-photon cooperativity* $C_0 = g_0^2/\kappa\gamma$ is an important quantity in many continuously driven optomechanical systems and has shown to be a genuine figure of merit for generating non-Gaussian states [115].

Meanwhile, we define single-photon *quantum-coherent coupling* as $g_0 > \{\kappa, \bar{N}\gamma\}$. From Chapter 3, we know that $\bar{N}\gamma$ represents the mechanical thermal decoher-

[5] Note that one could also choose a squeezed state with a large $\Delta X_{\rm M}$ to illustrate this point.

[6] Optical spring effect: change in the effective mechanical frequency due to the radiation-pressure interaction.

[7] Single-photon weak coupling is defined by $g_0 < \{\kappa, \gamma\}$.

ence rate. Single-photon quantum-coherent coupling is therefore an important requirement to generate steady-state mechanical Wigner negativity via the nonlinear optomechanical interaction itself. In Part II of this thesis, the ratio of g_0/κ is of interest for engineering interesting quantum states, however, single-photon quantum-coherent coupling, or $C_0 > \{1, \bar{N}\}$ is not required, as a number of techniques will be utilized including short pulsed interactions and state preparation by measurement.

One may also define the optomechanical single-photon *ultra-strong coupling regime* as $g_0 \gtrsim \{\omega_{\rm M}, \kappa\}$ [116, 117]. If Eq. (6.3) is rewritten in terms of the position and momentum quadratures as

$$H = \hbar\omega_{\rm C} a^\dagger a + \frac{\hbar\omega_{\rm M}}{2}\left(X_{\rm M}^2 + P_{\rm M}^2\right) - \hbar\sqrt{2} g_0 a^\dagger a X_{\rm M}, \tag{6.6}$$

the quantity $\sqrt{2}g_0/\omega_{\rm M}$ appears as the dimensionless mechanical displacement in position due to one photon trapped inside the cavity [92]. This can be seen heuristically by setting $a^\dagger a$ to one and completing the square in the above equation to give

$$H_{\rm M}^{(1)} = \frac{\hbar\omega_{\rm M}}{2}\left[\left(X_{\rm M} - \sqrt{2}\frac{g_0}{\omega_{\rm M}}\right)^2 + P_{\rm M}^2\right], \tag{6.7}$$

where $H_{\rm M}^{(1)}$ is the mechanical Hamiltonian in the subspace of 1 photon [118]. Further, note that the optical and interaction part of the optomechanical Hamiltonian can be written as $\hbar\left(\omega_{\rm C} - \sqrt{2}g_0 X_{\rm M}\right) a^\dagger a$ and so when $g_0/\kappa \gtrsim 1$, a mechanical displacement on the order of the zero-point fluctuations cause a shift in the cavity frequency on the order of κ or larger. Thus, the optomechanical single-photon blockade may be achieved in the ultra-strong coupling regime, where a single photon shifts the resonant frequency of the cavity enough that another photon is now off-resonant with the cavity [118, 119, 120]. For completeness, single-photon *deep-strong coupling*[8] is defined as $g_0 > \{\omega_{\rm M}, \kappa\}$. Furthermore, one can define corresponding strong coupling regimes for quadratic coupling of the photon number to the mechanical position operator: i.e. replace g_0 by $g_0^{(2)}$.

Finally, in the optomechanics literature some works use the terms *strong coupling*, *ultra-strong coupling*, and *deep-strong coupling* interchangeably. This is because the ratio $\omega_{\rm M}/\kappa$ is typically also stated which removes any ambiguity. Here, I use separate terms for easier comparison to the wider field of quantum light-matter interactions as in Ref. [121].

Linearized optomechanics

As is more commonly done in the optomechanics community, one can also define the strong, quantum-coherent, ultra-strong, and deep strong coupling regimes in terms of an enhanced coupling rate $g = \alpha_{\rm c} g_0$, where $\alpha_{\rm c}$ is the mean intracavity

[8] The optomechanical single-photon photon blockade does not require deep strong coupling as it depends on $g_0/\omega_{\rm M}$, $\kappa/\omega_{\rm M}$, *and* the laser detuning [119].

amplitude. However, this enhancement requires a linearized approximation to be made to the optomechanical interaction, which prohibits the generation of non-Gaussian states via the optomechanical interaction itself—see Section 6.3. Strong coupling has been achieved in the linearized regime with a range of optomechanical devices [122, 123, 124]. A signature of strong coupling in the linear regime is normal-mode splitting observed in the output noise power spectrum [125]. Furthermore, quantum-coherent coupling has also been explored across various devices in the linearized regime [126, 127]. Finally, ultra-strong coupling has been observed in the linearized regime via single-molecule optomechanics in picocavities [128].

Furthermore, one can also define the *linearized optomechanical cooperativity* $C = |\alpha_{\rm c}|^2 C_0$, which is also an important quantity in many continuously driven optomechanical systems. For example, to transduce quantum states of light via a mechanical mode with the linearized optomechanical interaction, one requires that $C > \bar{N}$ [129]. One can identify $2g^2/\kappa$ as the rate of transduction in a continuously driven system [130]. The condition $C > \bar{N}$ therefore states that for efficient quantum optomechanical transduction, the optomechanical state swap rate $2g^2/\kappa$ must be larger than the mechanical decoherence rate $\bar{N}\gamma$. Note that $2g^2/\kappa$ is also the linear measurement rate $k_{\rm L}$ in continuously driven optomechanics as I will discuss in Section 6.3.3. The rate at which phonons and photons are swapped is therefore equal to the rate at which information is imprinted on the optical field about the mechanical mode.

6.2.2 The large optomechanical phase shift regime

Having briefly described the strong coupling regime, I now introduce the particular regime of interest for Part III of this thesis, which we term the *large optomechanical phase shift regime*. This regime is defined by $g_0\sqrt{\langle X_{\rm M}^2\rangle}/\kappa \gtrsim 0.1$, which can be understood as the condition for a small-angle approximation to break down as follows. Namely, in *nonlinear optomechanics*, see Section 6.4, $g_0\sqrt{\langle X_{\rm M}^2\rangle}/\kappa$ quantifies the optical phase shift as light passes in and out of an optomechanical cavity. Such optical phase shift correspond to rotations in optical phase space. For large intracavity amplitudes and when $g_0\sqrt{\langle X_{\rm M}^2\rangle}/\kappa \ll 1$, a small angle approximation may be utilized and these optomechanical phase rotations are well approximated by a displacement along the phase amplitude quadrature of light, which are requirements of the regime of *linearized optomechanics*.

Part III focuses on the large phase shift regime when Eq (6.3) is valid. Experiments such as Refs [74, 131, 132, 133, 134, 135] operate in such a regime.

6.2.3 The sideband-resolution parameter: cooling, heating, and measurements

The sideband-resolution parameter is given by $\omega_{\rm M}/\kappa$. Systems with $\omega_{\rm M} \gg \kappa$ are said to operate in the *resolved sideband regime*, while systems with $\kappa \gg \omega_{\rm M}$

operate in the *unresolved sideband regime*. I now briefly motivate the sideband resolution parameter as a useful quantity.

Resolved sideband regime

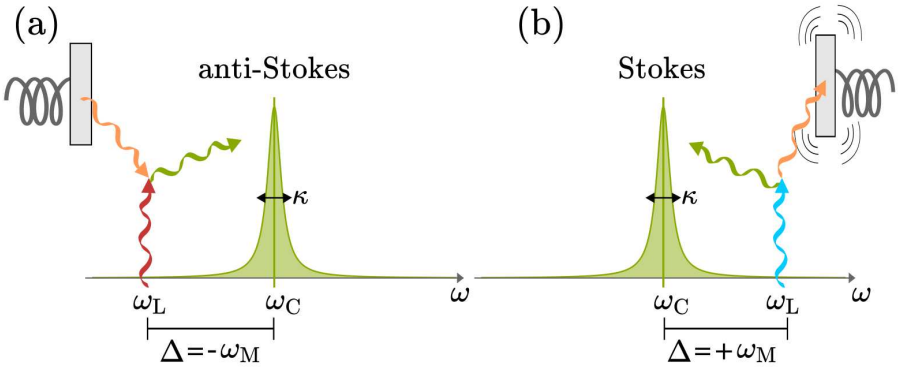


Figure 6.2: **Stokes and anti-stokes scattering in the resolved sideband regime.** A cavity is driven at ω_{L}, which is detuned by $\Delta = \omega_{\mathrm{L}} - \omega_{\mathrm{C}}$ from the cavity frequency ω_{C}. The cavity spectrum, centred at ω_{C}, is plotted (in green) as a function of frequency ω. The width of this spectrum κ satisfies $\omega_{\mathrm{M}} \gg \kappa$, so that a drive on the red ($\Delta = -\omega_{\mathrm{M}}$) and blue ($\Delta = +\omega_{\mathrm{M}}$) is well outside the cavity Lorentzian. (a) Driving on the red sideband ($\Delta = -\omega_{\mathrm{M}}$) preferentially selects the anti-Stokes scattering of photons into the cavity mode as the cavity spectrum enhances these processes. This takes energy away from the mechanical oscillator, which leads to cooling. (b) Driving on the blue sideband ($\Delta = +\omega_{\mathrm{M}}$) enhances Stokes scattering into the cavity mode, which leads to amplification of the mechanical oscillations. Here, the orange arrow represents a mechanical phonon at ω_{M}, green corresponds to a cavity photon at ω_{C}, and the drive photons are red in (a) and blue in (b).

The optomechanical interaction couples light and mechanics and therefore allows for the interconversion of quanta of light and mechanics. Consider the case where the cavity is driven at a frequency ω_{L} detuned from the cavity frequency by $\Delta = \omega_{\mathrm{L}} - \omega_{\mathrm{C}}$. Due to the finite cavity width κ, the drive photon may enter the cavity despite being off resonance. Two commonly studied interactions are: (i) *Stokes scattering*—a drive photon may then be converted into a cavity photon at ω_{C} and a mechanical phonon ω_{M} if $\omega_{\mathrm{L}} = \omega_{\mathrm{C}} + \omega_{\mathrm{M}}$ ($\Delta = +\omega_{\mathrm{M}}$) is satisfied, and (ii) *anti-Stokes scattering*—a drive photon and a mechanical phonon may be converted into a cavity photon if $\omega_{\mathrm{L}} + \omega_{\mathrm{M}} = \omega_{\mathrm{C}}$ ($\Delta = -\omega_{\mathrm{M}}$). Stokes scattering introduces quanta of energy to the mechanical mode of oscillation, while anti-Stokes scattering removes phonons from the oscillator. If the

sidebands are resolved, $\omega_{\rm M} \gg \kappa$, the scattering of light into the cavity mode is preferentially enhanced and the (anti-)Stokes process dominates over other scattering processes. However, if the sidebands aren't resolved, other scattering processes have a significant probability of occurring too—some of these processes will swap quanta into the mechanical mode, while other will swap quanta out of the mechanical mode. For a continuously driven sideband resolved system, driving on the red-detuned mechanical sideband ($\Delta = -\omega_{\rm M}$) enhances anti-Stokes scattering into the cavity mode, which leads to mechanical cooling [136], while driving on the blue-detuned mechanical sideband ($\Delta = \omega_{\rm M}$) enhances Stokes scattering into the cavity mode, which leads to mechanical amplification [137]. This is illustrated by Fig. 6.2. As it is difficult to preferentially enhance the anti-Stokes process in an unresolved sideband system, other cooling strategies should be employed—see below.

Unresolved sideband regime

The unresolved sideband regime $\kappa \gg \omega_{\rm M}$ is favourable for position measurements of the mechanical oscillator and is sometimes referred to as the *good measurement regime* [138]. In the unresolved sideband regime, the cavity field can be adiabatically eliminated $\dot{a} = 0$, which leads to an input-output relation of the form $a_{\rm out}(t) = f(X_{\rm M})a_{\rm in}(t)$, where f is the $X_{\rm M}$-dependent cavity response function. Measurement of the output field at time t then tells the observer about the mechanical oscillator at that time t also[9]. This allows one to derive a SME for the mechanical oscillator that describes a weak continuous measurement, whereas without adiabatic elimination of the cavity mode, the SME must also describe the cavity mode and its correlations with the mechanical mode. See Part III for more details on the adiabatic approximation and the derivation of the SMEs in this regime. Depending on the ratio of the measurement rate to the mechanical frequency, one can cool states close to the quantum ground state or prepare squeezed states via continuous position measurement—see Section 14.2.2.

Pulsed optomechanics requires $\tau_{\rm in}^{-1} \gg \omega_{\rm M}$, where $\tau_{\rm in}$ is the temporal width of the input pulse, and hence naturally operates in the unresolved sideband regime when $\kappa \sim \tau_{\rm in}$ or $\kappa \gg \tau_{\rm in}$. Interestingly, pulsed optomechanics can be also used to cool the mechanical mode—see Section 6.3 and Refs [139] and [140]. This cooling mechanism relies on a distinct principle compared to continuously driven systems. There, the standard continuous cooling utilizes the anti-Stokes scattering process, which relies on the interconversion of photons and phonons. Instead, cooling via pulsed optomechanics effectively squeezes the mechanical mode into a cooled state over a series of optomechanical interactions and measurements.

[9] Of course, to satisfy the no-signalling condition, this condition is not strictly true as the finite travel time of light has been ignored. However, this travel time will typically be much much shorter than all other relevant timescales.

6.3 Linearized cavity optomechanics and when it applies

In the single-photon weak coupling regime, it is common that the nonlinear optomechanical interaction term in Eq. (6.3) is linearized about some mean intracavity amplitude $\langle a \rangle = \alpha_c$. This process effectively boosts the optomechanical coupling rate from g_0 to the *linearized optomechanical coupling strength* $g = |\alpha_c| g_0$ at the expense of linearizing the optomechanical interaction.

Physically, linearization is achieved by sending in a large number of photons into the cavity, subject to certain conditions—see discussion on the validity of the linearization procedure below. Mathematically, this corresponds to moving into a displaced frame about α_c: $D^\dagger(\alpha_c) a D(\alpha_c) = \alpha_c + a$. In this new frame, it is assumed that $|\alpha_c| \gg |\langle a \rangle|$, i.e. a represents some small quantum fluctuations, described by field operator a, on top of a large classical mean field $\alpha_c \in \mathbb{C}$. Hence, in this new displaced frame the interaction term in Eq. (6.3) transforms to

$$
\begin{aligned}
H_{\text{INT}} &= -\hbar g_0 \alpha_c^2 (b + b^\dagger) - \hbar g (a + a^\dagger)(b + b^\dagger) - \hbar g_0 a^\dagger a (b + b^\dagger) && (6.8)\\
&\approx H_{\text{K}} + H_{\text{LIN}}, && (6.9)\\
H_{\text{K}} &= -\hbar g_0 \alpha_c^2 (b + b^\dagger), && (6.10)\\
H_{\text{LIN}} &= -\hbar g (a + a^\dagger)(b + b^\dagger). && (6.11)
\end{aligned}
$$

Here, $\alpha_c \in \mathbb{R}$ is assumed without loss of generality as it simply sets the phase reference for the optical field. The term H_{K} represents a Kerr-like effect, where the cavity length depends on the intensity of the mean field. This term leads to interesting phenomena in classical optomechanics, for example optical bistability[10], which was observed in optomechanics as early as 1983 [141]. For the purposes of this thesis however, the term H_{K} can be transformed away by shifting the mechanical position coordinate to coincide with the new equilibrium cavity length at $x = 0$. Moreover, the term H_{LIN} represents a linear coupling between the cavity field a and the mechanical mode b. Importantly, it has been assumed the term $\hbar g_0 a^\dagger a (b + b^\dagger)$ can be dropped from the Hamiltonian as it depends quadratically on the cavity field operator a in the displaced frame, which is assumed to take only small values—see Section 6.3.1.

6.3.1 Validity of the linearization procedure and beyond

Note this section contains many spoilers for theory introduced in later sections of this thesis. However, it is instructive to take a sneak peak at some results so the reader is able to answer questions such as "does this equation apply to this physical system?" or "are these nonlinear terms even relevant to this system?". Importantly, the unitaries introduced in this section include the input-output theory of the cavity.

[10] Optical bistability: the existence of two stable solutions of the intracavity mean photon number $|\alpha_c|^2$.

Validity of the linearization procedure

To see where the linear approximation breaks down, it is simplest to borrow a result from Part III. The optomechanical interaction, including the effects of the cavity, is described by the unitary $U = \mathrm{e}^{\mathrm{i}\varphi(X_\mathrm{M})n_\mathrm{L}}$, where $\varphi(X_\mathrm{M})$ is the nonlinear X_M-dependent optical phase shift and n_L is the number operator of the field entering or leaving the cavity. For a pulsed interaction, n_L is defined over the entire temporal envelope, while in the continuous case n_L (and therefore the unitary $U = \mathrm{e}^{\mathrm{i}\varphi(X_\mathrm{M})n_\mathrm{L}}$ too) is defined over an infinitesimal $\mathrm{d}t$.

However, as discussed below there is an intermediate regime between linear optomechanics and the exact theory, where the nonlinear phase is approximated to first order in position: $\varphi(X_\mathrm{M}) \approx \mu X_\mathrm{M}$. Here,

$$\mu = \frac{\sqrt{8}g_0}{\kappa} \tag{6.12}$$

is the *nonlinear optomechanical coupling strength*. In this case, the above unitary becomes $U = \mathrm{e}^{\mathrm{i}\mu n_\mathrm{L} X_\mathrm{M}}$. Again, this unitary is either defined over: (i) the entire temporal envelope for a pulsed interaction, or (ii) a $\mathrm{d}t$ for a continuous interaction. Consider then the effect of the unitary on an initial input optical coherent state $|\alpha\rangle$, with $\alpha = X_\alpha/\sqrt{2} \in \mathbb{R}$. The mechanical position-dependent optical rotation is shown in Fig. 6.3 for a given position X_M. Of course, the mechanical position operator can take a continuum of values and the variance in position is denoted by σ^2.

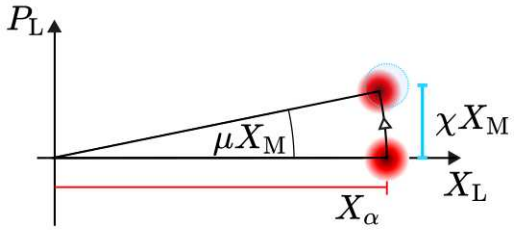


Figure 6.3: **Validity of linearized optomechanics.** Here, an optical coherent state $|\alpha\rangle$, with $\alpha = X_\alpha/\sqrt{2} \in \mathbb{R}$, rotates through a phase space angle μX_M. More precisely, the initial optical state represented by the red blob at $X_\mathrm{L} = X_\alpha$, $P_\mathrm{L} = 0$ rotates through an angle μX_M to the second red blob at $X_\mathrm{L} = X_\alpha \cos \mu X_\mathrm{M}$, $P_\mathrm{L} = X_\alpha \sin \mu X_\mathrm{M}$. This rotation may be modelled by the nonlinear optomechanical unitary $U = \mathrm{e}^{\mathrm{i}\mu n_\mathrm{L} X_\mathrm{M}}$. If the optical rotation is sufficiently small, the rotation may be approximated by a displacement along the P_L axis of phase space–see the blue line and faint blue blob. This displacement is described by the linearized optomechanical unitary $U = \mathrm{e}^{\mathrm{i}\chi X_\mathrm{L} X_\mathrm{M}}$.

Fig. 6.3 shows the optical coherent state rotates through an angle μX_M as it enters and leaves the cavity. The arc length scribed in phase space is given by

$\mu X_{\rm M} X_\alpha = \chi X_{\rm M}$. As $\mu = \sqrt{8} g_0/\kappa$ and the mean incident[11] photon number over the interaction is $N_{\rm P} = |\alpha|^2 = X_\alpha/2$, χ is

$$\chi = \frac{\sqrt{8} g_0 X_\alpha}{\kappa} = \frac{4 g_0 \sqrt{N_{\rm P}}}{\kappa}. \tag{6.13}$$

Here, χ is the *linearized optomechanical coupling strength*[12]. For small optical rotations $\mu X_{\rm M} \ll 1$—which becomes $\mu\sigma \ll 1$ if the range of possible $X_{\rm M}$ values is considered—the arc is well approximated by a vertical line in phase space parallel to the phase $P_{\rm L}$ axis [11]. Hence, when $\mu\sigma \ll 1$ the unitary $U = {\rm e}^{{\rm i}\mu n_{\rm L} X_{\rm M}}$ may be approximated by the linearized optomechanical unitary $U = {\rm e}^{{\rm i}\chi X_{\rm L} X_{\rm M}}$ as this unitary generates optical phase space displacements along the phase $P_{\rm L}$ axis—see the blue line in Fig. 6.3. Again this unitary is either defined over the temporal pulse for a pulsed interaction, or over a dt for a continuously driven system. See Section 6.3.2 for more details.

Linearization requires large intracavity amplitudes

It is important to remember that even if $\mu\sigma \ll 1$, if $X_\alpha \sim 1$ then linearized optomechanics is *not* valid. In which case, one should turn to the exact theory described by $U = {\rm e}^{{\rm i}\varphi(X_{\rm M}) n_{\rm L}}$. A small value of X_α implies a small intracavity field $|\alpha_{\rm c}| \sim 1$. In order to derive the linearized Hamiltonian $H_{\rm LIN}$, it was assumed that $|\alpha_{\rm c}| \gg |\langle a \rangle|$ in the displaced frame. However, if $|\alpha_{\rm c}| \sim 1$ this initial assumption is no longer valid.

To summarize, linearized cavity optomechanics requires $|\alpha_{\rm c}| \gg |\langle a \rangle|$ and $\mu\sigma \ll 1$. For this reason, one may also refer to linearized optomechanics as the regime of small optomechanical phase shifts (see Section 6.2.2) provided $X_\alpha \gg 1$.

Hierarchy of approximations in this thesis

When the nonlinear quantum optomechanical Hamiltonian of Eq. (6.3) holds, a hierarchy of approximations may be identified. Here, I assume the common scenario of an initial mechanical Gaussian state of width σ and $\langle X_{\rm M} \rangle = 0$ and a large input optical amplitude $X_\alpha \gg 1$, which allows this hierarchy to be parametrized simply by $\mu\sigma$. Note that if the mechanical state is prepared with a mean very far from zero, one should use the exact case so the cavity response, including the π-phase shift limit, is properly modelled—see below.

Most approximated regime: Linearized cavity optomechanics.— Valid if $\mu\sigma \ll 1$ so the optical rotation generated by the $a^\dagger a X_{\rm M}$ interaction is sufficiently well described by a displacement along the phase quadrature. In this regime, the coupling between the mechanics and optics is linear $(a + a^\dagger)(b + b^\dagger)$ so only Gaussian states can be generated by this interaction. The discussion from the

[11] The reader should not confuse the amplitude of the incident field α with the intracavity amplitude $\alpha_{\rm c}$.

[12] A reader who has read ahead will notice that I am implicitly assuming an adiabatic cavity in this discussion.

previous section, together with the results of Ref. [7], imply that linear optomechanics is described by the unitary $U = e^{i\chi X_M X_L}$.

Middleground: Cavity-free nonlinear optomechanics.— Valid if $\mu\sigma \lesssim 1$, or more precisely, if the cubic term in μX_M in Eq. (6.101) is much less than the linear term. This regime captures the inherent nonlinearity of optomechanics. However, this regime does not account for the nonlinear phase response of the cavity as in Ref. [7]. Moreover, for large optical rotations $\mu\sigma > 1$, the unitary $U = e^{i\mu n_L X_M}$ predicts the optical phase shift from the cavity can be arbitrarily large. This is not physical as when the mechanical position deviates so far as to make the incoming light completely off resonant, the light should simply reflect off the input mirror and acquire a π phase shift.

Exact case: Cavity-enhanced nonlinear optomechanics.— Always valid providing Eq. (6.3) holds and the cavity is one-sided[13]. Furthermore, the unitary $U = e^{i\varphi(X_M)n_L}$ applies for any value of X_α, even if $X_\alpha \sim 1$. The nonlinear optical X_M-dependent phase becomes significantly different from μX_M when $\mu\sigma \sim 1$—see Eq. (6.101). However, for small optical rotations, while this exact description is completely accurate, it may be unnecessarily complicated. Note that $\mu\sigma \sim 1$ describes the large optomechanical phase shift regime of Section 6.2.2, but is also needed for small optomechanical phase shifts if $X_\alpha \sim 1$.

6.3.2 Pulsed optomechanics

History of pulsed optomechanics theory

Vladimir Braginsky and co-workers introduced the idea of classical pulsed optomechanics in the context of gravitational wave detection [142, 143, 144]. By using short pulses of light, much shorter than the mechanical period, back-action evading measurements of mechanical position can be performed. In other words, the pulsed interaction is much shorter than the free harmonic evolution of the mechanical oscillator. Hence, information can be extracted about the mechanical position via the optical pulse before the momentum back action noise[14] can evolve into mechanical position. Braginsky called these types of interactions *stroboscopic quantum non-demolition interactions*[15], which is why some works may refer to pulsed optomechanics as stroboscopic optomechanics.

In Ref. [139], M.R.V. and colleagues utilized pulsed optomechanics to explore the quantum regime. Specifically, in this work the mechanical mode is treated quantum mechanically and the pulsed optomechanical interaction $U = e^{i\chi X_M X_L}$ derives from the linearized regime of optomechanics. This section describes linearized pulsed optomechanics in some detail, but before I turn to this I will take the opportunity to describe the next key steps in pulsed optomechanics.

Pulsed quantum optomechanics was then brought into the nonlinear regime by I.P. and co-workers in Ref. [145]. The nonlinear cavity-free unitary $U =$

[13] Although note that intrinsic cavity losses can be modelled by a beamsplitter model for loss as discussed in Chapter 3 to remedy this.

[14] Simply due to the radiation-pressure force on the oscillator.

[15] In this thesis, back action evasion (BAE) and quantum non-demolition (QND) are often used synonymously.

$e^{i\mu X_M n_L}$, discussed in the previous section, was introduced in this work. Finally, in Ref [7], and throughout this thesis, we introduce the cavity-enhanced unitary described by $U = e^{i\varphi(X_M)n_L}$.

The linearized optomechanical pulsed interaction

First, I present a derivation of the linearized optomechanical unitary $U = e^{i\chi X_M X_L}$ inspired by the derivation from Bennett *et al.* in Ref. [146]. Interestingly, Ref. [146] details how a series of pulsed optomechanical linearized interactions can be used to swap the states of light and mechanics.

Inserting, $H_{\rm LIN}$ into Eqs (3.3), (3.40), and (3.41) gives

$$\dot{a} = i\sqrt{2}gX_M - \kappa a + \sqrt{2\kappa}a_{\rm in}, \tag{6.14}$$

$$\dot{X}_M = 0, \tag{6.15}$$

$$\dot{P}_M = \sqrt{2}g(a + a^\dagger). \tag{6.16}$$

Importantly, the free evolution and dissipation of the mechanical mode has not been included. This is because in pulsed optomechanics the interaction time is much shorter than the mechanical period and so the mechanical position X_M is time-independent over the interaction. For an input pulse of temporal width $\tau_{\rm in}$, pulsed optomechanics requires $\tau_{\rm in}^{-1} \gg \omega_M$. Furthermore, pulsed optomechanics assumes either long pulses $\kappa \gg \tau_{\rm in}^{-1}$ [147, 146] or short pulses $\kappa \sim \tau_{\rm in}^{-1}$ [139] so $\kappa \gtrsim \tau_{\rm in}^{-1}$ is always guaranteed. Hence, pulsed optomechanics naturally coincides with the unresolved sideband regime or 'good measurement regime' of optomechanics $\kappa \gg \omega_M$. Here, the detuning is also taken to be zero $\Delta = 0$. See Ref. [7] for equations with the detuning included.

The cavity field a can then be adiabatically[16] eliminated $\dot{a} = 0$ if $\kappa \gg \tau_{in}^{-1}$. From Eq. (6.14), the relation between the input field $a_{\rm in}$ and the adiabatic cavity mode is then

$$a(t) = i\frac{\sqrt{2}g}{\kappa}X_M + \sqrt{\frac{2}{\kappa}}a_{\rm in}(t). \tag{6.17}$$

Using the input-output relation $a_{\rm out}(t) = \sqrt{2\kappa}a(t) - a_{\rm in}(t)$ gives

$$a_{\rm out}(t) = a_{\rm in}(t) + i\sqrt{\frac{4g^2}{\kappa}}X_M. \tag{6.18}$$

Meanwhile, the quadrature noise operators of the input and output modes are

[16] For more details on the the adiabatic approximation see Part III.

defined as

$$X_{\rm L}^{\rm in} = \frac{1}{\sqrt{2}}\left(a_{\rm in}+a_{\rm in}^{\dagger}\right), \tag{6.19}$$

$$X_{\rm L}^{\rm out} = \frac{1}{\sqrt{2}}\left(a_{\rm out}+a_{\rm out}^{\dagger}\right), \tag{6.20}$$

$$P_{\rm L}^{\rm in} = -\frac{\rm i}{\sqrt{2}}\left(a_{\rm in}-a_{\rm in}^{\dagger}\right), \tag{6.21}$$

$$P_{\rm L}^{\rm out} = -\frac{\rm i}{\sqrt{2}}\left(a_{\rm out}-a_{\rm out}^{\dagger}\right). \tag{6.22}$$

$$\tag{6.23}$$

Introducing the temporal envelope of the pulse to be $f(t)$ with $\int\ {\rm d}t|f(t)|^2=1$, one can define the dimensionless input and output quadrature operators as

$$X_{\rm L} = \int\ {\rm d}t f(t) X_{\rm L}^{\rm in}(t), \tag{6.24}$$

$$X_{\rm L}' = \int\ {\rm d}t f(t) X_{\rm L}^{\rm out}(t), \tag{6.25}$$

$$P_{\rm L} = \int\ {\rm d}t f(t) P_{\rm L}^{\rm in}(t), \tag{6.26}$$

$$P_{\rm L}' = \int\ {\rm d}t f(t) P_{\rm L}^{\rm out}(t). \tag{6.27}$$

Remembering that $g=\alpha_{\rm c}g_0$, and that in this system $\alpha_{\rm c}$ is generally time dependent[17], Eq. (6.18) allows one to arrive at the input-output relations for the optical quadratures

$$X_{\rm L}' = X_{\rm L}, \tag{6.28}$$

$$P_{\rm L}' = P_{\rm L}+\sqrt{\frac{8g_0^2}{\kappa}}\int\ {\rm d}t\alpha_{\rm c}(t)f(t)\ X_{\rm M}. \tag{6.29}$$

Importantly, one can define the mean photon number of the input pulse as the integral over the input flux $|\alpha_{\rm in}(t)|^2$ or the integral over the pulsed envelope

$$\begin{aligned} N_{\rm P} &= \alpha^2 \\ &= \int\ {\rm d}t|\alpha_{\rm in}(t)|^2 \\ &= N_{\rm P}\int\ {\rm d}t|f(t)|^2. \end{aligned} \tag{6.30}$$

Hence, $\alpha_{\rm in}(t)=\sqrt{N_{\rm P}}f(t)$. Further, using the relation $\alpha_{\rm c}(t)=\sqrt{\frac{2}{\kappa}}\alpha_{\rm in}(t)$ from Appendix E, which is valid in the linear regime of optomechanics $\mu\sigma\ll 1$, one

[17] Even though the cavity is adiabatic, the cavity field will still follow the input pulse shape. Furthermore, in what follows $\alpha_{\rm c}\in\mathbb{R}$ is taken, which simply sets the phase reference and implies $\{\alpha_{\rm in},f(t)\}\in\mathbb{R}$. See Appendix E.

then has

$$\begin{aligned} P'_{\mathrm{L}} &= P_{\mathrm{L}} + \frac{4g_0}{\kappa}\int \mathrm{d}t\alpha_{\mathrm{in}}(t)f(t)\ X_{\mathrm{M}} \\ &= P_{\mathrm{L}} + \frac{4g_0\sqrt{N_{\mathrm{P}}}}{\kappa}\int \mathrm{d}t f^2(t)\ X_{\mathrm{M}} \\ &= P_{\mathrm{L}} + \chi X_{\mathrm{M}}. \end{aligned} \tag{6.31}$$

Here, the formula $\chi = \frac{4g_0\sqrt{N_{\mathrm{P}}}}{\kappa}$ for the linearized optomechanical coupling strength has been used.

Turning now to the equation of motion for the mechanical momentum, integrating Eq. (6.16) over the pulsed interaction, employing Eq. (6.17), and using the definition of X_{L} gives

$$\begin{aligned} P'_{\mathrm{M}} &= P_{\mathrm{M}} + \sqrt{2}g_0\int \mathrm{d}t\alpha_{\mathrm{c}}(t)(a+a^\dagger) \\ &= P_{\mathrm{M}} + \frac{2g_0}{\sqrt{\kappa}}\int \mathrm{d}t\alpha_{\mathrm{c}}(t)(a_{\mathrm{in}}+a_{\mathrm{in}}^\dagger) \\ &= P_{\mathrm{M}} + \frac{2\sqrt{2}g_0\sqrt{N_{\mathrm{P}}}}{\kappa}\int \mathrm{d}t f(t)(a_{\mathrm{in}}+a_{\mathrm{in}}^\dagger) \\ &= P_{\mathrm{M}} + \chi X_{\mathrm{L}} \end{aligned} \tag{6.32}$$

Here, P'_{M} is the mechanical momentum after the pulsed interaction, while P_{M} is the mechanical momentum before the interaction. Note that as the mechanical position is constant during the interaction, Eq. (6.15) implies

$$X'_{\mathrm{M}} = X_{\mathrm{M}}. \tag{6.33}$$

All together, Eqs (6.28), (6.31), (6.32), and (6.33) agree with the Heisenberg transformations

$$X'_{\mathrm{L}} = U^\dagger X_{\mathrm{L}} U = X_{\mathrm{L}}, \tag{6.34}$$
$$P'_{\mathrm{L}} = U^\dagger P_{\mathrm{L}} U = P_{\mathrm{L}} + \chi X_{\mathrm{M}}, \tag{6.35}$$
$$X'_{\mathrm{M}} = U^\dagger X_{\mathrm{M}} U = X_{\mathrm{M}}, \tag{6.36}$$
$$P'_{\mathrm{M}} = U^\dagger P_{\mathrm{M}} U = P_{\mathrm{M}} + \chi X_{\mathrm{L}}, \tag{6.37}$$
$$\tag{6.38}$$

when $U = \mathrm{e}^{\mathrm{i}\chi X_{\mathrm{L}} X_{\mathrm{M}}}$. This completes the derivation.

Agreement with the cavity-free unitary

The cavity-free nonlinear unitary, see Section 6.4.1, is $U = \mathrm{e}^{\mathrm{i}\mu n_{\mathrm{L}} X_{\mathrm{M}}}$, where n_{L} given by

$$n_{\mathrm{L}} = \int \mathrm{d}t a_{\mathrm{in}}^\dagger a_{\mathrm{in}}. \tag{6.39}$$

Instead of linearizing about the mean cavity field to arrive at $U = \mathrm{e}^{\mathrm{i}\chi X_{\mathrm{L}} X_{\mathrm{M}}}$ an alternative approach is to linearize about the mean input field. Namely, consider the transformation to the displaced frame $a_{\mathrm{in}} \rightarrow \alpha_{\mathrm{in}} + a_{\mathrm{in}}$, where $|\alpha_{\mathrm{in}}| \gg |\langle a_{\mathrm{in}} \rangle| = 0$. Choosing $\alpha_{\mathrm{in}} \in \mathbb{R}$, which simply sets the phase reference as before, the above transformation leads to

$$\begin{aligned} n_{\mathrm{L}} &= \int \mathrm{d}t \alpha_{\mathrm{in}}^2 + \int \mathrm{d}t \alpha_{\mathrm{in}}(t)(a_{\mathrm{in}} + a_{\mathrm{in}}^\dagger) + \int \mathrm{d}t a_{\mathrm{in}}^\dagger a_{\mathrm{in}} \\ &\approx \int \mathrm{d}t \alpha_{\mathrm{in}}^2 + \int \mathrm{d}t \alpha_{\mathrm{in}}(t)(a_{\mathrm{in}} + a_{\mathrm{in}}^\dagger), \end{aligned} \tag{6.40}$$

where the small term that is quadratic in a_{in} will now be dropped. Using Eq. (6.30), $\alpha_{\mathrm{in}}(t) = \sqrt{N_{\mathrm{P}}} f(t)$, and the definition of X_{L}, gives

$$n_{\mathrm{L}} \approx N_{\mathrm{P}} + \sqrt{2N_{\mathrm{P}}} X_{\mathrm{L}}. \tag{6.41}$$

As, $\langle n_{\mathrm{L}} \rangle = N_{\mathrm{P}}$, this clearly illustrates that a, X_{L}, P_{L} are zero mean operators in the displaced frame. Inserting, this form of n_{L} into the cavity-free nonlinear unitary then gives

$$\begin{aligned} \mathrm{e}^{\mathrm{i}\mu n_{\mathrm{L}} X_{\mathrm{M}}} &\approx \mathrm{e}^{\mathrm{i}\mu N_{\mathrm{P}} X_{\mathrm{M}}} \mathrm{e}^{\mathrm{i}\mu\sqrt{2N_{\mathrm{P}}} X_{\mathrm{L}} X_{\mathrm{M}}} \\ &= \mathrm{e}^{\mathrm{i}\Omega X_{\mathrm{M}}} \mathrm{e}^{\mathrm{i}\chi X_{\mathrm{L}} X_{\mathrm{M}}}, \end{aligned} \tag{6.42}$$

$$\Omega = \mu N_{\mathrm{P}} = \frac{\sqrt{8} g_0 N_{\mathrm{P}}}{\kappa}, \tag{6.43}$$

$$\chi = \mu\sqrt{2N_{\mathrm{P}}} = \frac{4 g_0 \sqrt{N_{\mathrm{P}}}}{\kappa}. \tag{6.44}$$

Hence, the linearized optomechanical pulsed unitary $U = \mathrm{e}^{\mathrm{i}\chi X_{\mathrm{L}} X_{\mathrm{M}}}$ is recovered. From the derivation of $U = \mathrm{e}^{\mathrm{i}\chi X_{\mathrm{L}} X_{\mathrm{M}}}$, it can be appreciated that the origin of this term is the linear part of the interaction Hamiltonian $H_{\mathrm{LIN}} = -\hbar g(a + a^\dagger)(b + b^\dagger)$. The term $\mathrm{e}^{\mathrm{i}\Omega X_{\mathrm{M}}}$ represents a deterministic classical momentum kick on the mechanical mode, which originates from the Kerr-like term $H_{\mathrm{K}} = -\hbar g_0 \alpha^2 (b + b^\dagger)$. As the value of Ω is known, it may be negated by an optical feedback force or taken into account in any post-processing of results—see Refs [2] and [139] for more discussion. Hence, in what follows the effect of the deterministic momentum kick term will typically be ignored.

Pulse shaping to optimize χ

The above analysis relied on the assumption that the cavity mode could be adiabatically eliminated: $\dot{a} = 0$. However, when $\dot{a} \neq 0$ choosing an input pulse shape $f(t) = \sqrt{\kappa}\mathrm{e}^{-\kappa|t|}$ maximizes the linearized optomechanical coupling strength

$$\chi_{\mathrm{max}} = \frac{2\sqrt{5} g_0 \sqrt{N_{\mathrm{P}}}}{\kappa}, \tag{6.45}$$

as shown in the Appendix of Ref. [139]. I do not repeat the derivation here but note that it relies on a linear coupling between the cavity amplitude quadrature

$X_{\rm L}$ and the mechanical position $X_{\rm M}$. In order to extract maximal information about $X_{\rm M}$, which is encoded on the phase quadrature of light $P_{\rm L}$, one finds that an input pulse shape $f(t)$ that matches the Lorentzian spectrum response of the cavity is optimal.

In Part II, Section 7.6, I discuss the optimization of the pulse shape to maximize the nonlinear optomechanical coupling strength in the unitary $e^{i\mu n_{\rm L} X_{\rm M}}$.

Mechanical state reconstruction

One of the main results introduced by Ref, [139] was to utilize optical pulses for mechanical state tomography. Eq. (6.31) implicitly assumes that the input pulse was sent towards the cavity at $t = 0$. Instead, if the input pulse is sent towards the cavity at a time $t = \theta/\omega_{\rm M}$, the output optical phase quadrature reads

$$P'_{\rm L}(\theta) = P_{\rm L} + \chi X_{\rm M}(\theta), \tag{6.46}$$

$$X_{\rm M}(\theta) = X_{\rm M}\cos\theta + P_{\rm M}\sin\theta. \tag{6.47}$$

Hence, information about any mechanical quadrature $X_{\rm M}(\theta)$ may be obtained by sending input pulses towards the cavity at different times and then performing phase quadrature measurements via optical homodyne.

More precisely, consider some quantum state preparation stage of an experiment, followed by these pulsed interactions and phase homodyne measurements. Then a repetitive series of state preparation followed by these phase quadrature measurements allows one to build up histograms of $P'_{\rm L}(\theta)$. Knowledge of χ and the statistics of the input pulse $P_{\rm L}$ enables one to extract the statistics of the mechanical state prepared in the state preparation stage.

In this thesis, it is proposed how this pulsed-based quantum state verification may be used to completely reconstruct the two-mode optical-mechanical and mechanical-mechanical entangled states in Refs [2] and[3]. Furthermore, in Ref. [6] we discuss how arbitrary quadrature moments of two-mode entangled states can be measured in an iterative verification process.

Mechanical squeezing and cooling via pulsed interaction and measurement

The concept of mechanical squeezing and cooling by pulsed interaction and measurement was introduced by M.R.V. *et al.* in the original quantum pulsed optomechanics work of Ref. [139]. In short, an optical coherent state interacts with the mechanical mode via the unitary $e^{i\chi X_{\rm L} X_{\rm M}}$. After the interaction, a phase homodyne measurement is made on the output optical state. As the optical phase quadrature contains information about the mechanical position $X_{\rm M}$, the uncertainty in $X_{\rm M}$ is reduced, potentially even below the zero point amplitude for large enough χ, i.e. mechanical quantum squeezing. At the same time, the mechanical momentum quadrature experiences back action from the quantum measurement. In this section, I assume an initial Gaussian state of light and mechanics. However, the formalism of Gaussian continuous variable quantum

mechanics reviewed in Chapter 4 is used to derive the results of Ref. [139]. This is precisely the method that was used in Ref. [2] to describe the mechanical precooling stage.

Consider therefore the quadrature vector $\mathbf{X} = (X_{\rm L}, P_{\rm L}, X_{\rm M}, P_{\rm M})^{\rm T}$ of the two mode state of light and mechanics, which allows one to define the initial covariance matrix

$$V = \begin{pmatrix} V_{\rm L} & 0 \\ 0 & V_{\rm M} \end{pmatrix}, \tag{6.48}$$

$$V_{\rm L} = \frac{1}{2}\mathbb{1}_2, \tag{6.49}$$

$$V_{\rm M} = \begin{pmatrix} V_X & V_{XP} \\ V_{XP} & V_P \end{pmatrix}, \tag{6.50}$$

Here, $V_{\rm L}$ is the initial covariance matrix of the input optical coherent state and $V_{\rm M}$ is the initial covariance matrix of the mechanical mode. Using the results of Chapter 4, the covariance matrix V transforms according to

$$\begin{aligned} V_{\rm OM} &= S_{\rm OM} V S_{\rm OM}^{\rm T} \\ &= \begin{pmatrix} A & C \\ C^{\rm T} & B \end{pmatrix}, \end{aligned} \tag{6.51}$$

due to the linearized optomechanical pulsed interaction, which has been written in block matrix form. Then the mechanical covariance matrix becomes

$$V_{\rm M}' = B - C^{\rm T}(\Pi_\varphi A \Pi_\varphi)^{\rm MP} C \tag{6.52}$$

after the phase quadrature measurement. Here, $\varphi = \pi/2$ as $X_{\rm L}(\varphi = \pi/2) = P_{\rm L}$. After some algebra, one may arrive at the final covariance matrix

$$V_{\rm M}' = \begin{pmatrix} V_X' & V_{XP}' \\ V_{XP}' & V_P' \end{pmatrix}, \tag{6.53}$$

$$V_X' = \frac{V_X}{1 + 2V_X\chi^2}, \tag{6.54}$$

$$V_{XP}' = \frac{V_{XP}}{1 + 2V_X\chi^2}, \tag{6.55}$$

$$V_P' = V_P + \frac{1}{2}\chi^2\left(1 - \frac{4V_{XP}^2}{1 + 2V_X\chi^2}\right). \tag{6.56}$$

I now set $V_X = V_P = \sigma^2$ and $V_{XP} = 0$ in what follows[18]. This situation could describe an initial mechanical thermal state $\sigma^2 = \bar{n} + \frac{1}{2}$, for example. In Fig. 6.4(a), the step denoted by Υ, which describes $V_{\rm M} \to V_{\rm M}'$, shows that the mechanical position quadrature is reduced and the mechanical momentum quadrature experiences back action noise. In the Schrödinger picture, this squeezing

[18] Note the steady state results, see below, do not rely on $V_X = V_P$.

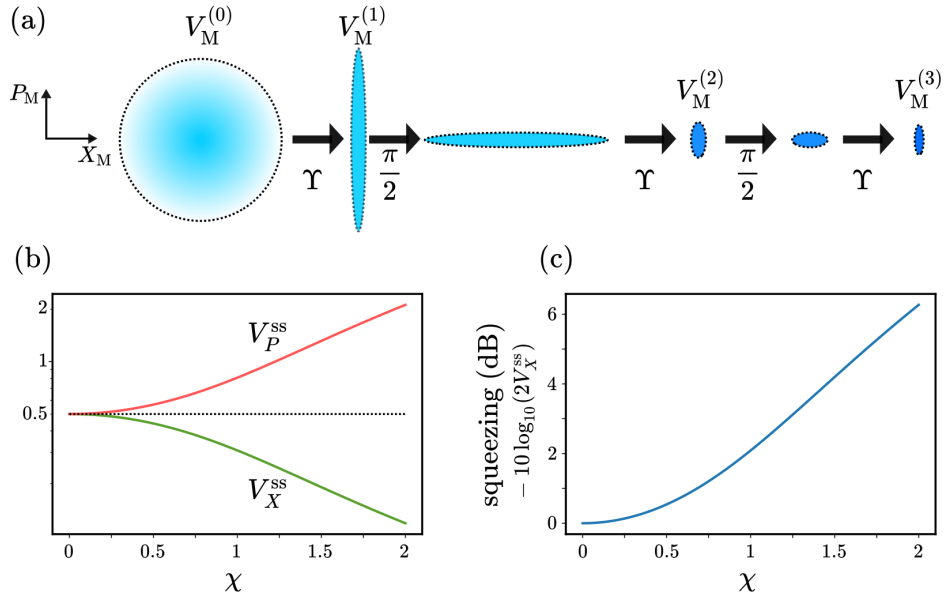


Figure 6.4: **Mechanical squeezing and cooling via pulsed interaction and measurement.** (a) Cartoon of mechanical squeezing and cooling via pulsed interaction and measurement. Here, $V_{\rm M}^{(n)}$ represents the mechanical state after the $n^{\rm th}$ step in the cooling procedure and is illustrated by an ellipse with a width given by the position $X_{\rm M}$ uncertainty and height given by the momentum $P_{\rm M}$ uncertainty. The steps denoted by Υ correspond to a reduction in position uncertainty by pulsed interaction and measurement. If the position variance $V_X^{(n)}$ at the $n^{\rm th}$ step is such that $V_X^{(n)} < 1/2$, this constitutes quantum squeezing and requires a large enough linearized optomechanical coupling strength χ—see Eq. (6.54). While the steps denoted by $\pi/2$ represent free mechanical evolution over a quarter period. (b) Steady state position and momentum variances as a function of the linearized optomechanical coupling strength χ. The steady state values are obtained in the limit of large step number n and are independent of the initial mechanical width σ. (c) The corresponding steady state mechanical position squeezing.

by interaction and measurement is described by the measurement operator

$$\begin{aligned}\Upsilon &= \langle P_{\rm L}|\, {\rm e}^{{\rm i}\chi X_{\rm L} X_{\rm M}}\, |0\rangle \\ &= \frac{1}{\pi^{1/4}} {\rm e}^{-\frac{1}{2}(P_{\rm L}-\chi X_{\rm M})^2}, \end{aligned} \tag{6.57}$$

from which the same measurement map $V_{\rm M} \rightarrow V'_{\rm M}$ was originally derived [139]. Here, the overlap formula from Appendix A has been used and we remind the reader that the input optical coherent pulse is equal to the vacuum state $|0\rangle$ in the displaced frame of linearized optomechanics.

Furthermore, one can cool the mechanical towards the ground state with repeated application of the measurement map $V_{\rm M} \rightarrow V'_{\rm M}$. Importantly, one must wait a quarter of a mechanical period (equal to a mechanical phase space angle of $\pi/2$) in-between applications of the map $V_{\rm M} \rightarrow V'_{\rm M}$ so that orthogonal quadratures may be successively squeezed. This is illustrated by Fig.6.4 (a), where the mechanical state after the $n^{\rm th}$ step in the cooling by pulsed interaction and measurement procedure is labelled by $V_{\rm M}^{(n)}$. The working principle of mechanical cooling via pulsed interaction and measurement has been demonstrated experimentally in Ref. [140].

One may then combine Eqs (6.54) and Eq. (6.56) to arrive at the recursive relations

$$V_X^{(n)} = \frac{V_X^{(n-2)} + \frac{1}{2}\chi^2}{1 + 2\left(V_X^{(n-2)} + \frac{1}{2}\chi^2\right)\chi^2}, \tag{6.58}$$

$$V_P^{(n)} = \frac{V_P^{(n-2)}}{1 + 2V_P^{(n-2)}\chi^2} + \frac{1}{2}\chi^2, \tag{6.59}$$

for the variances at the $n^{\rm th}$ step. Using these recursion relations and taking $V_X^{(0)} = V_X$, $V_P^{(0)} = V_P$, $V_X^{(1)} = V'_X$ from Eq. (6.54), and $V_P^{(1)} = V'_P$ from Eq. (6.56) allows one to determine the covariance matrix at any arbitrary step n in the procedure.

The mechanical covariance matrix reaches its steady state values $V_X^{\rm ss}$ and $V_P^{\rm ss}$ when $V_X^{(n)} = V_X^{(n-2)}$ and $V_P^{(n)} = V_P^{(n-2)}$. These steady state values are

$$V_X^{\rm ss} = -\frac{\chi^2}{4} + \frac{1}{4}\sqrt{\chi^4 + 4}, \tag{6.60}$$

$$V_P^{\rm ss} = +\frac{\chi^2}{4} + \frac{1}{4}\sqrt{\chi^4 + 4}, \tag{6.61}$$

and are plotted as a function of χ in Fig. 6.4(b). The steady state position squeezing in dB is plotted in Fig. 6.4(c), which is given by $-10\log_{10}(2V_X^{\rm ss})$. For small values of χ, the steady state[19] has high fidelity with the ground state, while higher values of χ prepare squeezed mechanical states.

[19] Note that the number of steps n required to reach the steady state values will depend on χ.

To quantify the success of the mechanical cooling procedure, one may define the effective mechanical thermal occupation $\bar{n}_{\rm eff} = \sqrt{\det(V_{\rm m})} - \frac{1}{2}$, which is related to the mechanical state purity $\mathrm{tr}\left(\rho^2\right)$ via $\bar{n}_{\rm eff} = \left(1/\,\mathrm{tr}\left(\rho^2\right) - 1\right)$ [50]. Inserting Eqs (6.60) and (6.61) leads to $\bar{n}_{\rm eff} = 0$, which implies the steady state mechanical states are pure $\mathrm{tr}\left(\rho^2\right) = 1$.

In Ref. [148], Brunelli and co-workers derived the steady state covariance matrix, described by $V_X^{\rm ss}$ and $V_P^{\rm ss}$, but also included the mechanical open system dynamics, modelled by Eq. (4.24), between each application of Υ. Brunelli *et. al* refer to this steady state cooling limit as *stroboscopic cooling*. Notably, for high-Q oscillators stroboscopic cooling is successful in preparing low $\bar{n}_{\rm eff}$ states. The authors also consider the case where the pulsed interaction and measurements are applied every half mechanical period, instead of every quarter period, as above. This means only the mechanical position is squeezed and in the steady state limit this is referred to as *stroboscopic squeezing*. Furthermore, in Ref. [2] we find that one application of Υ is sufficient for mechanical precooling in the optical-mechanical and mechanical-mechanical protocols as the unitary that generates the entanglement $\mathrm{e}^{\mathrm{i}\chi X_{\rm L} X_{\rm M}}$ is generated by the $X_{\rm M}$ quadrature and not the $P_{\rm M}$ quadrature—see Chapter 8 for more information.

6.3.3 Continuously driven optomechanics

I now briefly describe the elements of continuously driven linearized optomechanics that are relevant to this thesis. Much of the theoretical and experimental progress in cavity quantum optomechanics has been made in precisely this regime. Therefore, the reader should refer to Ref. [149] for a much more comprehensive review of this regime.

Resolved sideband regime: Stokes and anti-Stokes scattering

In a frame rotating at the laser frequency $\omega_{\rm L}$ and the mechanical frequency $\omega_{\rm M}$, the nonlinear optomechanical Hamiltonian of Eq. (6.3) is

$$H = -\hbar\Delta a^\dagger a - \hbar g_0 a^\dagger a(b\mathrm{e}^{-\mathrm{i}\omega_{\rm M} t} + b^\dagger \mathrm{e}^{+\mathrm{i}\omega_{\rm M} t}), \tag{6.62}$$

where the detuning is $\Delta = \omega_{\rm L} - \omega_{\rm C}$. In Eq. (6.8), the interaction term was linearized about the mean intracavity amplitude $\alpha_{\rm c}$ via $a \to \alpha_{\rm c} + a$ with $\alpha_{\rm c} \in \mathbb{R}$. Including the free evolution term in the linearization procedure gives

$$H = -\hbar\Delta\alpha_{\rm c}^2 - \hbar\Delta\alpha_{\rm c}(a + a^\dagger) - \hbar\Delta a^\dagger a + H_{\rm K} + H_{\rm LIN}, \tag{6.63}$$

$$H_{\rm K} = -\hbar g_0 \alpha_{\rm c}^2 (b\mathrm{e}^{-\mathrm{i}\omega_{\rm M} t} + b^\dagger \mathrm{e}^{\mathrm{i}\omega_{\rm M} t}), \tag{6.64}$$

$$H_{\rm LIN} = -\hbar g(a + a^\dagger)(b\mathrm{e}^{-\mathrm{i}\omega_{\rm M} t} + b^\dagger \mathrm{e}^{\mathrm{i}\omega_{\rm M} t}). \tag{6.65}$$

The term $-\hbar\Delta\alpha_{\rm c}^2$ is a constant term in the Hamiltonian and therefore will not appear in any equation of motion and is henceforth ignored. Meanwhile, the term $-\hbar\Delta\alpha_{\rm c}(a + a^\dagger)$ imparts a constant phase displacement to the optical mode and may be neglected via a transformation of the optical coordinates. Likewise,

as in the previous sections, the Kerr-like term may also be neglected by a suitable transformation of the mechanical coordinates. In the above linearization procedure the term $-\hbar g_0 a^\dagger a(b\mathrm{e}^{-\mathrm{i}\omega_\mathrm{M} t} + b^\dagger \mathrm{e}^{+\mathrm{i}\omega_\mathrm{M} t})$ was dropped, however the term $-\hbar\Delta a^\dagger a$ has been kept. This is because linearization only requires $\alpha_\mathrm{c} \gg 1$ and also $\mu\sigma \ll 1$ and does not imply anything about the size of Δ. In what follows $|\Delta| \sim \omega_\mathrm{M}$, which in general may be substantial and so the term $-\hbar\Delta a^\dagger a$ must be kept—even though $|\langle a^\dagger a\rangle|$ may be small. After these considerations the relevant part of the Hamiltonian to be studied is

$$H = -\hbar\Delta a^\dagger a + H_\mathrm{LIN}. \tag{6.66}$$

To determine the effect of the linearized optical-mechanical interaction at different detunings, one may now move to a rotating frame using $\tilde{H} = U_F^\dagger H U_F + \mathrm{i}\hbar\dot{U}_F^\dagger U_F$, with $U_F = \mathrm{e}^{+\mathrm{i}\Delta a^\dagger a t}$, which gives

$$\begin{aligned}\tilde{H} &= -\hbar g a b^\dagger \mathrm{e}^{\mathrm{i}(\Delta+\omega_\mathrm{M})t} + \mathrm{h.c.} \\ &\quad -\hbar g a b \mathrm{e}^{\mathrm{i}(\Delta-\omega_\mathrm{M})t} + \mathrm{h.c.}.\end{aligned} \tag{6.67}$$

By driving on either the red or blue sidebands $\Delta = \mp\omega_\mathrm{M}$, a rotating wave approximation (RWA)[20] may be made on the above Hamiltonian $\tilde{H}$, which is valid if $\omega_\mathrm{M} \gg \kappa$. The condition $\omega_\mathrm{M} \gg \kappa$ comes from κ being the largest decay rate in the system and implies one must work in the resolved sideband regime.

Driving on the red sideband $\Delta = -\omega_\mathrm{M}$ allows $\tilde{H}$ to be well approximated by

$$\tilde{H}_\mathrm{BS} = -\hbar g a b^\dagger + \mathrm{h.c.}, \tag{6.68}$$

which realizes an optomechanical beamsplitter operation. Meanwhile, driving on the blue sideband $\Delta = +\omega_\mathrm{M}$ allows $\tilde{H}$ to be written as

$$\tilde{H}_\mathrm{TMS} = -\hbar g a b + \mathrm{h.c.}, \tag{6.69}$$

which is the two-mode squeezer Hamiltonian. By including $\tilde{H}_\mathrm{BS}$ or $\tilde{H}_\mathrm{TMS}$ in the Heisenberg-Langevin and input-output equations for the cavity mode, the mathematics of either the anti-Stokes or Stokes scattering process can be described, which were discussed physically in Section 6.2.3.

Unresolved sideband regime: position measurement

As previously discussed in Section 6.2.3, the unresolved sideband regime $\kappa \gg \omega_\mathrm{M}$ allows for good position measurements. Note that unlike pulsed optomechanics, in a continuously driven system there is no concept of the input pulse temporal width and, instead, τ_in can represent the characteristic timescale over which the input varies. In the case $\kappa \gg \tau_\mathrm{in}^{-1}$, the interaction can be considered over a time slice Δt of the input drive and the limit $\Delta t \to \mathrm{d}t$ can be taken to derive an SME for position measurement. Moreover, as discussed in Section 6.2.3,

[20] See Section 3.2.3 and Fig. 3.8 in particular. If we work in the resolved sideband regime, the relevant terms oscillate at $\Delta \pm \omega_\mathrm{M}$ and the envelope decays slowly over a timescale $\sim 1/\kappa$.

the unresolved sideband regime allows for good position measurements because the intracavity field can be adiabatically eliminated. However, for adiabatic elimination in the pulsed regime $\kappa \gg \tau_{\rm in}^{-1} \gg \omega_{\rm M}$ is required. Therefore, if the drive is turned on suddenly, the very initial part of the intracavity dynamics may not be adiabatic, but as dynamics over much longer timescales than Δt will be typically considered (for example $\sim 1/\omega_{\rm M}$) any initial non-adiabatic part of the motion may be ignored. Furthermore, the SME presented below is Markovian—see Chapter 5—and so the initial part of the system's evolution will have no impact at long times.

In linearized optomechanics, information about the mechanical position $X_{\rm M}$ is only imprinted on the $P_{\rm L}$ quadrature of light. Hence, the phase quadrature $P_{\rm L}$ is monitored in a position measurement by continuous phase-homodyne detection. One can rewrite the measurement operator of Eq. (6.57), which describes a pulsed linearized optomechanical position measurement, as

$$\Upsilon = \frac{1}{\pi^{1/4}} \mathrm{e}^{-\frac{\chi^2}{2}(X_{\rm M} - P_{\rm L}/\chi)^2}. \tag{6.70}$$

Then one may consider this measurement operator over a Δt instead of a pulse with temporal width $\tau_{\rm in}$. To do this Eq. (6.30) is considered over a Δt, which implies the number of photons in the time slice Δt is

$$\begin{aligned} N_{\rm P} &= \alpha^2 = \frac{1}{2} X_\alpha^2 \\ &= |\alpha_{\rm in}|^2 \Delta t. \end{aligned} \tag{6.71}$$

Here, $\alpha = X_\alpha/\sqrt{2}$ has been used and note that the input flux to the cavity $|\alpha_{\rm in}|^2 = N_{\rm P}/\Delta t$ will typically be a constant in a continuously driven system[21]. From Section. 6.3.1, $\chi = \mu X_\alpha$ and together with Eq. (6.71) this implies the measurement operator $\Upsilon(\Delta t)$ that describes a time slice of the position measurement is

$$\Upsilon(\Delta t) = \frac{1}{\pi^{1/4}} \mathrm{e}^{-2k_{\rm L}\Delta t(X_{\rm M} - P_{\rm L}/\chi)^2}. \tag{6.72}$$

Here, the measurement rate k is half the input flux ($k = |\alpha_{\rm in}|^2/2$) such that

$$X_\alpha^2 = 4k\Delta t, \tag{6.73}$$

and using the result from Appendix E, the *linearized optomechanical measurement rate* is $k_{\rm L} = \mu^2 k = 2g^2/\kappa$.

Using the results of the general continuous homodyne measurement considered in Section 12.4.2 in Part III, the measurement output operator is identified as

$$c_{\rm L} = \sqrt{2k_{\rm L}} X_{\rm M}. \tag{6.74}$$

[21] The results presented below will still apply if the input flux is a function of time.

As $\Delta t \to \mathrm{d}t$, Eq. (12.15) immediately allows one to write down the SME for position measurement in linearized optomechanics

$$\mathrm{d}\rho = -\frac{\mathrm{i}}{\hbar}[H_0, \rho]\mathrm{d}t + \mathcal{D}[c_{\mathrm{L}}]\rho\mathrm{d}t + \sqrt{\eta}\mathcal{H}[c_{\mathrm{L}}]\rho\mathrm{d}W_{P_{\mathrm{L}}}. \tag{6.75}$$

Here, the measurement efficiency η and the mechanical free evolution generated by $H_0 = \hbar\omega_{\mathrm{M}} b^\dagger b$ has been included—see Section 12.4.4 for a justification as to why this term can be included in this way. Note the P_{L} measurement record discussed in Chapter 5 is simply given by

$$\mathrm{d}y_{P_{\mathrm{L}}} = \langle X_{\mathrm{M}} \rangle \, \mathrm{d}t + \frac{\mathrm{d}W_{P_{\mathrm{L}}}}{\sqrt{8\eta k_{\mathrm{L}}}}. \tag{6.76}$$

Notes on the continuous position measurement

In the SME of Eq. (6.75), I have not included the deterministic momentum kick as it is typically not present in a typical derivation of continuous position measurement [150, 71]. Ultimately, this deterministic momentum kick derives from the term $\mathrm{e}^{\mathrm{i}\Omega X_{\mathrm{M}}}$ from Section 6.3.2 considered over a $\mathrm{d}t$. In Section 14.2.2 this deterministic momentum kick is however included.

Furthermore, as Υ is a positive operator[22] one could have derived Eq. (6.75) entirely using the results of Ref. [71], which considers continuous Gaussian position measurements. See the discussion in [151] that explicitly talks about how to derive Eq. (6.75) using Ref. [71]. I make this point as the result in Section 12.4.2 is for general continuous homodyne measurements, which includes a unitary part in the polar decomposition of Υ. Hence, Eq. (12.15) can be used to derive more general SMEs in continuous optomechanics—see Ref. [7].

Steady state covariance matrix

The dynamics of the covariance matrix is deterministic and along with the first moments completely described the evolution of an initial Gaussian system. The steady state of the covariance matrix is given by

$$V_{XP}^{ss} = \frac{-\omega_{\mathrm{M}} + \sqrt{\omega_{\mathrm{M}}^2 + 16\eta k_{\mathrm{L}}^2}}{8\eta k_{\mathrm{L}}}, \tag{6.77}$$

$$V_X^{ss} = \sqrt{\frac{\omega_{\mathrm{M}} V_{XP}^{ss}}{4\eta k_{\mathrm{L}}}}, \tag{6.78}$$

$$V_P^{ss} = V_X^{ss} + \frac{8\eta V_{XP}^{ss} V_X^{ss} k_{\mathrm{L}}}{\omega_{\mathrm{M}}}, \tag{6.79}$$

which corresponds to the results of Section 14.2.2 with $\zeta = 1$. The derivation of these steady state values is sketched out in Appendix J.1.

[22] In the polar decomposition [62] of $\Upsilon = PU$ into a positive operator P and a unitary U, $\Upsilon = P$ and $U = \mathbb{1}$.

6.4 Nonlinear optomechanics

The intrinsic nonlinearity versus additional nonlinearities

In Section 6.1, I described how in this thesis I refer to $a^\dagger a X_{\rm M}$ as the intrinsic or inherent nonlinearity of quantum optomechanics. In Section 6.1, I also discussed nonlinearities of the form $a^\dagger a X_{\rm M}^n$ with $n \in \mathbb{Z}$ and $n \geq 2$, which arise from higher order terms in the expansion of the cavity frequency $\omega_{\rm C}(x)$ [108]. Apart from the optomechanical coupling, nonlinearities may be introduced into the system by modifying the potential of the mechanical mode. For example, the free Hamiltonian $H_0/\hbar = \frac{\omega_{\rm M}}{2}(X_{\rm M}^2 + P_{\rm M}^2)$ could be modified by including quartic terms $\sim X_{\rm M}^4$ to achieve a Duffing-type oscillator [152, 153], which can lead to nonlinear behaviour such as chaos [154].

Having reaffirmed that the nonlinearities this thesis is interested in for now originate from the $a^\dagger a X_{\rm M}$ coupling, I briefly describe some of the results of Part III. However, first I present an original derivation of the nonlinear cavity-free unitary $\mathrm{e}^{\mathrm{i}\mu n_{\rm L} X_{\rm M}}$ discussed earlier.

6.4.1 The nonlinear pulsed unitaries

The cavity-free unitary

Here, I will describe the nonlinear optomechanical pulsed unitary $\mathrm{e}^{\mathrm{i}\mu n_{\rm L} X_{\rm M}}$ first introduced in Ref. [145]. This unitary approximates the *cavity-enhanced unitary* $\mathrm{e}^{\mathrm{i}\varphi(X_{\rm M})n_{\rm L}}$ to only second order in $X_{\rm M}$. Therefore, despite the optomechanical coupling strength μ being proportional to g_0/κ in this derivation, one can view $\mathrm{e}^{\mathrm{i}\mu n_{\rm L} X_{\rm M}}$ as the *cavity-free unitary*. This is because without a cavity, one can derive the same unitary $\mathrm{e}^{\mathrm{i}\mu n_{\rm L} X_{\rm M}}$ for a cavity free scenario as in Ref. [155]. In this case, for a single reflection of an optical pulse of wavelength λ from the mechanical oscillator[23] $\mu = 4\pi x_0/\lambda$. Hence, while $\mathrm{e}^{\mathrm{i}\mu n_{\rm L} X_{\rm M}}$ models the nonlinearity of the radiation-pressure interaction, one must turn to $\mathrm{e}^{\mathrm{i}\varphi(X_{\rm M})n_{\rm L}}$ to accurately describe the nonlinear role of the cavity.

In nonlinear pulsed optomechanics, the Heisenberg-Langevin equations describing the dynamics generated by $H/\hbar = -\Delta a^\dagger a - g_0 a^\dagger a(b + b^\dagger)$ are

$$\dot{a} = \mathrm{i}\sqrt{2}g_0 a X_{\rm M} - \kappa a + \sqrt{2\kappa}a_{\rm in} \tag{6.80}$$

$$\dot{X}_{\rm M} = 0 \tag{6.81}$$

$$\dot{P}_{\rm M} = \sqrt{2}g_0 a^\dagger a, \tag{6.82}$$

for a resonant optical input in a frame rotating at the cavity frequency: $\Delta = 0$. Furthermore, as in the previous section, it is assumed that $\kappa \gg \tau_{\rm in}^{-1}$, where $\tau_{\rm in}$ is the characteristic timescale over which the input $a_{\rm in}$ changes. Hence, the cavity field can be adiabatically eliminated $\dot{a} = 0$. As before, it is also required that

[23] To derive this note that $\mathrm{e}^{\mathrm{i}\mu n_{\rm L} X_{\rm M}}$ implies the reflection of a single photon changes the mechanical momentum via $P_{\rm M} \to P_{\rm M} + \Delta P = P_{\rm M} + \mu$. The momentum carried by the photon is given by h/λ. Thus, after a reflection the oscillator experiences a $\Delta p = 2h/\lambda$ momentum change. In dimensionless units this corresponds to $\Delta P = \mu = \Delta p/p_0 = 4\pi x_0/\lambda$.

$\tau_{in}^{-1} \gg \omega_{\rm M}$ to ensure the mechanical position remains constant. The adiabatic cavity field is then given by

$$a(t) = \frac{\sqrt{2\kappa}}{\kappa - \mathrm{i}\sqrt{2}g_0 X_{\rm M}} a_{\rm in}(t). \tag{6.83}$$

Using the input-output relations for the cavity $a_{\rm out}(t) = \sqrt{2\kappa}a(t) - a_{\rm in}(t)$, and defining the nonlinear optomechanical coupling strength $\mu = \sqrt{8}g_0/\kappa$, then gives

$$\begin{aligned} a_{\rm out}(t) &= \frac{1 + \mathrm{i}\frac{\mu}{2}X_{\rm M}}{1 - \mathrm{i}\frac{\mu}{2}X_{\rm M}} a_{\rm in}(t) && (6.84)\\ &= \left(1 + \mathrm{i}\mu X_{\rm M} - \frac{1}{2}\mu^2 X_{\rm M}^2 - \frac{\mathrm{i}}{4}\mu^3 X_{\rm M}^3 + \ldots\right) a_{\rm in}(t) && (6.85)\\ &\approx \left(1 + \mathrm{i}\mu X_{\rm M} - \frac{1}{2}\mu^2 X_{\rm M}^2\right) a_{\rm in}(t) && (6.86)\\ &\approx \mathrm{e}^{\mathrm{i}\mu X_{\rm M}} a_{\rm in}(t). && (6.87) \end{aligned}$$

Therefore, $a_{\rm out}(t) = \mathrm{e}^{\mathrm{i}\mu X_{\rm M}} a_{\rm in}(t)$ to second order in $\mu X_{\rm M}$. Then defining the photon number operator $n_{\rm L}$ to be

$$\begin{aligned} n_{\rm L} &= \int_0^{\tau_p} a_{\rm in}^\dagger a_{\rm in}(t)\mathrm{d}t \\ &= \int_0^{\tau_p} a_{\rm out}^\dagger a_{\rm out}(t)\mathrm{d}t, && (6.88) \end{aligned}$$

allows the Heisenberg-Langevin equation for $P_{\rm M}$ to be integrated, leading to

$$\begin{aligned} P_{\rm M}(\tau_p) - P_{\rm M}(0) &= \frac{\mu}{1 + \left(\frac{\mu}{2}\right)^2 X_{\rm M}^2} n_{\rm L}, && (6.89)\\ &\approx \mu n_{\rm L}. && (6.90) \end{aligned}$$

Here, τ_p is the duration of the optomechanical interaction and the right-hand side has been approximated to second order in $\mu X_{\rm M}$. Eqs (6.87) and (6.90) can also be expressed as

$$\begin{aligned} a_{\rm out} &= U^\dagger a_{\rm in} U, && (6.91)\\ P_{\rm M}(\tau_p) &= U^\dagger P_{\rm M}(0) U, && (6.92) \end{aligned}$$

with $U = \mathrm{e}^{\mathrm{i}\mu n_{\rm L} X_{\rm M}}$, which completes the derivation of the free cavity unitary.

In Part II, Section 7.6, I will describe how a long input pulse, which allows the adiabatic approximation to be made, optimizes the optomechanical coupling strength μ. This is in contrast to the linearized regime, where the pulse shape is chosen to match the cavity response.

The cavity-enhanced unitary

In Ref. [7] I derive the unitary that accurately models a nonlinear pulsed optomechanical interaction in a cavity. The derivation is described in detail in

Part III, but in short, the cavity-enhanced unitary is $e^{i\varphi(X_M)n_L}$, where the optical X_M-dependent phase is given by

$$\varphi(X_M) = \arg(f), \tag{6.93}$$

$$f(X_M) = \frac{1+i\left(\frac{\mu}{2}X_M+\frac{\Delta}{\kappa}\right)}{1-i\left(\frac{\mu}{2}X_M+\frac{\Delta}{\kappa}\right)} \tag{6.94}$$

and $f(X_M)$ is the nonlinear response function of the cavity. A detuning Δ is also included if the input pulse is detuned from the cavity frequency ω_C at zero mechanical displacement. This unitary describes the Heisenberg transformations:

$$a_{out} = U^\dagger a_{in} U \tag{6.95}$$

$$= f(X_M)a_{in}, \tag{6.96}$$

$$= \frac{1+i\left(\frac{\mu}{2}X_M+\frac{\Delta}{\kappa}\right)}{1-i\left(\frac{\mu}{2}X_M+\frac{\Delta}{\kappa}\right)}a_{in}(t) \tag{6.97}$$

$$P_M(\tau_p) = U^\dagger P_M(0) U \tag{6.98}$$

$$= P_M(0) + \frac{\partial\varphi(X_M)}{\partial X_M}n_L \tag{6.99}$$

$$= \frac{\mu}{1+\left(\frac{\mu}{2}X_M+\frac{\Delta}{\kappa}\right)^2}n_L. \tag{6.100}$$

Setting $\Delta = 0$ and expanding $\varphi(X_M)$ in small μX_M about $\mu X_M = 0$ gives

$$\varphi(X_M) = \mu X_M - \frac{1}{12}(\mu X_M)^3 + \frac{1}{80}(\mu X_M)^5 - \ldots \tag{6.101}$$

Inserting, Eq. (6.101) into the cavity-enhanced unitary gives

$$e^{i\varphi(X_M)n_L} = \left[1 + i\mu X_M - \frac{1}{2}(\mu X_M)^2 - \frac{i}{4}(\mu X_M)^3 + \frac{1}{8}(\mu X_M)^4 + \ldots\right]^{n_L}. \tag{6.102}$$

Expanding, the cavity-free unitary in the same way gives

$$e^{i\mu n_L X_M} = \left[1 + i\mu X_M - \frac{1}{2}(\mu X_M)^2 - \frac{i}{6}(\mu X_M)^3 + \frac{1}{24}(\mu X_M)^4 + \ldots\right]^{n_L}. \tag{6.103}$$

Comparing Eq. (6.102) and Eq. (6.103), the terms in the square bracket agree to second order in μX_M.

6.4.2 Continuous nonlinear position measurements

The SMEs shown below apply for continuous position measurement in nonlinear cavity quantum optomechanics. Firstly, I show the cavity-free case and secondly I show the cavity-enhanced case. These SMEs were derived in Ref. [7] and I will discuss their derivations and implications in more detail in Part III. However, to complete this chapter on optomechanics, I briefly discuss these SMEs here.

As with continuous position measurement in the linearized regime, operation is carried out in the unresolved sideband regime of optomechanics $\kappa \gg \omega_{\mathrm{M}}$. This allows for adiabatic elimination[24] of the cavity mode and the derivation of the SME, which describes the continuous measurement. However, in the nonlinear regime, information about the mechanical position is not only encoded on the phase quadrature P_{L} of light but also the amplitude quadrature X_{L}. Hence, in the derivation of the SME a general-dyne measurement on the output light will be considered, see Fig. 6.5, which allows for measurement of both optical quadratures in a proportion determined by the beamsplitter coefficient ζ.

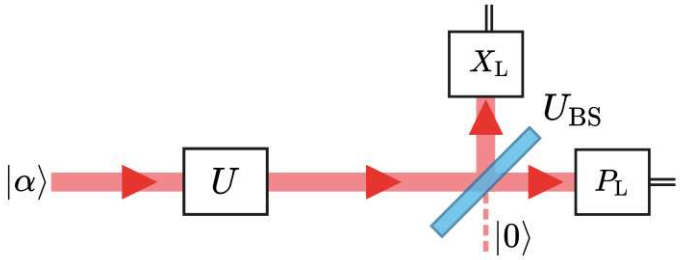


Figure 6.5: **Continuous nonlinear measurement of mechanical position via general-dyne detection.** An optomechanical cavity is continuously driven with an input coherent state $|\alpha\rangle$. Inside the cavity, the cavity mode interacts with the mechanics via the unitary U, which is $\mathrm{e}^{\mathrm{i}\mu n_{\mathrm{L}} X_{\mathrm{M}}}$ in the cavity-free case or $\mathrm{e}^{\mathrm{i}\varphi(X_{\mathrm{M}})n_{\mathrm{L}}}$ in the cavity-enhanced case. The output optical mode, and a vacuum mode, then impinge on a beamsplitter described by U_{BS}, with real transmission coefficient ζ. Amplitude (X_{L}) and phase (P_{L}) homodyne measurements are then made on the output modes. For $\zeta = 1$, a pure phase homodyne measurement is realized, while $\zeta = 0$ is a pure amplitude homodyne measurement, and $\zeta = 1/\sqrt{2}$ realizes a heterodyne measurement: projection onto a coherent state.

The derivation of the SMEs then proceeds similarly to the linear case: (i) the measurement operator describing a timeslice Δt is derived from the nonlinear unitaries introduced in the previous sections, and then (ii) the results of the general continuous homodyne measurement considered in Section 12.4.2 in Part III then allows one to immediately write down the SME.

The cavity-free case

Chapter 5 presents a derivation of the measurement operator that describes general-dyne position measurement via the nonlinear cavity-free unitary—see Eq. (5.5). One can again use Eq. (6.73) to write this measurement operator

[24] Note that the SMEs may be derived outside the unresolved sideband regime if adiabatic elimination of the cavity mode is still valid. In which case, one needs to carefully consider all the relevant rates of the system dynamics—see Ref. [7] for more details.

over a timeslice Δt as

$$\begin{aligned}
\Upsilon(\Delta t) &= \Upsilon_{X_{\rm L}}(\Delta t)\Upsilon_{P_{\rm L}}(\Delta t), \qquad (6.104)\\
\Upsilon_{X_{\rm L}}(\Delta t) &= \exp\Bigg[-2k(1-\zeta^2)\Delta t\left(\cos\mu X_{\rm M} - \frac{X_{\rm L}}{X_\alpha\sqrt{1-\zeta^2}}\right)^2\\
&+ {\rm i}4k(1-\zeta^2)\Delta t\left(\frac{X_{\rm L}}{X_\alpha\sqrt{1-\zeta^2}}\right)\sin\mu X_{\rm M}\\
&- {\rm i}2k(1-\zeta^2)\Delta t\cos\mu X_{\rm M}\sin\mu X_{\rm M}\Bigg],\\
\Upsilon_{P_{\rm L}}(\Delta t) &= \exp\Bigg[-2k\zeta^2\Delta t\left(\sin\mu X_{\rm M} - \frac{P_{\rm L}}{X_\alpha\zeta}\right)^2\\
&- {\rm i}4k\zeta^2\Delta t\left(\frac{P_{\rm L}}{X_\alpha\zeta}\right)\cos\mu X_{\rm M} + {\rm i}2k\zeta^2\Delta t\cos\mu X_{\rm M}\sin\mu X_{\rm M}\Bigg].
\end{aligned}$$

Then using the results from Section 12.4.2, Eq. (6.104) implies the output measurement operators are given by

$$\begin{aligned}
c_{X_{\rm L}} &= \sqrt{1-\zeta^2}c, \qquad (6.105)\\
c_{P_{\rm L}} &= -{\rm i}\zeta c, \qquad (6.106)\\
c &= \sqrt{2k}{\rm e}^{{\rm i}\mu X_{\rm M}}. \qquad (6.107)
\end{aligned}$$

After some algebra, Eq. (6.104) also implies the SME is given by

$$\begin{aligned}
{\rm d}\rho &= -\frac{\rm i}{\hbar}[H_0,\rho]{\rm d}t + \mathcal{D}[c]\rho{\rm d}t\\
&+ \sqrt{(1-\zeta^2)\eta_{X_{\rm L}}}\mathcal{H}[c]\rho{\rm d}W_{X_{\rm L}} + \zeta\sqrt{\eta_{P_{\rm L}}}\mathcal{H}[-{\rm i}c]\rho{\rm d}W_{P_{\rm L}}, \qquad (6.108)
\end{aligned}$$

where the measurement efficiencies of the amplitude and phase homodyne detectors have been introduced, $\eta_{X_{\rm L}}$ and $\eta_{P_{\rm L}}$, respectively, and included the free harmonic evolution of the mechanical oscillator $H_0/\hbar = \omega_{\rm M} b^\dagger b$. Finally, the measurement records are

$$\begin{aligned}
{\rm d}y_{X_{\rm L}} &= \langle\cos\mu X_{\rm M}\rangle\,{\rm d}t + \frac{{\rm d}W_{X_{\rm L}}}{\sqrt{8\eta_{X_{\rm L}}k(1-\zeta^2)}}, \qquad (6.109)\\
{\rm d}y_{P_{\rm L}} &= \langle\sin\mu X_{\rm M}\rangle\,{\rm d}t + \frac{{\rm d}W_{P_{\rm L}}}{\sqrt{8\eta_{P_{\rm L}}k\zeta^2}}. \qquad (6.110)
\end{aligned}$$

Expanding the above to first order in position $X_{\rm M}$ and setting $\zeta = 1$ returns the results for a linearized continuous measurement of position. In this way, one also naturally recovers the deterministic momentum kick term described in Section 6.3.3.

The cavity-enhanced case

To round of this section, I will simply state the results for a continuous position measurement in nonlinear optomechanics, which are derived and discussed in great detail in Part III. The SME, measurement output operators, and measurement records are given by

$$\begin{aligned}
\mathrm{d}\rho &= -\frac{\mathrm{i}}{\hbar}[H_0,\rho]\mathrm{d}t + \mathcal{D}[c]\rho\mathrm{d}t \\
&+ \sqrt{(1-\zeta^2)\eta_{X_\mathrm{L}}}\mathcal{H}[c]\rho\mathrm{d}W_{X_\mathrm{L}} + \zeta\sqrt{\eta_{P_\mathrm{L}}}\mathcal{H}[-\mathrm{i}c]\rho\mathrm{d}W_{P_\mathrm{L}}, && (6.111)\\
c_{X_\mathrm{L}} &= \sqrt{1-\zeta^2}c, && (6.112)\\
c_{P_\mathrm{L}} &= -\mathrm{i}\zeta c, && (6.113)\\
c &= \sqrt{2k}f(X_\mathrm{M}), && (6.114)\\
\mathrm{d}y_{X_\mathrm{L}} &= \langle A(X_\mathrm{M})\rangle\,\mathrm{d}t + \frac{\mathrm{d}W_{X_\mathrm{L}}}{\sqrt{8\eta_{X_\mathrm{L}}k(1-\zeta^2)}}, && (6.115)\\
\mathrm{d}y_{P_\mathrm{L}} &= \langle B(X_\mathrm{M})\rangle\,\mathrm{d}t + \frac{\mathrm{d}W_{P_\mathrm{L}}}{\sqrt{8\eta_{P_\mathrm{L}}k\zeta^2}} && (6.116)
\end{aligned}$$

where the operator-valued functions A and B are related to the nonlinear cavity response function $f(X_\mathrm{M})$ of Eq. (6.94) via

$$\begin{aligned}
f &= A(X_\mathrm{M}) + \mathrm{i}B(X_\mathrm{M}), && (6.117)\\
A(X_\mathrm{M}) &= \frac{1-\left(\frac{\mu}{2}X_\mathrm{M}+\frac{\Delta}{\kappa}\right)^2}{1+\left(\frac{\mu}{2}X_\mathrm{M}+\frac{\Delta}{\kappa}\right)^2}, && (6.118)\\
B(X_\mathrm{M}) &= \frac{2\left(\frac{\mu}{2}X_\mathrm{M}+\frac{\Delta}{\kappa}\right)}{1+\left(\frac{\mu}{2}X_\mathrm{M}+\frac{\Delta}{\kappa}\right)^2}. && (6.119)
\end{aligned}$$

Here, Δ is the detuning of the drive from the cavity frequency. Note the SME for the cavity-free case, Eq. (6.108), may be derived by approximating the functions A and B by $A \approx \cos\mu X_\mathrm{M}$ and $B \approx \sin\mu X_\mathrm{M}$, which is valid to second order in X_M when $\Delta = 0$.

In the linearized regime of optomechanics, the mechanical state remains Gaussian under continuous position monitoring. In Part III, from the cavity-enhanced SME, the *stochastic Gaussian regime* of continuous position measurement is derived. This describes situations where the mechanical state remains Gaussian beyond the linearized regime of optomechanics.

Part II

Quantum state engineering

Chapter 7

Growing mechanical cat states

This chapter draws heavily from Ref. [1] and also corrects some minor typographical errors present in the original publication.

Cavity quantum optomechanics provides a rich avenue for engineering quantum states of mechanical oscillation by taking advantage of the tools of both quantum optics and quantum measurement theory. Here, I detail how pulsed nonlinear optomechanical interactions[1] $e^{i\mu n_L X_M}$ followed by photon counting measurements can 'grow' a mechanical Schrödinger cat state over a series of steps in a multistep protocol. Thus, this protocol provides a route to overcome the challenge presented by low optomechanical coupling strengths μ.

I first discuss the relevant works in this research direction, namely engineering large superposition states of mechanical motion, before spending some time discussing the multi-photon counting scheme of Ref. [155], which the scheme presented in this thesis builds upon. I then detail the multistep protocol for 'growing' nonclassical mechanical Schrödinger cat states towards the macroscopic scale. For clarity, the protocol is first presented without including open-system dynamics, but I later introduce optical loss and discuss the effect this has on the heralding probability of the protocol. The mechanical open system dynamics are also taken into account and I derive the mechanical Wigner distribution of these thermalized Schrödinger cat states.

After introducing the protocol, I explain what is meant by "non-classical" and "macroscopic" in a quantifiable way and I also introduce a simplified measure of macroscopicity based on the quantum Fisher information. Using experimental parameter sets taken from recent solid-material and ultra-cold atom implementations, these non-classicality and macroscopicity measures are used to quantify the success of the protocol with respect to the number of steps.

[1] Note that in the cavity-free unitary $e^{i\mu n_L X_M}$ is considered here as the cavity-enhanced unitary $e^{i\varphi(X_M)n_L}$ had not been derived yet.

Alongside this, parameter sets for improved performance are proposed and the behaviour of the states produced is explored in near-future realizations of our multistep scheme.

Finally, I present a new derivation in this thesis for the optimal pulse shape to enhance the nonlinear optomechanical coupling strength μ. Here, I show that the optimal pulse shape is one that is much longer than the inverse of the cavity decay rate and I explain how these long pulses can overcome potential issues with the timing of the photon counters.

7.1 Towards macroscopic quantum states

Quantum state preparation protocols

Studying macroscopic quantum states has a myriad of motivations that range from quantum technology development to deepening our understanding of the foundations of physics. Notably, observing the dynamics of such states can put tighter bounds on objective wavefunction collapse models [156, 157, 158]. In particular, the generation of macroscopic quantum states allows one to design interferometric experiments of objective collapse models [159, 5], which provide a more unambiguous test of collapse than their non-interferometric counterparts [160]—see Appendix D of Chapter 5. Moreover, creating macroscopic quantum states provides a path to test the interplay of macroscopic quantum phenomena and quantum gravity on a table top [161, 95, 162]. For example, the interplay between macroscopic quantum states and gravity becomes apparent in the study of predicted deformations of the canonical commutation relations [145, 163] and in gravitationally mediated entanglement proposals [164, 165, 166]. Current experimental platforms pursuing the preparation of macroscopic quantum states include molecule interferometry [167], superconducting circuits [168, 169], ultracold atoms [170], and cavity quantum optomechanical systems [45].

The multistep protocol introduced here contributes to the field of cavity quantum optomechanics, which utilizes optical forces and the quantum control of light to generate and study non-classical states of mechanical motion. The field has diversified significantly over the last two decades and a number of quite different experimental platforms and protocols are now being explored. Prominent deterministic protocols to generate non-classical mechanical states include the generation of mechanics-field entanglement [161, 95, 171], and non-Gaussian state preparation via light-to-mechanics optomechanical state-swap [172, 93, 173, 146]. Utilizing measurement provides a powerful non-deterministic approach for state preparation with prominent examples including mechanical squeezing via measurement [139, 174, 7], superposition state preparation via position-squared measurements [175, 176, 132] phonon addition/subtraction [177, 178, 179, 180, 4, 181], and sequential measurement schemes [182, 183].

This line of research lays the foundation for the development of optomechan-

ical quantum technologies such as microwave-to-optical conversion [184, 185, 186], weak force sensing [187, 188], and quantum information applications [189], by establishing and improving the quantum coherence of mechanical motion.

Macroscopic quantum states

Macroscopicity is a useful concept in quantum physics. For example, in the quantum-to-classical transition, the more macroscopic a quantum state is the more susceptible it is to decoherence mechanisms [39]. Both conventional and objective collapse models scale with the size or macroscopicity of the quantum state, which helps explain why we don't see quantum states at classical length scales.

However, I have used the term 'macroscopic' quite liberally thus far without yet defining it. In fact, defining macroscopicity is an active area of research [190], but loosely speaking, a macroscopic quantum state is both (i) a state of a system which is somehow larger[2] than 'textbook' microscopic quantum states, such as atoms or optical cavity modes, and (ii) still retains a significant amount of quantum coherence despite, by its very nature, being more susceptible to decoherence mechanisms. Macroscopic quantum states are therefore very fragile by nature, which motivates our macroscopic state preparation protocol that operates in the pulsed regime of optomechanics; in pulsed optomechanics, quantum operations can easily be performed on the state over a timescale much smaller than the mechanical decoherence time.

A macroscopicity measure is one that quantifies the macroscopicity of a quantum state and its definition tends to depends on certain details of the physical system of interest. There exists a variety of measures of macroscopicity measures in the literature—see Ref. [190] for a review—but here I focus on macroscopicity measures designed for single-mode continuous-variable bosonic systems, as these describe the mechanical states generated in our multistep protocol. Such measures include the phase-space measure $\mathcal{I}$ introduced by Lee and Jeong [191], which measures the extent to which sharp features—caused by quantum interference effects—extend in phase space. The measure $\mathcal{I}$ averages over all phase-space directions and is shown to quantify how sensitive the macroscopic quantum state is to decoherence via the Lindblad master equation.

Other macroscopicity measures for single-mode continuous-variable bosonic systems include those based on the quantum Fisher information [192]. These measures also quantify the extent to which sharp features extend in phase space [193, 194]. However, these quantum-Fisher-information-based measures pick out an optimal direction in phase space rather than performing an average over all directions. Picking out an optimal direction in this way is closely related to the quantum Fisher information being a valuable measure in quantum metrology [195, 196, 197]. In determining the sensitivity of a quantum state to a physical transformation that depends on some small parameter[3], the

[2] Depending on the context, larger here could mean, more atoms, more mass, more modes, a greater spacial extent, or a greater extent of momenta—as in this work.

[3] In the context of quantum metrology, this small parameter is typically an angle θ, but

quantum Fisher information sets the ultimate bound on minimizing the measured variance of this small parameter. This bound is known as the quantum Cramér–Rao bound [198] and generalizes to the Heisenberg bound for quantum parameter estimation when one considers multiple independent measurements [195]. Macroscopic quantum states are therefore a useful resource in quantum metrology. For example, a macroscopic Schrödinger cat state could be used as an extremely sensitive probe for weak force sensing [199]. Moreover, it has been recently shown that postselection after the unitary transformation can lead to an enhancement of the quantum Fisher information for states with negative quasiprobability distributions [200, 201], which motivates the use of non-classical macroscopic *superposition* states combined with postselection for force sensing.

7.1.1 The multi-port protocol

The work presented below builds upon the theoretical and experimental work of Ringbauer and colleagues from Ref. [155]. Here the authors, propose a scheme where an optical pulse in the coherent state $|\psi\rangle = |\sqrt{2}\alpha\rangle$ is injected into one arm of a Mach-Zehnder interferometer. In the upper arm, the light interacts with a mechanical oscillator via the free-cavity nonlinear-pulsed optomechanical unitary $\mathrm{e}^{\mathrm{i}\mu n_{\mathrm{L}} X_{\mathrm{M}}}$. In the lower arm, the light acquires a phase shift ϕ and the optical modes are then projected onto a NOON state in the following way.

At the output of the Mach-Zehnder interferometer, the two output modes interact with $N_{\mathrm{p}}-2$ vacuum ancilla modes via an N_{p}-port optical interferometer. An N_{p}-port optical interferometer achieves linear interactions between a set of N_{p} input modes and can be achieved via an arrangement of beamsplitters and phase shifters—see Ref. [202]. The phases of the N_{p}-port optical interferometer are chosen such that an N_{p}-fold single photon coincidence click event heralds a measurement operator of the form

$$\Upsilon \propto \left(\mathrm{e}^{\mathrm{i}N_{\mathrm{p}}\mu X_{\mathrm{M}}} - \mathrm{e}^{\mathrm{i}\phi}\mathbb{1}\right) \tag{7.1}$$

that acts on the initial mechanical state. See Fig. 7.1 for the schematic of the multi-port protocol. The measurement operator Υ acts to create a quantum superposition of the initial mechanical state and a momentum-displaced version of the initial mechanical state. The size of the momentum displacement is given by $N_{\mathrm{p}}\mu/\sqrt{2}$ and so increasing N_{p} provides a route to increase the size and macroscopicity of the mechanical quantum state. However, as this multi-port protocol relies on the specific outcome of an N_{p}-fold single photon coincidence click event, the protocol is probabilistic and increasing N_{p} will lead to a diminishing heralding probability as discussed in Section 7.3.3—see Eq. (7.42).

Experimentally, the authors of Ref. [155] focus on the $N_{\mathrm{p}} = 2$ case and make the first observation of mechanical interference fringes—a key step towards observing a genuine quantum superposition state. Impressively, as discussed

can be associated with any another physical transformation, such as a displacement.

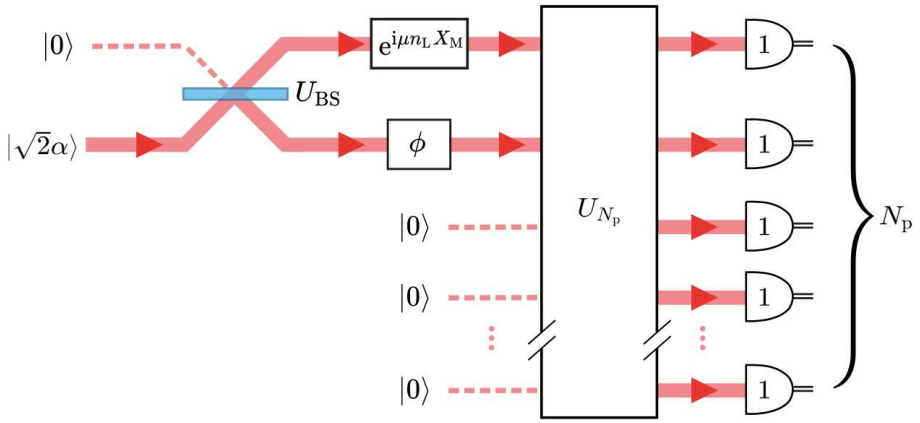


Figure 7.1: **Setup for the multi-port protocol.** An input optical pulse in the coherent state $|\sqrt{2}\alpha\rangle$ enters one port of a Mach-Zehnder interferometer. In the upper arm, the light interacts with the mechanical mode via the nonlinear free-cavity optomechanical unitary $e^{i\mu n_L X_M}$. While in the lower arm, the light acquires a phase shift ϕ. Together with a set of optical vacuum ancilla, a multiport interferometer of size N_p combined with the specific outcome of an N_p-fold single photon coincidence click event achieves a mechanical measurement operator of the form $\Upsilon \propto \left(e^{iN_p\mu X_M} - e^{i\phi}\mathbb{1}\right)$. This allows for the creation of mechanical superposition states. Figure adapted from Ref. [155].

in Section 6.4.1, the authors realize this experimental result even without the enhancement of the optomechanical coupling strength from a cavity.

In this work, instead of this $N_p = 2$ case being generalized to $N_p > 2$, the $N_p = 2$ setup is operated in a multistep fashion, which allows the size of the mechanical superposition to be grown over a series of steps. Furthermore, the case where the optical input pulse is in the single photon state $|\psi\rangle = |1\rangle$ is also considered and it is compared to the $|\psi\rangle = |\sqrt{2}\alpha\rangle$ input. Finally, I would like to point out that further work in this direction could combine the multi-port design of Ref. [155] and the multistep method of operation, which I will now introduce in detail.

7.2 The multistep protocol

7.2.1 Schrödinger cat states

Before detailing the multistep protocol, it is useful to have in mind what is the target mechanical state. Therefore, consider a measurement operator of the form $D(\beta) + e^{i\phi}\mathbb{1}$, which is a linear combination of the displacement operator

$D(\beta)$ and the identity operator multiplied by a phase. The action of the this measurement operator on the zero boson state $|0\rangle$ produces the pure Schrödinger cat state [203]

$$|\Psi\rangle = \mathcal{N}\left(|\beta\rangle + \mathrm{e}^{\mathrm{i}\phi}|0\rangle\right), \tag{7.2}$$

$$\mathcal{N} = \frac{1}{\sqrt{2\left(1+\cos\phi\ \mathrm{e}^{-\frac{1}{2}|\beta|^2}\right)}}. \tag{7.3}$$

For $\phi = 0$, $|\Psi\rangle$ is an *even cat state*, while for $\phi = \pi$, $|\Psi\rangle$ is an *odd cat state*. By expanding the coherent state $|\beta\rangle$ in the number basis and taking the limit $|\beta| \to 0$, one finds that the even cat state approaches $|0\rangle$. Whereas, as $|\beta| \to 0$ the odd state approaches the single boson state $|1\rangle$. Importantly, the state $|1\rangle$ possesses Wigner negativity, while $|0\rangle$ does not. Therefore, if an experiment is constrained by small values of $|\beta|$ and the goal is to generate a non-classical state, then one should focus on the odd cat state, with $\phi = \pi$. Note here that Wigner negativity is a key signature of non-classicality and will be discussed in Section 7.4.1.

I will now discuss how one can realize an operation of the form $D(\beta) + \mathrm{e}^{\mathrm{i}\phi}\mathbb{1}$, which acts an a mechanical state. Furthermore, I will discuss how one can effectively increase the size of $|\beta|$ in a multistep protocol.

7.2.2 The setup and overview

Fig. 7.2 shows the setup for achieving a measurement operator of the form $D(\beta) + \mathrm{e}^{\mathrm{i}\phi}\mathbb{1}$ on a mechanical oscillator. A pulse of light in the quantum state $|\psi\rangle$ is first injected into one of the input arms of a Mach-Zehnder interferometer. This pulse first reaches a 50:50 beamsplitter, described by U_{BS}, and mixes with optical vacuum $|0\rangle$. The output light from the beamsplitter is then split into the upper and lower arms of the interferometer. Here, a mechanical mode is placed in the top arm and a phase shifter is placed in the bottom arm. The mechanical mode interacts with the optical mode in a cavity via the nonlinear pulsed optomechanical unitary $\mathrm{e}^{\mathrm{i}\mu n_{\mathrm{L}} X_{\mathrm{M}}}$. From Chapter 6 the reader may appreciate that this means the system must operate in the unresolved sideband regime of optomechanics $\kappa \gg \omega_{\mathrm{M}}$, such that mechanical free evolution and open-system dynamics can be ignored during the optomechanical interaction. After the phase shift and optomechanical interaction, the light then recombines on another 50:50 beamsplitter and the output light is finally sent towards two photon counters. The projection of the light by the photon counters onto number states achieves a measurement operator on the mechanical subspace that is a combination of displacement operations and the identity operation. Thus, a mechanical superposition state is created, which can take the form of the Schrödinger cat state described in the previous section.

Temporal mode matching of the two optical pulses impinging on the final beamsplitter may be ensured by placing a cavity, with an identical response

function to that of the optomechanical cavity, in the bottom arm of the interferometer. However, as will be discussed in Section 7.6, optical pulses that allow for the cavity mode of the optomechanical cavity to be adiabatically eliminated actually maximize the optomechanical interaction strength μ. In this case, the input and output pulse shapes to the optomechanical cavity are equal to a very good approximation. Therefore, in this adiabatic regime, placing a cavity in the bottom arm of the interferometer is not necessary for good mode matching at the second beamsplitter.

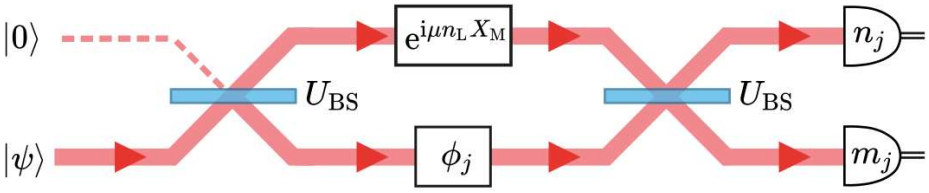


Figure 7.2: **Growing mechanical Schrödinger cat states in a multistep protocol: the j$^{\text{th}}$ step of the N step protocol.** An input pulse of light $|\psi\rangle$ is injected into one arm of a Mach-Zehnder interferometer and then mixes with optical vacuum $|0\rangle$ on a 50:50 beamsplitter U_{BS}. In the upper arm of the Mach-Zehnder, the optical mode interacts with a mechanical mode via $e^{i\mu n_L X_M}$, while in the lower arm the light picks up a phase ϕ_j. After this, the light mixes on another 50:50 beamsplitter and at the beamsplitter outputs, m_j and n_j photons are measured by photon counters.

A single step of the multistep protocol consists of an input pulse propagating through the interferometer, interacting with the mechanical mode, and then being detected by the photon counters. By sending in N input pulses and detecting N click events on the photon counters, an N-step protocol is realized. Furthermore, by controlling the phase shift at each step, the multistep protocol can increase the size of the mechanical spatial superposition.

7.2.3 Mathematical details and choice of phase in the multistep process

Measurement operator for a single step

First, I introduce subscripts 1 and 2 for the two optical modes in the upper arm a_1 and lower arm a_2, respectively. Then, by consulting Fig. 7.2 and the example of the measurement operator construction in Chapter 5, one may immediately write down the measurement operator that describes the j^{th} step of the protocol for an $\{m_j, n_j\}$ click event:

$$\Upsilon^{(j)}_{m_j,n_j} = \langle m_j| \langle n_j| U_{\text{BS}} e^{i\mu a_1^\dagger a_1 X_M} e^{i\phi_j a_2^\dagger a_2} U_{\text{BS}} |\psi\rangle |0\rangle . \tag{7.4}$$

Here, an $\{m_j, n_j\}$ click event corresponds to detecting m_j photons in the detector at the output of optical mode 1, and n_j photons at the output of mode 2. Furthermore, ϕ_j is the phase shift imparted to the lower optical mode on the j^{th} step and $j \in \mathbb{Z}$ with $1 \leq j \leq N$. Here, two cases are considered: (i) where the input pulse is in a coherent state $|\psi\rangle = \left|\sqrt{2}\alpha\right\rangle$ and (ii) where the input pulse is in a single photon state $|\psi\rangle = |1\rangle$.

In the Heisenberg picture, the transformation of the optical annihilation operators[4] are given by $U_{\text{BS}}^{\dagger} a_1 U_{\text{BS}} = \frac{1}{\sqrt{2}}(a_1 + a_2)$ and $U_{\text{BS}}^{\dagger} a_2 U_{\text{BS}} = \frac{1}{\sqrt{2}}(a_1 - a_2)$. Meanwhile, in the Schrödinger picture, the action of this unitary U_{BS} on the bipartite coherent state $|\alpha\rangle|\beta\rangle$ is given by $U_{\text{BS}}|\alpha\rangle|\beta\rangle = \left|\frac{1}{\sqrt{2}}(\alpha+\beta)\right\rangle\left|\frac{1}{\sqrt{2}}(\alpha-\beta)\right\rangle$. Furthermore, the action of the beamsplitter on the state $|1\rangle|0\rangle$ is $U_{\text{BS}}|1\rangle|0\rangle = \frac{1}{\sqrt{2}}(|1\rangle|0\rangle + |0\rangle|1\rangle)$ and the action of U_{BS} on the state $|0\rangle|1\rangle$ is $U_{\text{BS}}|0\rangle|1\rangle = \frac{1}{\sqrt{2}}(|1\rangle|0\rangle - |0\rangle|1\rangle)$. Using these beamsplitter relations, Eq. (7.4) becomes

$$\Upsilon_{m_j,n_j}^{(j)} = \begin{cases} \frac{e^{-|\alpha|^2}}{\sqrt{m_j! n_j!}} \frac{\alpha^{m_j+n_j}}{(\sqrt{2})^{m_j+n_j}} (e^{i\mu X_{\text{M}}} + e^{i\phi_j}\mathbb{1})^{m_j} (e^{i\mu X_{\text{M}}} - e^{i\phi_j}\mathbb{1})^{n_j} \\ \qquad\qquad \text{for } |\psi\rangle = \left|\sqrt{2}\alpha\right\rangle, \\ \frac{1}{2}[(e^{i\mu X_{\text{M}}} + e^{i\phi_j}\mathbb{1})\delta_{m_j,1}\delta_{n_j,0} + (e^{i\mu X_{\text{M}}} - e^{i\phi_j}\mathbb{1})\delta_{m_j,0}\delta_{n_j,1}] \\ \qquad\qquad \text{for } |\psi\rangle = |1\rangle. \end{cases} \tag{7.5}$$

For either input optical pulse, a $\{1,0\}$ or $\{0,1\}$ click event corresponds to a measurement operator that is proportional to $D(\beta) + e^{i\phi}\mathbb{1}$ with $\beta = i\mu/\sqrt{2}$. Hence, when acting on the ground state the operators $\Upsilon_{1,0}^{(j)}$ and $\Upsilon_{0,1}^{(j)}$ will generate a mechanical Schrödinger cat state along the momentum axis of mechanical phase space.

As discussed in Section 7.2.1, if $\mu \ll 1$ the action of $\Upsilon_{1,0}^{(j)}$ and $\Upsilon_{0,1}^{(j)}$ on the ground state will be well approximated by either the ground state or the single phonon state, depending on the choice of phase ϕ_j. Namely, if one wishes to approximate the single photon state in the small μ limit then one must aim to generated an odd cat state. Therefore, if one heralds a $\{1,0\}$ click event then $\phi_j = \pi$ must be chosen and if one heralds a $\{0,1\}$ click event then $\phi_j = 0$ must be chosen. Crucially, the phase shift occurs *before* the click event, so one can only herald the desired state in a probabilistic way, which is discussed more below.

I now consider how to grow the size of the mechanical Schrödinger cat state along the momentum axis via multiple steps, i.e. multiple applications of $\Upsilon_{1,0}^{(j)}$ and/or $\Upsilon_{0,1}^{(j)}$ on the initial mechanical state.

[4] By comparison with the most general beamsplitter transformation matrix of Eq. (2.31) in Chapter 2, the unitary U_{BS} corresponds to a matrix $\underline{\underline{B}}$ with $\lambda = -\pi$, $t = r = \frac{1}{\sqrt{2}}e^{i\frac{\pi}{2}}$, which realizes the Hadamard matrix $\underline{\underline{B}} = \frac{1}{\sqrt{2}}\begin{pmatrix} 1 & 1 \\ 1 & -1 \end{pmatrix}$.

Multiple steps and how to grow cats

I would like to remind the reader that the protocol operates in the pulsed regime of optomechanics. Therefore, free mechanical evolution and mechanical open system dynamics are negligible over one step of the protocol. However, to apply the measurement operator of Eq. (7.5) multiple times on the initial mechanical state, one must wait one full free mechanical period in between steps of the protocol[5]. This ensures that the displacements in mechanical phase space always occur along the momentum axis, in the positive direction, which allows one to 'grow' the size of the spatial superposition. However, the mechanical open-system dynamics that occurs between steps must be carefully modelled. I will return to this important detail in Section 7.3.4, but first I ignore the open-system dynamics for clarity and ease of presentation.

Let the initial mechanical state be ρ_{in}, then after N steps, the mechanical state is given by

$$\rho_N = \frac{1}{\mathcal{P}_N}(\Upsilon^{(N)}_{m_N,n_N}...\Upsilon^{(2)}_{m_2,n_2}\Upsilon^{(1)}_{m_1,n_1} \circ \rho_{\text{in}}), \tag{7.6}$$

where the circle notation for the quantum operations has been used: $\Upsilon \circ \rho = \Upsilon\rho\Upsilon^\dagger$. Here, the heralding probability to obtain a particular series of N output click events is

$$\mathcal{P}_N = \text{tr}(\Upsilon^{(N)}_{m_N,n_N}...\Upsilon^{(2)}_{m_2,n_2}\Upsilon^{(1)}_{m_1,n_1} \circ \rho_{\text{in}}). \tag{7.7}$$

For the specific case of a series of $\{0,1\}$ click events, the final mechanical state is

$$\rho_N \propto \prod_{j=1}^{N}\left[D(\text{i}\mu/\sqrt{2}) - \text{e}^{\text{i}\phi_j}\mathbb{1}\right] \circ \rho_{\text{in}}. \tag{7.8}$$

Here, ρ_N comprises $N+1$ copies of the initial mechanical state along the momentum axis of phase space, with each copy separated by μ. Many interesting superposition states can be generated by controlling the phase shift ϕ_j at each step. However, as the goal here is to increase the size of a Schrödinger cat state, the correct choice of phases is $\phi_j = 2\pi j/N$, which cancels of all the cross terms in Eq. (7.8), leaving only the outer two momentum components:

$$\rho_N = \rho_{\text{SCS}} \propto [D(\text{i}N\mu/\sqrt{2}) - \mathbb{1}] \circ \rho_{\text{in}}. \tag{7.9}$$

Here, ρ_{SCS} is the generalization of the odd Schrödinger cat state from Section 7.2.1 but with the initial ground state $|0\rangle$ replaced with a potentially mixed state ρ_{in}. Indeed, in what follows I assume the initial mechanical state is a thermal state with a mean thermal occupation $\bar{n}$:

$$\rho_{\text{in}} = \rho_{\bar{n}} = (\pi\bar{n})^{-1}\int \text{d}^2\beta \text{e}^{-|\beta|^2/\bar{n}}\,|\beta\rangle\langle\beta|\,. \tag{7.10}$$

[5]One can also consider the scenario where several steps of the protocol are carried out within a time interval that is much shorter than the mechanical period. However, eventually free mechanical evolution must occur as the step number is increased further and further. Thus, I focus on the situation where one waits a mechanical period in between steps, which allows the protocol to be generalized to high step numbers more straightforwardly.

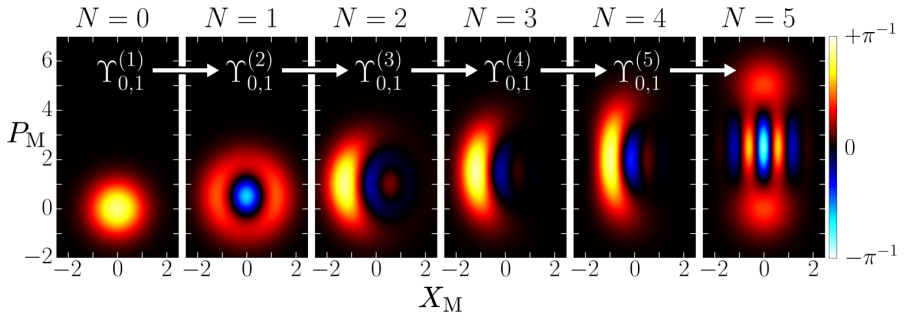


Figure 7.3: **Growing mechanical Schrödinger cat states in a multistep protocol: the evolution of the Wigner distribution.** Here, the Wigner distribution is plotted at each step of a five-step protocol for $\mu = 1$ and $\bar{n} = 0.1$. Between each plot the measurement operator $\Upsilon_{0,1}^{(j)}$ is applied to the previous mechanical state. The phases applied on the first, second, third, fourth, and fifth steps are $\phi_1 = 0$, $\phi_2 = 2\pi/5$, $\phi_3 = 4\pi/5$, $\phi_4 = 6\pi/5$, and $\phi_5 = 8\pi/5$, respectively. The final plot of this figure is the Schrödinger cat state, consisting of two population terms centred at $P_{\mathrm{M}} = 0$ and $P_{\mathrm{M}} = 5$, with quantum interference fringes between these two terms centred at $P_{\mathrm{M}} = 2.5$. Note these interference fringes lead to phase space negativity.

To visualize the multistep process one may calculate a representation of the state ρ_{SCS} in the phase space formed by the position X_{M} and momentum P_{M} operators. In this work, the Wigner quasiprobability distribution is chosen—see Chapter 2. The Wigner distribution of Eq. (7.9) is given by

$$\begin{aligned} W_{\mathrm{SCS}}(X_{\mathrm{M}}, P_{\mathrm{M}}) &= \frac{\mathcal{N}_{\mathrm{SCS}}}{\pi(1+2\bar{n})}\left\{\exp\left[\frac{-X_{\mathrm{M}}^2 - P_{\mathrm{M}}^2}{1+2\bar{n}}\right] + \exp\left[\frac{-X_{\mathrm{M}}^2 - (P_{\mathrm{M}} - N\mu)^2}{1+2\bar{n}}\right]\right. \\ &- \left. 2\cos(N\mu X_{\mathrm{M}})\exp\left[\frac{-X_{\mathrm{M}}^2 - (P_{\mathrm{M}} - N\mu/2)^2}{1+2\bar{n}}\right]\right\}, \qquad (7.11) \\ \mathcal{N}_{\mathrm{SCS}} &= \frac{1}{2\left[1 - \mathrm{e}^{-N^2\mu^2(1+2\bar{n})/4}\right]}. \qquad (7.12) \end{aligned}$$

Here, $\mathcal{N}_{\mathrm{SCS}}$ ensures normalization $\iint \mathrm{d}X_{\mathrm{M}}\mathrm{d}P_{\mathrm{M}} W_{\mathrm{SCS}}(X_{\mathrm{M}}, P_{\mathrm{M}})=1$ and the overlap formula between a coherent state and a quadrature state from Appendix A was used to calculate the Wigner distribution via Eq. (2.46) from Chapter 2. Fig. 7.3 shows an example of how the mechanical Schrödinger cat state grows in phase space over a five step process.

The odd cat state ρ_{SCS} in Eq. (7.9) may also be obtained by observing a series of $\{1, 0\}$ click events instead of a series of $\{0, 1\}$. However, in this case the appropriate choice of phases to generate the odd cat state is $\phi_j = 2\pi j/N + \pi$.

Whereas, a series of $\{1,0\}$ click events with phases $\phi_j = 2\pi j/N$ generates a state of the form $\rho'_N = \propto \left(D(\mathrm{i}\mu/\sqrt{2})^N - (-1)^N \mathbb{1}\right) \circ \rho_{\mathrm{in}}$, which alternates between and odd and even cat state with N.

Notes on other mechanical state this protocol can prepare

Even though our protocol focuses on the generation of Schrödinger cat states, the work presented here—which builds upon Ref. [155]—can be generalized to create a whole variety of interesting states in two-dimensional mechanical phase space. This can be done by varying the phase at each step and the duration between steps of the protocol, which effectively changes the direction of the mechanical kicks in phase space. For example, a superposition of four distinct coherent states located at the vertices of a square can be created [155], which were coined quantum compass states by Zurek [204]. Furthermore, complex patterns such as orthographic projections of hypercubes[6] can be created in mechanical phase space [205].

7.3 Open system dynamics and heralding probability

7.3.1 Heralding probability and optical loss

Heralding probability without optical loss

To calculate the heralding probability $\mathcal{P}_N$ for the multistep state-preparation protocol to successfully generate ρ_{SCS}, one may simply set the trace of Eq. (7.9) equal to one and then compare the result with the generalized quantum measurement from Chapter 5. For an initial thermal state $\rho_{\mathrm{in}} = \rho_{\bar{n}}$, and using $\phi_j = 2\pi j/N$, $m_j = 0$, and $n_j = 1$ for all j, this procedure gives

$$\mathcal{P}_N = \begin{cases} 2^{1-N} \mathrm{e}^{-2N|\alpha|^2} |\alpha|^{2N} \Big\{ 1 - \exp\big[-N^2\mu^2(1+2\bar{n})/4\big] \Big\} & \text{for } |\psi\rangle = \big|\sqrt{2}\alpha\big\rangle \\ 2^{1-2N} \Big\{ 1 - \exp\big[-N^2\mu^2(1+2\bar{n})/4\big] \Big\} & \text{for } |\psi\rangle = |1\rangle. \end{cases} \tag{7.13}$$

The single photon input $|\psi\rangle = |1\rangle$ shows better scaling in the heralding probability[7] with the step number N. This better scaling occurs for all coherent amplitudes, as can been seen if the first heralding probability in Eq. (7.13) is maximized with respect to $|\alpha|$ to obtain $|\alpha|_{\max} = 1/\sqrt{2}$, which maximizes the probability for $\{0,1\}$ and $\{1,0\}$ measurements. This different scaling in $\mathcal{P}_N$ with N is simply the result of photon number conservation; for a single photon input the only possible output clicks are $\{0,1\}$ and $\{1,0\}$, which are the desired outcomes for growing Schrödinger cat states. However, the coherent input pulse allows m_j and n_j to take on any integer value greater than or equal to zero.

[6] Hypercube: the n-dimensional generalization of a square $n = 2$, e.g. $n = 3$ gives the cube and $n = 4$ gives the tesseract.

[7] Note that Ref. [1] is missing a factor of 2^{-N} in $\mathcal{P}_N$.

Beamsplitter model for loss for a general input state

However, it is important to note that any optical loss in the multistep protocol will affect $\mathcal{P}_N$ and, in principle, the final mechanical state too. To model such losses a beamsplitter model for loss is utilized, which is described in Chapter 3 and is shown in Fig. 7.4. Namely, optical losses and detector inefficiencies are modelled with beamsplitters of intensity transmission η placed before the final beamsplitter[8]. These beamsplitters introduce interactions with the environmental optical modes in the upper and lower arms of the interferometer. These environmental optical modes are labelled by the annihilation operators a_3 and a_4.

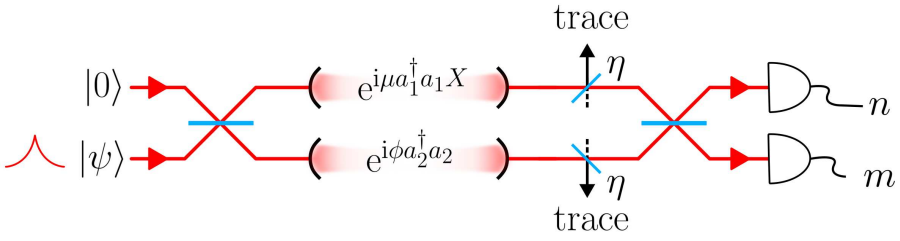


Figure 7.4: **Beamsplitter model for optical loss for each step in the multistep protocol.** Beamsplitters of intensity transmission η are placed just before the final beamsplitter to model loss to the optical environment. The input environmental modes interact with the interferometer modes on these beam splitters. A trace operation is then performed over the output environmental modes that leads to loss of optical information, which affects the state of the mechanical mode. At $\eta = 1$, these beam splitters are fully transmissive and the protocol operates at perfect optical efficiency.

From Chapter 3, we know that at high optical frequencies the input environmental modes are well approximated by the vacuum state and therefore the measurement operator corresponding to losing k photons in the upper arm and l photons in the lower arm, at any step in the protocol, is

$$\Upsilon_{m,n,k,l} = \langle m| \langle n| \langle k| \langle l| U_{12}U_{24}U_{13}e^{i\mu a_1^\dagger a_1 X_M} e^{i\phi a_2^\dagger a_2} U_{12} |\psi\rangle |0\rangle |0\rangle |0\rangle . \quad (7.14)$$

Here, the step index j has been dropped for clarity of presentation. Further, subscripts have been included on the beamsplitter unitaries to indicate the modes that they interfere. U_{12} describes the 50:50 beamsplitters that operate on the interferometer modes as outlined in Section 7.2.3, while U_{13} and U_{24} act according

[8]Here, equal optical in the upper and lower modes is assumed. However, if there is an asymmetry between the optical loss in the upper and lower arms of the interferometer, this may be compensated for by changing the transmission coefficient of the first beamsplitter to balance the amplitudes at the final beamsplitter.

to

$$U_{13}^{\dagger} a_1 U_{13} = \sqrt{\eta} a_1 + (\sqrt{1-\eta}\,) a_3, \tag{7.15}$$

$$U_{24}^{\dagger} a_2 U_{24} = \sqrt{\eta} a_2 + (\sqrt{1-\eta}\,) a_4. \tag{7.16}$$

To describe the loss of information to the optical environment a trace operation must be performed over the output environmental states, such that after an $\{m, n\}$ click event the state of the mechanical mode is given by

$$\rho' = \frac{\sum_{k,l} \Upsilon_{m,n,k,l} \circ \rho}{\mathrm{tr}(\sum_{k,l} \Upsilon_{m,n,k,l} \circ \rho)}. \tag{7.17}$$

Here, ρ is the state of the mechanical mode before the optomechanical interaction.

Optical loss with a single photon state input

For a single photon optical input pulse $|\psi\rangle = |1\rangle$, the measurement operator incorporating optical loss becomes

$$\begin{aligned}
\Upsilon_{m,n,k,l} &= \frac{1}{2}\sqrt{\eta}(\mathrm{e}^{\mathrm{i}\mu X_{\mathrm{M}}} + \mathrm{e}^{\mathrm{i}\phi}\mathbb{1})\delta_{m,1}\delta_{n,0}\delta_{k,0}\delta_{l,0} \\
&+ \frac{1}{2}\sqrt{\eta}(\mathrm{e}^{\mathrm{i}\mu X_{\mathrm{M}}} - \mathrm{e}^{\mathrm{i}\phi}\mathbb{1})\delta_{m,0}\delta_{n,1}\delta_{k,0}\delta_{l,0} + \sqrt{\frac{1-\eta}{2}}\mathrm{e}^{\mathrm{i}\mu X_{\mathrm{M}}}\delta_{m,0}\delta_{n,0}\delta_{k,1}\delta_{l,0} \\
&+ \sqrt{\frac{1-\eta}{2}}\mathrm{e}^{\mathrm{i}\phi}\mathbb{1}\delta_{m,0}\delta_{n,0}\delta_{k,0}\delta_{l,1}.
\end{aligned} \tag{7.18}$$

By comparing $\Upsilon_{m,n,k,l}$ with $\Upsilon_{m,n}$, it may be seen that for a $\{0,1\}$ or $\{1,0\}$ click event the only effect of optical loss is to reduce the heralding probability at each step by a factor of η, i.e. with optical loss the heralding probability to successfully create ρ_{SCS} of Eq. (7.9) is

$$\mathcal{P}_N = 2^{1-2N}\eta^N\Big\{1 - \exp\big[-N^2\mu^2(1+2\bar{n})/4\big]\Big\}. \tag{7.19}$$

With the single photon input, it is clear from $\Upsilon_{m,n,k,l}$ that the heralded mechanical state ρ_{SCS} is not affected and in this way the protocol is resilient to optical loss and detector inefficiencies. Explicitly, $\Upsilon_{1,0,k,l} = \sqrt{\eta}\Upsilon_{1,0}$ and $\Upsilon_{0,1,k,l} = \sqrt{\eta}\Upsilon_{0,1}$. Moreover, optical loss can only lead to a $\{0,0\}$ click event, which prevents the next step of the protocol—which consists of a string of either $\{1,0\}$ or $\{0,1\}$ click events—and so an experimental run with a $\{0,0\}$ click is discarded.

Optical loss with a coherent state input

For a coherent state optical input pulse $|\psi\rangle = \big|\sqrt{2}\alpha\big\rangle$, the measurement operator incorporating optical loss is

$$\begin{aligned}
\Upsilon_{m,n,k,l} = \frac{\mathrm{e}^{-|\alpha|^2}}{\sqrt{m!n!k!l!}} \frac{(\sqrt{\eta}\alpha)^{m+n}[(\sqrt{1-\eta})\alpha]^{k+l}}{(\sqrt{2})^{m+n}} \\
\times(\mathrm{e}^{\mathrm{i}\mu X_{\mathrm{M}}} + \mathrm{e}^{\mathrm{i}\phi}\mathbb{1})^m(\mathrm{e}^{\mathrm{i}\mu X_{\mathrm{M}}} - \mathrm{e}^{\mathrm{i}\phi}\mathbb{1})^n\mathrm{e}^{\mathrm{i}k\mu X_{\mathrm{M}}}\mathrm{e}^{\mathrm{i}l\phi}\mathbb{1}.
\end{aligned} \tag{7.20}$$

From Eq. (7.17), it may be seen that the terms depending on the index l have no operational effect on the mechanical mode and may be summed separately to give

$$\sum_{l=0}^{\infty} \frac{|(\sqrt{1-\eta})\alpha|^{2l}}{l!} = \mathrm{e}^{(1-\eta)|\alpha|^2}. \tag{7.21}$$

This is because the l-dependent terms correspond to optical loss in the lower arm of the interferometer and so do not directly affect the mechanical mode. However, the k-dependent terms affect the mechanical mode via

$$\sum_{k=0}^{\infty} \frac{|(\sqrt{1-\eta})\alpha|^{2k}}{k!} \mathrm{e}^{\mathrm{i}k\mu X_{\mathrm{M}}} \rho\ \mathrm{e}^{-\mathrm{i}k\mu X_{\mathrm{M}}}. \tag{7.22}$$

This quantum map describes momentum diffusion of the mechanical mode in the following way. Consider the situation where k photons are lost to the optical environment—this leads to a momentum kick of size $k\mu/\sqrt{2}$ on the mechanical mode. But as the environment does not 'keep record' of k, all possible k must be summed over in accordance with the photon number distribution of the coherent pulse. This weighted summation over all possible momentum kicks $k\mu/\sqrt{2}$ is precisely the momentum diffusion advertised.

However, in the limit $(1-\eta)|\alpha|^2 \ll 1$ these k-dependent terms leave the mechanical mode unchanged. In this regime, carrying out the trace operation leads to an effective measurement operator, for a $\{m,n\}$ photon detection event, given by

$$\Upsilon_{m,n} = \frac{\mathrm{e}^{-\eta|\alpha|^2}}{\sqrt{m!n!}} \frac{(\sqrt{\eta}\alpha)^{m+n}}{(\sqrt{2})^{m+n}} (\mathrm{e}^{\mathrm{i}\mu X_{\mathrm{M}}} + \mathrm{e}^{\mathrm{i}\phi}\mathbb{1})^m (\mathrm{e}^{\mathrm{i}\mu X_{\mathrm{M}}} - \mathrm{e}^{\mathrm{i}\phi}\mathbb{1})^n, \tag{7.23}$$

which is identical to Eq. (7.5) aside from the transformation $\alpha \to \eta\alpha$. In this regime the heralding probability is given by

$$\mathcal{P}_N \quad = \quad 2^{1-N} \mathrm{e}^{-2N\eta|\alpha|^2} \eta^N |\alpha|^{2N} \Big\{ 1 - \exp\big[-N^2\mu^2(1+2\bar{n})/4\big] \Big\}. \tag{7.24}$$

Crucially, as $\Upsilon_{m,n}$ has only been changed in the prefactor, the final mechanical state ρ_{SCS} will also be unchanged by optical loss.

When $(1-\eta)|\alpha|^2 \ll 1$ *cannot* be satisfied then the measurement operator takes the form

$$\Upsilon_{m,n,k} = \Upsilon_{m,n}\Theta_k, \tag{7.25}$$

where $\Theta_k = C_k\ D(\mathrm{i}k\mu/\sqrt{2})$, with $C_k = [(\sqrt{1-\eta})\alpha]^k/\sqrt{k!}$. Note that because Θ_k is a function of X_{M}, it commutes with all other operators in $\Upsilon_{m,n}$. As such, in the multistep protocol the effect of optical loss may be computed by commuting all of the Θ_k operators to left, which modifies Eq. (7.9) to

$$\rho_N \propto \sum_{k_1,k_2,\ldots,k_N=0}^{\infty} \Theta_{k_N}\Theta_{k_{N-1}}\ldots\Theta_{k_1}[D(\mathrm{i}N\mu/\sqrt{2}) - \mathbb{1}] \circ \rho_{\mathrm{in}}. \tag{7.26}$$

In the case of a coherent input state and in the presence of optical loss, the Wigner distribution of the mechanical mode after N steps of the protocol is therefore

$$W_\eta(X_{\rm M},P_{\rm M}) = \frac{\mathcal{N}_\eta}{\pi(1+2\bar{n})}\sum_{k_1,k_2,\ldots,k_N=0}^{\infty}|C_{k_N}|^2|C_{k_{N-1}}|^2\ldots|C_{k_1}|^2$$
$$\Bigg\{\exp\Big[\frac{-X_{\rm M}^2-(P_{\rm M}-\mu\sum_{i=1}^N k_i)^2}{1+2\bar{n}}\Big]+\exp\Big[\frac{-X_{\rm M}^2-(P_{\rm M}-N\mu-\mu\sum_{i=1}^N k_i)^2}{1+2\bar{n}}\Big]$$
$$-2\cos(N\mu X_{\rm M})\exp\Big[\frac{-X_{\rm M}^2-(P_{\rm M}-N\mu/2-\mu\sum_{i=1}^N k_i)^2}{1+2\bar{n}}\Big]\Bigg\}, \tag{7.27}$$

where the normalization is given by

$$\frac{1}{2\mathcal{N}_\eta} = \sum_{k_1,k_2,\ldots,k_N=0}^{\infty}|C_{k_N}|^2|C_{k_{N-1}}|^2\ldots|C_{k_1}|^2\Big\{1-{\rm e}^{-(N^2\mu^2(1+2\bar{n})/4}\Big\}. \tag{7.28}$$

$W_\eta(X_{\rm M},P_{\rm M})$ describes a mechanical state consisting of a statistical mixture of Schrödinger cat states described by the Wigner distribution $W_{\rm SCS}(X,P)$ from Eq. (7.11). Hence, one may write $W_\eta(X_{\rm M},P_{\rm M})$ as

$$W_\eta(X_{\rm M},P_{\rm M}) = \frac{\mathcal{N}_\eta}{\mathcal{N}_{\rm SCS}}\sum_{k_1,k_2,\ldots,k_N=0}^{\infty}|C_{k_N}|^2|C_{k_{N-1}}|^2\ldots|C_{k_1}|^2\times$$
$$W_{\rm SCS}\Big(X_{\rm M},P_{\rm M}-\mu\sum_{i=1}^N k_i\Big). \tag{7.29}$$

The first term in this sum represents the mechanical state in the absence of loss, while higher order terms in $(1-\eta)|\alpha|^2$ represent states displaced from this by integer multiples of μ along the momentum axis. This incoherent mixing of states in the mechanical phase-space distribution is the manifestation of mechanical decoherence induced by optical loss. For an arbitrary α and η, the full heralding probability for state preparation in the presence of optical loss is given by

$$P_N = \sum_{k_1,k_2,\ldots,k_N=0}^{\infty}|C_{k_N}|^2|C_{k_{N-1}}|^2\ldots|C_{k_1}|^2 2^{1-N}{\rm e}^{-2N\eta|\alpha|^2}\eta^N|\alpha|^{2N}\times$$
$$\Big\{1-\exp\big[-(N^2\mu^2(1+2\bar{n})/4\big]\Big\}, \tag{7.30}$$

which reduces to Eq. (7.24) in the limit $(1-\eta)|\alpha|^2 \ll 1$.

As the goal here is the generation of a Schrödinger cat state, in what follows, I will assume the condition $(1-\eta)|\alpha|^2 \ll 1$ is met. However, in Section 7.5.4 I will consider the effect of optical loss on the final mechanical state when the condition $(1-\eta)|\alpha|^2 \ll 1$ is *not* met in more detail.

Heralding probability with optical loss

To summarize, for a single photon input pulse $|\psi\rangle = |1\rangle$, or for a weak coherent input pulse $|\psi\rangle = \left|\sqrt{2}\alpha\right\rangle$, which satisfies $(1-\eta)|\alpha|^2 \ll 1$, the effect of optical loss on the multistep protocol is to leave the mechanical state ρ_{SCS} unchanged, but also to change the heralding probability from Eq. (7.13) to

$$\mathcal{P}_N = \begin{cases} 2^{1-N}\mathrm{e}^{-2N\eta|\alpha|^2}\eta^N|\alpha|^{2N}\left\{1-\exp\left[-N^2\mu^2(1+2\bar{n})/4\right]\right\} & \text{for } |\psi\rangle = \left|\sqrt{2}\alpha\right\rangle \\ 2^{1-2N}\eta^N\left\{1-\exp\left[-N^2\mu^2(1+2\bar{n})/4\right]\right\} & \text{for } |\psi\rangle = |1\rangle. \end{cases} \tag{7.31}$$

Even with optical loss and detector inefficiencies, the case where $|\psi\rangle = |1\rangle$ shows more favourable scaling in the heralding probability $\mathcal{P}_N$ with step number N. With optical loss, the optimal coherent amplitude to maximize the heralding probability is now given by $\sqrt{\eta}|\alpha|_{\max} = 1/\sqrt{2}$. However, smaller values of $|\alpha|$ may be needed to satisfy $(1-\eta)|\alpha|^2 \ll 1$ at realistic detector efficiencies.

7.3.2 Experimental considerations

Photon counters

With single photon input pulses $|\psi\rangle = |1\rangle$, low-dark-count avalanche-photodiodes (APDs) can be used—which may also be referred to as single-photon avalanche diodes (SPADs)—or superconducting nanowire single-photon detectors (SNSPDs) may also be used. In the absence of loss, only $\{0,1\}$ or $\{1,0\}$ click events are possible, so photon-number resolution is not required. In the presence of loss $\{0,0\}$ events are possible, which leads to a loss of mechanical non-classicality and therefore runs of the experiment where these events occur are discarded. In this way, the protocol is made resilient to detector inefficiency and optical loss by selecting a successful run of the experiment at the cost of a reduced success probability—see Eq. (7.31). Dark counts present a second unavoidable deleterious effect as they introduce false positive measurement outcomes. To minimize the frequency of these events, the detection time window may be gated to the pulse arrival time.

When coherent input pulses are used $|\psi\rangle = \left|\sqrt{2}\alpha\right\rangle$, the protocol is best suited for high efficiency, low-noise, photon-number resolving detectors. As the number of steps in the protocol increases past $N = 2$ then, depending on the experimental parameter regime, the total probability of obtaining the cat state may become smaller than the probability of observing a $\{0,2\}$, $\{2,0\}$ or $\{1,1\}$ at any particular step throughout the state preparation protocol. Therefore, in certain parameter regimes—such as $\mu < 1$ and coherent amplitudes $|\alpha| \sim 1$—if the detectors are not capable of photon-number resolution one cannot be confident that a true sequence of $\{0,1\}$ or $\{1,0\}$ events has been recorded and that optical loss has not led to a misidentification in the string of events, which would reduce the mechanical non-classicality. However, if the above demands on detector performance are satisfied—in particular that optical loss is low—then one may include $\{0,0\}$ click events within the string of click events and therefore

boost the heralding probability for state generation[9]. This is because the measurement operator for a coherent input pulse and a $\{0,0\}$ event is proportional to identity and so leaves the mechanical mode unchanged when mechanical decoherence can be neglected.

Experimental run time

Following the discussions of the heralding probability for state preparation, I now offer an approximate timescale over which the experiment may be carried out. Suppose that input pulses are applied every period and the mechanics is allowed to relax during a time T_r between each run of the experiment, where a run involves N steps of the protocol. Here, $T_\mathrm{r} = \min\{1/\gamma, 2\times 10^3\pi/\omega_\mathrm{M}\}$, meaning that the mechanical mode returns to the initial state over the inverse of the intrinsic mechanical decay rate γ. Or, if the quality factor of the mechanical mode Q is too high for this to be practical, one may assume that the mechanical mode can be brought back to the initial state over 10^3 mechanical periods, e.g. via active-feedback. Furthermore, in order to obtain sufficient experimental statistical data, many runs of the experiment will need to be completed. Supposing that one thousand runs of the experiment will be sufficient, it will take a total time of approximately

$$T_\mathrm{tot} = 10^3(2\pi N/\omega_\mathrm{M} + T_\mathrm{r})/\mathcal{P}_N. \tag{7.32}$$

Note that this expression can be used for both of the optical inputs considered in this work by appropriate choice of $\mathcal{P}_N$. In Section 7.5, I will evaluate T_tot for parameter sets taken from experiments.

Furthermore, it is desirable that the decoherence time of the mechanics $1/\Gamma$ is much greater than the time taken to perform a run of the experiment $2\pi N/\omega_\mathrm{M}$ in order to limit the effects of decoherence in the state preparation. Here $\Gamma = (2\bar{n}_\mathrm{b}+1)\gamma$ and $\bar{n}_\mathrm{b}$ is the occupation of the thermal bath, which is not necessarily in thermal equilibrium with the mechanical mode. This leads to the condition $Q/(2\bar{n}_\mathrm{b}+1) \gg 2\pi N$, which is easily met in most ultracold atom implementations and solid-material optomechanical systems operating at cryogenic temperatures—see Section 7.5.

Source of the input pulses

It is clear that single photon input pulses has several distinct advantages over coherent input pulses, such as a more favourable scaling of the heralding probability $\mathcal{P}_N$ with step number N, resilience of the final mechanical state against optical loss, and the ability to *not* use photon-number-resolving detectors. However, as the development of an ideal-single photon source is still an active area of research—see for example Ref. [206]—the choice $|\psi\rangle = |1\rangle$ will add an additional level of complexity to the experimental protocol. Nevertheless, much progress

[9] This is not true for the single photon input states as, in this case, the measurement operator for a $\{0,0\}$ click is not given by identity.

in on-demand deterministic single photon sources has been made in recent years. These on-demand single photon sources include quantum dots [207, 208] and single-atoms sources that work in the strong coupling regime of cavity QED [209]. Moreover, placing these single photon sources inside an optical cavity provides a route to control the temporal shape of the single photon pulses. Note that probabilistic single photon sources could also be used, for example via parametric down conversion followed by heralding a signal photon. However, the probabilistic nature of these single photon sources would reduce the overall heralding probability $\mathcal{P}_N$ of our multistep protocol.

At present, the requirement of creating a high fidelity single photon input pulse every mechanical period is therefore the main disadvantage of choosing $|\psi\rangle = |1\rangle$. Whereas, an ideal source of weak coherent pulses can be readily achieved via standard techniques, such as Mach-Zehnder modulation for example, which allow for a well-defined repetition rate and control over the temporal pulse shapes. In pulsed optomechanics, this pulse duration τ must be brief from the point of view of the mechanical period $2\pi/\omega_{\text{M}}$, but allowing this period τ to be much larger than the inverse of the cavity linewidth, $\tau \gg 1/\kappa$, will lead to a maximization of the optomechanical coupling strength μ as discussed in Section 7.6. Moreover, achieving a Gaussian temporal profile for the input pulses also avoids the need to gate the detection window[10] to achieve a constant value of μ—see Section 7.6.

7.3.3 Scaling of the heralding probability with step number

An optimal value N?

By examining Eq. (7.31), one may ask if the maximum value of $\mathcal{P}_N$ could occur for some value of $N > 1$? It would be surprising if $\mathcal{P}_N$ was maximized with some $N > 1$, as it would suggest that the heralding probability increases as the non-classicality and macroscopicity of the state grows[11]. In probabilistic state preparation tasks, it is often the case that the outcomes that correspond to more non-classical states occur with lower probability. In the context of interferometric state preparation protocols, postselecting the most unlikely measurements outcomes is sometimes referred to as *dark port detection* and is a useful way to amplify the non-classical features of the heralded state [210]. Our intuition tells us that nature favours more classical states and so the heralding probability should decrease with N.

While using intuition is valuable, the calculation should also be carried out. I will now prove that for integer $N \geq 1$, $\mathcal{P}_N$ is maximum for $N = 1$ and decreases with increasing N. Furthermore, here I present just the $|\psi\rangle = |1\rangle$ case, while the case for $|\psi\rangle = \left|\sqrt{2}\alpha\right\rangle$ is proven in the exact same way.

[10] Of course, the detection window should still be gated to minimize the effect of dark counts as previously mentioned.

[11] Here, I investigate if this is the case with the corrected formula for $\mathcal{P}_N$.

I will first show that $\mathcal{P}_1 \geq \mathcal{P}_2$. Setting $b = \mu^2(1+2\bar{n})/4$ and noting $b \geq 0$, one has that $\mathcal{P}_1 = \frac{1}{2}\eta\left(1-\mathrm{e}^{-b}\right)$ and $\mathcal{P}_2 = \frac{1}{8}\eta\left(1-\mathrm{e}^{-4b}\right)$, then $\mathcal{P}_1 \geq \mathcal{P}_2$ is true providing

$$\begin{aligned} 4 &\geq \eta f_1(b), & (7.33)\\ f_1(b) &= \frac{1-\mathrm{e}^{-4b}}{1-\mathrm{e}^{-b}}, & (7.34) \end{aligned}$$

for $b \geq 0$. It is straightforward to show that $f_1(b)$ is a decreasing function of b, i.e. $\dfrac{\partial f_1}{\partial b} = -\mathrm{e}^{-3b}[3+\mathrm{e}^b(2+\mathrm{e}^b)] \leq 0$ for $b \geq 0$. Therefore, to maximize the function $f_1(b)$ the limit $b \to 0$ should be taken, which is most easily done via L'Hôpital's rule:

$$\lim_{b\to 0} f_1(b) = 4, \tag{7.35}$$

which implies the inequality $4 \geq \eta f_1(b)$ is true and thus $\mathcal{P}_1 \geq \mathcal{P}_2$ is true with equality at $\eta = 0$ or $b = 0$, i.e. zero detection efficiency or no optomechanical interaction $\mu = 0$.

Having proved $\mathcal{P}_1 \geq \mathcal{P}_2$ I will now show that $\mathcal{P}_N \geq \mathcal{P}_{N+1}$, which is true providing

$$\begin{aligned} 4 &\geq \eta f_N(b), & (7.36)\\ f_N(b) &= \frac{1-\mathrm{e}^{-(N+1)^2 b}}{1-\mathrm{e}^{-N^2 b}}, & (7.37) \end{aligned}$$

for $b \geq 0$. Note that $f_N(b)$ is a decreasing function of b, i.e. $\dfrac{\partial f_N}{\partial b} \leq 0$ for $b \geq 0$. Explicitly,

$$\begin{aligned} \frac{\partial f_N}{\partial b} &= -\frac{\mathrm{e}^{-b(1+2N)}}{(\mathrm{e}^{bN^2}-1)^2} g(b), & (7.38)\\ g(b) &= 1+2N+\mathrm{e}^{b(1+N)^2}N^2 - \mathrm{e}^{bN^2}(N+1)^2, & (7.39) \end{aligned}$$

and one can see that $g(b) \geq 0$ as

$$\begin{aligned} \mathrm{e}^{b(1+N)^2}N^2 - \mathrm{e}^{bN^2}(N+1)^2 &= \sum_{m=0}^{\infty}\left[\frac{b^m(1+N)^{2m}N^2}{m!} - \frac{b^m N^{2m}(1+N)^2}{m!}\right]\\ &= \sum_{m=0}^{\infty}\frac{b^m}{m!}\left[(1+N)^{2m}N^2 - N^{2m}(1+N)^2\right]\\ &\geq 0 \qquad (7.40) \end{aligned}$$

for $b \geq 0$. Hence, $\dfrac{\partial f_N}{\partial b} \leq 0$ for $b \geq 0$ and so to maximize the function $f_N(b)$, one takes the limit as $b \to 0$ via L'Hôpital's rule:

$$\lim_{b\to 0} f_N(b) = 1 + \frac{2}{N} + \frac{1}{N^2} \leq 4 \tag{7.41}$$

for $N \geq 1$ with equality at $N = 1$. Hence, $4 \geq \eta f_N(b)$ and $\mathcal{P}_N \geq \mathcal{P}_{N+1}$ for all integer $N \geq 1$, with equality at $b = 0$ or $\eta = 0$.

Combining these two results, it therefore follows that for integer $N \geq 1$, $\mu \neq 0$, and $\eta > 0$, $\mathcal{P}_N$ is maximum for $N = 1$ and, furthermore, $\mathcal{P}_N$ decreases with increasing N.

Comparison with the multi-photon counting protocol

It is constructive to compare the heralding probabilities of the protocol introduced here with the multi-photon counting scheme introduced in Ref. [155]. There, mechanical state generation is achieved via the interaction with a coherent state of light $\left|\sqrt{2}\alpha\right\rangle$, followed by a projection of the optical mode onto a NOON state. If $N_{\rm p}$ is the size of multi-port implemented in this scheme, then the heralding probability for state generation is given by

$$\begin{aligned}\mathcal{P}_{N_{\rm p}} &= 2N_{\rm p}^{-N_{\rm p}}\mathrm{e}^{-2|\alpha|^2}|\alpha|^{2N_{\rm p}} \\ &\quad\times\Big\{1-(-1)^{N_{\rm p}}\exp\big[-N_{\rm p}^2\mu^2(1+2\bar{n})/4\big]\cos(N_{\rm p}\phi)\Big\}, \quad (7.42)\end{aligned}$$

where ϕ is the phase imparted by the phase shifter. By choosing $\phi = \pi$, this heralding probability may be rewritten—along with the two heralding probabilities from Eq. (7.13)—as a scaling S multiplied by $\left\{1-\exp\left[-N'^2\mu^2(1+2\bar{n})/4\right]\right\}$, where $N' = N$ or $N_{\rm p}$. Optimizing these scalings over coherent amplitudes, and assuming that $\eta = 1$, leads to

$$S_{\rm (i)} = 2^{1-2N}\mathrm{e}^{-N} \quad (7.43)$$

$$S_{\rm (ii)} = 2^{1-2N} \quad (7.44)$$

$$S_{\rm (iii)} = 2^{1-N_{\rm p}}\mathrm{e}^{-N_{\rm p}}, \quad (7.45)$$

where (i) and (ii) refer to the scalings for $|\psi\rangle = \left|\sqrt{2}\alpha\right\rangle$ and $|\psi\rangle = |1\rangle$ in our multistep scheme, respectively, while (iii) is the optimal scaling from Ref. [155]. Comparison of $S_{\rm (i)}$ with $S_{\rm (iii)}$ indicates that the heralding probability scales more favourably with multi-port size than with step number for the case of a coherent input $\left|\sqrt{2}\alpha\right\rangle$. However, Eq. (7.44) shows that the multistep protocol with a single photon input gives the best heralding probability.

With the above probabilities in mind, I would like to further note that the multi-photon counting scheme in Ref. [155] and the multistep protocol introduced here may be combined. In such a scheme, the momentum transfer to the mechanics per step would increase to $N_{\rm p}\mu$, where $N_{\rm p} \geq 2$, and thus coherent states would be required as the optical input states.

7.3.4 Mechanical decoherence

Decoherence model

The fidelity between the final mechanical state of the protocol and the desired Schrödinger cat state will be limited by interactions with the mechanical thermal

environment. Here, the decoherence of the mechanical mode is modelled through the semigroup mapping [211, 14]

$$\rho_{\rm out} = (\pi\bar{n}_{\rm th})^{-1}\int {\rm d}^2\beta {\rm e}^{-|\beta|^2/\bar{n}_{\rm th}} D(\beta)\rho_{\rm in}D^\dagger(\beta), \tag{7.46}$$

which describes an admixture of thermal phonons to the input state $\rho_{\rm in}$. In this thermalization process, $\bar{n}_{\rm th}$ can be thought of as the mean number of phonons added to the mechanics by the thermal environment between each step of the protocol—so note that $\bar{n}_{\rm th}$ will be much lower than the mean thermal occupation of the bath: $\bar{n}_{\rm th} \ll \bar{n}_{\rm b}$. By expanding Eq. (7.46) using $\bar{n}_{\rm th} \to \bar{n}_{\rm th} + \delta\bar{n}_{\rm th}$, to first order in $\delta\bar{n}_{\rm th}$, it may be seen that the thermalization process is equivalent to the standard single-phonon quantum master equation that describes the evolution of a state in contact with a high temperature bath $\bar{n}_{\rm b} \gg 1$. Explicitly, expanding Eq. (7.46) to first order in $\delta\bar{n}_{\rm th}$ and then treating this quantity as an infinitesimal $\delta\bar{n}_{\rm th} \to {\rm d}\bar{n}_{\rm th}$ gives

$$\frac{{\rm d}\rho}{{\rm d}\bar{n}_{\rm th}} = \mathcal{D}[b]\rho + \mathcal{D}[b^\dagger]\rho. \tag{7.47}$$

Following Ref. [211], one may then change variables via $\bar{n}_{\rm th} = \gamma\bar{n}_{\rm b}t$, which gives

$$\frac{{\rm d}\rho}{{\rm d}t} = \gamma\bar{n}_{\rm b}\mathcal{D}[b]\rho + \gamma\bar{n}_{\rm b}\mathcal{D}[b^\dagger]\rho. \tag{7.48}$$

Comparison of Eq. (7.48) to Eq. (3.8) from Chapter 3, tells us that in this scheme the convention that the mechanical decay rate γ is an intensity[12] quantity is used, which is to be kept in mind when quoting values from the literature. Furthermore, for ease of computation the free mechanical evolution is not explicitly included in Eq. (7.48). This is because our protocol works by applying the measurement operator $\Upsilon_{0,1}^{(j)}$ to the mechanics once every mechanical period.

In other words, Eq. (7.48) may be integrated in between steps of the protocol, to obtain Eq. (7.46), where $\bar{n}_{\rm th}$ is then the mean number of thermal phonons added to the state during this time. Mathematically, the requirement for a high temperature bath is $\bar{n}_{\rm b} \gg 1$, which remains an appropriate limit for many mechanical quantum systems even at cryogenic temperatures.

To approximate the number of phonons added between each step, I use $\bar{n}_{\rm th} = \gamma\bar{n}_{\rm b}t$ and take t equal to one mechanical period. Furthermore, at these high bath temperatures $\bar{n}_{\rm b} \approx \bar{n}_{\rm b} + 1/2$. Together, this gives

$$\bar{n}_{\rm th} \approx \pi(2\bar{n}_{\rm b} + 1)/Q. \tag{7.49}$$

The Wigner function in the presence of decoherence

As in Section 7.2.3 I assume that the mechanical mode is initially in the thermal state $\rho_{\bar{n}}$ and I apply the measurement operator $\Upsilon_{0,1}^{(j)}$ at each step. Eq. (7.46) is

[12] Rather than an amplitude quantity as in Chapter 3, hence the factor of 2 difference.

now used to model the decoherence during the mechanical period between each step. This may be computed analytically, and the Wigner distribution after N iterations of this step-thermalization process is

$$W_{\bar{n}_{\rm th}}(X_{\rm M}, P_{\rm M}) = \mathcal{N} \sum_{l_1,m_1,\ldots,l_N,m_N=0}^{1} \left\{ \exp\left[\mathrm{i} \sum_{i=1}^{N} (l_i - m_i)(\mu X_{\rm M} - \phi_i - \pi) - \frac{1}{2}\bar{n}_{\rm th} \sum_{i=1}^{N} \xi_i^2 \right] \exp\left[- \frac{(X_{\rm M} + \mathrm{i}\bar{n}_{\rm th} \sum_{i=1}^{N} \xi_i)^2}{1 + 2\bar{n} + 2N\bar{n}_{\rm th}} - \frac{(P_{\rm M} - \frac{1}{2}\sum_{i=1}^{N}(l_i + m_i)\mu)^2}{1 + 2\bar{n} + 2N\bar{n}_{\rm th}} \right] \right\}, \quad (7.50)$$

where $\xi_i = \sum_{j=1}^{i}(l_j - m_j)\mu$ and $\mathcal{N}$ ensures normalization. For $\bar{n}_{\rm th} = 0$, this Wigner distribution returns to Eq. (7.11) so the $\bar{n}_{\rm th}$ dependent terms in Eq. (7.50) may be identified as a damping and shifting of the interference features of the Wigner distribution. This decoherence effect leads to an imperfect cancellation of the N population terms in the mechanical cat state.

7.4 Quantifying the cats

In this section I discuss the non-classicality and macroscopicity of the states produced by this protocol. I then demonstrate that significant non-classicality and macroscopicity for realistic experimental scenarios can be generated. The non-classicality measures investigated are based on the negativity of the Wigner distribution, while the macroscopicity measures studied are the phase-space measure $\mathcal{I}$, introduced in Ref. [191], and a measure based on the quantum Fisher information [198]. Definitions and descriptions of these non-classicality and macroscopicity measures are given below.

7.4.1 Non-classicality

In stark contrast to classical joint probability distributions, the Wigner distributions may become negative, and hence negativity in the Wigner distribution is a signature of non-classicality. Therefore, I present two measures of non-classicality based on the Wigner distribution—its minimum value (min W) and its total negative volume δ [212].

The absolute minimum value any properly normalized Wigner distribution may take is $-1/\pi$ [18]. When the multistep protocol is applied to an initial thermal state, and decoherence is ignored between steps, the final mechanical state is given by Eq. (7.11). In this case, the minimum value of $W_{\rm SCS}$ occurs at $X_{\rm M} = 0$, $P_{\rm M} = N\mu/2$ and is given by

$$\min W_{\rm SCS} = -\frac{1}{\pi(1 + 2\bar{n}))} \frac{\{1 - \exp[-N^2\mu^2/4(1 + 2\bar{n})]\}}{\{1 - \exp[-N^2\mu^2(1 + 2\bar{n})/4]\}}. \quad (7.51)$$

For this state, in the limit of large momentum separation $N\mu$, the minimum of the Wigner distribution becomes $-1/\pi(1 + 2\bar{n})$, and therefore the states pro-

duced in the multistep protocol approach the absolute minimum value for min W in the limit $\bar{n} \to 0$.

The total negative volume of the Wigner distribution δ [212] is calculated using

$$\delta = \frac{1}{2}\left(\int\int |W(X,P)| \mathrm{d}X \mathrm{d}P - 1 \right), \tag{7.52}$$

which is strictly greater than or equal to zero. Furthermore, in F.1 I show that for Schrödinger cat states this measure is always less than $1/\pi$. This upper bound is reached for $N\mu \gg 1$ even in the case where the mechanical mode supports an initial non-zero mean thermal occupation. However, the introduction of mechanical decoherence ($\bar{n}_{\mathrm{th}} \neq 0$) between steps causes the value of δ to reduce and drop below this maximal value, as will be discussed in the results section below.

7.4.2 Macroscopicity

The phase space measure $\mathcal{I}$

The phase-space measure of macroscopicity for a single-mode Wigner distribution introduced by Lee and Jeong in Ref. [191] is defined as

$$\mathcal{I} = -\frac{\pi}{2} \int_{-\infty}^{+\infty} \int_{-\infty}^{+\infty} W(X,P)(\nabla^2 + 2) W(X,P) \mathrm{d}X \mathrm{d}P, \tag{7.53}$$

where ∇^2 is the Laplacian in phase space. $\mathcal{I}$ quantifies the size of the superposition by measuring the degree to which the sharp features, caused by interference effects, extend in phase space. In Ref. [191], Lee and Jeong show that pure Schrödinger cat states belong to a class of states that saturate the upper bound that can be reached by $\mathcal{I}$, namely the expectation value of the number operator. Note that $\mathcal{I}$ has been used to quantify macroscopicity in other optomechanics-based mechanical-state generation schemes such as in Ref. [183].

Quantum Fisher information based measure $N_{\mathrm{eff}}(\rho)$ and pure states

Quantum Fisher information (QFI) $\mathcal{F}$ is typically used as a tool in parameter estimation [197], however, more recently QFI has been used as a genuine measure of macroscopic quantum effects in spin ensembles [193] and in photonic systems [194]. The macroscopicity of a state ρ can be quantified by its sensitivity to translations in phase space. First note that the translated state is given by $\rho_\tau = \mathrm{e}^{-\mathrm{i}\tau X_\theta} \rho \mathrm{e}^{\mathrm{i}\tau X_\theta}$, with $X_\theta = (a\mathrm{e}^{-\mathrm{i}\theta} + a^\dagger \mathrm{e}^{\mathrm{i}\theta})/\sqrt{2}$. Differentiation with respect to the small real parameter τ gives the equation

$$\frac{\partial \rho_\tau}{\partial \tau} = \mathrm{i}[\rho_\tau, X_\theta]. \tag{7.54}$$

The QFI with respect to these phase-space translations, $\mathcal{F}_\tau$, is then calculated[13] for each θ via [213]

$$\mathcal{F}_\tau = \sum_{m\neq n} \frac{2}{\lambda_m + \lambda_n} |\langle\psi_m| \frac{\partial\rho_\tau}{\partial\tau} |\psi_n\rangle|^2, \tag{7.55}$$

where the spectral decomposition of ρ_τ is given by

$$\rho_\tau = \sum_m \lambda_m |\psi_m\rangle\langle\psi_m| . \tag{7.56}$$

Finally, a maximization over all θ is performed and the QFI-based macroscopicity measure for a single mode of a bosonic system is therefore[14] [193, 194]

$$N_{\text{eff}}(\rho) = \frac{1}{2}\max_\theta \mathcal{F}_\tau. \tag{7.57}$$

As the QFI corresponds to the classical Fisher information (CFI) maximized over all possible POVMs [198], one may also write $N_{\text{eff}}(\rho)$ as

$$N_{\text{eff}}(\rho) = \frac{1}{2}\max_{\theta,\text{POVMs}} F_\tau, \tag{7.58}$$

where

$$F_\tau = \int \mathrm{d}x \frac{1}{p_\tau(x)}\Big(\frac{\partial p_\tau(x)}{\partial\tau}\Big)^2 \tag{7.59}$$

is the CFI. Here, $p_\tau(x) = \text{tr}[\rho_\tau E(x)]$ for POVM element $E(x)$, and as before $\rho_\tau = \mathrm{e}^{-\mathrm{i}\tau X_\theta}\rho\mathrm{e}^{\mathrm{i}\tau X_\theta}$, and $X_\theta = (a\mathrm{e}^{-\mathrm{i}\theta} + a^\dagger\mathrm{e}^{\mathrm{i}\theta})/\sqrt{2}$.

However, the measure $N_{\text{eff}}(\rho)$ is computationally difficult to calculate for mixed states, as diagonalization of the density matrix—or, equivalently, a maximization over all POVMs—is required to obtain the QFI. Whereas for pure states no such diagonalization or maximization is required. Namely, from Eq. (7.54)

$$\langle\psi_m| \frac{\partial\rho_\tau}{\partial\tau} |\psi_n\rangle = \mathrm{i}(\lambda_m - \lambda_n)\langle\psi_m| X_\theta |\psi_n\rangle , \tag{7.60}$$

and then inserting this into Eq. (7.55) gives the alternative expression for the QFI

$$\mathcal{F}_\tau = \sum_{m\neq n} \frac{2(\lambda_m - \lambda_n)^2}{\lambda_m + \lambda_n} |\langle\psi_m| X_\theta |\psi_n\rangle|^2. \tag{7.61}$$

[13] The reader should not view this as the 'core' definition of the QFI. Instead, one should view the QFI as the classical analogue of the Fisher information maximized over all POVMs or as the expectation value of the symmetric logarithmic derivative squared–see Ref. [213]. Eq. (7.55) is thus merely a useful starting point for the analysis.

[14] The subscript on $N_{\text{eff}}(\rho)$ comes from Ref. [193], where this quantity was introduced and is referred to as the 'effective size' of the state.

If $\rho_\tau = |\psi\rangle\langle\psi|$ is a pure state then in the spectral decomposition $\lambda_1 = 1$ and $\lambda_m = 0$ for $m \neq 1$. Further, $|\psi_1\rangle = |\psi\rangle$ and so Eq. (7.61) becomes

$$\begin{aligned}\mathcal{F}_\tau &= 2\sum_{m\neq 1} |\langle\psi_m| X_\theta |\psi\rangle|^2 + 2\sum_{n\neq 1} |\langle\psi| X_\theta |\psi_n\rangle|^2 \\ &= 4\sum_{n\neq 1} \langle\psi| X_\theta |\psi_n\rangle\langle\psi_n| X_\theta |\psi\rangle . \end{aligned} \tag{7.62}$$

Identity may then be decomposed as

$$\mathbb{1} = |\psi\rangle\langle\psi| + \sum_{n\neq 1} |\psi_n\rangle\langle\psi_n| \tag{7.63}$$

and insert $\sum_{n\neq 1} |\psi_n\rangle\langle\psi_n|$ into Eq. (7.62) using this expression. This gives

$$\begin{aligned}\mathcal{F}_\tau &= 4\left[\langle\psi| X_\theta^2 |\psi\rangle - (\langle\psi| X_\theta |\psi\rangle)^2\right] \\ &= 4\mathrm{Var}(X_\theta). \end{aligned} \tag{7.64}$$

Hence, for pure states the QFI, with respect to X_θ, simply reduces to four times the variance of X_θ. In particular, for the pure Schrödinger cat state, with $\bar{n} = \bar{n}_{\mathrm{th}} = 0$,

$$\mathcal{F}_\tau = 2 + \frac{N^2\mu^2}{1-\exp(-N^2\mu^2/4)} - N^2\mu^2\cos^2\theta, \tag{7.65}$$

which is maximum at $\theta = \pi/2$. Hence,

$$N_{\mathrm{eff}}(\rho_{\mathrm{SCS}}) = 1 + \frac{N^2\mu^2}{2\left[1-\exp(-N^2\mu^2/4)\right]}. \tag{7.66}$$

Encouragingly, QFI has been shown to satisfy a set of conditions for measures of macroscopic coherence in Ref. [214]. Therefore I will now present a measure based on QFI as an alternative measure of macroscopicity, which is easy to calculate for mixed states.

Alternative quantum Fisher information based measure $\mathcal{M}$ and mixed states

To alleviate the difficulty of maximizing over all possible POVMS when the state is mixed, the set of POVMs is restricted to $E(X_\lambda) = |X_\lambda\rangle\langle X_\lambda|$, where $0 \leq \lambda < \pi$, which corresponds to quadrature measurements at an angle λ from the position axis. I therefore introduce a macroscopicity measure $\mathcal{M}$ that satisfies $\mathcal{M} \leq \mathcal{N}_{\mathrm{eff}}(\rho)$. To analyze the macroscopicity of mixed states, the simplified QFI-based measure proposed is

$$\mathcal{M} = \frac{1}{2}\max_{\theta,\lambda} F_\tau, \tag{7.67}$$

where F_τ is the CFI given in Eq. (7.59) but with $p_\tau = \langle X_\lambda| \rho_\tau |X_\lambda\rangle$.

Eq. (7.67) is still difficult to calculate as it requires maximization over two variables θ and λ. Fortunately, this expression can be simplified by rewriting the state ρ_τ in the Glauber-Sudarshan P representation,

$$\begin{aligned}\rho_\tau &= \mathrm{e}^{-\mathrm{i}\tau X_\theta}\rho\mathrm{e}^{\mathrm{i}\tau X_\theta} \\ &= \int_{-\infty}^{+\infty}\int_{-\infty}^{+\infty} P_0(X,P)\mathrm{e}^{-\mathrm{i}\tau X_\theta}\,|\gamma\rangle\langle\gamma|\,\mathrm{e}^{\mathrm{i}\tau X_\theta}\,\mathrm{d}^2\gamma \\ &= \int_{-\infty}^{+\infty}\int_{-\infty}^{+\infty} P_\tau(X,P)\,|\gamma\rangle\langle\gamma|\,\mathrm{d}^2\gamma, \end{aligned} \tag{7.68}$$

with coherent amplitude $\gamma = (X+iP)/\sqrt{2}$. Here $P_\tau(X,P)$ is the P function of the state ρ_τ, while $P_0(X,P)$ is the P function of state ρ. Considering the action of the displacement operators on the coherent states $|\gamma\rangle$ allows one to see that $P_\tau(X,P) = P_0(X-\tau\sin\theta, P+\tau\cos\theta)$, and consequently $W_\tau(X,P) = W_0(X-\tau\sin\theta, P+\tau\cos\theta)$. The Radon transformation [18]

$$p_\tau(X_\lambda) = \int_{-\infty}^{+\infty} W_\tau(X\cos\lambda - P\sin\lambda, X\sin\lambda + P\cos\lambda)\mathrm{d}P \tag{7.69}$$

may then be employed to show that $p_\tau(X_\lambda) = p_0[X_\lambda - \tau\sin(\theta+\lambda)]$. Inserting this into Eq. (7.59) and making the substitution $X_\lambda^{'} = X_\lambda - \tau\sin(\theta+\lambda)$ leads to the expression $F_\tau = \sin^2(\theta+\lambda)F_{X_\lambda}$. Here,

$$F_{X_\lambda} = \int_{-\infty}^{+\infty}\mathrm{d}X_\lambda \frac{1}{p_0(X_\lambda)}\Big(\frac{\partial p_0(X_\lambda)}{\partial X_\lambda}\Big)^2, \tag{7.70}$$

is the CFI of the quadrature X_λ, which is much easier to calculate than F_τ as no explicit reference is made to the phase-space translations which is used to test the sensitivity of the state ρ. Hence the macroscopicity measure employed is $\mathcal{M} = \frac{1}{2}\max_{\theta,\lambda}\{\sin^2(\theta+\lambda)F_{X_\lambda}\}$, which is clearly maximum when the phase-space translations are parallel to the quadrature X_λ, $\theta+\lambda = \pm\pi/2$. Finally, the simplified expression for $\mathcal{M}$ is

$$\mathcal{M} = \frac{1}{2}\max_\lambda F_{X_\lambda}. \tag{7.71}$$

Importantly, this form of $\mathcal{M}$ only requires maximization over *one variable*, the phase space angle λ, rather than the two variables θ and λ as originally suggested by the form of Eq. (7.67).

Furthermore, the states which are produced in the multistep protocol contain interference terms that oscillate along the X_{M} axis of phase space, and hence the maximization is achieved at $\lambda = 0$. Further, the CFI of the Schrödinger cat state, with $\bar{n} \neq 0$ and $\bar{n}_{\mathrm{th}} = 0$, is given by

$$F_X = \frac{2}{2\bar{n}+1} + \frac{N^2\mu^2}{1-\exp[-N^2\mu^2(2\bar{n}+1)/4]}, \tag{7.72}$$

and hence

$$\mathcal{M} = \frac{1}{2\bar{n}+1} + \frac{N^2\mu^2}{2\left\{1-\exp[-N^2\mu^2(2\bar{n}+1)/4]\right\}} \tag{7.73}$$

By comparing Eqs (7.66) and (7.73), for a pure Schrödinger cat state, $\bar{n} = \bar{n}_{\rm th} = 0$, one has that $\mathcal{M} = N_{\rm eff}(\rho_{\rm SCS})$. Therefore, for a pure Schrödinger cat state, $\bar{n} = \bar{n}_{\rm th} = 0$, it is clear that a quadrature measurement along $X_{\rm M}$ is in fact the optimal POVM measurement, which provides further motivation for restricting the class of POVMs to quadrature measurements.

Aside.—As the cat state is orientated along the momentum axis of phase space, a quadrature measurement along $X_{\rm M}$ effectively scans over the interference fringes. A value of $\theta = \pi/2$ in ρ_τ, then translates the state such the interference fringes move parallel to the $X_{\rm M}$ axis. Using this physical intuition, when the cat state is *thermal* one expects that (i) an $X_{\rm M}$ quadrature measurement is the POVM that maximizes the QFI and (ii) therefore $\theta = \pi/2$ gives $N_{\rm eff}(\rho_{\rm SCS}) = \mathcal{M}$ in Eq. (7.73)—see above for the proof this is true in the pure case.

More generally, one may expect that the optimal POVM measurement that gives the QFI of a thermal Schrödinger cat state is a quadrature measurement along the orthogonal direction to which the Schrödinger cat state is orientated, i.e. scanning over the interference fringes. Therefore $N_{\rm eff}(\rho_{\rm SCS}) = \mathcal{M}$. Then, letting this optimal POVM be an X_λ quadrature measurement, one may expect the correct choice of θ that maximizes $N_{\rm eff}(\rho_{\rm SCS})$ is then $\theta = \lambda \pm \pi/2$. The reasoning for this is as the state ρ_τ is translated in phase space, the interference fringes move parallel to the X_λ axis. Note that this postulate is not proven for mixed states in this thesis and so I stick to using $\mathcal{M}$ as the macroscopicity measure.

7.5 Results

7.5.1 Cats versus kittens

In this multistep protocol, the non-classicality and macroscopicity of the final state depends on $N\mu$ and the initial thermal occupation of the mechanical mode. As an example, consider the ideal case $\bar{n} = \bar{n}_{\rm th} = 0$, where the RMS width of the initial Gaussian state is $\sqrt{\langle X^2\rangle} = 1/\sqrt{2}$. For $N\mu < 1/\sqrt{2}$, the final state of the mechanical mode resembles a single-phonon Fock state. This can be seen by taking the limit $N\mu \to 0$ in Eq. (7.9), which gives $[D(\mathrm{i}N\mu/\sqrt{2}) - \mathbb{1}]\,|0\rangle \approx \mathrm{i}N\mu X\,|0\rangle \propto |1\rangle$. Varying the value of $N\mu$ in the range $N\mu < 1/\sqrt{2}$ has very little effect on the non-classicality and macroscopicity measures of these states. For example, when $N\mu$ is increased from 10^{-4} to 0.1, δ remains approximately 0.2131, this equalling the value of δ for a single-phonon Fock state $\delta_{|1\rangle} = 2\mathrm{e}^{-0.5} - 1 \simeq 0.2131$. The macroscopicity measure $\mathcal{M}$ also remains

clamped in this interval at 3—this being equal to the value of $\mathcal{M}$ for the state $|1\rangle$.

When $N\mu$ is increased above the width of the initial Gaussian state, the state becomes more macroscopic. For example, when $N\mu = 2$, the non-classicality measure δ remains saturated at the value of the single-phonon Fock state, whereas $\mathcal{M}$ has increased rapidly to 4.16. The phase-space distribution now resembles a 'kitten' state—a Schrödinger cat state with a small separation between population terms. As $N\mu$ is increased even further, such that $N\mu > 4/\sqrt{2}$, the non-classicality and macroscopicity measures increase more dramatically. At $N\mu = 4$, δ reaches 0.2462 and $\mathcal{M}$ increases to 9.15. When $N\mu > 4/\sqrt{2}$, the separation of the two Gaussian population terms is greater than four times the RMS width of the ground state, such that the diameter of the interference fringes—given by twice the RMS width of the ground state— does not overlap with the width of the population components. Moreover, when $N\mu > 4/\sqrt{2}$ the mechanical mode is a bona fide Schrödinger cat state as the overlap between the two Gaussian population terms is negligible (less than 1.83%).

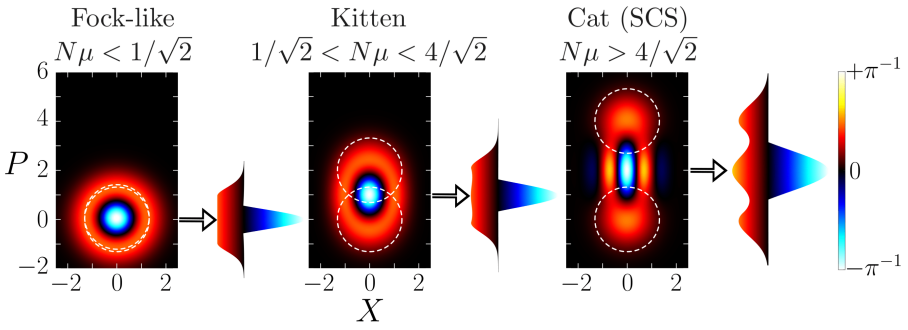


Figure 7.5: **Wigner distributions of the single-phonon Fock-like state, kitten state, and Schrödinger cat state (SCS) that can be generated by our scheme.** This figure shows how the ratio of $N\mu$ and the initial width of the mechanical mode determines the nature of the final state produced in the multistep protocol. Here, $\bar{n} = 0$, $\bar{n}_{\rm th} = 0$ and $N\mu$ increases from left to right as 0.1, 2 and 4. White-dashed circles of radius $\sqrt{2}$—twice the RMS width of the ground state—are placed around each of the Gaussian population terms. When $N\mu > 4/\sqrt{2}$ these circles do not overlap and the mechanical mode is in a cat state. Side-views of the Wigner distributions parallel to the position axis are also plotted to highlight the difference between the three different regimes of states. All these distributions are computed from Eq. (7.11).

In the impure case, initial thermal occupation, or thermal decoherence, leads to a smearing of the population terms and a reduction in the quantum interference fringe visibility. The decoherence process modelled by Eq. (7.46) reduces

the non-classicality and macroscopicity of the state in a non-trivial way as the state grows, such that at a certain step number the non-classicality and macroscopicity may begin to decrease as the multistep protocol proceeds. This is discussed in more detail below and computed numerically. Fig. 7.5 illustrates the three different regimes of states generated in the protocol depending upon the value of $N\mu$. In particular, the side-view of this figure shows how the two peaks from the Gaussian population terms in the phase-space distribution begin to become resolvable when $N\mu$ increases past $1/\sqrt{2}$, before becoming fully distinct when $N\mu > 4/\sqrt{2}$.

7.5.2 Experimental parameters

Table 7.1 lists a range of parameter sets taken from recent experiments that implement ultracold atom or solid-material realizations of optomechanical systems. In order to expose the mechanical quantum features, which lie beneath any thermal fluctuations, the mechanical system must be cooled close to its ground state. Therefore, in this table for the solid state devices it is assumed that the mechanical resonator is pre-cooled to $\bar{n} = 0.1$ and the bath temperature is 100 mK. This can be done using a combination of cryogenics, back-action cooling and active-feedback cooling methods [45]. The table also includes a range of proposed parameter sets that enable improved performance with our protocol. Here, the following case is considered: the optical input state is a single-photon pulse $|\psi\rangle = |1\rangle$, the step number is $N = 3$, and one thousand runs of the multistep protocol have been completed at an optical efficiency of 90%, such that $\eta = 0.9$. Therefore, the column headed $T_{\rm tot}$ indicates the approximate total time taken[15] to complete an experiment where one thousand successful runs are obtained. If a weak coherent pulse $|\psi\rangle = \left|\sqrt{2}\alpha\right\rangle$ is chosen as the input state then the protocol takes approximately twenty times longer when $N = 3$. The final four columns show the values of the non-classicality and macroscopicity measures calculated using Eq. (7.50) and the definition of these measures from Section 7.4.1 and 7.4.2.

[15] As compared to Ref. [1], the aforementioned missing factor of 2^{-N} in $\mathcal{P}_N$ has been included when calculating these values for $T_{\rm tot}$. Note this correction only affects the case for the single photon inputs $|\psi\rangle = |1\rangle$ and not the case for the coherent state inputs $|\psi\rangle = \left|\sqrt{2}\alpha\right\rangle$. Therefore, to approximate the time taken for an experiment with coherent state inputs, one needs to multiply the values of $T_{\rm tot}$ in Table 7.1 by 20 and *not* a factor of ~ 100 as stated in the original manuscript.

Table 7.1: **Present-day experimental and proposed parameter sets**. Here, one thousand runs of the multistep protocol have been considered using single photons as the optical input states $|\psi\rangle = |1\rangle$. Each run consists of $N = 3$ steps with 10% optical loss at each step. All ultracold atom setups are assumed to be operating at $\bar{n} = 0$ and at a low bath occupancy, while it is assumed that the solid-material setups are operating at $\bar{n} = 0.1$ in a thermal bath which has been cooled to 100 mK. Parameter set (i) is a currently realizable proposal for generating macroscopic Schrödinger cat states in ultracold atoms, while parameter sets (ii), (iii) are proposals for generating macroscopic states in near-future solid-material systems.

Ref.	μ	$\omega_{\rm M}/2\pi$(Hz)	Q	$\bar{n}_{\rm th}$	$T_{\rm tot}$(s)	min W	δ	$\mathcal{I}$	$\mathcal{M}$
Ultracold atom systems									
[131]	17.8	37×10^3	581	5.41×10^{-3}	113	-0.047	0.115	1.71	11.6
[74]	15.4	50×10^3	314	7.14×10^{-3}	46.5	-0.046	0.116	1.28	9.06
(i)	15.0	50×10^3	785	4.00×10^{-3}	112	-0.049	0.142	2.05	13.7
Solid-material systems									
[112]	9.64×10^{-5}	4.30×10^6	7.54×10^5	4.05×10^{-3}	4.08×10^8	-0.172	0.117	0.323	1.91
[133]	8.44×10^{-3}	3.74×10^6	3.74×10^4	9.40×10^{-2}	6.12×10^4	-0.023	0.010	-0.032	0.512
(ii)	0.10	1.00×10^6	6.28×10^6	2.09×10^{-3}	1650	-0.178	0.122	0.351	2.09
(iii)	1.00	1.00×10^6	6.28×10^6	2.09×10^{-3}	47.2	-0.230	0.165	0.886	4.39

I would like to highlight that the generation of a truly macroscopic Schrödinger cat state is currently achievable using ultracold implementations of optomechanical devices over realistic timescales. The proposed parameter set (i) is currently realizable and serves as a suggestion for slight improvements that can be made to individual parameters for an even better performance of the scheme. The solid state systems in Ref. [112] and [133], as well as proposal (ii), operate in the regime where $N\mu < 1/\sqrt{2}$. The protocol is successful in generating macroscopic states for the parameters from Ref. [112] and (ii), as macroscopicity values much larger than that of the initial thermal state are generated. For reference, the macroscopicity of a thermal state is given by $\mathcal{M} = 1/(2\bar{n} + 1)$ as can be seen by setting $\mu = 0$ in Eq. (7.73), which equals 0.83 for $\bar{n} = 0.1$. However, in this regime true Schrödinger cat states cannot be generated as $N\mu > 4/\sqrt{2}$ is required. Given the current rate of experimental advances, it is encouraging that μ need only be increased by a factor of one hundred to allow for the generation of Schrödinger cat states in solid-material devices when $N = 3$. Importantly, this requirement on the improvement of μ is relaxed even further when N is increased. Proposal (iii) illustrates the success of the protocol in preparing macroscopic Schrödinger cat states when this requirement on $N\mu > 4/\sqrt{2}$ is met.

The parameter set from Ref. [133] generates little non-classicality and macroscopicity despite the relatively large value of μ. This is due to the rapid thermalization of the mechanical mode in between steps, which is a consequence of the low quality factor. The performance of the protocol rapidly diminishes as $\bar{n}_{\rm th}$ is increased in magnitude past 10^{-2}, and note that the value of $\bar{n}_{\rm th}$ depends upon the quality factor and the temperature of the thermal bath.

Values for the mean number of phonons added to the mechanical mode were calculated using Eq. 7.49. The values of the measures of non-classicality and

macroscopicity reached in this multistep protocol are sensitive to the value of $\bar{n}_{\rm th}$, in fact, for a given value of μ and $\bar{n}_{\rm th}$, there may be a point where increasing the step number past a certain value leads to a reduction in the non-classicality and macroscopicity of the state. The plots in the next section illustrate this point and demonstrate that for a given parameter set an optimal step number can be chosen by considering the total time required and calculating the measures from Eq. 7.50. I will now study the non-classicality and macroscopicity of the mechanical states in more detail.

7.5.3 The non-classicality and macroscopicity

The plots in Figs. 7.6 through 7.9 consider the dependence of the non-classicality and macroscopicity measures on step number for $\bar{n}_{\rm th} = \{10^{-5}, 10^{-3}, 10^{-2}\}$, $\bar{n} = \{0, 0.1, 1\}$, and $\mu = \{0.1, 1\}$. As expected, the introduction of decoherence between steps filters out the high-frequency contributions to the Wigner distribution, which leads to a decrease in the non-classicality and macroscopicity values. Step numbers ranging from zero through to seven are considered and note that the case where $\bar{n}_{\rm th} = 10^{-5}$ performs as well as the ideal case, with $\bar{n}_{\rm th} = 0$, to within five percent by the end of the seventh step for all measures. Therefore, if optomechanical devices could be produced with sufficiently high quality factors operating at millikelvin temperatures, such that $\bar{n}_{\rm th} \approx 10^{-5}$, then Eq. 7.11 would serve as an accurate tool for analysis up to at least seven steps. The cases where $\bar{n}_{\rm th} = 10^{-3}$ are also considered, which was considered in Table 7.1, and $\bar{n}_{\rm th} = 10^{-2}$, which represents a situation where thermal interactions are much stronger. Furthermore, I assume that either single photons or weak coherent states, satisfying $(1-\eta)|\alpha|^2 \ll 1$, are used as input states such that the presence of optical loss has no effect on the phase distribution of the final mechanical state.

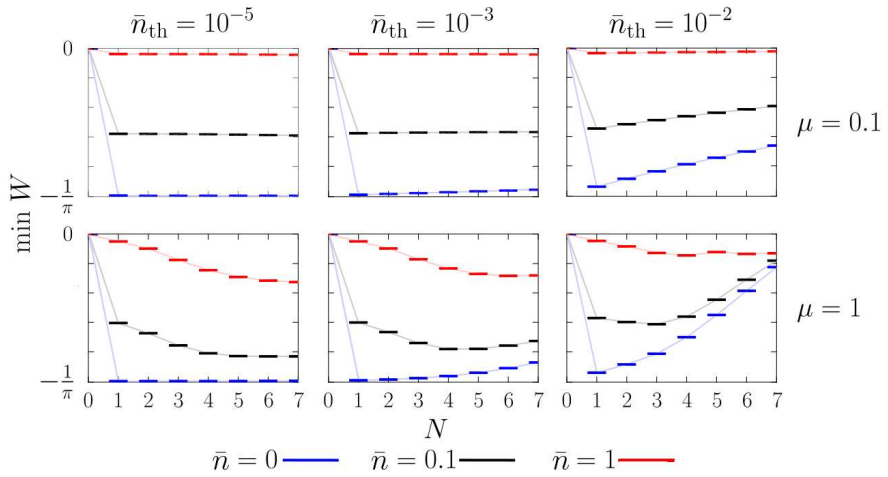


Figure 7.6: **Minimum of the Wigner distribution min W plotted as a function of step number N for a range of μ, $\bar{n}_{\rm th}$, and $\bar{n}$.** In the ideal case, $\bar{n} = \bar{n}_{\rm th} = 0$, this non-classicality measure saturates at the minimum possible value of $-1/\pi$ irrespective of the value of μ. Although the Wigner distribution has greater negativity for $\mu = 1$ and for small decoherence ($\bar{n}_{\rm th} = 10^{-5}$), the lower value of μ produces a state with a min W more resilient to the thermal decoherence as N increases.

The non-classicality measures plotted in Figs. 7.6 and 7.7 are very sensitive to initial thermal occupation, which reduces the prominence of any non-classical features of the final mechanical state. The amount of thermal occupation, and therefore the reduction in 'phase-space sharpness', is further increased by the decoherence process modelled in between steps of the protocol. Generally speaking, Figs. 7.6 and 7.7 show that states with the highest values of $N\mu$, and therefore the sharpest phase-space features, are more susceptible to thermal decoherence effects. This is the conventional quantum-to-classical transition in action. Note that, even after seven steps of the multistep protocol the states with $\mu = 1$ experiencing heavy thermalization, $\bar{n}_{\rm th} = 10^{-2}$, still retain significant non-classicality—approximately one-fifth of the maximal values for each non-classicality measure.

The macroscopicity measures are plotted in Figs. 7.8 and 7.9 and by comparing these plots it may be seen that these two measures scale similarly with N. This is because both $\mathcal{I}$ and $\mathcal{M}$ measure macroscopicity via the degree to which sharp features extend in phase space. $\mathcal{I}$ measures this sharpness by averaging over the whole of phase space, while $\mathcal{M}$ selects an optimal direction in phase space. The multistep protocol discussed above is deemed successful if it can grow mechanical superposition states towards macroscopic values even in the presence of thermal occupation and decoherence. For the chosen parameter range, Figs. 7.8 and 7.9 show that this goal is possible for $\mu = 0.1$ only for small $\bar{n}_{\rm th}$. The plots for $\mu = 0.1$ and $\bar{n}_{\rm th} = 10^{-3}, 10^{-2}$ show a decrease in $\mathcal{I}$ and

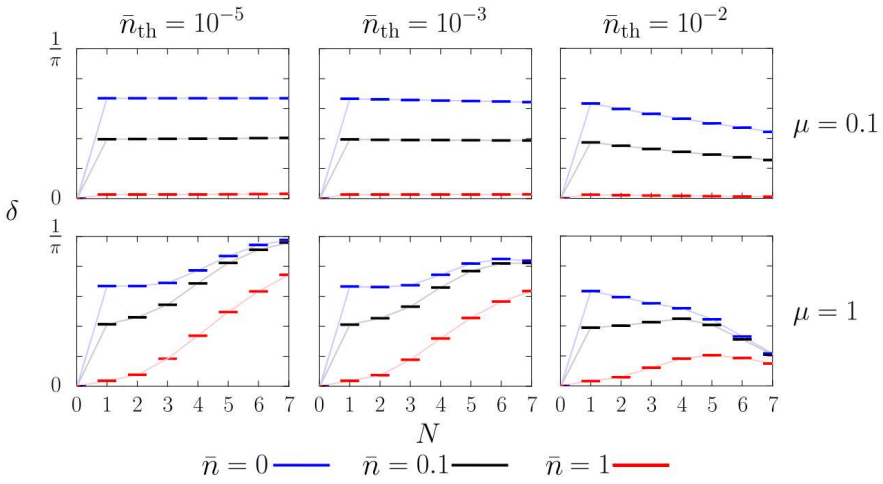


Figure 7.7: **Total negative volume in phase space δ plotted as a function of step number N for a range of μ, $\bar{n}_{\rm th}$, and $\bar{n}$.** States produced in the large $N\mu$ regime with $\bar{n}_{\rm th} = 0$ saturate the maximum value of this non-classicality measure for a Schrödinger cat state, $\delta_{\rm max} = 1/\pi$, independent of the value of $\bar{n}$. The plots also show that for $\bar{n} = 0$, $\bar{n}_{\rm th} \approx 0$, and $N\mu < 4/\sqrt{2}$ the value of δ is equal to that of the single-phonon Fock state. The states with lower phase-space separation are better at retaining their δ values as N increases when decoherence effects are considered.

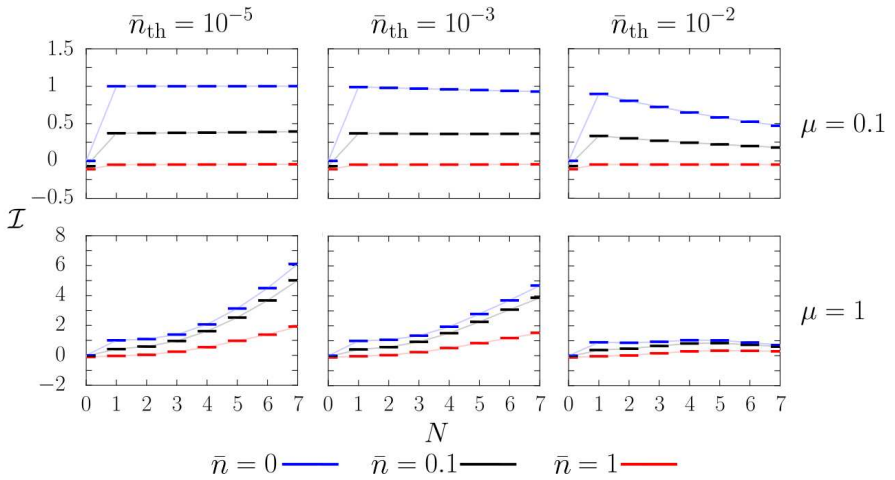


Figure 7.8: **The phase-space macroscopicity measure $\mathcal{I}$ plotted as a function of step number N for a range of μ, $\bar{n}_{\rm th}$, and $\bar{n}$.** With the set of parameters denoted in the figure, the plots demonstrate the regime where the multistep protocol is successful in growing macroscopicity—as measured by $\mathcal{I}$—with step number N. The plots also identify the regime where $\mathcal{I}$ decreases with step number when decoherence effects begin to dominate.

$\mathcal{M}$ with step number. While the corresponding plot at $\bar{n}_{\rm th} = 10^{-5}$ produces an increase in these measures with step number—this increase is slight and not visible in Fig. 7.8. But perhaps more interestingly, for $\mu = 1$, the macroscopicity of the decohered states increases as the state grows for $N \leq 5$ even in the case of heavy thermalization, $\bar{n}_{\rm th} = 10^{-2}$. This demonstrates that the protocol is capable of generating significant macroscopicity even when decoherence and initial thermal occupation of the mechanical mode are accounted for. It must however be noted that past $N = 5$ the protocol leads to a decrease in macroscopicity, meaning that 5 steps is the optimal step number for $\mu = 1$ and $\bar{n}_{\rm th} = 10^{-2}$. For a given coupling strength and decoherence rate this result indicates that by analysing Eq. (7.50) an optimal step number can be established.

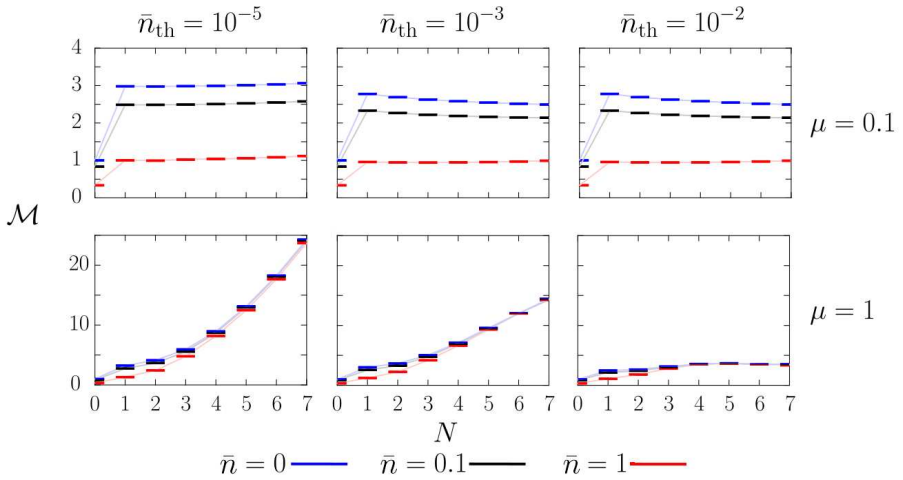


Figure 7.9: **The quantum Fisher information based macroscopicity measure $\mathcal{M}$ plotted as a function of step number N for a range of μ, $\bar{n}_{\rm th}$, and $\bar{n}$.** $\mathcal{M}$ scales similarly to $\mathcal{I}$, reflecting the similarity of the two measures, and the same general results discussed in the caption of Fig. 7.8 apply here too. However, as compared to Fig. 7.8, the increase in macroscopicity with step number N is just visible when $\mu = 0.1$ and $\bar{n}_{\rm th} = 10^{-5}$.

7.5.4 Effect of optical loss

From Section 7.3.1 we know that for a coherent state input pulse $|\psi\rangle = |\sqrt{2}\alpha\rangle$, if $(1-\eta)|\alpha|^2 \ll 1$ is *not* satisfied then the final mechanical state will not be given by $\rho_{\rm SCS}$. In this case, the non-classicality and macroscopicity of the final mechanical state will also be reduced, however these changes can be made negligible for a given value of η by reducing the amplitude of the input coherent state such that $(1-\eta)|\alpha|^2 \ll 1$ is satisfied. In Fig. 7.10 the effect of optical loss on the phase-space distribution of the heralded mechanical state is illustrated. The asymmetry about $P_{\rm M} = 0$ in the final phase-space plot is explained by the interpretation of $W_\eta(X_{\rm M}, P_{\rm M})$ as a statistical mixture of Schrödinger cat states, each displaced by integer multiples of μ along the momentum axis. In this way it may be seen that positive and negative areas of phase-space will combine in order to produce regions of reduced visibility as in the final phase-space plot of Fig. 7.10. Interestingly, Fig. 7.10 shows that the macroscopicity measure $\mathcal{M}$ is unaffected by optical loss. This is because this measure depends entirely on the position probability marginal $p(X_{\rm M})$, and by integrating Eq. (7.29) one finds that $p_\eta(X_{\rm M}) = p_{\rm SCS}(X_{\rm M})$.

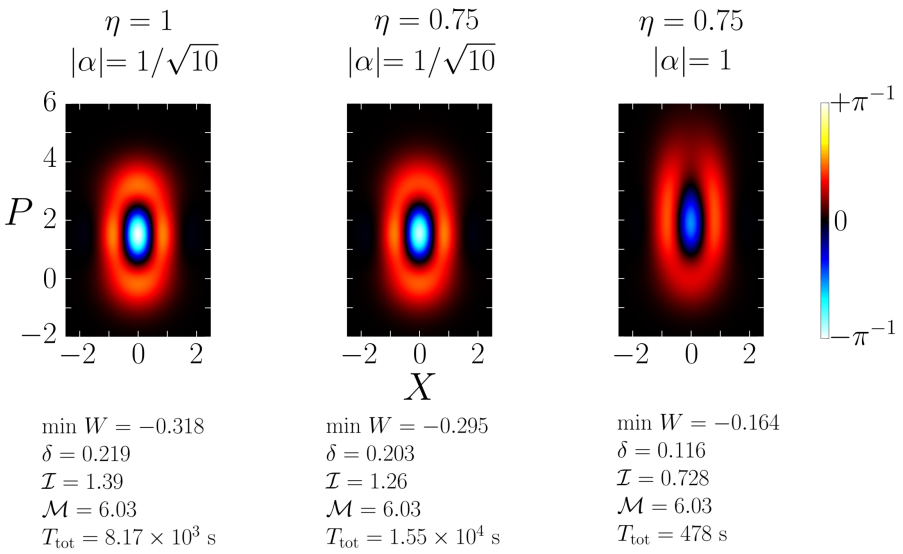


Figure 7.10: **The effect of optical loss and detector inefficiencies on the final mechanical state.** This shows the effects of optical loss on the performance of a multistep protocol consisting of $N = 3$ steps with a coherent state chosen as the optical input. The performance is quantified in terms of the non-classicality measures, the macroscopicity measures, and the total time taken to complete an experiment where one thousand successful runs are obtained. Parameters from proposal (iii) of Table 7.1 are taken, but thermal effects are ignored so that the effect of loss is isolated ($\mu = 1$, $\bar{n} = 0$). The phase-space plot at $\eta = 1$ and $|\alpha| = 1/\sqrt{10}$ (left) illustrates the case when the protocol operates at perfect optical efficiency. Conversely, the phase-space plot at $\eta = 0.75$ and $|\alpha| = 1/\sqrt{10}$ (middle) shows the effect that optical loss has in a regime where $(1 - \eta)|\alpha|^2 \ll 1$. Here, the main effect of loss is to decrease $T_{\rm tot}$, while the phase-space measures are not changed significantly. The final plot illustrates a regime where optical loss leads to significant mechanical decoherence (right).

I would like to reiterate that the deleterious effects of optical loss to the mechanical state are avoided by choosing single photons or weak coherent states as the input states.

7.6 Optimizing the pulse shape

7.6.1 Pulse shape in the original work

In Appendix A of the original work [1], an input pulse shape $f(t) = \sqrt{\kappa}\mathrm{e}^{-\kappa|t|}$ was assumed to optimize the optomechanical coupling strength μ. This shape was chosen as it produces an intracavity field that matches the Lorentzian response of the cavity. Furthermore, it was shown in Ref. [139] that in the linearized regime, this pulse shape optimizes the linear optomechanical coupling strength χ. In the original calculation of Ref. [1], a value of $\mu = 3g_0/\sqrt{2}\kappa$ was calculated assuming the pulse shape $f(t) = \sqrt{\kappa}\mathrm{e}^{-\kappa|t|}$. However, this value for μ is less than the value achieved by a long pulse in the adiabatic regime—see Section 6.4.1, where $\mu = \sqrt{8}g_0/\kappa$. I will now show that this long pulsed drive actually maximizes the optomechanical coupling strength and is advantageous for a number of reasons.

Minimal pulse distortion

In the adiabatic regime $\kappa \gg \tau^{-1}$, the shape of the output pulse is well approximated by the shape of the input pulse, see Eq. (6.87). In the work of Ref. [145], working in the adiabatic regime was motivated by this property of minimal pulse distortion.

7.6.2 Optimization with long pulses

Heisenberg-Langevin equations

Without making the adiabatic approximation, solving the Heisenberg-Langevin equation from Section 6.4 for the intracavity field gives

$$a(t) = \sqrt{2\kappa}\mathrm{e}^{(-\kappa+\mathrm{i}\sqrt{2}X_{\mathrm{M}}g_0)t}\int_{-\infty}^{t} a_{\mathrm{in}}(t')\mathrm{e}^{(\kappa-\mathrm{i}\sqrt{2}X_{\mathrm{M}}g_0)t'}\mathrm{d}t'. \tag{7.74}$$

Note that X_{M} is not time-dependent in the pulsed regime. Inserting $a(t)$ into the Heisenberg-Langevin equation for P_{M} gives

$$\begin{aligned} P'_{\mathrm{M}} - P_{\mathrm{M}} &= \sqrt{2}g_0\int a^\dagger a(t)\mathrm{d}t \\ &= \sqrt{8}g_0\kappa\int_{-\infty}^{+\infty}\mathrm{d}t\mathrm{e}^{-2\kappa t}\int_{-\infty}^{t}\mathrm{d}t'\int_{-\infty}^{t}\mathrm{d}t''\mathrm{e}^{(\kappa+\mathrm{i}\sqrt{2}X_{\mathrm{M}}g_0)t'}\times \\ &\qquad \mathrm{e}^{(\kappa-\mathrm{i}\sqrt{2}X_{\mathrm{M}}g_0)t''}a^\dagger_{\mathrm{in}}(t')a_{\mathrm{in}}(t''). \end{aligned} \tag{7.75}$$

Here, the prime indicates the momentum operator after the optomechanical interaction and the limits of the first integral are taken at $\pm\infty$ so that the whole optomechanical interaction is integrated over[16].

[16] Later in this derivation I will introduce the pulse shape, which determines the duration of the interaction.

From Section 6.4, we know that the unitary $U = \mathrm{e}^{\mathrm{i}\mu n_{\mathrm{L}} X_{\mathrm{M}}}$ produces the transformation[17]

$$P'_{\mathrm{M}} - P_{\mathrm{M}} = \mu n_{\mathrm{L}}. \tag{7.76}$$

Furthermore, Section 6.4 informs us that Eq. (7.76) accurately describes the interaction to second order in X_{M}. Hence, to derive a value for μ, one may take the expectation values of Eqs (7.75) and (7.76) and set them equal to each other, which gives

$$\mu \langle n_{\mathrm{L}} \rangle = \sqrt{8} g_0 \kappa \int_{-\infty}^{+\infty} \mathrm{d}t \mathrm{e}^{-2\kappa t} \int_{-\infty}^{t} \mathrm{d}t' \int_{-\infty}^{t} \mathrm{d}t'' \times \left\langle \mathrm{e}^{(\kappa + \mathrm{i}\sqrt{2} X_{\mathrm{M}} g_0) t'} \mathrm{e}^{(\kappa - \mathrm{i}\sqrt{2} X_{\mathrm{M}} g_0) t''} a^{\dagger}_{\mathrm{in}}(t') a_{\mathrm{in}}(t'') \right\rangle. \tag{7.77}$$

The term

$$\left\langle \mathrm{e}^{(\kappa + \mathrm{i}\sqrt{2} X_{\mathrm{M}} g_0) t'} \mathrm{e}^{(\kappa - \mathrm{i}\sqrt{2} X_{\mathrm{M}} g_0) t''} a^{\dagger}_{\mathrm{in}}(t') a_{\mathrm{in}}(t'') \right\rangle \tag{7.78}$$

may be factored as

$$\mathrm{e}^{\kappa t'} \mathrm{e}^{\kappa t''} \left\langle \mathrm{e}^{\mathrm{i}\sqrt{2} X_{\mathrm{M}} g_0 (t' - t'')} \right\rangle \left\langle a^{\dagger}_{\mathrm{in}}(t') a_{\mathrm{in}}(t'') \right\rangle \tag{7.79}$$

as the input pulse is uncorrelated with the initial mechanical state.

The problematic term

The mechanical phase term

$$\left\langle \mathrm{e}^{\mathrm{i}\sqrt{2} X_{\mathrm{M}} g_0 (t' - t'')} \right\rangle$$

is problematic as it depends on the mechanical state before the pulse is sent in. This is evident if the expectation value is calculated in the X_{M} basis, so that for a given initial mechanical probability distribution $P_{\mathrm{in}}(X_{\mathrm{M}})$ one has

$$\left\langle \mathrm{e}^{\mathrm{i}\sqrt{2} X_{\mathrm{M}} g_0 (t' - t'')} \right\rangle = \int \mathrm{d}X_{\mathrm{M}} P_{\mathrm{in}}(X_{\mathrm{M}}) \mathrm{e}^{\mathrm{i}\sqrt{2} X_{\mathrm{M}} g_0 (t' - t'')}. \tag{7.80}$$

For example, if $P_{\mathrm{in}}(X_{\mathrm{M}})$ is a zero-mean Gaussian state of width σ then

$$\begin{aligned} \left\langle \mathrm{e}^{\mathrm{i}\sqrt{2} X_{\mathrm{M}} g_0 (t' - t'')} \right\rangle &= \sum_{n}^{\infty} \frac{\left[\mathrm{i}\sqrt{2} g_0 (t' - t'')\right]^n}{n!} \langle X_{\mathrm{M}}^n \rangle \\ &= \mathrm{e}^{-g_0^2 \sigma^2 (t' - t'')^2}, \end{aligned} \tag{7.81}$$

which may be calculated using the Gaussian integrals listed in Appendix C. Importantly, $\left\langle \mathrm{e}^{\mathrm{i}\sqrt{2} X_{\mathrm{M}} g_0 (t' - t'')} \right\rangle \neq 1$ is true when the exponential is expanded

[17] In the non-adiabatic regime n_{L} may be a more complicated function of the input and output fields than in the adiabatic regime.

to second order in $X_{\rm M}$. The unitary $e^{i\mu n_{\rm L} X_{\rm M}}$ models the system dynamics to second order in $X_{\rm M}$. Hence, the dependence of the mechanical phase term on the mechanical state is a problem, not just in general, but even for the second-order-in-$X_{\rm M}$ description.

Nevertheless, we are only interested in optimizing μ and not calculating it in full generality for any pulse shape. Therefore, by noting that this term always satisfies

$$\left\langle e^{i\sqrt{2}X_{\rm M} g_0(t'-t'')} \right\rangle \leq 1, \tag{7.82}$$

in what follows I take the mechanical phase term to equal one to maximize μ in Eq. (7.77).

Of course, it would be problematic for our multistep protocol if μ varied between steps as suggested by Eq. (7.80). If μ varied between steps due the dependence on the mechanical state at each step, then cancelling all but the extremal momentum components, with suitable phase choices, will become imperfect. Therefore, the protocol would not wholly succeed in growing cat states. Fortunately, as we shall see, long pulses **both** maximize the value of μ *and* produce a μ that is independent of the mechanical state.

Pulse shaping with single photons or coherent states

In this Heisenberg description, the correlation function

$$\left\langle a_{\rm in}^\dagger(t') a_{\rm in}(t'') \right\rangle \tag{7.83}$$

is taken with respect to the initial optical input state. In our multistep protocol it was assumed this was either a single photon state or a coherent state of light. To calculate the above correlation function one must define these inputs states in terms of the input operators and the pulse shape as follows.

I will introduce the *temporal number states*

$$|1\rangle_t = a_{\rm in}^\dagger(t)\,|0\rangle\,, \tag{7.84}$$

$$|n\rangle_t = \frac{a_{\rm in}^{\dagger n}(t)}{\sqrt{n!}}\,|0\rangle\,. \tag{7.85}$$

Here, the mode labels 't' on the kets denote a single photon or n photons being created at a specific time t. These states also obey

$${}_t\langle n|m\rangle_{t'} = \delta_{n,m}\delta(t-t') \tag{7.86}$$

However, the input optical pulse is comprised of a temporal envelope $f(t)$ of such temporal number states, which is normalized by $\int |f(t)|^2 {\rm d}t = 1$. For example, the single photon input pulse is given by

$$|1\rangle = \int {\rm d}t f(t)\,|1\rangle_t \tag{7.87}$$

$$= \int {\rm d}t f(t) a_{\rm in}^\dagger(t)\,|0\rangle\,. \tag{7.88}$$

Taking the expectation value $\left\langle a_{\rm in}^\dagger(t')a_{\rm in}(t'')\right\rangle$ with respect to the single photon input pulse then gives

$$\left\langle a_{\rm in}^\dagger(t')a_{\rm in}(t'')\right\rangle = f^*(t')f(t''), \tag{7.89}$$

by virtue of Eq. (7.85).

Moreover, one may also define the input coherent pulse in terms of the temporal number states

$$|\alpha\rangle = \int {\rm d}t f(t)\,|\alpha\rangle_t \tag{7.90}$$

$$= \int {\rm d}t f(t){\rm e}^{-|\alpha|^2/2}\sum_{n=0}^{\infty}\frac{\alpha^n}{\sqrt{n}}\,|n\rangle_t\,. \tag{7.91}$$

Calculating $\left\langle a_{\rm in}^\dagger(t')a_{\rm in}(t'')\right\rangle$ with respect to the coherent input pulse then gives

$$\left\langle a_{\rm in}^\dagger(t')a_{\rm in}(t'')\right\rangle = |\alpha|^2 f^*(t')f(t''). \tag{7.92}$$

Here, $|\alpha|^2$ is the mean photon number of the coherent pulse. One may therefore write the correlation function, for either input pulse, as

$$\left\langle a_{\rm in}^\dagger(t')a_{\rm in}(t'')\right\rangle = \langle n_{\rm L}\rangle\, f^*(t')f(t''). \tag{7.93}$$

In Appendix F.2 I show that this result is valid for any input optical pulse—not just the single photon and coherent state pulses assumed in our multistep protocol.

Optimization over pulse shapes

Inserting Eq. (7.93) into Eq. (7.77) and taking $\left\langle {\rm e}^{{\rm i}\sqrt{2}X_{\rm M}g_0(t'-t'')}\right\rangle = 1$ gives

$$\mu = \sqrt{8}g_0\kappa\int_{-\infty}^{+\infty}{\rm d}t{\rm e}^{-2\kappa t}\int_{-\infty}^{t}{\rm d}t'\int_{-\infty}^{t}{\rm d}t''{\rm e}^{\kappa t'}{\rm e}^{\kappa t''}f^*(t')f(t''), \tag{7.94}$$

which may be rewritten as

$$\mu = \sqrt{8}g_0\kappa\int_{-\infty}^{+\infty}dt|g(t)|^2, \tag{7.95}$$

with

$$g(t) = {\rm e}^{-\kappa t}\int_{-\infty}^{t}dt'{\rm e}^{\kappa t'}f(t'). \tag{7.96}$$

Then by utilising the useful result $\int_{-\infty}^{t}dt' = \int_{-\infty}^{+\infty}dt'\Theta(t-t')$, where $\Theta(t)$ is the Heaviside function defined by

$$\Theta(t) = \begin{cases} 0 & \text{for } t<0 \\ 1 & \text{for } t>0, \end{cases} \tag{7.97}$$

$g(t)$ may be rewritten as a simple convolution $g(t) = f * h(t)$, with $h(t) = \Theta(t)\mathrm{e}^{-\kappa t}$. Paserval's identity from Appendix B may then be used on the expression for μ, namely

$$\mu = \sqrt{8} g_0 \kappa \int_{-\infty}^{+\infty} d\omega |\tilde{g}(\omega)|^2. \tag{7.98}$$

Here $\tilde{g}(\omega)$ is a Fourier transform of a convolution and hence $\tilde{g}(\omega) = \sqrt{2\pi}\tilde{f}(\omega)\tilde{h}(\omega)$. An expression for $\tilde{h}(\omega)$ may be calculated as

$$\begin{aligned} \tilde{h}(\omega) &= \frac{1}{\sqrt{2\pi}} \int_{-\infty}^{+\infty} \mathrm{d}t \mathrm{e}^{-i\omega t} h(t) && (7.99) \\ &= \frac{1}{\sqrt{2\pi}} \int_{-\infty}^{+\infty} \mathrm{d}t \mathrm{e}^{-i\omega t} \Theta(t) \mathrm{e}^{-\kappa t} && (7.100) \\ &= \frac{1}{\sqrt{2\pi}} \frac{1}{\kappa + i\omega}. && (7.101) \end{aligned}$$

Then by introducing $F(\omega) = |\tilde{f}(\omega)|^2$ one can further massage μ into the neater form

$$\mu = \sqrt{8} g_0 \kappa \int_{-\infty}^{+\infty} d\omega \frac{1}{\kappa^2 + \omega^2} F(\omega) = \sqrt{8} g_0 \pi \int_{-\infty}^{+\infty} d\omega L(\omega) F(\omega), \tag{7.102}$$

where I have introduced the Lorentzian function with L^1-norm, such that

$$L(\omega) = \frac{\kappa}{\pi} \frac{1}{\kappa^2 + \omega^2} \tag{7.103}$$

and $\int_{-\infty}^{+\infty} d\omega L(\omega) = 1$. It is clear that the integral over $F(\omega)$ is unity as

$$\begin{aligned} 1 &= \int_{-\infty}^{+\infty} dt |f(t)|^2 && (7.104) \\ &= \int_{-\infty}^{+\infty} d\omega |\tilde{f}(\omega)|^2 && (7.105) \\ &= \int_{-\infty}^{+\infty} d\omega F(\omega) = 1. && (7.106) \end{aligned}$$

To maximize μ, one must therefore maximize $\int_{-\infty}^{+\infty} d\omega L(\omega) F(\omega)$ which is done by noting that $\max\{L(\omega)\} = L(0) = 1/\pi\kappa$, so that

$$\begin{aligned} \int_{-\infty}^{+\infty} d\omega L(\omega) F(\omega) &\leq \int_{-\infty}^{+\infty} d\omega L(0) F(\omega) && (7.107) \\ &= L(0) \int_{-\infty}^{+\infty} d\omega F(\omega) = L(0) = 1/\pi\kappa. && (7.108) \end{aligned}$$

Where the fact that $\int_{-\infty}^{+\infty} d\omega F(\omega) = 1$ has been used. Equality is reached when $F(\omega) = \delta(\omega)$, which leads to a maximal value for μ in this pulsed regime:

$$\mu_{\max} = \frac{\sqrt{8}g_0}{\kappa}. \tag{7.109}$$

This infinitely narrow spectral intensity corresponds to a flat pulse shape in the time domain, which violates the approximation that X_{M} is constant.

However, the adiabatic approximation of Section 6.4 resulted in a value of $\mu = \mu_{\max}$. Hence, providing $\kappa \gg \omega_{\mathrm{M}}$, a long pulse (of any shape $f(t)$) satisfying $\kappa \gg \tau_{\mathrm{in}}^{-1} \gg \omega_{\mathrm{M}}$ leads to the optimal value of μ, which is also independent of the mechanical state.

7.7 Detector timing with long pulses

7.7.1 Time dependence of μ

The derivation in Section 6.4.1 assumed long pulses of duration τ_{in}, which satisfy $\kappa \gg \tau_{\mathrm{in}}^{-1} \gg \omega_{\mathrm{M}}$. This allowed the assumption that the cavity is adiabatic with $\dot{a} = 0$, which produced $\mu = \sqrt{8}g_0/\kappa$. From the previous section, it may be seen that this value of μ is optimal in nonlinear pulsed optomechanics.

For concreteness, consider now a rectangular pulse shape with $f(t) = \tau_{\mathrm{in}}^{-1}$ for $0 \leq t \leq \tau_{\mathrm{in}}$ and $f(t) = 0$ otherwise. In this case, μ will vary over a short timescale $\sim 1/\kappa$ before it reaches this maximum—as can be seen from Eq. (7.74). However, for a long rectangular pulse with $\tau_{\mathrm{in}} \gg \kappa^{-1}$, this period over which μ varies is much smaller than the pulse width. A sketch of μ as a function of time is shown in Fig. 7.11.

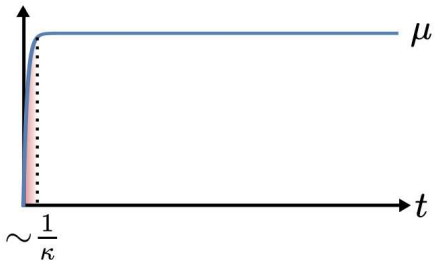


Figure 7.11: **Sketch of the dependence of the nonlinear optomechanical coupling strength μ on time for a rectangular input pulse shape.** From Eq. (7.74) it may be seen that for a long pulsed drive, the cavity field $a(t)$ approaches its steady state over a timescale $1/\kappa$. Therefore, μ will saturate to a value of $\mu = \sqrt{8}g_0/\kappa$ over a time $\sim 1/\kappa$. For the long pulse drive, which has a characteristic width τ_{in} satisfying, $\tau_{\mathrm{in}} \gg 1/\kappa$, this time period where μ varies is negligible. This period is shaded in red in the above sketch.

7.7.2 Detector timing

Photon trajectories

Consider the situation when a single photon is detected at a time t. Time zero is set by the input pulse being sent towards the cavity, i.e. when the leading edge of the input pulse, of temporal width τ_{in}, enters the cavity.

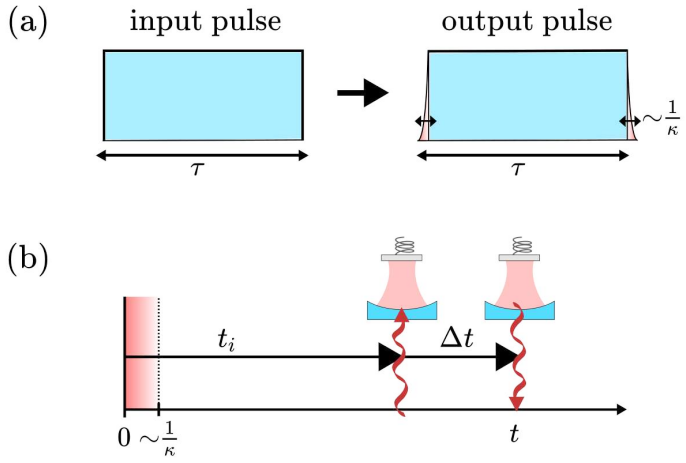


Figure 7.12: **Single photon detection after the nonlinear optomechanical interaction with long pulses.** (a) Cartoon of the input rectangular pulse shape and the corresponding output pulse shape. In the regime where $\tau \gg 1/\kappa$, the output pulse shape is well approximated by the input pulse shape except for the leading and trailing tails. These tails on the output pulse are of negligible width $\sim 1/\kappa$ and are exaggerated in this cartoon. (b) Detection time and gating. The photon may enter from the input pulse into the cavity at any time t_i in the interval $0 \leq t_i \leq \tau$. This is depicted by the wavy-red arrow entering the cavity. Here, t_i is marked from the leading edge of the pulse that enters the cavity at time zero. The photon then may leave the cavity to go into the output pulse after remaining in the cavity for Δt, which is depicted by the second wavy-red arrow. A photon is then detected at time $t = t_i + \Delta t$. This detection event corresponds to the weighted coherent sum of over possible photon trajectories, characterized by all possible values of t_i and Δt that sum to t. Gating the detector so that early times $\sim 1/\kappa$ are not accepted ensures that $\mu = \sqrt{8}g_0/\kappa$. For $\kappa \gg \tau^{-1}$, this gating has a negligible effect on the heralding probability.

One possible photon trajectory that corresponds to a detection event at t is: the photon in the input pulse enters the cavity at time $t_i \leq \tau_{\text{in}}$ and remains in

the cavity for Δt. To a good approximation, the photon is immediately detected after it leaves the cavity, hence $t = t_i + \Delta t$. This trajectory is shown in Fig. 7.12.

However, there exists a continuum of distinct photon trajectories for each detection time t. These corresponds to all different times the photon could enter the cavity in the interval t_i, and all the different times the photon can remain in the cavity for Δt satisfying $t = t_i + \Delta t$. All these different possible trajectories must be added together in a weighted coherent sum for a given detection event. The weighting of each trajectory is determined by the input and output pulse shapes, which are the same in the adiabatic approximation. See Eq. (6.87), which implies the output pulse has the same shape as the input pulse for an adiabatic cavity. Here, I have assumed a rectangular input—and therefore output—pulse shape. However, in reality the output pulse will be slightly smoothed by the cavity. This is shown in the cartoon of Fig. 7.12(a), which shows that the rectangular output pulse gains small tails of width $1/\kappa$.

Problem trajectories and detector gating

One can now look back to Fig. 7.11 to identify potentially problematic trajectories for a given detection time t. Namely, trajectories where the photon is detected at $t \lesssim 1/\kappa$ correspond to $\mu < \sqrt{8} g_0/\kappa$. This is because the cavity hasn't had time to reach a steady state at these early times. I refer to such photon trajectories as *problem trajectories*.

Therefore, the detector may be gated so only detection events later than $\sim 1/\kappa$ are accepted to avoid the problem trajectories. Therefore, the detector should be gated so that detections at early times, corresponding to the red shaded area in Fig. 7.12(b), are not accepted. In order for this gating to have a negligible effect on the total photon heralding probability, it is required that the probability of detecting in the interval of problem trajectories is much less than the pulse width. This leads to

$$\kappa \gg \tau_{\text{in}}^{-1}, \tag{7.110}$$

which is a condition that is already met by working in the long pulsed regime.

Avoiding the problematic trajectories and detector gating with pulse shaping

The need for detector gating at early times described in the previous section was because—for a the rectangular pulse shape considered—the adiabatic approximation $\dot{a} = 0$ was not valid at short times $\sim 1/\kappa$. However, as discussed in the linearized regime of pulsed optomechanics in Ref. [147], choosing a Gaussian input pulse shape ensures the cavity field follows the input pulse adiabatically even at early times in the beginning of the pulse.

For the rectangular pulse shape considered in the previous section, adiabatic elimination is not be valid for early times in the beginning of the pulse as the cavity mode is initially in the vacuum state and it will take some time for the cavity field to respond to the abrupt change in the input. However, if at these

early times the input varies slowly compared to $1/\kappa$—as with the Gaussian pulse shape—then the adiabatic elimination of the cavity mode will be valid for the entire dynamics of the cavity field. Therefore, choosing a pulse shape that slowly varies at every point in the pulse shape allows the approximation $\dot{a} = 0$ to be made at all times and therefore avoids the needs to gate the detector. Adopting a long Gaussian input pulse in the nonlinear regime of pulsed optomechanics was suggested in Ref. [6].

Dark counts

Finally, one should carefully compare τ with the rate of detector dark counts. If the rate of dark counts is comparable to $1/\tau$, one may gate the detection times about some small window to avoid the deleterious effects of these dark counts.

7.8 Conclusion and outlook

Conclusion

I have discussed our measurement-based multistep protocol for macroscopic quantum state preparation of mechanical motion via cavity quantum optomechanics from Ref. [1]. This protocol not only allows for the increase in nonclassicality and macroscopicity with step number, but also relaxes the requirement on the optomechanical coupling strength μ needed to prepare well-separated mechanical superposition states. Here, I have focused primarily on the preparation of mechanical Schrödinger cat states, which consist of a superposition of two distinct momentum states. This is achieved by setting the phase within an optical interferometer, at each step of the N-step protocol, to be the N^{th} root of unity. I would also like to highlight that by varying the phase ϕ_j introduced at each step, our scheme opens up the possibility of preparing a broad range of non-classical mechanical states.

The protocol presented in this thesis may be implemented with readily available optical inputs: single photons $|\psi\rangle = |1\rangle$ or weak coherent states $|\psi\rangle = |\sqrt{2}\alpha\rangle$. I have discussed the advantages and disadvantages of both input choices. For example, providing $(1-\eta)|\alpha|^2 \ll 1$, both inputs provide resilience to optical loss. Whereas a more favourable heralding probability is obtained with single photons, and weak coherent inputs are more readily achieved in the lab. Using parameters from recent experiments, I have described the effect that initial thermal occupation and mechanical decoherence has on the heralded mechanical state. Our scheme may be used to grow macroscopic Schrödinger cat states in present-day ultracold atom implementations of cavity optomechanical systems. Furthermore, our scheme provides an experimentally feasible route to grow macroscopic mechanical superposition states in solid-material devices using present-day, and expected near-future, experimental parameters.

Outlook

This protocol provides a new path towards the long-standing goal of quantum state generation at a truly macroscopic scale, which would allow for the study of wavefunction collapse and the interface between quantum mechanics and gravity to be explored. I would also like to note that this protocol can be readily adapted to be employed in systems which interact via a spin-phonon coupling, e.g. of the form $H_{\text{int}} = \hbar\lambda\sigma_z X$. Prominent examples of such systems include mechanical oscillators with nitrogen-vacancy centres [215, 216] and superconducting electromechanical platforms [217, 218, 219].

Since the publication of Ref. [1], I have proved in Section 7.6 that long pulses, which enable adiabatic elimination of the cavity mode, maximize the optomechanical coupling strength μ in the cavity-free unitary $\mathrm{e}^{\mathrm{i}\mu n_{\text{L}} X_{\text{M}}}$. Moreover, since the publication of this work, the cavity-enhanced unitary $\mathrm{e}^{\mathrm{i}\varphi(X_{\text{M}})n_{\text{L}}}$ has been derived in Ref. [7]–see Part III—which also operates in this adiabatic limit. Further work in this direction could therefore involve using the unitary $\mathrm{e}^{\mathrm{i}\varphi(X_{\text{M}})n_{\text{L}}}$ to design macroscopic superposition state preparation protocols. In particular, combining the multistep protocol presented here, the multi-port protocol of Ref. [155], and the unitary $\mathrm{e}^{\mathrm{i}\varphi(X_{\text{M}})n_{\text{L}}}$ would be enable a plethora of probabilistic preparation possibilities.

Chapter 8

Generating and verifying mechanical entanglement

This section draws heavily from Ref. [2], where this work was originally published. I also briefly discuss Refs [3] and [6], first-authored by P.N. and L.K.N., respectively, where J.C. made theoretical contributions.

Entanglement generation at a macroscopic scale offers an exciting avenue to develop new quantum technologies and study fundamental physics on a tabletop. Cavity quantum optomechanics provides an ideal platform to generate and exploit such phenomena owing to the precision of quantum optics combined with recent experimental advances in optomechanical devices. In this chapter, I detail our proposals to prepare and verify both optical-mechanical and mechanical-mechanical entanglement, which operate outside the resolved-sideband regime. These schemes employ pulsed interactions with a duration much less than the mechanical period and, together with homodyne measurements, can both generate and characterize these types of entanglement. The entanglement generated by our schemes is quantified using the logarithmic negativity and is analyzed with respect to the strength of the pulsed optomechanical interactions for realistic experimental scenarios including mechanical decoherence and optical loss. Two separate schemes for mechanical entanglement generation are introduced and compared: one scheme based on an optical interferometric design, and the other comprising sequential optomechanical interactions. The pulsed nature of our protocols provides more direct access to these quantum correlations in the time domain, with applications including quantum metrology and tests of quantum decoherence. By considering a parameter set based on recent experiments, the feasibility to generate significant entanglement with our schemes, even with large optical losses, is demonstrated. Finally, I provide an overview of Refs [3] and [6], which go beyond the entanglement protocols proposed in Ref. [2], and provide an outlook for further works in this direction.

8.1 Entanglement in optomechanics

In quantum optics, entanglement has been observed in many experimental scenarios including light with continuous variables [220, 221, 222], in discrete optical systems [223, 224, 225, 226], with the electronic states of neutral atoms [227, 228, 229], and between nitrogen-vacancy centres [230]. Moreover, entanglement is critical in quantum technologies demonstrating an advantage over their classical counterparts [195, 231, 232], and also allows for fundamental physics questions to be studied [233].

Beyond optical systems, entanglement between motional degrees of freedom is also being pursued, with the first experimental realization of spatially-separated mechanical entanglement being between the motion of pairs of ions [234]. Interestingly for this thesis, one promising route to study motional entanglement for more massive systems is provided by cavity quantum optomechanics—see Chapter 6. The theoretical study of both optical-mechanical and mechanical-mechanical entanglement via optomechanics is an active area of research, and has led to several experimental works in this direction. Here, I briefly provide a description of some notable studies into both optical-mechanical and mechanical-mechanical entanglement.

First, I will focus on the progress made in developing theoretical proposals for optical-mechanical entanglement. Even before the turn of the century, photon-phonon transfer operations were proposed as a way to generate optical-mechanical entanglement [235]. Here, a nonclassical state of light interacts with a mechanical oscillator via the light-mechanics beamsplitter interactions[1] to generate optical-mechanical entanglement [236]. Here, the nonclassicality of the input states of light is a necessary condition for creating the entanglement [237]. As a result of these early proposals, a number of further studies into the generation and verification of Gaussian optical-mechanical entanglement have now been carried out that focus on the linearized dynamics about the steady state of a continuously driven system [238, 239]. Steady-state optomechanical systems are subject to certain stability conditions, which prevent operation in parts of parameter space, particularly for operation on the blue sideband in the resolved-sideband regime. To enable operation in this part of parameter space and alleviate these stability conditions, using long-pulsed optical drives have been proposed [130], and the effect of high thermal occupation [240], multiple interactions, pulse shaping, and different optical detunings have also been studied for such long optical pulses [241].

To complement the research into optical-mechanical entanglement, there are a number of proposals for generating mechanical-mechanical entanglement via optomechanics. Namely, the steady-state of two mechanical oscillators interacting with the same entangling optical field has been studied to investigate Gaussian entanglement in the linearized regime of optomechanics [242]. To achieve this type of entanglement a variety of different experimental configurations have been proposed, such as placing two mechanical membranes within

[1] Note that the light-mechanics beamsplitter operation requires operation in the resolved-sideband regime $\omega_{\mathrm{M}} \gg \kappa$ as detailed in Chapter 6.

the same optical cavity [243], the injection of squeezed light into both a double cavity system [244] and a ring cavity design [245], and the placement of two levitating nanobeads interacting in the same central potential [246]. Reservoir engineering techniques [247] can also to be utilized to generate mechanical-mechanical entanglement in the steady state, such as via multi-tone driving of an optomechanical system containing two mechanical oscillators [248]. Recently, Brunelli and colleagues carried out a more comprehensive theoretical study of steady-state Gaussian entanglement [249], which investigates optical-mechanical, mechanical-mechanical, and tripartite mechanical-optical-mechanical entanglement. Crucially, Ref. [249] is capable of describing any value of the sideband-ratio resolution parameter $\omega_{\mathrm{M}}/\kappa$ and does not make the rotating-wave or adiabatic approximations used in previous works.

Long-pulsed linear optomechanical interactions and linear optical measurements, such as homodyne or heterodyne, can also be used to swap optical-mechanical entanglement to the mechanical subspace and thus generate Gaussian entanglement [250, 251]. To generate and witness non-Gaussian mechanical entanglement, the linear optical measurements can be substituted with photon-counting measurements [252, 253]. Note that photon-counting measurements realize a nonlinear measurement on the optical field quadratures, which introduces a nonlinearity into the system that generates the non-Gaussianity.

Now, I briefly review the experimental progress that has been made in generating entanglement between electromagnetic fields and mechanical modes of oscillation. In the resolved-sideband regime, long-pulsed optomechanical interactions have enabled the generation of entanglement between microwave fields and mechanical motion [254]. In this work, optical-quadrature measurements were used to verify this type entanglement by calculating an EPR variance [255]. Moving now to the optical domain, photon-counting measurements have been used to witness non-classical optomechanical correlations between optical pulses and phonon modes in bulk diamond via Raman scattering [177], and then similarly in a nanomechanical resonator operating in the resolved-sideband regime [179].

Now I will turn to the experimental progress in entanglement generation between two mechanical oscillators. Firstly, mechanical entanglement has been generated between two spatially-separated diamonds using an interferometric pump-probe scheme and photon-counting measurements on Stokes scattered photons [256]. After this, entanglement has been similarly generated between mechanical resonators in the resolved-sideband regime of cavity optomechanics [257]. Notably, Refs [256] and [257] generate their mechanical entanglement by building upon the famous DLCZ protocol [258] that has previously enabled the generation of entanglement between spatially separated atomic ensembles [259]. Building on the aforementioned reservoir engineering proposal of Ref. [248], entanglement has now been realized between two micromechanical drum oscillators [260]. Here, the oscillators form the two end mirrors of a microwave optomechanical device. Finally, I note that recent experiments with microwave fields utilizing the ideas of quantum mechanics free subsystems [261] and pulsed electromechanics [262], respectively, have now pushed the forefront

of mechanics-mechanics entanglement experiments even further.

8.1.1 Linearized pulsed optomechanics for generating and verifying entanglement

Having briefly outlined the theoretical and experimental progress in studying entanglement in optomechanics, I will now describe how linearized pulsed optomechanics[2] provides an alternative route for entanglement generation and verification. In the previous chapter, I discussed how pulsed optomechanics is a useful tool in the preparation of non-classical quantum states, both in the linearized [183] and nonlinear regimes [155, 1]. Furthermore, linearized pulsed optomechanics has been shown to be a route for generating optical-mechanical correlations [263] and is a useful tool in numerous state verification schemes [139, 264]. Here, the first protocols for preparing and verifying entanglement between two mechanical modes in the regime of linearized pulsed optomechanics is introduced. The entanglement proposals presented in this thesis have several key advantages owing to their operation in the linearized pulsed regime. Firstly, over the optomechanical interactions both mechanical evolution and decoherence can be ignored. Secondly, as opposed to the nonlinear regime, the linearized regime enables the generation and full characterization of Gaussian continuous-variable entangled states. Note that continuous-variable systems allows for greater entanglement than is possible in low-dimensional discrete variable states. Thirdly, our protocols operate with pulses, which allows for more direct access to the entanglement in the time domain and enables operation in discrete time steps.

To elucidate our mechanical-mechanical entanglement protocol, I first introduce a protocol for the generation and full characterization of optical-mechanical entanglement via linearized pulsed optomechanics. Then I compare and contrast interferometric and non-interferometric configurations for mechanical-mechanical entanglement generation and analyze the utility of optical squeezing in each case. Here, it may be seen that optical squeezing provides a route to increase the resilience of the entangled state to optical loss and mechanical decoherence.

8.1.2 Experimental realization and future work

Although most of the progress in optomechanical entanglement has occurred in the resolved-sideband regime, as discussed in the previous section, unresolved-sideband experiments have now advanced to a point where the entanglement schemes I will discuss below are realizable even with current-day experimental parameters. For example, as discussed in Chapter 6 mechanical cooling via pulsed-interaction and measurement has been successfully realized in experiments [140, 114], and developments in sliced-photonic crystal devices now

[2]The concepts and tools for pulsed optomechanics in the quantum regime was developed in Ref. [139] and discussed in Section 6.3.2 of Chapter 6. Pulsed optomechanics operates in the unresolved sideband regime, where $\kappa \gg \omega_{\mathrm{M}}$, and uses pulses which are much much shorter than the mechanical period.

allow for large optomechanical coupling rates [265, 133, 266]. Owing to the slow thermal timescales involved, pulsed optomechanical interactions also provide an experimental route to achieve resilience to optics-induced thermal heating effects [267]. As will be discussed below, these experimental advances in pulsed optomechanics enable our optical-mechanical entanglement scheme to be realized with present-day parameters, and mechanical-mechanical entanglement can be realized even with total optical efficiencies much less than unity, i.e. of order 10%—see in Section 8.5.

Investigating optical-mechanical and mechanical-mechanical entanglement in the unresolved-sideband regime via pulsed optomechanics enables a broad range of applications. Firstly, for quantum science and technologies, applications include the development of new quantum sensors [102] and quantum parameter estimation techniques [268], performing optical-to-mechanical state swaps [146] and achieving optomechanical transduction [269], and enabling entanglement distillation via optomechanics [270]. Secondly, for fundamental science, applications include measuring decoherence rates in massive systems [271, 272], investigating non-classical correlations mediated by gravity [164, 165, 166], and placing new bounds on free parameters in generalized uncertainty principle models by exploring optomechanical geometric phases [145, 147, 273, 163].

8.2 Pulsed optomechanics, Gaussian operations, and optical-mechanical entanglement

In this section, I describe the physical operations that are used in our protocols for optomechanical entangled state preparation and verification. Moreover, I will work in the linearized regime of pulsed optomechanics, see Section 6.3.2, and utilize the tools of continuous-variable Gaussian quantum optics from Chapter 4.

8.2.1 The optomechanical interaction and Gaussian continuous variable quantum mechanics

From Section 6.3.2, in particular Eq. (6.42), a linearized pulsed-optomechanical interaction is described by the unitary operator $U_{\mathrm{LIN}} = \mathrm{e}^{\mathrm{i}\Omega X_{\mathrm{M}}}\mathrm{e}^{\mathrm{i}\chi X_{\mathrm{L}}X_{\mathrm{M}}}$. However, from here on, I will use $U_{\mathrm{OM}} = \mathrm{e}^{\mathrm{i}\chi X_{\mathrm{L}}X_{\mathrm{M}}}$ to describe the optomechanical interaction, as the deterministic part $\mathrm{e}^{\mathrm{i}\Omega X_{\mathrm{M}}}$ may either be compensated for via a mechanical displacement operation or subtracted from the measurement results in postprocessing [139].

As the linearized optomechanical Hamiltonian, H_{LIN} from Eq. (6.8), is bilinear in annihilation and creation operators, the unitary it generates will transform Gaussian states into other Gaussian states [47]. Such states can be fully characterized by the first and second moments of their quadrature vector $\mathbf{X} = (\mathbf{X}_{\mathrm{L}}, \mathbf{X}_{\mathrm{M}})^{\mathrm{T}} = (X_{\mathrm{L}}, P_{\mathrm{L}}, X_{\mathrm{M}}, P_{\mathrm{M}})^{\mathrm{T}}$. Here, the quadrature vectors for each mode are given by $\mathbf{X}_{\mathrm{L}} = (X_{\mathrm{L}}, P_{\mathrm{L}})^{\mathrm{T}}$ and $\mathbf{X}_{\mathrm{M}} = (X_{\mathrm{M}}, P_{\mathrm{M}})^{\mathrm{T}}$. Here, I will only consider initial Gaussian states of light and mechanics, and moreover, I will only consider unitary operations that preserve their Gaussian nature. Therefore, the symplectic

formalism for Gaussian unitary interactions, which was outlined in Chapter 4, will be utilized from here on.

Furthermore, non-unitary Gaussian operations—optical loss, mechanical decoherence and optical homodyne measurements—are also described in Chapter 4. The decoherence of each mode is modelled using a phase-insensitive Gaussian channel, which corresponds to each mode interacting with a Gaussian environment on a beamsplitter [274, 275]. In Hilbert space, the action of these phase-insensitive Gaussian decoherence channels on state ρ is $\mathcal{E}_\eta(\rho)$ and $\mathcal{E}_\gamma(\rho)$, where η and γ are the efficiency of the optical channel and the damping rate of the mechanical mode, respectively. In the pulsed regime of optomechanics, the mechanical decoherence may be neglected over the course of the optomechanical interactions and optical measurements.

Quantum states are described using either density matrices in Hilbert space or as covariance matrices in phase space. I use these descriptions interchangeably and the corresponding symplectic transformations, together with unitary and non-unitary operations, can be found in Chapter 4. For later convenience, the circle notation is used for quantum operations on density matrices, i.e. $M \circ \rho = M\rho M^\dagger$.

8.2.2 Mechanical precooling

Following a pulsed optomechanical interaction with an optical homodyne measurement allows one to reduce thermal noise along an axis of mechanical phase space, which was described in Section 6.3.2. I will refer to this cooling by pulsed interaction and measurement as 'mechanical precooling' as it will precede each of our proposed entanglement schemes. Mathematically, this precooling stage is described by

$$\rho \to \mathcal{E}_\gamma(U_{\text{ROT}}(\pi/2)\left|P_{\text{L}}\right\rangle\left\langle P_{\text{L}}\right| \circ \mathcal{E}_\eta(U_{\text{OM}} \circ \rho)). \tag{8.1}$$

Mechanical precooling, Eq. (8.1), begins with a pulsed optomechanical interaction U_{OM}, followed by optical decoherence, described by $\mathcal{E}_\eta$, and it is assumed that the optical environment is well described by the vacuum state. Subsequently, a homodyne measurement of the phase-quadrature, with projector $\left|P_{\text{L}}\right\rangle\left\langle P_{\text{L}}\right|$, is made on the light which projects the mechanical mode into a squeezed thermal state with a lower effective thermal occupation [139]. The mechanical state is then allowed to evolve freely over a quarter of a period prior to the generation of optical-mechanical entanglement, described by the unitary $U_{\text{ROT}}(\theta) = \mathrm{e}^{\mathrm{i}\theta b^\dagger b}$ with $\theta = \pi/2$. During this time, the mechanical mode interacts with a thermal environment with mean occupation $\bar{N}$ at a rate γ, described by $\mathcal{E}_\gamma$. In this way, Eq. (8.1) prepares a mechanical state with reduced thermal noise along the momentum quadrature of phase space.

The results of Chapter 4 may be used to neatly compute the analytic result of Eq. (8.1) on the first and second moments of the quadrature vector. In full, U_{OM} corresponds to symplectic matrix S_{OM} in Eq. (4.13), the decoherence channels $\mathcal{E}_\eta(\rho)$ and $\mathcal{E}_\gamma(\rho)$ correspond to map of Eq. (4.24), the homodyne measurement

of the $P_{\rm L}$ quadrature $|P_{\rm L}\rangle\langle P_{\rm L}|$ is given by the measurement map[3] of Eqs (4.18) and (4.19), and the single mode unitary rotation $U_{\rm ROT}(\theta)$ corresponds to the symplectic matrix $S_{\rm ROT}(\theta)$ in Eq. (4.10). Then, if the initial state of the optical-mechanical system is given by the covariance matrix

$$\sigma_{\rm IN} = \frac{1}{2}\begin{pmatrix} 1 & 0 & 0 & 0 \\ 0 & 1 & 0 & 0 \\ 0 & 0 & 1+2\bar{n} & 0 \\ 0 & 0 & 0 & 1+2\bar{n} \end{pmatrix}, \tag{8.2}$$

where $\bar{n}$ is the initial mechanical occupation, then the precooled state of the mechanics is given by

$$\sigma_{\rm COOL} = \begin{pmatrix} V_{\rm X} & 0 \\ 0 & V_{\rm P} \end{pmatrix}. \tag{8.3}$$

Here,

$$2V_{\rm X} = 1 + 2\bar{N} + 2{\rm e}^{-\gamma t}(\bar{n}-\bar{N}) + {\rm e}^{-\gamma t}\chi^2 \tag{8.4}$$

$$2V_{\rm P} = (1+2\bar{N})(1-{\rm e}^{-\gamma t}) + {\rm e}^{-\gamma t}\frac{1+2\bar{n}}{1+\eta\chi^2(1+2\bar{n})}. \tag{8.5}$$

Comparing these equations to Eqs (6.54) and (6.56), one sees that the cooling map includes the interactions with the optical and mechanical environments.

8.2.3 Optomechanical entanglement

The symplectic formalism outlined in Chapter 4 may then be used to efficiently compute the generation of optical-mechanical entanglement. The generation of an entangled optomechanical state is achieved via interaction of light and mechanics through $U_{\rm OM}$. However, the optical mode will then be subject to optical loss described by the channel $\mathcal{E}_\eta$. After this optical loss channel, the mechanical state evolves freely through a phase-space angle θ, described by the unitary $U_{\rm ROT}(\theta) = {\rm e}^{{\rm i}\theta b^\dagger b}$. During this time, the mechanical mode interacts with a thermal environment described by $\mathcal{E}_\gamma$. Including this decoherence, the map that describes the generation of an optical-mechanical entangled state from initial state ρ is therefore

$$\rho \to \mathcal{E}_\gamma(U_{\rm ROT}(\theta)\circ\mathcal{E}_\eta(U_{\rm OM}\circ\rho)). \tag{8.6}$$

Note that the phase insensitive channel commutes with the free evolution of the mechanical mode, i.e. $\mathcal{E}_\gamma(U_{\rm ROT}\circ\rho) = U_{\rm ROT}\circ\mathcal{E}_\gamma(\rho)$. Both the precooling and entangling stages are illustrated in the circuit diagram of Fig. 8.1.

Taking $\frac{1}{2}\mathbb{1}_2 \oplus \sigma_{\rm COOL}$ as the initial covariance matrix of light and mechanics, one may then use the results of Chapter 4 to describe each operation in Eq. (8.6). After this calculation, the entangled state has the covariance matrix

$$\sigma_{\rm LM} = \begin{pmatrix} A_{\rm LM} & C_{\rm LM} \\ C_{\rm LM}^{\rm T} & B_{\rm LM} \end{pmatrix}, \tag{8.7}$$

[3]Note that Eqs (4.18) and (4.19) correspond to a projection onto a general Gaussian state. To describe the $P_{\rm L}$ homodyne measurement, one may use Eq. (4.20) with $\varphi = \pi/2$.

with

$$A_{\mathrm{LM}} = \begin{pmatrix} a_{11} & 0 \\ 0 & a_{22} \end{pmatrix}, \tag{8.8}$$

$$B_{\mathrm{LM}} = \begin{pmatrix} b_{11} & 0 \\ 0 & b_{22} \end{pmatrix}, \tag{8.9}$$

$$C_{\mathrm{LM}} = \begin{pmatrix} 0 & c_{12} \\ c_{21} & 0 \end{pmatrix}, \tag{8.10}$$

where

$$2a_{11} = 1 \tag{8.11}$$

$$2a_{22} = 1 + (1 + 2V_{\mathrm{X}}\eta\chi^2) \tag{8.12}$$

$$2b_{11} = (1 + 2\bar{N})(1 - \mathrm{e}^{-\gamma t}) + 2V_{\mathrm{X}}\mathrm{e}^{-\gamma t} \tag{8.13}$$

$$2b_{22} = (1 + 2\bar{N})(1 - \mathrm{e}^{-\gamma t}) + (2V_{\mathrm{P}} + \chi^2)\mathrm{e}^{-\gamma t} \tag{8.14}$$

$$2c_{12} = \mathrm{e}^{-\gamma t/2}\sqrt{\eta}\chi \tag{8.15}$$

$$2c_{21} = 2V_{\mathrm{X}}\mathrm{e}^{-\gamma t/2}\sqrt{\eta}\chi. \tag{8.16}$$

For brevity, σ_{LM} is presented in a frame rotating at the mechanical frequency, $\theta = 0$, and the mechanical entanglement protocols are also presented in the same rotating frame. However, as the decoherence channel $\mathcal{E}_\gamma$ and the unitary operation described by U_{ROT} commute, the form of σ_{LM} in a non-rotating frame may be obtained by computing $\mathbb{1}_2 \oplus S_{\mathrm{ROT}}(\theta)\sigma_{\mathrm{LM}}\mathbb{1}_2 \oplus S^{\mathrm{T}}_{\mathrm{ROT}}(\theta)$.

Quantifying the entanglement

In order to quantify entanglement, the logarithmic negativity $E_{\mathcal{N}}(\sigma)$ is employed, which was introduced in Chapter 4 and applies to bipartite continuous variable Gaussian states [60]. To recap, the logarithmic negativity $E_{\mathcal{N}}(\sigma)$ of a general bipartite covariance matrix σ, cf. Eq. (4.5), is given by

$$E_{\mathcal{N}}(\sigma) = \max\{0, -\log_2(2\tilde{\nu}_-)\}, \tag{8.17}$$

where the minimum symplectic eigenvalue is

$$\tilde{\nu}_- = \sqrt{\frac{\tilde{\Delta} - \sqrt{\tilde{\Delta}^2 - 4\det\sigma}}{2}}, \tag{8.18}$$

and $\tilde{\Delta} = \det A + \det B - 2\det C$.

8.2.4 Experimental parameters

The proposed system parameters are listed in Table 8.1, which are based on the sliced-silicon nanobeam devices from Refs [114, 265, 133]. In the following, I also discuss the parameters I change from these experiments, namely the thermal occupation $\bar{n}$ and the optical efficiency η.

In Ref. [114], a reduction in the thermal occupation from $\bar{n} = 22,200$ to an effective occupation of $3,400$ was achieved using a series of pulsed-optomechanical interactions at 3.2 K. Therefore, multiple precooling steps can be used to increase the environmental temperature at which the protocol can operate at. However, to simplify the discussions, I do not consider multiple precooling steps and assume a bath temperature of approximately 0.1 K, hence $\bar{n} = \bar{N} = 500$. Such temperatures are readily achieved with commercially available dilution refrigerators. Furthermore, in the table an improved optical efficiency of $\eta = 0.855$ is proposed. Optical efficiencies of 1.3% have been achieved in experiments, and without implementing further cooling techniques a reduction in the uncertainty below the zero-point fluctuations may be achieved with $\eta > 8\%$ [114, 133]. In Section 8.5, I further discuss the requirements on optical efficiency that our protocols present. In particular, the optical-mechanical entanglement protocol can generate entanglement at very low optical efficiencies, less than 1%, while the protocols for generating mechanical entanglement require total optical efficiencies greater than 10%. As noted in Ref. [133], improvements to the optical design and employing new waveguide coupling techniques provide an encouraging route for further experimental progress in pulsed optomechanics.

Table 8.1: **List of proposed experimental parameters for the optical-mechanical and mechanical entanglement protocols.** The parameter values are based on the sliced-silicon nanobeam system that appears in Refs [114, 265, 133]. Here, it is assumed that the mechanical oscillator and its environment are in equilibrium, hence $\bar{n} = \bar{N} = 500$—this corresponds to a temperature of approximately 0.1 K. An improved optical efficiency of $\eta = 0.855$ is proposed. This optical efficiency may be decomposed into a part that accounts for output cavity coupling losses from the cavity, η_{CAV}, and a part that accounts for homodyne detection efficiency η_{DET}. Here, a range of values for the optomechanical interaction strength χ is considered.

System parameter	Value
$\omega_{\text{M}}/2\pi$	4 MHz
$\gamma/2\pi$	100 Hz
$\bar{n} = \bar{N}$	500
$\kappa/2\pi$	20 GHz
$g_0/2\pi$	30 MHz
η_{CAV}	0.9
η_{DET}	0.95

Now I will apply the theory discussed in this section to design protocols for generating and verifying both optical-mechanical and mechanical-mechanical entanglement.

8.3 Optical-mechanical entanglement in pulsed optomechanics

8.3.1 Optical-mechanical entanglement generation

The proposed setup for the preparation of an entangled state of light and mechanics is shown in Fig. 8.1. A pulse of light in a coherent state $|\alpha\rangle$ is injected into an optomechanical cavity, which then interacts via the entangling unitary U_{OM} with a mechanical oscillator in an initial thermal state with mean thermal occupation $\bar{n}$. This interaction, followed by optical loss and mechanical decoherence is described by Eq. (8.6) and generates an entangled state of light and mechanics.

Prior to the entangling stage, the precooling stage, described by Eq. (8.1), creates an initial mechanical state which can be utilized to generate more entanglement for a given interaction strength χ. This increase in performance is due to the reduction in thermal noise in the direction of the phase-space translations generated by the optomechanical unitary, and hence a higher amount of entanglement can be prepared between light and mechanics. Multiple precooling stages can be employed to further increase the degree of entanglement generated. However, within the range of parameters considered here, I find that additional stages are unnecessary and lead to a negligible increase in the amount of entanglement generated.

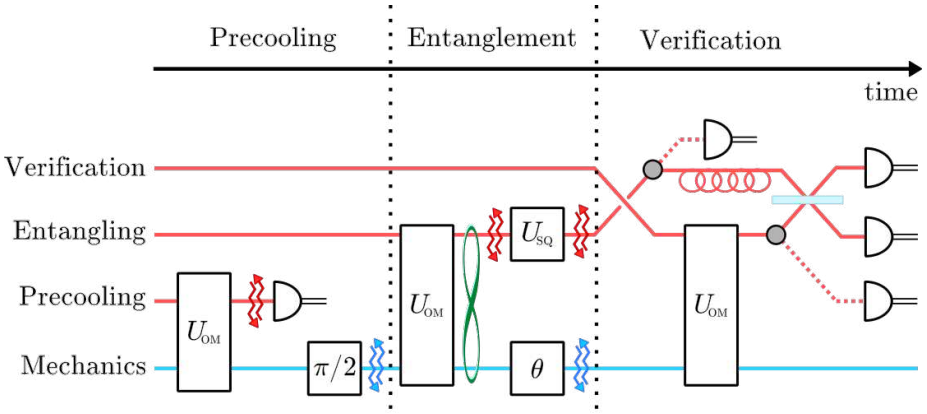


Figure 8.1: **Scheme for pulsed optical-mechanical entanglement preparation and verification.** Circuit diagram for the separate stages of the protocol—mechanical precooling, entanglement generation, and verification—with red lines corresponding to the optical modes and the blue line representing the mechanical mode. The interaction between the optical pulses and the mechanical state is given by $U_{\mathrm{OM}} = \mathrm{e}^{\mathrm{i}\chi X_{\mathrm{L}} X_{\mathrm{M}}}$. Following the precooling stage, the mechanical oscillator freely evolves over a phase-space angle $\theta = \pi/2$. Then, after the generation of the optical-mechanical entanglement, indicated by the green figure eight, the mechanics rotates through an angle θ. Including an optional optical squeezer U_{SQ} increases the amount of optomechanical entanglement generated. The jagged arrows indicate optical loss or mechanical decoherence, while the detectors represent optical homodyne measurements. Finally, the dashed red lines in the verification stage indicate the different paths the optical pulses may take, which may be achieved via the grey optical switches. Verification of the optical and mechanical blocks of the optical-mechanical covariance matrix is achieved by directly homodyning the entangling and verification pulses, respectively. To access the correlations block, the entangling and verification pulses interfere on a beamsplitter and the optical output modes are homodyned. To realize this interference, the entangling pulse is sent down a delay line, indicated by the red overlapping circles, and then the verification pulse is sent towards the beamsplitter.

8.3.2 Optical-mechanical entanglement verification

Once an entangled state of light and mechanics has been generated, the full phase-space structure of the two-mode Gaussian state can be reconstructed. In this reconstruction process many runs of an experiment will be needed to build up adequate statistics for the different quadrature combinations. Experimentally, it will be important to track the first moments vector to accurately construct probability histograms of each observed quadrature. More specifically, in order to reconstruct the statistics of each quadrature the first moment must

be recorded and subtracted from the measurement results, removing the effects of the random homodyne measurement outcomes from the data. Tracking the first moments vector may be achieved by considering the action of each Gaussian unitary and non-unitary process in the precooling and entangling stages of the protocol, as well as recording the measurement outcomes of the homodyne detection events. As mentioned in Section 8.2, when constructing the probability histograms of the mechanical quadratures, the projection of the deterministic momentum transfer along the mechanical quadrature under consideration may also be subtracted from the measurement results to avoid the necessity of a feedback force.

Turning now to the reconstruction of the covariances, the reconstructed covariance matrix is referred to as σ_{VER}, which in block matrix form is

$$\sigma_{\text{VER}} = \begin{pmatrix} A_{\text{VER}} & C_{\text{VER}} \\ C_{\text{VER}}^{\text{T}} & B_{\text{VER}} \end{pmatrix}, \tag{8.19}$$

and, in the absence of decoherence processes, will approach the covariance matrix σ prepared immediately after the entangling stage. In the analysis, I assume that the interaction strength χ and the total optical efficiency η are precisely known, which allows σ_{VER} to be constructed accurately. So that the reader may easily follow the symplectic transformations, I present formulae for σ_{VER} without the inclusion of optical loss in only the verification stage—optical losses are present in the precooling and entangling stages. However, including optical loss in the formulas for σ_{VER} is straightforward and does not affect the results presented. In Appendix G.1, I discuss how the elements of σ_{VER} are obtained in more detail and how to include optical loss in the formulas for σ_{VER}.

After the optomechanical interaction in the entangling stage of the protocol, the optical pulse exits the cavity and either a homodyne measurement is made on a rotated quadrature $P_{\text{L}}(\varphi) = P_{\text{L}} \cos\varphi - X_{\text{L}} \sin\varphi$, or the light is sent down a delay line. If the entangling pulse of light is directly homodyned, this allows the A_{VER} block of σ_{VER} to be determined and the required set of homodyne measurement angles may be noted from the expression

$$A_{\text{VER}} = \begin{pmatrix} \text{Var}(X_{\text{L}}) & \frac{1}{2}[\text{Var}(P_{\text{L}}(\frac{3\pi}{4})) - \text{Var}(P_{\text{L}}(\frac{\pi}{4}))] \\ \frac{1}{2}[\text{Var}(P_{\text{L}}(\frac{3\pi}{4})) - \text{Var}(P_{\text{L}}(\frac{\pi}{4}))] & \text{Var}(P_{\text{L}}) \end{pmatrix}. \tag{8.20}$$

After the entangling pulse has been homodyned, a verification pulse in a pure coherent state is then introduced into the cavity after a controllable time delay $t = \theta/\omega_{\text{M}}$ in which time the mechanics evolves freely and undergoes some decoherence. This decoherence of the mechanical mode between the interaction with the entangling and verification pulses leads to imperfect reconstruction of the covariance matrix σ. After the optomechanical interaction, the quadrature vector of the verification pulse is $\mathbf{X}_{\text{V}}(\theta) = (X_{\text{V}}(\theta), P_{\text{V}}(\theta))^{\text{T}}$. The $X_{\text{V}}(\theta)$ quadrature contains no information about the mechanical mode, however the phase quadrature of the verification pulse reads $P_{\text{V}}(\theta) = P_{\text{IN}} + \chi X_{\text{M}}(\theta)$, where the initial optical phase quadrature P_{IN} introduces noise in the reconstruction process and $X_{\text{M}}(\theta) = X_{\text{M}} \cos\theta + P_{\text{M}} \sin\theta$. Note that the argument θ of $P_{\text{V}}(\theta)$ refers to

the phase-space evolution of the mechanics and not a rotation in the optical subspace. To access the B_{VER} block of the covariance matrix, optical homodyne measurements are made directly on the $P_{\text{V}}(\theta)$ quadrature at various time delays and the input noise $\text{Var}(P_{\text{IN}})$ can be subtracted to increase the accuracy of the reconstruction process. Importantly, to verify the B_{VER} block the homodyne measurement outcomes on the entangling pulse of light must be ignored so the light is traced out in the reconstruction process. The mechanical block is then given by

$$B_{\text{VER}} = \frac{1}{\chi^2}\begin{pmatrix} \text{Var}(P_{\text{V}}(0)) - \text{Var}(P_{\text{IN}}) & \frac{1}{2}[\text{Var}(P_{\text{V}}(\frac{\pi}{4})) - \text{Var}(P_{\text{V}}(\frac{3\pi}{4}))] \\ \frac{1}{2}[\text{Var}(P_{\text{V}}(\frac{\pi}{4})) - \text{Var}(P_{\text{V}}(\frac{3\pi}{4}))] & \text{Var}(P_{\text{V}}(\frac{\pi}{2})) - \text{Var}(P_{\text{IN}}) \end{pmatrix}. \tag{8.21}$$

To access the C_{VER}-block elements of the covariance matrix, the entangling light is not directly homodyned, but instead it is sent down a path towards a controllable delay line, while the verification pulse is sent down another path. These two pulses interact with each other on a 50:50 beamsplitter and each individual output is directly homodyned. Redirection of the entangling and verification pulses may be achieved by using an optical switch. The timescale over which this optical switch operates must be less than a quarter of the mechanical cycle as this corresponds to the time between the precooling pulse and the entangling pulse of light. This means there is no need for high-speed switching or small-scale integrated operation, one can use a larger switch that operates with very low optical loss, such as a Pockels cell.

The beamsplitter operation, which mixes the entangling and verification pulses, is described by the 4×4 symplectic matrix $S_{\text{BS}}(\alpha,\beta)$ given by Eq. (4.12), where α and β are the real beamsplitter parameters. To access every element of C_{VER}, two different beamsplitter configurations are required: $S_{\text{BS}}(\frac{\pi}{4},0)$ and $S_{\text{BS}}(\frac{\pi}{4},\frac{\pi}{2})$. These two configurations may be implemented with a single 50:50 beamsplitter and a controllable phase shifter. The quadrature vectors after the $S_{\text{BS}}(\frac{\pi}{4},0)$ and $S_{\text{BS}}(\frac{\pi}{4},\frac{\pi}{2})$ operations are defined as $(\mathbf{X}'_{\text{V}}(\theta),\mathbf{X}'_{\text{L}}(\theta))^{\text{T}}$ and $(\mathbf{X}''_{\text{V}}(\theta),\mathbf{X}''_{\text{L}}(\theta))^{\text{T}}$, respectively. Then the C_{VER} block is determined by

$$C_{\text{VER}} = \frac{1}{2\chi}\begin{pmatrix} \text{Var}(P''_{\text{V}}(2\pi)) - \text{Var}(X''_{\text{L}}(2\pi)) & \text{Var}(P''_{\text{V}}(\frac{5\pi}{2})) - \text{Var}(X''_{\text{L}}(\frac{5\pi}{2})) \\ \text{Var}(P'_{\text{V}}(2\pi)) - \text{Var}(P'_{\text{L}}(2\pi)) & \text{Var}(P'_{\text{V}}(\frac{5\pi}{2})) - \text{Var}(P'_{\text{L}}(\frac{5\pi}{2})) \end{pmatrix}. \tag{8.22}$$

Interference between the entangling and verification pulses is necessary to obtain the optomechanical covariances. Whereas, if there was no interference one would only be able to access the A_{VER} and B_{VER} blocks and not the full covariance matrix. Note, an addition of 2π has been included in the arguments of the C_{VER} elements, which corresponds to a full rotation of the mechanical mode in phase space. The necessity of this additional 2π is explained shortly when the conservative approaches to entanglement estimation are explained. Furthermore, when the additional factor of 2π is included, the time between the entangling and verification pulses is always greater than the time between the precooling and entangling pulses.

8.3.3 Optical squeezing and non-monotonic behaviour

Here, I investigate the non-monotonic behaviour in the logarithmic negativity with increasing interaction strength in the presence of both optical loss and mechanical decoherence, and how the protocol can be made more resilient to these decoherence effects by using optical squeezers.

After the optomechanical interaction between the entangling pulse and the precooled mechanical oscillator, the reduced state of the optical mode will satisfy $\mathrm{Var}(P_{\mathrm{L}}) > \mathrm{Var}(X_{\mathrm{L}})$. This is due to the phase-space displacements generated by U_{OM} along the P_{L} axis of optical phase space, which are proportional to the mechanical position quadrature operator. The optical mode is then subject to the phase-insensitive decoherence channel $\mathcal{E}_{\eta}$, which introduces vacuum noise and degrades the optomechanical correlations. However, to reduce these deleterious effects, an optical squeezer may be applied immediately after the optomechanical interaction. Optical squeezing is a useful way to protect single-mode quantum states from interactions with the environment, for example squeezers may be used to improve state fidelity in teleportation [276] and the performance of quantum memory devices [277]. Furthermore, the utility of such operations in protecting quantum coherence has been investigated theoretically [278, 279, 280] and verified experimentally [281]. Unlike these recent applications of optical squeezing, in this work optical squeezing is utilized to protect the entanglement of a bipartite state specifically. Eq. (8.6), which describes the generation of optical-mechanical entanglement, is therefore modified to

$$\rho \to \mathcal{E}_{\gamma}(U_{\mathrm{ROT}}(\theta) \circ \mathcal{E}_{\eta_{\mathrm{DET}}}(U_{\mathrm{SQ}} \circ \mathcal{E}_{\eta_{\mathrm{CAV}}}(U_{\mathrm{OM}} \circ \rho))). \tag{8.23}$$

Here, the squeezing unitary is $U_{\mathrm{SQ}} = \exp\{\frac{r}{2}[(a^{\dagger})^2 - a^2]\}$, with real squeezing parameter r. Moreover, the channel $\mathcal{E}_{\eta_{\mathrm{CAV}}}$ represents losses from the optical cavity and $\mathcal{E}_{\eta_{\mathrm{DET}}}$ is the channel describing detection inefficiencies. It is assumed that the optical squeezer can be turned off during the precooling and verification stages of the protocol. However, if for a particular experimental implementation of our scheme, operating the squeezer in this way is not feasible, then the description of the precooling and verification stages is straightforwardly modified by using the symplectic transformation $S_{\mathrm{SQ}}(r)$, which is given by Eq. (4.11).

In the entanglement scheme presented in this thesis, interest is placed on how squeezing operations allow for the protection of entanglement—rather than quantum superposition as studied in Refs [278, 279, 280, 281]. For a Gaussian bosonic channel, it is well known that the output state with maximum purity and minimum von-Neumann entropy corresponds to a coherent state input [282, 283]. Likewise, when a squeezing operation is applied to an input state of fixed given purity, the input state that maximizes the output purity and minimizes the output entropy, with respect to the real squeezing parameter r, is given by a symmetric mode in phase space, i.e. a thermal state, see Appendix G.2 for a proof. This may suggest that the optical squeezing parameter $r_{\mathrm{SYM}} = \frac{1}{4}\ln\left[1 - \eta_{\mathrm{CAV}} + \eta_{\mathrm{CAV}}(1 + 2V_{\mathrm{X}}\chi^2)\right]$, which symmetrizes the optical mode such that $\mathrm{Var}(P_{\mathrm{L}}) = \mathrm{Var}(X_{\mathrm{L}})$, is a good candidate for the optimal squeezing parameter to also maximize the output logarithmic negativity. Here, V_{X} is the position

variance of the precooled mechanical state—see Eq. (8.4).

However, the entangling unitary U_{OM} generates optomechanical correlations which are distributed asymmetrically between the optical phase and amplitude quadratures. Namely, only the optical phase quadrature contains information about the mechanical position, which may be lost to the optical environment leading to a reduction in the logarithmic negativity. Furthermore, the optical environment will be less sensitive to displacements along the phase quadrature for an optical state of a given purity with $\text{Var}(P_{\text{L}}) > \text{Var}(X_{\text{L}})$. Therefore, a state with $\text{Var}(P_{\text{L}}) > \text{Var}(X_{\text{L}})$ at the input of the optical loss channel $\mathcal{E}_{\eta_{\text{DET}}}$, reduces the sensitivity of the optical environment to the mechanical position quadrature and the optomechanical correlations.

A balance between a symmetric optical phase-space distribution, which minimizes the output entropy of the optical decoherence channel, and an optical phase-space distribution with $\text{Var}(P_{\text{L}}) > \text{Var}(X_{\text{L}})$, which reduces the sensitivity of the optical environment to optomechanical correlations, leads to the optimal squeezing parameter r_{OPT} that maximizes the logarithmic negativity. In the upper plot of Fig. 8.2, r_{OPT} is plotted as a function of the interaction strength χ. This plot shows the logarithmic negativity of the optical-mechanical entangled state as a function of r and χ. Here, the entangled state has been subject to both optical and mechanical decoherence processes since the time of entanglement generation. For comparison, I also present r_{SYM} as a function of χ, and note that $r_{\text{SYM}} > r_{\text{OPT}}$ for all χ—demonstrating the balance between the two effects described above. The experimental implementation of this squeezing operation, which is introduced to protect entanglement in pulsed optomechanics, is made feasible by experimental advances in squeezing pulses of light [284, 285] and non-classical continuous travelling waves of light [286].

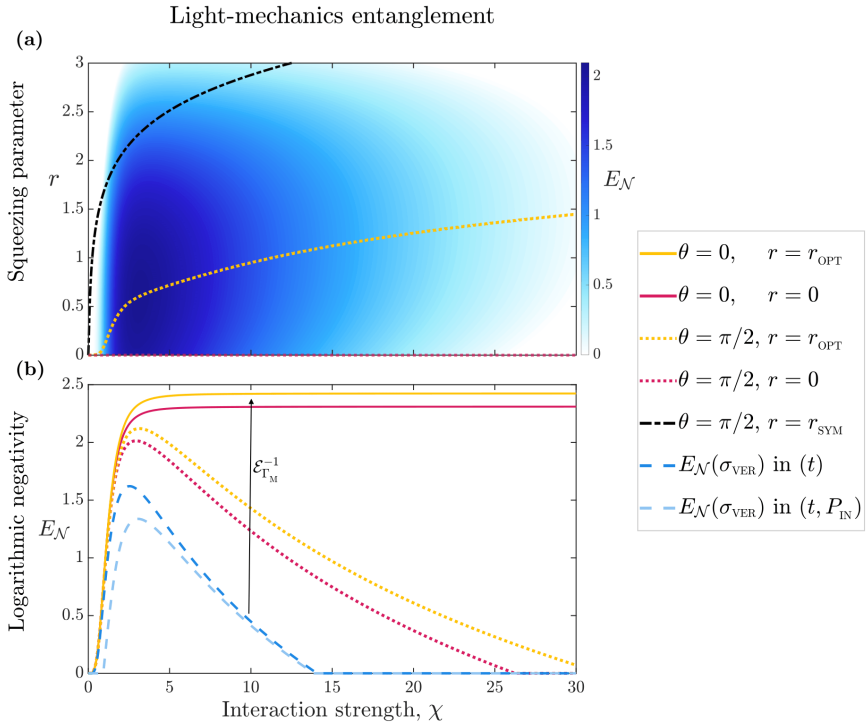


Figure 8.2: **Logarithmic negativity generated between a pulse of light and a precooled mechanical state. Upper:** Contour plot of logarithmic negativity $E_{\mathcal{N}}(\sigma)$ as a function of optomechanical interaction strength χ and the optical squeezing parameter r—with other system parameters corresponding to those listed in Table 8.1. Here, the mechanical state has evolved, and decohered, through a phase-space angle of $\theta = \pi/2$ after the time of entanglement generation. The maximum achievable logarithmic negativity is $E_{\mathcal{N}} = 2.12$, which requires $\chi = 3.12$ and $r = 0.60$. Without the use of an optical squeezer, a value of $E_{\mathcal{N}} = 2.01$ is obtained with $\chi = 2.94$. The squeezing parameter $r_{\rm SYM}$ symmetrizes the optical mode after the optomechanical interaction, while $r = r_{\rm OPT}$ maximizes $E_{\mathcal{N}}(\sigma)$ as a function of χ. The contour plot shows $r_{\rm SYM} > r_{\rm OPT}$ for all χ, which demonstrates that an asymmetric optical phase-space distribution is optimal for maximizing entanglement. **Lower:** Plot showing logarithmic negativity as a function of interaction strength χ in the presence of both optical loss and mechanical decoherence. The plot also shows that two conservative approaches, which ensure that the logarithmic negativity is not overestimated, can verify a significant amount of entanglement, i.e. $E_{\mathcal{N}}(\sigma_{\rm VER}) > 1$, for a range of χ. Here, θ refers to the angle through which the mechanical oscillator evolves in phase-space after the optomechanical interaction. The conservative approach in time, which accounts for different times between the entangling and verification pulses, is denoted by (t), while the conservative approach in time and noise, which also accounts for lack of knowledge about the optical noise on the verification pulse, is denoted by $(t, P_{\rm IN})$. At large χ the two conservative approaches show the same limiting behaviour as the contribution of the optical noise becomes less relevant. The arrow indicates that better approximations of σ can be made from $\sigma_{\rm VER}$ by applying the inverse of the mechanical decoherence map to each element, which is explored further in Appendix G.1.

Importantly, as is evident from the lower plot of Fig. 8.2, non-monotonic behaviour in the logarithmic negativity is observed when both optical loss and mechanical decoherence are present after the generation of entanglement. The existence of this non-monotonic behaviour is because—at large values of χ—the increase in the magnitude of the optomechanical correlations with interaction strength scales in the same way as the decrease in the logarithmic negativity due to the decoherence of either the optical or mechanical mode alone. Hence, when both optical and mechanical decoherence processes are present, the logarithmic negativity first rises to a maximum before tending towards zero as χ is increased and decoherence processes outweigh the effect of the entangling optomechanical unitary. When the optical squeezing operation can be applied before the decoherence channels, the non-monotonic behaviour in logarithmic negativity can be completely eliminated. In this case, the entangled state is made more resilient to loss of information to the environment before it enters the decoherence channels and so higher values of $E_{\mathcal{N}}(\sigma)$ can be reached than in Fig. 8.2. I refer the reader to Appendix G.3 for a discussion of this case.

8.3.4 Conservative approaches to entanglement estimation

Here, I consider the time order in which elements of the covariance matrix must be measured to conservatively estimate the entanglement generated in the protocol.

The lower plot in Fig. 8.2 also demonstrates how accurately the optical-mechanical entanglement is measured in the verification process. As it is necessary to allow the mechanical oscillator to undergo free mechanical evolution to obtain information about the rotated mechanical quadratures $X_{\mathrm{M}}(\theta)$, the problem that different elements of the covariance matrix must be measured at different times is encountered, having suffered different amounts of mechanical decoherence. Moreover, care must be taken when calculating the logarithmic negativity from the reconstructed covariance matrix, in particular one must ensure that $E_{\mathcal{N}}(\sigma) \geq E_{\mathcal{N}}(\sigma_{\mathrm{VER}})$, meaning that the logarithmic negativity is not overestimated. To ensure this condition, one must demand that the elements of C_{VER} are accessed at later times than those of A_{VER} and B_{VER}, hence the addition of 2π in the argument of the elements in Eq. (8.22). Therefore, the C_{VER} elements experience a larger amount of decoherence than the A_{VER} and B_{VER} elements, meaning that the optical-mechanical correlations cannot be falsely enhanced in the verification process. This approach is referred to as *conservative in time*, and the conservative nature of this approach is demonstrated in the lower plot of Fig. 8.2. Moreover, I consider the case in which state reconstruction is performed without assuming that the noise statistics of the verification pulse $\mathrm{Var}(P_{\mathrm{IN}})$ is known and can be subtracted. Similarly, this approach is referred to as *conservative in time and noise*.

If the mechanical damping rate γ and thermal occupation $\bar{n}$ are well known, the inverse of the mechanical decoherence may be applied to each element of σ_{VER} to compensate for decoherence, as illustrated in the lower plot of Fig. 8.2

by the vertical arrow. The application of the inverse map to the elements of σ_{VER} that depend on two different times is more involved and is described in Appendix G.1. Also, if decoherence can be accurately compensated for in this way, the need to be conservative with respect to time is no longer needed and so additional factors of 2π can be removed from the arguments of the C_{VER}-elements.

8.4 Mechanical-mechanical entanglement in pulsed optomechanics

Our proposal for preparing an entangled state of two mechanical oscillators builds upon the optical-mechanical entanglement described in the previous section. In this section, I describe schemes for converting entanglement between two optical-mechanical systems to entanglement between two mechanical oscillators using optical homodyne measurements. In particular, two such complementary schemes are introduced. One scheme employs an optical interferometric design and therefore necessitates the introduction of two optical modes, while the other scheme comprises a non-interferometric setup. For each scheme, I compute the amount of entanglement that can be prepared and verified.

8.4.1 Interferometric scheme

Generating entanglement

The interferometric protocol to entangle two mechanical modes is shown in the circuit diagram of Fig. 8.3, where, for brevity, the details of the precooling stage have been omitted. The entanglement stage of the protocol starts with a pulse of light in a coherent state impinging on one input port of a Mach-Zehnder interferometer. The other input port is in the vacuum state, such that after the first 50:50 beamsplitter interaction, described by U_{BS}, two coherent pulses of light propagate in the upper and lower arms towards the two mechanical modes. I label the quadratures of the optical modes $\mathbf{X}_{\text{L1}} = (X_{\text{L1}}, P_{\text{L1}})^{\text{T}}$ and $\mathbf{X}_{\text{L2}} = (X_{\text{L2}}, P_{\text{L2}})^{\text{T}}$, and the mechanical modes with which these light modes interact as $\mathbf{X}_{\text{M1}}$ and $\mathbf{X}_{\text{M2}}$, respectively. Each light mode interacts with its respective mechanical mode through the unitary U_{OM}, hence the total optomechanical interaction is described by $U_{\text{OM}} \otimes U_{\text{OM}} = U_{\text{OM}}^{\otimes 2}$. After these interactions, the decoherence channel $\mathcal{E}_{\eta_{\text{CAV}}}$ describing optical cavity losses acts on the two-mode optical subspace, and optional unitary squeezing operations $U_{\text{SQ}}^{\otimes 2}$ may be applied to each optical mode to increase the final amount of entanglement generated. Following this, the optical modes experience the loss channel $\mathcal{E}_{\eta_{\text{DET}}}$ and then pass through a 50:50 beamsplitter, which erases which-path information about the optomechanical interactions. Here, the ordering of the final loss channel and beamsplitter is arbitrary as they both lead to the same final mechanical state. To turn the optical-mechanical entanglement to mechanical-mechanical entanglement, optical homodyne measurements are made on the rotated quadratures $X_{\text{L1}}(\varphi)$ and

$X_{\mathrm{L2}}(\psi)$, described by the projector $|X_{\mathrm{L1}}(\varphi), X_{\mathrm{L2}}(\psi)\rangle\langle X_{\mathrm{L1}}(\varphi), X_{\mathrm{L2}}(\psi)|$. After the mechanical entanglement has been generated, the first and second mechanical modes evolve through phase-space angles θ and ϕ, respectively, which is described by $U_{\mathrm{ROT}}(\theta,\phi) = U_{\mathrm{ROT}}(\theta)\otimes U_{\mathrm{ROT}}(\phi)$. Different periods of mechanical free evolution can be achieved using controllable delay lines, as is shown in Fig. 8.3 and discussed in further detail below. During this free evolution the mechanical oscillators decohere via the channel $\mathcal{E}_\gamma$. Including mechanical decoherence, the interferometric entanglement protocol is therefore given by

$$\rho \to \mathcal{E}_\gamma(U_{\mathrm{ROT}}(\theta,\phi)\,|X_{\mathrm{L1}}(\varphi), X_{\mathrm{L2}}(\psi)\rangle\langle X_{\mathrm{L1}}(\varphi), X_{\mathrm{L2}}(\psi)|\,U_{\mathrm{BS}}\circ \mathcal{E}_{\eta_{\mathrm{DET}}}(U_{\mathrm{SQ}}^{\otimes 2}\circ\mathcal{E}_{\eta_{\mathrm{CAV}}}(U_{\mathrm{OM}}^{\otimes 2}U_{\mathrm{BS}}\circ\rho))). \tag{8.24}$$

From Eq. (8.24), one finds that at the input ports of the homodyne detectors the optical phase quadratures P_{L1} and P_{L2} contain information about the mechanical EPR quadratures $X_{\mathrm{M1}} \pm X_{\mathrm{M2}}$, whilst no knowledge of mechanical position can be gleaned from the the corresponding optical amplitude quadratures, X_{L1} and X_{L2}. In what follows, the homodyne angles are therefore set to one of two equivalent configurations given by $(\varphi,\psi) = \{(0,\pi/2),(\pi/2,0)\}$. These configurations correspond to Bayesian inference of a mechanical EPR quadrature, which projects the mechanics into an entangled state. Conversely, if both phase quadratures are measured, then no mechanical entanglement can be created, as this would allow information about each mechanical quadrature to be obtained separately. Interestingly, there exists other optimal homodyne angles than those stated above, which also maximize the logarithmic negativity. These angles correspond to a balance between the Bayesian inference of an EPR quadrature and an effective unitary operation, and this is discussed further in Appendix G.4.

If the initial state of each mechanical oscillator is described by the covariance matrix σ_{COOL}, the covariance matrix of each light mode interacting with the mechanical modes is $\frac{1}{2}\mathbb{1}_2$, and the homodyne angles are chosen to be $(\varphi,\psi) = (0,\pi/2)$, then by using the results of Chapter 4 and Eq. (8.24) the final bipartite mechanical covariance matrix is given by

$$\sigma_{\mathrm{INT}} = \begin{pmatrix} A_{\mathrm{INT}} & C_{\mathrm{INT}} \\ C_{\mathrm{INT}}^{\mathrm{T}} & B_{\mathrm{INT}} \end{pmatrix}, \tag{8.25}$$

$$A_{\mathrm{INT}} = B_{\mathrm{INT}} = \begin{pmatrix} a_{11} & 0 \\ 0 & a_{22} \end{pmatrix}, \tag{8.26}$$

$$C_{\mathrm{INT}} = \begin{pmatrix} c_{11} & 0 \\ 0 & c_{22} \end{pmatrix}, \tag{8.27}$$

where

$$
\begin{aligned}
2a_{11} &= (1+2\bar{N})(1-\mathrm{e}^{-\gamma t}) + 2V_{\mathrm{X}}\mathrm{e}^{-\gamma t}\left(1 - \frac{\eta V_{\mathrm{X}}\chi^2}{\mathrm{e}^{2r}(1-\eta_{\mathrm{DET}}) + \eta_{\mathrm{DET}}(1+2V_{\mathrm{X}}\eta_{\mathrm{CAV}}\chi^2)}\right), \\
2a_{22} &= (1+2\bar{N})(1-\mathrm{e}^{-\gamma t}) + \mathrm{e}^{-\gamma t}\left[2V_{\mathrm{P}} + \chi^2 - \frac{1}{2}\left(\frac{\mathrm{e}^{2r}\eta\chi^2}{1+\eta_{\mathrm{DET}}(\mathrm{e}^{2r}-1)}\right)\right], \\
c_{11} &= \frac{\mathrm{e}^{-\gamma t}\eta V_{\mathrm{X}}^2\chi^2}{\mathrm{e}^{2r}(1-\eta_{\mathrm{DET}}) + \eta_{\mathrm{DET}}(1+2V_{\mathrm{X}}\eta_{\mathrm{CAV}}\chi^2)}, \\
c_{22} &= -\frac{1}{4}\left(\frac{\mathrm{e}^{2r}\mathrm{e}^{-\gamma t}\eta\chi^2}{1+\eta_{\mathrm{DET}}(\mathrm{e}^{2r}-1)}\right).
\end{aligned}
$$

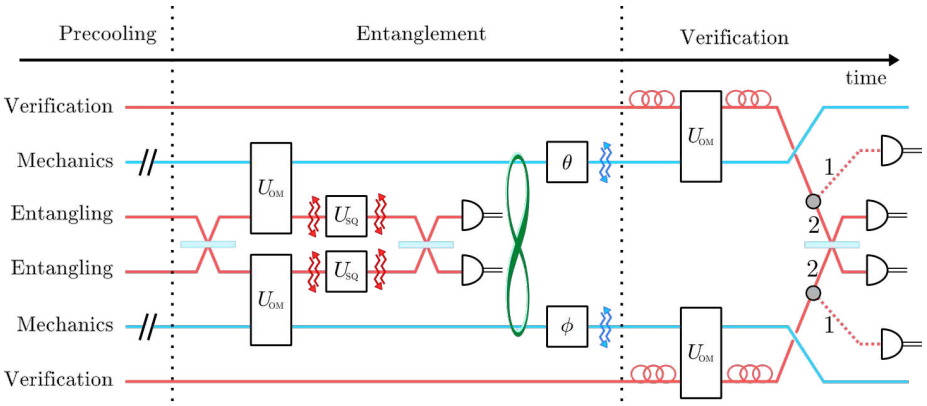


Figure 8.3: **Interferometric scheme for mechanical entanglement preparation and verification.** Circuit diagram for the preparation and verification stages after the precooling stage has taken place. The angles through which the first and second mechanical modes freely evolve are given by θ and ϕ, respectively. By virtue of the optical switches (grey dots) and controllable delay lines (red overlapping circles), the setup allows for mechanical precooling, entangled state preparation, and verification. Each mechanical mode is initially precooled by an interaction with a precooling pulse, followed by an optical phase-quadrature measurement. This is achieved by setting the optical switches to position 1. Mechanical entanglement is generated by first establishing pairwise optical-mechanical entanglement, and then converting this to mechanical entanglement via optical interference and homodyne measurements. Setting the optical switches to position 2 allows for this. The blocks of the covariance matrix, which correspond to each mechanical oscillator, are reconstructed by interacting each mechanical mode with a verification pulse and directly homodyning the optical outputs, which requires the optical switches to be set to position 1. Instead, if the optical switches are set to position 2, then the mechanical-mechanical correlations can be measured.

The reduced state of each mechanical mode is identical, $A_{\mathrm{INT}} = B_{\mathrm{INT}}$, mean-

ing the Gaussian state is symmetric, which allows the entanglement of formation to be computed analytically [287, 288]. But as this entanglement measure is also a monotonically decreasing function of $\tilde{\nu}_-$, it is an equivalent measure to $E_{\mathcal{N}}$.

Verifying entanglement

The state prepared by the precooling and entangling stages, as illustrated in Fig. 8.3, can be reconstructed by sending a subsequent verification pulse into the input port of the interferometer. The verification pulses in the upper and lower arms then interact with the mechanical oscillators after time delays $t_1 = \theta/\omega_{\mathrm{M}}$ and $t_2 = \phi/\omega_{\mathrm{M}}$, respectively. The phase quadrature of the verification pulse in the upper arm of the Mach-Zehnder interferometer evolves from P_{IN1} to $P_{\mathrm{V1}}(\theta) = P_{\mathrm{IN1}} + \chi X_{\mathrm{M1}}(\theta)$, during the optomechanical interaction. While the verification pulse in the lower arm evolves from P_{IN2} to $P_{\mathrm{V2}}(\phi) = P_{\mathrm{IN2}} + \chi X_{\mathrm{M2}}(\phi)$. As in the optical-mechanical entanglement scheme, for clarity, I present results for the verification procedure without the inclusion of optical loss and refer the reader to Appendix G.1 for a more complete discussion, including optical loss.

The covariance matrix obtained in the verification procedure is σ_{VER}, which has the same block-matrix form as Eq. (8.19). However, now both the A_{VER} and B_{VER} blocks correspond to a covariance matrix of a reduced mechanical state. These matrix blocks are obtained by performing phase homodyne measurements on the verification pulses after they interact with the mechanical modes. To allow for this direct detection, optical switches are placed after the optomechanical interactions in Fig. 8.3 to redirect the verification pulses away from the second 50:50 beamsplitter of the Mach-Zehnder interferometer. The elements of the A_{VER} and B_{VER} blocks, which depend on the mechanical phase-space angles θ and ϕ, respectively, are therefore given by equivalent expressions to Eq. (8.21)—with $P_{\mathrm{V}}(\theta)$ replaced by $P_{\mathrm{V1}}(\theta)$ or $P_{\mathrm{V2}}(\phi)$.

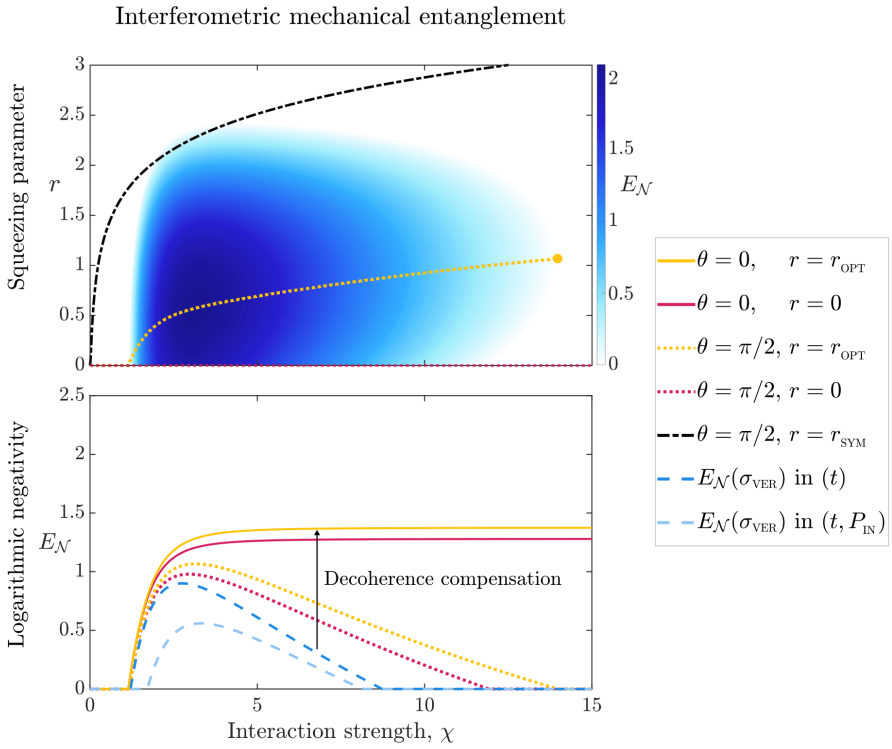


Figure 8.4: **Logarithmic negativity of the entangled mechanical state generated by the interferometric scheme. Upper:** Contour plot of logarithmic negativity $E_{\mathcal{N}}(\sigma)$ as a function of optomechanical interaction strength χ and squeezing parameter r. Here, the other system parameters correspond to those listed in Table 8.1. Since the time of entanglement generation, each mechanical oscillator has rotated, and decohered, over a quarter of a mechanical period. The maximum logarithmic negativity is $E_{\mathcal{N}} = 1.07$, which corresponds to $\chi = 3.15$ and $r = 0.57$. Without the use of a squeezer, the protocol achieves $E_{\mathcal{N}} = 0.98$ with $\chi = 2.97$. The curve corresponding to the optimal squeezing parameter terminates at the point where, even with squeezing, no entanglement can be generated. Note that the formula for r_{SYM} is the same as in the optical-mechanical case. **Lower:** Logarithmic negativity in the presence of both optical loss and mechanical decoherence after state preparation, and conservative approaches for entanglement verification. The plot shows the case where the two mechanical modes have freely evolved through the same phase-space angles, $\theta = \phi$, and hence have decohered by the same amount. Here, r_{OPT} is the optimal squeezing parameter to maximize the logarithmic negativity. The arrow indicates that with an inverse transform, better approximations to the entanglement generated at $\theta = \phi = 0$ can be made from the statistics gathered using the conservative approaches. In this non-unitary process, entanglement is generated for $\chi \gtrsim 1.15$.

On the other hand, the correlations between the two mechanical modes, defined by the C_{VER}-block elements, are obtained by mixing the two verification pulses on a beamsplitter after the optomechanical interactions. Similarly to the verification of optical-mechanical entanglement, it is the interference of these two optical pulses that allows for the full reconstruction of the covariance matrix. After this operation, the resulting phase quadrature operators at the beamsplitter outputs are given by $P_{\text{V}\pm}(\theta,\phi) = (P_{\text{V}_1}(\theta) \pm P_{\text{V}_2}(\phi))/\sqrt{2}$. Homodyne measurements are then performed on these quadratures in order to construct C_{VER}. Introducing $\delta(\theta,\phi) = \text{Var}(P_{\text{V}+}(\theta,\phi)) - \text{Var}(P_{\text{V}-}(\theta,\phi))$ allows one to write C_{VER} as

$$C_{\text{VER}} = \frac{1}{2\chi^2}\begin{pmatrix} \delta(2\pi,2\pi) & \delta(2\pi,\frac{5\pi}{2}) \\ \delta(\frac{5\pi}{2},2\pi) & \delta(\frac{5\pi}{2},\frac{5\pi}{2}) \end{pmatrix}. \tag{8.28}$$

The off-diagonal elements of C_{VER}, correspond to different periods of free evolution for each mechanical mode. To introduce this difference—and to ensure the recombination of the verification pulses on the final beamsplitter—controllable delay lines may be inserted before and after the optomechanical interactions in the interferometer of Fig. 8.3. I have again included an additional factor of 2π in the arguments of the C_{VER}-block such that the logarithmic negativity is conservatively estimated as discussed in Section 8.3.

Fig. 8.4 shows the logarithmic negativity of the entangled state of two mechanical oscillators, and demonstrates how optical squeezing may be used to increase the amount of entanglement generated. The squeezing changes the phase-space distributions of the light modes to ensure the protocol remains robust to decoherence processes in the large χ limit. The lower plot of Fig. 8.4 also reaffirms the conclusions of Section 8.3. Namely, that the origin of the non-monotonic behaviour in the logarithmic negativity is due to the presence of both optical loss and mechanical decoherence. Conservative approaches for state verification are also shown in the lower plot of Fig. 8.4. As in the case of the optical-mechanical entanglement protocol, the statistics obtained via the conservative approaches may be compensated for by using an inverse decoherence map.

The interferometric scheme introduced above offers an alternative strategy to the mechanical entanglement scheme presented in Ref. [250]—which utilizes Stokes scattering in the resolved-sideband regime. Namely, in this work, the potential to generate entanglement using short optical pulses in the unresolved sideband regime is explored, which allows rapid preparation and verification of entanglement, and a full-state-characterization procedure using these short optical pulses is introduced and detailed.

8.4.2 Non-interferometric scheme

Generating entanglement

The non-interferometric scheme for entanglement preparation and verification using pulsed optomechanics is shown in the circuit diagram of Fig. 8.5. As

before, a precooling stage is implemented to increase the amount of mechanical-mechanical entanglement generated. The entangling stage is then initiated by a pulse of coherent light entering an optomechanical cavity and interacting with the first mechanical mode—identified by its quadrature vector $\mathbf{X}_{\mathrm{M1}}$. The light is then subject to optical losses, each described by $\mathcal{E}_{\eta_{\mathrm{CAV}}}$, corresponding to the output-cavity-coupling and input-cavity-coupling efficiencies of the first and second cavities, respectively. Here, I assume equal out-coupling and in-coupling efficiencies, which are given by η_{CAV}. An optional optical squeezer may be placed between these two optical loss channels to provide resilience to interactions with the optical environment.

For the first optomechanical interaction, it was sufficient to absorb the input-cavity-coupling losses into the definition of the interaction strength χ, but when the light interacts with the second mechanical mode—described by $\mathbf{X}_{\mathrm{M2}}$—it is important to separate out this effect. This is because the light incident on the second cavity contains information about X_{M1}, and so input coupling losses lead to loss of information about the mechanical position and a reduction in the final amount of entanglement generated. The attenuation of the light between the two optomechanical interactions leads to a reduction in the optomechanical interaction strength: $\chi \to \eta_{\mathrm{CAV}}\chi$. Hence the second optomechanical interaction is modified from $U_{\mathrm{OM}} = \mathrm{e}^{\mathrm{i}\chi X_{\mathrm{L}} X_{\mathrm{M}}}$ to $U'_{\mathrm{OM}} = \mathrm{e}^{\mathrm{i}\eta_{\mathrm{CAV}}\chi X_{\mathrm{L}} X_{\mathrm{M}}}$.

After the optomechanical interaction with the second mechanical oscillator, the light passes through the optical loss channels $\mathcal{E}_{\eta_{\mathrm{CAV}}}$ and $\mathcal{E}_{\eta_{\mathrm{DET}}}$, with an optional squeezing operation in between. Finally, a homodyne measurement is made on the phase quadrature of light which contains information about an EPR-like quadrature variable of X_{M1} and X_{M2}. Hence, this measurement projects the mechanical subspace into an entangled state via Bayesian inference of a joint-mechanical quadrature—see Appendix G.4 for a more complete discussion. This non-interferometric entanglement protocol, followed by free mechanical evolution $U_{\mathrm{ROT}}(\theta, \phi)$ and mechanical decoherence $\mathcal{E}_\gamma$, is represented by Eq. (8.29).

$$\begin{aligned}\rho \to \mathcal{E}_\gamma(U_{\mathrm{ROT}}(\theta,\phi)\,|P_{\mathrm{L}}\rangle\,\langle P_{\mathrm{L}}| \circ \mathcal{E}_{\eta_{\mathrm{DET}}}(U_{\mathrm{SQ}}\circ \\ \mathcal{E}_{\eta_{\mathrm{CAV}}}(U'_{\mathrm{OM}} \circ \mathcal{E}_{\eta_{\mathrm{CAV}}}(U_{\mathrm{SQ}} \circ \mathcal{E}_{\eta_{\mathrm{CAV}}}(U_{\mathrm{OM}} \circ \rho))))).\end{aligned} \tag{8.29}$$

Eq. (8.29) describes the generation of an entangled state of two mechanical oscillators using the non-interferometric scheme. As in the previous subsection, if the initial state of each mechanical oscillator is described by the covariance matrix σ_{COOL}, and the initial covariance matrix of the light mode is $\frac{1}{2}\mathbb{1}_2$, then

the final bipartite mechanical covariance matrix is

$$\sigma_{\rm NON} = \begin{pmatrix} A_{\rm NON} & C_{\rm NON} \\ C_{\rm NON}^{\rm T} & B_{\rm NON} \end{pmatrix}, \tag{8.30}$$

$$A_{\rm NON} = \begin{pmatrix} a_{11} & 0 \\ 0 & a_{22} \end{pmatrix}, \tag{8.31}$$

$$B_{\rm NON} = \begin{pmatrix} b_{11} & 0 \\ 0 & b_{22} \end{pmatrix}, \tag{8.32}$$

$$C_{\rm NON} = \begin{pmatrix} c_{11} & 0 \\ 0 & c_{22} \end{pmatrix}, \tag{8.33}$$

where

$$\begin{aligned}
2a_{11} &= (1+2\bar{N})(1-\mathrm{e}^{-\gamma t}) + \mathrm{e}^{-\gamma t} V_{\rm X} J_a \\
2a_{22} &= (1+2\bar{N})(1-\mathrm{e}^{-\gamma t}) + \mathrm{e}^{-\gamma t}(2V_{\rm P} + \chi^2) \\
2b_{11} &= (1+2\bar{N})(1-\mathrm{e}^{-\gamma t}) + \mathrm{e}^{-\gamma t} V_{\rm X} J_b \\
2b_{22} &= (1+2\bar{N})(1-\mathrm{e}^{-\gamma t}) + \mathrm{e}^{-\gamma t}\left[2V_{\rm P} + \eta_{\rm CAV}^2 \chi^2 [1 + \eta_{\rm CAV}(\mathrm{e}^{2r}-1)]\right] \\
c_{11} &= -\frac{1}{8}\mathrm{e}^{2r} V_{\rm X}^2 \mathrm{e}^{-\gamma t} \eta_{\rm CAV}^3 \eta_{\rm DET} \chi^2 J_c \\
c_{22} &= \frac{1}{2}\mathrm{e}^{r} \mathrm{e}^{-\gamma t} \eta_{\rm CAV}^2 \chi^2 .
\end{aligned}$$

The functions J_a, J_b, and J_c are given in Appendix G.5.

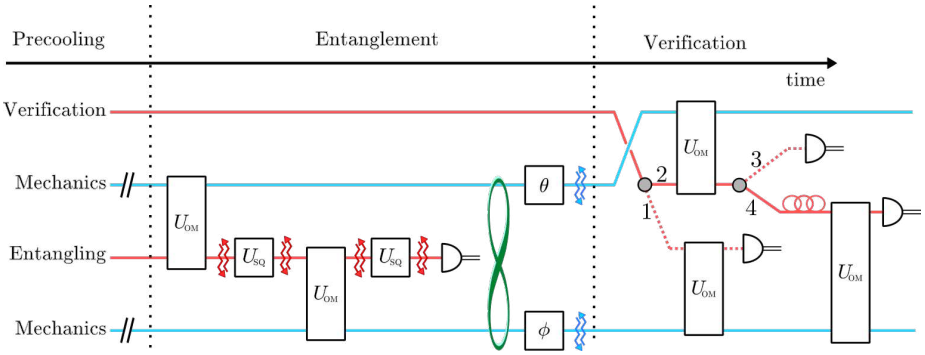


Figure 8.5: **Non-interferometric scheme for mechanical-mechanical entanglement preparation and verification.** Circuit diagram of the protocol. Here, a single homodyne detector and controllable delay line suffice to realize the precooling, entangling, and verification stages of the protocol. For each mechanical mode, the precooling stage consists of an interaction with the precooling pulse followed by a phase-quadrature measurement on the output pulse. For the first mechanical mode, this is achieved using the switch settings 2 and 3, respectively, while for the second mechanical mode switch settings 1 and 4 are required. Mechanical entanglement is generated by choosing the switch settings 2 and 4 and homodyning the optical output, which corresponds to Bayesian inference of a joint mechanical quadrature. In the verification procedure, the same combination of paths as in the precooling stage will yield the blocks of the covariance matrix corresponding to each mechanical oscillator, while the optical-switch setting 2 and 4 allows the mechanical-mechanical correlations to be accessed.

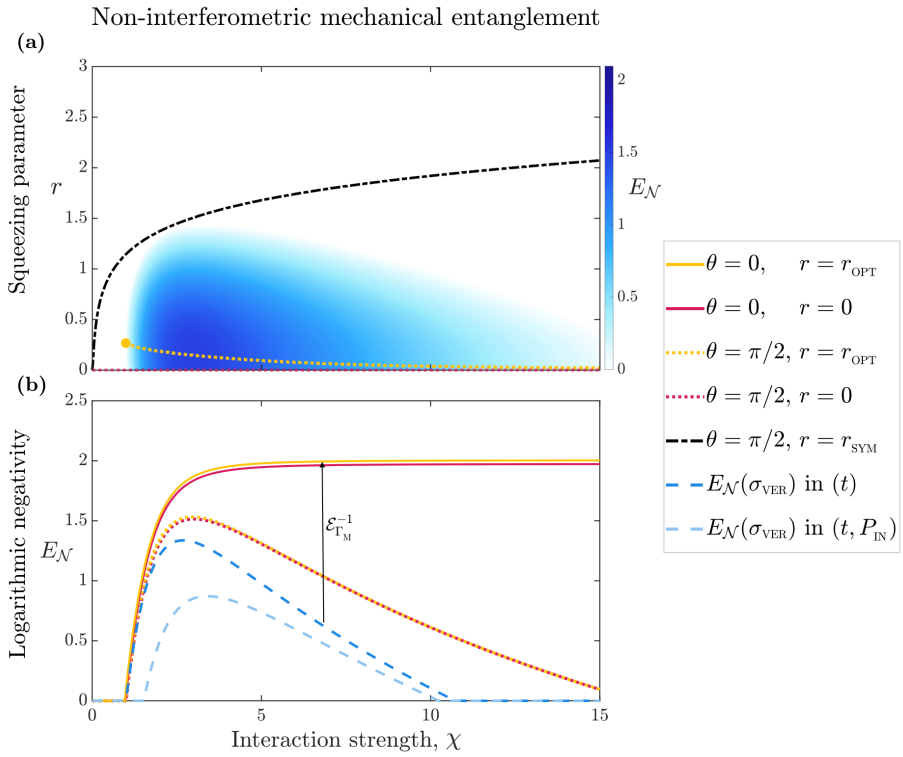


Figure 8.6: **Logarithmic negativity of the entangled mechanical state generated by the non-interferometric scheme. Upper:** Contour plot of logarithmic negativity $E_{\mathcal{N}}(\sigma)$ as a function of optomechanical interaction strength χ and squeezing parameter r—with other system parameters corresponding to those listed in Table 8.1. Here, each mechanical mode has decohered over a quarter of a period since the time of entanglement generation. The maximum of the logarithmic negativity is $E_{\mathcal{N}} = 1.53$, which corresponds to $\chi = 2.97$ and $r = 0.15$. Without the use of an optical squeezer the protocol achieves $E_{\mathcal{N}} = 1.51$ with $\chi = 3.00$. As compared to the previous entanglement schemes, the asymmetry in the optomechanical interactions leads to a different form for $r_{\rm SYM}$, which is given by the real-positive solution of a quartic equation in e^{2r}. Also in contrast to the previous schemes, the first point in the contour plot with $E_{\mathcal{N}}(\sigma) > 0$ corresponds to finite value of $r_{\rm OPT}$, which is highlighted with the yellow circle. **Lower:** Logarithmic negativity of the entangled state, showing the effect of mechanical decoherence and optical squeezing on $E_{\mathcal{N}}(\sigma)$, and conservative approaches for mechanical state verification. As the mechanical modes evolve and undergo decoherence, the optical squeezing operations become less useful—demonstrated by the convergence of the orange and red curves. In addition to conservative approaches, the physical requirement that $\phi \geq \theta$ leads to further decay of the elements of $\sigma_{\rm VER}$. In this non-unitary process, for these system parameters, entanglement is generated for $\chi \gtrsim 1$.

Verifying entanglement

Focusing on the verification procedure, the $A_{\rm VER}$ and $B_{\rm VER}$ blocks of the verified covariance matrix $\sigma_{\rm VER}$ are obtained by addressing each mechanical oscillator individually with a pulse of light, which is achieved by the use of optical switches as shown in Fig. 8.5. The $A_{\rm VER}$ and $B_{\rm VER}$ blocks are therefore given by an equivalent expression to Eq. (8.21). A single verification pulse, with an initial phase quadrature $P_{\rm IN}$, is then used to construct $C_{\rm VER}$. By allowing both mechanical modes to evolve over a phase-space angle θ and implementing a controllable delay line between the two mechanical modes, such that the second mechanical oscillator evolves over a total phase-space angle ϕ, the phase quadrature entering the homodyne detector is given by $P_{\rm V}(\theta,\phi) = P_{\rm IN} + \chi(X_{\rm M1}(\theta) + X_{\rm M2}(\phi))$. Due to the non-interferometric arrangement, one has the condition $\phi \geq \theta$, which leads to further decay of the $C_{\rm VER}$-elements—on top of the decay due to *conservative in time* approach. By defining $\epsilon(\theta,\phi) = {\rm Var}(P_{\rm V}(\theta,\phi)) - {\rm Var}(P_{\rm V}(\theta,\phi+\pi))$, one finds that the elements describing the mechanical correlations are given by

$$C_{\rm VER} = \frac{1}{4\chi^2}\begin{pmatrix} \epsilon(2\pi,2\pi) & \epsilon(2\pi,\frac{5\pi}{2}) \\ -\epsilon(\frac{5\pi}{2},3\pi) & \epsilon(\frac{5\pi}{2},\frac{5\pi}{2}) \end{pmatrix}. \tag{8.34}$$

Plots analysing the behaviour of the logarithmic negativity obtained using the non-interferometric scheme are shown in Fig. 8.6, and it may be seen that the protocol is relatively insensitive to the squeezing operations as compared to the optical-mechanical and interferometric entanglement schemes. This difference in sensitivity occurs because there is an additional optomechanical interaction and loss channel which further modifies the same optical phase-space distribution towards the ideal, slightly asymmetric, state with ${\rm Var}(P_{\rm L}) > {\rm Var}(X_{\rm L})$. This additional modification to the phase-space distribution means a lower squeezing parameter r is needed to protect the state from optical loss and mechanical decoherence. The lower plot of Fig. 8.6 shows the logarithmic negativity which may be measured in the verification process, compared to the logarithmic negativity of the unverified state at different times since entanglement generation.

8.5 Comparison between the entanglement protocols

In this section, I compare the three entanglement schemes outlined above. In particular, I discuss the relative importance of the squeezing operations, the fidelity of the verification procedure, and the sensitivity to the cavity coupling efficiency. Focus will be placed primarily on the interferometric and non-interferometric mechanical entanglement schemes to establish which one is favourable for preparing and verifying entangled mechanical states.

In Fig. 8.7, the logarithmic negativity generated in each of the three entanglement schemes is compared and the relative importance of optical squeezing in each scheme is also analyzed. More specifically, in this figure, I plot the percentage increase in the logarithmic negativity due to the use of optical squeezers, and

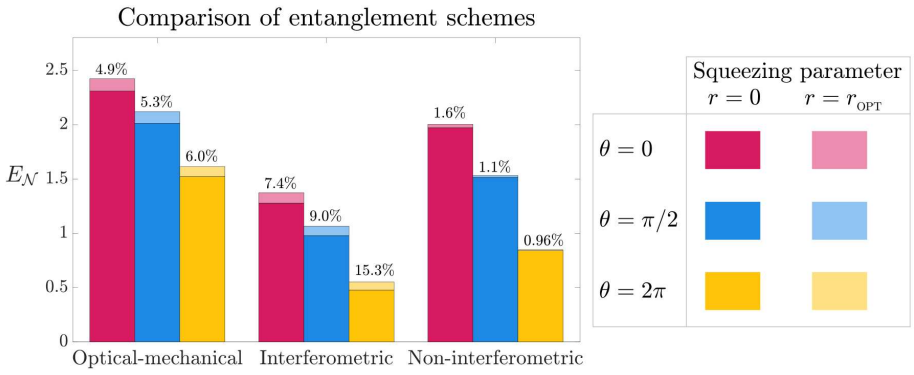


Figure 8.7: **Comparison of entanglement schemes with and without optical squeezers.** The maximum logarithmic negativity $E_{\mathcal{N}}(\sigma)$ generated using the three different entanglement schemes: optical-mechanical, interferometric, and non-interferometric. The squeezing parameter is taken to either be $r = 0$ or the value which maximizes logarithmic negativity $r = r_{\mathrm{OPT}}$. The phase-space angle θ over which the mechanical modes rotate and decohere, after the time of entanglement generation, is taken to be 0, $\pi/2$, or 2π. For the mechanical entanglement schemes, the second mechanical phase-space angle is taken to be $\phi = \theta$. The percentage increase in $E_{\mathcal{N}}(\sigma)$, as a result of optimal squeezing, is listed above each bar.

find that squeezing is most useful in the interferometric scheme and least useful in the non-interferometric scheme. It is interesting to note that as the mechanical oscillators evolve and decohere after the instance of entanglement generation, the percentage increase in logarithmic negativity rises for the optical-mechanical and interferometric entanglement schemes, while the percentage increase drops towards 0% for the non-interferometric scheme. This is due to the active role the second optomechanical interaction has on the optical phase-space distribution in the non-interferometric scheme. For the parameter values listed in Table 8.1, a squeezing parameter of $r \approx 0.60$ is required to reach maximum logarithmic negativity for the optical-mechanical and interferometric entanglement protocols, which is experimentally feasible. However, it is experimentally simpler to implement the entanglement protocol without the use of optical squeezers, in which case the non-interferometric scheme is advantageous.

In the conservative approaches for state verification, the C_{VER} elements in the non-interferometric protocol must be measured at later times than those in the interferometric protocol. Despite this requirement, the logarithmic negativity of the verified state $E_{\mathcal{N}}(\sigma_{\mathrm{VER}})$ is much higher in the non-interferometric scheme than in the interferometric scheme—as is evident from the lower plots of Figs. 8.4 and 8.6. Specifically, in the interferometric scheme, the conservative in time approach reaches a maximum logarithmic negativity of $E_{\mathcal{N}}(\sigma_{\mathrm{VER}}) = 0.90$, as compared to the non-interferometric scheme which reaches $E_{\mathcal{N}}(\sigma_{\mathrm{VER}}) = 1.34$.

To aid experimental development, the behaviour of the logarithmic negativity with cavity coupling efficiency is described, keeping all other parameters in Table 8.1 the same. Furthermore, I also set all the squeezing parameters to $r = 0$ for this analysis and assume that the input-cavity-coupling and output-cavity-coupling efficiencies are both given by η_{CAV}. Therefore interest is placed on finding the minimum value of η_{CAV} required to satisfy the condition $E_{\mathcal{N}}(\sigma) > 0$ in each of the three schemes. Table 8.2 lists this minimum value of η_{CAV} for different values of the phase-space angle through which the mechanical modes evolve and decohere after entanglement generation. It is found that the optical-mechanical system can still be entangled, even after the mechanical mode has decohered over a full period, for $\eta_{\text{CAV}} > 0.0065$. This entanglement scheme is therefore currently experimentally feasible. The mechanical entanglement schemes lead to stricter requirements on the cavity coupling efficiency, with the non-interferometric scheme being favourable in this regard. However, if one calculates the total optical efficiency in each of the two schemes, it is found that only relatively low efficiencies are required to generate entanglement. More specifically, by using Table 8.2 and Eqs (8.24) and (8.29), one can calculate that in order to generate entanglement, total optical efficiencies of 50% and 11% are required for the interferometric and non-interferometric schemes, respectively. Here, the total optical efficiency in the interferometric design is given by the efficiency of a single optical path, i.e. the product of the cavity coupling efficiency and the detection efficiency, while for the linear non-interferometric design the total efficiency is given by product of all the intensity efficiencies along the optical path. Moreover, Table 8.2 also shows the minimum cavity coupling efficiency required to verify entanglement in each of the schemes, i.e. to satisfy $E_{\mathcal{N}}(\sigma_{\text{VER}}) > 0$ in the case of no squeezing. These values correspond to minimum total optical efficiencies of 0.63%, 60%, and 16% to verify entanglement in the optical-mechanical, interferometric, and non-interferometric schemes, respectively.

Table 8.2: **Minimum cavity coupling efficiency for entanglement generation and verification.** The table shows the minimum cavity coupling efficiency η_{CAV} required to retain an entangled state after each mechanical oscillator rotates through a phase-space angle θ whilst undergoing some decoherence, and the minimum cavity coupling efficiency required to verify the entangled state using the conservative in time approach. Other system parameters correspond to those given in Table 8.1, apart from the optical squeezing parameter r—which is set to zero here. The total optical efficiency is given by the product of the intensity efficiencies along the optical path.

Entanglement scheme	$\theta = 0$	$\theta = \pi/2$	$\theta = 2\pi$	Verification
Optical-mechanical	>0	0.00040	0.0065	0.0066
Interferometric	0.53	0.59	0.70	0.63
Non-interferometric	0.48	0.52	0.61	0.55

To summarize this comparison between schemes, in the parameter range

considered, the non-interferometric design allows for both the preparation and verification of a higher amount of mechanical entanglement—both with and without the use of optical squeezers. The non-interferometric scheme also provides a route for generating entangled mechanical states if the cavity coupling efficiency is the major source of technical difficulty. In fact, the only regime studied in which the interferometric design is preferable, is when the output coupling efficiency from the cavities is set to unity, but the input coupling efficiency remains less than unity. In this case, the non-monotonic behaviour in the logarithmic negativity with increasing interaction strength χ is removed as the optical squeezers act before any decoherence channels, and so the entangled state may then be made resilient to optical loss and mechanical decoherence—see G.3 for a detailed discussion. However, if both input and output coupling efficiencies are set to unity, then the non-interferometric scheme allows for higher values of logarithmic negativity to be reached, and also allows the non-monotonic behaviour to be avoided.

8.6 Summary of the entanglement protocols

I have detailed our schemes for the generation and verification of optical-mechanical and mechanical-mechanical entanglement via pulsed optomechanics. These schemes naturally operate in the unresolved-sideband regime and use linear optomechanical interactions and optical homodyne measurements to generate Gaussian entanglement. To increase the amount of entanglement generated, even in the presence of both mechanical decoherence and optical loss, one may utilize optical squeezers and an additional precooling stage. I also detailed how the elements of the covariance matrices must be measured at distinct times. To address this problem, I discussed how a state verification procedure may be carried out in order to accurately measure the entanglement.

The two mechanical entanglement schemes introduced here have been compared using a set of parameters based on current state-of-the-art experiments. Here,the non-interferometric design outperforms the interferometric design in two main ways: (i) the non-interferometric scheme is able to prepare and verify more entanglement as characterized by the logarithmic negativity $E_{\mathcal{N}}$, and (ii) with the non-interferometric design, entanglement can be prepared and verified at a lower minimum total optical efficiency of 16%—even without the enhancement of optical squeezing.

Crucially, generating and verifying optical-mechanical entanglement can even be achieved with optical efficiencies much less than 1% and so can be realized with present-day experiments.

8.7 Further entanglement works

8.7.1 Entangling modes of the same resonator

Here I briefly discuss the work of Ref. [3], where this work was originally published. P.N. was the first author of this work and J.C. made theoretical contributions.

The interferometric and non-interferometric schemes, outlined above, generate entanglement between spatially separated optomechanical systems. However, in Ref. [3] a scheme to generate and verify entanglement between two mechanical modes in a single mechanical structure is detailed. For example, these two mechanical modes can be two vibrating membranes in an optical cavity [289, 290, 291] or a sliced photonic crystal nanobeam with two non-degenerate flexural modes [292]. Ref. [148] also proposes a scheme to generate bipartite mechanical entanglement in a single optomechanical system stroboscopically via a train of many short pulses, but here a minimal two pulse sequence is explored that can generate mechanical entanglement within a single mechanical period of both modes.

Our protocol begins with a pulsed optomechanical interaction between an input pulse and the two mechanical modes described by the unitary $U_{\rm OM}^{\otimes 2} = \mathrm{e}^{\mathrm{i}X_{\rm L}(\chi_1 X_{\rm M1}+\chi_2 X_{\rm M2})}$, where χ_1 and χ_2 are the coupling strengths for each mechanical mode. After this, a phase $P_{\rm L}$ homodyne measurement is made on the output pulse, which reduces uncertainty in the joint mechanical quadrature $X_{\rm a} \propto \chi_1 X_{\rm M1} + \chi_2 X_{\rm M2}$. If the initial bipartite state of the mechanical modes is ρ_0, then after the pulsed interaction and measurement the state is $\rho_1 \propto |P_{\rm L}\rangle\langle P_{\rm L}| U_{\rm OM}^{\otimes 2} \circ \rho_0$. As in Ref. [2], the measurement map $\rho_0 \to \rho_1$ can be described completely in terms of the transformations of the first and second moments using the Gaussian continuous variable formalism of Chapter 4.

Following the first pulsed interaction and measurement, the entanglement generation protocol proceeds by a period of free mechanical evolution and then a second pulsed interaction and phase quadrature measurement. As our protocol must apply for two non-degenerate mechanical modes of the same optomechanical structure, we account for a frequency difference between the two modes $\omega_1 \neq \omega_2$. To illustrate this point further, our proposal is centred around the case $\omega_2 = 3\omega_1$. Then, if the second pulsed interaction and measurement is applied after a time $t = \pi/2\omega_1 = 3\pi/2\omega_2$, the uncertainty in the joint mechanical quadrature $P_{\rm b} \propto \chi_1 P_{\rm M1} - \chi_2 P_{\rm M2}$ is now reduced. The second pulsed interaction may be summarized by the measurement map $\rho_2 \propto |P_{\rm L}\rangle\langle P_{\rm L}| U_{\rm OM}^{\otimes 2} U_{\rm ROT}(\omega_2 t) \otimes U_{\rm ROT}(\omega_1 t) \circ \rho_1$. The period of free evolution above is motivated by the Duan-type inequality for inseparability [255]

$$\Delta X_+ \Delta P_- < \frac{1}{2} \tag{8.35}$$

and the fact that as $\chi_2 \to \chi_1$, one has $X_{\rm a} \to X_+ = (X_{\rm M1} + X_{\rm M2})/\sqrt{2}$ and $P_{\rm b} \to P_- = (P_{\rm M1} - P_{\rm M2})/\sqrt{2}$. However, the logarithmic negativity $E_{\mathcal{N}}(\sigma)$ is still used to exactly quantify the amount of entanglement generated.

The verification procedure proceeds in a familiar way, by sending verification pulses at fixed time delays from the last entangling pulse in order to reconstruct the covariance matrix of the two-mode state. As in Ref. [2], mechanical decoherence and optical loss between the entangling and verification pulses are modelled by the maps $\mathcal{E}_{\gamma_i}$ and $\mathcal{E}_\eta$. Here, the fact that the two oscillators may have different quality factors[4] $Q_i = \omega_i/\gamma_i$ is accounted for. The condition to successfully generate *and* verify entanglement numerically is also explored. Moreover, in the case $\chi_1 = \chi_2 = \chi$ and $Q_1 = Q_2 = Q$, the neat conditions for entanglement generation and verification are found: (i) $\eta\chi > 1\sqrt{2}$ and (ii) $2\pi\bar{n}_1/Q > 1$. Condition (i) is due to the non-unitary nature of the entanglement generation protocol and mirrors the condition $\chi \gtrsim 1$ from the interferometric and non-interferometric schemes—c.f. Figs. 8.4 and 8.6. Noting that[5] $\eta\chi = 0.11$ has already been achieved in Ref. [114], condition (i) is within reach of near-future experiments. Meanwhile, condition (ii) is related to mechanical decoherence and dissipation between the entangling and verification pulses.

To assess the robustness of the protocol to experimental deviations and imperfections, the effect of varying both the ratio ω_2/ω_1 and the time delay between the two entangling pulses is numerically computed. It is seen that by varying the time delay between the entangling pulses, the frequency mismatch can be compensated for. Furthermore, the effect of varying the ratio χ_2/χ_1 is numerically investigated. By carefully adjusting the sequence of pulses in the generation and verification stages one finds that significant entanglement can be generated even when $\chi_1 \neq \chi_2$.

8.7.2 Two-mode mechanical cat states

Here I briefly discuss the work of Ref. [6], where this work was originally published. L.K.N. was the first author of this work and J.C. made theoretical contributions.

Up until now in this chapter, all the entangled states generated have been Gaussian states. In Ref. [6], the generation and verification of two-mode non-Gaussian states is studied. In particular, a protocol to create a two-mode Schrödinger-cat state in the displacement of two spatially separated mechanical oscillators is devised. In optomechanics, theoretical progress has been made in studying the generation and entanglement properties of two-mode mechanical Schrödinger-cat states [252, 293, 294], and here we contribute to this research direction by proposing a scheme to generate *and* verify non-Gaussian mechanical entanglement with pulsed optomechanics in the unresolved sideband regime. To generate non-Gaussian entanglement, the protocol utilizes the nonlinear cavity-free unitary interaction $\mathrm{e}^{\mathrm{i}\mu n_{\mathrm{L}} X_{\mathrm{M}}}$ and photon counting measurements. Moreover,

[4] The theory presented in Ref. [3] is applicable to the case $Q_1 \neq Q_2$, however, in the results section of this work the case $Q_1 = Q_2$ is focused on, which implies the thermal decoherence rates $\sim \bar{n}_i\gamma_i$ are also equal.

[5] There is a slight discrepancy in the definition of χ between Refs [2] and [3]. As Ref. [3] considers just one optomechanical system, it allows η to be absorbed neatly into the definition of χ. However, here I adhere to the definition of Section 6.3.2 and do not absorb η into χ.

the protocol can be understood as a two-mechanical-mode generalization of the protocol discussed in Chapter 7. Namely, before the phase shifter in setup of Fig. 7.2, a second mechanical mode is placed in the lower arm of the Mach-Zehnder interferometer such that the mechanical modes are in a parallel configuration[6]. Detecting an $\{m,n\}$ click event then realizes a two-mechanical-mode version of the measurement operator in Eq. (7.5), which is

$$\Upsilon_{m,n} = \begin{cases} \frac{\mathrm{e}^{-|\alpha|^2}}{\sqrt{m!n!}} \frac{\alpha^{m+n}}{(\sqrt{2})^{m+n}} (\mathrm{e}^{\mathrm{i}\mu X_{\mathrm{M}1}} + \mathrm{e}^{\mathrm{i}\phi+\mathrm{i}\mu X_{\mathrm{M}2}})^m (\mathrm{e}^{\mathrm{i}\mu X_{\mathrm{M}1}} - \mathrm{e}^{\mathrm{i}\phi+\mathrm{i}\mu X_{\mathrm{M}2}})^n & \\ \qquad\qquad\qquad\qquad\qquad\qquad \text{for } |\psi\rangle = \left|\sqrt{2}\alpha\right\rangle, & \\ \frac{1}{2}[(\mathrm{e}^{\mathrm{i}\mu X_{\mathrm{M}1}} + \mathrm{e}^{\mathrm{i}\phi+\mathrm{i}\mu X_{\mathrm{M}2}})\delta_{m,1}\delta_{n,0} + (\mathrm{e}^{\mathrm{i}\mu X_{\mathrm{M}1}} - \mathrm{e}^{\mathrm{i}\phi+\mathrm{i}\mu X_{\mathrm{M}2}})\delta_{m,0}\delta_{n,1}] & \\ \qquad\qquad\qquad\qquad\qquad\qquad \text{for } |\psi\rangle = |1\rangle. & \end{cases} \tag{8.36}$$

Considering an initial two-mode mechanical ground state, a $\{1,0\}$ click event generates the two-mode Schrödinger-cat state

$$|\psi\rangle = \mathcal{N}\left(\left|\frac{\mathrm{i}\mu}{\sqrt{2}}\right\rangle|0\rangle + \mathrm{e}^{\mathrm{i}\phi}|0\rangle\left|\frac{\mathrm{i}\mu}{\sqrt{2}}\right\rangle\right), \tag{8.37}$$

which is the two-mode generalization of the single-mode Schrödinger-cat state in Eq. (7.2), where $\mathcal{N}$ is again the state normalization. Generalizing to an initial two-mode thermal state $\rho_i = \rho_{\bar{n}_1} \otimes \rho_{\bar{n}_2}$, a $\{1,0\}$ click event generates the thermal two-mode Schrödinger-cat state $\rho_f \propto \left[D\left(\mathrm{i}\mu/\sqrt{2}\right) \otimes \mathbb{1} + \mathrm{e}^{\mathrm{i}\phi}\mathbb{1} \otimes D\left(\mathrm{i}\mu/\sqrt{2}\right)\right] \circ \rho_i$—c.f. the single-mode version in Eq. (7.9). Meanwhile, the heralding probability is for a $\{1,0\}$ click event is

$$\mathcal{P} = \begin{cases} \mathrm{e}^{-2|\alpha|^2}|\alpha|^2\left\{1 + \exp\left[-\mu^2(1+\bar{n}_1+\bar{n}_2)/2\right]\cos\phi\right\} & \text{for } |\psi\rangle = \left|\sqrt{2}\alpha\right\rangle, \\ \frac{1}{2}\left\{1 + \exp\left[-\mu^2(1+\bar{n}_1+\bar{n}_2)/2\right]\cos\phi\right\} & \text{for } |\psi\rangle = |1\rangle. \end{cases} \tag{8.38}$$

which again can be compared to the single-mode version of Eq. (7.13) when $\phi = \pi$. The initial mechanical state dependency in Eq. (8.38) is evident through the $\bar{n}_1$ and $\bar{n}_2$ terms in the exponentials and as $\bar{n}_1$, $\bar{n}_2 \to \infty$, this dependency drops outs.

As the two-mode cat states are non-Gaussian, the logarithmic negativity can be zero (and so the minimum symplectic eigenvalue can be $\tilde{\nu} > 1/2$) even if the state is entangled. However, violation of the PPT criterion remains a sufficient condition for entanglement for non-Gaussian states. Even though violation of the PPT criterion does not capture all non-Gaussian entanglement, by itself Simon's condition $\tilde{\nu} < 1/2$—which only depends on the first and second moments of the state—only explores a small class of PPT-violating states.

[6]The protocol also considers a series configuration, where the two mechanical modes are placed in the same arm of the interferometer, one after another. But in Ref. [6] it is shown that in the pure case, the states generated are equivalent to the states generated in the parallel configurations by local unitary transformations. In the absence of loss, the entanglement properties of the two states are therefore the same.

Therefore, as discussed in Chapter 4 to detect entanglement in our protocol, the class of negative-partial-transpose (NPT) based entanglement criteria developed by Shchukin and Vogel using arbitrarily high-order moments of the two mode state [61] is employed. In particular, focus is placed on the two NPT criteria: (i) $D_5 < 0$, which is equivalent to Simon's condition $\tilde{\nu} < 1/2$ and is a necessary and sufficient condition for two-mode Gaussian states to be entangled, and (ii) $S_3 < 0$, given by Eq. (4.29), which is a sufficient condition for a state to be entangled. As Simon's condition D_5 captures all two-mode Gaussian entanglement, if one finds parameters for which the two-mode cat states satisfy $S_3 < 0$ but *not* Simon's condition, then one can conclude that truly non-Gaussian entanglement has been generated. To further quantify the non-Gaussian nature of the two-mode cat states, one may employ the quantum relative entropy $\delta(\rho_f) = S(\rho_{\mathrm{G}}) - S(\rho_f)$ between the cat state and a reference Gaussian state built from the first and second moments of the cat state [295, 296]. As $\delta(\rho_f)$ is an exact measure of non-Gaussianity [297], this allows one to confirm that the non-Gaussianity increases as $\phi \to \pi$ and μ increases. It is interesting to note that in Ref. [1], $\phi = \pi$ was chosen to maximize non-classicality, whereas in this two-mode work, $\phi = \pi$ is chosen to maximize non-Gaussianity. In both cases, $\phi = \pi$ minimizes the heralding probability—nature often makes it difficult for us to make interesting states!

To verify the non-Gaussian entanglement, one only needs to measure the moments that make up the specific NPT criteria that one is interested in and full mechanical state tomography does not need to be employed. In our case, interest is placed on D_5 and S_3, which go up to fourth-order moments, see Eq. (4.29). However, we propose an entanglement verification procedure that is capable of measuring arbitrarily high-order moments and is therefore applicable to the whole class of NPT criteria, and indeed also other entanglement and non-classicality tests that depend on measuring high-order moments [298, 299, 300]. Our verification pulses are resonant with a different optical mode than the generation pulses. This optical mode is chosen so that the interaction can be described by the linearized pulsed optomechanical unitary $\mathrm{e}^{\mathrm{i}\chi X_{\mathrm{L}} X_{\mathrm{M}}}$, which means all the mechanical information will be imprinted purely on the phase quadrature of light. Therefore in this work, our verification procedure generalizes the verification procedure of Refs [2] and [3] by computing arbitrarily high-order mechanical moments from the phase homodyne measurement results. By modelling mechanical decoherence and optical loss between the entangling and verification stages, we demonstrate that non-Gaussian mechanical entanglement is accessible in current state-of-the-art experiments with additional mechanical precooling stages.

8.8 Conclusion and outlook

The work detailed in this chapter shows the potential of pulsed optomechanics for generating optical-mechanical and mechanical-mechanical entanglement. The protocols I have discussed here provide a promising path for the develop-

ment of new quantum technologies, entangled resources for quantum-information-based tasks, and for the exploration of the foundations of physics using the tools of quantum optics. Future research in this direction could involve combining the ideas of Refs [3] and [6], which would allow one to explore the generation of two mode cat states in a single mechanical structure. Likewise, one could consider multiple steps to grow the non-Gaussian entangled states of Ref. [6] *á la* the multistep protocol of Chapter 7. Further work in this direction could also involve using the cavity-enhanced unitary $e^{i\varphi(X_M)n_L}$ to generate and verify non-Gaussian entanglement or studying multipartite entanglement between a collection of oscillators [301]. To detect non-Gaussian entanglement using optimized NPT criteria, the framework developed in Ref. [10] will be useful.

Chapter 9

Non-Gaussian state preparation via multi-phonon subtraction and addition in Brillouin optomechanics

This chapter draws heavily from Ref. [4], where this work was originally published. G.E., L.F., J.J.P., and A.Ø.S. were the first authors of this work. J.C. made theoretical contributions.

Addition and subtraction operations provide a very powerful non-unitary method to generate non-classical quantum states in bosonic systems. In this section I describe the experiment carried out by G.E., L.F., J.J.P., A.Ø.S., *et al.* from Ref. [4] and the underlying theory that models this experiment. Firstly, I motivate this experiment by discussing addition and subtractions in quantum optics. Then I briefly introduce Brillouin optomechanics and describe how addition and subtraction operations can be used to generate non-Gaussian mechanical states. I then provide a theoretical analysis of the states generated by multi-phonon subtraction and addition. Finally, I compare these theoretical predictions to the experimental results of Ref. [4].

9.1 Addition, subtraction, and quantum state tomography in bosonic systems

9.1.1 Addition and subtraction operations in optical systems

Addition or subtraction of quanta to/from bosonic states is an alternative route to generate non-classical quantum states compared to the scheme introduced in Chapter 7. For example, rather than applying a measurement operator that is a superposition of two unitary operators, single photon subtraction from the squeezed vacuum state is a route to generate the small amplitude Schrödinger kitten states[1] in optical systems. Photon subtraction from the squeezed vacuum state may be achieved by first mixing with vacuum on a beamsplitter and then a photon is subtracted from the squeezed vacuum when a single photon is detected at one of the beamsplitter outputs. Note that the reflectivity of the beamsplitter can be adjusted to limit the probability of a two photon-subtraction event. This scheme was first proposed by Dakna *et al.* in Ref. [302] for an optical system and then later realized in an experiment that reconstructed the Wigner function via optical homodyne tomography [303]. In this experiment, the non-Gaussian dip in between the two maxima of the kitten state was observed in phase space. However, improvements to this experimental scheme, particularly in the overall efficiency[2], then allowed observation of Wigner negativity in these kitten states [285, 304]. As discussed in Section 7.4.1, Wigner negativity is a clear indication of the non-classical behaviour of a quantum state.

The addition of a single quanta to a coherent state is another way to produce a non-classical quantum state [305]. Zavatta and colleagues experimentally generated the single-photon added state via a spontaneous parametric down-conversion process in a BBO crystal [306]. Here, the detection of a single photon in the idler mode heralded the addition of a single photon in the seed coherent field. Furthermore, in this experiment the Wigner function was reconstructed via optical homodyne tomography and Wigner negativity was clearly observed. Later, Zavatta *et al.* performed single photon addition to thermal states of light [307]. By varying the thermal occupation of this optical mode, the experiment was able to see the Wigner negativity degrade with increasing thermal occupation.

Beyond quantum state generation, addition and subtraction operations allow for the investigation of more fundamental aspects of quantum mechanics in bosonic systems. For example, applying these addition and subtraction operations in different orders to the same initial state must produce distinct quantum states due to non-commutativity of the annihilation of creation operators, which

[1] In Section 7.5.1, I discussed how the multistep protocol could produce these kitten states in mechanical systems for $N\mu < 4/\sqrt{2}$.

[2] In fact, as I will discuss in Section 9.1.8, we will see that the effect of optical loss is to smooth the Wigner function, which leads to a reduction in non-classical features. This smoothed Wigner function is precisely the s-parametrized Wigner distribution of Section 2.8 with $s < 0$.

has been experimentally confirmed in optical systems [308, 309, 310]. Moreover, quantum operations at the single-quanta level are an important aspect of quantum technologies including quantum computing [311] and quantum key distribution [312].

9.1.2 Quantum state tomography

In order to determine the quantum states realized by photon addition and subtraction operations, the quantum mechanical state must be reconstructed somehow in the experiment. In optical systems, optical homodyne tomography has been used to great success to reconstruct not only the Wigner functions of the optical states described above, but also a wide range of interesting non-classical quantum states [313].

Outside optical systems, quantum state tomography has also been used to great success. For example in molecular systems, early experiments reconstructed an s-parametrized Wigner distribution of a vibrating molecule. In this experiment the s parameter was negative, meaning a smoothed version of the Wigner function was measured [314]—see Section 2.8. In a later experiment, the Wigner distributions of a dissociating of molecule were reconstructed [315].

More recently, exciting progress has been in the field of circuit quantum acoustodynamics, where microwave fields, along with superconducting quantum circuits, have been utilized to generate and control quantum states of acoustic modes [316]. Furthermore, quantum state tomography of phonon Fock states has been successfully carried out in these systems and Wigner negativity has clearly been observed [317, 318].

9.1.3 Looking ahead to Brillouin optomechanical systems

Thinking ahead to phonon addition and subtraction operations in Brillouin optomechanics—see Section 9.1.4—what lessons can be learned from the optical systems described here? Firstly, we know that if (i) the thermal occupation of the mechanical mode is too high [307] or (ii) if the optical efficiency of the readout scheme is too low [285], then it will not be possible to observe Wigner negativity. However, we know that a large thermal occupation or a small optical efficiency does not preclude the observation of the non-Gaussianity of the phonon added/subtracted states [303]. Therefore, observing non-Gaussianity in these Brillouin optomechanical systems is a key first step towards observing non-classicality.

Furthermore, the exciting progress made in the microwave domain with superconducting circuit electromechanics [317, 318], further motivates the investigation of the measurement and control of acoustic modes in optomechanical systems operating at optical frequencies.

9.1.4 Brillouin optomechanics with whispering gallery microresonators

Whispering gallery microresonators are quickly becoming an attractive system for quantum state preparation protocols with several cooling and Brillouin-scattering-induced transparency experiments now having been performed [319, 320, 321]. In particular, the Brillouin-Mandelstam scattering interaction [322, 323]—see Eq. (9.1)—between optical and acoustic waves provides a route to manipulate the quantum mechanical state of the acoustic modes via the tools of conventional quantum optics. Moreover, owing to the large frequencies of the acoustic modes, these systems can be be brought close to the quantum ground state by use of cryogenics alone and without the need of more involved cooling techniques. Furthermore, these whispering gallery mode systems—which can be made, for example, from silica and barium fluoride—can provide much lower optical absorption rates than more ubiquitous silicon-based optomechanical systems [324]. These low optical absorption rates limit the effect of optics-induced heating on the mean phononic occupation. Together, the high mechanical frequencies and low optics-induced heating in these systems will allow low thermal occupations to be reached in near future devices. *See the PhD theses of collaborators G.E. [324], J.J.P. [325], and A.Ø.S. [326] for more experimental information on Brillouin optomechanics with whispering gallery mode microresonators.*

In Ref. [124], G.E. and colleagues observed strong optomechanical coupling in a fused-silica microresonator which is an important prerequisite for performing efficient optics-mechanics state swapping— see Section 6.2. Further elucidating the promise of Brillouin optomechanics in whispering gallery microresonators for quantum state preparation tasks. Later, in Ref. [180], G.E. *et al.* realized single phonon addition and subtraction in a barium fluoride optical microresonator. Here, the authors saw the doubling of the variance of the mechanical state, which is a clear signature of a successful addition/subtraction event—see Section 9.1.6. In each of these experiments, the backwards Brillouin scattering process [327] was utilized which provides excellent mode discrimination between the forwards-travelling pump field and the backwards-travelling signal field.

These initial experiments by G.E. *et al.* motivated the experiment conducted by G.E., L.F., J.J.P., A.Ø.S. *et al.* In this work, full state tomography of the mechanical mode was performed and non-Gaussianity in the mechanical s-parametrized Wigner function was observed. I will discuss this work in detail in this chapter, with emphasis placed on the theoretical components, but first I give a brief introduction to the underlying physics of the Brillouin optomechanical Hamiltonian.

A brief overview of the underlying physics and Hamiltonian

Brillouin scattering involves the interaction between two optical modes and an acoustic mode, described by the three-wave mixing Hamiltonian

$$H = \hbar\omega_1 a_1^\dagger a_1 + \hbar\omega_2 a_2^\dagger a_2 + \hbar\omega_{\rm M} b^\dagger b + \hbar g_0 \left(a_1 a_2^\dagger b + a_1^\dagger a_2 b^\dagger\right). \quad (9.1)$$

Here, $\omega_1 < \omega_2$ is assumed. In cavity quantum optomechanics, radiation pressure is the underlying physical mechanism that leads to the Hamiltonian of Eq. (6.3). While in Brillouin optomechanics, the underlying physical phenomena that lead to the Hamiltonian of Eq. (9.1) are *electrostriction* and *photoelasticity* [328]. Electrostriction describes the displacement of atoms in a medium towards regions of high optical intensity, while photoelasticity describes how the refractive index of light changes according to the density profile of the acoustic mode in the medium. This interplay between light and mechanics—namely, how the light affects the mechanics, and in turn how the mechanics affects the light—is very reminiscent of the radiation-pressure interaction described in Chapter 6. Moreover, the symmetries between Brillouin optomechanics and conventional cavity optomechanics can be put on a stronger theoretical footing as in Ref. [329]. However, as will be shown explicitly, the exact same Stokes and anti-Stokes scattering processes enabled in the resolved-sideband regime of continuous-wave linearized optomechanics—see Section 6.2.3—can be performed in Brillouin optomechanics. Importantly, these Stokes and anti-Stokes scattering processes lay the foundations for the phonon addition and subtraction experiments.

Fig. 9.1(a) shows a Blender rendering of the barium fluoride optical microresonator used in Refs [180] and [4]. Here, an optical pump field is evanescently coupled[3] into the microresonator via a tapered optical fiber. This optical field then interacts with an acoustic mode of the microresonator to produce a frequency-shifted optical signal via Eq. (9.1). If the two optical modes are separated by the mechanical frequency, this Brillouin scattering process is resonantly enhanced. However, searching for three modes that satisfy this requirement can require much experimental effort [324]. Finally, the scattered signal photons couple out of the microresonator through the tapered optical fiber and may then be detected by the experimenter. In the three-wave Brillouin scattering process, energy and momentum must be conserved and hence

$$\omega_{\rm M} = \omega_2 - \omega_1, \quad (9.2)$$

$$\hbar k_{\rm M} = \hbar k_2 - \hbar k_1, \quad (9.3)$$

must be satisfied. Here, k_i are the wave vectors of the optical and mechanical fields. Note that the pump field may coincide with either the lower frequency (ω_1) or the higher frequency (ω_2) optical mode, which will affect which mechanical mode ($\omega_{\rm M}$) must be chosen. I will now closely follow the linearization procedure of Section 6.3 to describe these two situations which lead to a beamsplitter or two-mode-squeezer-type Hamiltonian.

[3] Note the coupling of light in and out of the microresonator is described by the input-output formalism of Chapter 3.

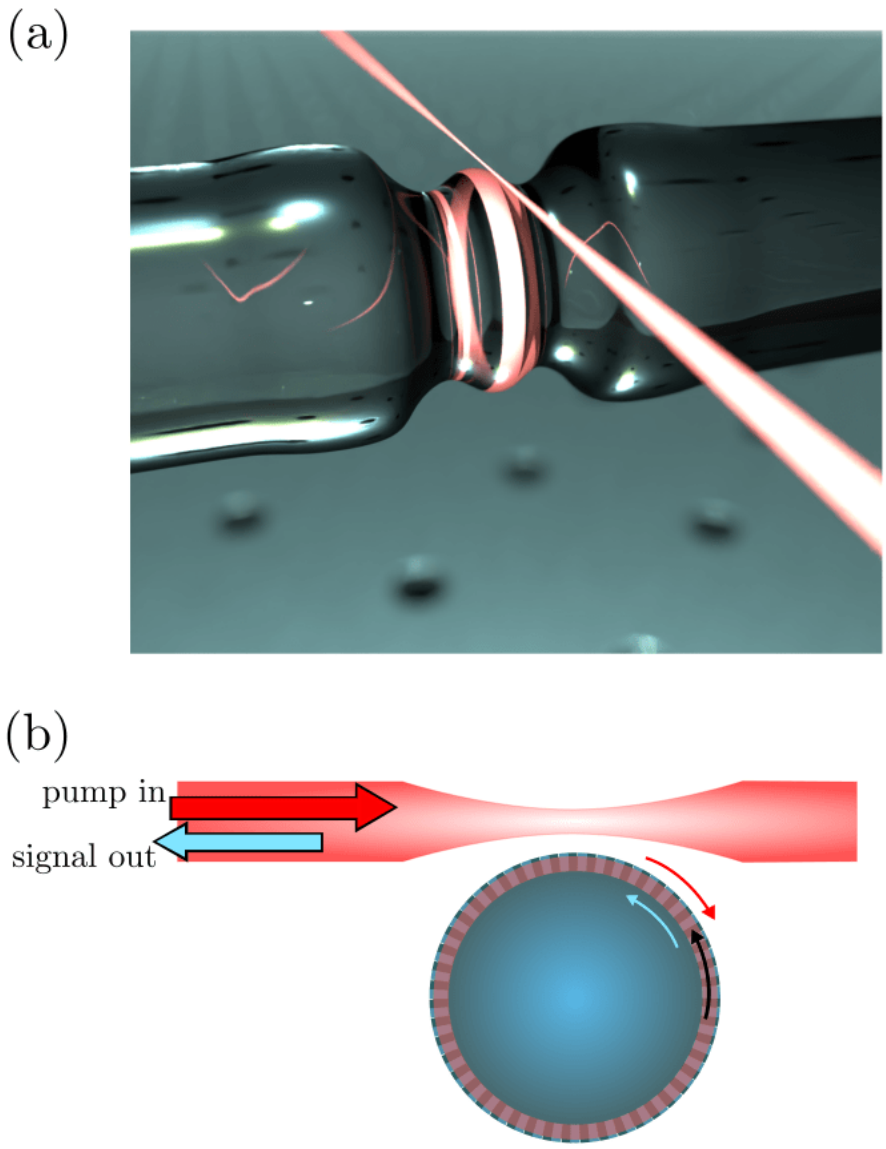


Figure 9.1: **Brillouin optomechanics experiments performed by the Quantum Measurement Lab.** (a) Rendering of the whispering-gallery-mode microresonator. Light (red) propagates in a tapered optical fiber and is then coupled into the microresonator where it interacts with the high-frequency acoustic waves. (b) Backwards Brillouin scattering in the microresonator to achieve the beamsplitter Hamiltonian between the signal field (blue arrow) and the mechanical mode (black arrow). The strong pump field (red arrow) is tuned at the lower optical frequency $\omega_{\mathrm{P}} = \omega_1$, which leads to the anti-Stokes scattering process. The higher frequency signal field $\omega_{\mathrm{S}} = \omega_2$ propagates in the reverse direction to the pump allowing for excellent mode discrimination. Figure adapted from Ref. [124].

Beamsplitter Hamiltonian.—Driving the lower frequency field, $\omega_{\rm P} = \omega_1$, leads to the anti-Stokes scattering process and realization of a beamsplitter-type Hamiltonian—cf. 6.2(a). Mathematically, this corresponds to moving to the displaced frame[4], i.e. setting $a_1 \to \alpha_{\rm c} + a_1$ in Eq. (9.1) and ignoring the small quantum fluctuations in a_1, which is valid if $\alpha_{\rm c} \gg |a_1|$. We then arrive at the beamsplitter Hamiltonian

$$H_{\rm BS} \quad = \quad \hbar g a_2^\dagger b + \text{h.c.} \tag{9.4}$$

Here, $g = \alpha_{\rm c} g_0$ is the linearized optomechanical coupling rate. The realization of this optomechanical beamsplitter allows phonons to be subtracted from the acoustic mode via the scheme proposed by Vanner *et al.* in Ref. [178]. Note the mathematically similarities to the all optical scheme proposed by Dakna *et al.* in Ref. [302]. Fig. 9.1(b) shows a backwards Brillouin scattering process in a whispering gallery microresonator that achieves the beamsplitter Hamiltonian.

Two mode squeezer Hamiltonian.—Meanwhile, driving the higher frequency optical field, $\omega_{\rm P} = \omega_2$, leads to the Stokes scattering process and realization of a two-mode-squeezer-type Hamiltonian—cf. 6.2(b). Following the same linearization process described above, one has

$$H_{\rm TMS} \quad = \quad \hbar g a_1 b + \text{h.c.} \tag{9.5}$$

This optomechanical two-mode-squeezer allows one to add phonons to the mechanical mode in an analogy to the all-optical experiment by Zavatta and colleagues [306].

Up to a minus sign these Hamiltonians are precisely the beamsplitter and two-mode-squeezer-type Hamiltonians derived in Section 6.3.3. Note that compared to conventional linearized quantum optomechanics, no rotating wave approximation was made to arrive at the final result.

9.1.5 Experimental protocol and simplified setup

Phonon addition and subtraction protocol

Fig. 9.2 shows a simplified schematic for the multi-phonon addition/subtraction protocol our team employed using Brillouin optomechanics. Driving the lower optical mode of the microresonator with a strong pump field achieves the beamsplitter interaction $H_{\rm BS}$ as described in the previous section. Measuring n-photons in the signal field then directly causes the n-phonon subtraction event [178]. For an initial mechanical thermal state $\rho_{\bar{n}}$, with mean thermal occupation $\bar{n}$, the n-phonon subtracted thermal mechanical state is then

$$\rho_{n-} \propto b^n \rho_{\bar{n}} b^{\dagger n}. \tag{9.6}$$

[4] As before, I take the mean field amplitude inside the microresonator to be real without loss of generality, i.e. $\alpha_{\rm c} \in \mathbb{R}$.

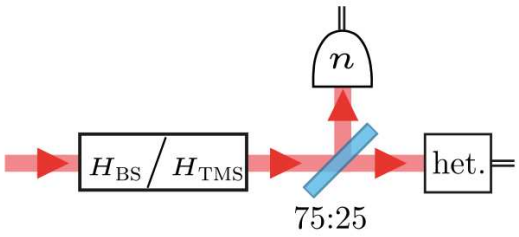


Figure 9.2: **Simplified experimental setup for multi-phonon addition and subtraction.** The beamsplitter (two-mode-squeezer) interaction is driven by the strong pump field in the coherent state $|\alpha\rangle$ and an n-phonon subtraction (addition) operation is heralded by the detection of n scattered photons—cf. Eq. (9.6) (Eq. (9.7)). The anti-Stokes (Stokes) field from the Brillouin optomechanical system is not only used for state preparation via measurement, but it is also used for state verification. The n-click photon detection event in the 25% arm triggers the recording of the heterodyne signal in the 75% arm, which is used for mechanical state readout. Figure simplified from Ref. [4].

In the experiment, the linearized optomechanical coupling rate was $g/2\pi = 10\,\text{MHz}$, the intrinsic mechanical decay rate was $\gamma/2\pi = 3.26\,\text{MHz}$, and the amplitude decay rate of the signal mode was $\kappa_1/2\pi = 46.9\,\text{MHz}$. Hence, the system operates in the weak coupling regime of optomechanics $g < (\kappa_1+\gamma)/2$—see Section 6.2. Therefore, the probability of detecting one photon far exceeds the probability of detecting n-photons in the signal mode for $n \geq 2$. This allows for high-fidelity single phonon subtraction operation using SPADs—see Section 7.3.2—while one can perform n-phonon subtraction by splitting the signal mode and detecting an n-fold coincidence click. In Ref. [4], single- and two-phonon subtraction was experimentally studied.

Meanwhile, driving the upper optical mode of the microresonator with a strong pump field achieves the optomechanical two-mode-squeezer $H_{\rm TMS}$. Measuring n-photons in the signal field then directly causes the n-phonon addition event [306]. For an initial mechanical thermal state $\rho_{\bar{n}}$, with mean thermal occupation $\bar{n}$, the n-phonon added thermal mechanical state is

$$\rho_{n+} \propto b^{\dagger n}\rho_{\bar{n}}b^{n}. \tag{9.7}$$

Although the phonon added states were not generated in the experiment of Ref. [4], phonon addition was performed in Ref. [180], and in Section 9.1.6 the similarity between ρ_{n-} and ρ_{n+} is studied in detail.

Laser cooling of the mechanical mode

At 300 K and a high mechanical frequency of $\omega_{\rm m}/2\pi = 8.16$ GHz, the thermal occupation[5] of the mechanical mode is $\bar{n}_{\rm th} \simeq 766$. However, in the experiment

[5] Calculated via Eq. (2.18)

the anti-Stokes field was used to laser cool the mechanical mode to $\bar{n} \approx 453$ via sideband cooling. Therefore, the state $\rho_{\bar{n}}$ in Eqs (9.6) and (9.7) correspond to this laser-cooled value of $\bar{n}$. The principle of sideband cooling was discussed in Section 6.2.3, but to see mathematically how laser cooling works the reader should refer to the discussion around Eq. (10.57).

Even at room temperature, the thermal occupation of the mechanical mode is relatively low owing to the high mechanical frequency. Despite this, and the laser cooling, the thermal occupation is still too high to see non-classicality—see Section 9.1.10. However, a first key step towards observing non-classicality will be observing the non-Gaussian dip in the mechanical Wigner function. Furthermore, operation at cryogenic temperatures opens a route to see truly non-classical features in these whispering gallery-mode microresonator systems.

Verification via heterodyne detection

Importantly, the signal field resulting from the Brillouin scattering process is not only used for mechanical state preparation. From the experimental schematic shown in Fig. 9.2, 75% of the signal field is sent towards a heterodyne detector. Moreover, when the detector measures an n-photon click in the 25% arm, this triggers the recording of the heterodyne signal from which the mechanical state may be read out in the following way.

The heterodyne detector measures the Q function of the incoming optical field. Further, the mechanical state will be transduced onto the signal field with some efficiency via the optomechanical beamsplitter interaction. Along with other optical inefficiencies, this means the measured optical Q function will correspond to a measurement of an s-parametrized Wigner function of the mechanical state with $s < -1$.

I discuss state verification via heterodyne detection further in Sections 9.1.9 and 9.1.10.

9.1.6 Multiphonon subtraction and addition to a thermal state: density operator, phonon number statistics, quasiprobability distributions, and moments

In this work, the detection of n photons in the signal field is approximated as an addition/subtraction of n phonons from the mechanical state. In Chapter 10, it is shown how the detection of n photons more accurately corresponds to both (i) the addition/subtraction of n phonons *and* (ii) a redistribution of the phonon number probabilities. However, deep within the weak coupling regime the redistribution of the phonon number probabilities may be neglected as this corresponds to a higher order process in g as discussed above.

In this section, I focus on the mathematics of the multiphonon subtracted and added states. Firstly, I will discuss their density operators in the number basis before calculating their phase-space representations as quasiprobability distributions.

Initial thermal state

Consider an initial laser-cooled thermal state $\rho_{\bar{n}}$ of a mechanical oscillator with mean occupation number $\bar{n}$

$$\rho_{\bar{n}} = \frac{1}{1+\bar{n}} \sum_{m=0}^{\infty} \left(\frac{\bar{n}}{1+\bar{n}} \right)^m |m\rangle\langle m| \tag{9.8}$$

$$= (1-x) \sum_{m=0}^{\infty} x^m |m\rangle\langle m|. \tag{9.9}$$

Here, $x = \bar{n}/(1+\bar{n})$ and $\bar{n} = x/(1-x)$.

n phonon subtraction

An n-phonon subtraction operation to $\rho_{\bar{n}}$ creates the state

$$\rho_{n-} = \frac{b^n \rho_{\bar{n}} b^{\dagger n}}{\mathrm{tr}\left(b^n \rho_{\bar{n}} b^{\dagger n}\right)}, \tag{9.10}$$

The mean phonon number of the n-phonon-subtracted state ρ_{n-} is given by

$$\langle b^\dagger b \rangle_{n-} = \frac{\mathrm{tr}\left(b^{n+1} \rho_{\bar{n}} b^{\dagger n+1}\right)}{\mathrm{tr}\left(b^n \rho_{\bar{n}} b^{\dagger n}\right)}. \tag{9.11}$$

Here, the trace terms $\mathrm{tr}\left(b^k \rho_{\bar{n}} b^{\dagger k}\right)$ with $k \in \mathbb{N}$, may be calculated by using $b^k|m\rangle = \sqrt{m!/(m-k)!}|m-k\rangle$ for $m \geq k$ and $b^k|m\rangle = 0$ otherwise, to arrive at

$$\mathrm{tr}\left(b^k \rho_{\bar{n}} b^{\dagger k}\right) = (1-x) \sum_{l,m=0}^{\infty} \frac{m!}{(m-k)!} x^m \delta_{m-k,l} \tag{9.12}$$

$$= (1-x) \sum_{m=0}^{\infty} \frac{m!}{(m-k)!} x^m \tag{9.13}$$

$$= \frac{k!}{(1-x)^k} x^k \tag{9.14}$$

$$= k! \bar{n}^k. \tag{9.15}$$

Here, the useful sum from Appendix C has been used.

This expression for the trace may be inserted into Eqs (9.10) and (9.11) to give the explicit form of the density operator ρ_{n-} and the mean phonon number $\langle b^\dagger b \rangle_{n-}$

$$\rho_{n-} = \sum_{m=0}^{\infty} p_{n-}(m) |m\rangle\langle m|, \tag{9.16}$$

$$p_{n-}(m) = (1-x)^{n+1} x^m \binom{m+n}{n}, \tag{9.17}$$

$$\langle b^\dagger b \rangle_{n-} = (n+1)\bar{n}. \tag{9.18}$$

n phonon addition

An n-phonon addition operation to the state ρ_n yields

$$\rho_{n+} = \frac{b^{\dagger n}\rho_{\bar{n}}b^n}{\mathrm{tr}\left(b^{\dagger n}\rho_{\bar{n}}b^n\right)}, \tag{9.19}$$

which has mean occupation

$$\begin{aligned}\langle b^\dagger b\rangle_{n+} &= \mathrm{tr}\left(b^\dagger b\rho_{n+}\right) &(9.20)\\ &= \mathrm{tr}\left(bb^\dagger\rho_{n+}\right) - \mathrm{tr}\left(\rho_{n+}\right) &(9.21)\\ &= \frac{\mathrm{tr}\left(b^{\dagger n+1}\rho_{\bar{n}}b^{n+1}\right)}{\mathrm{tr}\left(b^{\dagger n}\rho_{\bar{n}}b^n\right)} - 1. &(9.22)\end{aligned}$$

Here, $[b, b^\dagger] = 1$ was used in the second line. The trace terms $\mathrm{tr}\left(b^{\dagger k}\rho_{\bar{n}}b^k\right)$ may be calculated using $b^{\dagger k}\left|m\right\rangle = \sqrt{(m+k)!/m!}\left|m+k\right\rangle$, which allows one to arrive at

$$\begin{aligned}\mathrm{tr}\left(b^{\dagger k}\rho_{\bar{n}}b^k\right) &= (1-x)\sum_{l,m=0}^{\infty}\frac{(m+k)!}{m!}x^m\delta_{m+k,l} &(9.23)\\ &= (1-x)\sum_{l=0}^{\infty}\frac{l!}{(l-k)!}x^{l-k} &(9.24)\\ &= \frac{k!}{(1-x)^k} &(9.25)\\ &= k!(1+\bar{n})^k. &(9.26)\end{aligned}$$

Here, the sum in Appendix C has again been used.

This expression for $\mathrm{tr}\left(b^{\dagger k}\rho_{\bar{n}}b^k\right)$ may be inserted in Eqs (9.19) and (9.20) to calculate the density operator and the mean phonon number of the n-phonon-added state ρ_{n+}, which are given by

$$\begin{aligned}\rho_{n+} &= \sum_{m=0}^{\infty}p_{n+}(m)|m\rangle\langle m|, &(9.27)\\ p_{n+}(m) &= (1-x)^{n+1}x^{m-n}\binom{m}{n}, &(9.28)\\ \langle b^\dagger b\rangle_{n+} &= (n+1)\bar{n}+n. &(9.29)\end{aligned}$$

Here, the binomial coefficient $\binom{m}{n} = 0$ for $m < n$, such that phonon-number states $|m\rangle$ with $m < n$ of ρ_{n+} are unoccupied. This property also leads to the observation that the phonon-number distribution of ρ_{n+} and ρ_{n-} are equal up to a shift, hence

$$p_{n+}(m) = p_{n-}(m-n). \tag{9.30}$$

Comparison to the more general results of Ref. [330].—Note that the results presented here for the states ρ_{n-} and ρ_{n+} agree with those presented by Barnett

et al. in Ref. [330]. In Ref. [330], moment-generating functions were used to calculate the factorial moments of these states. Simply put, the results for $\langle b^\dagger b\rangle_{n-}$ and $\langle b^\dagger b\rangle_{n+}$ agree with the first factorial moments presented in Ref. [330].

Similarity between ρ_{n-} and ρ_{n+} and the high $\bar{n}$ limit

Eq. (9.30) informs us that the states ρ_{n-} and ρ_{n+} are similar. To further study the similarity of the states ρ_{n-} and ρ_{n+}, one may calculate the quantum state fidelity between them [17]

$$F(\rho_{n-},\rho_{n+}) = \left(\mathrm{tr}\left(\sqrt{\sqrt{\rho_{n+}}\rho_{n-}\sqrt{\rho_{n+}}}\right)\right)^2, \tag{9.31}$$

$$\tag{9.32}$$

which is strictly less than one $F(\rho_{n-},\rho_{n+}) < 1$ as $\rho_{n-} \neq \rho_{n+}$. By using $[\rho_{n-},\rho_{n+}] = 0$, one finds that

$$F(\rho_{n-},\rho_{n+}) = \left(\sum_m \sqrt{p_{n-}(m)p_{n+}(m)}\right)^2 \tag{9.33}$$

$$= \left(\frac{(1-x)^{n+1}x^{-n/2}}{n!}\sum_{m=n}^{\infty} x^m\sqrt{\frac{(m+n)!}{(m-n)!}}\right)^2 \tag{9.34}$$

$$= \left((1-x)^{n+1}x^{-n/2}\sum_{m=0}^{\infty} x^m\sqrt{\binom{m}{n}\binom{m+n}{n}}\right)^2 \tag{9.35}$$

Utilizing $\binom{m+n}{n} < \binom{m}{n}$, a lower bound for the fidelity is derived as follows

$$F(\rho_{n-},\rho_{n+}) = \left((1-x)^{n+1}x^{-n/2}\sum_{m=0}^{\infty} x^m\sqrt{\binom{m}{n}\binom{m+n}{n}}\right)^2 \tag{9.36}$$

$$> \left((1-x)^{n+1}x^{-n/2}\sum_{m=0}^{\infty} x^m\binom{m}{n}\right)^2 \tag{9.37}$$

$$= x^n \tag{9.38}$$

$$= \left(\frac{\bar{n}}{1+\bar{n}}\right)^n. \tag{9.39}$$

Therefore, $F(\rho_{n-},\rho_{n+})$ is bounded from below and above via

$$\left(\frac{\bar{n}}{1+\bar{n}}\right)^n < F(\rho_{n-},\rho_{n+}) < 1. \tag{9.40}$$

For finite n, this lower bound approaches one from below as $\bar{n}$ increases, and hence the two states are approximately the same in the high $\bar{n}$ limit. As mentioned in Section 9.1.5, the experiment achieved a laser-cooled occupation of $\bar{n} \approx 453$. Thus, the *lower bound* for the fidelity is 0.998. This motivates the experiment only generating the phonon-subtracted state ρ_{n-} as the state ρ_{n+} would be almost exactly identical at these temperatures.

Variances and a more stringent similarity condition for ρ_{n-} and ρ_{n+}

Moreover, to arrive at a more stringent condition on $\bar{n}$ and n for the states ρ_{n-} and ρ_{n+} to be similar, it is demanded that the separation of the means

$$\langle b^\dagger b\rangle_{n+} - \langle b^\dagger b\rangle_{n-} = n \tag{9.41}$$

is much less than the standard deviations in phonon number $\sqrt{\mathrm{Var}\left(\rho_{n+}, b^\dagger b\right)}$ and $\sqrt{\mathrm{Var}\left(\rho_{n-}, b^\dagger b\right)}$. Therefore, one must first calculate (i) $\mathrm{Var}\left(\rho_{n-}, b^\dagger b\right)$ and (ii) $\mathrm{Var}\left(\rho_{n+}, b^\dagger b\right)$.

(i) $\mathrm{Var}\left(\rho_{n-}, b^\dagger b\right)$.—Here, the expression for $\mathrm{tr}\left(b^{\dagger k}\rho_{\bar{n}}b^k\right)$ was used to find

$$\begin{aligned}
\left\langle (b^\dagger b)^2\right\rangle_{n-} &= \mathrm{tr}\left(b^\dagger b b^\dagger b \rho_{n-}\right) && (9.42)\\
&= \mathrm{tr}\left((b^\dagger b^\dagger b b + b^\dagger b)\rho_{n-}\right) && (9.43)\\
&= \frac{\mathrm{tr}\left(b^{n+2}\rho_{\bar{n}}(b^\dagger)^{n+2}\right)}{\mathrm{tr}\left(b^n\rho_{\bar{n}}(b^\dagger)^n\right)} + \frac{\mathrm{tr}\left(b^{n+1}\rho_{\bar{n}}(b^\dagger)^{n+1}\right)}{\mathrm{tr}\left(b^n\rho_{\bar{n}}(b^\dagger)^n\right)} && (9.44)\\
&= \bar{n}^2(n^2+3n+2) + \bar{n}(n+1), && (9.45)
\end{aligned}$$

so then

$$\begin{aligned}
\mathrm{Var}\left(\rho_{n-}, b^\dagger b\right) &= \left\langle (b^\dagger b)^2\right\rangle_{n-} - \left(\left\langle b^\dagger b\right\rangle_{n-}\right)^2 && (9.46)\\
&= \bar{n}(\bar{n}+1)(n+1). && (9.47)
\end{aligned}$$

(ii) $\mathrm{Var}\left(\rho_{n+}, b^\dagger b\right)$.—Using the expression for $\mathrm{tr}\left(b^{\dagger k}\rho_{\bar{n}}b^k\right)$

$$\begin{aligned}
\left\langle (b^\dagger b)^2\right\rangle_{n+} &= \mathrm{tr}\left(b^\dagger b b^\dagger b \rho_{n+}\right) && (9.48)\\
&= \mathrm{tr}\left((b b b^\dagger b^\dagger - 3 b b^\dagger + 1)\rho_{n+}\right) && (9.49)\\
&= \frac{\mathrm{tr}\left((b^\dagger)^{n+2}\rho_{\bar{n}}b^{n+2}\right)}{\mathrm{tr}\left((b^\dagger)^n\rho_{\bar{n}}b^n\right)} - 3\frac{\mathrm{tr}\left((b^\dagger)^{n+1}\rho_{\bar{n}}b^{n+1}\right)}{\mathrm{tr}\left((b^\dagger)^n\rho_{\bar{n}}b^n\right)} + 1 && (9.50)\\
&= (\bar{n}+1)^2(n+2)(n+1) - 3(n+1)(\bar{n}+1) + 1, && (9.51)
\end{aligned}$$

which leads to

$$\begin{aligned}
\mathrm{Var}\left(\rho_{n+}, b^\dagger b\right) &= \left\langle (b^\dagger b)^2\right\rangle_{n+} - \left(\left\langle b^\dagger b\right\rangle_{n+}\right)^2 && (9.52)\\
&= \bar{n}(\bar{n}+1)(n+1). && (9.53)
\end{aligned}$$

Therefore one has

$$\mathrm{Var}\left(\rho_{n-}, b^\dagger b\right) = \mathrm{Var}\left(\rho_{n+}, b^\dagger b\right) = \bar{n}(\bar{n}+1)(n+1), \tag{9.54}$$

which also agrees with results calculated from moment-generating functions from Ref. [330].

So the stringent condition for the two states to be similar is

$$\frac{\langle b^\dagger b\rangle_{n+} - \langle b^\dagger b\rangle_{n-}}{\sqrt{\mathrm{Var}\left(\rho_{n+}, b^\dagger b\right)}} \ll 1, \tag{9.55}$$

which gives

$$\bar{n} \gg \left(-(1+n) + \sqrt{4n^3 + 5n^2 + 2n + 1}\right) / \left(2(1+n)\right), \tag{9.56}$$

where the right-hand side of this inequality is an increasing function of n. Hence, at high values of n, the condition for the mechanical state generated by an n-phonon subtraction to a thermal state to be the same as that generated by an n-phonon addition operation is

$$\bar{n} \gg \sqrt{n}. \tag{9.57}$$

Quasiprobability distributions and high-order moments of the states

By examining Eqs (9.10) and (9.19) and comparing them to the formulae for the quasiprobability distributions of Section 2.8, one can anticipate that ρ_{n-} will admit a very simple P function, while ρ_{n+} should have a very simple Q function. Furthermore, from Section 2.8 and Ref. [18], we know that the P function is useful for calculating normally-ordered expectation values such as $\left\langle b^{\dagger k} b^k \right\rangle$, while the Q-function is useful for calculating anti-normally-ordered expectation values such as $\left\langle b^k b^{\dagger k} \right\rangle$. I will now dive into the calculation of the quasiprobability distributions and the moments.

P function of ρ_{n-} and $\left\langle b^{\dagger k} b^k \right\rangle_{n-}$.— From Section 2.8, the P function $P(\beta)$ of a quantum state is related to its density operator ρ through

$$\rho \quad = \quad \int \mathrm{d}^2\beta \; P(\beta) |\beta\rangle\langle\beta|. \tag{9.58}$$

Further, the P function of the thermal state $\rho_{\bar{n}}$ is given by $P_{\bar{n}}(\beta) = \frac{1}{\pi\bar{n}} \mathrm{e}^{-|\beta|^2/\bar{n}}$. Using Eq. (9.10) and $b\,|\beta\rangle = \beta\,|\beta\rangle$, one finds that the P function of ρ_{n-} is

$$P_{n-}(\beta) = \frac{1}{n!\bar{n}^n} |\beta|^{2n} P_{\bar{n}}(\beta). \tag{9.59}$$

Note that $P_{n-}(\beta)$ only depends on the magnitude of β, which demonstrates the rotational symmetry of the state in phase space. From Section 2.8, we know that the P-function is the most convenient way to calculate normally-ordered expectation values of creation and annihilation operators. Using, Eq. (2.60) one has that

$$\begin{aligned}
\left\langle b^{\dagger k} b^k \right\rangle_{n-} &= \int \mathrm{d}^2\beta \; P_{n-}(\beta) |\beta|^{2k} && (9.60)\\
&= \int \mathrm{d}^2\beta \; \frac{1}{n!\bar{n}^n} |\beta|^{2(n+k)} P_{\mathrm{th}}(\beta) && (9.61)\\
&= \frac{(n+k)!\bar{n}^k}{n!} \int \mathrm{d}^2\beta \; \frac{1}{(n+k)!\bar{n}^{n+k}} |\beta|^{2(n+k)} P_{\mathrm{th}}(\beta) && (9.62)\\
&= \frac{(n+k)!\bar{n}^k}{n!} \int \mathrm{d}^2\beta P_{(n+k)-}(\beta) && (9.63)\\
&= \frac{(n+k)!\bar{n}^k}{n!}, && (9.64)
\end{aligned}$$

where in the last line $\int \mathrm{d}^2\beta\ P(\beta) = 1$ was used to avoid explicitly calculating the integral.

Q function of ρ_{n-} and $\langle b^k b^{k\dagger}\rangle$.—The Q function of a quantum state ρ is again

$$Q(\beta) = \frac{1}{2\pi}\langle\beta|\,\rho\,|\beta\rangle\,, \tag{9.65}$$

and the Q function of the thermal state $\rho_{\bar{n}}$ is $Q_{\rm th}(\beta) = \frac{1}{\pi(\bar{n}+1)}\mathrm{e}^{-|\beta|^2/(\bar{n}+1)}$. Using Eq. (9.19) and $b\,|\beta\rangle = \beta\,|\beta\rangle$, one finds that the Q function of ρ_{n+} is

$$Q_{n+}(\beta) = \frac{1}{n!(1+\bar{n})^n}|\beta|^{2n}Q_{\rm th}(\beta), \tag{9.66}$$

which is also rotationally invariant in phase space. Finally using Eq. (2.56) one has that

$$\langle b^k b^{\dagger k}\rangle_{n+} = \int \mathrm{d}^2\beta\ Q(\beta)|\beta|^{2k} \tag{9.67}$$

$$= \frac{(n+k)!(1+\bar{n})^{n+k}}{n!(1+\bar{n})^n}\times \frac{1}{(n+k)!(1+\bar{n})^{n+k}}\int \mathrm{d}^2\beta\ |\beta|^{2(n+k)}Q_{\rm th}(\beta) \tag{9.68}$$

$$= \frac{(n+k)!(1+\bar{n})^k}{n!}\int \mathrm{d}^2\beta\ Q_{(n+k)+}(\beta) \tag{9.69}$$

$$= \frac{(n+k)!(1+\bar{n})^k}{n!}, \tag{9.70}$$

where once again the normalization of the quasiprobability distribution

$$\int \mathrm{d}^2\beta\ Q(\beta) = 1$$

was used.

Notably, the quasiprobability distributions in Eqs (9.59) and (9.66) provide a simple and convenient expression from which other, more experimentally relevant, probability marginals and s-parameterized Wigner functions may be calculated.

9.1.7 Probability distributions

In the previous section, I completely characterized the n-phonon subtracted/added states. Namely, I calculated the density operator and the appropriate quasiprobability distribution for each. However, to interpret the experimental data from the heterodyne detectors, it will be convenient to have an expression for the position probability of the states[6].

[6] As was seen in the previous section, the states ρ_{n-} and ρ_{n+} are rotationally symmetric and so one may choose any rotated quadrature operator here.

Probability distributions from the number basis

Of course, one can find simple expressions for the position marginals from the density operators of ρ_{n-} and ρ_{n+}, which are expanded in the number basis. Namely, the position probabilities of the n-phonon subtracted/added states are

$$\begin{aligned} \mathrm{pr}_{n\pm}(X_{\mathrm{M}}) &= \langle X_{\mathrm{M}}| \rho_{n\pm} |X_{\mathrm{M}}\rangle & (9.71)\\ &= \sum_{m=0}^{\infty} p_{n\pm}(m)|\psi_m(X_{\mathrm{M}})|^2, & (9.72) \end{aligned}$$

where $\psi_m(X_{\mathrm{M}}) = H_m(X_{\mathrm{M}})\mathrm{e}^{-X_{\mathrm{M}}^2/2}/\sqrt{2^m m!\sqrt{\pi}}$ is the wavefunction of the m^{th} Fock state and $H_m(X_{\mathrm{M}})$ is the m^{th} Hermite polynomial. Due to the rotational symmetry of the states, the probability marginals are invariant under the transformation $X_{\mathrm{M}} \to X_{\mathrm{M}}(\theta) = X_{\mathrm{M}}\cos\theta + P_{\mathrm{M}}\sin\theta$.

However, this expression for $\mathrm{pr}_{n\pm}(X_{\mathrm{M}})$ is an infinite sum and when analyzing the experimental data from the heterodyne detectors, it would be more convenient to deal with only finite sums. As the experiment only generated the n-phonon subtracted states, I will now compute a finite-sum-form of $\mathrm{pr}_{n-}(X_{\mathrm{M}})$.

Finite sum of the probability distribution for the n-phonon subtracted state

From the expression of ρ_{n-} in terms of the P function and Eq. (9.59), one may calculate the position marginal of ρ_{n-} to be

$$\begin{aligned} \mathrm{pr}_{n-}(X_{\mathrm{M}}) &= \int d^2\beta\ P_{n-}(\beta)|\langle X_{\mathrm{M}}|\beta\rangle|^2 \\ &= \frac{\exp\left(-\frac{X_{\mathrm{M}}^2}{1+2\bar{n}}\right)}{n!\pi^{\frac{3}{2}}\sqrt{1+2\bar{n}}} \sum_{k=0}^{n}\sum_{l=0}^{k} \binom{n}{k}\binom{2k}{2l} \Gamma\left[n-k+\frac{1}{2}\right]\Gamma\left[l+\frac{1}{2}\right] X_{\mathrm{M}}^{2(k-l)} \frac{(2\bar{n})^{k-l}}{(1+2\bar{n})^{2k-l}}, \end{aligned} \tag{9.73}$$

where the formula for the Gaussian integral in Appendix C was used. Here, the gamma functions are given by

$$\Gamma\left[m+\frac{1}{2}\right] = \frac{(2m)!}{4^m m!}\sqrt{\pi} \tag{9.74}$$

for $m \in \mathbb{N}$.

9.1.8 The measured marginals and the s-parametrized Wigner function

In this section I calculate the marginals of the mechanical state ρ_{n-} that are measured by the heterodyne detection in the experiment. Due to both inefficient detection and the type of optical detection utilized[7], the measured marginals *do*

[7] I.e. heterodyne detection being used as opposed homodyne detection.

not correspond to the actual probability marginals of the mechanical state ρ_{n-} in Eq. (9.73). Instead, the marginals measured by the experiment correspond to the marginals of an s-parametrized Wigner function with $s < -1$. The experiment can therefore be used to reconstruct an s-parametrized Wigner function of the mechanical state ρ. Moreover, I derive conditions on how efficient the measurement must be to observe mechanical non-Gaussianity.

Again, I focus on the state ρ_{n-} in this analysis as these were the states actually generated in the experiment.

Inefficiencies in the measurement

The total measurement efficiency η of the mechanical state includes mechanics-light transduction efficiency and optical detection efficiencies. An inefficient measurement of the mechanical state marginal $\mathrm{pr}(X_{\mathrm{M}})$ is described by a beamsplitter model for loss

$$\mathrm{pr}(X_{\mathrm{M}};\eta) = \frac{1}{\sqrt{\pi(1-\eta)}} \int_{-\infty}^{+\infty} dX' \ \mathrm{pr}(X') \exp\left(-\frac{\eta}{1-\eta}(X' - X_{\mathrm{M}}/\sqrt{\eta})^2\right), \tag{9.75}$$

where $\mathrm{pr}(X_{\mathrm{M}};\eta)$ is the marginal of the optical field to be measured—see Ref. [331] for a derivation. Inserting $\mathrm{pr}_{n-}(X_{\mathrm{M}})$ into Eq. (9.75) yields

$$\mathrm{pr}_{n-}(X_{\mathrm{M}};\eta) = \frac{\exp\left[-X_{\mathrm{M}}^2\left(\frac{1}{1-\eta} - \frac{B^2}{A}\right)\right]}{n!\pi^2\sqrt{(1+2\bar{n})(1-\eta)A}} \sum_{k=0}^{n}\sum_{l=0}^{k}\sum_{p=0}^{k-l} \binom{n}{k}\binom{2k}{2l}\binom{2(k-l)}{2p} \times$$
$$\Gamma\left[n-k+\frac{1}{2}\right]\Gamma\left[l+\frac{1}{2}\right]\Gamma\left[p+\frac{1}{2}\right]\left(\frac{BX_{\mathrm{M}}}{A}\right)^{2(k-l-p)} \frac{(2\bar{n})^{k-l}}{(1+2\bar{n})^{2k-l}} A^{-p}, \tag{9.76}$$

where $A = 1/(1+2\bar{n}) + \eta/(1-\eta)$ and $B = \sqrt{\eta}(1-\eta)$.

An equivalent expression to Eq. (9.75), describing the effect of the beamsplitter model is given by the P-function transformation: $P'(\beta) = \frac{1}{\eta}P(\beta/\sqrt{\eta})$, where $P'(\beta)$ is the P function of the optical field to be measured. Using (9.59), the P function of ρ_{n-} therefore transforms according to $P'_{n-}(\beta) = P_{n-}(\beta;\bar{n}\to\eta\bar{n})$, which is a simple rescaling of the initial mean phonon number of the thermal state. According to Eq. (9.73), the effect of inefficient measurement on the marginal $\mathrm{pr}_{n-}(X_{\mathrm{m}})$ is also to rescale $\bar{n}$ in the same way: $\bar{n}\to\eta\bar{n}$. Hence, $\mathrm{pr}_{n-}(X_{\mathrm{m}};\eta) = \mathrm{pr}_{n-}(X_{\mathrm{m}};\bar{n}\to\eta\bar{n})$.

Heterodyne detection

Heterodyne detection projects the optical state ρ entering the detector onto a coherent state $|\alpha\rangle$. An outcome $\alpha\in\mathbb{C}$ occurs with probability proportional to $\mathrm{Tr}(|\alpha\rangle\langle\alpha|\rho) = \langle\alpha|\rho|\alpha\rangle$. Hence, as the Husimi-$Q$ function is defined as $Q(\alpha) = \frac{1}{2\pi}\langle\alpha|\rho|\alpha\rangle$, heterodyne detection allows one to measure the Q function of the optical state ρ.

In the case of a perfect measurement of the mechanical state, $\eta = 1$, heterodyne detection measures the Q function of the mechanical state. When $\eta = 1$,

the marginals of the Q function are related to the mechanical state marginals $\mathrm{pr}(X_\mathrm{m})$ via a convolution with a Gaussian

$$\mathrm{pr}(X_\mathrm{M}; s=-1) = \int dP_\mathrm{m}\ Q(X_\mathrm{M}, P_\mathrm{M}) \tag{9.77}$$

$$= \frac{1}{\sqrt{\pi}} \int dX'\ \mathrm{pr}(X')\mathrm{e}^{-(X_\mathrm{M}-X')^2}. \tag{9.78}$$

This equation is again phase-invariant and $s=-1$ refers to condition for the s-parametrized Wigner function $W_s(X_\mathrm{M}, P_\mathrm{M})$ to equal the Q function.

The measured marginals

The measured marginals $\mathrm{Pr}_{n-}(X_\mathrm{M})$ are then given by inserting the expression for $\mathrm{pr}(X_\mathrm{M};\eta)$ into the integral of Eq. (9.78). This gives the neat expression for the measured marginal of the n-phonon subtracted state

$$\mathrm{Pr}_{n-}(X_\mathrm{M}) = \frac{1}{\sqrt{\pi}} \int dX'\ \mathrm{pr}_{n-}(X';\eta)\mathrm{e}^{-(X_\mathrm{M}-X')^2} \tag{9.79}$$

$$= \frac{1}{\sqrt{\pi(2-\eta)}} \int dX'\ \mathrm{pr}_{n-}(X')\mathrm{e}^{-\frac{\eta}{2-\eta}(X'-X_\mathrm{M}/\sqrt{\eta})^2} \tag{9.80}$$

$$= \frac{\exp\left(-\frac{X_\mathrm{M}^2}{2(1+\eta\bar{n})}\right)}{n!\pi^2\sqrt{2(1+\eta\bar{n})}} \sum_{k=0}^{n}\sum_{l=0}^{k}\sum_{r=0}^{k-l} \binom{n}{k}\binom{2k}{2l}\binom{2(k-l)}{2r} \Gamma\left[n-k+\frac{1}{2}\right] \Gamma\left[l+\frac{1}{2}\right]\Gamma\left[r+\frac{1}{2}\right] X_\mathrm{M}^{2(k-l-r)} \frac{(2\eta\bar{n})^{k-l}}{(1+2\eta\bar{n})^{l+r}[2(1+\eta\bar{n})]^{2(k-l)-r}}, \tag{9.81}$$

where in the second line the Gaussian integral from Appendix C was used.

Importantly, the measured marginals $\mathrm{Pr}_{n-}(X_\mathrm{M})$ are exactly equal to the marginals of an s-parametrized Wigner function of the mechanical state ρ_{n-}, which will be shown shortly, but first I calculate the s-parametrized Wigner function itself.

The s-parametrized Wigner function

For a general quantum state, the s-parametrized Wigner function can be computed by convolving the P function with a two-dimensional Gaussian

$$W_s(X_\mathrm{M}, P_\mathrm{M}) = \frac{1}{\pi(1-s)} \iint_{-\infty}^{\infty} dX'_\mathrm{M} dP'_\mathrm{M}\ P(X'_\mathrm{M}, P'_\mathrm{M}) \times \exp\left(-\frac{(X_\mathrm{M}-X'_\mathrm{M})^2+(P_\mathrm{M}-P'_\mathrm{M})^2}{1-s}\right). \tag{9.82}$$

Here, for n-phonon subtraction, the s-parametrized Wigner function can be calculated by using (9.59) for the P function. The full form of the s-parametrized

Wigner function for an n-phonon subtracted state is then

$$W_s(X_{\rm M},P_{\rm M}) = \frac{2^{-n}\bar{n}^{-1-n}}{\pi^2(1-s)n!}\iint_{-\infty}^{\infty} dX'_{\rm M}dP'_{\rm M}\Bigg[\left(X'^2_{\rm M}+P'^2_{\rm M}\right)^n \times \exp\left(-\frac{X'^2_{\rm M}+P'^2_{\rm M}}{2\bar{n}}-\frac{(X'_{\rm M}-X_{\rm M})^2+(P'_{\rm M}-P_{\rm M})^2}{1-s}\right)\Bigg], \quad (9.83)$$

where $\beta=(X_{\rm M}+{\rm i}P_{\rm M})/\sqrt{2}$ has been used. Introducing,

$$G_s(X_{\rm M},P_{\rm M}) = \frac{1}{\pi(1-s)}\exp\left(-\frac{X^2_{\rm M}+P^2_{\rm M}}{1-s}\right) \quad (9.84)$$

then allows $W_s(X_{\rm M},P_{\rm M})$ to be written more compactly as

$$W_s(X_{\rm M},P_{\rm M}) = \left(P_{n-} * G_s\right)(X_{\rm M},P_{\rm M}) \ , \quad (9.85)$$

where $*$ represents the two-dimensional convolution.

But what is the value of s? As will be shown now, it depends on the value of η.

The value of s and the equivalence to the marginals of the s-parametrized Wigner function

In the case of inefficient detection, $\eta<1$, the Q function measured by heterodyne detection is smoothed according to

$$Q(X_{\rm M},P_{\rm M}) = \frac{1}{\eta}W_s(X_{\rm M}\eta^{-1/2},P_{\rm M}\eta^{-1/2}), \quad (9.86)$$

$$s = \frac{1}{\eta}(\eta-2), \quad (9.87)$$

which is a result taken from Ref. [332]. Therefore, inefficient heterodyne measures the s-parametrized Wigner function $W_s(X_{\rm M},P_{\rm M})$ of the mechanical state with $s<-1$. Using Eq. (9.86), one finds that the marginal distribution $\Pr(X_{\rm M})$ of the field measured by heterodyne is

$$\Pr(X_{\rm M}) = \int dP_{\rm m}\ Q(X_{\rm M},P_{\rm M}) \quad (9.88)$$

$$= \frac{1}{\eta}\int dP_{\rm m}\ W_s(X_{\rm M}\eta^{-1/2},P_{\rm M}\eta^{-1/2}) \quad (9.89)$$

$$= \frac{1}{\sqrt{\eta}}\int dP\ W_s(X_{\rm M}\eta^{-1/2},P_{\rm M}) \quad (9.90)$$

$$= \frac{1}{\sqrt{\pi|s|\eta}}\int dX'\ {\rm pr}(X'){\rm e}^{-|s|^{-1}(X'-X_{\rm M}/\sqrt{\eta})^2}. \quad (9.91)$$

In the last line of Eq. (9.91), the following relation between the marginal distribution ${\rm pr}(X_{\rm M})$ and the marginal of the s-parametrized Wigner function ${\rm pr}(X_{\rm M};s)$

was used:

$$\mathrm{pr}(X_{\mathrm{M}};s) \quad = \quad \frac{1}{\sqrt{\pi|s|}}\int dX'\ \mathrm{pr}(X')\mathrm{e}^{-|s|^{-1}(X_{\mathrm{M}}-X')^2}, \tag{9.92}$$

valid for $s<0$.

Crucially, Eq. (9.91) is equal to Eq. (9.80) when $s=(\eta-2)/\eta$. Therefore, it has been shown that the experiment measures the marginals of $W_s(X_{\mathrm{M}},P_{\mathrm{M}})$, given by $\mathrm{Pr}_{n-}(X_{\mathrm{M}})$ with $s=(\eta-2)/\eta$.

Conditions to observe non-Gaussianity

Now I will focus on the states generated by the experiment. Explicitly, the measured marginal distributions of the thermal state $\rho_{\bar{n}}$, single-phonon subtracted state ρ_{1-}, and two-phonon subtracted state ρ_{2-} are

$$\mathrm{Pr}_{\bar{n}}(X_{\mathrm{M}}) = \frac{1}{\sqrt{2\pi(1+\eta\bar{n})}}\exp\left[-\frac{X_{\mathrm{M}}^2}{2(1+\eta\bar{n})}\right], \tag{9.93}$$

$$\begin{aligned}\mathrm{Pr}_{1-}(X_{\mathrm{M}}) =& \frac{1}{\sqrt{8\pi(1+\eta\bar{n})}}\exp\left[-\frac{X_{\mathrm{M}}^2}{2(1+\eta\bar{n})}\right]\times \\ & \left(\frac{2+\eta\bar{n}}{1+\eta\bar{n}}+\frac{4\eta\bar{n}}{[2(1+\eta\bar{n})]^2}X_{\mathrm{M}}^2\right),\end{aligned} \tag{9.94}$$

$$\begin{aligned}&\mathrm{Pr}_{2-}(X_{\mathrm{M}}) = \frac{1}{\sqrt{8\pi(1+\eta\bar{n})}}\exp\left[-\frac{X_{\mathrm{M}}^2}{2(1+\eta\bar{n})}\right]\times \\ &\left(\frac{8+8\eta\bar{n}+3(\eta\bar{n})^2}{4(1+\eta\bar{n})^2}+\frac{4\eta\bar{n}+(\eta\bar{n})^2}{2(1+\eta\bar{n})^3}X_{\mathrm{M}}^2+\frac{(2\eta\bar{n})^2}{[2(1+\eta\bar{n})]^4}X_{\mathrm{M}}^4\right),\end{aligned} \tag{9.95}$$

which simplify to the marginals of the mechanical Q functions when $\eta=1$.

For $\eta\bar{n}\leq 2$, a maximum of the measured distribution of the single-phonon subtracted state $\mathrm{Pr}_{1-}(X_{\mathrm{M}})$ occurs at $X_{\mathrm{M}}=0$. While for $\eta\bar{n}>2$, the maxima occur at $X_{\mathrm{M}}=\pm X_1$

$$X_1=\sqrt{\frac{(1+\eta\bar{n})(\eta\bar{n}-2)}{\eta\bar{n}}}. \tag{9.96}$$

and a local minimum is located at $X_{\mathrm{M}}=0$. Hence, the condition to produce the non-Gaussian ring shape, characterized by a dip at $X_{\mathrm{M}}=0$, is $\eta\bar{n}>2$.

I now sketch how to relate the location of the maxima of $\mathrm{Pr}_{1-}(X_{\mathrm{M}})$ to the radius at which the maxima occur in W_s. Firstly, consider the simple expression for the P function of the single-phonon subtracted state by choosing $n=1$ in Eq. (9.59). Then, one may find that the maxima of $P_{1-}(\beta)$ occur at a radius $\sqrt{2\bar{n}}$ from the origin. Integrating $P_{1-}(\beta)$ over one quadrature then gives an

expression for marginal of this P function: $\mathrm{pr}_{1-}(X_{\mathrm{M}}; s = +1)$. The maxima of $\mathrm{pr}_{1-}(X_{\mathrm{M}}; s = +1)$ occur at $X_{\mathrm{M}} = \pm\sqrt{\bar{n}}$. Hence, there is a factor of $\sqrt{2}$ difference between the distance of the maxima from the origin of $\mathrm{pr}_{1-}(X_{\mathrm{M}}; s = +1)$ and $P_{1-}(\beta)$. Secondly, Eq. (9.92), and a two-dimensional convolution from the P function to W_s, is used to show that this factor of $\sqrt{2}$ difference persists at the level of $\mathrm{Pr}_{1-}(X_{\mathrm{M}})$ and W_s. Hence, for ρ_{1-} the maxima of $W_s(X_{\mathrm{M}}, P_{\mathrm{M}})$ occur at a radius of

$$r_1 = \sqrt{2}X_1. \tag{9.97}$$

For $\eta\bar{n} > 2\sqrt{6} - 4$, the maxima for the measured distribution of two-phonon subtracted state $\mathrm{Pr}_{2-}(X_{\mathrm{M}})$ occur at $X_{\mathrm{M}} = \pm X_2$

$$X_2 = \sqrt{\frac{1+\eta\bar{n}}{\eta\bar{n}}\left[-4 + \eta\bar{n} + \sqrt{2(4+(\eta\bar{n})^2)}\right]}, \tag{9.98}$$

and a minimum exists at $X_{\mathrm{M}} = 0$. A similar calculation to the one sketched above gives that for ρ_{2-} the maxima of $W_s(X_{\mathrm{M}}, P_{\mathrm{M}})$ occur at a radius

$$r_2 = \sqrt{2}X_2. \tag{9.99}$$

In this case, the condition to observe non-Gaussianity in the two-phonon subtracted state is $\eta\bar{n} > 2\sqrt{6} - 4$.

In the experiment $\eta\bar{n} = 4.1$ is achieved, as the overall efficiency[8] is $\eta = 0.91\%$ and $\bar{n} = 453$, which satisfies the condition to observe non-Gaussianity in both the single- and two-phonon subtracted state.

9.1.9 The heterodyne signal as a function of time for verification

Variance of the measured marginals at time equals zero

From Eqs (9.93), (9.94), and (9.95), one can compute the variance of the measured marginals $\mathrm{Pr}_{\bar{n}}(X_{\mathrm{M}})$, $\mathrm{Pr}_{1-}(X_{\mathrm{M}})$, and $\mathrm{Pr}_{2-}(X_{\mathrm{M}})$ to be

$$V = 1 + \eta\bar{n}, \tag{9.100}$$
$$V_{1-} = 1 + 2\eta\bar{n}, \tag{9.101}$$
$$V_{2-} = 1 + 3\eta\bar{n}, \tag{9.102}$$

respectively. Here, I have once again used the Gaussian integrals from Appendix C. It is instructive to pause a moment and analyze these expressions.

Firstly, when $\eta = 0$, the variances of the measured marginals equal 1, regardless of the state. Importantly, $V = 1$ is the variance of the Q function of optical vacuum, so when the measurement of the mechanical mode is completely inefficient only the intrinsic quantum noise of the heterodyne measurement is registered. Secondly, note that each instance of $\bar{n}$ is multiplied by η. This

[8] See Sections 9.1.9 and 9.1.10.

is because the total measurement efficiency describes how well the mechanical signal is transduced onto the optical state entering the heterodyne detector. Finally, note how the doubling and tripling enters in the variances of the measured marginals V_{1-} and V_{2-}.

Time varying heterodyne signals and measuring η

Calculations by G.E. for the single-phonon subtracted state and J.J.P for the two-phonon subtracted state.
From the Heisenberg-Langevin equations describing the optomechanical interaction, the variance of the optical mode is derived to be

$$\langle X_{\mathrm{L}}(\tau)\rangle_{1-} = \frac{1}{2} + \frac{\bar{n}_{\mathrm{th}} g^2}{\kappa(\kappa+\gamma)}\left(1 + \left(\frac{\kappa \mathrm{e}^{-\gamma|\tau|} - \gamma \mathrm{e}^{-\kappa|\tau|}}{\kappa-\gamma}\right)^2\right) \quad (9.103)$$

for the single-phonon subtracted case, and

$$\langle X_{\mathrm{L}}(\tau)\rangle_{2-} = \frac{1}{2} + \frac{\bar{n}_{\mathrm{th}} g^2}{\kappa(\kappa+\gamma)}\left(1 + 2\left(\frac{\kappa \mathrm{e}^{-\gamma|\tau|} - \gamma \mathrm{e}^{-\kappa|\tau|}}{\kappa-\gamma}\right)^2\right) \quad (9.104)$$

for the two-phonon subtracted case—see the Supplemental Materials of Refs [180] and [4]. Here, $\tau = 0$ is the time at which the n-phonon subtraction event is heralded.

To find an expression for the variances of the heterodyne signal, one must take into account any optical losses and the extra 1/2 quanta of noise the heterodyne measurement adds, which gives

$$\sigma^2_{1-}(\tau) = 1 + \eta\bar{n}_{\mathrm{th}}\left(1 + \left(\frac{\kappa \mathrm{e}^{-\gamma|\tau|} - \gamma \mathrm{e}^{-\kappa|\tau|}}{\kappa-\gamma}\right)^2\right), \quad (9.105)$$

$$\sigma^2_{2-}(\tau) = 1 + \eta\bar{n}_{\mathrm{th}}\left(1 + 2\left(\frac{\kappa \mathrm{e}^{-\gamma|\tau|} - \gamma \mathrm{e}^{-\kappa|\tau|}}{\kappa-\gamma}\right)^2\right), \quad (9.106)$$

for the single-phonon and two-phonon subtraction events, respectively. The functions $\sigma^2_{1-}(\tau)$ and $\sigma^2_{2-}(\tau)$ are plotted over the experimental data in the results section: Section 9.1.10. The heterodyne variance for the thermal state is time independent and is given by $\sigma^2 = 1 + \eta\bar{n}_{\mathrm{th}}$.

Measuring η and s and normalization of the signal

Far away from the subtraction event $|\tau| \to \infty$, Eqs (9.105) and (9.106) both tend towards the heterodyne variance of the thermal state $\sigma^2 = \eta\bar{n}_{\mathrm{th}} + 1$. The variance of the measured thermal distribution and knowledge of $\bar{n}_{\mathrm{th}}$ therefore allows one to determine the efficiency $\eta = (\sigma^2 - 1)/\bar{n}_{\mathrm{th}}$ and s parameter $s = (\eta - 2)/\eta$. From the experimental data, see Section 9.1.10, the overall efficiency was determined to be $\eta = 0.91\%$, which implies $s = -219$. With the knowledge of the measurement efficiency, the heterodyne quadrature signal can then be

normalized to units of mechanical zero-point fluctuations. More explicitly, to normalize to mechanical zero-point units the quadrature axes are divided by $\sqrt{\eta}$, i.e. $\sigma^2 = 1 + \eta\bar{n}_{\rm th} \rightarrow \sigma^2/\eta = 1/\eta + \bar{n}_{\rm th}$.

Taking $\tau = 0$, one has that

$$\sigma^2_{1-}(0) = 1 + 2\eta\bar{n}_{\rm th}, \tag{9.107}$$

$$\sigma^2_{2-}(0) = 1 + 3\eta\bar{n}_{\rm th}. \tag{9.108}$$

Note that $\sigma^2_{1-}(0)$ and $\sigma^2_{2-}(0)$ do not agree exactly with the expressions for the variances of the expected measured marginals V_{1-} and V_{2-} of the single and two phonon subtracted states. This is because the mechanical state readout is continuous wave and so the mechanical bath influences the optical mode, which can be seen from the γ dependence in Eqs (9.105) and (9.106). Therefore, in the results section, when constructing the measured marginals $\Pr(X_{\rm M})$ and s-parametrized Wigner distributions $W_s(X_{\rm M}, P_{\rm M})$ from the experimental data one can rescale the widths of these distributions by the square root of the cooling factor. More concretely,

$$V_{n-} - 1 = \frac{\bar{n}}{\bar{n}_{\rm th}}(\sigma^2_{n-} - 1), \tag{9.109}$$

which is approximately

$$V_{n-} \approx \frac{\bar{n}}{\bar{n}_{\rm th}}\sigma^2_{n-}. \tag{9.110}$$

9.1.10 Experimental Results

Data analysis performed by A.Ø.S. Experiments performed by G.E., L.F., J.J.P., and A.Ø.S.

Fig. 9.3 shows the experimental s-parametrized Wigner distributions of the states $\rho_{\bar{n}}$, ρ_{1-}, and ρ_{2-}. Each of these phase-space distributions were reconstructed from 2.4×10^5 heterodyne time traces. Importantly, mechanical non-Gaussianity may be clearly observed in the phase-space distributions of ρ_{1-} and ρ_{2-}. This is because $\eta\bar{n} = 4.1$, which satisfies the conditions derived to observe the non-Gaussian dips from Section 9.1.8. Moreover, the white-dashed lines in Fig. 9.3 show the predicted location of the maxima of the states ρ_{1-} and ρ_{2-} from Eqs (9.97) and (9.99), which show excellent agreement with the experimentally observed maxima.

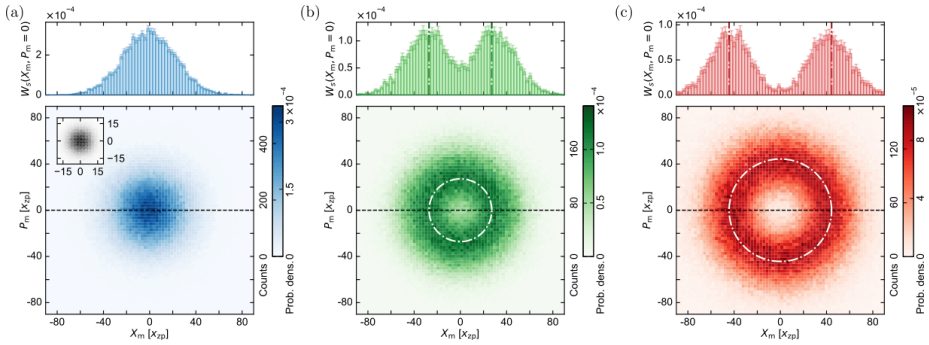


Figure 9.3: **Experimental s-parametrized Wigner functions W_s (bottom row), with slices through the momentum quadrature (top row).** Here, (a) is the initial mechanical thermal state $\rho_{\bar{n}}$, (b) is the single-phonon subtracted state ρ_{1-} and (c) is the two-phonon subtracted state ρ_{2-}. The phase-space distributions are normalized to units of the mechanical zero point fluctuations x_0 as described in the previous section. Non-Gaussianity generated from the initial thermal state is observed via the single-phonon subtraction operation, which further increases with the two-phonon subtraction operation. The dash-dotted lines indicate the theoretically predicted maxima for the W_s functions, which are given by Eqs (9.97) and (9.99). The phase-space distribution of the optical vacuum contribution is shown in the inset in panel (a). *Figure taken from Ref. [4] and made by A.Ø.S.*

Fig. 9.4(a) shows the variances of the heterodyne signal (in units of optical vacuum noise) as a function of time calculated from the experimental data. One clearly observes the expected doubling and tripling of the variance between the mechanical thermal state $\rho_{\bar{n}}$ and the states ρ_{1-} and ρ_{2-}, respectively. Furthermore, the theoretically expected curves σ^2_{1-} and σ^2_{2-} are plotted in dashed lines and show excellent agreement with the data. The small discrepancy between the experimental observations and the theoretical predictions was attributed to the filtering in the quadrature demodulation, the small level of dark counts in the SPADs, and the optical filtering performed in the heralding arm[9]. Fig. 9.4(c) plots the measured mechanical marginal distributions $\Pr(X_{\rm M})$ at the time of the phonon heralding event, for the initial thermal mechanical state $\Pr_{\bar{n}}(X_{\rm M})$, single-phonon subtracted state $\Pr_{1-}(X_{\rm M})$, and two-phonon subtracted state $\Pr_{2-}(X_{\rm M})$. Dashed lines are given by the theoretical predictions of Eqs (9.93), (9.94), and (9.95), which agree well with the experiment.

[9] Note that higher order corrections in g predict a decrease in the doubling and tripling of the variances, in agreement with these experimental observations—see Eq. (10.53). However, the calculation of Eq. (10.53) is performed without open system dynamics, so an open-system version this calculation must be performed to see if these experimental observations agree with theory when higher orders in g are taken into account.

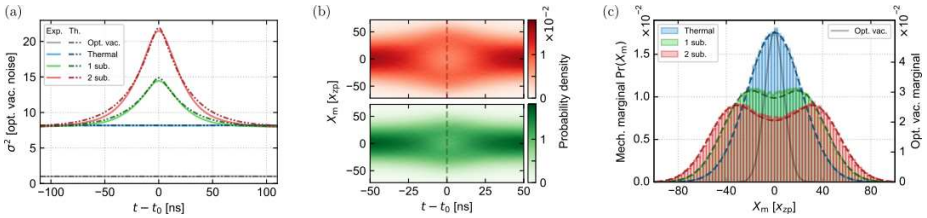


Figure 9.4: **Time evolution and non-Gaussian marginals of the heralded mechanical states.** (a) Time evolution of the heterodyne variance in units of optical vacuum noise about the heralding event for single-phonon subtracted thermal state σ^2_{1-} and two-phonon subtracted thermal state σ^2_{2-}, plotted in green and red, respectively. The optical vacuum is plotted in gray and the variance of the thermal state is plotted in blue. Experimentally obtained variances are shown as solid lines, and the predictions of the theoretical model, given by Eqs (9.105) and (9.106) are shown as dotted-dashed lines. At the time of the heralding event, the ratio of the heterodyne variance to the optical vacuum noise increases by a factor of 1.94 and 2.94 relative to the initial thermal state for single- and two-phonon subtraction, respectively. (b) Marginal distributions for the X_{M}-quadrature of the single-phonon subtracted state (green) and the two-phonon subtracted state (red) as a function of time. (c) Measured mechanical marginal distributions $\Pr(X_{\mathrm{M}})$ at the time of the heralding event, $t = t_0$, for the initial thermal mechanical state $\Pr_{\bar{n}}(X_{\mathrm{M}})$ (blue), single-phonon subtracted state $\Pr_{1-}(X_{\mathrm{M}})$ (green), and two-phonon subtracted state (red) $\Pr_{2-}(X_{\mathrm{M}})$. Dashed lines are given by the theoretical predictions of Eqs (9.93), (9.94), and (9.95). *Figure taken from Ref. [4] and made by A.Ø.S.*

9.1.11 Conclusion and outlook

The overall efficiency $\eta = 0.91\%$ of this experiment realized an s parameter of $s = -219$, which corresponds to a 15 times improvements to the current state-of-the-art optics-based mechanical tomography, Ref. [114], which is an experiment that operates in the pulsed regime optomechanics. Furthermore, the experimental results detailed above demonstrate how multi-phonon addition and subtraction operations can effectively generate mechanical non-Gaussianity, even at room temperature.

Importantly, the generation of mechanical non-Gaussianity is a key step towards observing mechanical non-classicality. By performing these same experiments at cryogenic temperatures and with improvements to the s-parameter, one can see how the observation of mechanical non-Gaussianity can be achieved in these Brillouin optomechanical systems. As the Q function is always positive, one must achieve an $s > -1$ to observe negativity in the mechanical phase-space distribution. Assuming homodyne detection ($s = 0$) is utilized in future experiments, the s parameter is given by $s = (\eta - 1)/\eta$. Therefore, to satisfy $s > -1$ and be able to observe mechanical negativity, one must achieve

an overall measurement efficiency of over 50% [331]. These improvements to the overall measurement inefficiency may be achieved via (i) further tapered fiber and microresonator device optimization, (ii) utilizing a Stokes process for mechanical state preparation and the anti-Stokes process for mechanical state readout to make for a more independent readout, which would allow one to remove the beamsplitter for photodetection.

Finally, note that combining phonon subtraction/addition operations with the techniques of pulsed optomechanics, such as mechanical squeezing described in Section 6.3.2, provides a route for generating squeezed phonon subtracted states—the mechanical version of the optical scheme from Dakna *et al.* in Ref. [302]—as well as other interesting superposition states. This scheme was proposed in Ref. [182] and requires a single mechanical mode to interact with two separate cavity modes: one operating in the resolved sideband regime to facilitate the phonon addition/subtraction operations and one operating in the unresolved sideband regime to enable pulsed optomechanics.

Chapter 10

Cooling via zero-photon detection

This chapter provides a brief introduction to theoretical framework developed in Ref. [8]. E.C.J. and K.D.M. jointly led the experiment detailed in Ref. [9], which utilizes this framework.

Compared to multi-photon detection, the detection of zero photons is quite often overlooked. Indeed, in the last chapter, it was shown how detecting one or more photons can lead to the generation of interesting quantum states. However, the detection of zero photons also provides one with the opportunity to manipulate quantum mechanical states in interesting ways. In this chapter, I first discuss this fact more broadly within the field of quantum optics. Then, I describe how one can cool a mechanical oscillator via a combination of the optomechanical beamsplitter interaction and a zero photon measurement on the optical output mode. Moreover, I also use this theory to refine the description of multi-phonon subtraction via optomechanics from the previous chapter. This refinement allows one to account for higher orders in g and thus see the interplay between the phonon subtraction operation and the redistribution of phonon number probabilities due to the knowledge gain from the measurement. I compare this cooling by zero-photon detection to standard laser cooling techniques and also account for optical loss and measurement inefficiency. Finally, I discuss future steps for this project, which involve accurately modelling the optomechanical open-system dynamics, an outlook towards quantum state tomography, and the experimental verification of cooling via zero-photon detection.

10.0.1 Zero-photon detection in quantum optics

In Section 9, I discussed how the addition and subtraction of quanta to/from bosonic systems is a useful method for generating interesting quantum states. In particular, I discussed how in quantum optics these operations have been

used to generate and observe Wigner negativity, while in Ref. [4] we saw how single- and multi-phonon subtraction operations successfully generated mechanical non-Gaussianity in Brillouin optomechanics. Notably, I also discussed how subtraction and addition operations lead to an increase the mean occupation of the quantum state.

Quite surprisingly, it has also been shown that for all single-mode quantum states[1] 'subtracting zero photons' results in a reduction in the mean occupation of the state [333]. In practice, subtracting zero photons is done by first mixing the state of interest with an ancillary mode via a beamsplitter unitary. Then zero photons are detected at the output of the ancillary mode, which is said to subtract zero photons from the state of interest. However, in what follows, I will sometimes refer to 'zero photon subtraction' as 'zero-photon detection' to avoid confusion. In optical systems, these zero-photon detection events, are useful in probabilistic noiseless attenuation protocols for quantum communication applications [334, 335]. Experimental work in successfully heralding zero photons in the presence of optical loss and dark counts [336], has allowed experiments to verify this reduction in the mean occupation due to zero photon subtraction for a range of optical input states [337].

The zero subtraction protocol described above, although counter-intuitive, can be understood through Bayesian inference as follows. Let the state of interest ρ have some mean occupation $\bar{n}$ and some uncertainty in the photon number. Then, let the state ρ interact with an ancillary mode via a beamsplitter unitary. For the sake of simplicity, let this ancillary mode be in the vacuum state $|0\rangle$. Now consider the situation when zero photons are detected at the output of the ancillary mode, which, of course, occurs with some finite probability. Crucially, some information has been gained about the state of interest, regardless of how transmissive the beamsplitter unitary was. Therefore, as ρ represents the state of knowledge of the quantum state ρ, it must be updated. Namely, due to both (i) the original uncertainty in the photon number of ρ and (ii) the detection of zero photons, the mean occupation of the state can only decrease. Note that this reduction in the mean occupation relied on there being on initial uncertainty in the photon number, i.e. you can only gain more knowledge about the photon number if you are uncertain about it in the first place[2].

Beyond the purely optical systems discussed above, the concept of 'measuring no photons' is certainly very useful, for example in driving atoms towards decoherence free subspaces in cavity QED [338, 339]. However, this concept has not been previously explored in optomechanics. I will now introduce such a proposal for cooling a mechanical thermal state via zero-photon detection using a measurement operator approach. Namely, I will focus on the simple case of a pulsed optomechanical interaction followed by a photon number measurement to elucidate the key physics. The full framework, including open-system dynamics and continuous monitoring, is described in Ref. [8].

[1] Apart from pure Fock states.

[2] Therefore, for pure Fock states, which have zero uncertainty in the photon number, the above analysis does not apply as discussed in Ref. [337].

10.0.2 The optomechanical beamsplitter unitary

In Sections 6.3.3 and 9.1.4, we saw how the optomechanical beamsplitter Hamiltonian can be achieved in cavity quantum optomechanics and Brillouin optomechanics, respectively. The optomechanical beamsplitter Hamiltonian is given by

$$H_{\text{BS}} = \hbar g(ab^\dagger + a^\dagger b), \tag{10.1}$$

which can be compared to the L_1 Jordan-Schwinger operator

$$L_1 \quad = \quad \frac{1}{2}\left(a_1^\dagger a_2 + a_2^\dagger a_1\right) \tag{10.2}$$

from Section 2.6. Therefore, relabelling $b = a_1$ and $a = a_2$ the optomechanical beamsplitter interaction is described by the Hamiltonian

$$H_{\text{BS}} = \hbar g(a_1 a_2^\dagger + a_2 a_1^\dagger), \tag{10.3}$$

which leads to the unitary

$$U = \mathrm{e}^{-2\mathrm{i}\zeta L_1}. \tag{10.4}$$

with $\zeta = gt \in [0, \infty)$.

More convenient forms for the optomechanical beamsplitter unitary

Using the results of Section 2.6, the optomechanical beamsplitter unitary $U = \mathrm{e}^{-2\mathrm{i}\zeta L_1}$ can be recast into the more convenient form as follows. Firstly, recall that a beamsplitter transformation can be written as the Heisenberg matrix transformation

$$\begin{pmatrix} a_1' \\ a_2' \end{pmatrix} \quad = \quad \underline{\underline{B}} \begin{pmatrix} a_1 \\ a_2 \end{pmatrix}, \tag{10.5}$$

where

$$\underline{\underline{B}} \quad = \quad \begin{pmatrix} B_{11} & B_{12} \\ B_{21} & B_{22} \end{pmatrix} \tag{10.6}$$

$$= \quad \mathrm{e}^{\mathrm{i}\Lambda/2} \begin{pmatrix} \cos\Theta/2\mathrm{e}^{\mathrm{i}(\Psi+\Phi)/2} & \sin\Theta/2\mathrm{e}^{\mathrm{i}(\Psi-\Phi)/2} \\ -\sin\Theta/2\mathrm{e}^{-\mathrm{i}(\Psi-\Phi)/2} & \cos\Theta/2\mathrm{e}^{-\mathrm{i}(\Psi+\Phi)/2} \end{pmatrix}. \tag{10.7}$$

Secondly, recall that the same transformation can be written as

$$\begin{pmatrix} a_1' \\ a_2' \end{pmatrix} \quad = \quad U^\dagger \begin{pmatrix} a_1 \\ a_2 \end{pmatrix} U, \tag{10.8}$$

with

$$U \quad = \quad \mathrm{e}^{\mathrm{i}\Lambda L_0}\mathrm{e}^{\mathrm{i}\Psi L_3}\mathrm{e}^{\mathrm{i}\Theta L_2}\mathrm{e}^{\mathrm{i}\Phi L_3}. \tag{10.9}$$

So what are the right choices of Λ, Θ, Φ and Ψ to produce the optomechanical beamsplitter $U = \mathrm{e}^{-2\mathrm{i}\zeta L_1}$?

To find the values of the variables Λ, Θ, Φ and Ψ, $\Omega = -2\zeta$ is first introduced, and thus $U = \mathrm{e}^{-2\mathrm{i}\zeta L_1}$ becomes $U = \mathrm{e}^{\mathrm{i}\Omega L_1}$, which allows one to write the optomechanical beamsplitter transformation as

$$\begin{pmatrix} a_1' \\ a_2' \end{pmatrix} = \mathrm{e}^{-\mathrm{i}\Omega L_1} \begin{pmatrix} a_1 \\ a_2 \end{pmatrix} \mathrm{e}^{\mathrm{i}\Omega L_1} \tag{10.10}$$

$$= \underline{\underline{B}} \begin{pmatrix} a_1 \\ a_2 \end{pmatrix} \tag{10.11}$$

$$= \begin{pmatrix} f(\Omega) \\ g(\Omega) \end{pmatrix} \tag{10.12}$$

Therefore, one must find the elements of $\underline{\underline{B}}$ with the initial conditions that $B_{11}(\Omega = 0) = B_{22}(\Omega = 0) = 1$ and $B_{12}(\Omega = 0) = B_{21}(\Omega = 0) = 0$ subject to the conditions of Eqs (2.24) and (2.25) from Section 2.6. Differentiating $f(\Omega)$ gives

$$\begin{aligned} \frac{\partial f}{\partial \Omega} &= \frac{\partial B_{11}}{\partial \Omega} a_1 + \frac{\partial B_{12}}{\partial \Omega} a_2 \\ &= -\mathrm{i}\mathrm{e}^{-\mathrm{i}\Omega L_1} [L_1, a_1] \mathrm{e}^{\mathrm{i}\Omega L_1} \\ &= \frac{\mathrm{i}}{2} \mathrm{i}\mathrm{e}^{-\mathrm{i}\Omega L_1} a_2 \mathrm{e}^{\mathrm{i}\Omega L_1} \\ &= \frac{\mathrm{i}}{2} g(\Omega). \end{aligned} \tag{10.13}$$

Similarly, differentiating $g(\Omega)$ gives

$$\frac{\partial g}{\partial \Omega} = \frac{\mathrm{i}}{2} f(\Omega). \tag{10.14}$$

In terms of the beamsplitter matrix elements, Eqs (10.13) and(10.14) give

$$\frac{\partial B_{11}}{\partial \Omega} = \frac{\mathrm{i}}{2} B_{21} \tag{10.15}$$

$$\frac{\partial B_{12}}{\partial \Omega} = \frac{\mathrm{i}}{2} B_{22} \tag{10.16}$$

$$\frac{\partial B_{21}}{\partial \Omega} = \frac{\mathrm{i}}{2} B_{11} \tag{10.17}$$

$$\frac{\partial B_{22}}{\partial \Omega} = \frac{\mathrm{i}}{2} B_{12}. \tag{10.18}$$

Combining Eqs (10.15) and (10.17) gives

$$\frac{\partial^2 B_{11}}{\partial \Omega} = -\frac{1}{4} B_{11}, \tag{10.19}$$

which has a solution $B_{11} = \cos \Omega/2$ such that $B_{11}(\Omega = 0) = 1$. Solving for the rest of the beamsplitter matrix elements gives

$$\underline{\underline{B}} = \begin{pmatrix} \cos \Omega/2 & \mathrm{i} \sin \Omega/2 \\ \mathrm{i} \sin \Omega/2 & \cos \Omega/2 \end{pmatrix}. \tag{10.20}$$

Thus, the optomechanical beamsplitter matrix may be achieved by choosing $\Lambda = 0$, $\Theta = \Omega$, $\Psi = \pi/2$, and $\Phi = -\pi/2$. Hence, the optomechanical beamsplitter can be written as

$$\begin{aligned} U &= \mathrm{e}^{\mathrm{i}\frac{\pi}{2}L_3}\mathrm{e}^{\mathrm{i}\Omega L_2}\mathrm{e}^{-\mathrm{i}\frac{\pi}{2}L_3} \\ &= \mathrm{e}^{\mathrm{i}\frac{\pi}{2}L_3}\mathrm{e}^{-2\mathrm{i}\zeta L_2}\mathrm{e}^{-\mathrm{i}\frac{\pi}{2}L_3}. \end{aligned} \tag{10.21}$$

Finally, one may then use Eq. (2.38) of Section 2.6 to rewrite the optomechanical beamsplitter as

$$U = T^{\hat{n}_1}\mathrm{e}^{-R^* a_2^\dagger a_1}\mathrm{e}^{R a_1^\dagger a_2}T^{-\hat{n}_2}, \tag{10.22}$$

$$T = \cos\zeta, \tag{10.23}$$

$$R = -\mathrm{i}\sin\zeta. \tag{10.24}$$

10.0.3 n-click detection without open-system dynamics

The measurement operator for n clicks

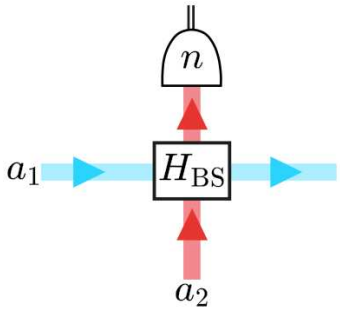


Figure 10.1: **Optomechanical beamsplitter and n-click detection.** Mechanical mode a_1 (blue) and optical mode a_2 (red) interact via a beamsplitter type interaction H_{BS}, with beamsplitter transmission coefficient $T = \cos\zeta$, where $\zeta = gt$. n clicks are then detected in the output optical mode, which yields the measurement operator Υ_n acting on the mechanical mode.

To arrive at the optomechanical beamsplitter Hamiltonian H_{BS}, we found that in Sections 6.3.3 and 9.1.4, one must operate in the linearized regime of optomechanics. Therefore, the interaction has been expanded about some large intracavity amplitude α_{c}, such that the optical mode a_2 (a) is now in the vacuum state. Hence, using Eq. (10.22) the measurement operator for an n-click

event is

$$\begin{aligned}\Upsilon_n &= {}_2\langle n|\, U\, |0\rangle_2 \\ &= T^{\hat{n}_1}\, {}_2\langle n|\, \mathrm{e}^{-R^* a_2^\dagger a_1} \mathrm{e}^{R a_1^\dagger a_2} T^{-\hat{n}_2}\, |0\rangle_2 \\ &= T^{\hat{n}_1}\, {}_2\langle n|\, \mathrm{e}^{-R^* a_2^\dagger a_1} \mathrm{e}^{R a_1^\dagger a_2}\, |0\rangle_2 \\ &= T^{\hat{n}_1}\, {}_2\langle n|\, \mathrm{e}^{-R^* a_2^\dagger a_1}\, |0\rangle_2 \,, \end{aligned} \tag{10.25}$$

where $T^{-\hat{n}_2}\,|0\rangle = |0\rangle$ and $\mathrm{e}^{R a_1^\dagger a_2}\,|0\rangle = |0\rangle$ was used, which may be seen by taking a series expansion of the exponential operators where only the identity term contributes. Then using $(a^\dagger)^m\,|0\rangle = \sqrt{m!}\,|m\rangle$

$$\begin{aligned}\Upsilon_n &= T^{\hat{n}_1} \sum_{m=0}^{\infty} \frac{(-R^* a_1)^m}{m!}\, {}_2\langle n|\, (a_2^\dagger)^m\, |0\rangle_2 \\ &= \frac{(-R^*)^n}{\sqrt{n!}} T^{\hat{n}_1} a_1^n, \end{aligned} \tag{10.26}$$

which agrees with the more general measurement operator of the form $\langle n|\, U\, |m\rangle$ derived in Ref. [340].

Therefore, the optomechanical beamsplitter followed by an n-click event is physically (i) an n-phonon subtraction event followed by (ii) a redistribution of the phonon number probabilities. Furthermore, note that as $T = \cos\zeta$, with $\zeta = gt$, to first order in g one has that $T^{\hat{n}_1} \approx \mathbb{1}$. Hence, for zero-photon detection, Υ_0 is non-trivial only if the second order in ζ is non-negligible.

In further calculations, it will also be convenient to sometimes swap the order of the phonon-redistribution term and n-phonon subtraction term in Eq. (10.26). Using

$$\mathrm{e}^{\varphi \hat{n}} f(a) = f(a\mathrm{e}^{-\varphi} a)\mathrm{e}^{\varphi \hat{n}} \tag{10.27}$$

with $\varphi = \ln(T)$ from Appendix A, which gives

$$\begin{aligned} T^{\hat{n}_1} a_1^n &= (a_1 \mathrm{e}^{-\ln(T)})^n (\mathrm{e}^{\ln(T)})^{\hat{n}_1} \\ &= \frac{1}{T^n} a_1^n T^{\hat{n}_1}. \end{aligned} \tag{10.28}$$

Hence,

$$\Upsilon_n = \frac{1}{\sqrt{n!}} \left(\frac{-R^*}{T}\right)^n a_1^n T^{\hat{n}_1}. \tag{10.29}$$

Finally, in Appendix H, I show that the set of measurement operators $\{\Upsilon_n\}$ form a complete map, which is a requirement measurement operators must meet as previously discussed in Chapter 5.

Detecting zero photons and change in the thermal occupation

I will now compute how detecting zero photon changes the thermal occupation of an initial mechanical state. To this end, consider an initial thermal state

$$\begin{aligned}\rho_{\bar{n}} &= \sum_{m=0}^{\infty} p_m \left|m\right\rangle \left\langle m\right| \\ &= \frac{1}{1+\bar{n}} \sum_{m=0}^{\infty} \left(\frac{\bar{n}}{1+\bar{n}}\right)^m \left|m\right\rangle \left\langle m\right| \\ &= (1-x) \sum_{m=0}^{\infty} x^m \left|m\right\rangle \left\langle m\right|, \end{aligned} \tag{10.30}$$

with $x = \bar{n}/(1+\bar{n})$ and $\bar{n} = x/(1-x)$. A zero photon detection event gives the mechanical state

$$\rho_0 = \frac{\Upsilon_0 \rho_{\bar{n}} \Upsilon_0^\dagger}{\mathcal{P}_0}, \tag{10.31}$$

with the heralding probability $\mathcal{P}_0$ and measurement operator Υ_0 given by

$$\mathcal{P}_0 = \mathrm{tr}\left(\Upsilon_0^\dagger \Upsilon_0 \rho_{\bar{n}}\right), \tag{10.32}$$

$$\Upsilon_0 = T^{\hat{n}_1}. \tag{10.33}$$

$$\tag{10.34}$$

Hence,

$$\rho_0 = (1-xT^2) \sum_{m=0}^{\infty} (xT^2)^m \left|m\right\rangle \left\langle m\right|, \tag{10.35}$$

$$\begin{aligned}\mathcal{P}_0 &= \frac{1-x}{1-xT^2} \\ &= \frac{1}{1+\bar{n}(1-T^2)} \\ &= \frac{1}{1+\bar{n}(1-\cos^2\zeta)} \end{aligned} \tag{10.36}$$

with reduced thermal occupation

$$\begin{aligned}\bar{n}_0 &= \frac{xT^2}{1-xT^2} \\ &= \frac{\bar{n}T^2}{1+\bar{n}(1-T^2)} \\ &= \frac{\bar{n}\cos^2\zeta}{1+\bar{n}(1-\cos^2\zeta)}. \end{aligned} \tag{10.37}$$

When $\zeta = 0$, $\bar{n}_0 = \bar{n}$ and $\underline{\underline{B}} = \mathbb{1}$. When $\zeta = gt = (2m+1)\pi/2$, for $m \in \mathbb{N}$, $\bar{n}_0 = 0$, and $\underline{\underline{B}} = -\mathrm{i}\sigma_x$. In this case, $a_1 \to -\mathrm{i}a_2$ and $a_2 \to a_1$, which is a complete optomechanical state swap.

Comparison to a simple unitary optomechanical state swap

It is instructive to compare the change in the thermal occupation induced by the zero-photon detection scheme with the change induced by just the beamsplitter interaction itself. Note that the Heisenberg equations of motion induced by the beamsplitter Hamiltonian $H_{\rm BS} = \hbar g(a_1 a_2^\dagger + a_2 a_1^\dagger)$ are

$$\dot{a}_1(t) = \frac{\mathrm{i}}{\hbar}[H_{\rm BS}, a_1] = -\mathrm{i}g a_2(t), \tag{10.38}$$

$$\dot{a}_2(t) = \frac{\mathrm{i}}{\hbar}[H_{\rm BS}, a_2] = -\mathrm{i}g a_1(t), \tag{10.39}$$

which are solved by

$$a_1(t) = a_1(0)\cos\zeta - \mathrm{i}a_2(0)\sin\zeta, \tag{10.40}$$

$$a_2(t) = a_2(0)\cos\zeta - \mathrm{i}a_1(0)\sin\zeta. \tag{10.41}$$

Taking the initial state of the mechanical mode to be the thermal state, the initial state of the optical mode to be the vacuum state, and the initial system to be uncorrelated

$$\langle n_1(0)\rangle = \left\langle a_1^\dagger a_1(0)\right\rangle = \bar{n}, \tag{10.42}$$

$$\langle n_2(0)\rangle = \left\langle a_2^\dagger a_2(0)\right\rangle = 0, \tag{10.43}$$

and all cross terms at time zero, such as $\left\langle a_2^\dagger a_1(0)\right\rangle$, are zero. Together, with the solution for $a_1(t)$, this implies that the thermal occupation of the mechanical mode as a function of time is

$$\langle n_1(t)\rangle = \bar{n}\cos^2\zeta. \tag{10.44}$$

When $\zeta = gt = (2m+1)\pi/2$, for $m \in \mathbb{N}$, a perfect state swap with the optical mode is realized.

Fig. 10.2 plots the how Eq. (10.44) compares to the zero-photon detection scheme described by Eq. (10.37). From this figure, it is clear that the zero-photon detection scheme performs much better in cooling the mechanical mode.

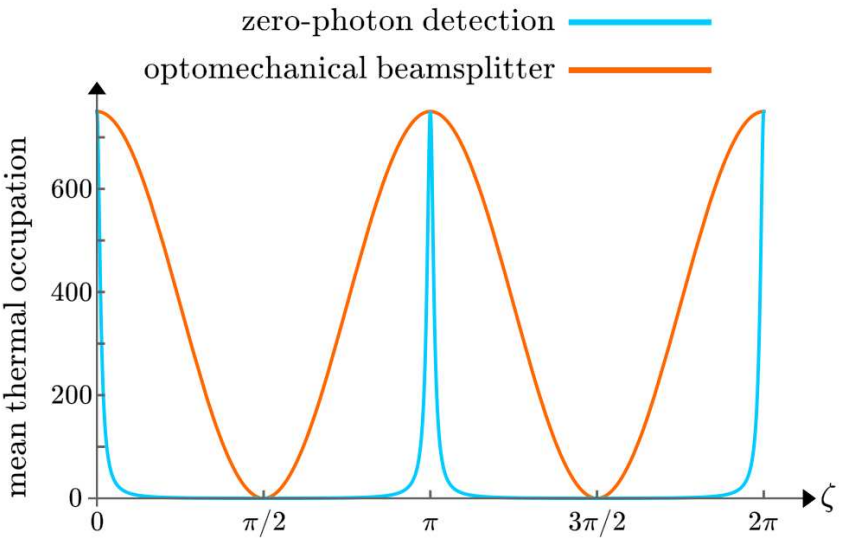


Figure 10.2: **Zero click detection versus the optomechanical beamsplitter/laser cooling.** Plot of the thermal occupation of the mechanical mode against $\zeta = gt$ for (i) zero-photon detection in blue given by Eq. (10.37) and (ii) the unitary optomechanical beamsplitter interaction in orange given by Eq. (10.44). Here, the initial occupation of the mechanical mode is taken to be $\bar{n} = 750$. At $\zeta = gt = (2m+1)\pi/2$, for $m \in \mathbb{N}$, each case achieves a perfect state swap between the optical vacuum mode and the thermal mechanical mode. However, at all over times the zero-photon detection scheme performs much better in cooling the mechanical mode. *n.b. As will soon be shown, the thermal occupation of the mechanical mode induced by the optomechanical beamsplitter unitary is the same as the laser cooled state in the absence of environmental interactions.*

Detecting n clicks and change in the thermal occupation

Detecting n-click event changes the initial thermal state $\rho_{\bar{n}}$ according to

$$\rho_n = \frac{\Upsilon_n \rho_{\bar{n}} \Upsilon_n^\dagger}{\mathcal{P}_n}, \tag{10.45}$$

$$\mathcal{P}_n = \mathrm{tr}\left(\Upsilon_n^\dagger \Upsilon_n \rho_{\bar{n}}\right) \tag{10.46}$$

Using Eq. (10.29) and $a^n |m\rangle = \sqrt{m!/(m-n)!}\,|m-n\rangle$ for $m \geq n$ or zero otherwise, one finds that

$$\begin{aligned}
\Upsilon_n \rho_{\bar{n}} \Upsilon_n^\dagger &= \frac{(1-x)}{n!}\left(\frac{|R|^2}{|T|^2}\right)^n \sum_{m=0}^{\infty} x^m a_1^n T^{\hat{n}_1} |m\rangle \langle m| T^{\hat{n}_1} (a_1^\dagger)^n \\
&= (1-x)\left(\frac{|R|^2}{|T|^2}\right)^n (xT^2)^n \sum_{m=0}^{\infty} (xT^2)^m \frac{(m+n)!}{m!n!} |m\rangle \langle m| \\
&= (1-x)(x|R|^2)^n \sum_{m=0}^{\infty} (xT^2)^m \frac{(m+n)!}{m!n!} |m\rangle \langle m| \qquad (10.47)
\end{aligned}$$

Therefore,

$$\begin{aligned}
\mathcal{P}_n &= (1-x)\left(\frac{|R|^2}{|T|^2}\right)^n (xT^2)^n \sum_{m=0}^{\infty} (xT^2)^m \frac{(m+n)!}{m!n!} \\
&= (1-x)\frac{(x|R|^2)^n}{(1-xT^2)^{n+1}}, \qquad (10.48)
\end{aligned}$$

where

$$\sum_{m=0}^{\infty} \frac{(m+n)!}{m!n!} x^m = \frac{1}{(1-x)^{n+1}} \qquad (10.49)$$

from Appendix C was used.

One can then check that the heralding probabilities are properly normalized via

$$\begin{aligned}
1 &= \sum_{n=0}^{\infty} \mathcal{P}_n \\
&= \frac{(1-x)}{1-xT^2} \sum_{n=0}^{\infty} \left(\frac{(x|R|^2)}{(1-xT^2)}\right)^n = 1. \qquad (10.50)
\end{aligned}$$

Here, the evaluation of the infinite summation is valid as $x < 1 \implies (x|R|^2)/(1-xT^2) < 1$.

With

$$\frac{(m+n)!}{m!n!} = \binom{m+n}{n} \qquad (10.51)$$

the explicit form of ρ_n is then

$$\rho_n = (1-xT^2)^{n+1} \sum_{m=0}^{\infty} (xT^2)^m \binom{m+n}{n} |m\rangle \langle m|\,. \qquad (10.52)$$

Then comparing Eq. (10.52) with Eqs (9.16), (9.17), and (9.18) one may deduce that the thermal occupation of the mechanical mode after n clicks is

$$\langle \hat{n}_1 \rangle_n = (n+1)\bar{n}_0, \qquad (10.53)$$

where n_0 is given by Eq. (10.37). Note that Eq. (10.53) generalizes the results of Eq. (9.18) to include the higher order terms in g.

Laser cooling and comparison with zero-photon detection

As opposed to zero-photon or n-photon detection, one may instead consider the laser cooled state as described in Section 9.1.5. During laser cooling, no information of the photon number is acquired and so the laser cooled state is simply given by the weighted sum over all possible click events

$$\rho_{\mathrm{LC}} = \sum_n \mathcal{P}_n \rho_n. \tag{10.54}$$

The thermal occupation of the laser cooled state is then

$$\begin{aligned} \langle \hat{n}_1 \rangle_{\mathrm{LC}} &= \bar{n}_{\mathrm{LC}} = \sum_n \mathcal{P}_n \langle \hat{n}_1 \rangle_n \\ &= \bar{n}_0 \frac{(1-x)}{1-xT^2} \sum_{n=0}^{\infty} (n+1) \left(\frac{(x|R|^2)}{(1-xT^2)} \right)^n \\ &= \bar{n}_0 \frac{1-xT^2}{1-x}, \end{aligned} \tag{10.55}$$

where

$$\sum_{m=0}^{\infty} (m+1) x^m = \frac{1}{(1-x)^2} \tag{10.56}$$

was used

Using Eq. (10.37) one then finds that the thermal occupation of the laser cooled state is

$$\bar{n}_{\mathrm{LC}} = \bar{n} T^2 \tag{10.57}$$

$$= \bar{n} \cos^2 \zeta \tag{10.58}$$

$$= \langle n_1(t) \rangle , \tag{10.59}$$

which, as expected, is exactly equal to the thermal occupation induced by the simple optomechanical beamsplitter unitary.

Moreover, the thermal occupation via zero-photon detection $\bar{n}_0$ is related to the laser cooled occupation $\bar{n}_{\mathrm{LC}}$ via

$$\bar{n}_0 = \frac{\bar{n}_{\mathrm{LC}}}{1 + \bar{n}(1-T^2)}, \tag{10.60}$$

so $\bar{n}_0 < \bar{n}_{\mathrm{LC}}$ and it is proven that zero-photon detection is always better than laser cooling *for a given value of* T *and therefore* t.

Detector timing and repeated zero-photon detection scheme

In practice it may be difficult to achieve an arbitrary ζ, for example, due to the presence of dark counts. In which case, a short optical input pulse may be used to limit the effect of dark counts. As in Ref. [336], the initial optical state may be

split into two modes, one going towards the optomechanical beamsplitter, and one acting as a reference pulse going towards a reference APD. The reference pulse may then be used to herald the zero-photon event, i.e. when there is zero-photon "coincidence click" between the detector in the arm of the reference pulse and the detector at the output of the beamsplitter interaction.

Repeating this process many times, by recording a series of zero-photon events, allows one to cool the mechanical mode further and further in a probabilistic way. Note that as $\zeta \to 0$, $\mathcal{P}_0 \to 1$ in Eq. (10.36), irrespective of the initial thermal occupation $\bar{n}$. Thus, for small values of ζ, this process achieves a sequence of infinitely frequent measurements, reminiscent of the quantum Zeno effect [341]. However, as the mechanical mode is driven towards a target state, rather than being stabilized in its current state, this effect is more accurately described as the quantum watchdog effect [342].

10.0.4 Zero-photon detection with optical loss

Here, the calculation for zero-photon detection is repeated but now the effects of optical loss are also included. To this end, I include an additional optical mode a_3 to model these losses on a beamsplitter model for loss as in Fig. 10.3.

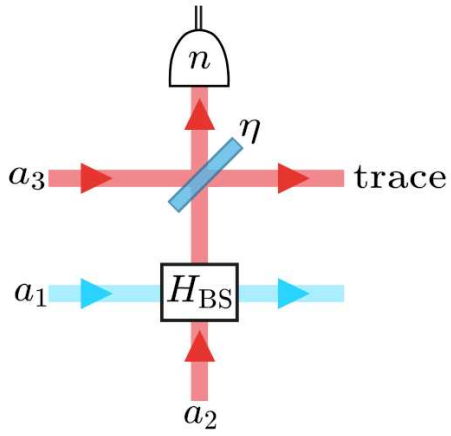


Figure 10.3: **Optomechanical beamsplitter and n-click detection with optical loss.** Mechanical mode a_1 (blue) and optical mode a_2 (red) interact via a beamsplitter type interaction $H_{\rm BS}$, with beamsplitter transmission coefficient $T = \cos\zeta$, where $\zeta = gt$. Following this, optical loss is modelled via interaction with another vacuum optical mode a_3 on a beamsplitter of transmission coefficient $t = \sqrt{\eta}$. n clicks are then detected in the output of optical mode a_2 and a trace operation is performed at the output of optical mode a_3.

The measurement operator for 0 clicks in output mode 2 and m photons lost

to the environment in output mode 3 is

$$\begin{aligned}\Upsilon_{0m} &= {}_3\langle m|\ {}_2\langle 0|\, U_{23}U_{12}\,|0\rangle_2\,|0\rangle_3 \\ &= {}_2\langle 0|\, \upsilon_m U_{12}\,|0\rangle_2\,, \end{aligned} \tag{10.61}$$

with

$$U_{12} = T^{\hat{n}_1}\mathrm{e}^{-R^* a_2^\dagger a_1}\mathrm{e}^{R a_1^\dagger a_2}T^{-\hat{n}_2}, \tag{10.62}$$

$$U_{23} = t^{\hat{n}_2}\mathrm{e}^{-r^* a_3^\dagger a_2}\mathrm{e}^{r a_2^\dagger a_3}t^{-\hat{n}_3}, \tag{10.63}$$

and

$$\begin{aligned}\upsilon_m &= {}_3\langle m|\, U_{23}\,|0\rangle_3 \\ &= \frac{1}{\sqrt{m!}}(-r^*)^m t^{\hat{n}_2}a_2^m = \frac{1}{\sqrt{m!}}\left(\frac{-r^*}{t}\right)^m a_2^m t^{\hat{n}_2}, \end{aligned} \tag{10.64}$$

where Eq. (10.22) was used to represent the two beamsplitter unitaries U_{12} and U_{23}, between modes 1 and 2 and modes 2 and 3, respectively. As before, the optomechanical beamsplitter, now labelled U_{12}, has $T = \cos\zeta$ and $R = -\mathrm{i}\sin\zeta$. While have chosen the beamsplitter U_{23} with $t = \sqrt{\eta}$ and $r = \sqrt{1-\eta}$ to model loss, such that $|t|^2 + |r|^2 = 1$. Furthermore, Eqs (10.26) and (10.29) have been used to write the last line in two different ordering.

This measurement operator is then

$$\begin{aligned}\Upsilon_{0m} &= \frac{1}{\sqrt{m!}}(-r^*)^m\ {}_2\langle 0|\, t^{\hat{n}_2}a_2^m T^{\hat{n}_1}\mathrm{e}^{-R^* a_2^\dagger a_1}\mathrm{e}^{R a_1^\dagger a_2}T^{-\hat{n}_2}\,|0\rangle_2 \\ &= \frac{1}{\sqrt{m!}}(-r^*)^m T^{\hat{n}_1}\ {}_2\langle 0|\, a_2^m \mathrm{e}^{-R^* a_2^\dagger a_1}\,|0\rangle_2 \\ &= (-r^*)^m T^{\hat{n}_1}\ {}_2\langle m|\sum_{n=0}^{\infty}\frac{(-R^* a_1)^n}{n!}(a_2^\dagger)^n\,|0\rangle_2 \\ &= \frac{1}{\sqrt{m!}}(-r^*)^m(-R^*)^m T^{\hat{n}_1}a_1^m \\ &= (-r^*)^m\Upsilon_m. \end{aligned} \tag{10.65}$$

Note that for $r = 0$ (no loss), $\Upsilon_{0m} = \delta_{0,m}\Upsilon_m = \Upsilon_0$.

The state after optical loss and a zero-photon event is then a trace over all possible outcomes m, which gives[3]

$$\begin{aligned}\rho_0' &= \frac{\sum_n \Upsilon_{0n}\rho_{\bar{n}}\Upsilon_{0n}}{\mathrm{tr}\left(\sum_n \Upsilon_{0n}\rho_{\bar{n}}\Upsilon_{0n}\right)} \\ &= \frac{\sum_n |r|^{2n}\Upsilon_n\rho_{\bar{n}}\Upsilon_n}{\mathrm{tr}\left(\sum_n |r|^{2n}\Upsilon_n\rho_{\bar{n}}\Upsilon_n\right)}, \end{aligned} \tag{10.66}$$

$$\mathcal{P}_0' = \mathrm{tr}\left(\sum_n |r|^{2n}\Upsilon_n\rho_{\bar{n}}\Upsilon_n\right). \tag{10.67}$$

[3]Note the index has been changed from m to n to avoid confusion later.

Using Eq. (10.47), one then has

$$\begin{aligned}\sum_n |r|^{2n}\Upsilon_n\rho_{\bar{n}}\Upsilon_n &= (1-x)\sum_{n=0}^{\infty}(x|r|^2|R|^2)^n \times \\ &\sum_{m=0}^{\infty}(xT^2)^m\frac{(m+n)!}{m!n!}\,|m\rangle\langle m| \end{aligned} \tag{10.68}$$

and so

$$\begin{aligned}\mathcal{P}_0' &= (1-x)\sum_{n=0}^{\infty}(x|r|^2|R|^2)^n\sum_{m=0}^{\infty}(xT^2)^m\frac{(m+n)!}{m!n!} \\ &= (1-x)\sum_{n=0}^{\infty}(x|r|^2|R|^2)^n\frac{1}{(1-xT^2)^{n+1}} \\ &= \frac{(1-x)}{1-xT^2}\sum_{n=0}^{\infty}\left(\frac{x|r|^2|R|^2}{1-xT^2}\right)^n \\ &= \frac{(1-x)}{1-x(T^2+|r|^2|R|^2)}. \end{aligned} \tag{10.69}$$

When the process is lossless, $r = 0$, and $\mathcal{P}_0' = \mathcal{P}_0$ as expected. The density matrix may then be calculated via

$$\begin{aligned}\rho_0' &= \left[1-x(T^2+|r|^2|R|^2)\right]\sum_{n=0}^{\infty}(x|r|^2|R|^2)^n \times \\ &\sum_{m=0}^{\infty}(xT^2)^m\binom{m+n}{n}|m\rangle\langle m|\,. \end{aligned} \tag{10.70}$$

At $r = 0$ one has that $\rho_0' = \rho_0$ as only the $n = 0$ survives. Using Eq. (10.52) then gives

$$\rho_0' = \frac{\left[1-x(T^2+|r|^2|R|^2)\right]}{1-xT^2}\sum_{n=0}^{\infty}\left(\frac{x|r|^2|R|^2}{1-xT^2}\right)^n\rho_n, \tag{10.71}$$

which satisfies $\mathrm{tr}(\rho_0') = 1$ as $\mathrm{tr}(\rho_n) = 1$.

Then the mean phonon number of ρ_0' is

$$\begin{aligned}
\bar{n}_0' &= \mathrm{tr}\left(a_1^\dagger a_1 \rho_0'\right) \\
&= \frac{\left[1 - x(T^2 + |r|^2|R|^2)\right]}{1 - xT^2} \sum_{n=0}^{\infty} \left(\frac{x|r|^2|R|^2}{1 - xT^2}\right)^n \mathrm{tr}\left(a_1^\dagger a_1 \rho_n\right) \\
&= \bar{n}_0 \frac{\left[1 - x(T^2 + |r|^2|R|^2)\right]}{1 - xT^2} \sum_{n=0}^{\infty} \left(\frac{x|r|^2|R|^2}{1 - xT^2}\right)^n (n+1) \\
&= \bar{n}_0 \frac{1 - xT^2}{1 - x(|T|^2 + |r|^2|R|^2)}, \qquad (10.72) \\
&= \frac{\bar{n}T^2}{1 + \eta\bar{n}(1 - T^2)} = \frac{\bar{n}_{\mathrm{LC}}}{1 + \eta\bar{n}(1 - T^2)} \qquad (10.73)
\end{aligned}$$

where Eq. (10.56) was used.

Fig. 10.4 shows the effect of optical loss on the zero-photon cooling scheme. When there is no loss ($r = 0$ and $\eta = 1$), $\bar{n}_0' = \bar{n}_0$. Meanwhile, when there is zero optical efficiency ($r = 1$ and $\eta = 0$), $\bar{n}_0' = \bar{n}_{\mathrm{LC}}$. Hence, even in the presence of optical loss, zero-photon detection cannot perform worse than laser cooling.

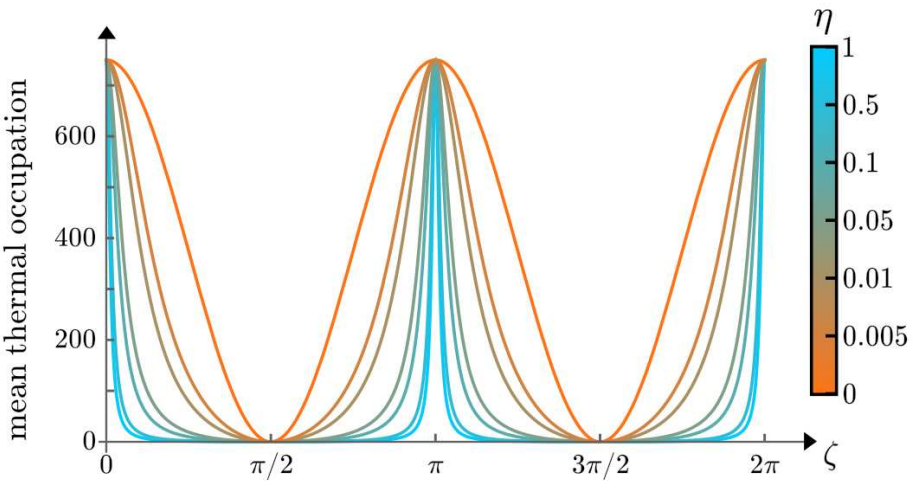


Figure 10.4: **Zero click detection in the presence of optical loss.** Plot of the thermal occupation of the mechanical mode against $\zeta = gt$ for zero-photon detection given by Eq. (10.73). Here, the initial occupation of the mechanical mode is again taken to be $\bar{n} = 750$. At $\zeta = gt = (2m+1)\pi/2$, for $m \in \mathbb{N}$, perfect state swapping between the optical vacuum mode and the thermal mechanical mode is achieved regardless of the optical efficiency η. Here, $\eta = 1$ corresponds to the blue curve in Fig. 10.4, which represents perfect zero-photon detection, while $\eta = 0$ corresponds to the orange curve in Fig. 10.4, which represents laser cooling/unitary optomechanical state swapping.

10.0.5 Conclusion and outlook

Here, I have presented a simple description of mechanical cooling via optomechanical coupling and zero-photon detection. I have demonstrated how this protocol performs better than standard laser cooling and is robust towards optical loss. However, to accurately model the experiment in Ref. [9] mechanical open-system dynamics must be properly accounted for. To this end, the following SME for the optomechanical system can be used

$$\begin{aligned} \mathrm{d}\rho = &-\frac{i}{\hbar}[H,\rho]\mathrm{d}t + \mathcal{G}[a]\rho\mathrm{d}N - \eta\kappa_{\mathrm{ex}}\mathcal{H}\left[a^\dagger a\right]\mathrm{d}t + 2\kappa_{\mathrm{ex}}(1-\eta)\mathcal{D}\left[a\right]\rho\mathrm{d}t \\ &+2\kappa_{\mathrm{i}}\mathcal{D}\left[a\right]\rho\mathrm{d}t + 2\gamma(\bar{N}+1)\mathcal{D}[b]\rho dt + 2\gamma\bar{N}\mathcal{D}[b^\dagger]\rho\mathrm{d}t. \end{aligned} \tag{10.74}$$

Here, η is again the optical detection efficiency, κ_{ex} (κ_{i}) is the external (intrinsic) amplitude coupling rate of the cavity mode from Chapter 3, γ is the amplitude decay rate of the mechanical mode, $\bar{N}$ is the occupation of the mechanical thermal environment, and H includes the free evolution of the mechanical mode and the optomechanical beamsplitter Hamiltonian. Moreover, from Chapter 5, the superoperators $\mathcal{H}$ and $\mathcal{D}$ are defined via $\mathcal{H}[O]\rho = O\rho + \rho O^\dagger - \left\langle O + O^\dagger \right\rangle \rho$ and $\mathcal{D}[O]\rho = O\rho O^\dagger - \frac{1}{2}\{O^\dagger O, \rho\}$. I have also returned to the convention of Chapter 2— a is the cavity mode field operator and b is the mechanical annihilation operator—to avoid any confusion. Notably, the superoperator $\mathcal{G}$ is defined via $\mathcal{G}[O] = O\rho O^\dagger / \left\langle O^\dagger O \right\rangle - \rho$ and describes the stochastic process of continuous photodetection—see Ref. [63]. Here, over a given time increment $\mathrm{d}t$, the stochastic increment for photodetection is $\mathrm{d}N = 0$ for a zero-photon event or $\mathrm{d}N = 1$ for one-photon event. Note that $\mathrm{d}N^2 = \mathrm{d}N$.

To see how Eq. (10.74) can be used to describe the experimental results of Ref. [9], the reader is referred to Ref. [8]. Notably, Ref. [8] also considers the case where the optomechanical beamsplitter unitary is replaced by the optomechanical two mode squeezer. Perhaps surprisingly, it is shown that mechanical cooling via zero-photon detection can still be achieved via the two mode squeezing interaction. Further work in this direction will relax requirements for laser cooling from the thermal state, allow for more accurate theoretical predictions of the mechanical occupation after an n-click event, and enable the unwanted mechanical heating effects from the two mode squeezing interaction to be mitigated.

Part III

Nonlinear cavity quantum optomechanics

Chapter 11

The nonlinear cavity-enhanced optomechanical interaction

This chapter draws heavily from Ref. [7], where this work was originally published. Unpublished material which goes beyond the linear coupling to position $a^\dagger a X_{\mathrm{M}}$ is also included.

In Chapter 6, I discussed linearized and cavity-free nonlinear optomechanics in both the pulsed and continuous regimes of operation. In this chapter a framework of nonlinear cavity quantum optomechanics for adiabatic cavities is introduced. In particular, I introduce several new unitaries that describe pulsed and continuous optomechanical interactions in various regimes of optomechanics. Firstly, I focus on an interaction Hamiltonian with linear coupling to the position operator: $a^\dagger a X_{\mathrm{M}}$. From this I derive the cavity-enhanced nonlinear unitary, which accurately includes the physics of the nonlinear response of the cavity. As was discussed in Chapter 6, I then detail how this unitary recovers the linearized and cavity-free interactions in certain limits. Secondly, I also go well beyond the linear coupling to position $a^\dagger a X_{\mathrm{M}}$, which was the focus of Ref. [7], to describe arbitrary nonlinear coupling to the mechanical position. In other words, I derive the cavity-enhanced nonlinear unitary for a dispersively coupled system $\omega_{\mathrm{C}}(x)a^\dagger a$, up to arbitrary order in position. I then introduce the cavity-free and linearized limits of this more general optomechanical interaction. Table 11.1 provides a summary of all the different regimes of optomechanics discussed in this chapter.

11.1 Linear coupling to position

In this section, consider a cavity quantum optomechanical system described by the cubic interaction Hamiltonian $H_{\rm INT} = -\hbar g_0 a^\dagger a(b + b^\dagger)$—see Eq. (6.3). Here, the dimensionless position quadrature of the mechanical oscillator $X_{\rm M} = (b+b^\dagger)/\sqrt{2}$ is *linearly coupled* the the intracavity photon number operator $a^\dagger a$. I will consider more general couplings of the position to $a^\dagger a$ in Section 11.2.

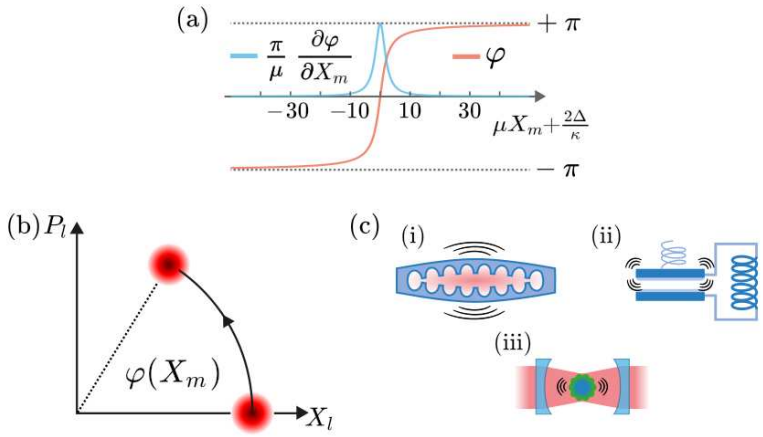


Figure 11.1: **Nonlinear cavity quantum optomechanical position measurement scheme.** (a) Plot of the optical phase $\varphi(X_{\rm M})$ and the mechanical momentum kick per photon $\partial\varphi(X_{\rm M})/\partial X_{\rm M}$ arising from the cavity-enhanced nonlinear optomechanical interaction. Here, μ is the dimensionless coupling strength and $X_{\rm M}$ is the mechanical position quadrature. At $\mu X_{\rm M} = -\frac{2\Delta}{\kappa}$, $\varphi(X_{\rm M}) = 0$ and $\partial\varphi(X_{\rm M})/\partial X_{\rm M} = \mu$. (b) In optical phase space there is a position-dependent rotation of an input coherent state owing to the nonlinearity of the radiation-pressure interaction as well as the full cavity response. This framework goes well beyond both the linearized regime, which approximates the rotation as a phase displacement, and treatments where the interaction is modelled as the unitary $e^{i\mu n_{\rm L} X_{\rm M}}$. (c) This framework is broadly applicable and example nonlinear optomechanical systems include: (i) photonic crystals, (ii) microwave LC resonators, (iii) levitation-based or cold-atom implementations.

By solving the Heisenberg-Langevin equations of motion for the optomechanical system, as will be detailed below, the nonlinear optomechanical interaction for an adiabatic cavity is described by the unitary $U = e^{i\varphi(X_{\rm M})n_{\rm L}}$. Here, the nonlinear phase is $\varphi(X_{\rm M}) = \arg(f)$, which is plotted in Fig. 11.1(a), where $f = \left[1 + i\left(\frac{\mu}{2}X_{\rm M} + \frac{\Delta}{\kappa}\right)\right] / \left[1 - i\left(\frac{\mu}{2}X_{\rm M} + \frac{\Delta}{\kappa}\right)\right]$, the nonlinear optomechanical coupling strength is $\mu = \sqrt{8}g_0/\kappa$, and the cavity detuning is Δ. Importantly, $n_{\rm L}$ is the photon number operator of the field entering or leaving the cavity[1], which

[1]Note, one should not confuse the intracavity photon number operator $a^\dagger a$ with $n_{\rm L}$.

for a pulse is defined over the entire temporal envelope, while in the continuous case is defined over an infinitesimal $\mathrm{d}t$. Hence, in the continuous case U represents an infinitesimal unitary from time t to $t+\mathrm{d}t$, which is sufficient to derive the SME.

When $\Delta = 0$, this nonlinear optomechanical phase agrees with the phase modelled in previous works to second order in X_{M} [1, 145], and the higher order terms in X_{M} account for the nonlinearity of the cavity-based radiation-pressure interaction. Moreover, to second order in X_{M}, the unitary $\mathrm{e}^{\mathrm{i}\varphi(X_{\mathrm{M}})n_{\mathrm{L}}}$ agrees with the cavity-free unitary $\mathrm{e}^{\mathrm{i}\mu n_{\mathrm{L}}X_{\mathrm{M}}}$, which will be discussed further in Section 11.1.4. Fig. 11.1(b) shows the rotation of an optical coherent state $|\alpha\rangle$ after the optomechanical interaction. For significant optical rotations, information about the mechanical position is encoded on both the phase P_{L} and amplitude X_{L} quadratures, signalling the breakdown of the linearized regime.

Fig. 11.1(c) gives some examples for cavity quantum optomechanical systems, which may be described by the nonlinear cavity-enhanced unitary $\mathrm{e}^{\mathrm{i}\varphi(X_{\mathrm{M}})n_{\mathrm{L}}}$. Such systems include, nanostring mechanical oscillators [132], sliced photonic crystal nanobeam resonators [133, 266], microwave nanoelectromechanical resonators [343], levitated optomechanical systems [344], and ultracold atom implementations [74, 345]. Compared to systems working in the linearized regime of optomechanics, large optical amplitudes are not required[2] in these intrinsically nonlinear systems. This allows for reduced optical absorption heating [346] compared to strategies that rely on large input powers.

11.1.1 Pulsed interaction

Adiabatic elimination of the cavity field

Pulsed optomechanics coincides with the unresolved sideband regime of optomechanics $\kappa \gg \omega_{\mathrm{M}}$ [139]. In this regime, the Heisenberg-Langevin equations describing the dynamics generated by $H/\hbar = -\Delta a^\dagger a - g_0 a^\dagger a(b+b^\dagger)$ are

$$\dot{a} = \mathrm{i}(\sqrt{2}g_0 X_{\mathrm{M}} + \Delta)a - \kappa a + \sqrt{2\kappa}a_{\mathrm{in}} \tag{11.1}$$

$$\dot{X}_{\mathrm{M}} = 0 \tag{11.2}$$

$$\dot{P}_{\mathrm{M}} = \sqrt{2}g_0 a^\dagger a, \tag{11.3}$$

for an input pulse with angular carrier frequency ω_{L} in a frame rotating at the cavity frequency ω_{C}. Here, the detuning is $\Delta = \omega_{\mathrm{L}} - \omega_{\mathrm{C}}$ and free mechanical evolution and dissipation are neglected as the interaction time is much less than the mechanical period. The operator $a_{\mathrm{in}}(t)$ describes the time-dependent input to the cavity mode and $X_{\mathrm{M}} = (b+b^\dagger)/\sqrt{2}$. Furthermore, in pulsed optomechanics the cavity field can be adiabatically eliminated $\dot{a} = 0$ if $\kappa \gg \tau_{in}^{-1}$, where τ_{in} is the characteristic timescale over which the input a_{in} changes. This may be

[2] Linearization is only valid for large optical amplitudes and in the limit of very small rotations—see Section 6.3.

shown in more detail by integrating Eq (11.1):

$$a(t) = \sqrt{2\kappa}\int_{-\infty}^{t} \mathrm{d}t'\; a_{\mathrm{in}}(t')\mathrm{e}^{-[\kappa-\mathrm{i}(\sqrt{2}g_0X_{\mathrm{M}}+\Delta)]|t-t'|}. \tag{11.4}$$

Generally, if $h(t')$ is a slowly varying function, such that $\kappa \gg \tau_h^{-1}$, where τ_h is the characteristic timescale over which the function $h(t')$ changes,

$$\begin{aligned} h(t')\mathrm{e}^{-\kappa|t-t'|} &\simeq h(t')\frac{2}{\kappa}\delta(t-t') \\ &= h(t)\frac{2}{\kappa}\delta(t-t') \\ &\simeq h(t)\mathrm{e}^{-\kappa|t-t'|}. \end{aligned} \tag{11.5}$$

Here, $\lim_{\kappa\to\infty}\frac{\kappa}{2}\mathrm{e}^{-\kappa|t-t'|} = \delta(t-t')$ has been used. This property (11.5) implies that $a_{\mathrm{in}}(t')\mathrm{e}^{-[\kappa-\mathrm{i}(\sqrt{2}g_0X_{\mathrm{M}}+\Delta)]|t-t'|} = a_{\mathrm{in}}(t)\mathrm{e}^{-[\kappa-\mathrm{i}(\sqrt{2}g_0X_{\mathrm{M}}+\Delta)]|t-t'|}$ if $\kappa \gg \tau_{in}^{-1}$, regardless of g_0, X_{M}, and Δ. The expression for $a(t)$ in Eq. (11.4) then becomes

$$\begin{aligned} a(t) &= \sqrt{2\kappa}a_{\mathrm{in}}(t)\int_{-\infty}^{t}\mathrm{d}t'\;\mathrm{e}^{-[\kappa-\mathrm{i}(\sqrt{2}g_0X_{\mathrm{M}}+\Delta)](t-t')} \\ &= \frac{\sqrt{2\kappa}}{\kappa-\mathrm{i}(\sqrt{2}g_0X_{\mathrm{M}}+\Delta)}a_{\mathrm{in}}(t), \end{aligned} \tag{11.6}$$

which amounts to adiabatic elimination of the cavity field $\dot{a}=0$ in Eq. (11.1).

Input-output relations

Using the input-output relations for the cavity $a_{\mathrm{out}}(t) = \sqrt{2\kappa}a(t) - a_{\mathrm{in}}(t)$, and defining the nonlinear optomechanical coupling strength $\mu = \sqrt{8}g_0/\kappa$, then gives

$$a_{\mathrm{out}}(t) = \frac{1+\mathrm{i}\left(\frac{\mu}{2}X_{\mathrm{M}}+\frac{\Delta}{\kappa}\right)}{1-\mathrm{i}\left(\frac{\mu}{2}X_{\mathrm{M}}+\frac{\Delta}{\kappa}\right)}a_{\mathrm{in}}(t). \tag{11.7}$$

While defining the photon number operator n_{L} to be[3]

$$\begin{aligned} n_{\mathrm{L}} &= \int_0^{\tau_p} a_{\mathrm{in}}^{\dagger}a_{\mathrm{in}}(t)\mathrm{d}t \\ &= \int_0^{\tau_p} a_{\mathrm{out}}^{\dagger}a_{\mathrm{out}}(t)\mathrm{d}t, \end{aligned} \tag{11.8}$$

allows Eq. (11.3) to be integrated, and using (11.6), one arrives at

$$P_{\mathrm{M}}(\tau_p) - P_{\mathrm{M}}(0) = \frac{\mu}{1+\left(\frac{\mu}{2}X_{\mathrm{M}}+\frac{\Delta}{\kappa}\right)^2}n_{\mathrm{L}}. \tag{11.9}$$

[3]Remember that in the adiabatic limit, the input and output pulses have the same temporal shape, as can be seen from Eq. (11.7).

Here, τ_p is the duration of the pulsed optomechanical interaction.

Introducing the nonlinear cavity response function

$$f(X_{\rm M}) = \frac{1 + {\rm i}\left(\frac{\mu}{2}X_{\rm M} + \frac{\Delta}{\kappa}\right)}{1 - {\rm i}\left(\frac{\mu}{2}X_{\rm M} + \frac{\Delta}{\kappa}\right)} \tag{11.10}$$

and the nonlinear phase

$$\varphi(X_{\rm M}) = \arg(f), \tag{11.11}$$

allows Eqs (11.7) and (11.9) to be written as

$$a_{\rm out} = f(X_{\rm M})a_{\rm in}, \tag{11.12}$$

$$P_{\rm M}(\tau_p) = P_{\rm M}(0) + \frac{\partial\varphi(X_{\rm M})}{\partial X_{\rm M}}n_{\rm L}, \tag{11.13}$$

which are equivalent to Heisenberg transformations

$$a_{\rm out} = U^\dagger a_{\rm in} U, \tag{11.14}$$

$$P_{\rm M}(\tau_p) = U^\dagger P_{\rm M}(0) U. \tag{11.15}$$

with the nonlinear pulsed optomechanical unitary given by $U = {\rm e}^{{\rm i}\varphi(X_{\rm M})n_{\rm L}}$. The equivalence between Eqs (11.12) and (11.14), may be understood via the equation for phase-space rotations $a_{\rm out} = {\rm e}^{{\rm i}\phi n_{\rm L}} a_{\rm in} {\rm e}^{-{\rm i}\phi n_{\rm L}} = (\cos\phi - {\rm i}\sin\phi)\, a_{\rm in}$. While the Hadamard lemma from Appendix A along with $[\varphi(X_{\rm M}), P_{\rm M}] = {\rm i}\dfrac{\partial\varphi(X_{\rm M})}{\partial X_{\rm M}}$, is used to derive the equivalence between Eqs (11.13) and (11.15). I will now discuss $\varphi(X_{\rm M})$ and its derivative more carefully.

Thinking about the phase $\varphi(X_{\rm m})$ more carefully

The nonlinear cavity response function $f(X_{\rm M})$ can be decomposed as $f(X_{\rm M}) = A(X_{\rm M}) + {\rm i}B(X_{\rm M})$ with

$$A(X_{\rm M}) = \frac{1 - \left(\frac{\mu}{2}X_{\rm M} + \frac{\Delta}{\kappa}\right)^2}{1 + \left(\frac{\mu}{2}X_{\rm M} + \frac{\Delta}{\kappa}\right)^2}, \tag{11.16}$$

$$B(X_{\rm M}) = \frac{2\left(\frac{\mu}{2}X_{\rm M} + \frac{\Delta}{\kappa}\right)}{1 + \left(\frac{\mu}{2}X_{\rm M} + \frac{\Delta}{\kappa}\right)^2}. \tag{11.17}$$

Therefore, one has

$$\begin{aligned}\varphi(X_{\rm M}) &= \arg\left(A+{\rm i}B\right) &(11.18)\\ &= \arctan\left(\frac{B}{A}\right)+F(A,B), &(11.19)\end{aligned}$$

$$F(A,B) = \begin{cases} 0 & \text{if } A>0 \\ +\pi & \text{if } A<0, \quad B\geq 0 \\ -\pi & \text{if } A<0, \quad B<0 \\ +\pi/2 & \text{if } A=0, \quad B>0 \\ -\pi/2 & \text{if } A=0, \quad B<0 \\ \text{undefined} & \text{if } A=B=0 \end{cases} \tag{11.20}$$

Note the case $A=B=0$ never arises as $A=0$ at $\mu X_{\rm M}/2+\Delta/\kappa=\pm 2$ and $B=0$ at $\mu X_{\rm M}/2+\Delta/\kappa=0$, but now one clearly sees why $-\pi<\varphi<\pi$ in Fig. 11.1(a). This π-phase limit is a key characteristic of the *cavity*-enhanced aspect of the unitary $\mathrm{e}^{{\rm i}\varphi(X_{\rm M})n_{\rm L}}$.

Furthermore, note that $A^2+B^2=1$ and as $\varphi(X_{\rm M})=\arg(f)=\arg(A+{\rm i}B)$, one has

$$\mathrm{e}^{{\rm i}\varphi}=\cos\varphi+{\rm i}\sin\varphi=f=A+{\rm i}B \tag{11.21}$$

and hence A and B can be rewritten as

$$\begin{aligned}A(X_{\rm M}) &= \cos\left[\varphi(X_{\rm M})\right], &(11.22)\\ B(X_{\rm M}) &= \sin\left[\varphi(X_{\rm M})\right], &(11.23)\end{aligned}$$

which clarifies that $U=\mathrm{e}^{{\rm i}\varphi(X_{\rm M})n_{\rm L}}$ rotates an initial coherent state through an angle $\varphi(X_{\rm M})$ for a given value of $X_{\rm M}$, i.e.

$$\begin{aligned}\mathrm{e}^{{\rm i}\varphi(X_{\rm M})n_{\rm L}}\left|\alpha\right\rangle &= \left|\alpha\mathrm{e}^{{\rm i}\varphi(X_{\rm M})}\right\rangle \\ &= \left|\alpha f(X_{\rm M})\right\rangle \\ &= \left|\alpha\left(A(X_{\rm M})+{\rm i}B(X_{\rm M})\right)\right\rangle \\ &= \left|\alpha\left(\cos\left[\varphi(X_{\rm M})\right]+{\rm i}\sin\left[\varphi(X_{\rm M})\right]\right)\right\rangle. &(11.24)\end{aligned}$$

Using the expression for $\varphi(X_{\rm M})$ in Eq. (11.19), then allows one to compute the derivative most straightforwardly

$$\frac{\partial\varphi(X_{\rm M})}{\partial X_{\rm M}} = \frac{\mu}{1+\left(\frac{\mu}{2}X_{\rm M}+\frac{\Delta}{\kappa}\right)^2}. \tag{11.25}$$

From Eq. (11.13), $\dfrac{\partial\varphi(X_{\rm M})}{\partial X_{\rm M}}$ represents momentum kick per photon, which is maximum when $\mu X_{\rm M}=-2\Delta/\kappa$. This implies that to achieve the maximum momentum kick, one must carefully consider the interplay between the detuning

of the drive from the cavity resonance Δ and the distribution of $X_{\rm M}$, which is discussed more in Chapter 14. More simply, taking $X_{\rm M}$ to be a constant value, one may choose a detuning $\Delta = -\frac{1}{2}\mu\kappa X_{\rm M}$ so that the input light is now effectively on resonance for a cavity with $X_{\rm M} \neq 0$. At $\mu X_{\rm M} = -\frac{2\Delta}{\kappa}$, $\varphi(X_{\rm M}) = 0$ and $\partial\varphi(X_{\rm M})/\partial X_{\rm M} = \mu$, which is equal to the nonlinear optomechanical coupling strength μ. Thus, the coupling strength μ indicates the maximum possible momentum kick per photon.

Agreement with the free-cavity and linearized unitaries

To second order in $X_{\rm M}$, and when $\Delta = 0$, $U = \mathrm{e}^{\mathrm{i}\varphi(X_{\rm M})n_{\rm L}}$ agrees with the nonlinear unitary $\mathrm{e}^{\mathrm{i}\mu X_{\rm M} n_{\rm L}}$. Setting $\Delta = 0$ and expanding $\varphi(X_{\rm M})$ in small $\mu X_{\rm M}$ about $\mu X_{\rm M} = 0$ gives

$$\varphi(X_{\rm M}) = \mu X_{\rm M} - \frac{1}{12}(\mu X_{\rm M})^3 + \frac{1}{80}(\mu X_{\rm M})^5 - \ldots \tag{11.26}$$

The higher orders in $X_{\rm M}$ account for the nonlinearity of the cavity response function. Furthermore, the linearized unitary $\mathrm{e}^{\mathrm{i}\chi X_{\rm L} X_{\rm M}}$ is recovered in the limit of small optical rotations and large intracavity amplitude: $a \to \alpha_c + \delta a$ and $|\alpha_c| \gg \delta a$. This was shown explicitly in Section 6.3.2, but to summarize: (i) small rotations and $\Delta = 0$ imply $\mathrm{e}^{\mathrm{i}\varphi(X_{\rm M})n_{\rm L}} \to \mathrm{e}^{\mathrm{i}\mu X_{\rm M} n_{\rm L}}$, and then (ii) linearization via $a \to \alpha_c + \delta a$ implies $\mathrm{e}^{\mathrm{i}\mu X_{\rm M} n_{\rm L}} \to \mathrm{e}^{\mathrm{i}\Omega X_{\rm M}}\mathrm{e}^{\mathrm{i}\chi X_{\rm L} X_{\rm M}}$.

11.1.2 Continuous infinitesimal unitary

Here, I construct the infinitesimal unitary that will be used to derive the SME. I derive the infinitesimal unitary in the interaction picture to carefully account for the effects of mechanical evolution.

Heisenberg-Langevin equations

For convenience, the optomechanical Hamiltonian of Eq. (6.3) is once again

$$\begin{aligned} H &= \hbar\omega_{\rm C} a^\dagger a + \hbar\omega_{\rm M} b^\dagger b - \hbar g_0 a^\dagger a(b + b^\dagger) \\ &= H_0 + H_{\rm INT}, && (11.27)\\ H_0 &= \hbar\omega_{\rm C} a^\dagger a + \hbar\omega_{\rm M} b^\dagger b, && (11.28)\\ H_{\rm INT} &= -\hbar g_0 a^\dagger a(b + b^\dagger). && (11.29) \end{aligned}$$

Transforming from the lab frame to a rotating frame using $\tilde{H} = U_F^\dagger H U_F + \mathrm{i}\hbar\dot{U}_F^\dagger U_F$, with $U_F = \mathrm{e}^{-\mathrm{i}\omega_{\rm L} a^\dagger a t - \mathrm{i}\omega_{\rm M} b^\dagger b t}$ gives

$$\begin{aligned} \tilde{H}/\hbar &= -\Delta a^\dagger a - g_0 a^\dagger a(b\mathrm{e}^{-\mathrm{i}\omega_{\rm M} t} + b^\dagger \mathrm{e}^{+\mathrm{i}\omega_{\rm M} t}), \\ &= -\Delta a^\dagger a - \sqrt{2} g_0 a^\dagger a \tilde{X}_{\rm M} && (11.30)\\ \tilde{X}_{\rm M} &= X_{\rm M}\cos\omega_{\rm M} t + P_{\rm M}\sin\omega_{\rm M} t, && (11.31)\\ \tilde{P}_{\rm M} &= P_{\rm M}\cos\omega_{\rm M} t - X_{\rm M}\sin\omega_{\rm M} t. && (11.32) \end{aligned}$$

In this rotating frame, the Heisenberg-Langevin equations with optical driving of the cavity are given by

$$\dot{X}_{\rm M} = -\sqrt{2}g_0 a^\dagger a \sin\omega_{\rm M} t, \tag{11.33}$$
$$\dot{P}_{\rm M} = \sqrt{2}g_0 a^\dagger a \cos\omega_{\rm M} t, \tag{11.34}$$
$$\dot{a} = +{\rm i}\left[\sqrt{2}g_0(X_{\rm M}\cos\omega_{\rm M} t + P_{\rm M}\sin\omega_{\rm M} t) + \Delta\right] a - \kappa a + \sqrt{2\kappa}a_{\rm in}. \tag{11.35}$$

Again, I have not included mechanical interactions with the bath as they aren't a part of the construction of the infinitesimal unitary. These mechanics-bath interactions will be included in the SME via a Lindblad dissipator. Solving these equations over an arbitrary infinitesimal time window $t \to t + {\rm d}t$ gives

$$X_{\rm M}(t+{\rm d}t) = X_{\rm M}(t) - \sqrt{2}g_0 a^\dagger a \sin(\omega_{\rm M} t){\rm d}t, \tag{11.36}$$
$$P_{\rm M}(t+{\rm d}t) = P_{\rm M}(t) + \sqrt{2}g_0 a^\dagger a \cos(\omega_{\rm M} t){\rm d}t, \tag{11.37}$$
$$a(t+{\rm d}t) = a(t) + {\rm i}\left(\sqrt{2}g_0\tilde{X}_{\rm M} + \Delta\right) a{\rm d}t - \kappa a{\rm d}t + \sqrt{2\kappa}a_{\rm in}{\rm d}t. \tag{11.38}$$

Good position measurements

In the 'good position measurement', the cavity field adiabatically follows the mechanical oscillator [138]. Such a measurement is readily achieved in the unresolved sideband regime $\kappa \gg \omega_{\rm M}$, as the cavity field responds quickly to the mechanical motion and adiabatically follows the mechanical oscillator [132]. Outside the unresolved sideband regime, adiabatic elimination of the cavity mode is also valid, provided the cavity decay rate exceeds other rates in the Hamiltonian [347].

I will now describe adiabatic elimination of the cavity mode in the unresolved sideband regime for a continuous drive, which enables a good position measurement. To see how adiabatic elimination of the cavity mode can be achieved outside of the unresolved sideband regime, see Appendix E.3.

Adiabatic elimination and input-output relations

Solving Eq. (11.35) over a short time interval $t - \tau \to t$ gives

$$a(t) = a(t-\tau){\rm e}^{-(\kappa - {\rm i}\Delta)\tau} + \int_{t-\tau}^{t} {\rm d}t' \left[\sqrt{2\kappa}a_{\rm in}(t') + {\rm i}\sqrt{2}g_0\tilde{X}_{\rm M}(t')a(t')\right] {\rm e}^{-[\kappa - {\rm i}\Delta](t-t')}. \tag{11.39}$$

As we are interested in deriving an infinitesimal unitary, we will shortly take the limit $\tau \to {\rm d}t$. The first term on the right-hand side of Eq. (11.39) is approximately zero when $\kappa\tau \gg 1$. The $a_{\rm in}(t')$ term may be pulled out of the integral and evaluated at t if the timescale on which it varies, $\tau_{\rm in}$, satisfies $\tau_{\rm in} \gg \tau \gg \kappa^{-1}$. Likewise, the $\tilde{X}_{\rm M}(t')$ term may be pulled out of the integral if $\kappa \gg \tau^{-1} \gg \omega_{\rm M}$. Notably, these inequalities are readily satisfied in the

unresolved sideband regime and in the limit $\tau \to \mathrm{d}t$. Thus, Eq. (11.39) now becomes

$$a(t) = \sqrt{2\kappa}\frac{a_{\mathrm{in}}(t)}{\kappa - \mathrm{i}\Delta}\left[1 - \mathrm{e}^{-(\kappa - \mathrm{i}\Delta)\tau}\right] + \mathrm{i}\sqrt{2}g_0\tilde{X}_{\mathrm{M}}(t)\int_{t-\tau}^{t}\mathrm{d}t' a(t')\mathrm{e}^{-[\kappa - \mathrm{i}\Delta](t-t')}. \tag{11.40}$$

As before, the $\mathrm{e}^{-(\kappa-\mathrm{i}\Delta)\tau}$ term is approximately zero when $\kappa\tau \gg 1$. Now, because $\kappa\tau \gg 1$, the integral term in Eq. (11.40) is only non-zero about $t' = t$, which enables the $a(t')$ to be pulled out of the integral and evaluated at t, and taking the limit $\tau \to \mathrm{d}t$, Eq. (11.40) now becomes

$$a(t) = \frac{\sqrt{2\kappa}a_{\mathrm{in}}(t)}{\kappa - \mathrm{i}\Delta} + \frac{\mathrm{i}\sqrt{2}g_0\tilde{X}_{\mathrm{M}}(t)a(t)}{\kappa - \mathrm{i}\Delta}, \tag{11.41}$$

which may be rearranged as

$$a(t) = \frac{\sqrt{2\kappa}a_{\mathrm{in}}(t)}{\kappa - \mathrm{i}\left(\sqrt{2}g_0\tilde{X}_{\mathrm{M}} + \Delta\right)}. \tag{11.42}$$

Therefore, in the adiabatic regime, the cavity field rapidly reaches the steady state $\dot{a} = 0$ on the order of $1/\kappa$ and so together with Eq. (11.42), the cavity input-output relation gives

$$a_{\mathrm{out}}(t) = \frac{1 + \mathrm{i}\left(\frac{\mu}{2}\tilde{X}_{\mathrm{M}}(t) + \frac{\Delta}{\kappa}\right)}{1 - \mathrm{i}\left(\frac{\mu}{2}\tilde{X}_{\mathrm{M}}(t) + \frac{\Delta}{\kappa}\right)}a_{\mathrm{in}}(t). \tag{11.43}$$

Notably, no statement was made about the size of the optomechanical coupling rate g_0.

The definition of the photon number operator in Eq. (11.8) implies that over a time increment $\mathrm{d}t$ the photon number operator outside the cavity is $n_{\mathrm{L}}(\mathrm{d}t) = a_{\mathrm{in}}^{\dagger}a_{\mathrm{in}}\mathrm{d}t$. Together with Eqs (11.36) and (11.37), this also implies

$$X_{\mathrm{M}}(t + \mathrm{d}t) = X_{\mathrm{M}}(t) - \frac{\mu}{1 + \left(\frac{\mu}{2}\tilde{X}_{\mathrm{M}} + \frac{\Delta}{\kappa}\right)^2}\sin(\omega_{\mathrm{M}}t)n_{\mathrm{L}}(\mathrm{d}t), \tag{11.44}$$

$$P_{\mathrm{M}}(t + \mathrm{d}t) = P_{\mathrm{M}}(t) + \frac{\mu}{1 + \left(\frac{\mu}{2}\tilde{X}_{\mathrm{M}} + \frac{\Delta}{\kappa}\right)^2}\cos(\omega_{\mathrm{M}}t)n_{\mathrm{L}}(\mathrm{d}t). \tag{11.45}$$

I now make an ansatz for the infinitesimal unitary in this interaction picture to be $U_I(\mathrm{d}t) = \mathrm{e}^{\mathrm{i}\varphi(\tilde{X}_{\mathrm{M}})n_{\mathrm{L}}(\mathrm{d}t)}$. Here, the dependence on $\mathrm{d}t$ is explicitly labelled. Similarly to the derivation of the pulsed nonlinear unitary, this ansatz can be shown to give the same expression as Eqs (11.43), (11.44) and (11.45) through

$$a_{\mathrm{out}}(t) = U_I^{\dagger}(\mathrm{d}t)a_{\mathrm{in}}(t)U_I(\mathrm{d}t), \tag{11.46}$$

$$X_{\mathrm{M}}(t + \mathrm{d}t) = U_I^{\dagger}(\mathrm{d}t)X_{\mathrm{M}}(t)U_I(\mathrm{d}t), \tag{11.47}$$

$$P_{\mathrm{M}}(t + \mathrm{d}t) = U_I^{\dagger}(\mathrm{d}t)P_{\mathrm{M}}(t)U_I(\mathrm{d}t). \tag{11.48}$$

To derive the last two equations, the Hadamard lemma was again employed and the following property was used: for a function $f(X_{\rm M}, P_{\rm M})$ of the two conjugate variables,

$$[f(X_{\rm M}, P_{\rm M}), X_{\rm M}] = -{\rm i}\frac{\partial f}{\partial P_{\rm M}}, \tag{11.49}$$

$$[f(X_{\rm M}, P_{\rm M}), P_{\rm M}] = +{\rm i}\frac{\partial f}{\partial X_{\rm M}}. \tag{11.50}$$

11.1.3 Dimensionless input and output operators

The $a_{\rm in}$ and $a_{\rm out}$ operators have dimensions of $\mathrm{s}^{-1/2}$. If one wants to work with dimensionless operators of the input and output pulses then

$$a_i = a_{\rm in}\sqrt{\tau} \tag{11.51}$$

may be introduced, where τ is either (i) the input pulse duration τ_p or (ii) the infinitesimal $\mathrm{d}t$ in the continuous case. This leads to the definition for the input photon number operator

$$n_{\rm L} = a_i^\dagger a_i, \tag{11.52}$$

which agrees with the definition Eq. (11.8) for short τ_p or if $a_{\rm in}^\dagger a_{\rm in}$ is approximately constant over the pulse envelope. In the adiabatic approximation, the output temporal shape will match the input temporal shape, so it is also valid to define the annihilation operator of the output pulse

$$a_o = a_{\rm out}\sqrt{\tau}. \tag{11.53}$$

Furthermore, the optomechanical interaction conserves photon number so

$$n_{\rm L} = a_o^\dagger a_o = a_i^\dagger a_i. \tag{11.54}$$

One may then multiply the left- and right-hand sides of the input-output equations by $\sqrt{\tau}$ to get a transformation for the dimensionless input-output operators. For example in the pulsed case, by multiplying Eq. (11.14) by $\sqrt{\tau}$, one has that

$$\begin{aligned} a_o &= {\rm e}^{-{\rm i}\varphi(X_{\rm M})n_{\rm L}} a_i {\rm e}^{{\rm i}\varphi(X_{\rm M})n_{\rm L}} \\ &= {\rm e}^{-{\rm i}\varphi(X_{\rm M})a_i^\dagger a_i} a_i {\rm e}^{{\rm i}\varphi(X_{\rm M})a_i^\dagger a_i} \\ &= {\rm e}^{{\rm i}\varphi(X_{\rm M})} a_i \\ &= f(X_{\rm M}) a_i. \end{aligned} \tag{11.55}$$

11.1.4 The cavity free limit

From Section 6.4.1, it was shown that for a cavity-free optomechanical system the pulsed optomechanical unitary is ${\rm e}^{{\rm i}\mu n_{\rm L} X_{\rm M}}$. Moreover, we now know that the

cavity-free unitary may be recovered by expanding the cavity-enhanced unitary to second order in $X_{\rm M}$ as discussed above. Therefore, the infinitesimal unitary in this interaction picture for the cavity free case is $U_I(\mathrm{d}t) = \mathrm{e}^{\mathrm{i}\mu n_{\rm L}(\mathrm{d}t)\tilde{X}_{\rm M}}$.

Due to the Euler identity

$$\mathrm{e}^{\mathrm{i}\mu X_{\rm M}} = \cos\mu X_{\rm M} + \mathrm{i}\sin\mu X_{\rm M}, \tag{11.56}$$

the equivalent of the A and B functions from Eqs (11.16) and (11.17) are

$$A(X_{\rm M}) = \cos\mu X_{\rm M} \tag{11.57}$$
$$B(X_{\rm M}) = \sin\mu X_{\rm M}. \tag{11.58}$$

Crucially, because $-\infty < \mu X_{\rm M} < \infty$, there is no π-phase limit for the cavity-free interaction. However, from Section 6.4.1 we know that truly cavity-free optomechanics is limited to $\mu = 4\pi x_0/\lambda$ and hence achieving a phase shift beyond π will require a mechanical state with a large spread in $X_{\rm M}$. In other words, for a mechanical state with a standard deviation in $X_{\rm M}$ of σ, one requires (i) $\mu\sigma \gtrsim 1$ and (ii) no cavity present[4] to begin to see these large phase shifts beyond π.

11.2 Arbitrary nonlinear position coupling

From Chapter 6, we know that for a single cavity mode and single mechanical mode, the dispersively coupled optomechanical Hamiltonian is given by

$$H = \hbar\omega_{\rm C}(x)a^\dagger a + \hbar\omega_{\rm M}b^\dagger b. \tag{11.59}$$

In the previous section, I considered the expansion of $\omega_{\rm C}(x)$ to first order in position. However, there is a growing amount of experimental evidence that in certain optomechanical systems, the function $\omega_{\rm C}(x)$ must be expanded to higher orders in position to accurately describe the intrinsically nonlinear physics. A combination of first and second order couplings have been seen in nanomechanical cantilever systems [108], photonic crystals [348], and with levitated nanoparticles [349]. Further, membrane-in-the-middles systems [78, 350] provide a route to tune the relative strengths of the first and second order couplings by carefully controlling the membrane position within the cavity. Moreover, couplings up to third order have been observed in microwave optomechanics [351] and even up to quartic order in membrane-in-the-middle systems [352].

Excitingly, the recent work of Ref. [353] in the classical domain with nanomechanical cantilevers has studied the nonlinearities induced by *both* the higher order terms in $\omega_{\rm C}(x)$ *and* the nonlinearity due to the cavity enhancement. Here, I provide an extension of the formalism developed in the previous sections to provide a quantum model that accounts for both types of nonlinearities: namely, nonlinear position coupling and the cavity enhancement.

[4] Otherwise, the unitary $\mathrm{e}^{\mathrm{i}\mu n_{\rm L}X_{\rm M}}$ is no longer valid if $\mu\sigma \gtrsim 1$.

11.2.1 The expanded optomechanical Hamiltonian

Expanding $\omega_{\rm C}(x)$ in position about $x = 0$ gives

$$\begin{aligned}\omega_{\rm C}(x) &= \omega_{\rm C}(0) + \frac{\partial\omega_{\rm C}}{\partial x}|_{x=0}x + \frac{1}{2}\frac{\partial^2\omega_{\rm C}}{\partial x^2}|_{x=0}x^2 + \ldots + \frac{1}{n!}\frac{\partial^n\omega_{\rm C}}{\partial x^n}|_{x=0}x^n + \ldots \\ &= \omega_{\rm C}(0) + \frac{1}{\sqrt{2}}\frac{\partial\omega_{\rm C}}{\partial x}|_{x=0}x_0(b+b^\dagger) + \frac{1}{4}\frac{\partial^2\omega_{\rm C}}{\partial x^2}|_{x=0}x_0^2(b+b^\dagger)^2 + \\ &\quad \ldots + \frac{1}{n!(\sqrt{2})^n}\frac{\partial^n\omega_{\rm C}}{\partial x^n}|_{x=0}x_0^n(b+b^\dagger)^n + \ldots, \end{aligned} \tag{11.60}$$

where $x = x_0X_{\rm M}$ and $X_{\rm M} = (b+b^\dagger)/\sqrt{2}$ was used. The optomechanical Hamiltonian is therefore given by[5]

$$H = H_0 + H_{\rm INT}, \tag{11.61}$$

$$H_0 = \hbar\omega_{\rm C}a^\dagger a + \hbar\omega_{\rm M}b^\dagger b, \tag{11.62}$$

$$H_{\rm INT} = -\hbar a^\dagger a\sum_{n=1}^{\infty}\left[g_0^{(n)}(b+b^\dagger)^n\right], \tag{11.63}$$

$$g_0^{(n)} = -\frac{1}{n!(\sqrt{2})^n}\frac{\partial^n\omega_{\rm C}}{\partial x^n}|_{x=0}x_0^n, \tag{11.64}$$

where $\omega_{\rm C}(0) = \omega_{\rm C}$ is used for brevity.

Furthermore, the operator-valued function

$$\mathcal{G}(X_{\rm M}) = \sum_{n=1}^{\infty}g_0^{(n)}(b+b^\dagger)^n \tag{11.65}$$

$$= \sum_{n=1}^{\infty}(\sqrt{2})^n g_0^{(n)}X_{\rm M}^n \tag{11.66}$$

can be defined, allowing the interaction term in the Hamiltonian to be written as

$$H_{\rm INT} = -\hbar a^\dagger a\mathcal{G}(X_{\rm M}). \tag{11.67}$$

11.2.2 Pulsed interaction

Heisenberg-Langevin equations for an adiabatic cavity

As before I consider the regime of pulsed optomechanics, where free mechanical evolution and dissipation may be ignored over the optomechanical interaction. Hence, the Heisenberg-Langevin equations generated by Eq. (11.61) in

[5] Note that I use the convention $x_0 = \sqrt{\frac{\hbar}{m\omega_{\rm M}}}$ from Chapter 2.

this regime are

$$\dot{X}_{\rm M} = 0, \tag{11.68}$$

$$\dot{P}_{\rm M} = \frac{\rm i}{\hbar}[H, P_{\rm M}], \tag{11.69}$$

$$\dot{a} = \frac{\rm i}{\hbar}[H, a] - \kappa a + \sqrt{2\kappa}a_{\rm in}. \tag{11.70}$$

Focusing first on the cavity mode, and using Eq. (11.61), one has

$$\dot{a} = {\rm i}\left[\mathcal{G}(X_{\rm M}) + \Delta\right] - \kappa a + \sqrt{2\kappa}a_{\rm in}, \tag{11.71}$$

where the detuning has been introduced $\Delta = \omega_{\rm L} - \omega_{\rm C}$.

Working in the same regime as in Section 11.1.1, the cavity mode may be adiabatically eliminated, which gives

$$a = \frac{\sqrt{2\kappa}}{\kappa - {\rm i}(\mathcal{G} + \Delta)}a_{\rm in}, \tag{11.72}$$

and then the input-output relation $a_{\rm out} = \sqrt{2\kappa}a - a_{\rm in}$ may be used to arrive at

$$a_{\rm out} = f(X)a_{\rm in}, \tag{11.73}$$

$$f(X_{\rm M}) = \frac{\kappa + {\rm i}(\mathcal{G} + \Delta)}{\kappa - {\rm i}(\mathcal{G} + \Delta)}, \tag{11.74}$$

where $f(X_{\rm M})$ is now more general than in Section 11.1.1. One may also multiply by $\sqrt{\tau}$, giving $a_o = f(X)a_i$, which is the expression for the dimensionless annihilation input-output operators.

The mechanical mode

Turning to the mechanical momentum, the equation for $\dot{P}_{\rm M}$ is

$$\dot{P}_{\rm M} = -{\rm i}a^\dagger a \sum_{n=1}^{\infty} (\sqrt{2})^n g_0^{(n)} [X_{\rm M}^n, P_{\rm M}] \tag{11.75}$$

$$= a^\dagger a \sum_{n=1}^{\infty} (\sqrt{2})^n g_0^{(n)} n X_{\rm M}^{n-1} \tag{11.76}$$

$$= \frac{\partial \mathcal{G}(X_{\rm M})}{\partial X_{\rm M}} a^\dagger a, \tag{11.77}$$

where $[X_{\rm M}^n, P_{\rm M}] = {\rm i}n X_{\rm M}^{n-1}$ was used. Inserting Eq. (11.72) for the cavity mode and integrating over τ leads to

$$P'_{\rm M} = P_{\rm M} + \frac{\partial \mathcal{G}(X_{\rm M})}{\partial X_{\rm M}} \frac{2\kappa}{\kappa^2 + (\mathcal{G} + \Delta)^2} n_{\rm L}, \tag{11.78}$$

where $P'_{\rm M} = P_{\rm M}(\tau)$ and $P_{\rm M} = P_{\rm M}(0)$.

The pulsed unitary

Now I make the ansatz $U = \mathrm{e}^{\mathrm{i}\varphi(X_{\mathrm{M}})n_{\mathrm{L}}}$ and show it works for both the optical and mechanical mode transformations, i.e. Eqs (11.73) and (11.78). Once again, $\varphi(X_{\mathrm{M}})$ is different, and more general, than the same expression in Section 11.1.1. Firstly, for the optical mode

$$\begin{aligned} a_{\mathrm{out}} &= U^{\dagger}a_{\mathrm{in}}U && (11.79)\\ &= \mathrm{e}^{-\mathrm{i}\varphi(X_{\mathrm{M}})n_{\mathrm{L}}}a_{\mathrm{in}}\mathrm{e}^{\mathrm{i}\varphi(X_{\mathrm{M}})n_{\mathrm{L}}} && (11.80)\\ &= \mathrm{e}^{\mathrm{i}\varphi(X_{\mathrm{M}})}a_{\mathrm{in}}, && (11.81)\end{aligned}$$

which agrees with Eq. (11.73) if

$$\varphi = \arg(f), \tag{11.82}$$

which can be satisfied as $|f|^2 = 1$. Now turning to the mechanics. The position is simply preserved by the unitary transformation $X'_{\mathrm{M}} = U^{\dagger}X_{\mathrm{M}}U = X_{\mathrm{M}}$. However, the transformation for the momentum operator is

$$\begin{aligned} P'_{\mathrm{M}} &= U^{\dagger}P_{\mathrm{M}}U && (11.83)\\ &= \mathrm{e}^{-\mathrm{i}\varphi(X_{\mathrm{M}})n_{\mathrm{L}}}P_{\mathrm{M}}\mathrm{e}^{\mathrm{i}\varphi(X_{\mathrm{M}})n_{\mathrm{L}}}. && (11.84)\end{aligned}$$

I will use the Hadamard lemma to simplify this expression, but let's first again decompose $f = A + \mathrm{i}B$

$$\begin{aligned} A(X_{\mathrm{M}}) &= \frac{1-\left(\frac{\mathcal{G}}{\kappa}+\frac{\Delta}{\kappa}\right)^2}{1+\left(\frac{\mathcal{G}}{\kappa}+\frac{\Delta}{\kappa}\right)^2}, && (11.85)\\ B(X_{\mathrm{M}}) &= \frac{2\left(\frac{\mathcal{G}}{\kappa}+\frac{\Delta}{\kappa}\right)}{1+\left(\frac{\mathcal{G}}{\kappa}+\frac{\Delta}{\kappa}\right)^2}. && (11.86)\end{aligned}$$

After this I focus on the first commutator in the Hadamard lemma, which is

$$[\varphi(X_{\mathrm{M}}), P_{\mathrm{M}}] = \mathrm{i}\frac{\partial\varphi(X_{\mathrm{M}})}{\partial X_{\mathrm{M}}}. \tag{11.87}$$

To evaluate this note that

$$\varphi(X_{\mathrm{M}}) = \arg(f) = \arctan\left(\frac{B}{A}\right) + F(A,B) \tag{11.88}$$

where, $F(A,B)$ depends on the quadrant of phase space f via Eq. (11.20). However, one need not specify the value of $F(A,B)$ as it is the derivative that is interesting

$$\begin{aligned} \frac{\partial\varphi(X_{\mathrm{M}})}{\partial X_{\mathrm{M}}} &= \frac{\partial}{\partial X_{\mathrm{M}}}\arctan\left(\frac{B}{A}\right) && (11.89)\\ &= \frac{\partial\mathcal{G}(X_{\mathrm{M}})}{\partial X_{\mathrm{M}}}\frac{2\kappa}{\kappa^2+(\mathcal{G}+\Delta)^2}, && (11.90)\end{aligned}$$

which is just a function of $X_{\rm M}$ so all higher order terms in the Hadamard lemma vanish and therefore

$$P'_{\rm M} = P_{\rm M} + \frac{\partial \mathcal{G}(X_{\rm M})}{\partial X_{\rm M}} \frac{2\kappa}{\kappa^2 + (\mathcal{G} + \Delta)^2} n_{\rm L}, \tag{11.91}$$

which agrees with Eq. (11.78). Thus, $U = \mathrm{e}^{\mathrm{i}\varphi(X_{\rm M})n_{\rm L}}$ is the correct unitary for the nonlinear pulsed optomechanical interaction with arbitrary position coupling.

11.2.3 Continuous infinitesimal unitary

The derivation of Section 11.1.2 may be repeated for the arbitrary nonlinear coupling to mechanical position given by $H_{\rm INT} = -\hbar a^\dagger a \mathcal{G}(X_{\rm M})$ to find the unitary that describes an infinitesimal time step from t to $t + \mathrm{d}t$. However, as we learnt from this section, the limit $\tau \to \mathrm{d}t$ may simply be taken to arrive at $U_I(\mathrm{d}t) = \mathrm{e}^{\mathrm{i}\varphi(\tilde{X}_{\rm M})n_{\rm L}(\mathrm{d}t)}$, where $\varphi = \arg(f)$, which now describes the arbitrary nonlinear position coupling via Eq. (11.74).

11.2.4 The cavity free limit

Similar to the linear position coupling to $a^\dagger a$, there exists a 'cavity free' limit for the arbitrary position coupling to $a^\dagger a$. In this regime, the cavity free unitary generalizes to $U = \mathrm{e}^{2\mathrm{i}\frac{\mathcal{G}(X_{\rm M})}{\kappa}n_{\rm L}}$, which agrees with the unitary $\mathrm{e}^{\mathrm{i}\mu n_{\rm L} X_{\rm M}}$ in the limit of linear coupling: $g_0^{(1)} = g_0$ and $g_0^{(n)} = 0$ for $n \neq 1$.

Once again, the Euler identity is used, which gives

$$\mathrm{e}^{2\mathrm{i}\frac{\mathcal{G}(X_{\rm M})}{\kappa}} = \cos\left(\frac{2\mathcal{G}(X_{\rm M})}{\kappa}\right) + \mathrm{i}\sin\left(\frac{2\mathcal{G}(X_{\rm M})}{\kappa}\right), \tag{11.92}$$

and so the A and B functions are then

$$A(X_{\rm M}) = \cos\left(\frac{2\mathcal{G}(X_{\rm M})}{\kappa}\right) \tag{11.93}$$

$$B(X_{\rm M}) = \sin\left(\frac{2\mathcal{G}(X_{\rm M})}{\kappa}\right). \tag{11.94}$$

Importantly, as $-\infty < X_{\rm M} < \infty$ and $\mathcal{G}(X_{\rm M})$ is a simply polynomial operator-valued function of $X_{\rm M}$, there is also no π-phase limit and this is why we refer to $U = \mathrm{e}^{2\mathrm{i}\frac{\mathcal{G}(X_{\rm M})}{\kappa}n_{\rm L}}$ as the cavity free limit.

Details on reaching the cavity free limit

To show that $U = \mathrm{e}^{2\mathrm{i}\frac{\mathcal{G}(X_{\rm M})}{\kappa}n_{\rm L}}$ agrees with the unitary $\mathrm{e}^{\mathrm{i}\varphi(X_{\rm M})n_{\rm L}}$ in the cavity free limit limit, set $\Delta = 0$ and then expand both the functions $\mathrm{e}^{2\mathrm{i}\frac{\mathcal{G}(X_{\rm M})}{\kappa}}$ and $\mathrm{e}^{\mathrm{i}\varphi(X_{\rm M})}$ in $X_{\rm M}$. It is then seen that $\mathrm{e}^{2\mathrm{i}\frac{\mathcal{G}(X_{\rm M})}{\kappa}}$ is equal to $\mathrm{e}^{\mathrm{i}\varphi(X_{\rm M})}$ *up to second order* in the $g_0^{(n)}$ coefficients. In other words, by expanding in $X_{\rm M}$, one finds that

$$\mathrm{e}^{2\mathrm{i}\frac{\mathcal{G}(X_{\rm M})}{\kappa}} = \mathrm{e}^{\mathrm{i}\varphi(X_{\rm M})} + \mathcal{O}(g_0^{(n)} g_0^{(m)} g_0^{(l)}). \tag{11.95}$$

11.3 Summary of all the optomechanical unitaries

For an adiabatic cavity with the optomechanical interaction Hamiltonian $H_{\rm INT}$ and a drive detuned from resonance by Δ, the pulsed optomechanical unitary is $\mathrm{e}^{\mathrm{i}\varphi(X_{\rm M})n_{\rm L}}$ and the continuous unitary describing an infinitesimal time step from t to $t+\mathrm{d}t$ is $U_I(\mathrm{d}t)=\mathrm{e}^{\mathrm{i}\varphi(\tilde{X}_{\rm M})n_{\rm L}(\mathrm{d}t)}$. Here, $\mathrm{e}^{\mathrm{i}\varphi(X_{\rm M})}=f(X_{\rm M})=A(X_{\rm M})+\mathrm{i}B(X_{\rm M})$. Table 11.1 gives the expressions for $H_{\rm INT}$, $f(X_{\rm M})$, $A(X_{\rm M})$, and $B(X_{\rm M})$ in the different regimes of optomechanics described above—as well as discussing linearized optomechanics for both arbitrary-position and linear-position coupling.

What is the point of this table?

In what follows, many of the results can be extended to the various regimes described by Table 11.1 by choosing the functions $f(X_{\rm M})$, $A(X_{\rm M})$, and $B(X_{\rm M})$ appropriately. For example, in Chapter 12, the measurement operator and SME can be used to describe these different regimes, simply by replacing the functions $A(X_{\rm M})$, and $B(X_{\rm M})$ according to Table 11.1.

Linearized optomechanics

Table 11.1 also shows the linearized unitary $\mathrm{e}^{\mathrm{i}\Omega X_{\rm M}}\mathrm{e}^{\mathrm{i}\chi X_{\rm L}X_{\rm M}}$, which may be derived from the cavity free unitary $\mathrm{e}^{\mathrm{i}\mu n_{\rm L}X_{\rm M}}$ by linearizing via $n_{\rm L}\to N_{\rm P}+\sqrt{2N_{\rm P}}X_{\rm L}$ as in Section 6.3.2. Note that as $\mathrm{e}^{\mathrm{i}\Omega X_{\rm M}}\mathrm{e}^{\mathrm{i}\chi X_{\rm L}X_{\rm M}}$ no longer describes a rotation, it is no longer appropriate to assign it a function $f(X_{\rm M})$. However, I have put an entry in the $B(X_{\rm M})$ function to indicate that the phase quadrature $P_{\rm L}$ does contain information about the mechanical position. Meanwhile, the entry for the $A(X_{\rm M})$ function is left blank as no information about $X_{\rm M}$ is encoded in the $X_{\rm L}$ quadrature in the linearized regime.

In Table 11.1, I also introduce the linearized regime with nonlinear position coupling $\mathrm{e}^{2\mathrm{i}\frac{\mathcal{G}(X_{\rm M})}{\kappa}N_{\rm P}}\mathrm{e}^{2\sqrt{2}\mathrm{i}\frac{\mathcal{G}(X_{\rm M})\sqrt{N_{\rm P}}}{\kappa}X_{\rm L}}$, which may be derived from the cavity free unitary $\mathrm{e}^{2\mathrm{i}\frac{\mathcal{G}(X_{\rm M})}{\kappa}n_{\rm L}}$ by linearizing via $n_{\rm L}\to N_{\rm P}+\sqrt{2N_{\rm P}}X_{\rm L}$.

Clarifying comment on the term 'cavity free'

Note the term 'cavity free' could be slightly misleading in this chapter. Here, I mean that these cavity free unitaries have the *same form*[6] as an interaction taking place with no cavity present. Hence there is no π-phase limit encoded in these unitaries[7]. There may still be the enhancement to the interaction from the cavity due to multiple reflections, which can be seen via the presence of κ in the cavity free and linearized unitaries. However, the nonlinearity of the cavity response is not apparent in these cases.

[6] With different coefficients, i.e. $\mu=\sqrt{8}g_0/\kappa$ is replaced by $\mu=4\pi x_0/\lambda$ when there is no actual cavity present—see the Supplementary of Ref. [155].

[7] Of course, if a cavity is present there ultimately must be a π-phase limit and so these cavity free unitaries are not valid for large optical rotations $\mu\sigma$ if a cavity is present.

Table 11.1: **Summary of all the optomechanical unitaries in the adiabatic regime.** (i) Cavity-enhanced with arbitrary nonlinear position coupling. Here, $\mathcal{G}(X_{\rm M}) = \sum_{n=1}^{\infty}(\sqrt{2})^n g_0^{(n)} X_{\rm M}^n$ and $\varphi = \arg(f)$. (ii) Cavity-enhanced with linear position coupling, which corresponds to taking $g_0^{(1)} = g_0$ and $g_0^{(n)} = 0$ for $n \neq 1$. Here, $\varphi = \arg(f)$ too. (iii) Cavity-free with arbitrary nonlinear position coupling. (iv) Cavity-free with linear position coupling. Here, $\mu = \sqrt{8} g_0/\kappa$. (v) Linearized optomechanics with nonlinear position coupling. Here, $\alpha_{\rm c}$ is the mean intracavity amplitude and $N_{\rm P}$ is the mean number of photons in the input pulse. (vi) Linearized optomechanics with linear position coupling. Here, $g = \alpha g_0$ and $\chi = \mu\sqrt{2N_{\rm P}}$. Note that unitaries (iii)-(vi) do not typically include a detuning Δ and the Kerr-like terms ($\propto N_{\rm P}$) have been left out of (v) and (vi) for space.

	$H_{\rm INT}/\hbar$	U	$f(X_{\rm M})$	$A(X_{\rm M})$	$B(X_{\rm M})$
(i)	$-\mathcal{G}(X_{\rm M})a^\dagger a$	$\mathrm{e}^{\mathrm{i}\varphi(X_{\rm M})n_{\rm L}}$	$\mathrm{e}^{\mathrm{i}\varphi(X_{\rm M})} = \dfrac{\kappa + \mathrm{i}(\mathcal{G}+\Delta)}{\kappa - \mathrm{i}(\mathcal{G}+\Delta)}$	$\dfrac{1-\left(\frac{\mathcal{G}}{\kappa}+\frac{\Delta}{\kappa}\right)^2}{1+\left(\frac{\mathcal{G}}{\kappa}+\frac{\Delta}{\kappa}\right)^2}$	$\dfrac{2\left(\frac{\mathcal{G}}{\kappa}+\frac{\Delta}{\kappa}\right)}{1+\left(\frac{\mathcal{G}}{\kappa}+\frac{\Delta}{\kappa}\right)^2}$
(ii)	$-\sqrt{2}g_0 a^\dagger a X_{\rm M}$	$\mathrm{e}^{\mathrm{i}\varphi(X_{\rm M})n_{\rm L}}$	$\mathrm{e}^{\mathrm{i}\varphi(X_{\rm M})} = \dfrac{1+\mathrm{i}\left(\frac{\mu}{2}X_{\rm M}+\frac{\Delta}{\kappa}\right)}{1-\mathrm{i}\left(\frac{\mu}{2}X_{\rm M}+\frac{\Delta}{\kappa}\right)}$	$\dfrac{1-\left(\frac{\mu}{2}X_{\rm M}+\frac{\Delta}{\kappa}\right)^2}{1+\left(\frac{\mu}{2}X_{\rm M}+\frac{\Delta}{\kappa}\right)^2}$	$\dfrac{2\left(\frac{\mu}{2}X_{\rm M}+\frac{\Delta}{\kappa}\right)}{1+\left(\frac{\mu}{2}X_{\rm M}+\frac{\Delta}{\kappa}\right)^2}$
(iii)	$-\mathcal{G}(X_{\rm M})a^\dagger a$	$\mathrm{e}^{2\mathrm{i}\frac{\mathcal{G}(X_{\rm M})}{\kappa}n_{\rm L}}$	$\mathrm{e}^{2\mathrm{i}\frac{\mathcal{G}(X_{\rm M})}{\kappa}}$	$\cos\left(\dfrac{2\mathcal{G}(X_{\rm M})}{\kappa}\right)$	$\sin\left(\dfrac{2\mathcal{G}(X_{\rm M})}{\kappa}\right)$
(iv)	$-\sqrt{2}g_0 a^\dagger a X_{\rm M}$	$\mathrm{e}^{\mathrm{i}\mu n_{\rm L} X_{\rm M}}$	$\mathrm{e}^{\mathrm{i}\mu X_{\rm M}}$	$\cos\mu X_{\rm M}$	$\sin\mu X_{\rm M}$
(v)	$-\sqrt{2}\alpha_{\rm c}\mathcal{G}(X_{\rm M})X_{\rm L}$	$\mathrm{e}^{2\sqrt{2}\mathrm{i}\frac{\mathcal{G}(X_{\rm M})\sqrt{N_{\rm P}}}{\kappa}X_{\rm L}}$	N/A	N/A	$\sim \mathcal{G}(X_{\rm M})$
(vi)	$-2gX_{\rm L}X_{\rm M}$	$\mathrm{e}^{\mathrm{i}\chi X_{\rm L}X_{\rm M}}$	N/A	N/A	$\sim X_{\rm M}$

11.4 Conclusion and outlook

Here, I have developed the framework of nonlinear cavity quantum optomechanics for adiabatic cavities. The nonlinearity of this framework includes the intrinsic nonlinearity of the radiation-pressure interaction, the nonlinear role of the cavity, and the nonlinearities coming from arbitrarily high-orders of mechanical position in the expansion of the cavity frequency. I have also demonstrated how this more general theory recovers the cavity-free and linearized regimes of optomechanics.

The unitary interactions introduced here have a wide range of applications in nonlinear optomechanics including developing quantum state engineering protocols, studying fundamental physics in strongly interacting light-matter devices, and extending the toolset of quantum metrology. Finally, the theory developed here may be utilized to achieve position measurement in nonlinear optomechanics, which I describe in the next chapter.

Chapter 12

The nonlinear measurement operator and stochastic master equation for position measurement

This chapter draws heavily from Ref. [7], where this work was originally published.

In linearized optomechanics the mechanical position is linearly transduced onto the phase quadrature of light. Phase homodyne measurements are then made on the light field, which constitutes a position measurement. This very simple description describes much of position measurement in optomechanics both theoretically and experimentally. However, in the previous chapter we saw that beyond the linearized regime of optomechanics the mechanical position is imprinted onto the optical field in a much more interesting and complex way. Mechanical information is transduced onto both the phase and amplitude quadratures of light and for large optical rotations, the response of the cavity means that mechanical position is nonlinearly transduced as well.

Building on the theory of the last chapter, a general-dyne detection scheme for position measurement is now introduced. By measuring both the phase and amplitude quadratures, general-dyne detection allows mechanical information to be measured in a more optimal way. Furthermore, as both pulsed and infinitesimal unitaries have been derived for the nonlinear optomechanical interaction, I now develop a theory for both pulsed *and* continuous position measurements. Mathematically, this corresponds to deriving both a measurement operator and a stochastic master equation to describe the pulsed and continuous measurements respectively. I would like to remind the reader that by choosing the A and B functions according to Table 11.1, the general theory presented here can

be used to describe position measurement for all the regimes of adiabatic optomechanics. In Chapters 13 and 14, I will discuss the general theory developed here for the case of a linearly coupled optomechanical system in a greater level of detail.

12.1 The need for a theory of nonlinear position measurement

Position measurements in optomechanics are important for a broad range of sensing applications, as well as a variety of quantum measurement and control protocols. Thus far, theory and experiment have focused on the linearized regime of optomechanics to achieve position measurements. Nevertheless, the optomechanical sensing of position underpins a plethora of technologies including the detection of single-spins [187] and bacterial resistance to antibiotics [354], the development of ultrasensitive measurements of accelerations [355, 356] and magnetic fields [357, 358], yoctogram resolution mass sensing [359, 360], and weak force sensors operating at the zeptonewton scale [361, 88]. Precision linear position measurement also provides a valuable tool for tests of fundamental physics, notably with the detection of gravitational waves by LIGO [84, 85], paving the way for the search of new physics [362]. Direct gravitational detection of dark matter with arrays of mechanical sensors [363, 364] has been proposed, as have methods to explore modifications to Newtonian gravity beyond the standard model with optomechanics [365, 366]. A continuous position measurement made with light is limited by radiation-pressure back-action and photon shot noise [68, 367]. A careful balance between these two noise sources defines the standard quantum limit (SQL) [368], which underpins the sensitivity of a wide range of optomechanics experiments [110, 369, 112]. However, back-action evading (BAE) measurements may be employed to surpass the SQL [143] by measuring only one mechanical quadrature, which can be achieved via a number of techniques such as two-tone drives [370, 371, 372] and using pulses much shorter than the mechanical period [142, 139, 140]. Together with feedback cooling techniques [373, 374] and exploiting output correlations between amplitude and phase fluctuations [375], position measurement sensitivity has recently been observed below the SQL in experiment [376].

These optomechanical measurement techniques operate in the linearized regime of optomechanics where the inherently nonlinear interaction [97] is linearized about the intracavity amplitude. Nonlinearities may then be introduced via a Duffing-type nonlinearity to the mechanical mode [152, 153] or by dispersively coupling to the position squared [78, 377] to observe nonlinear dynamics such as mechanical self oscillations [378, 379] and chaos [380, 381]. However, when the intrinsic optomechanical nonlinearity itself produces significant optical rotations, corrections to linear optomechanical phenomena [382, 383, 384, 385] and distinctly nonlinear effects [118, 119, 386] can be observed. In this regime, the mechanical signal is transduced onto both optical phase and amplitude

quadratures, allowing for selective position-squared measurements [176], and the generation of macroscopic superposition states [161, 155] and non-Gaussian mechanical entanglement [293, 6, 387]. Optomechanics experiments are now becoming highly nonlinear as increasingly larger optomechanical coupling rates are achieved [112, 113, 114]. A combination of the importance of optomechanical position measurements and recent observations of optical rotations that cannot be described by previous frameworks [132, 133, 134], elucidates the need for a nonlinear theory of optomechanical position measurements, which is capable of describing *both* the nonlinearity of radiation pressure *and* the nonlinear role of the cavity.

Using the theory developed in the last chapter, I now describe our position measurement scheme for nonlinear cavity quantum optomechanics based on general-dyne detection.

12.2 General-dyne detection scheme

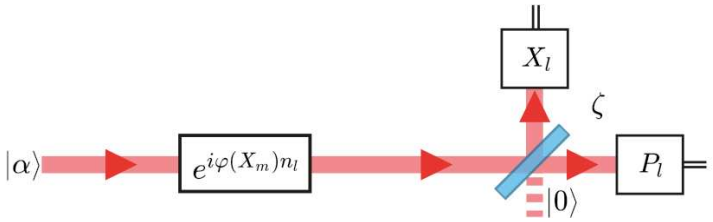


Figure 12.1: **General-dyne measurement scheme.** An optical coherent state $|\alpha\rangle$ interacts with a mechanical oscillator and is then measured by a general-dyne detector, which may be realized with a beamsplitter $U_{\rm bs}$ of variable transmission coefficient ζ, vacuum on one input, and amplitude and phase homodyne measurements at the outputs.

Beyond the linearized regime of optomechanics, information about the mechanical position is encoded on *both* the phase $P_{\rm L}$ and amplitude $X_{\rm L}$ quadratures of light after an optomechanical interaction. Hence, a general-dyne measurement scheme to extract mechanical position information encoded on both optical quadratures may be employed to best measure the mechanical position. In the general-dyne position measurement scheme, Fig. 12.1, the optical state after the nonlinear optomechanical interaction $U = \mathrm{e}^{\mathrm{i}\varphi(X_{\rm M})n_{\rm L}}$ is measured by the general-dyne detector, At the output of the optomechanical cavity, the optical mode mixes with vacuum $|0\rangle$ at a beamsplitter, described by $U_{\rm bs}$. While at the beamsplitter outputs, light is sent towards the phase $P_{\rm L}$ or amplitude $X_{\rm L}$ homodyne, in a proportion determined by the beamsplitter coefficient ζ.

Below I discuss how this general-dyne measurement scheme can be operated in a pulsed or continuous fashion. Mathematically, pulsed operation leads to a measurement operator description, while continuous operation is described by

a SME. In Chapters 13 and 14, I then focus on the linear coupling to position $a^\dagger a X_{\rm M}$ and explore each of these approaches in a much greater level of detail, as in Ref. [7].

12.3 Measurement operator

Eq. (11.24) may be generalized to describe the different regimes in Table 11.1. Namely, the nonlinear pulsed unitary $U = \mathrm{e}^{\mathrm{i}\varphi(X_{\rm M})n_{\rm L}}$ acts on the input coherent state $|\alpha\rangle$ via

$$U|\alpha\rangle = |\alpha\left(A(X_{\rm M}) + \mathrm{i}B(X_{\rm M})\right)\rangle\,, \tag{12.1}$$

where the cavity response function has been decomposed into its real and imaginary parts $f(X_{\rm M}) = A(X_{\rm M}) + \mathrm{i}B(X_{\rm M})$ and where, for each regime of adiabatic optomechanics introduced in the previous chapter, the functions A and B are given by Table 11.1. Hence, U rotates the initial coherent state through an angle $\varphi(X_{\rm M})$ for a given value of $X_{\rm M}$.

The nonlinear pulsed optomechanical interaction, followed by optical general-dyne measurement as in Fig. 12.1, therefore yields the measurement operator

$$\begin{aligned}
\Upsilon &= \langle X_{\rm L}|\langle P_{\rm L}|U_{\rm bs}U|\alpha\rangle|0\rangle \\
&= \left\langle X_{\rm L}\middle|\sqrt{1-\zeta^2}\alpha(A(X_{\rm M})+\mathrm{i}B(X_{\rm M}))\right\rangle\langle P_{\rm L}|\zeta\alpha(A(X_{\rm M})+\mathrm{i}B(X_{\rm M}))\rangle \\
&= \frac{1}{\sqrt{\pi}}\exp\Big[-\frac{1}{2}\Big(X_{\rm L}-\sqrt{1-\zeta^2}X_\alpha A(X_{\rm M})\Big)^2 \\
&\qquad -\frac{1}{2}\left(P_{\rm L}-\zeta X_\alpha B(X_{\rm M})\right)^2 - \mathrm{i}\zeta X_\alpha P_{\rm L}A(X_{\rm M}) \\
&\qquad +\mathrm{i}\sqrt{1-\zeta^2}X_\alpha X_{\rm L}B(X_{\rm M}) - \frac{\mathrm{i}}{2}(1-2\zeta^2)X_\alpha^2 A(X_{\rm M})B(X_{\rm M})\Big],
\end{aligned} \tag{12.2}$$

where $\alpha = X_\alpha/\sqrt{2}$ and X_α is assumed real without loss of generality. Here, the formula for the overlap between a quadrature state and a coherent state from Appendix A was used.

12.4 Stochastic master equation

In Chapter 11, I derived the infinitesimal[1] unitary operator $U_I(\Delta t)$ to describe the time step $t \to t + \Delta t$ of a continuous optomechanical interaction. To be careful, and to highlight the core physics, I worked in the interaction picture and thus moved to a rotating frame. I will do the same here again to derive the SME describing a continuous position measurement via optical general-dyne detection. After this, I will return to the lab frame.

[1] Here, I work with a time interval Δt and will later take the limit $\Delta t \to \mathrm{d}t$.

12.4.1 Infinitesimal measurement operator in rotating frame

The infinitesimal measurement operator $\Upsilon_I(\Delta t)$ describes the action of the continuous general-dyne measurement of Fig. 12.1 over a small time increment Δt. In the rotating frame, it is given by

$$\begin{aligned}\Upsilon_I(\Delta t) &= \langle X_{\rm L}|\langle P_{\rm L}|U_{\rm bs}U_I(\Delta t)|\alpha\rangle|0\rangle \\ &= \left\langle X_{\rm L}\middle|\sqrt{1-\zeta^2}\alpha\left(A(\tilde{X_{\rm M}})+{\rm i}B(\tilde{X_{\rm M}})\right)\right\rangle\left\langle P_{\rm L}\middle|\zeta\alpha\left(A(\tilde{X_{\rm M}})+{\rm i}B(\tilde{X_{\rm M}})\right)\right\rangle \\ &= \Upsilon_I(X_{\rm L})\Upsilon_I(P_{\rm L}), \end{aligned} \tag{12.3}$$

$$\Upsilon_I(X_{\rm L}) = \frac{1}{\pi^{\frac{1}{4}}}\exp\Big[-\frac{a^2}{2}(A(\tilde{X_{\rm M}})-\frac{X_{\rm L}}{a})^2+{\rm i}a^2\frac{X_{\rm L}}{a}B(\tilde{X_{\rm M}})-\frac{\rm i}{2}a^2A(\tilde{X_{\rm M}})B(\tilde{X_{\rm M}})\Big], \tag{12.4}$$

$$\Upsilon_I(P_{\rm L}) = \frac{1}{\pi^{\frac{1}{4}}}\exp\Big[-\frac{b^2}{2}(B(\tilde{X_{\rm M}})-\frac{P_{\rm L}}{b})^2-{\rm i}b^2\frac{P_{\rm L}}{b}A(\tilde{X_{\rm M}})+\frac{\rm i}{2}b^2A(\tilde{X_{\rm M}})B(\tilde{X_{\rm M}})\Big], \tag{12.5}$$

where the measurement operator has been split up into a part corresponding to the $X_{\rm L}$ measurement and the $P_{\rm L}$ measurement. I have also introduced the shorthands

$$a = \sqrt{1-\zeta^2}X_\alpha, \tag{12.6}$$

$$b = \zeta X_\alpha, \tag{12.7}$$

which will be used frequently from here on out. Once again, Table 11.1 gives the different forms of the A and B operators for the different regimes of optomechanics.

The Δt dependence in $\Upsilon_I(\Delta t)$ comes in as the mean number of input photons in a Δt is $N_{\rm P} = |\alpha|^2 = \frac{1}{2}X_\alpha^2 = |\alpha_{\rm in}|^2\Delta t$—see Section 6.3.3 where this is justified. Here, α is the dimensionless input amplitude, which depends on Δt, whereas $\alpha_{\rm in}$ is the input field amplitude in units of $\mathrm{s}^{-1/2}$ and does not depend on Δt. For later convenience I define the measurement rate to be half of the input flux $k = |\alpha_{\rm in}|^2/2$ so

$$X_\alpha^2 = 4k\Delta t. \tag{12.8}$$

12.4.2 A general continuous homodyne measurement

To derive the SME for the continuous optomechanical general-dyne position measurement, first consider the SME that results from a continuous homodyne measurement of the Hermitian observable $X = X^\dagger$. Over a time increment Δt, the measurement operator for such a measurement is given by the following

$$\upsilon(\Delta t) = \frac{1}{\pi^{\frac{1}{4}}}\exp\left[-2k\Delta t(X-\bar{X})^2+4{\rm i}k\Delta t\bar{X}Y-2{\rm i}k\Delta tXY\right], \tag{12.9}$$

$$\bar{X} = \langle X\rangle + \frac{1}{\sqrt{8k}}\frac{\Delta W}{\Delta t}, \tag{12.10}$$

$$c_\upsilon = \sqrt{2k}(X+{\rm i}Y). \tag{12.11}$$

To see why this operator realizes a continuous homodyne measurement, compare the form of Eq. (12.9) to the overlap formulae in Appendix A.

The measurement operator ν is similar to the operator used in Ref. [71] to derive continuous position measurement but the operator ν is not just a positive operator but also includes additional unitary terms that describe homodyne-measurement back action. Here, k is the measurement rate, $\bar{X}$ is the measurement record, Y is another Hermitian operator, satisfying $[X, Y] = 0$, that leads to back action, and c_υ will turn out to be the measurement output operator. The Wiener increment ΔW is a Gaussian random variable with zero mean and variance Δt, which obeys the Itô rule $(\Delta W)^2 = \Delta t$. The Itô rule is strictly only true in the limit $\Delta t \to \mathrm{d}t$, $\Delta W \to \mathrm{d}W$, but this limit will be taken shortly in order to derive the SME.

The homodyne measurement operator may be written as

$$\upsilon(\Delta t) \propto \mathrm{e}^{-2k\Delta t[X^2 - 2\langle X\rangle(X+\mathrm{i}Y)+\mathrm{i}XY]+\sqrt{2k}(X+\mathrm{i}Y)\Delta W},$$

ignoring terms in the exponential which are not operators and so will only affect the state normalization. Then considering an infinitesimal change in the state $|\psi(t+\mathrm{d}t)\rangle = |\psi(t)\rangle + \mathrm{d}\,|\psi\rangle = \mathcal{N}\lim_{\Delta t\to \mathrm{d}t}\upsilon(\Delta t)\,|\psi(t)\rangle$, and expanding to first order in Δt with the Itô rule, gives

$$\begin{aligned} |\psi(t+\mathrm{d}t)\rangle &= |\psi(t)\rangle + \mathrm{d}\,|\psi\rangle \qquad (12.12)\\ &= \lim_{\Delta t\to \mathrm{d}t}\mathcal{N}\left\{1 - k\Delta t[X^2 + Y^2 - 4\langle X\rangle(X+\mathrm{i}Y)] + \sqrt{2k}(X+\mathrm{i}Y)\Delta W\right\}|\psi(t)\rangle. \end{aligned}$$

Here, the normalization of the state is given by

$$\mathcal{N} \;=\; 1 - k\Delta t\,\langle X\rangle^2 - \sqrt{2k}\,\langle X\rangle\,\Delta W. \qquad (12.13)$$

This leads to the stochastic Schrödinger equation for a general continuous homodyne measurement

$$\mathrm{d}\,|\psi\rangle = \left\{-k[(X - \langle X\rangle)^2 + Y^2 - 2\mathrm{i}\,\langle X\rangle\,Y]\mathrm{d}t + \sqrt{2k}[X - \langle X\rangle + \mathrm{i}Y]\mathrm{d}W\right\}|\psi\rangle. \qquad (12.14)$$

Following the derivation in Ref. [71], one may then use $\mathrm{d}\rho = \mathrm{d}\,|\psi\rangle\,\langle\psi| + |\psi\rangle\,\mathrm{d}\,\langle\psi| + \mathrm{d}\,|\psi\rangle\,\mathrm{d}\,\langle\psi|$ to derive the SME for general homodyne measurement

$$\begin{aligned} \mathrm{d}\rho &= -k[X^2\rho + \rho X^2 - 2X\rho X + Y^2\rho + \rho Y^2 - 2Y\rho Y - 2\mathrm{i}Y\rho X + 2\mathrm{i}X\rho Y]\mathrm{d}t\\ &+ \sqrt{2k}[(X+\mathrm{i}Y)\rho + \rho(X - \mathrm{i}Y) - 2\langle X\rangle\rho]\mathrm{d}W,\\ &= \mathcal{D}[c_\upsilon]\rho\mathrm{d}t + \mathcal{H}[c_\upsilon]\rho\mathrm{d}W. \qquad (12.15) \end{aligned}$$

Here, it may be seen that c_υ is the measurement output operator. The first term in Eq. (12.15) represents measurement back action and the Lindblad superoperator is given by $\mathcal{D}[O]\rho = O\rho O^\dagger - \frac{1}{2}\{O^\dagger O, \rho\}$. While the second term in Eq. (12.15) describes localization of X, with the measurement superoperator being $\mathcal{H}[O]\rho = O\rho + \rho O^\dagger - \langle O + O^\dagger\rangle\,\rho$, which is nonlinear in ρ.

12.4.3 SME in the rotating frame

Writing out the individual homodyne measurement operators $\Upsilon_I(X_{\rm L})$ and $\Upsilon_I(P_{\rm L})$ in the form of Eqs (12.9), (12.10), and (12.11) gives

$$\Upsilon(X_{\rm L}) = \frac{1}{\pi^{\frac{1}{4}}} \exp\Big[-\frac{a^2}{2}(A(\tilde{X}_{\rm M}) - \frac{X_{\rm L}}{a})^2 + {\rm i}a^2\frac{X_{\rm L}}{a}B(\tilde{X}_{\rm M}) - \frac{\rm i}{2}a^2 A(\tilde{X}_{\rm M})B(\tilde{X}_{\rm M})\Big], \tag{12.16}$$

$$\frac{X_{\rm L}}{a} = \Big\langle A(\tilde{X}_{\rm M})\Big\rangle + \frac{1}{\sqrt{8k(1-\zeta^2)}}\frac{\Delta W_{X_{\rm L}}}{\Delta t}, \tag{12.17}$$

$$\tilde{c}_{X_{\rm L}} = \sqrt{2k(1-\zeta^2)}f(\tilde{X}_{\rm M}), \tag{12.18}$$

and

$$\Upsilon(P_{\rm L}) = \frac{1}{\pi^{\frac{1}{4}}} \exp\Big[-\frac{b^2}{2}(B(\tilde{X}_{\rm M}) - \frac{P_{\rm L}}{b})^2 - {\rm i}b^2\frac{P_{\rm L}}{b}A(\tilde{X}_{\rm M}) + \frac{\rm i}{2}b^2 A(\tilde{X}_{\rm M})B(\tilde{X}_{\rm M})\Big], \tag{12.19}$$

$$\frac{P_{\rm L}}{a} = \Big\langle B(\tilde{X}_{\rm M})\Big\rangle + \frac{1}{\sqrt{8k\zeta^2}}\frac{\Delta W_{P_{\rm L}}}{\Delta t}, \tag{12.20}$$

$$\tilde{c}_{P_{\rm L}} = -{\rm i}\sqrt{2k\zeta^2}f(\tilde{X}_{\rm M}). \tag{12.21}$$

Here, the Δt dependence comes in through Eq. (12.8) to give $a^2 = 4k(1-\zeta^2)\Delta t$ and $b^2 = 4k\zeta^2\Delta t$. The Wiener increments from the two homodyne measurements are independent $\Delta W_i \Delta W_j = \delta_{i,j}\Delta t$.

Then using the result of Eq. (12.15), in the rotating frame the continuous general-dyne measurement produces the nonlinear SME

$$\begin{aligned} {\rm d}\tilde{\rho} &= \mathcal{D}[\tilde{c}_{X_{\rm L}}]\tilde{\rho}{\rm d}t + \mathcal{D}[\tilde{c}_{P_{\rm L}}]\tilde{\rho}{\rm d}t + \mathcal{H}[\tilde{c}_{X_{\rm L}}]\tilde{\rho}{\rm d}W_{X_{\rm L}} + \mathcal{H}[\tilde{c}_{P_{\rm L}}]\tilde{\rho}{\rm d}W_{P_{\rm L}} \qquad (12.22)\\ &= 2k\left(f(\tilde{X}_{\rm M})\tilde{\rho}f(-\tilde{X}_{\rm M}) - \tilde{\rho}\right){\rm d}t \\ &+ \sqrt{2k(1-\zeta^2)}\left(f(\tilde{X}_{\rm M})\tilde{\rho} + \tilde{\rho}f(-\tilde{X}_{\rm M}) - 2\Big\langle A(\tilde{X}_{\rm M})\Big\rangle\tilde{\rho}\right){\rm d}W_{X_{\rm L}} \\ &+ \sqrt{2k\zeta^2}\left(-{\rm i}f(\tilde{X}_{\rm M})\tilde{\rho} + {\rm i}\tilde{\rho}f(-\tilde{X}_{\rm M}) - 2\Big\langle B(\tilde{X}_{\rm M})\Big\rangle\tilde{\rho}\right){\rm d}W_{P_{\rm L}}, \qquad (12.23)\end{aligned}$$

where $\tilde{\rho}$ is the mechanical state in the rotating frame. Then introducing $\tilde{c} = \sqrt{2k}f(\tilde{X}_{\rm M})$ so that $\tilde{c}_{X_{\rm L}} = \sqrt{1-\zeta^2}\,\tilde{c}$, and $\tilde{c}_{P_{\rm L}} = -{\rm i}\zeta\tilde{c}$, allows the nonlinear SME to be written as

$${\rm d}\tilde{\rho} = \mathcal{D}[\tilde{c}]\tilde{\rho}{\rm d}t + \sqrt{1-\zeta^2}\mathcal{H}[\tilde{c}]\tilde{\rho}{\rm d}W_{X_{\rm L}} + \zeta\mathcal{H}[-{\rm i}\tilde{c}]\tilde{\rho}{\rm d}W_{P_{\rm L}}, \tag{12.24}$$

with ${\rm d}W_i{\rm d}W_j = \delta_{i,j}{\rm d}t$, $\mathbb{E}[{\rm d}W_i] = 0$, for $i,j = X_{\rm L}, P_{\rm L}$. Here, the stochastic average is represented by $\mathbb{E}$ to differentiate from the quantum expectation value.

12.4.4 SME in the lab frame

The state in the lab frame is $\rho(t) = U_F(t)\tilde{\rho}(t)U_F^\dagger(t)$, where the transformation unitary[2] is $U_F = \mathrm{e}^{-\mathrm{i}\omega_{\mathrm{M}} b^\dagger b t}$ as in Chapter 11. Therefore, one has that

$$\begin{aligned}
\rho(t+\mathrm{d}t) &= U_{\mathrm{F}}(t+\mathrm{d}t)\tilde{\rho}(t+\mathrm{d}t)U_{\mathrm{F}}^\dagger(t+\mathrm{d}t) \\
&= U_{\mathrm{F}}(t)U_{\mathrm{F}}(\mathrm{d}t)\tilde{\rho}(t+\mathrm{d}t)U_{\mathrm{F}}^\dagger(t)U_{\mathrm{F}}^\dagger(\mathrm{d}t) \\
&= U_{\mathrm{F}}(t)U_{\mathrm{F}}(\mathrm{d}t)\left(\tilde{\rho}(t)+\mathrm{d}\tilde{\rho})\right)U_{\mathrm{F}}^\dagger(t)U_{\mathrm{F}}^\dagger(\mathrm{d}t) \\
&= U_{\mathrm{F}}(t)U_{\mathrm{F}}(\mathrm{d}t)\tilde{\rho}(t)U_{\mathrm{F}}^\dagger(t)U_{\mathrm{F}}^\dagger(\mathrm{d}t) + U_{\mathrm{F}}(t)\mathrm{d}\tilde{\rho}(t)U_{\mathrm{F}}^\dagger(t), \quad (12.25)
\end{aligned}$$

where in the last line terms producing higher order terms than $\mathrm{d}t$ have been dropped. So

$$\begin{aligned}
\rho(t+\mathrm{d}t) &= U_{\mathrm{F}}(\mathrm{d}t)U_{\mathrm{F}}(t)\tilde{\rho}(t)U_{\mathrm{F}}^\dagger(t)U_{\mathrm{F}}^\dagger(\mathrm{d}t) + U_{\mathrm{F}}(t)\mathrm{d}\tilde{\rho}(t)U_{\mathrm{F}}^\dagger(t) \\
&= U_{\mathrm{F}}(\mathrm{d}t)\rho(t)U_{\mathrm{F}}^\dagger(\mathrm{d}t) + U_{\mathrm{F}}(t)\mathrm{d}\tilde{\rho}(t)U_{\mathrm{F}}^\dagger(t) \\
&= (1-\mathrm{i}H_0/\hbar\mathrm{d}t)\,\rho(t)\,(1+\mathrm{i}H_0/\hbar\mathrm{d}t) + U_{\mathrm{F}}(t)\mathrm{d}\tilde{\rho}(t)U_{\mathrm{F}}^\dagger(t), \quad (12.26)
\end{aligned}$$

where $H_0 = \hbar\omega_{\mathrm{M}} b^\dagger b$ is the free mechanical Hamiltonian and terms higher order than $\mathrm{d}t$ have been dropped. Therefore, as $\rho(t+\mathrm{d}t) = \rho(t) + \mathrm{d}\rho$, one can identify

$$\mathrm{d}\rho = -\frac{\mathrm{i}}{\hbar}[H_0,\rho]\mathrm{d}t + U_F(t)\mathrm{d}\tilde{\rho}(t)U_F^\dagger(t). \quad (12.27)$$

By then using $U_F^\dagger U_F = \mathbb{1}$, $X_{\mathrm{M}}^n = U_F \tilde{X}_{\mathrm{M}}{}^n U_F^\dagger$ and $c = U_F\tilde{c}U_F^\dagger = \sqrt{2k}f(X_{\mathrm{M}})$, one has that

$$U_F\mathcal{D}[\tilde{c}]\tilde{\rho}U_F^\dagger = \mathcal{D}[c]\rho. \quad (12.28)$$

Then using that expectation values are the same in the rotating and the lab frame $\langle\tilde{c}\rangle = \mathrm{tr}\,(\tilde{c}\tilde{\rho}) = \mathrm{tr}\left(U_F^\dagger c U_F U_F^\dagger \rho U_F\right) = \mathrm{tr}\,(c\rho) = \langle c\rangle$,

$$U_F\mathcal{H}[\tilde{c}]\tilde{\rho}U_F^\dagger = \mathcal{H}[c]\rho. \quad (12.29)$$

Hence,

$$U_F(t)\mathrm{d}\tilde{\rho}(t)U_F^\dagger(t) = \mathcal{D}[c]\rho\mathrm{d}t + \sqrt{1-\zeta^2}\mathcal{H}[c]\rho\mathrm{d}W_{X_{\mathrm{L}}} + \zeta\mathcal{H}[-\mathrm{i}c]\rho\mathrm{d}W_{P_{\mathrm{L}}}, \quad (12.30)$$

which shows that the nonlinear SME for an ideal continuous optomechanical general-dyne position measurement is

$$\mathrm{d}\rho = -\frac{\mathrm{i}}{\hbar}[H_0,\rho]\mathrm{d}t + \mathcal{D}[c]\rho\mathrm{d}t + \sqrt{1-\zeta^2}\mathcal{H}[c]\rho\mathrm{d}W_{X_{\mathrm{L}}} + \zeta\mathcal{H}[-\mathrm{i}c]\rho\mathrm{d}W_{P_{\mathrm{L}}}. \quad (12.31)$$

[2]Note, the cavity part $\hbar a^\dagger a$ of H_0 does not act on the mechanical subspace so is ignored here.

There was an easier way all along

The SME was derived in the lab frame by first calculating the SME in the rotating frame. This method was chosen to isolate the more interesting physics from the simple free evolution. Although for a continuous nonlinear position measurement, the SME could have been more directly derived by expanding $\rho(t+\mathrm{d}t) = \mathrm{e}^{-\mathrm{i}H_0(t+\mathrm{d}t)/\hbar}\Upsilon\rho(t)\Upsilon^\dagger\mathrm{e}^{\mathrm{i}H_0(t+\mathrm{d}t)/\hbar}$ to first order in $\mathrm{d}t$ in the lab frame. This indeed produces the same SME as Eq. (12.31). Note that $\rho(t) = U_F(t)\tilde{\rho}(t)U_F^\dagger(t)$ implies $\rho(t+\mathrm{d}t) = U_F(t+\mathrm{d}t)\tilde{\rho}(t)U_F^\dagger(t+\mathrm{d}t)$ and in the mechanical subspace $U_F(t) = \mathrm{e}^{-\mathrm{i}H_0t/\hbar}$, which explains the t dependence in the above transformation.

However, one may also worry about the order of these terms. Is $\rho(t+\mathrm{d}t) = \Upsilon\mathrm{e}^{-\mathrm{i}H_0(t+\mathrm{d}t)/\hbar}\rho(t)\mathrm{e}^{\mathrm{i}H_0(t+\mathrm{d}t)/\hbar}\Upsilon^\dagger$ the right way instead? In fact, one need not worry about the free Hamiltonian not commuting with Υ. This is because, for a continuous measurement, both Υ and $\mathrm{e}^{-\mathrm{i}H_0(t+\mathrm{d}t)/\hbar}$ depend on $\mathrm{d}t$ and any terms that arise in the SME from the non-commutativity Υ and $\mathrm{e}^{-\mathrm{i}H_0\mathrm{d}t/\hbar}$ will be of order higher than $\mathrm{d}t$ so will not appear in the SME. More explicitly, ignoring any terms higher than $\mathrm{d}t$, one has $\Upsilon\mathrm{e}^{-\mathrm{i}H_0(t+\mathrm{d}t)/\hbar} = \mathrm{e}^{O\mathrm{d}t}\mathrm{e}^{-\mathrm{i}H_0(t+\mathrm{d}t)/\hbar}\Upsilon$, where O is a Hermitian mechanical operator arising from the non-commutativity. The inclusion of this O will then modify the SME according to $\mathrm{d}\rho \to \mathrm{e}^{O\mathrm{d}t}\mathrm{d}\rho\mathrm{e}^{O\mathrm{d}t}$. However, as $\mathrm{d}\rho$ only depends on terms proportional to $\mathrm{d}t$ and $\mathrm{d}W$, any modifications to the SME from $\mathrm{d}\rho \to \mathrm{e}^{O\mathrm{d}t}\mathrm{d}\rho\mathrm{e}^{O\mathrm{d}t}$ will be higher order than $\mathrm{d}t$ and so $\mathrm{e}^{O\mathrm{d}t}$ can be safely ignored.

Mechanical dissipation, inefficient detection and the total stochastic master equation

Inefficient detection is accounted for by the transformation $\mathcal{H}[O] \to \sqrt{\eta}\mathcal{H}[O]$, where η is the detection efficiency [63]. In general, the efficiencies of the P_L and X_L homodyne measurement may be different, so I label these efficiencies η_{X_L} and η_{P_L}, respectively. While mechanical interactions with the high-temperature environment[3] may be accounted for with an additional Lindblad dissipator $L = \sqrt{\frac{4\gamma k_\mathrm{B}T}{\hbar\omega_\mathrm{M}}}X_\mathrm{M} + \mathrm{i}\theta\sqrt{\frac{\hbar\omega_\mathrm{M}\gamma}{4k_\mathrm{B}T}}P_\mathrm{M}$, which models quantum Brownian motion for $\theta = 1$, or momentum diffusion for $\theta = 0$ [39] as detailed in Chapter 3. Here, T is the temperature of the environment and γ is the mechanical decay rate.

Summary

To summarize, the total SME for continuous general-dyne measurement is

$$\boxed{\begin{aligned}\mathrm{d}\rho &= -\frac{\mathrm{i}}{\hbar}[H_0,\rho]\mathrm{d}t + \mathcal{D}[c]\rho\mathrm{d}t + \mathcal{D}[L]\rho\mathrm{d}t \\ &+ \sqrt{(1-\zeta^2)\eta_{X_\mathrm{L}}}\mathcal{H}[c]\rho\mathrm{d}W_{X_\mathrm{L}} + \zeta\sqrt{\eta_{P_\mathrm{L}}}\mathcal{H}[-\mathrm{i}c]\rho\mathrm{d}W_{P_\mathrm{L}}\end{aligned}} \tag{12.32}$$

[3] See the discussion of quantum Brownian motion in Chapter 3. Note that in Ref. [7], the occupation of the thermal environment is much greater than 1.

where $c = \sqrt{2k} f(X_{\mathrm{M}})$ and $f(X_{\mathrm{M}})$ depends on the regime of optomechanics from Table 11.1.

12.5 Conclusion and outlook

In this chapter, a scheme for position measurement that accounts for the nonlinearity of the cavity-enhanced radiation pressure interaction with arbitrary coupling to the mechanical position has been developed. This scheme is capable of describing both pulsed and continuous measurements, which utilize generaldyne measurements to access mechanical information imprinted on both optical quadratures.

This new framework describes existing and future experiments entering the nonlinear regime of optomechanics, which allow for reduced optics-induced heating compared to strategies that rely on large optical amplitudes. Furthermore, this formalism will allow for new and refined state preparation and measurement protocols that take into account the nonlinearity of the cavity-based optomechanical interaction. In particular, one can study the non-Gaussian momentum distribution induced by the nonlinear unitary and subsequent measurements. Finally, the general framework introduced here will allow for exploration of the SQL in inherently nonlinear systems and enable the development of new quantum sensing protocols.

Chapter 13

Pulsed position measurements

This chapter draws heavily from Ref. [7], where this work was originally published.

In this chapter, I describe pulsed position measurement via optical generaldyne detection, which is described by Υ from Eq. (12.2). Moreover, I will focus on the nonlinear cavity-enhanced optomechanical interaction with linear coupling to position $a^\dagger a X_{\mathrm{M}}$ as in Ref. [7]. To recap, this pulsed interaction is described by the unitary $U = \mathrm{e}^{\mathrm{i}\varphi(X_{\mathrm{M}})n_{\mathrm{L}}}$ with $\varphi(X_{\mathrm{M}}) = \arg(f)$ and $f = \left[1 + \mathrm{i}\left(\frac{\mu}{2}X_{\mathrm{M}} + \frac{\Delta}{\kappa}\right)\right] / \left[1 - \mathrm{i}\left(\frac{\mu}{2}X_{\mathrm{M}} + \frac{\Delta}{\kappa}\right)\right]$. Furthermore, in this chapter I will consider the case of a resonant input pulse $\Delta = 0$ as I also assume an initial mechanical state with $\langle X_{\mathrm{M}}\rangle = 0$, this setting maximizes the amount of light that can enter the cavity. In this case, the A and B functions are given by

$$A(X_{\mathrm{M}}) = \frac{1 - \left(\frac{\mu}{2}X_{\mathrm{M}}\right)^2}{1 + \left(\frac{\mu}{2}X_{\mathrm{M}}\right)^2}, \tag{13.1}$$

$$B(X_{\mathrm{M}}) = \frac{\mu X_{\mathrm{M}}}{1 + \left(\frac{\mu}{2}X_{\mathrm{M}}\right)^2}. \tag{13.2}$$

I would like to remind the reader that as the pulsed optomechanical interaction is much shorter than the mechanical period, mechanical free evolution and dissipation is negligible during the interaction, and so the measurements described in this chapter are back action evading position measurements [143, 139].

13.1 Pulsed measurement map

13.1.1 Kraus map and heralding probability

The action of a nonlinear pulsed measurement on an initial mechanical state ρ_i is described by the Kraus map

$$\rho_f = \frac{\Upsilon \rho_i \Upsilon^\dagger}{\mathcal{P}}, \tag{13.3}$$

$$\mathcal{P} = \mathrm{tr}\left(\Upsilon^\dagger \Upsilon \rho_i\right), \tag{13.4}$$

where Υ is given by Eq. (12.2), ρ_f is the mechanical state after the measurement, and $\mathcal{P}$ is the heralding probability for a particular $(X_\mathrm{L}, P_\mathrm{L})$ general-dyne outcome. Eq. (13.3) implies that the position probability changes according to

$$P_f(X_\mathrm{M}) = \frac{F(X_\mathrm{M}) P_i(X_\mathrm{M})}{\mathcal{P}}, \tag{13.5}$$

where $P_i(X_\mathrm{M}) = \langle X_\mathrm{M}| \rho_i |X_\mathrm{M}\rangle$, $P_f(X_\mathrm{M}) = \langle X_\mathrm{M}| \rho_f |X_\mathrm{M}\rangle$, and the filtering function $F(X_\mathrm{M}) = \langle X_\mathrm{M}| \Upsilon^\dagger \Upsilon |X_\mathrm{M}\rangle$ filters the initial probability distribution to produce the final mechanical position probability. Explicitly, the filtering function is

$$F = \frac{1}{\pi} \exp\left[-(X_\mathrm{L} - aA(X_\mathrm{M}))^2 - (P_\mathrm{L} - bB(X_\mathrm{M}))^2\right], \tag{13.6}$$

where A and B are now functions of the variable X_M and are not operators and a and b are defined in Eqs (12.6) and (12.7).

While the map Eq. (13.3) applies for any input mechanical state ρ_i, in what follows an initial mechanical Gaussian state with position probability distribution

$$P_i(X_\mathrm{M}) = \frac{1}{\sqrt{2\pi\sigma^2}} \mathrm{e}^{-X_\mathrm{M}^2/2\sigma^2} \tag{13.7}$$

is assumed. Here, $\sigma^2 = \bar{n} + \frac{1}{2}$ for a thermal state.

13.1.2 The output optical state

Equivalence of $\mathcal{P}$ and the Husimi-Q function

The heralding probability $\mathcal{P}$ for $(X_\mathrm{L}, P_\mathrm{L})$ outcomes $\mathcal{P} = \int \mathrm{d}X_\mathrm{M} F(X_\mathrm{M}) P_i(X_\mathrm{M})$ is given explicitly by

$$\mathcal{P}(X_\mathrm{L}, P_\mathrm{L}) = \frac{1}{\pi} \int \mathrm{d}X_\mathrm{M} P_i(X_\mathrm{M}) \mathrm{e}^{-(X_\mathrm{L} - \sqrt{1-\zeta^2} X_\alpha A)^2 - (P_\mathrm{L} - \zeta X_\alpha B)^2}. \tag{13.8}$$

For $\zeta = 1/\sqrt{2}$, the general-dyne measurement realizes heterodyne detection and therefore measures the Husimi-Q function of the reduced state of the optical mode ρ_L after the optomechanical interaction. Explicitly, the Q function is

$$Q(\beta) = \frac{1}{2\pi} \langle \beta| \rho_\mathrm{L} |\beta\rangle, \tag{13.9}$$

where

$$\begin{aligned}\rho_{\rm L} &= {\rm tr}_{\rm M}\left(U\left|\alpha\right\rangle\left\langle\alpha\right|\rho_i U^\dagger\right)\\ &= \int {\rm d}X_{\rm M}\ P_i(X_{\rm M})\left|\alpha(A+{\rm i}B)\right\rangle\left\langle\alpha(A+{\rm i}B)\right|,\end{aligned} \tag{13.10}$$

Therefore

$$\begin{aligned}Q(\beta) &= \frac{1}{2\pi}\int {\rm d}X_{\rm M}\ P_i(X_{\rm M})\left|\left\langle\beta|\alpha(A+{\rm i}B)\right\rangle\right|^2\\ &= \frac{1}{2\pi}\int {\rm d}X_{\rm M}\ P_i(X_{\rm M}){\rm e}^{-|\beta-\alpha(A+{\rm i}B)|^2}.\end{aligned} \tag{13.11}$$

Then writing the complex amplitudes as $\alpha(A+{\rm i}B) = X_\alpha(A+{\rm i}B)/\sqrt{2}$ and $\beta = (X_\beta + {\rm i}P_\beta)/\sqrt{2}$ gives

$$Q(X_\beta,P_\beta) = \frac{1}{2\pi}\int {\rm d}X_{\rm M}\ P_i(X_{\rm M}){\rm e}^{-\frac{1}{2}(X_\beta - X_\alpha A)^2-\frac{1}{2}(P_\beta - X_\alpha B)^2}. \tag{13.12}$$

The Husimi-Q function is normalized such that

$$\int {\rm d}^2\beta Q(\beta) = \frac{1}{2}\int\int {\rm d}X_\beta {\rm d}P_\beta Q(X_\beta,P_\beta) = 1.$$

Finally, rescaling the coordinates $X_\beta = \sqrt{2}X_{\rm L}$ and $P_\beta = \sqrt{2}P_{\rm L}$ gives

$$Q(X_{\rm L},P_{\rm L}) = \frac{1}{\pi}\int {\rm d}X_{\rm M}\ P_i(X_{\rm M}){\rm e}^{-(X_{\rm L}-\frac{1}{\sqrt{2}}X_\alpha A)^2-(P_\beta-\frac{1}{\sqrt{2}}X_\alpha B)^2}, \tag{13.13}$$

which is equal to $\mathcal{P}(X_{\rm L},P_{\rm L})$ at $\zeta = 1\sqrt{2}$. For $0<\zeta<1$, general-dyne detection measures the Q function of the optical mode after the optomechanical interaction with rescaled coordinates $(X_{\rm L},P_{\rm L})$.

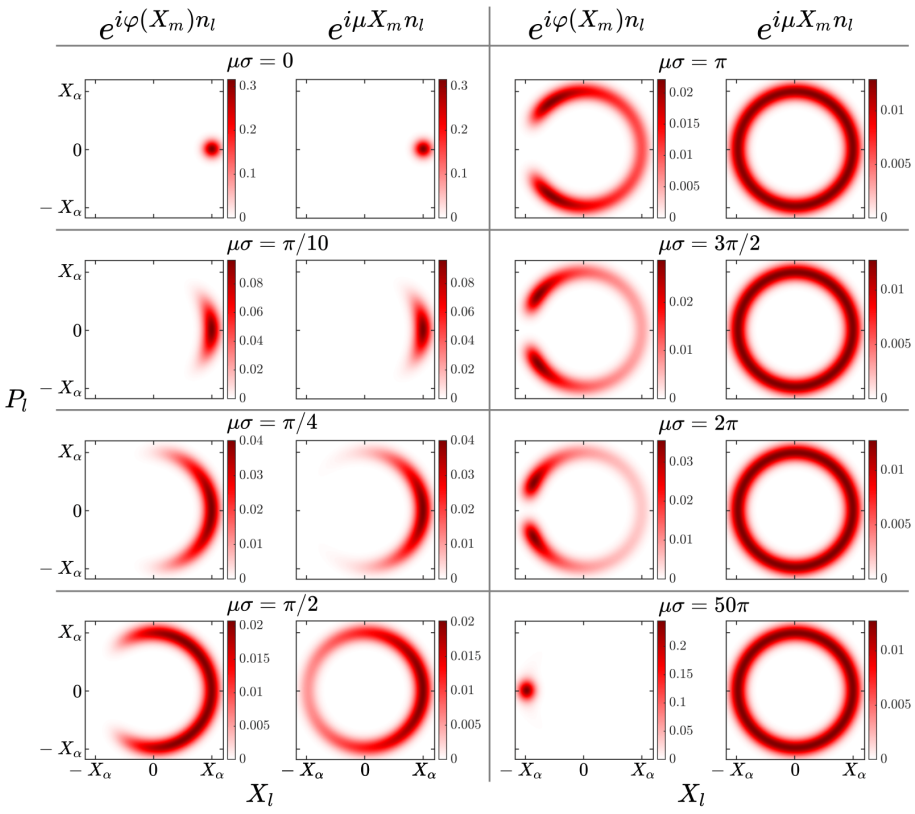


Figure 13.1: Q **functions of the optical state after the optomechanical interaction.** Here, shown for $X_\alpha = 10$, $\Delta = 0$, and various values of $\mu\sigma$ are shown, where σ^2 is the initial variance of the mechanical state. Cavity-enhanced $e^{i\varphi(X_M)n_L}$ columns: the Q functions for a nonlinear optomechanical interaction that incorporates the nonlinear cavity response function. Cavity-free $e^{i\mu X_M n_L}$ columns: the same case but with the nonlinear optomechanical unitary approximated to first order in position X_M. Note that in the expansion of $\varphi(X_M)$, the second order term in X_M with $\Delta = 0$ is zero. For the cavity-enhanced interaction, the π-phase limit is seen at large optical rotations, for example at $\mu\sigma = 50\pi$, the optical coherent state has almost fully rotated $\pm\pi$ in phase space.

For plots of the Wigner function of ρ_L with non-zero detuning see Section 15.5.

Nonlinearity of the optomechanical phase of the cavity and π-phase limit

Fig. 13.1 shows the Q functions of the optical state after the optomechanical interactions and compares the results of $e^{i\varphi(X_M)n_L}$ with that induced by $e^{i\mu X_M n_L}$, demonstrating the nonlinear optomechanical phase shift. Furthermore, for any finite value of X_M, in the limit $\mu \to \infty$, one has $A \to -1$ and $B \to 0$. Hence, in this limit $\mathcal{P} = F = \frac{1}{\pi}\exp\left[-(X_L + a)^2 - P_L^2\right]$ and $P_f(X_M) = P_i(X_M)$. This means the optical coherent state has fully rotated $\pm\pi$ in phase space (see Fig. 13.1) and no information is gained about the mechanics. Note that the contribution at $X_M = 0$, that leads to $P_f(X_M) \neq P_i(X_M)$, becomes narrower and narrower in the limit of $\mu\sigma \to \infty$, where σ is the initial width of the Gaussian mechanical state, as shown in Fig. 13.2.

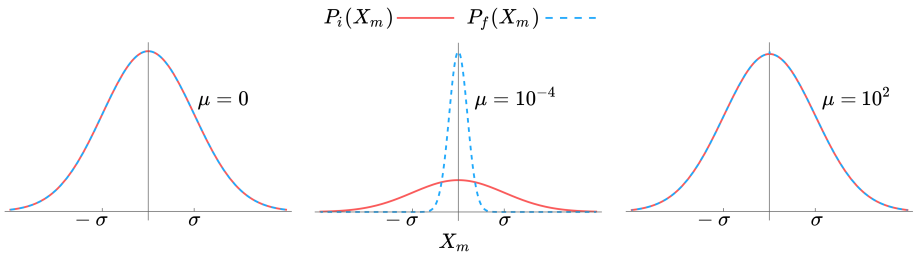


Figure 13.2: **π-phase limit in cavity optomechanics.** An initial mechanical state with width $\sigma = 5000$ and position marginal $P_i(X_M)$ is plotted. Here, $X_\alpha = 10$, $\Delta = 0$, $\zeta = 0.7$ and the output position marginal $P_f(X_M)$ is plotted with increasing values of μ for an $X_L = a$, $P_L = 0$ outcome, as an example. When $\mu = 0$, there is no measurement so $P_f(X_M) = P_i(X_M)$ and no information is gained about the mechanics, when $\mu = 10^{-4}$ $P_f(X_M) \neq P_i(X_M)$, indicating information about X_M has been gained. As $\mu\sigma \to \infty$, the π-phase limit is approached and once again no information is gained about the mechanics. For $\mu = 10^2$, $P_f(X_M) \approx P_i(X_M)$ with only a small deviation at $X_M = 0$.

13.1.3 Mechanical state tomography from the output light

Akin to the protocol described in pulsed linearized optomechanics [139], measuring the distribution $\mathcal{P}(X_L, P_L)$, or equivalently $Q(X_L, P_L)$, allows one to measure the position probability of the initial mechanical state $P_i(X_M)$. From the expression $\mathcal{P} = \int \mathrm{d}X_M F(X_M) P_i(X_M)$, it may be seen that this requires knowledge of the filtering function F and a deconvolution of $\mathcal{P}(X_L, P_L)$—see Ref. [139] for more details.

Allowing the mechanical mode to rotate through a phase a space angle $\theta = \omega_M t$ then allows one to measure all the rotated mechanical marginals $P_i(X_\theta)$. Then the Wigner function of the mechanical mode can be determined from the set of rotated marginals via an inverse Radon transformation [18].

13.2 Gaussian approximation to pulsed measurement

In this section, I derive a Gaussian approximation to the position measurement map of Eq. (13.5). To do so the coordinate system is changed from the standard phase-space coordinates $(X_{\rm L}, P_{\rm L})$ to the 'general-dyne coordinates' (z, δ). Here, the coordinate z parametrizes points on the classical trajectory[1] of the coherent state in the general-dyne measurement space, while the coordinate δ spans every other point by extending perpendicularly from this trajectory. For a given outcome (z, δ), the filtering function $F = \Upsilon^\dagger \Upsilon$ may then be expanded in position $X_{\rm M}$ about its maximum at $z = X_{\rm M}/\mu$, $\delta = 0$ to give the Gaussian approximation to the position measurement.

Note that this Section only focuses on the position marginal of the mechanical mode. However, a full Gaussian approximation can be applied to the measurement map of Eq. (13.3), i.e. one may find the Gaussian approximation of Υ rather than just $F = \Upsilon^\dagger \Upsilon$. In this case one may derive the Gaussian transformation for the first moments vector and the covariance matrix. This derivation is shown in Appendix I and also utilizes 'general-dyne coordinates'.

13.2.1 General-dyne coordinates

To perform a Gaussian approximation to the general-dyne measurement, the filtering function must be expanded about its maximum. To do this, one must first compute $\dfrac{\partial F}{\partial X_{\rm M}}|_{X_{\rm L}, P_{\rm L}} = 0$, which gives

$$bP_{\rm L}A - aX_{\rm L}B + (a^2 - b^2)AB = 0 \tag{13.14}$$

To proceed, the use of 'general-dyne coordinates' must be motivated. To this end, note that Eq. (13.14) is also the result of minimizing the distance D from the ellipse scribed by $(aA(z), bB(z))$, $z \in (-\infty, +\infty)$ to a general point in $(X_{\rm L}, P_{\rm L})$ space, with $D = \sqrt{(X_{\rm L} - aA(z))^2 + (P_{\rm L} - bB(z))^2}$ and

$$A(z) = \frac{1 - (z/2)^2}{1 + (z/2)^2}, \tag{13.15}$$

$$B(z) = \frac{z}{1 + (z/2)^2}. \tag{13.16}$$

Namely, $\dfrac{{\rm d}(D)^2}{{\rm d}z} = 0$ leads to Eq. (13.14) with $\mu X_{\rm M}$ replaced by z and the minimum distance is $D = \delta$. Then, if one inserts $X_{\rm L} = aA(z) + \delta_{X_{\rm L}}$ and $P_{\rm L} = bB(z) + \delta_{P_{\rm L}}$ with $\delta = \sqrt{\delta_{X_{\rm L}}^2 + \delta_{P_{\rm L}}^2}$ into Eq (13.14) one has that

$$\delta_{P_{\rm L}} = \frac{aB}{bA}\delta_{X_{\rm L}}. \tag{13.17}$$

[1] In other words, the trajectory the coherent state would follow if $X_{\rm M}$ was replaced by a classical variable z.

Thus, one may construct two similar right-angled triangles with acute angle ψ satisfying

$$\sin(\psi) = \frac{aB}{\sqrt{b^2A^2 + a^2B^2}} = \frac{\delta_{P_{\rm L}}}{\delta}, \tag{13.18}$$

$$\cos(\psi) = \frac{bA}{\sqrt{b^2A^2 + a^2B^2}} = \frac{\delta_{X_{\rm L}}}{\delta}, \tag{13.19}$$

$$\tan(\psi) = \frac{aB}{bA} = \frac{\delta_{P_{\rm L}}}{\delta_{X_{\rm L}}}. \tag{13.20}$$

This motivates choosing the general-dyne coordinates (z, δ) to parametrize the measurement space

$$X_{\rm L} = aA(z) + \delta\frac{bA(z)}{\sqrt{b^2A^2 + a^2B^2}}, \tag{13.21}$$

$$P_{\rm L} = bB(z) + \delta\frac{aB(z)}{\sqrt{b^2A^2 + a^2B^2}}, \tag{13.22}$$

with $z \in (-\infty, +\infty)$ and $\delta \in [-\min(a, b), \infty)$. Fig. 13.3 illustrates how general-dyne coordinates span the space of measurement outcomes. Namely, the coordinate z parametrizes points on the classical trajectory of the coherent state in the general-dyne measurement space, while the coordinate δ spans every other point by extending perpendicularly from this trajectory.

The Jacobian for the transformation from $(X_{\rm L}, P_{\rm L})$ space to general-dyne coordinates (z, δ) is

$$J(z, \delta) = \begin{pmatrix} \frac{\partial X_{\rm L}}{\partial z} & \frac{\partial X_{\rm L}}{\partial \delta} \\ \frac{\partial P_{\rm L}}{\partial z} & \frac{\partial P_{\rm L}}{\partial \delta} \end{pmatrix}. \tag{13.23}$$

Hence, the Jacobian determinant is

$$\det J = \frac{4}{4 + z^2}\left[\sqrt{a^2B^2 + b^2A^2} + \delta\frac{ab}{a^2B^2 + b^2A^2}\right], \tag{13.24}$$

which describes the transformation of the area element $\mathrm{d}X_{\rm L}\mathrm{d}P_{\rm L} \to |\det J|\mathrm{d}z\mathrm{d}\delta$ upon the change of coordinates.

13.2.2 Gaussian approximation to the filtering function F and its validity

Inserting the general-dyne coordinates into Eq. (13.6) and expanding to second order about the maximum of the filtering function at $\mu X_{\rm M} = z$, $\delta = 0$ gives

$$F = \frac{1}{\pi}\mathrm{e}^{-\delta^2 - \beta(\mu X_{\rm M} - z)^2}, \tag{13.25}$$

$$\beta = \frac{16}{(4 + z^2)^2}\left[a^2B^2(z) + b^2A^2(z) + \delta\frac{ab}{\sqrt{a^2B^2(z) + b^2A^2(z)}}\right]. \tag{13.26}$$

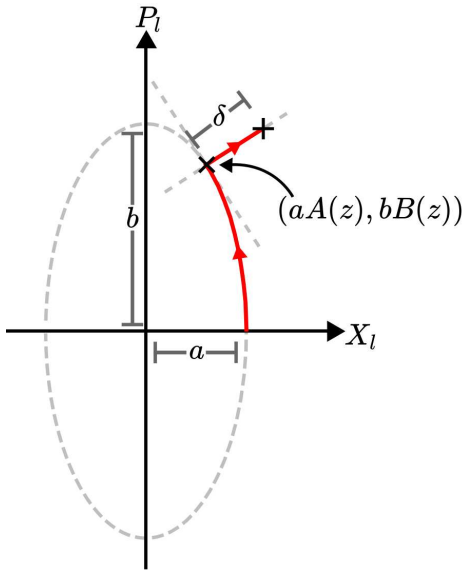


Figure 13.3: **General-dyne coordinates** (z, δ)**.** In the measurement space, the classical trajectory of the optical state is an ellipse, which is scribed parametrically by z via $(aA(z), bB(z))$ for $z \in (-\infty, +\infty)$. Moreover, $\delta \in [-\min(a, b), \infty)$ spans every other point in the measurement space by extending perpendicularly from the ellipse. In this way the δ coordinate takes into account the intrinsic quantum uncertainty of measurement outcomes.

The Gaussian approximation is valid when the expansion about the maximum of the filtering function at $\mu X_{\text{M}} = z$ is valid. Hence, $|\mu X_{\text{M}} - z|$ should be a small quantity and the filtering function should have a width less than one. This condition is

$$\frac{1}{\sqrt{2\beta}} < 1. \tag{13.27}$$

For small optical rotations, the Gaussian approximation works well as linearized optomechanics is recovered. Hence, I investigate Eq. (13.27) for larger optical rotations. For large X_α and z, one has $\beta = 16\zeta^2 X_\alpha^2 / z^4$. Note that the heralding probability will decay in the δ direction with the width of the initial coherent state, so one may consider $\delta \sim 1$ in this approximation. Hence, Eq. (13.27) gives $z^2 < 4\sqrt{2}\zeta X_\alpha$ to leading order in X_α and z. Note that for the Gaussian approximation $z \approx \mu X_{\text{M}}$ so when one considers the range of z^2 values, one may replace z^2 in the inequality with the expectation value $\mu^2 \langle X_{\text{M}}^2 \rangle$. Therefore, the Gaussian approximation is valid when

$$\mu^2 \sigma^2 < 4\sqrt{2}\zeta X_\alpha, \tag{13.28}$$

where σ is the initial width of the mechanical state. Fig. 13.4 demonstrates the validity of the Gaussian approximation when Eq. 13.27 is met. As is evident

from Fig. 13.4, when Eq. 13.27 is violated, there are only small deviations from the Gaussian approximation. Therefore, Eq. (13.28) is a conservative inequality for the Gaussian approximation, as most outcomes z will lie within a width of $\mu\sigma$.

For a good measurement, the outcome z should give accurate information about the position. Hence, the variance in position should be small enough that the outcome z accurately pins down the mechanical position, explaining the left-hand side of Eq. (13.28). Note that information about $X_{\rm M}$ from the measurement increases with the input amplitude X_α and for large rotations $\zeta \lesssim 1$ is the optimal setting[2], explaining the right hand side of Eq. (13.28). The condition for a Gaussian measurement is the same as the condition for a good measurement of position.

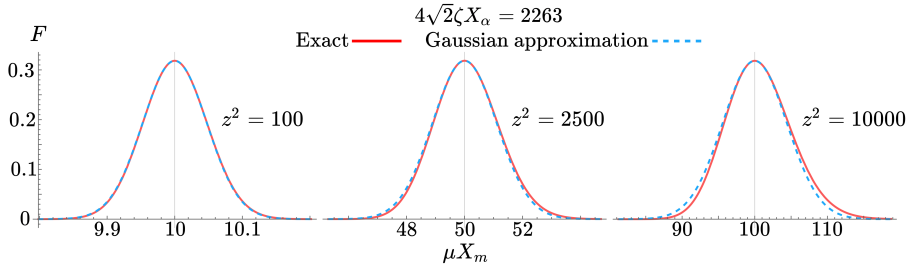


Figure 13.4: Validity of the Gaussian approximation. Here, $\zeta = 0.8$, $X_\alpha = 500$, and $\delta = 0$, such that $4\sqrt{2}\zeta X_\alpha = 2263$. When $z = 10$, the $z^2 < 4\sqrt{2}\zeta X_\alpha$ is met and the Gaussian approximation to F is valid. At $z = 50$, $z^2 > 4\sqrt{2}\zeta X_\alpha$ and one begins to see some small deviations between the filtering function F and its Gaussian approximation. When $z = 100$, $z^2 \gg 4\sqrt{2}\zeta X_\alpha$ and these deviations are more clear.

Other subtle points

For small optical amplitudes, there is significant overlap between the initial optical coherent state—and indeed every rotated optical state—with the origin of phase space. In this way, small optical amplitudes prevent good position measurements and render the Gaussian approximation invalid. To ensure negligible overlap with origin one requires $X_\alpha > 3/\sqrt{2}$. In other words, the coherent state is at least 3 standard deviations away from the origin of phase space.

Furthermore, $P_{\rm L}$ measurements near $\varphi = \pm\pi/2$ and $X_{\rm L}$ measurements near $\varphi = 0, \pm\pi$ preclude good position measurements and the Gaussian approximation. For these measurement settings, many optical rotations have very similar projections onto the $P_{\rm L}$ or $X_{\rm L}$ axis. These measurements will be far from optimal so they do not affect the study of optimal ζ. I will discuss this point further in Section 13.4, however it is first convenient to finish the analysis of the Gaussian approximation in $X_{\rm M}$.

[2]See Section 13.4.

13.2.3 The output mechanical position probability and the heralding probability for a (z, δ) outcome

Within this Gaussian approximation, for the initial mechanical Gaussian state $P_i(X_{\rm M}) = {\rm e}^{-X_{\rm M}^2/2\sigma^2}/\sqrt{2\pi\sigma^2}$, the output position probability distribution is given by

$$P_f(X_{\rm M}) = \frac{1}{\sqrt{2\pi\sigma_f^2}} \exp\left[-\frac{(X_{\rm M}-\bar{X})^2}{2\sigma_f^2}\right], \tag{13.29}$$

$$\sigma_f^2 = \frac{\sigma^2}{1+2\mu^2\sigma^2\beta}, \tag{13.30}$$

$$\bar{X} = \frac{z}{\mu}\frac{2\mu^2\sigma^2\beta}{1+2\mu^2\sigma^2\beta}. \tag{13.31}$$

While the heralding probability is given by

$$\mathcal{P}(z,\delta) = \int {\rm d}X_{\rm M}\ F(X_{\rm M})P_i(X_{\rm M}) \tag{13.32}$$

$$= \frac{1}{\pi\sqrt{1+2\mu^2\sigma^2\beta}} \exp\left[-\delta^2 - \frac{\beta}{1+2\mu^2\sigma^2\beta}z^2\right]. \tag{13.33}$$

Averaging over all measurement outcomes (z, δ) gives

$$\mathbb{E}[\sigma_f^2] = \int {\rm d}z \int {\rm d}\delta \mathcal{P}(z,\delta)|\det\ J|\sigma_f^2. \tag{13.34}$$

Large X_α approximation

When $X_\alpha \gg 1$

$$\beta \approx \frac{16}{(4+z^2)^2}\left(a^2B^2 + b^2A^2\right), \tag{13.35}$$

$$|\det\ J| \approx \frac{4}{4+z^2}\sqrt{a^2B^2+b^2A^2} = \sqrt{\beta}, \tag{13.36}$$

which are δ independent. So one may integrate out δ trivially to get

$$\mathcal{P}(z) = \int {\rm d}\delta \mathcal{P}(z,\delta)|\det\ J| \tag{13.37}$$

$$= \sqrt{\frac{\beta}{\pi(1+2\mu^2\sigma^2\beta)}} \exp\left\{-\frac{\beta z^2}{1+2\mu^2\sigma^2\beta}\right\} \tag{13.38}$$

Note the limits of δ may be taken at $\pm\infty$ when $X_\alpha \gg 1$.

13.3 Optical loss

For the pulsed measurement, mechanical dissipation may be ignored during the optomechanical measurement. However, information about the mechanical oscillator may still be lost to the optical environment. These losses include intrinsic cavity losses and the general-dyne detection inefficiencies. To study the effect of such losses, a beamsplitter model for loss is employed after the optomechanical interaction [331]. To this end, an extra environmental vacuum mode can be introduced that interacts with the output optical mode on a beamsplitter of transmission coefficient η. Consider then a position-quadrature measurement $|Z\rangle$ made by the environment. The measurement operator now becomes

$$\begin{aligned}
\Upsilon' &= \langle Z| \langle X_{\rm L}| \langle P_{\rm L}| U_{\rm bs} U_\eta U |\alpha\rangle |0\rangle |0\rangle && (13.39)\\
&= \left\langle Z \middle| \sqrt{1-\eta^2}\alpha(A+{\rm i}B)\right\rangle \langle X_{\rm L}| \langle P_{\rm L}| U_{\rm bs} |\eta\alpha(A+{\rm i}B)\rangle |0\rangle && (13.40)\\
&= \Theta_Z \Upsilon_\eta, && (13.41)\\
\Upsilon_\eta &= \langle X_{\rm L}| \langle P_{\rm L}| U_{\rm bs} |\eta\alpha(A+{\rm i}B)\rangle |0\rangle && (13.42)\\
\Theta_Z &= \left\langle Z \middle| \sqrt{1-\eta^2}\alpha(A+{\rm i}B)\right\rangle, && (13.43)
\end{aligned}$$

where U_η is the beamsplitter modelling loss. To account for loss of information a trace over the environment must be taken: $Z \in (-\infty, +\infty)$. Note that as Υ_η and Θ_Z are both functions of the position operator $X_{\rm M}$, $[\Upsilon_\eta, \Theta_Z] = 0$, and the measurement map may be written as

$$\begin{aligned}
\rho'_f &= \frac{1}{\mathcal{P}'} \int {\rm d}Z\ \Upsilon' \rho_i \Upsilon'^\dagger \\
&= \frac{1}{\mathcal{P}'} \Upsilon_\eta \left(\int {\rm d}Z\ \Theta_Z \rho_i \Theta_Z^\dagger \right) \Upsilon_\eta^\dagger, && (13.44)\\
\mathcal{P}' &= {\rm tr}\left(\int {\rm d}Z\ \Upsilon'^\dagger \Upsilon' \rho_i \right). && (13.45)
\end{aligned}$$

The measurement operator in Eq. (13.42) is simply the lossless operator Υ of Eq. (12.2) with a reduced optical amplitude $\alpha \to \eta\alpha$. Hence, the action of Υ_η on the position distribution of the initial state is known and so to study the effects of optical loss on the position measurement it suffices to analyze the transformation

$$\rho'_i = \int {\rm d}Z\ \Theta_Z \rho_i \Theta_Z^\dagger, \qquad (13.46)$$

which can be thought of as a change in the mechanical initial state ρ_i due to optical loss.

As the operator Θ_Z is only a function of $X_{\rm M}$

$$\begin{aligned} P_i'(X_{\rm M}) &= \langle X_{\rm M}|\,\rho_i'\,|X_{\rm M}\rangle \\ &= \int {\rm d}Z\ \langle X_{\rm M}|\,\Theta_Z^\dagger\Theta_Z\,|X_{\rm M}\rangle\,P_i(X_{\rm M}) \\ &= \int {\rm d}Z\ \left\langle\sqrt{1-\eta^2}\alpha(A+{\rm i}B)\middle|Z\right\rangle\left\langle Z\middle|\sqrt{1-\eta^2}\alpha(A+{\rm i}B)\right\rangle P_i(X_{\rm M}) \\ &= P_i(X_{\rm M}), \end{aligned} \tag{13.47}$$

where $\int {\rm d}Z\ |Z\rangle\langle Z| = 1$ has been used. Therefore, as $P_i'(X_{\rm M}) = P_i(X_{\rm M})$, Eq. (13.44) indicates that the effect of optical loss on the measurement is to reduce α. This is because the optomechanical unitary U is only a function of mechanical position $X_{\rm M}$ but not momentum $P_{\rm M}$, so measurements made by the environment induce changes in the momentum direction of the mechanical phase space.

As the position distribution of the mechanical state changes in a trivial way with optical loss, it is instructive to study the phase-space distribution of the state of ρ_i' in Eq. (13.46). The Wigner quasiprobability distribution of ρ_i' is given by

$$\begin{aligned} W_i'(X_{\rm M},P_{\rm M}) &= \frac{1}{2\pi}\int {\rm d}u\ {\rm e}^{{\rm i}P_{\rm M}u}\,\langle X_{\rm M}-u/2|\,\rho_i'\,|X_{\rm M}+u/2\rangle \\ &= \frac{1}{2\pi}\int {\rm d}u\ {\rm e}^{{\rm i}P_{\rm M}u}\,\langle X_{\rm M}-u/2|\,\rho_i\,|X_{\rm M}+u/2\rangle\,\mathcal{L}(\mu X_{\rm M},u), \end{aligned} \tag{13.48}$$

$$\mathcal{L}(\mu X_{\rm M},u) = \int {\rm d}Z\ \Theta_Z(\mu X_{\rm M}-\mu u/2)\Theta_Z^\dagger(\mu X_{\rm M}+\mu u/2), \tag{13.49}$$

where the dependence of the function Θ_Z on $X_{\rm M}$ and the dummy variable u is now made clear in its argument. Explicitly, the function $\mathcal{L}(\mu X_{\rm M},u)$ is given by

$$\mathcal{L}(\mu X_{\rm M},u) = \exp\left\{\frac{1}{2}(1-\eta^2)X_\alpha^2\left[\frac{16{\rm i}\mu u}{(\mu u-4{\rm i})^2-4\mu^2X_{\rm M}^2}\right]\right\} \tag{13.50}$$

and satisfies $\mathcal{L}(\mu X_{\rm M},0)=1$.

Firstly, I proceed with a Gaussian approximation to Eq. (13.48) and then check its validity. Hence, consider ρ_i to be some initial Gaussian state with first moments vector $\langle\mathbf{r}\rangle = (\langle X_{\rm M}\rangle,\langle P_{\rm M}\rangle)^{\rm T}$ and covariance matrix $V_{i,j} = \frac{1}{2}\langle\{r_i,r_j\}\rangle - \langle r_i\rangle\langle r_j\rangle$. Here, $V_{1,1} = V_X = \sigma^2$ is the initial position variance, $V_{1,2} = V_{2,1} = V_{XP}$ is the mechanical covariance, and $V_{2,2} = V_P$ is the initial momentum variance. For small optical rotations $\mu\sigma$ and large X_α, the argument of the exponential in $\mathcal{L}(\mu X_{\rm M},0) = 1$ may be expanded to quadratic order. Then, within this Gaussian approximation Eq.(13.48) changes the first and second

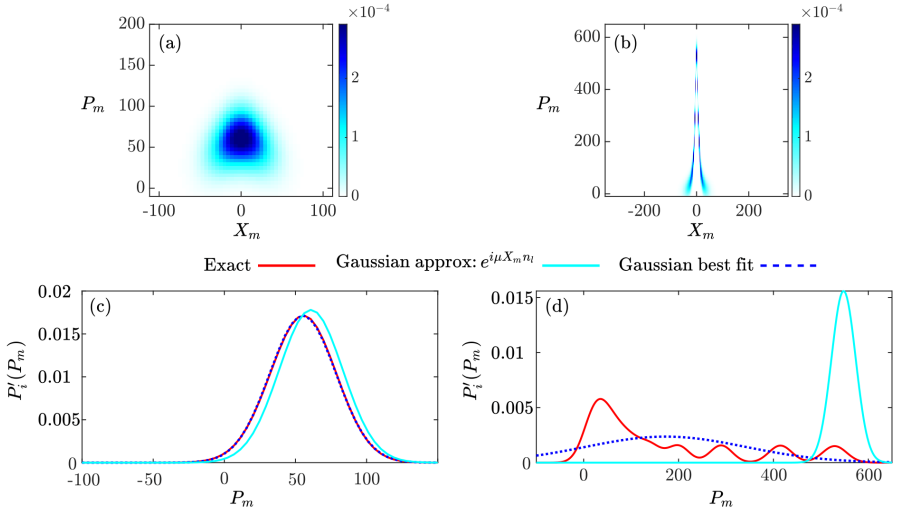


Figure 13.5: **Non-Gaussianity in the mechanical Wigner phase-space distribution along the momentum axis due to optical loss.** Here, $X_\alpha = 200$, $\eta = 0.95$, and the initial mechanical state ρ_i has a covariance matrix with entries $V_X = V_P = \sigma^2 = 500$, $V_{XP} = 0$, and zero means. (a) Wigner distribution $W_i'(X_\mathrm{M}, P_\mathrm{M})$ with $\mu\sigma = 2\pi/9$. (b) Wigner distribution $W_i'(X_\mathrm{M}, P_\mathrm{M})$ with $\mu\sigma = 2\pi$. (c) Momentum marginal for $\mu\sigma = 2\pi/9$. (d) Momentum marginal for $\mu\sigma = 2\pi$. Exact case—red: computed by integrating $W_i'(X_\mathrm{M}, P_\mathrm{M})$ over X_M. Gaussian approximation from $\mathrm{e}^{\mathrm{i}\mu X_\mathrm{M} n_\mathrm{L}}$: corresponding to Eqs (13.51)-(13.55)—cyan. Gaussian best fit—blue dashed.

moments according to

$$V_X \rightarrow V_X, \tag{13.51}$$
$$V_{XP} \rightarrow V_{XP}, \tag{13.52}$$
$$V_P \rightarrow V_P + \frac{1}{2}(1-\eta^2)\mu^2 X_\alpha^2, \tag{13.53}$$
$$\langle X_\mathrm{M}\rangle \rightarrow \langle X_\mathrm{M}\rangle, \tag{13.54}$$
$$\langle P_\mathrm{M}\rangle \rightarrow \langle P_\mathrm{M}\rangle + \frac{1}{2}(1-\eta^2)\mu X_\alpha^2. \tag{13.55}$$

To explain, Eqs (13.51)-(13.55), optical loss causes a mean number of photons $\frac{1}{2}(1-\eta^2)X_\alpha^2$ to be lost to the environment. Then to quadratic order in the optomechanical interaction, the interaction is described by the cavity-free unitary $U \approx \mathrm{e}^{\mathrm{i}\mu X_\mathrm{M} n_\mathrm{L}}$, therefore the effect of optical loss is to cause a mean momentum kick $\mu\frac{1}{2}(1-\eta^2)X_\alpha^2$. The variance in the number of photons lost to environment is also $\frac{1}{2}(1-\eta^2)X_\alpha^2$ so the mechanical momentum variances increases by $\mu^2\frac{1}{2}(1-\eta^2)X_\alpha^2$.

Fig. 13.5 shows the exact Wigner distributions $W_i'(X_\mathrm{M}, P_\mathrm{M})$ of Eq. (13.48) and the corresponding momentum marginals $P_i'(P_\mathrm{M}) = \int \mathrm{d}P_\mathrm{M} W_i'(X_\mathrm{M}, P_\mathrm{M})$. For

small optical rotations $\mu\sigma$, the Gaussian approximations of Eqs (13.51)-(13.55) work well. However, at high values of $\mu\sigma$, the state is now highly non-Gaussian along the momentum marginal, which means a Gaussian approximation cannot be made in $P_{\rm M}$. However, optical loss does not affect the validity of the Gaussian approximation in $X_{\rm M}$ and the description of the position measurement.

To study the full transformation, including the non-Gaussianity of the momentum distribution, one may consider the quasiprobability of Eq. (13.44).

13.4 Results

After exploring the Gaussian approximation, I will now return back to the exact theory of pulsed position measurement described by Eq. (13.3). The pulsed general-dyne measurement changes the mechanical variance from σ^2 to σ_f^2, which depends on the outcome $(X_{\rm L}, P_{\rm L})$. Here, σ_f^2 is the variance of the position distribution of the final state $P_f(X_{\rm M})$, which is in general not a Gaussian distribution. As $X_{\rm L}$ and $P_{\rm L}$ are continuous variables, one may average over all measurement outcomes to quantify the success in reducing the position variance[3]

$$\mathbb{E}[\sigma_f^2] \quad = \quad \int \mathrm{d}X_{\rm L} \int \mathrm{d}P_{\rm L} \mathcal{P}(X_{\rm L}, P_{\rm L}) \sigma_f^2. \tag{13.56}$$

Fig. 13.6(b) shows the averaged variance $\mathbb{E}[\sigma_f^2]$ as a function of $\mu\sigma$ for the optimal beamsplitter transmission coefficient $\zeta_{\rm opt}$, which allows for quantum squeezing well below the ground state width, shown by the shaded grey region. Here, $\zeta_{\rm opt}$ is computed numerically and is plotted in Fig. 13.6(c). At small and large values of $\mu\sigma$, the Q-function is aligned mostly along the $P_{\rm L}$ axis. Hence, the optimal beamsplitter transmission coefficient is close to $\zeta = 1$. While for intermediate values of $\mu\sigma$, Q is aligned mostly parallel to the $X_{\rm L}$ axis, so the optimal setting is closer to $\zeta = 0$. For comparison, Fig. 13.6(b) also plots $\mathbb{E}[\sigma_f^2]$ for a phase-homodyne measurement $\zeta = 1$ and at small optical rotations $\mu\sigma$, agreement is affirmed with the linear theory, shown by the small green shaded region. With increasing optical rotation $\mu\sigma$, this pulsed scheme allows for BAE position measurement well beyond the validity of the linearized regime. Moreover, Fig. 13.6(b) shows that the amount quantum squeezing continues to increase as one exits the linearized regime.

13.4.1 Range of $\mu\sigma$ and the Gaussian approximation

In Fig. 13.6, a range of $\mu\sigma$ from 0 to 2π is explored. As $\mu\sigma$ increases past $\sim \pi/2$ the optimal value of $\mathbb{E}[\sigma_f^2]$ begins to fall again. This is in part due to less light being able to get into the cavity to gain information about the mechanical mode. Of course, one may compensate for this by varying Δ as will be discussed in Chapter 15. However, past a certain value of $\mu\sigma$ other optical modes could be

[3] By accepting only specific outcomes or considering a window of outcomes $X_a < X_{\rm L} < X_b$, $P_a < P_{\rm L} < P_b$ one can achieve lower conditional variances than $\mathbb{E}[\sigma_f^2]$ in a probabilistic way.

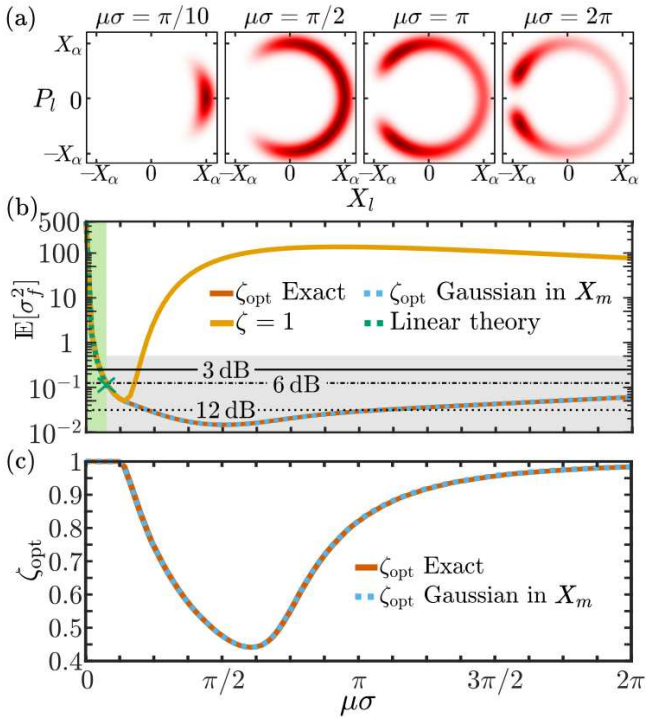


Figure 13.6: **Pulsed back action evading position measurement.** Here, an on-resonant pulse $\Delta = 0$ is considered. (a) Q functions of the optical mode after the optomechanical interaction with increasing optical rotation $\mu\sigma$ and $X_\alpha = 10$. Colour scale: white, at $Q = 0$, through to dark red, at $Q = \max(Q)$. Note the optical phase-space distribution after the pulsed interaction is equal to the general-dyne probability distribution $\mathcal{P}$ when $\zeta = 1/\sqrt{2}$. The maxima of $\mathcal{P}$ do not coincide with the input optical state at $X_{\text{L}} = X_\alpha = 10$, demonstrating the nonlinearity of the cavity transfer function. (b) The mechanical position variance averaged over all measurement outcomes is plotted for the optimal beamsplitter transmission coefficient ζ_{opt} as a function of $\mu\sigma$ with $X_\alpha = 200$, $\sigma^2 = 500$. The grey shaded area indicates quantum squeezing and for these parameters squeezing even below 12 dB can be achieved. The exact theory agrees with the Gaussian approximation in position X_{M}. A comparison to a phase-homodyne measurement $\zeta = 1$ is shown and agreement with the linear theory is also confirmed at small values of $\mu\sigma$. The green shaded area indicates where the linearized regime is valid, which ends at $\mu\sigma = 0.25$ when the linear theory deviates from the exact theory by more than 10%. (c) Plot of the optimal ζ as a function of $\mu\sigma$ shows agreement between the exact case and the Gaussian approximation in X_{M}.

excited within the cavity. If light scatters into these modes and they become populated then the unitary $e^{i\varphi(X_M)n_L}$ is no longer valid. To find a condition for the validity of the single optical mode description, and therefore $e^{i\varphi(X_M)n_L}$, consider the change in the cavity frequency ω_C with the mechanical position $x = x_0 X_M$

$$\begin{aligned} \Delta\omega_C &= |\omega_C(x) - \omega_C(0)| \\ &= \sqrt{2} g_0 |X_M| \\ &\simeq \sqrt{2} g_0 \sigma. \end{aligned} \tag{13.57}$$

Further, the cavity finesse is defined by $\mathcal{F}_C = \Delta\omega_{FSR}/\kappa$, where $\Delta\omega_{FSR}$ is the free spectral range, i.e. the frequency separation between neighbouring optical modes. Scattering into the neighbouring optical mode is negligible—and the single optical mode description is valid—when $\Delta\omega_C < \Delta\omega_{FSR}$, which gives

$$\mu\sigma < 2\mathcal{F}_C; \tag{13.58}$$

a condition which is easily met in many cavity optomechanical implementations [86]. See Chapter 6 for more discussions on the validity of the single optical mode optomechanical Hamiltonian.

Fig. 13.6 also includes the Gaussian approximation to the position measurement detailed in Section 13.2. This approximation agrees with the exact theory as shown in Fig. 13.6. Note that in the limit $\mu\sigma \to \infty$ the Gaussian approximation trivially holds for an initial Gaussian state as $P_f(X_M) = P_i(X_M)$ as explained in Section 13.1.

13.4.2 Measuring only the phase quadrature

As discussed in Section 13.2, outside the linear regime a pure P_L measurement, $\zeta = 1$, is not the optimal measurement setting. Furthermore, it is noteworthy that in Fig 13.6 at higher values of $\mu\sigma$, ζ_{OPT} is close to $\zeta = 1$ but the setting $\zeta = 1$ performs poorly compared to ζ_{OPT}. Fig. 13.7 studies the difference between a $\zeta = 0.99$ and a $\zeta = 1$ measurement to illustrate how sending only a small fraction of the light towards the X_L homodyne can greatly improve the position measurement.

Outside the linear regime, a pure P_L measurement may be poor as many different optical rotations (values of X_M) correspond to the same value of P_L as illustrated by Fig. 13.7. This produces non-Gaussian features in the output mechanical probability distribution $P_f(X_M)$. However, by sending even a small fraction of light towards the X_L homodyne, the non-Gaussianity is greatly reduced. In Fig. 13.7, $\zeta = 0.99$ is chosen because, for the parameters used in this figure, the non-Gaussianity is completely removed.

However, when $\mu\sigma$ is very large, P_L measurements become optimal again. For example, see the Q-function when $\mu\sigma = 50\pi$ in Fig. 13.1; information about the mechanical position is encoded mostly along the P_L quadrature and the optical Q-function is zero away from where the probability is concentrated. Therefore,

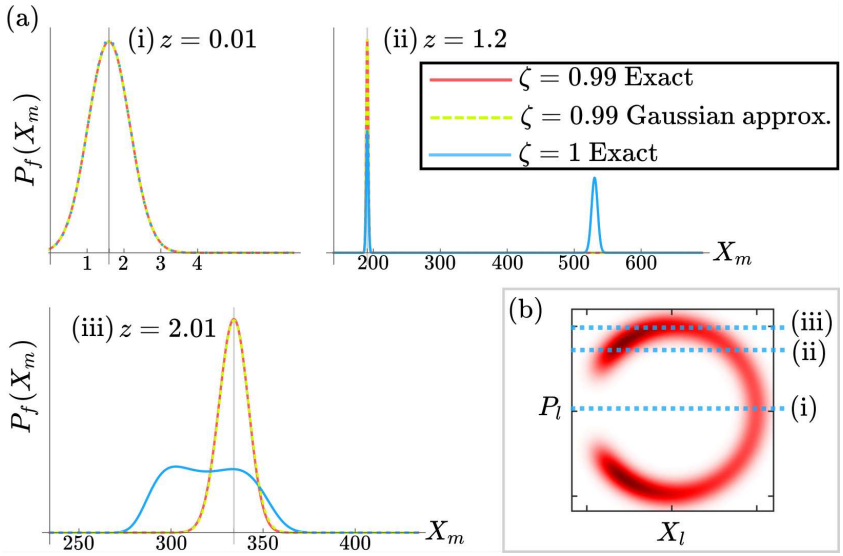


Figure 13.7: Measuring only the P_{L} quadrature leads to suboptimal position measurements outside the linearized regime. (a) The output position probability $P_f(X_{\mathrm{M}})$ for $\zeta = 0.99$ and $\zeta = 1$ for various z at $\delta = 0$. Here, $\sigma = 500$, $X_\alpha = 200$, and $\mu\sigma = \pi$. The Gaussian approximation in X_{M} works extremely well for $\zeta = 0.99$, however for z outside the linear regime, $\zeta = 1$ precludes a Gaussian approximation. (i) $z = 0.01$: for small values of z, both $\zeta = 0.99$ and $\zeta = 1$ lead to a Gaussian $P_f(X_{\mathrm{M}})$. (ii) $z = 1.2$: an example of a value of z outside the linear regime. A pure P_{L}-homodyne measurement ($\zeta = 1$) leads to a bimodal $P_f(X_{\mathrm{M}})$. (iii) $z = 2.01$: at even higher values of z, the P_{L} measurement produces a very non-Gaussian $P_f(X_{\mathrm{M}})$. (b) Depiction of how P_{L} measurements lead to the output position probabilities in cases (i), (ii), and (iii). The Gaussian, bimodal, and non-Gaussian nature of $P_f(X_{\mathrm{M}})$ in cases (i), (ii), and (iii), respectively, are reflected in how the lines $P_{\mathrm{L}} = X_\alpha B(z)$ overlap with the optical Q-functions. Note this diagram is not to scale as the Q-function has been rescaled to a much smaller value of X_α so that the phase-space features can be resolved.

the bimodal and non-Gaussian features present in Fig. 13.7, with $\mu\sigma = \pi$, are no longer present.

13.5 Conclusion and outlook

Here, I have developed the general framework of pulsed measurement from Chapter 12 for the case of a linearly position-coupled optomechanical system ($a^\dagger a X_{\mathrm{M}}$) in a much greater level of detail. By studying the output optical phase-space distribution using the Husimi Q representation, the π-phase limit is observed, which is a key signature of the nonlinear cavity-enhanced interaction.

Furthermore, by introducing a system of coordinates, dubbed 'general-dyne coordinates', it has been shown that an extremely accurate Gaussian approximation to the position measurement can be made. I also carefully analyzed when this Gaussian approximation applies and noted the instances when the general-dyne scheme generates mechanical non-Gaussianity.

In the results section, I demonstrated that the variance of the output mechanical state can be reduced well below the quantum ground state and that our framework is applicable well outside the region where the linearized regime of position measurement is valid. I also demonstrated that one can determine the optimal beamsplitter coefficient for the general-dyne detection scheme and that both the Gaussian and large X_α approximations can be used to greatly reduced the numerical computation time of finding ζ_{OPT}.

Finally, the optical loss calculations show interesting mechanical non-Gaussianity in the momentum direction of phase-space. As such, the theory introduced in this chapter is capable in aiding the development of non-Gaussian quantum superposition state preparation protocols in the regime of nonlinear cavity-enhanced optomechanics—see Ref. [13].

Chapter 14

Continuous position measurements

This chapter draws heavily from Ref. [7], where this work was originally published.

In Chapter 12 I derived the SME of Eq. (12.31), which describes continuous position measurement in nonlinear optomechanics via general-dyne detection. For convenience the SME is again[1]

$$\mathrm{d}\rho = -\frac{\mathrm{i}}{\hbar}[H_0,\rho]\mathrm{d}t + \mathcal{D}[c]\rho\mathrm{d}t + \sqrt{1-\zeta^2}\mathcal{H}[c]\rho\mathrm{d}W_{X_\mathrm{L}} + \zeta\mathcal{H}[-\mathrm{i}c]\rho\mathrm{d}W_{P_\mathrm{L}},$$

where $c = \sqrt{2k}f(X_\mathrm{M})$ and $f(X_\mathrm{M}) = A(X_\mathrm{M}) + \mathrm{i}B(X_\mathrm{M})$.

In this chapter, I focus on nonlinear optomechanics with linear position coupling. By consulting Table 11.1, one may see that in this regime $f = \left[1+\mathrm{i}\left(\frac{\mu}{2}X_\mathrm{M}+\frac{\Delta}{\kappa}\right)\right]/\left[1-\mathrm{i}\left(\frac{\mu}{2}X_\mathrm{M}+\frac{\Delta}{\kappa}\right)\right]$ and

$$\begin{aligned} A(X_\mathrm{M}) &= \frac{1-\left(\frac{\mu}{2}X_\mathrm{M}+\frac{\Delta}{\kappa}\right)^2}{1+\left(\frac{\mu}{2}X_\mathrm{M}+\frac{\Delta}{\kappa}\right)^2}, \\ B(X_\mathrm{M}) &= \frac{2\left(\frac{\mu}{2}X_\mathrm{M}+\frac{\Delta}{\kappa}\right)}{1+\left(\frac{\mu}{2}X_\mathrm{M}+\frac{\Delta}{\kappa}\right)^2}. \end{aligned}$$

Firstly, I detail how the measurement records are defined, before then confirming agreement with the limiting cases of cavity-free and linearized optomechanics.

I then describe how the SME for continuous position measurement predicts a new regime: the *stochastic Gaussian* regime. Like linearized optomechanics, this regime allows for a complete description of the mechanical dynamics using just the first and second mechanical moments. Unlike linearized optomechanics,

[1] Here, I have left out the optical loss and mechanical dissipation for clarity—see Eq. (12.32) for the full expression

the stochastic Gaussian regime can describe arbitrarily large optical rotations and all the interesting physics that comes with that.

14.1 Measurement records

From Chapter 5 and 12, one may deduce that the measurement records for the $X_{\rm L}$ and $P_{\rm L}$ homodyne detectors comprising the continuous general-dyne measurement are

$$\mathrm{d}y_{X_{\rm L}} = \langle A\rangle\,\mathrm{d}t + \frac{\mathrm{d}W_{X_{\rm L}}}{\sqrt{8\eta_{X_{\rm L}}(1-\zeta^2)k}}, \tag{14.1}$$

$$\mathrm{d}y_{P_{\rm L}} = \langle B\rangle\,\mathrm{d}t + \frac{\mathrm{d}W_{P_{\rm L}}}{\sqrt{8\eta_{P_{\rm L}}\zeta^2 k}}. \tag{14.2}$$

From these measurement records and the expectation values of $\langle A\rangle$ and $\langle B\rangle$ from the previous time step, an observer may estimate the mechanical density operator at the next time step using the SME of Eq. (12.32) [71]. Notably, the measurement records measured by an observer would appear fairly noisy due to the stochastic terms in Eqs (14.1) and (14.2).

For visualization purposes, the general-dyne measurement records are integrated over some finite integration time τ as follows

$$X_{\rm L}(t) = \sqrt{\frac{4k\eta_{X_{\rm L}}(1-\zeta^2)}{\tau}}\int_{t-\tau}^{t}\mathrm{d}y_{X_{\rm L}}, \tag{14.3}$$

$$P_{\rm L}(t) = \sqrt{\frac{4k\eta_{P_{\rm L}}\zeta^2}{\tau}}\int_{t-\tau}^{t}\mathrm{d}y_{P_{\rm L}}, \tag{14.4}$$

which enables the phase-space asymmetry, discussed in Section 14.3.3, to be identified more clearly. We will refer to $X_{\rm L}(t)$ and $P_{\rm L}(t)$ as the integrated general-dyne measurement currents. These measurement currents are defined such that in the absence of an optomechanical interaction at $\mu = 0$, the variances are $\mathbb{E}(X_{\rm L}^2) - \mathbb{E}(X_{\rm L})^2 = \mathbb{E}(P_{\rm L}^2) - \mathbb{E}(P_{\rm L})^2 = 1/2$ and the means are $\mathbb{E}(X_{\rm L}) = \sqrt{4k\eta_{X_{\rm L}}(1-\zeta^2)\tau}$ and $\mathbb{E}(P_{\rm L}) = 0$. The integration time is chosen such that $X_\alpha = \sqrt{4k\tau}$, so that for $\mu = 0$, $\mathbb{E}(X_{\rm L}) = X_\alpha\sqrt{\eta_{X_{\rm L}}(1-\zeta^2)}$. In other words, in the absence of any interaction, the measurement records are processed so that the $X_{\rm L}(t)$ and $P_{\rm L}(t)$ measurement currents enable a coherent state with an amplitude $\sqrt{\eta_{X_{\rm L}}(1-\zeta^2)}$ to be visualized.

14.2 Agreement with cavity-free and linearized optomechanics

The SME of Eq. (12.31) is a general theory of nonlinear cavity-enhanced position measurement that encompasses both cavity-free and linearized optomechanics, as well as new regimes of operation. Therefore, before I explore a new regime of

operation predicted by Eq. (12.31), I will first confirm agreement with cavity-free and linearized continuous measurements.

14.2.1 Cavity-free continuous measurements

In Chapter 6 I derived the cavity-free SME for continuous position measurements, which is given by Eq. (6.108). Now one can see explicitly how Eq. (6.108) is the cavity free limit of Eq. (12.31) by looking at the measurement output operator $c = \sqrt{2k}\mathrm{e}^{\mathrm{i}\varphi(X_{\mathrm{M}})}$, which becomes $c = \sqrt{2k}\mathrm{e}^{\mathrm{i}\mu X_{\mathrm{M}}}$ in the cavity free limit—see Section 11.1.4.

14.2.2 Standard linearized continuous measurements

For small optical rotations $\mu\sigma \ll 1$ and zero detuning $\Delta = 0$, $c = \sqrt{2k}f(X_{\mathrm{M}}) \approx \sqrt{2k} + \mathrm{i}c_{\mathrm{L}}$ with $c_{\mathrm{L}} = \sqrt{2k_{\mathrm{L}}}X_{\mathrm{M}}$ and $k_{\mathrm{L}} = \mu^2 k$. Further, from Appendix E, one also has that measurement rate is $k_{\mathrm{L}} = 2g^2/\kappa$ in the linearized regime. Then, using the following properties of the superoperators, with $\gamma \in \mathbb{C}$

$$\mathcal{H}[c+\gamma]\rho = \mathcal{H}[c]\rho, \tag{14.5}$$

$$\mathcal{D}[c+\gamma]\rho = \mathcal{D}[c]\rho + \frac{1}{2}[\gamma^* c - \gamma c^\dagger, \rho], \tag{14.6}$$

the nonlinear SME in Eq. (12.31) returns the continuous SME of standard linearized optomechanics

$$\begin{aligned}\mathrm{d}\rho = &-\frac{\mathrm{i}}{\hbar}[H_0,\rho]\mathrm{d}t + \mathrm{i}2\mu k[X_{\mathrm{M}},\rho]\mathrm{d}t + \mathcal{D}[c_{\mathrm{L}}]\rho\mathrm{d}t \\ &+\sqrt{1-\zeta^2}\mathcal{H}[\mathrm{i}c_{\mathrm{L}}]\rho\mathrm{d}W_{X_{\mathrm{L}}} + \zeta\mathcal{H}[c_{\mathrm{L}}]\rho\mathrm{d}W_{P_{\mathrm{L}}}.\end{aligned} \tag{14.7}$$

Here, there is also a term corresponding to the X_{L} measurement in the generaldyne detection—compare Eq. (14.7) to Eq. (6.75), which only includes the phase homodyne measurement. Note that the superoperator term corresponding to the X_{L} measurement can be rewritten as $\mathcal{H}[\mathrm{i}c_{\mathrm{L}}]\rho = \mathrm{i}\mu\sqrt{2k}[X_{\mathrm{M}},\rho]$, which does not localize the position operator. Furthermore, the term $\mathrm{i}2\mu k[X_{\mathrm{M}},\rho]\mathrm{d}t$ represents a *deterministic* momentum kick on the mechanical oscillator, which leads to a shift in the equilibrium mean position and is typically transformed away. Note this transformation is only valid if in the lab frame if $\mu\sigma \ll 1$. Furthermore, in the linearized regime one can rewrite $2\mu k = \sqrt{2}g_0|\alpha_c|^2 = \sqrt{2}g|\alpha_c|$ in Eq. (14.7) to write the deterministic momentum kick term in a more familiar form.

Steady state solutions

Being a linear SME, Eq. (14.7) admits a complete description of a continuous measurement on an initial Gaussian state through the adjoint equations for the first and second moments of the vector $\mathbf{X} = (X_{\mathrm{M}}, P_{\mathrm{M}})^{\mathrm{T}}$. For Eq. (14.7), the inherent stochasticity of the continuous measurement decouples from the covariance matrix elements, which may be then solved deterministically [71].

Introducing optical loss η in the measurement process, the steady state (infinite time) solutions to Eq. (14.7) are

$$V_{XP}^{ss} = \frac{-\omega_{\rm M} + \sqrt{\omega_{\rm M}^2 + 16\zeta^2\eta\left(1-\eta+\zeta^2\eta\right)k_{\rm L}^2}}{8\zeta^2\eta k_{\rm L}}, \tag{14.8}$$

$$V_X^{ss} = \sqrt{\frac{\omega_{\rm M} V_{XP}^{ss}}{4\zeta^2\eta k_{\rm L}}}, \tag{14.9}$$

$$V_P^{ss} = V_X^{ss} + \frac{8\zeta^2\eta V_{XP}^{ss} V_X^{ss} k_{\rm L}}{\omega_{\rm M}}. \tag{14.10}$$

As the derivation of these steady state values requires some mathematics that will be introduced in the next section, I refer the reader to Appendix J.1 for a derivation.

The minimum squeezing variance $V_{\rm min}$

In the linearized regime, mechanical information is only encoded on the $P_{\rm L}$ quadrature of light and so from here on I set $\zeta = 1$ in Eqs (14.8), (14.9), and (14.10). I will now discuss the squeezing of the mechanical mode via continuous position measurement.

Quantum squeezing below the ground state width is achieved if, for some mechanical quadrature $X_\theta = X_{\rm M}\cos\theta + P_{\rm M}\sin\theta$, one has that $\mathrm{Var}(X_\theta) < 1/2$. When $\mathrm{Var}(X_\theta)$ reaches its minimum value at $\theta_{\rm min}$, this is called the minimum squeezing variance $\mathrm{Var}(X_{\theta_{\rm min}}) \equiv V_{\rm min}$ and it corresponds to the minimum eigenvalue of the covariance matrix V. For a continuous position measurement, the amount of squeezing depends on the ratio of the measurement rate to the mechanical frequency $k_{\rm L}/\omega_{\rm M}$. For the steady state solutions above, the minimum squeezing variance $V_{\rm min}$ and the minimum squeezing angle $\theta_{\rm min}$ are plotted in Figs. 14.1 and 14.2, respectively. As $k_{\rm L}/\omega_{\rm M} \to \infty$, Eq. (14.8) gives $V_{XP}^{ss} \to 1/2\eta$, which is non-zero[2] and implies the covariance matrix V is *not* diagonal in this limit. Therefore, even in the limit $k_{\rm L}/\omega_{\rm M} \to \infty$, one always has $V_{\rm min} < V_X^{ss}$. However, as shown in Fig. 14.2 as $k_{\rm L}/\omega_{\rm M} \to \infty$ the minimum squeezing angle $\theta_{\rm min} \to 0$, which implies one gets infinitesimally close to true position squeezing.

For small values of $k_{\rm L}/\omega_{\rm M} \ll 1$ and $\eta < 1$, one does not extract mechanical position information fast enough to achieve mechanical squeezing, i.e. a precise position measurement. However, this means the mechanical state remains symmetric in phase space and so in this way one can cool the mechanical state by reducing uncertainty in both the mechanical position and momentum symmetrically—see Ref. [388] for an experimental demonstration of cooling via continuous position measurement for $k_{\rm L}/\omega_{\rm M} \ll 1$.

[2] Only the mechanical position is measured in optomechanics as the interaction Hamiltonian is a function of $X_{\rm M}$ and not $P_{\rm M}$. However, when the system freely evolves the mechanical position being measured at time t will depend on the mechanical momentum at $t' < t$. Hence, position and momentum become correlated in this way.

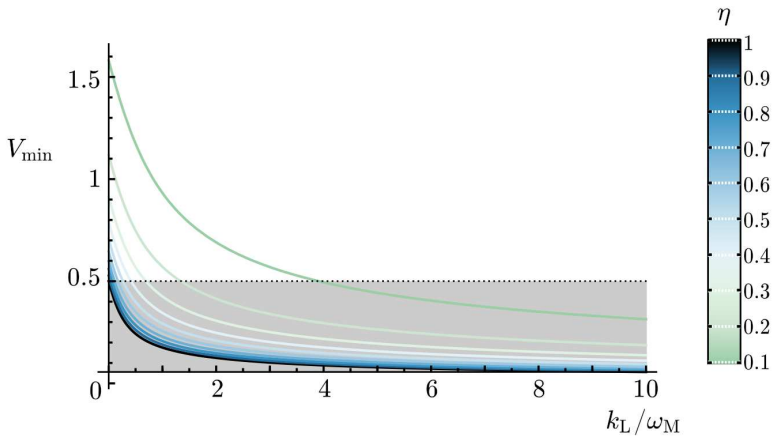


Figure 14.1: **Minimum squeezing variance $V_{\min}$.** Here, $V_{\min} \equiv \mathrm{Var}(X_{\theta_{\min}})$, where $\theta_{\min}$ is shown in Fig. 14.2. At high values of $k_{\mathrm{L}}/\omega_{\mathrm{M}}$ the state can become quantum squeezed (shown by the grey shaded region) for all values of η shown. As $k_{\mathrm{L}}/\omega_{\mathrm{M}} \to 0$ at $\eta = 1$, the state is cooled to the quantum ground state with $V_X = V_P = V_{\min} = 1/2$.

14.3 The stochastic Gaussian regime

From a mathematical perspective, the advantage of the linear regime is that for an initial Gaussian state the first and second moments provide a full description of the mechanical state evolution under continuous measurement [47], which is vastly more efficient than the description in the infinite dimensional Hilbert space. Physically, the linear regime allows for the preparation of mechanical Gaussian states, such as cooled states and squeezed states, which are useful for state preparation and quantum sensing.

However, here a new Gaussian limit of Eq. (12.31) is derived that goes beyond standard linear optomechanics, which can describe optomechanical position measurement for arbitrarily large optical rotations and optomechanical coupling rates, while still accurately describing the nonlinear response of the cavity and the π-phase limit. In linearized optomechanics the evolution of the mechanical covariance matrix is deterministic. While curiously in this new regime, the evolution of the mechanical covariance matrix is *stochastic* as the variances depend on the measurement outcomes. Thus, this new Gaussian regime of operation is identified as the *stochastic Gaussian* regime. I will now derive and explore the stochastic Gaussian regime.

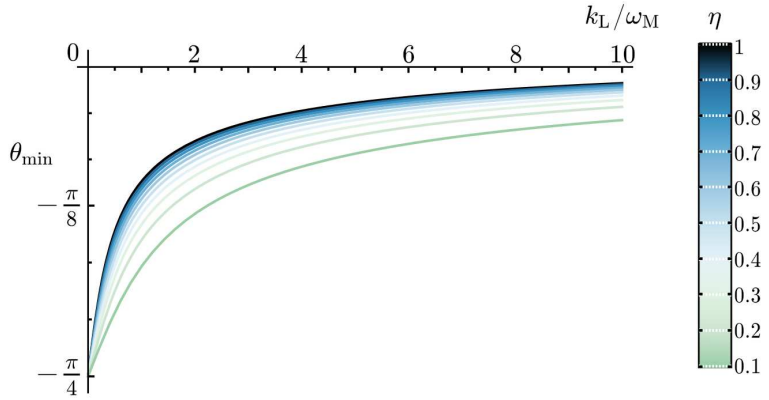


Figure 14.2: **Minimum squeezing angle θ_{min}.** As $k_{\text{L}}/\omega_{\text{M}} \to \infty$, the amount of squeezing increases and $\theta_{\text{min}} \to 0$ meaning the mechanics tends towards a position squeezed state. As $k_{\text{L}}/\omega_{\text{M}} \to 0$, $\theta_{\text{min}} \to \pi/4$. However, in this limit the state becomes symmetric in phase space $V_X \approx V_P$—see Eqs (14.8), (14.9), and (14.10).

14.3.1 Derivation and mathematics

Expansion about the mean, measurement output operator and current

First, let's write $\mu X_{\text{M}} = \mu \langle X_{\text{M}} \rangle + \mu Y_{\text{M}}$ at every time step $t \to t + \mathrm{d}t$ in the SME. Note that as $\langle X_{\text{M}} \rangle$ will change with time, this transformation is time-dependent. Then one may expand c to first order in μY_{M} if $\langle \mu Y_{\text{M}} \rangle^2 \sim \text{Var}(\mu Y_{\text{M}}) \ll 1$ at each time step. Importantly, the infinitesimal phase shifts μY_{M} over each $t \to t + \mathrm{d}t$ may integrate to arbitrarily large optical rotations $\mu\sigma$ over a finite duration. By expanding about $\langle X_{\text{M}} \rangle$ at each time t, the physics of large optical rotations can be explored. Such large optical rotations cannot be described within the linearized regime, which requires $\mu^2\sigma^2 \ll 1$ and implies only small phase shifts.

To first order in μY_{M},

$$c = \sqrt{2k} f(\langle X_{\text{M}} \rangle) + \frac{\mathrm{i} c_{\text{L}}}{\left[1 - \mathrm{i}\left(\frac{\mu}{2}\langle X_{\text{M}} \rangle + \frac{\Delta}{\kappa}\right)\right]^2} \tag{14.11}$$

with $c_{\text{L}} = c_{\text{L}}^\dagger = \sqrt{2k_{\text{L}}} Y_{\text{M}}$. Here, $k_{\text{L}} = \mu^2 k$ and k_{L} is *not* equal to $2g^2/\kappa$, which is valid only for small optical rotations—see the discussion above on the the

linearized measurement rate. The measurement records are therefore

$$\mathrm{d}y_{X_{\mathrm{L}}} = A(\langle X_{\mathrm{M}}\rangle)\mathrm{d}t + \frac{\mathrm{d}W_{X_{\mathrm{L}}}}{\sqrt{8\eta_{X_{\mathrm{L}}}(1-\zeta^2)k}}, \tag{14.12}$$

$$\mathrm{d}y_{P_{\mathrm{L}}} = B(\langle X_{\mathrm{M}}\rangle)\mathrm{d}t + \frac{\mathrm{d}W_{P_{\mathrm{L}}}}{\sqrt{8\eta_{P_{\mathrm{L}}}\zeta k}}, \tag{14.13}$$

as by definition $\langle Y_{\mathrm{M}}\rangle = 0$. The difference with Eqs (14.1) and (14.2) is in taking the expectation value of X_{M} before entering it into the functions A and B. The measurement currents are defined in the same way as in the general nonlinear theory.

The stochastic Gaussian SME

Expanding the SME of Eq. (12.31) to first order in μY_{M} gives

$$\begin{aligned}\mathrm{d}\rho &= -\frac{\mathrm{i}}{\hbar}[H_0+H_1,\rho]\mathrm{d}t + \mathcal{D}\left[\frac{c_{\mathrm{L}}}{1+(\frac{\mu}{2}\langle X_{\mathrm{M}}\rangle+\frac{\Delta}{\kappa})^2}\right]\rho\mathrm{d}t \\ &\quad +\sqrt{1-\zeta^2}\mathcal{H}\left[\frac{\mathrm{i}c_{\mathrm{L}}}{\left[1-\mathrm{i}\left(\frac{\mu}{2}\langle X_{\mathrm{M}}\rangle+\frac{\Delta}{\kappa}\right)\right]^2}\right]\rho\mathrm{d}W_{X_{\mathrm{L}}} \\ &\quad +\zeta\mathcal{H}\left[\frac{c_{\mathrm{L}}}{\left[1-\mathrm{i}\left(\frac{\mu}{2}\langle X_{\mathrm{M}}\rangle+\frac{\Delta}{\kappa}\right)\right]^2}\right]\rho\mathrm{d}W_{P_{\mathrm{L}}},\end{aligned} \tag{14.14}$$

where the term H_1 now describes a *stochastic* momentum kick, explicitly given by

$$\frac{H_1}{\hbar} = -\frac{2\mu k}{1+(\frac{\mu}{2}\langle X_{\mathrm{M}}\rangle+\frac{\Delta}{\kappa})^2}Y_{\mathrm{M}}. \tag{14.15}$$

This momentum kick is stochastic due to the denominator in Eq. (14.15), which originates from the nonlinear cavity response. Therefore to study the effect of this term, I do not transform it away by shifting the X_{M} and P_{M} coordinates. Furthermore as $\mu\langle X_{\mathrm{M}}\rangle/2 + \Delta/\kappa \to \infty$, Eq. (14.14) tends towards $\mathrm{d}\rho = -\mathrm{i}[H_0/\hbar,\rho]\mathrm{d}t$ as the light is no longer resonant with the cavity and is simply reflected at the input.

Adding mechanical decoherence and optical loss to Eq. (14.14) and using Eq. (14.6) gives

$$\begin{aligned}\mathrm{d}\rho &= \frac{\mathrm{i}}{\hbar}[H_0+H_1+H_2,\rho]\mathrm{d}t + \mathcal{D}\left[\frac{c_{\mathrm{L}}}{1+(\frac{\mu}{2}\langle X_{\mathrm{M}}\rangle+\frac{\Delta}{\kappa})^2}\right]\rho\mathrm{d}t \\ &+ \mathcal{D}[L_Y]\rho\mathrm{d}t + \sqrt{(1-\zeta^2)\eta_{X_{\mathrm{L}}}}\mathcal{H}\left[\frac{\mathrm{i}c_{\mathrm{L}}}{\left[1-\mathrm{i}\left(\frac{\mu}{2}\langle X_{\mathrm{M}}\rangle+\frac{\Delta}{\kappa}\right)\right]^2}\right]\rho\mathrm{d}W_{X_{\mathrm{L}}} \\ &+ \zeta\sqrt{\eta_{P_{\mathrm{L}}}}\mathcal{H}\left[\frac{c_{\mathrm{L}}}{\left[1-\mathrm{i}\left(\frac{\mu}{2}\langle X_{\mathrm{M}}\rangle+\frac{\Delta}{\kappa}\right)\right]^2}\right]\rho\mathrm{d}W_{P_{\mathrm{L}}},\end{aligned} \tag{14.16}$$

where $H_2/\hbar = -\theta\gamma \langle X_{\rm M}\rangle P_{\rm M}$ and $L_Y = \sqrt{\frac{4\gamma k_{\rm B}T}{\hbar\omega_{\rm M}}}Y_{\rm M} + {\rm i}\theta\sqrt{\frac{\hbar\omega_{\rm M}\gamma}{4k_{\rm B}T}}P_{\rm M}$, which as before models quantum Brownian motion for $\theta = 1$, or momentum diffusion for $\theta = 0$.

Stochastic Riccati equations

Here, I recast Eq. (14.16) into a system of stochastic differential equations (SDEs), but, importantly, I include the linear term in the Hamiltonian, accounted for by the displacement vector $\mathbf{d}$. For more information on the derivation of SDEs in optomechanics, the reader is referred to Ref. [389]. Defining the vector $\mathbf{r} = (Y_{\rm M}, P_{\rm M})^{\rm T}$ the Hamiltonian is rewritten as

$$
\begin{aligned}
H &= \frac{1}{2}\mathbf{r}^T R\mathbf{r} + \mathbf{d}^T\Omega\mathbf{r}, && (14.17)\\
R &= \omega_{\rm M}\mathbb{1}, && (14.18)\\
\mathbf{d} &= \begin{pmatrix} -\theta\gamma\langle X_{\rm M}\rangle \\ -\omega_{\rm M}\langle X_{\rm M}\rangle + \dfrac{2\mu k}{1+\left(\frac{\mu}{2}\langle X_{\rm M}\rangle + \frac{\Delta}{\kappa}\right)^2}\end{pmatrix}, && (14.19)\\
\Omega &= \begin{pmatrix} 0 & 1 \\ -1 & 0\end{pmatrix}. && (14.20)
\end{aligned}
$$

Then writing the three independent measurement output operators in Eq. (14.16) as a vector $\mathbf{c} = C\mathbf{r}$ with

$$
\begin{aligned}
C &= \begin{pmatrix} C_{11} & 0 \\ C_{21} & 0 \\ C_{31} & C_{32}\end{pmatrix}, && (14.21)\\
C_{11} &= \frac{{\rm i}\sqrt{2k_{\rm L}(1-\zeta^2)}}{\left[1-{\rm i}\left(\frac{\mu}{2}\langle X_{\rm M}\rangle + \frac{\Delta}{\kappa}\right)\right]^2}, && (14.22)\\
C_{21} &= \frac{\sqrt{2k_{\rm L}\zeta^2}}{\left[1-{\rm i}\left(\frac{\mu}{2}\langle X_{\rm M}\rangle + \frac{\Delta}{\kappa}\right)\right]^2}, && (14.23)\\
C_{31} &= \sqrt{\frac{4\gamma k_{\rm B}T}{\hbar\omega_{\rm M}}}, && (14.24)\\
C_{32} &= {\rm i}\theta\sqrt{\frac{\hbar\omega_{\rm M}\gamma}{4k_{\rm B}T}}. && (14.25)
\end{aligned}
$$

Furthermore, I define the efficiency matrix $\boldsymbol{\eta} = {\rm diag}\,(\eta_{X_{\rm L}}, \eta_{P_{\rm L}}, 0)$ and the vector of Wiener increments ${\rm d}\mathbf{W} = ({\rm d}W_{X_{\rm L}}, {\rm d}W_{P_{\rm L}}, 0)^{\rm T}$. Here, the last element of ${\rm d}\mathbf{W}$ has been set to zero for simplicity as this term will always be multiplied by the last diagonal entry of $\boldsymbol{\eta}$, which is zero; the channel describing mechanical dissipation is only monitored by the environment and not by an observer.

I then introduce the drift matrix M, the diffusion matrix D, and the noise

matrix N

$$M = \Omega\left(R + \mathrm{Im}[C^\dagger(t)C(t)]\right), \tag{14.26}$$
$$D = -\Omega \mathrm{Re}[C^\dagger(t)C(t)]\Omega, \tag{14.27}$$
$$N = 2V\mathrm{Re}[C^{\mathrm{T}}(t)] - \Omega\mathrm{Im}[C^{\mathrm{T}}(t)], \tag{14.28}$$

and one finds that—given an initial Gaussian mechanical state—the dynamics described by Eq. (14.16) can be completely described by 5 independent SDEs. Namely, two SDES describing the evolution of the first moments

$$\mathrm{d}\left\langle \mathbf{r}\right\rangle = \left(M\left\langle \mathbf{r}\right\rangle + \mathbf{d}\right)\mathrm{d}t + N\sqrt{\boldsymbol{\eta}}\mathrm{d}\mathbf{W} \tag{14.29}$$

and a stochastic Riccati matrix equation describing the evolution of the 3 independent covariance matrix elements

$$\frac{\mathrm{d}V}{\mathrm{d}t} = MV + VM^{\mathrm{T}} + D - N\boldsymbol{\eta}N^{\mathrm{T}}. \tag{14.30}$$

Here, $V_{ij} = \left\langle\{r_i, r_j\}\right\rangle/2 - \left\langle r_i\right\rangle\left\langle r_j\right\rangle$ with $V_{11} = V_X$, $V_{12} = V_{21} = V_{XP}$, and $V_{22} = V_P$. As opposed to linearized optomechanics, the Riccati equation is no longer deterministic. The origin of this stochasticity comes from the dependence of the measurement output operators $\mathbf{c}$ on the stochastic mean position $\langle X_{\mathrm{M}}\rangle$. Furthermore, note that the covariance matrix is invariant under the transformation $X_{\mathrm{M}} = \langle X_{\mathrm{M}}\rangle + Y_{\mathrm{M}}$ at each time step, i.e. $V_X = \left\langle X_{\mathrm{M}}^2\right\rangle - \langle X_{\mathrm{M}}\rangle^2 = \left\langle Y_{\mathrm{M}}^2\right\rangle - \langle Y_{\mathrm{M}}\rangle^2$ and $V_{XP} = \left\langle\{X_{\mathrm{M}}, P_{\mathrm{M}}\}\right\rangle/2 - \langle X_{\mathrm{M}}\rangle\langle P_{\mathrm{M}}\rangle = \left\langle\{Y_{\mathrm{M}}, P_{\mathrm{M}}\}\right\rangle/2 - \langle Y_{\mathrm{M}}\rangle\langle P_{\mathrm{M}}\rangle$.

The condition $\mathrm{Var}(\mu Y_{\mathbf{m}}) \ll 1$

In general the condition $\mathrm{Var}(\mu Y_{\mathrm{M}}) \ll 1$ may not hold at short times, especially for larger initial thermal occupations than considered below in the results section. However, providing the nonlinear measurement brings the mechanical oscillator to a region where $\mathrm{Var}(\mu Y_{\mathrm{M}}) \ll 1$, then the stochastic Gaussian regime holds for the rest of the trajectory as Eqs (14.29) and (14.30) describe Markovian dynamics.

Choice of $\zeta = 1/\sqrt{2}$ and validity of the stochastic Gaussian regime

As opposed to the pulsed regime, in the continuous regime finding the optimal ζ is much more numerically intensive. For each given parameter set, many runs of the SDEs would need to be computed for each value of ζ. Also there is the additional complication of choosing a period of time to run these simulations as no steady state is reached as compared to the linearized regime of optomechanics. Hence, in the results section $\zeta = 1/\sqrt{2}$ is chosen for simplicity and because it limits stochastic fluctuations at short times, which leads to less variation run to run, as will now be explained.

If the initial condition of the SDEs is $\langle X_{\mathrm{M}}\rangle = 0$, such as a thermal state, expanding in small $\mu\langle X_{\mathrm{M}}\rangle$ is valid near $t = 0$. In this case, when Eq. (14.30)

is expanded in $\mu\langle X_{\rm M}\rangle$ then selecting $\zeta = 1/\sqrt{2}$ leads to a cancellation of all terms that are first order in $\langle X_{\rm M}\rangle$, provided $\eta_{X_{\rm L}} = \eta_{P_{\rm L}}$. Therefore, even though $\mathrm{Var}(\mu Y_{\rm M}) \ll 1$ may not hold in general near $t = 0$—especially for large thermal states—by selecting $\zeta = 1/\sqrt{2}$ one selects the general-dyne setting that most effectively limits the effect of stochastic fluctuations on the mechanical position variance at short times. This limits the variation in results from run to run of the SDEs and therefore one needs to compute fewer runs in total to achieve the same level of accuracy. Note that $\zeta = 1/\sqrt{2}$ and $\eta_{X_{\rm L}} = \eta_{P_{\rm L}}$ are *not* prerequisites for the stochastic Gaussian regime to hold but chosen here to simply demonstrate the working principle.

14.3.2 Connection to classical estimation theory

In linearized optomechanics, the equations of motion for the means and variances of the mechanical state correspond to the Kalman-Bucy filter of classical estimation theory. The extended Kalman-Bucy filter is a nonlinear version of the Kalman-Bucy filter, which linearizes about the current estimates of the means and variances. In this way, Eqs (14.29) and (14.30) of the stochastic Gaussian regime corresponds to the extended Kalman-Bucy filter of classical estimation theory.

14.3.3 Origin of the asymmetry in the general-dyne distribution: the stochastic momentum kick term

Consider an initial thermal mechanical state with $\langle X_{\rm M}\rangle = 0$. Even when $\Delta = 0$, there will still be an intrinsic asymmetry in the phase-space distribution of the integrated $(X_{\rm L}, P_{\rm L})$ general-dyne currents defined above. The mathematical origin of this asymmetry is the term $\mathbf{d}$ of Eq. (14.19). Namely, the term $2\mu k/\left(1 + (\frac{\mu}{2}\langle X_{\rm M}\rangle)^2\right)$ in $\mathbf{d}$ represents a stochastic momentum kick. In the linearized regime of optomechanics, this momentum kick term is deterministic and can be transformed away via a displacement operator. However, the intrinsic nonlinearity of the cavity-enhanced optomechanical interactions breaks the symmetry of momentum translations and this term must be accounted for. One may visualize the effect of this stochastic momentum kick by removing it in the simulations of Eqs (14.29) and (14.30) as shown in Fig. 14.3. Here, $\Delta = 0$ too as a non-zero Δ will also impart a phase shift to the optics, leading to an asymmetrical distribution.

Fig. 14.3(a) shows the distribution of the integrated general-dyne currents $(X_{\rm L}, P_{\rm L})$ without the term $2\mu k/\left(1 + (\frac{\mu}{2}\langle X_{\rm M}\rangle)^2\right)$ for a particular stochastic trajectory, while Fig. 14.3(b) includes the stochastic momentum kick. Comparison of these two figures confirms that $2\mu k/\left(1 + (\frac{\mu}{2}\langle X_{\rm M}\rangle)^2\right)$ is the mathematical origin of the asymmetry. Furthermore, the maxima of the phase-space distributions are located away from the initial coherent state $X_{\rm L} = X_\alpha\sqrt{\eta_{X_{\rm L}}(1-\zeta^2)}$, which is another signature of the nonlinear regime and is also present in the pulsed regime. The location of the maxima in Fig. 14.3(b) indicate that when the light passes in and out of the cavity, it receives a phase shift much larger

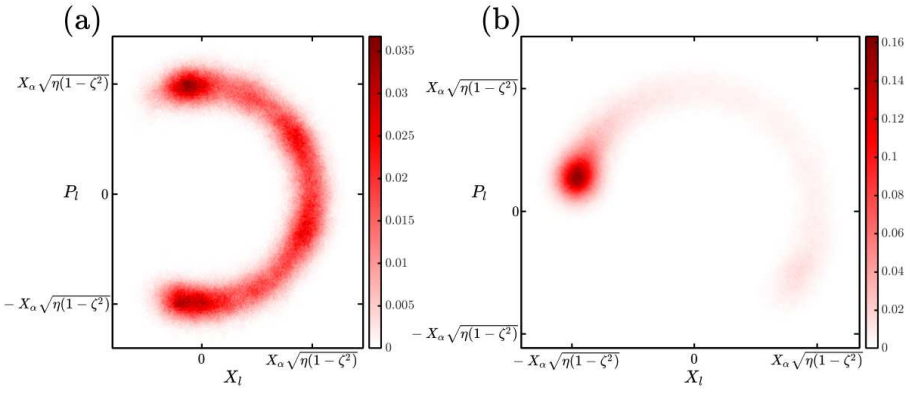


Figure 14.3: **General-dyne distribution of the integrated currents $(X_\mathrm{l}, P_\mathrm{l})$ as a 2D histogram.** Here, the phase-space distributions are recorded over 10 mechanical periods. Here, $X_\alpha = 10$, $\Delta = 0$, $\omega_\mathrm{M}/2\pi = 10\,\mathrm{MHz}$, $\mu = 0.05$, $\mu^2 k/\omega_\mathrm{M} = 6$, $\eta_{X_\mathrm{L}} = \eta_{P_\mathrm{L}} = 0.95$, $\gamma/2\pi = 1\,\mathrm{Hz}$, $\zeta = 1/\sqrt{2}$, $T = 100\,\mathrm{mK}$ and the initial mechanical state is in thermal equilibrium with its surroundings. (a) Without including the term $2\mu k/\left(1+(\frac{\mu}{2}\langle X_\mathrm{M}\rangle)^2\right)$ in $\mathbf{d}$. (b) Including the term $2\mu k/\left(1+(\frac{\mu}{2}\langle X_\mathrm{M}\rangle)^2\right)$ in $\mathbf{d}$, which describes a stochastic momentum kick.

than if the mean mechanical position was averaged around $\langle X_\mathrm{M}\rangle = 0$. Looking ahead to Fig. 14.5, one may see that $\langle X_\mathrm{M}\rangle$ is often located far from zero due to the stochastic momentum kick term.

14.3.4 Drive locking via a Butterworth filter

Physically, it is not possible to simply remove the stochastic momentum kick term described in the previous section, hence here I discuss the choice of the detuning Δ that locks the drive to the cavity frequency. At zero detuning $\Delta = 0$, the optical phase shift averaged over a given stochastic trajectory is positive as shown in Fig. 14.3(b). This is because the radiation-pressure force causes the time-averaged mean mechanical position to effectively detune the cavity away from resonance. Hence, to maximize the amount of light that enters the cavity, and ensure the time-averaged optical phase shift is zero, feedback is applied to the vary the detuning Δ of the drive laser. The goal of this feedback is to choose a Δ along the stochastic trajectory that effectively cancels the slowly varying component of $\langle X_\mathrm{M}\rangle$, while the dynamics and fluctuations of the mechanical position are still measured. Hence, a third-order Butterworth filter is applied to the time trace of $\langle X_\mathrm{M}\rangle$ estimated from the general-dyne measurement records, which enables a choice a Δ that cancels the slowly varying component of $\langle X_\mathrm{M}\rangle$. The Butterworth filter is a low-pass frequency filter with a flat frequency response in the pass-band and cut-off frequency, which is chosen to be at $0.5\omega_\mathrm{M}$.

To gain further insight, one may also take the real Fourier transform of the

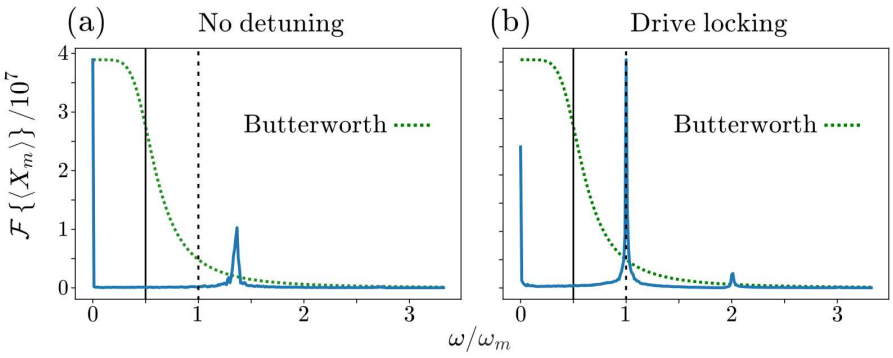


Figure 14.4: **Real Fourier transform of the mean mechanical position $\mathcal{F}\{\langle X_{\mathbf{m}}\rangle\}$.** (a) No detuning: $\Delta = 0$ and (b) drive locking: $\Delta = -\frac{1}{2}\mu\kappa\overline{\langle X_{\mathrm{M}}\rangle}$. Here, $X_\alpha/\sqrt{2} = 10$, $\omega_{\mathrm{M}}/2\pi = 10\,\mathrm{MHz}$, $\mu = 0.05$, $\mu^2 k/\omega_{\mathrm{M}} = 2$, $\eta = 0.95$, $\gamma/2\pi = 1\,\mathrm{Hz}$, $\zeta = 1/\sqrt{2}$, $T = 100\,\mathrm{mK}$ and the initial mechanical state is in thermal equilibrium. A third-order Butterworth filter is shown by the green-dashed line. Meanwhile, the cut-off frequency at $0.5\omega_{\mathrm{M}}$ of the Butterworth is shown by the vertical black line and the mechanical frequency ω_{M} is shown by the vertical dashed line. In (b), the Butterworth is used to calculate the detuning at each time step. The numerical simulations last 100 mechanical periods and the real Fourier transforms are calculated with data obtained in the last 90 periods to avoid the transient effects associated with the response time of the filter.

mean mechanical position $\mathcal{F}\{\langle X_{\rm M}\rangle\}$ over a given trajectory. When $\Delta = 0$, $\mathcal{F}\{\langle X_{\rm M}\rangle\}$ is shown in Fig. 14.4(a) for a given trajectory. Here, a peak in $\mathcal{F}\{\langle X_{\rm M}\rangle\}$ is seen at a higher frequency than $\omega_{\rm M}$, which is a demonstration of the optical spring effect. Note that at zero detuning, and for the chosen parameters, the intracavity power is too low to see higher order frequency components coming from the optical force. Fig. 14.4(b) shows $\mathcal{F}\{\langle X_{\rm M}\rangle\}$ for a particular trajectory but now when the detuning of the drive is chosen to cancel the slowly-varying component of $\langle X_{\rm M}\rangle$, which symmetrizes the optical phase space distribution as shown in the results section. Let this low frequency component of the mean mechanical position be $\overline{\langle X_{\rm M}\rangle}$. Then, it follows that the portion of $\mathcal{F}\{\langle X_{\rm M}\rangle\}$ which is captured by the third-order Butterworth filter corresponds to $\mathcal{F}\left\{\overline{\langle X_{\rm M}\rangle}\right\}$. Therefore, by calculating $\mathcal{F}\{\langle X_{\rm M}\rangle\}$ at each time step, the low-pass filtering allows one to calculate $\overline{\langle X_{\rm M}\rangle}$ at each time step too. From Eq. (14.16), for example, one can identify the correct choice of Δ to cancel the low frequency components is

$$\Delta = -\frac{1}{2}\mu\kappa\overline{\langle X_{\rm M}\rangle}. \tag{14.31}$$

In this way, the drive is locked to the cavity frequency, which changes as the time averaged mean mechanical position drifts away from zero. However, in the numerical simulations, or indeed an experiment, this cancellation of $\overline{\langle X_{\rm M}\rangle}$ must be done in a causal fashion, such that only information about $\mathcal{F}\{\langle X_{\rm M}\rangle\}$ at times $t' < t$ is used to compute the detuning Δ at time t. This explains why the cancellation of the low frequency components in Fig. 14.4(b) is imperfect.

Fig. 14.4(b) contains a peak in $\mathcal{F}\{\langle X_{\rm M}\rangle\}$ at $\omega_{\rm M}$, which shows that the optical spring effect is cancelled by the drive locking. Furthermore, this figure shows a small peak in $2\omega_{\rm M}$ as higher frequency components are now amplified as the drive locking allows more light into the cavity and thus a higher intracavity power. This peak at $2\omega_{\rm M}$ is a key signature of the nonlinear theory—not predicted by linearized optomechanics—and is due to quadratic contributions of $X_{\rm M}$ in the output operator c. In principle arbitrarily high-order frequency components may be present in $\mathcal{F}\{\langle X_{\rm M}\rangle\}$ in the nonlinear theory for *both* zero detuning and with drive locking.

Note that the order and frequency cut-off of the Butterworth are chosen to optimize the run time of the numerical simulations, while still demonstrating the working principle of the stochastic Gaussian regime. Choosing the optimal filtering procedure and choice of Δ is primarily a task for future experimental implementations and the filter chosen here is used to demonstrate the key physics.

14.4 Results

14.4.1 Solving the SDEs

The SDEs of Eqs (14.29) and (14.30) are solved via the Euler-Maruyama method, which is the simplest way to solve SDEs numerically [390]. To illustrate this method consider the SDE for some variable x

$$\mathrm{d}x \quad = \quad f(x,t)\mathrm{d}t + g(x,t)\mathrm{d}W. \tag{14.32}$$

To numerically solve this equation in some time interval $t \in [0,T]$ first approximate the SDE by

$$\Delta x \quad = \quad f(x,t)\Delta t + g(x,t)\Delta W, \tag{14.33}$$

where $\Delta t = T/N$ for a total of N time steps. Then starting from some initial condition $x = x_0$ at $t = 0$, the SDE may be solved iteratively according to $x_{n+1} = x_n + \Delta x_n$ with $\Delta x_n = f(x_n, n\Delta t)\Delta t + g(x_n, n\Delta t)\Delta W_n$ for $n = 0, 1, \ldots, N$. Here, the ΔW_n is a random number belonging to a Gaussian distribution of zero mean and variance Δt. The set of Wiener increments $\{\Delta W_n\}$, randomly chosen at each time step, then uniquely identify a particular stochastic trajectory. To calculate the mean and variance of the function $x(t)$, one finds the mean and average over many stochastic trajectories.

Eqs (14.29) and (14.30) comprise 5 SDEs. To this end, one may write $\mathbf{x} = (\langle Y_{\mathrm{M}}\rangle, \langle P_{\mathrm{M}}\rangle, V_X, V_{XP}, V_P)^{\mathrm{T}}$ and write Eqs (14.29) and (14.30) as a stochastic matrix equation

$$\mathrm{d}\mathbf{x} \quad = \quad \mathbf{f}(\mathbf{x},t)\mathrm{d}t + G(\mathbf{x},t)\mathrm{d}\mathbf{W}^*, \tag{14.34}$$

where $\mathrm{d}\mathbf{W}^* = (\mathrm{d}W_{X_{\mathrm{L}}}, \mathrm{d}W_{P_{\mathrm{L}}}, 0, 0, 0)^{\mathrm{T}}$. The Euler-Maruyama method may then be used to solve the system of SDEs and the set $\{\Delta W_{X_{\mathrm{L}},n}, \Delta W_{P_{\mathrm{L}},n}\}$, randomly chosen at each time step, then uniquely identify a particular stochastic trajectory. See Ref. [390] for more details on numerical solutions to systems of SDEs.

14.4.2 Figures of merit: The minimum squeezing variance V_{min} and the effective thermal occupation $\bar{n}_{\mathrm{eff}}$

When there is mechanical evolution in a optomechanical system under continuous position measurement, the squeezing will not exactly be along X_{M} as discussed in Section 14.2.2. Therefore, to quantify the amount of squeezing induced by the continuous position, I again use the minimum squeezing variance V_{min} along the stochastic trajectories, which corresponds to the minimum eigenvalue of V.

While V_{min} is the maximum amount of squeezing along the optimal direction in phase space, I also use the effective thermal occupation $\bar{n}_{\mathrm{eff}}$ to quantify the

reduction in uncertainty averaged through all directions in phase space [139]. Here, $\bar{n}_{\rm eff}$ is defined—and related to the state purity $\mathrm{tr}\left(\rho^2\right)$ [53]—via

$$\begin{aligned}\bar{n}_{\rm eff} &= \sqrt{\det\left(V\right)} - \frac{1}{2} \\ &= \frac{1}{2}\left(\frac{1}{\mathrm{tr}(\rho^2)} - 1\right). \end{aligned} \tag{14.35}$$

For a pure state $\mathrm{tr}\left(\rho^2\right) = 1$, one has that $\bar{n}_{\rm eff} = 0$.

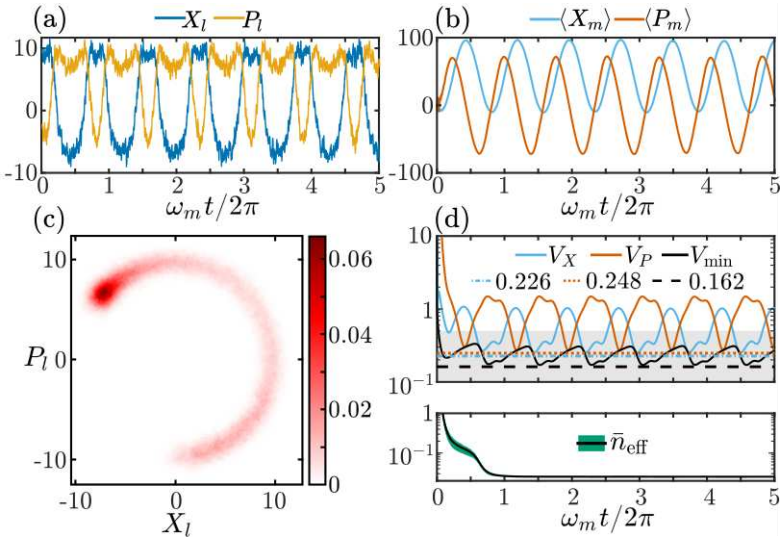


Figure 14.5: **Continuous position measurement in the stochastic Gaussian regime with $\Delta = 0$.** Here, $X_\alpha/\sqrt{2} = 10$, $\omega_{\rm M}/2\pi = 10\,\mathrm{MHz}$, $\mu = 0.05$, $\mu^2 k/\omega_{\rm M} = 2$, $\eta = 0.95$, $\gamma/2\pi = 1\,\mathrm{Hz}$, $\zeta = 1/\sqrt{2}$, $T = 100\,\mathrm{mK}$ and the initial mechanical state is in thermal equilibrium. (a) The integrated general-dyne measurement currents $X_{\rm L}$ and $P_{\rm L}$ plotted as a function of time for a given stochastic trajectory. (b) The corresponding trajectories of the mechanical means $\langle X_{\rm M}\rangle$ and $\langle P_{\rm M}\rangle$. (c) The same integrated general-dyne currents plotted as a 2D histogram, normalized to one. One may see that the optical phase shift averaged over this trajectory is positive. (d) The position variance V_X, the momentum variance V_P, and the generalized squeezing variance $V_{\rm min}$ for the same trajectory. Here, the dashed lines correspond to the mean of the minimum of each variance quantity over 100 runs, while the grey shaded area corresponds to quantum squeezing. The effective thermal occupation $\bar{n}_{\rm eff}$ plotted as a function of time averaged over 100 stochastic trajectories.

14.4.3 Zero detuning

Firstly, I run the simulations of Eqs (14.29) and (14.30) for the stochastic Gaussian regime with no detuning $\Delta = 0$, which produces the results shown in Fig. 14.5. In Appendix J.2, I include a gallery of results for different parameter sets. Fig. 14.5(a) shows the integrated general-dyne measurement currents with time for a given stochastic trajectory, while the means $\langle X_{\mathrm{M}} \rangle$ and $\langle P_{\mathrm{M}} \rangle$ are plotted in Fig. 14.5(b) for the same trajectory. Note how the evolution of $\langle X_{\mathrm{M}} \rangle$ and $\langle P_{\mathrm{M}} \rangle$ evolve harmonically at a higher frequency than ω_{M} in agreement with $\mathcal{F}\{\langle X_{\mathrm{M}} \rangle\}$ in Fig. 14.4(a). Meanwhile, Fig. 14.5(c) plots the general-dyne currents as a 2D histogram in optical phase space, which is asymmetric due to the lack of drive-locking at $\Delta = 0$. Fig. 14.5(d) shows the position variance V_X, the momentum variance V_P, and the minimum squeezing variance $V_{\min}$ for the same trajectory and the corresponding dashed lines indicate the mean of the minimum value of these quantities over 100 stochastic runs, each lasting 100 mechanical periods. The effective thermal occupation $\bar{n}_{\mathrm{eff}}$ averaged over the 100 runs is also plotted. These plots show that squeezing well below the ground-state width and effective ground-state cooling are achievable in the stochastic Gaussian regime. Importantly, an observer would use the measurement records of Eqs (14.1) and (14.2) to estimate the mechanical state at each time step as described above. The integrated general-dyne measurement currents plotted here are for visualization purposes. Further, in Appendix J.2 I show that quantum squeezing is still accessible at much lower measurement efficiencies, higher environmental temperatures, and higher mechanical decay rates than shown in Fig. 14.5.

Note that the noise is not visible in the evolution of $\langle X_{\mathrm{M}} \rangle$ and $\langle P_{\mathrm{M}} \rangle$ in Fig. 14.5(b). This is because the stochastic part of the evolution in Eq. (14.29) scales with $\sqrt{k_{\mathrm{L}}}$, while part of the deterministic evolution scales with k_{L}. In Fig. 14.5, $k_{\mathrm{L}} = 1.26 \times 10^7\,\mathrm{s}^{-1}$.

14.4.4 Drive locking

Here, I again run the simulations of Eqs (14.29) and (14.30) with the detuning $\Delta = -\frac{1}{2}\mu\kappa\overline{\langle X_{\mathrm{M}} \rangle}$ from the Butterworth filter described in Section 14.3.4. The results of which are shown in Fig. 14.6. Comparison between Figs. 14.5 and 14.6 shows this drive locking removes the asymmetry in the optical phase space distribution and improves the mechanical squeezing. Furthermore, the evolution of the first moments in Fig. 14.6(b) becomes less sinusoidal compared to the evolution in Fig. 14.5(b). Indeed, the evolution of $\langle X_{\mathrm{M}} \rangle$ and $\langle P_{\mathrm{M}} \rangle$ becomes anharmonic due to the $2\omega_{\mathrm{M}}$ component of the optical force in agreement with $\mathcal{F}\{\langle X_{\mathrm{M}} \rangle\}$ in Fig. 14.4(a). This is because the drive-locking modifies the radiation-pressure force the mechanical mode experiences by increasing the average intracavity intensity, which amplifies the nonlinear components of the optical force. In Appendix J.2, I explore a range of different parameters and even at $\eta = 0.5$, $\gamma = 100$ Hz, and $T = 4$ K, a significant quantum squeezing $V_{\min} \approx 0.3$ is observed and the mean of the minimum of $V_X < 1/2$.

Fig. 14.7 shows the the mean mechanical position $\langle X_{\mathrm{M}} \rangle$ and the detuning

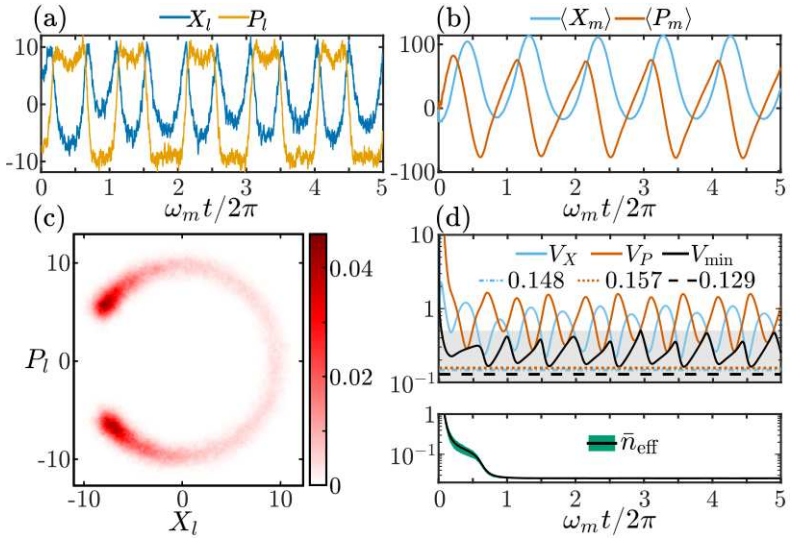


Figure 14.6: **Continuous position measurement in the stochastic Gaussian regime with drive locking $\Delta = -\frac{1}{2}\mu\kappa\overline{\langle X_{\mathbf{m}}\rangle}$.** Here, $X_\alpha/\sqrt{2} = 10$, $\omega_{\rm M}/2\pi = 10\,{\rm MHz}$, $\mu = 0.05$, $\mu^2 k/\omega_{\rm M} = 2$, $\eta = 0.95$, $\gamma/2\pi = 1\,{\rm Hz}$, $\zeta = 1/\sqrt{2}$, $T = 100\,{\rm mK}$, and the initial mechanical state is in thermal equilibrium. (a) The integrated general-dyne measurement currents $X_{\rm L}$ and $P_{\rm L}$ plotted as a function of time for a given stochastic trajectory. (b) The corresponding trajectories of the mechanical means $\langle X_{\rm M}\rangle$ and $\langle P_{\rm M}\rangle$. (c) The same integrated general-dyne currents plotted as a 2D histogram, normalized to one. (d) The position variance V_X, the momentum variance V_P, and the minimum eigenvalue $V_{\rm min}$ for the same trajectory. Here, the dashed lines correspond to the mean of the minimum of each variance quantity over 100 trajectories, while they grey shaded area indicates quantum squeezing. The effective thermal occupation $\bar{n}_{\rm eff}$ plotted as a function of time averaged over 100 stochastic trajectories. The shaded green areas indicate the upper and lower quartile ranges and are apparent at small times during the response time of the Butterworth filter.

$\Delta = -\frac{1}{2}\mu\kappa\overline{\langle X_{\rm M}\rangle}$ realized from the Butterworth filter for a single trajectory. While the time average of $\langle X_{\rm M}\rangle$ is far from zero, the function $\langle X_{\rm M}\rangle + 2\Delta/\mu\kappa$—and therefore $\mu\langle X_{\rm M}\rangle/2 + \Delta/\kappa$—time averages to ≈ 0. Thus demonstrating how both (i) the drive is locked to the optical cavity and (ii) the phase-space distribution of the light in Fig. 14.6 becomes symmetric. From Fig. 14.4 it may be seen that the tail of the Butterworth filter cuts into the frequency range around $\omega_{\rm M}$, which explains why Δ oscillates at $\omega_{\rm M}$ with a small amplitude. In an experiment, it may be difficult to modulate Δ at $\omega_{\rm M}$, in which case one could use a higher order Butterworth filter[3] so the tail of the Butterworth filter does not cut into $\omega_{\rm M}$, which would then produces a flat value of Δ—after the initial response time of the filter.

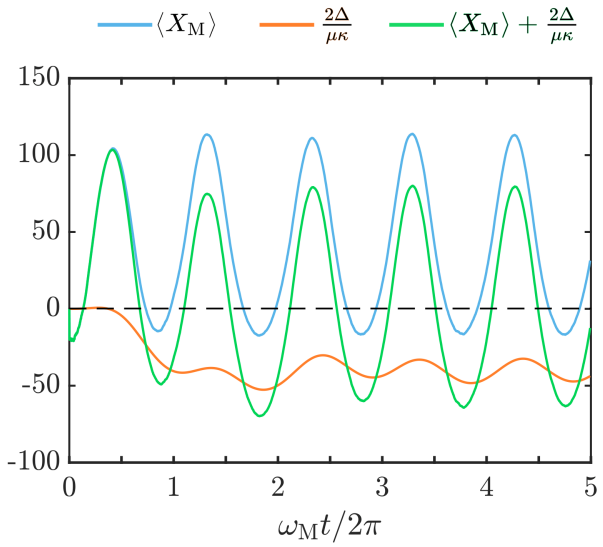


Figure 14.7: **The mechanical mean position $\langle X_{\mathbf{m}}\rangle$ and detuning Δ from the drive locking.** Here, the parameters are the same as in Fig. 14.6. The time average of $\langle X_{\rm M}\rangle$ is greater than zero, while the time average of $\Delta = -\frac{1}{2}\mu\kappa\overline{\langle X_{\rm M}\rangle}$ is negative. The appropriate sum of the two, $\langle X_{\rm M}\rangle + 2\Delta/\mu\kappa$, time averages to approximately zero (black-dashed line) after the initial response time of filter.

Finally, to demonstrate the stochastic nature of the numerical simulations more clearly, in Fig. 14.8, I plot the minimum squeezing variance $V_{\rm min}$, averaged over the 100 runs. Comparison with $\bar{n}_{\rm eff}$ in Fig. 14.6(d) indicates that the evolution of the covariance matrix elements is much more stochastic than the evolution of the state's purity.

[3]The numerical simulations are limited to a third-order Butterworth filter simply to manage the run time of the simulations.

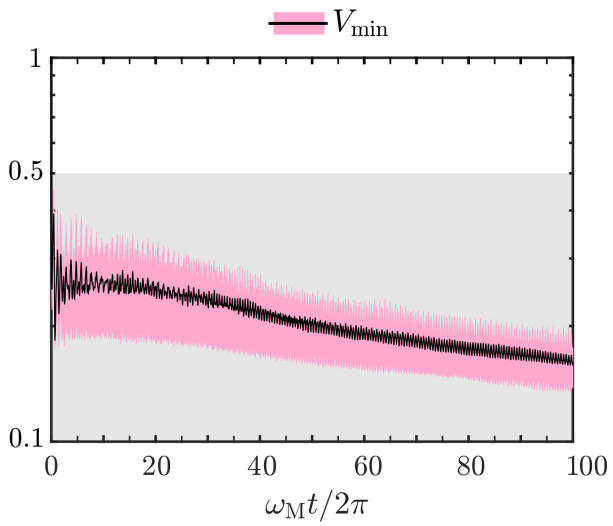


Figure 14.8: **The minimum squeezing variance $V_{\min}$ averaged over 100 runs.** Here, the parameters are the same as in Fig. 14.6. The black line shows the average time evolution of $V_{\min}$ over the 100 runs, while the pink shaded area indicates the upper and lower quartile range.

14.5 Conclusion and outlook

In this chapter I have further explored the theory of continuous position measurement developed in Chapter 12 for the specific case of linear-position coupling ($a^\dagger a X_{\mathrm{M}}$). Using the theory of Chapter 5 I first discussed the general-dyne measurement records, before then showing how the general nonlinear cavity-enhanced SME recovers the cavity-free and linearized SMEs in the appropriate limits. Furthermore, I have shown how the nonlinear SME predicts a new regime of operation: the 'stochastic Gaussian regime'. This regime accurately models the nonlinear dynamics of the interaction, including the cavity enhancement, is also capable of describing arbitrarily large optical rotations, and allows for efficient computation of the mechanical evolution via the first and second moments. I have then explained how operation in this regime leads to anharmonicity in the mechanical motion due to superlinear terms in X_{M} contributing to the optical force.

In the results section, I showed how quantum squeezing and effective ground state cooling are both achievable in the stochastic Gaussian regime even in the presence of optical loss and mechanical dissipation. In Appendix J.2 I present a gallery of results and still see significant quantum squeezing ($V_{\min} \approx 0.3$) at $\eta = 0.5$, $\gamma = 100\,\mathrm{Hz}$, and $T = 4\,\mathrm{K}$. Importantly, drive locking via a Butterworth filter removes the asymmetry in the output optical phase-space distribution by effectively cancelling the deterministic momentum kick and the optical spring

shift. This drive locking technique improves the quantum squeezing of the continuous measurement.

The SME presented here offers many opportunities for developing new quantum state engineering and measurement protocols. In particular, by tracing over all measurement outcomes the SME reduces to a deterministic master equation. By studying this master equation one may develop deterministic protocols for mechanical quantum state preparation. One such example is the deterministic preparation of mechanical squeezed states, which is described in the next chapter.

Chapter 15

Deterministic mechanical squeezing

This chapter draws heavily from Ref. [12], which is unpublished at the time of writing. P.N. is the first author of this work and J.C. made theoretical contributions.

Building upon the framework developed in the previous chapters, I will now detail a new method for achieving *deterministic* squeezing of a mechanical oscillator. In this chapter, I briefly motivate the utility of a deterministic squeezing protocol in nonlinear optomechanics, before I then discuss the underlying theory of the squeezing protocol in much more detail. As opposed to the measurement-outcome dependent squeezing protocols introduced in Chapters 13 and 14, a deterministic squeezing protocol is often more convenient and practical from an experimental point of view. I again focus on a linear coupling to position $a^\dagger a X_{\mathrm{M}}$, but the analysis presented here is readily applicable to the other regimes of optomechanics summarized in Table 11.1. Finally, I briefly study the phase-space features of the output optical state.

15.1 Mechanical squeezing in optomechanics

Squeezing light is most commonly achieved via nonlinear optical processes, such as degenerate parametric down conversion [391], but in mechanical systems one must take a different tack. By manipulating the evolution of a mechanical oscillator one can realize a squeezing operation. For example, sudden changes in the frequency of a quantum oscillator can lead to squeezing [392] and a well-timed series of such frequency changes induces even stronger squeezing [393]. In optomechanics, we have a wealth of techniques and different regimes of operation to manipulate the evolution of a mechanical oscillator with light via the radiation-pressure interaction. Here, I review a selection of such techniques to

motivate our protocol.

In the resolved sideband regime, parametric amplification is a useful method to generate mechanical squeezing [394, 395, 396], as are reservoir engineering schemes achieved via two-tone drives [397, 398]. Further squeezing techniques in this regime include BAE measurements by equally driving both mechanical sidebands [370] and optomechanical state swaps of squeezed states of light onto mechanics [399]. Meanwhile, in the unresolved sideband regime, there are also a number of interesting techniques to achieve squeezing. For example, it was recently shown that mechanical quantum squeezing can be achieved in a continuously driven system through a dynamical instability, achieved with an off-resonant interaction in the ultrastrong coupling regime [400] and in Chapter 14 we saw how a continuous position measurement can achieve squeezing when the measurement rate $\mu^2 k$ exceeds the mechanical frequency. Furthermore, I have extensively discussed how pulsed optomechanics and measurement [139, 7] can achieve measurement-based squeezing. Moreover, it was shown by Khosla *et al.* in Ref. [147] that by recycling the optical input pulsed over a sequence of four pulsed optomechanical interactions one can generate a geometric phase[1] proportional to X_{M}^2, which leads to *deterministic* mechanical squeezing. Mathematically, a similar X_{M}^2 squeezing type unitary can be achieved via a single pulsed interaction with an oscillator that has an X_{M}^2 nonlinear coupling to the photon number operator [402]. Conversely, by carefully controlling the input fields, measuring the degree of mechanical squeezing can be a useful tool for estimating the size of nonlinearities present in the system [403].

Here, I discuss our deterministic squeezing protocol that exploits the nonlinearities of cavity optomechanics. I show that mechanical squeezing can be achieved in both the limit of pulsed optomechanics and in the presence of mechanical evolution using a master equation approach. I also demonstrate that this regime can achieve quantum squeezing below the ground state width. In Ref. [12], this protocol is experimentally realized and 10 dB of mechanical thermal squeezing in a photonic crystal device is achieved. However, this thesis describes the underlying theory of this protocol, which I will now discuss.

15.2 An exact analysis

The SME of Eq. (12.31) reduces to a deterministic master equation (ME) when the X_{L} and P_{L} quadratures are unmeasured. This corresponds to setting $\eta = 0$ in Eq. (12.31), which gives

$$\mathrm{d}\rho \;=\; -\frac{\mathrm{i}}{\hbar}[H_0,\rho]\mathrm{d}t + \mathcal{D}[c]\rho\mathrm{d}t, \tag{15.1}$$

where once again $H_0/\hbar = \omega_{\mathrm{M}} b^\dagger b$, $c = \sqrt{2k} f(X_{\mathrm{M}})$,

$$f = \frac{1 + \mathrm{i}\left(\frac{\mu}{2}X_{\mathrm{M}} + \bar{\Delta}\right)}{1 - \mathrm{i}\left(\frac{\mu}{2}X_{\mathrm{M}} + \bar{\Delta}\right)},$$

[1] This optomechanical geometric phase is also useful in the generation [147] and preservation [401] of Wigner negativity.

and the normalized detuning is $\bar{\Delta} = \Delta/\kappa$. To describe the effects of mechanical dissipation one can also add the term $\mathcal{D}[L]\rho dt$ with $L = \sqrt{\frac{4\gamma k_B T}{\hbar\omega_M}} X_M + i\theta\sqrt{\frac{\hbar\omega_M\gamma}{4k_B T}} P_M$ to Eq. (15.1) as in Chapter 12.

Mechanical quantum squeezing with $\bar{\Delta} \neq 0$

Interestingly, deterministic mechanical squeezing can be achieved via Eq. (15.1) by setting $\bar{\Delta} \neq 0$. To do so, consider a short pulsed nonlinear optomechanical interaction. However, instead of a measurement operator approach, I will use the ME description, which readily allows for a period of mechanical evolution and dissipation to be included during the optomechanical interaction. Furthermore, the ME recovers the measurement operator description when the interaction period τ satisfies $\tau \ll 2\pi/\omega_M$.

To see why setting $\bar{\Delta} \neq 0$ allows for mechanical squeezing, consider the Heisenberg-Langevin equations for the optomechanical system operating in the unresolved sideband regime during a period where the mechanical evolution is negligible

$$\dot{a} = i(\sqrt{2}g_0 X_M + \Delta)a - \kappa a + \sqrt{2\kappa}a_{in} \tag{15.2}$$
$$\dot{X}_M = 0 \tag{15.3}$$
$$\dot{P}_M = \sqrt{2}g_0 a^\dagger a. \tag{15.4}$$

Then note that Eq. (15.1) is valid when the intracavity field can be adiabatically eliminated, which gives

$$a(t) = \frac{\sqrt{\kappa}}{\frac{\kappa}{2} - i\sqrt{2}g_0 X_M + \Delta} a_{in}(t) \tag{15.5}$$

from the Heisenberg-Langevin equations and so

$$\dot{X}_M = 0, \tag{15.6}$$
$$\dot{P}_M = s(t), \tag{15.7}$$

where the dimensionless force $s(t)$ on the mechanical mode is

$$s(t) = \sqrt{2}g_0 a^\dagger a = \frac{\mu}{1 + \left(\frac{\mu}{2}X_M + \bar{\Delta}\right)^2} a_{in}^\dagger a_{in}. \tag{15.8}$$

From Eq. (15.8), one may see that when $\bar{\Delta} \neq 0$, $s(t)$ produces a shearing force that generates correlations between the mechanical position and momentum V_{XP} as shown in Fig. 15.1. As the mechanical position variance is unchanged over the interaction, this shearing of the initial mechanical state produces squeezing[2] and a minimum squeezing variance of V_{min} that can go below the ground state width, i.e. quantum squeezing.

[2]To understand the origin of the squeezing mathematically, remember that V_{min} is the

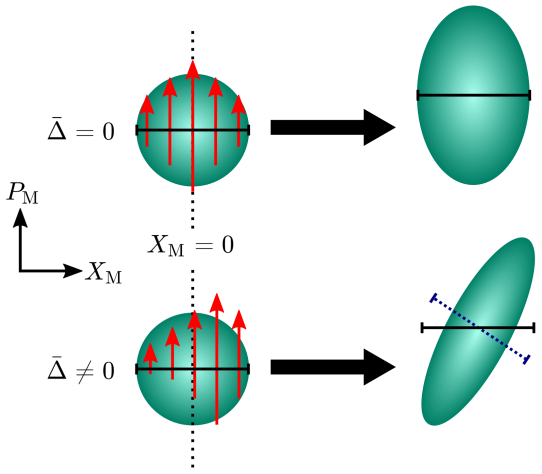


Figure 15.1: **Mechanical squeezing via shearing.** An initial thermal state with $V_X = V_P$ and $V_{XP} = 0$ is shown by the phase-space cartoons in the left of the figure. The initial width of the state $\sim \sqrt{V_X}$ is indicated by the black solid lines. $\bar{\Delta} = 0$: the force on the mechanical mode $s(t)$ (red arrows) is centred symmetrically about $X_{\rm M} = 0$ (black-dashed line) and is largest at $X_{\rm M} = 0$. Over a short pulsed interaction, no correlations between position and momentum are generated and so V_{XP} remains zero. $\Delta \neq 0$: the force $s(t)$ is now distributed asymmetrically about $X_{\rm M} = 0$ and is maximum at $X_{\rm M} = -2\bar{\Delta}/\mu$, which realizes a shearing force on the mechanical state. During a short pulsed interaction, the position variance does not change ($\dot{X}_{\rm M} = 0$), but the shearing force generates $V_{XP} \neq 0$. Hence, the state becomes squeezed along an angle tilted away from the $X_{\rm M}$-axis as indicated by the blue dashed line, which is the same length as the black solid lines.

Photon statistics of the input pulse

The photon number operator of the input pulse is

$$n_{\rm L} \quad = \quad \int_0^\tau \mathrm{d}t a_{\rm in}^\dagger a_{\rm in}. \tag{15.9}$$

Here, I choose the input pulse to be in the coherent state $|\alpha\rangle$, which obeys Poissonian statistics. Hence, the mean photon number is

$$\langle n_{\rm L} \rangle \quad = \quad N_{\rm P}, \tag{15.10}$$

minimum eigenvalue of the covariance matrix. Thus, even though V_P will change over the interaction, because V_X is unchanged and V_{XP} becomes non-zero, the minimum eigenvalue $V_{\rm min}$ must satisfy $V_{\rm min} < V_X$.

the variance is

$$\left\langle n_{\rm L}^2 \right\rangle - \left\langle n_{\rm L} \right\rangle^2 = N_{\rm P}, \tag{15.11}$$

and $\left\langle n_{\rm L}^2 \right\rangle$ is

$$\left\langle n_{\rm L}^2 \right\rangle = N_{\rm P}^2 + N_{\rm P}. \tag{15.12}$$

In the deterministic squeezing protocol the optical mode is not measured. Instead, the optical mode is traced out and so the Poissonian photon number statistics will influence the quantum noise imparted upon the mechanical mode.

15.3 Gaussian approximation to deterministic squeezing

Let the duration of the input pulse τ satisfy $\tau \ll 2\pi/\omega_{\rm M}$. From the point of view of the mechanics this means $\tau = {\rm d}t$ and propagating the mechanical equations of motion over this short time interval gives

$$X_{\rm M}(\tau) = X_{\rm M}(0), \tag{15.13}$$

$$P_{\rm M}(\tau) = P_{\rm M}(0) + \frac{\mu n_{\rm L}}{1 + \left(\frac{\mu}{2} X_{\rm M} + \bar{\Delta}\right)^2}. \tag{15.14}$$

Now I make a Gaussian approximation that proceeds by expanding the denominator in Eq. (15.14) about $\mu X_{\rm M} = 0$:

$$\frac{1}{1 + \left(\frac{\mu}{2} X_{\rm M} + \bar{\Delta}\right)^2} = \frac{1}{1+\bar{\Delta}^2} - \frac{\mu \bar{\Delta} X_{\rm M}}{(1+\bar{\Delta}^2)^2},$$

which is valid for small ${\rm Var}(\frac{\mu}{2} X_{\rm M}(0)) < 1$ and $\langle X_{\rm M}(0) \rangle = 0$. In this Gaussian approximation, Eqs (15.13) and (15.14) become

$$X_{\rm M}(\tau) = X_{\rm M}(0), \tag{15.15}$$

$$P_{\rm M}(\tau) = P_{\rm M}(0) + \frac{\mu n_{\rm L}}{1+\bar{\Delta}^2} - \frac{\mu^2 n_{\rm L} \bar{\Delta} X_{\rm M}}{(1+\bar{\Delta}^2)^2}. \tag{15.16}$$

A Gaussian transformation of the mechanical mode is completely described by the first and second mechanical moments. Hence, one must take the expectation value of $X_{\rm M}(\tau)$, $P_{\rm M}(\tau)$, $X_{\rm M}^2(\tau)$, $P_{\rm M}^2(\tau)$, and $X_{\rm M}(\tau)P_{\rm M}(\tau) + P_{\rm M}(\tau)X_{\rm M}(\tau)$ via Eqs (15.15) and (15.16) with $\langle X_{\rm M}(0) \rangle = 0$. For example, the $P_{\rm M}^2(\tau)$ term gives

$$\begin{aligned} \left\langle P_{\rm M}^2(\tau) \right\rangle &= \left\langle P_{\rm M}^2(0) \right\rangle + \frac{\mu^2 \left\langle n_{\rm L}^2 \right\rangle}{(1+\bar{\Delta}^2)^2} + \frac{\mu^4 \left\langle n_{\rm L}^2 \right\rangle \bar{\Delta}^2 V_X(0)}{(1+\bar{\Delta}^2)^4} \\ &- \frac{2\mu^2 \left\langle n_{\rm L} \right\rangle \bar{\Delta} V_{XP}(0)}{(1+\bar{\Delta}^2)^2} + \frac{2\mu \left\langle P_{\rm M}(0) \right\rangle \left\langle n_{\rm L} \right\rangle}{1+\bar{\Delta}^2}, \end{aligned} \tag{15.17}$$

where I have used that in the Heisenberg picture the state vectors remain time independent and so one can separate out the expectation values of the optical and mechanical mode.

Using the above expectation values for $\langle n_{\rm L}\rangle$ and $\langle n_{\rm L}^2\rangle$ then gives the Gaussian transformation for the first moments and covariance matrix elements:

$$\begin{aligned}
\langle X_{\rm M}(\tau)\rangle &= \langle X_{\rm M}(0)\rangle = 0, && (15.18)\\
\langle P_{\rm M}(\tau)\rangle &= \langle P_{\rm M}(0)\rangle + \frac{\mu N_{\rm P}}{1+\bar{\Delta}^2}, && (15.19)\\
V_X(\tau) &= V_X(0), && (15.20)\\
V_{XP}(\tau) &= V_{XP}(0) - \frac{\mu^2 N_{\rm P}\bar{\Delta}V_X(0)}{(1+\bar{\Delta}^2)^2}, && (15.21)\\
V_P(\tau) &= V_P(0) + \frac{\mu^2 N_{\rm P}}{(1+\bar{\Delta}^2)^2} + \frac{\mu^4(N_{\rm P}^2+N_{\rm P})\bar{\Delta}^2 V_X(0)}{(1+\bar{\Delta}^2)^4}\\
&\quad - \frac{2\mu^2 N_{\rm P}\bar{\Delta}V_{XP}(0)}{(1+\bar{\Delta}^2)^2}. && (15.22)
\end{aligned}$$

For later convenience I define

$$\sinh r = \frac{\mu^2 N_{\rm P}\bar{\Delta}}{(1+\bar{\Delta}^2)^2}, \qquad (15.23)$$

which is maximum at $\bar{\Delta} = \pm 1/\sqrt{3}$ and minimum at $\bar{\Delta} = 0$. This allows the Gaussian transformation of the covariance matrix elements—Eqs (15.20) to (15.22)—for the pulsed interaction to be written more neatly as

$$\begin{aligned}
V_X(\tau) &= V_X(0), && (15.24)\\
V_{XP}(\tau) &= V_{XP}(0) - V_X(0)\sinh r, && (15.25)\\
V_P(\tau) &= V_P(0) + \frac{\sinh r}{\bar{\Delta}} + V_X(0)\sinh^2 r\left(1+\frac{1}{N_{\rm P}}\right)\\
&\quad - 2V_{XP}(0)\sinh r. && (15.26)
\end{aligned}$$

15.3.1 Quantum noise contributions

To identify the quantum noise contributions, one may compare the semi-classical and fully quantum descriptions. A semi-classical treatment proceeds by treating the optical input mode classically, i.e. ignoring the quantum uncertainty in the input pulse: $\langle n_{\rm L}^2\rangle \to N_{\rm P}^2$ and $\langle n_{\rm L}^2\rangle - \langle n_{\rm L}\rangle^2 \to 0$. Hence, using Eq. (15.17) the semi-classical transformation of $V_P(\tau)$ is

$$V_P^{sc}(\tau) = V_P(0) + V_X(0)\sinh^2 r - 2V_{XP}(0)\sinh r. \qquad (15.27)$$

While, the semi-classical transformation of the first moments and other covariance matrix elements is identical to the quantum transformation, i.e. it is only

the momentum variance that is different. Subtracting $V_P^{sc}(\tau)$ from $V_P(\tau)$ gives the quantum noise contribution

$$\begin{aligned} V_Q(\tau) &= V_P(\tau) - V_P^{sc}(\tau) \\ &= \frac{\sinh r}{\bar{\Delta}} + V_X(0)\frac{\sinh^2 r}{N_{\rm P}}. \end{aligned} \tag{15.28}$$

These terms represent the optical quantum back action noise on the mechanical momentum quadrature. The first back action term $\sinh r/\bar{\Delta} = \mu^2 N_{\rm P}/(1+\bar{\Delta}^2)^2$ is maximal at $\bar{\Delta} = 0$, while the second term

$$\frac{V_X(0)\sinh^2 r}{N_{\rm P}} = \frac{\mu^4 N_{\rm P}\bar{\Delta}^2 V_X(0)}{(1+\bar{\Delta}^2)^4}$$

is zero at $\bar{\Delta} = 0$ and maximal at $\bar{\Delta} = \pm 1/\sqrt{3}$ and so is related to the shearing effect described above. Both quantum noise terms are proportional to $N_{\rm P}$, which is the quantum variance of the input coherent pulse. Moreover, both back action terms tend to zero as $|\bar{\Delta}| \rightarrow \infty$ and the light is no longer accepted by the cavity.

15.3.2 Matrix transformation

The initial first moments vector is $\langle \mathbf{X}(0)\rangle = (\langle X_{\rm M}(0)\rangle, \langle P_{\rm M}(0)\rangle)^{\rm T}$ and the initial covariance matrix is

$$V(0) = \begin{pmatrix} V_X(0) & V_{XP}(0) \\ V_{XP}(0) & V_P(0) \end{pmatrix}. \tag{15.29}$$

I now introduce (i) the symplectic matrix that represents the shearing and squeezing effect

$$S = \begin{pmatrix} 1 & 0 \\ -\dfrac{\mu^2 N_{\rm P}\bar{\Delta}}{(1+\bar{\Delta}^2)^2} & 1 \end{pmatrix} = \begin{pmatrix} 1 & 0 \\ -\sinh r & 1 \end{pmatrix}, \tag{15.30}$$

(ii) the displacement vector that captures the classical back action (a simple momentum displacement)

$$\mathbf{d} = \begin{pmatrix} 0 \\ \dfrac{\mu N_{\rm P}}{1+\bar{\Delta}^2} \end{pmatrix}, \tag{15.31}$$

and (iii) the quantum back action noise matrix

$$N = \begin{pmatrix} 0 & 0 \\ 0 & V_Q \end{pmatrix}. \tag{15.32}$$

Using S, $\mathbf{d}$, and N then allows one to write the Gaussian transformation after one pulse as

$$\langle \mathbf{X}(\tau)\rangle = S\langle \mathbf{X}(0)\rangle + \mathbf{d}, \tag{15.33}$$

$$V(\tau) = SV(0)S^{\rm T} + N. \tag{15.34}$$

I would like to remind the reader here that I have assumed $\langle X_{\rm M}(0)\rangle = 0$. In the absence of quantum back action noise ($N = 0$), Eqs (15.33) and (15.34) describe a bona fide symplectic transformation as described in Chapter 4, i.e. the semi-classical transformation is symplectic.

15.3.3 The squeezing factor

Now consider an initial thermal state $V_X(0) = V_P(0) = \bar{n}+1/2$ and $V_{XP}(0) = 0$. Then in the case of (i) $N_{\rm P} \gg 1$ and a large initial thermal occupation (ii)

$$\left(\bar{n} + \frac{1}{2}\right)\mu^2\left(N_{\rm P} - 1\right) \gg \frac{\left(1+\bar{\Delta}^2\right)^2}{\bar{\Delta}^2}, \tag{15.35}$$

the quantum back action noise N is negligible in Eq. (15.34) and hence the transformation is a bona fide symplectic transformation.

Defining the rotated quadrature $X_\theta = X_{\rm M}\cos\theta + P_{\rm M}\sin\theta$ then allows one to write the mechanical variance at a given angle θ as

$$\begin{aligned} V_\theta(\tau) &= V_X(\tau)\cos^2\theta + V_P(\tau)\sin^2\theta + 2V_{XP}\tau\cos\theta\sin\theta \\ &= \left(\bar{n}+\frac{1}{2}\right)\left[1 - 2\sinh r\sin 2\theta + 4\sinh^2 r\sin^2\theta\left(1+\frac{1}{2N_{\rm P}}\right)\right] \\ &\qquad +2\frac{\sinh r}{\bar{\Delta}}\sin^2\theta \\ &\approx \left(\bar{n}+\frac{1}{2}\right)\left[1 - 2\sinh r\sin 2\theta + 4\sinh^2 r\sin^2\theta\right], \end{aligned} \tag{15.36}$$

where in the last line the quantum back action noise terms have been ignored. In this approximation, taking the derivative $\dfrac{\partial V_\theta}{\partial\theta}$ and setting it equal to zero gives

$$\tan 2\theta^* = \frac{1}{\sinh r}, \tag{15.37}$$

which implies $\sin 2\theta^* = \pm 1/\cosh r$, $\cos 2\theta^* = \pm\tanh r$, and $\sin^2\theta^* = 1/(1+{\rm e}^{\pm 2r})$. Inserting these solutions for $\theta^* = \theta_{\rm min}, \theta_{\rm min}+\pi/2$ into $V_\theta(\tau)$ gives $\left(\bar{n}+\frac{1}{2}\right){\rm e}^{\mp 2r}$, which implies that the minimum and maximum variances of the mechanical state after one pulse are

$$V_{\rm min} = \left(\bar{n}+\frac{1}{2}\right){\rm e}^{-2|r|}, \tag{15.38}$$

$$V_{\rm max} = \left(\bar{n}+\frac{1}{2}\right){\rm e}^{+2|r|}. \tag{15.39}$$

Hence, it may be seen how the symplectic matrix $S(r)$ acts to squeeze the state along $\theta_{\rm min}$ with squeezing parameter r, which is maximal at $\bar{\Delta} = \pm 1\sqrt{3}$. Note that when quantum back action noise is comparable to the thermal noise, the optimal value of $|\bar{\Delta}|$ will not be $|\bar{\Delta}| = 1/\sqrt{3}$.

15.3.4 Agreement with the exact analysis

To confirm the validity of the Gaussian approximation, in Fig. 15.2 one may compare Eqs (15.18) to (15.22) to results obtained in QuTiP via a simulation of the ME of Eq. (15.1) using the inbuilt `mesolve` function [404]. In these simulations, I consider an initial ground state and the duration of the optomechanical interaction τ is 0.1% of the mechanical period $2\pi/\omega_{\rm M}$, which satisfies the short pulsed approximation $\tau \ll 2\pi/\omega_{\rm M}$—upon which the Gaussian approximation relies. In Fig. 15.2 it may be seen that the Gaussian approximation agrees well with the ME simulations[3] as the initial state also satisfies $\mu\sigma \ll 1$. Furthermore, I plot the minimum and maximum eigenvalues of the covariance matrix, $V_{\rm min}$ and $V_{\rm max}$, and the effective thermal occupation $\bar{n}_{\rm eff} = \det(V) - 1/2$, which quantifies the quantum back action noise.

[3]The analytic results for the Gaussian approximation depend on μ, $\bar{\Delta}$, and $N_{\rm P}$, whereas the ME is written in terms of μ, $\bar{\Delta}$ and k. I would therefore like remind the reader that in terms of k (equal to half the incoming photon flux), the mean number of incident photons is given by $N_{\rm P} = X_\alpha^2/2 = 2k\tau$.

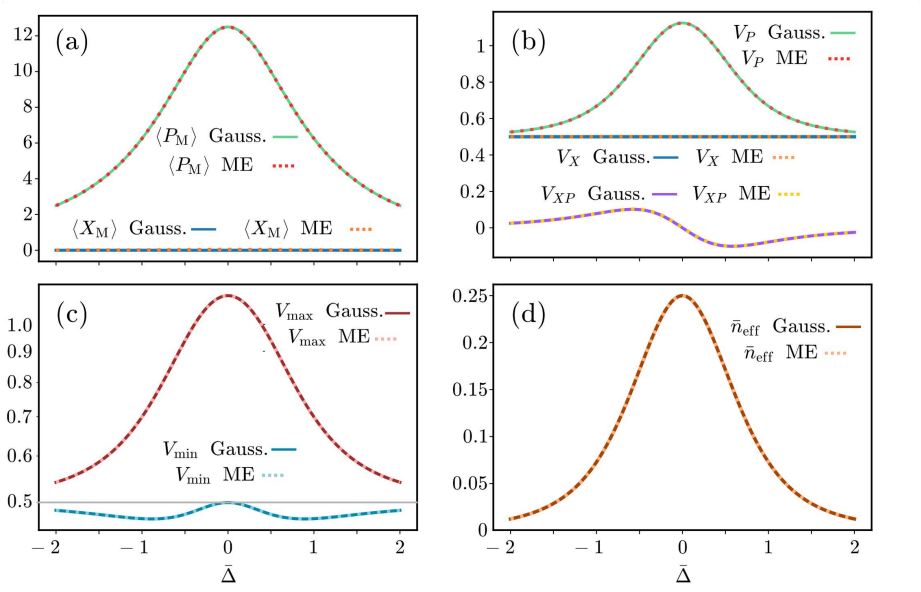


Figure 15.2: **Agreement between the Gaussian approximation and the master equation.** Here, the initial mechanical state is the ground state, $N_P = 250$, $\mu = 0.05$, $\omega_M/2\pi = 1\,\mathrm{MHz}$, and the duration of the pulse in the ME simulation is $\tau = 10^{-3} \times 2\pi/\omega_M$, which satisfies $\tau \ll 2\pi/\omega_M$. (a) Position and momentum means. (b) Elements of the covariance matrix. (c) Minimum and maximum squeezing variances. Here, squeezing below the quantum ground state V_{min} is achieved. The minimum value of $V_{min} = 0.4689$ is at $\bar{\Delta} = \pm 0.88$. (d) Effective thermal occupation.

Importantly, Fig. 15.2(c) confirms that quantum squeezing below the ground state width is possible $V_{min} < 1/2$. Moreover, from Fig. 15.2(d), it may be seen that the added back action noise, quantified by $\bar{n}_{eff}$, is comparable to the intrinsic quantum noise and so the minimum values of V_{min} in Fig. 15.2(c) are located at $|\bar{\Delta}| > 1/\sqrt{3}$.

15.3.5 Finite mechanical evolution

Now I study the effect of finite mechanical evolution and the difference between the Gaussian approximation, which assumes $\tau = \mathrm{d}t$, to the results obtained in QuTiP via a simulation of the ME of Eq. (15.1). In Fig. 15.3, the parameters are the same as in Fig. 15.2 *apart* from now τ is equal to 10% of the mechanical period $2\pi/\omega_M$, which means the mechanical mode will significantly evolve during the optomechanical interaction.

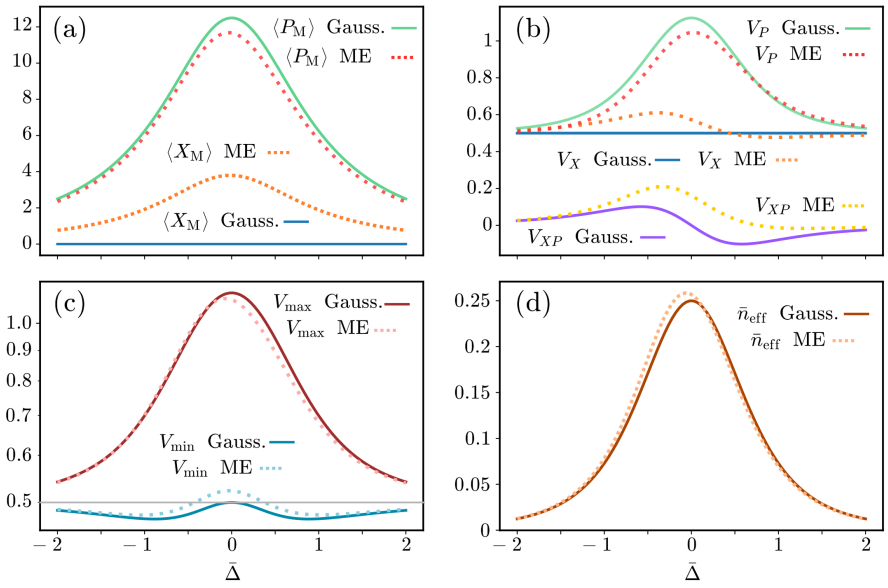


Figure 15.3: **Comparison between the Gaussian approximation with $\tau = \mathrm{d}t$ and the master equation with finite mechanical evolution.** Here, the initial mechanical state is the ground state, $N_P = 250$, $\mu = 0.05$, $\omega_M/2\pi = 1\,\mathrm{MHz}$, and the duration of the pulse in the ME simulation is $\tau = 0.2\pi/\omega_M$, which *does not* satisfy $\tau \ll 2\pi/\omega_M$. (a) Position and momentum means. (b) Elements of the covariance matrix. (c) Minimum and maximum squeezing variances. Here, squeezing below the quantum ground state V_{min} is seen. For the ME simulation, the minimum value of $V_{min} = 0.4761$ is at $\bar{\Delta} = -1.03$, while at $\bar{\Delta} = +1.03$, the minimum eigenvalue is slightly higher: $V_{min} = 0.4764$. (d) Effective thermal occupation.

Fig. 15.3 shows that quantum squeezing below the ground state width is still possible even when there is significant mechanical evolution during the optomechanical interaction.

Breaking the symmetry between $\pm\bar{\Delta}$

When the ME of Eq. (15.1) is used to model an optomechanical interaction of finite duration, the symmetry between $\pm\bar{\Delta}$ is broken and the red-detuned solution performs better than the blue-detuned solution—as noted in the caption of Fig. 15.3. Over a finite duration, the mechanical position will increase slightly during the interaction. This means the cavity frequency will decrease slightly via $\omega_C(x) = \omega_C(0) - \sqrt{2}g_0 X_M$ and so having an initially red-detuned drive, e.g. $\bar{\Delta} < 0$, will allow slightly more light into the cavity and hence the squeezing protocol will be more efficient.

15.4 The two pulse sequence

The classical back action evident from the non-zero value of $\langle P_{\rm M}\rangle$ in Eq. (15.19) may be undesirable. For instance, if one wishes to verify the squeezed state of light via a verification pulse—as described in Section 6.3.2—then the mechanical state readout will be more difficult when the mechanical mode is oscillating with a large amplitude due to the classical back action. This is because, as the verification pulse is entering and leaving the cavity, the large mechanical oscillation will force the cavity in and out of resonance with the input optical state, which manifests in a nonlinear transduction of the mechanical state onto the phase quadrature of light [114]. Thus a sequence of two pulses, with a specific separation in time, may be used to cancel the classical back action within the squeezing protocol as shown in Fig. 15.4. Within the infinitesimal pulse duration approximation ($\tau \approx {\rm d}t$) that leads to Eqs (15.18) to (15.22) this separation between pulses is simply half a period $T = \pi/\omega_{\rm M}$. I will now describe the mathematics of this two pulse sequence.

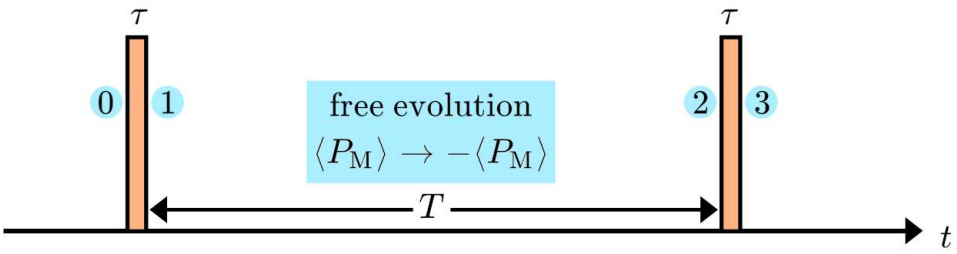


Figure 15.4: **Two pulse sequence for deterministic mechanical squeezing.** (0): the mechanical state just before the first pulse. (1): the mechanical state just after the first pulse. The pulse width τ is assumed to satisfy $\tau \ll 2\pi/\omega_{\rm M}$ in the analytic Gaussian approximation. However, this assumption can be relaxed with the ME approach. (2): the mechanical state just before the second pulse. Here, the mechanical mode has freely evolved such that the mean momentum evolves from $\langle P_{\rm M}(\tau)\rangle$ to $\langle P_{\rm M}(\tau+T)\rangle \to -\langle P_{\rm M}(\tau)\rangle$. (3): the final mechanical state just after the second pulse.

After the first pulsed interaction, the first moments vector and covariance matrix change via $\langle \mathbf{X}(0)\rangle \to \langle \mathbf{X}(\tau)\rangle$ and $V(0) \to V(\tau)$ according to Eqs (15.33) and (15.34). Then after half a mechanical period $T = \pi/\omega_{\rm M}$, the state evolves to $\langle \mathbf{X}(\tau+T)\rangle = (0, -\langle P_{\rm M}(\tau)\rangle)^{\rm T}$ and $V(\tau+T) = V(\tau)$, where again $\langle X_{\rm M}(0)\rangle = 0$ has been assumed. Finally, the second pulse is applied to compensate for

classical back action. Using Eqs (15.33) and (15.34) the state becomes

$$\begin{aligned}
\langle \mathbf{X}(2\tau+T)\rangle &= S\langle \mathbf{X}(\tau+T)\rangle + \mathbf{d} \\
&= \begin{pmatrix} 0 \\ -\langle P_{\rm M}(0)\rangle \end{pmatrix}, \qquad (15.40)\\
V(2\tau+T) &= SV(\tau+T)S^{\rm T}+N \qquad (15.41)\\
&= SV(\tau)S^{\rm T}+N \\
&= S\left[SV(\tau)S^{\rm T}+N\right]S^{\rm T}+N \\
&= S^2V(\tau)\left(S^{\rm T}\right)^2+SNS^{\rm T}+N \\
&= S^2V(\tau)\left(S^{\rm T}\right)^2+2N,
\end{aligned}$$

where $SNS^{\rm T}=N$ was used. Furthermore,

$$S^2 = \begin{pmatrix} 1 & 0 \\ -\dfrac{2\mu^2 N_{\rm P}\bar{\Delta}}{(1+\bar{\Delta}^2)^2} & 1 \end{pmatrix} = \begin{pmatrix} 1 & 0 \\ -2\sinh r & 1 \end{pmatrix}. \qquad (15.42)$$

Therefore, the two pulse transformation $V(2\tau+T)$ is identical to the single pulse transformation $V(\tau)$ *but* with $N_{\rm P}\to 2N_{\rm P}$ and the elimination of classical back action. Therefore,

$$\begin{aligned}
V_X(T+2\tau) &= V_X(0), \qquad (15.43)\\
V_{XP}(T+2\tau) &= V_{XP}(0)-2\sinh r V_X(0), \qquad (15.44)\\
V_P(T+2\tau) &= V_P(0)+4\sinh^2 r V_X(0)-4\sinh r V_{XP}(0)+2V_Q \qquad (15.45)\\
&= V_P(0)+4\sinh^2 r V_X(0)\left(1+\frac{1}{2N_{\rm P}}\right)\\
&\quad -4\sinh r V_{XP}(0)+2\frac{\sinh r}{\bar{\Delta}}.
\end{aligned}$$

Timing with finite duration interactions

As discussed previously, when the infinitesimal pulse duration approximation is relaxed, the deterministic squeezing protocol is still valid and one can use the ME description of Eq. (15.1). Moreover, a two pulse sequence can still be used to cancel the classical back action. However, in this case one must think more carefully about the timing T between the two pulses. Fig. 15.5 illustrates this point.

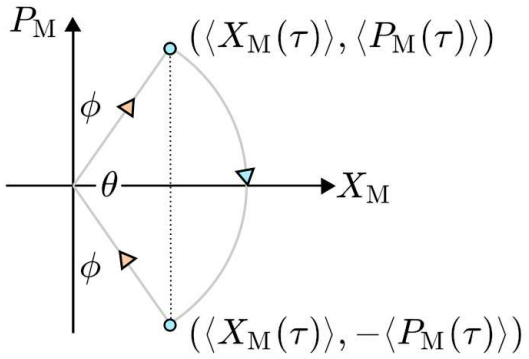


Figure 15.5: **Choosing the optimal time delay for finite duration optomechanical interactions.** For simplicity of this illustration, the initial mechanical state is assumed to be located at the origin of phase space. After the optomechanical interaction the mean of mechanical state is $\langle \mathbf{X}(\tau)\rangle = (\langle X_{\rm M}(\tau\rangle), \langle P_{\rm M}(\tau)\rangle)^{\rm T}$, which makes an angle ϕ with the $P_{\rm M}$ axis of mechanical phase space. Note that $\langle X_{\rm M}(\tau\rangle) \neq 0$ as the mechanics evolves in a modified potential during the optomechanical interaction. The mechanical mode is then allowed to freely evolve through $\theta = \omega_{\rm M} T = \pi - 2\phi$, before the second pulse is applied, which cancels the classical back action. *n.b. Here I am using the convention that the mechanical free evolution occurs in the clockwise convention.*

From Fig. 15.5, it may be seen that after the first pulse, of finite duration τ, the first moments are $\langle \mathbf{X}(\tau)\rangle = (\langle X_{\rm M}(\tau)\rangle, \langle P_{\rm M}(\tau)\rangle)^{\rm T}$, with $\langle X_{\rm M}(\tau)\rangle \neq \langle X_{\rm M}(0)\rangle = 0$ and $\langle P_{\rm M}(\tau)\rangle \neq \langle P_{\rm M}(0)\rangle$. The angle ϕ is defined via $\tan\phi = \langle X_{\rm M}(\tau)\rangle / \langle P_{\rm M}(\tau)\rangle$, which satisfies $\phi \to 0$ as $\tau \to {\rm d}t$ and $\langle X_{\rm M}(\tau)\rangle \to 0$. The mechanics then evolves for a phase space angle $\theta = \omega_{\rm M} T = \pi - 2\phi$, such that the first moments are $\langle \mathbf{X}(\tau + T)\rangle = (\langle X_{\rm M}(\tau)\rangle, -\langle P_{\rm M}(\tau)\rangle)^{\rm T}$. Finally, applying the second pulse will cancel the classical back, i.e. $\langle \mathbf{X}(2\tau + T)\rangle = (0, -\langle P_{\rm M}(0)\rangle)^{\rm T}$.

15.4.1 Results

Figs. 15.6 and 15.7 plots the analytic results of the two-pulse deterministic squeezing protocol for an initial thermal state and an initial ground state, respectively. For comparison, the results for a single-pulsed interaction are also plotted with dashed lines.

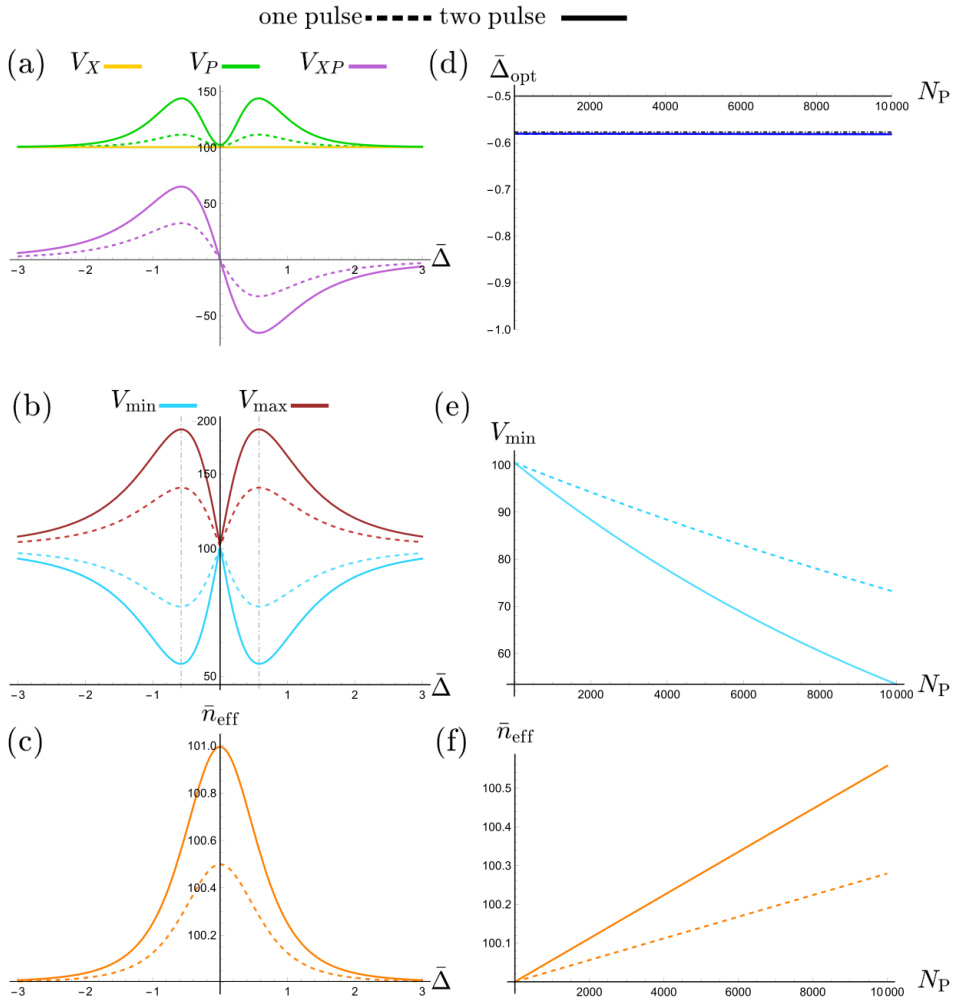


Figure 15.6: **One- and two-pulse squeezing protocol for an initial thermal state.** Here, the mechanical state before the squeezing protocol is a thermal state with $\bar{n} = 100$. Furthermore, $\mu = 0.05$ is chosen such that $\mu\sqrt{\bar{n} + 1/2} < 1$. Dashed lines: one-pulse protocol. Solid lines: two-pulse protocol that cancels classical back action. (a) The covariance matrix elements as a function of the normalized detuning $\bar{\Delta}$. (b) The minimum and maximum variances of the state as a function of $\bar{\Delta}$. Here, the dashed-vertical lines are at $\bar{\Delta} = \pm 1/\sqrt{3}$. (c) The effective thermal occupation as a function of $\bar{\Delta}$. (d) The optimal value of the normalized detuning $\bar{\Delta}_{\text{opt}}$ as a function of the mean photon number incident on the cavity N_{P}. The dashed-grey line is at $\bar{\Delta} = -1\sqrt{3}$, which lies just above the value of $\bar{\Delta}_{\text{opt}}$—the slight difference is due to quantum back action noise. Note $\bar{\Delta} = -\bar{\Delta}_{\text{opt}}$ is also an optimal value in this short-pulsed approximation. (e) The minimum squeezing variance $V_{\min}$ as a function of N_{P} for the optimal detuning $\bar{\Delta}_{\text{opt}}$. (f) The effective thermal occupation $\bar{n}_{\text{eff}}$ as a function of N_{P} for the optimal detuning $\bar{\Delta}_{\text{opt}}$.

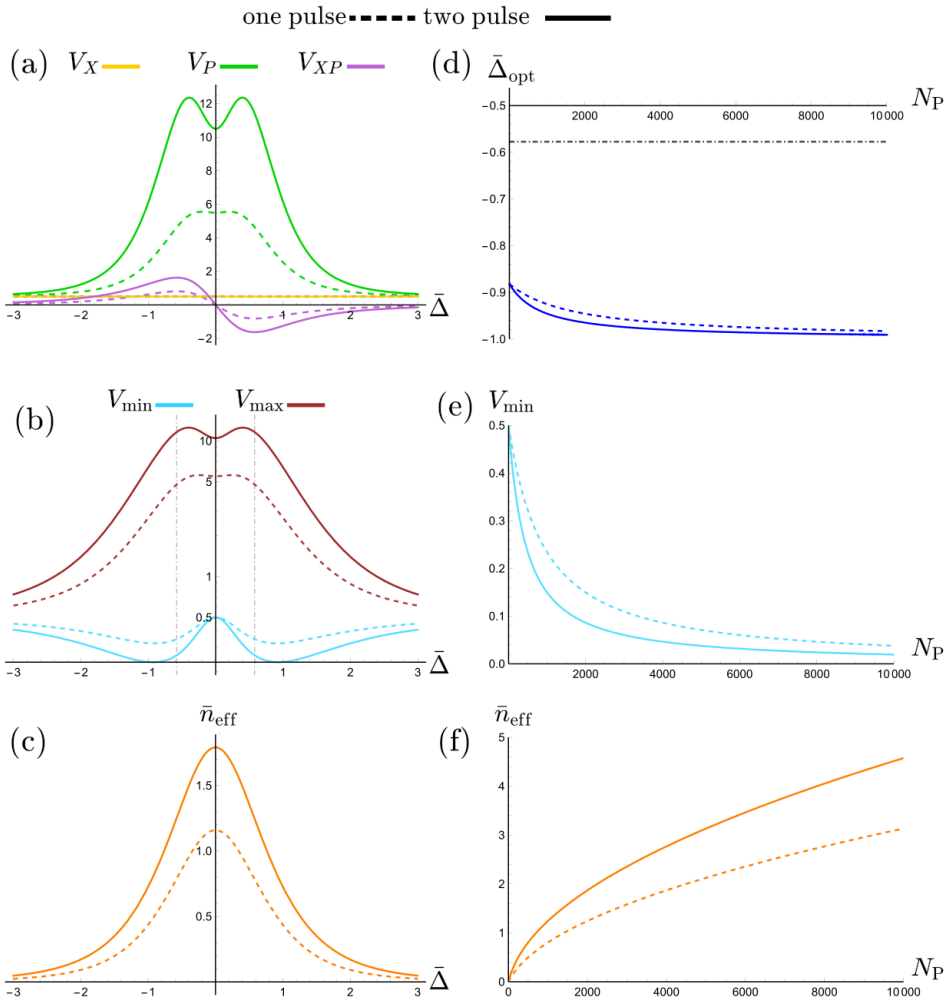


Figure 15.7: **One- and two-pulse squeezing protocol for an initial ground state.** Here, the mechanical state before the squeezing protocol is the ground state with $\bar{n} = 0$. Furthermore, $\mu = 0.1$ is chosen so $\mu\sqrt{1/2} < 1$. Dashed lines: one-pulse protocol. Solid lines: two-pulse protocol that cancels classical back action. (a) The covariance matrix elements as a function of the normalized detuning $\bar{\Delta}$. (b) The minimum and maximum variances of the state as a function of $\bar{\Delta}$. Here, the dashed-vertical lines are at $\bar{\Delta} = \pm 1/\sqrt{3}$. (c) The effective thermal occupation as a function of $\bar{\Delta}$. (d) The optimal value of the normalized detuning $\bar{\Delta}_{\text{opt}}$ as a function of the mean photon number incident on the cavity N_{P}. The dashed-grey line is at $\bar{\Delta} = -1\sqrt{3}$, which lies far from from $\bar{\Delta}_{\text{opt}}$—now the quantum back action noise is comparable to the intrinsic quantum noise of the initial state. Note $\bar{\Delta} = -\bar{\Delta}_{\text{opt}}$ is also an optimal value in this short-pulsed approximation. (e) The minimum squeezing variance $V_{\min}$ as a function of N_{P} for the optimal detuning $\bar{\Delta}_{\text{opt}}$. (f) The effective thermal occupation $\bar{n}_{\text{eff}}$ as a function of N_{P} for the optimal detuning $\bar{\Delta}_{\text{opt}}$.

It is therefore seen that the protocol successfully squeezes both an initial thermal state and an initial ground state. Importantly, Fig. 15.7 demonstrates one can expect to see quantum squeezing experimentally in states with low thermal occupations $\bar{n} \sim 1$. The main qualitative difference between Figs. 15.6 and 15.7 is related to the analysis of Section 15.3.3. Namely, when the intrinsic thermal noise of the initial state dominates over the quantum back action induced by the squeezing protocol, as in Fig. 15.6, the protocol can be well approximated as a pure squeezing unitary operation—with optimal normalized detuning $|\bar{\Delta}_{\rm opt}| = 1/\sqrt{3}$. Whereas, when the quantum back action noise becomes comparable to the initial state uncertainty, as in Fig. 15.7, the protocol can no longer be approximated as a simple unitary transformation.

Visualizing the quantum back action

In our deterministic squeezing protocol the mechanical state is Gaussian, hence one can use Eq. (4.3) to plot the Wigner function of the Gaussian mechanical state in phase space. However, to visualize the effect of quantum back action it is useful to think about a specific contour of the Wigner function. For example, the FWHM of the Wigner function is given by the equation for the ellipse

$$(2\bar{n}_{\rm eff}^2 + 1)\ln(2) = V_P X_{\rm M}^2 - 2V_{XP} X_{\rm M} P_{\rm M} + V_X P_{\rm M}^2. \tag{15.46}$$

To see the effect of quantum back action, one may consider the contour in Eq. (15.46) without the quantum back action terms $2V_Q$ contributing to the momentum variance in Eq. (15.45). Plots of these two contours—the one including quantum back action and the one which does not—are shown in Fig. 15.8. Here, one can now visualize that at low values of $\bar{n}$, the quantum back action is comparable to the intrinsic quantum noise. While at higher values of $\bar{n}$, the thermal noise is the dominant contribution.

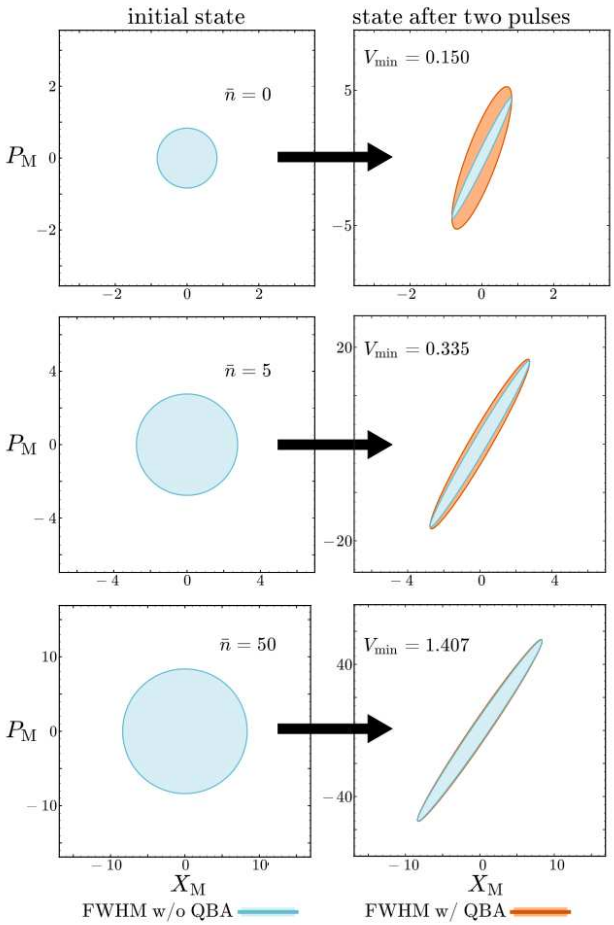


Figure 15.8: **Visualizing the effect of quantum back action noise.** The FWHM contour is plotted for the mechanical Wigner function before and after the two-pulse deterministic-squeezing protocol for an initial ground state, a thermal state with $\bar{n} = 5$, and a thermal state with $\bar{n} = 50$. Here, $\mu = 0.1$, $N_{\mathrm{P}} = 10^3$, and $\bar{\Delta} = \bar{\Delta}_{\mathrm{opt}}$ is chosen to minimize $V_{\min}$. The blue contour represents the FWHM of the Wigner function without quantum back action noise, while the orange contour represents the FWHM with quantum back action noise. *n.b. For the state after two pulses, the axes have an unequal aspect ratio to make the QBA contribution clearer.*

15.5 Is optical squeezing possible?

Outside the adiabatic regime, the optomechanical interaction can be utilized to generate squeezed states of light. Namely, pondermotive squeezing of light can be achieved in the the resolved sideband regime via a blue-detuned drive [382, 405]. After introducing the deterministic mechanical squeezing protocol above, which also relies on a detuned drive, one may then ask if this mechanism can produce squeezed optical states in the unresolved sideband regime for adiabatic cavities. To investigate this question, I take the optical state $\rho_{\rm L}$ after the optomechanical interaction, see Eq. (13.10), and compute its Wigner function.

15.5.1 The Wigner function with detuning

Inserting $\rho_{\rm L}$ from Eq. (13.10) into Wigner's formula Eq. (2.46) gives the expression for the optical Wigner function at the output of the nonlinear optomechanical interaction

$$W_{\rm L}(X_{\rm L},P_{\rm L}) \;=\; \frac{1}{\pi}\int \mathrm{d}X_{\rm M}\; P_i(X_{\rm M})\mathrm{e}^{-[X_{\rm L}-X_\alpha A(X_{\rm M})]^2-[P_{\rm L}-X_\alpha B(X_{\rm M})]^2}, \quad (15.47)$$

Note that when there is no optomechanical interaction $\mu=0$ one has

$$A(0) \;=\; \frac{1-\bar{\Delta}^2}{1+\bar{\Delta}^2}, \quad (15.48)$$

$$B(0) \;=\; \frac{2\bar{\Delta}}{1+\bar{\Delta}^2}, \quad (15.49)$$

and therefore $W_{\rm L}(X_{\rm L},P_{\rm L})$ is just a rotated coherent state

$$W_{\rm L}(X_{\rm L},P_{\rm L}) \;=\; \frac{1}{\pi}\mathrm{e}^{-[X_{\rm L}-X_\alpha A(0)]^2-[P_{\rm L}-X_\alpha B(0)]^2}. \quad (15.50)$$

Is the optical state squeezed?

Using the form of $\rho_{\rm L}$ from Eq. (13.10) one can also calculate any moment of an arbitrary rotated quadrature operator $X_{\rm L}(\theta)=X_{\rm L}\cos\theta+P_{\rm L}\sin\theta$ via

$$\langle X_{\rm L}^n(\theta)\rangle = \mathrm{tr}_{\rm L}(X_{\rm L}^n(\theta)\rho_{\rm L}). \quad (15.51)$$

By performing the trace over the optical subspace in the $X_{\rm L}(\theta)$ basis, one finds

$$\langle X_{\rm L}^n(\theta)\rangle = \frac{1}{\sqrt{\pi}}\int \mathrm{d}X_{\rm M}P_i(X_{\rm M})\times \int \mathrm{d}X_{\rm L}(\theta)X_{\rm L}^n(\theta)\mathrm{e}^{-(X_{\rm L}(\theta)-X_\alpha A(X_{\rm M})\cos\theta-X_\alpha B(X_{\rm M})\sin\theta)^2}. \quad (15.52)$$

Using the Gaussian integrals from Appendix C one finds

$$\langle X_{\rm L}(\theta)\rangle = \int {\rm d}X_{\rm M} P_i(X_{\rm M})\ X_\alpha \left[A(X_{\rm M})\cos\theta + B(X_{\rm M})\sin\theta\right], \tag{15.53}$$

$$\begin{aligned}\left\langle X_{\rm L}^2(\theta)\right\rangle &= \int {\rm d}X_{\rm M} P_i(X_{\rm M})\ \left\{\frac{1}{2} + X_\alpha^2\left[A(X_{\rm M})\cos\theta + B(X_{\rm M})\sin\theta\right]^2\right\}. \\ &= \frac{1}{2} + \int {\rm d}X_{\rm M} P_i(X_{\rm M})\ X_\alpha^2\left[A(X_{\rm M})\cos\theta + B(X_{\rm M})\sin\theta\right]^2. \end{aligned} \tag{15.54}$$

The variance of the rotated quadrature is then

$${\rm Var}(X_{\rm L}(\theta)) = \left\langle X_{\rm L}^2(\theta)\right\rangle - \left(\langle X_{\rm L}(\theta)\rangle\right)^2. \tag{15.55}$$

The optical state is squeezed if there exists a value of θ for which ${\rm Var}(X_{\rm L}(\theta)) < \frac{1}{2}$. Furthermore, note that as the initial width of the mechanical state $\sigma \to 0$, the initial mechanical probability distribution tends towards a delta function $P_i(X_{\rm M}) \to \delta(X_{\rm M})$. Therefore, in the limit $\sigma \to 0$, ${\rm Var}(X_{\rm L}(\theta)) = \frac{1}{2}$ as expected.

Results and Wigner function plots

By examining the expression for $\rho_{\rm L}$

$$\rho_{\rm L} = \int {\rm d}X_{\rm M}\ P_i(X_{\rm M})\left|\alpha(A+{\rm i}B)\right\rangle\left\langle\alpha(A+{\rm i}B)\right|,$$

it may be seen that $\rho_{\rm L}$ is a phase-diffused rotated coherent state. Thus, despite the choice of $\Delta \neq 0$ producing deterministically squeezed states of the mechanical mode, one does not expect $\rho_{\rm L}$—even with $\Delta \neq 0$—to show squeezing as $\rho_{\rm L}$ is an incoherent mixture of coherent (non-squeezed) states. To show this definitively I write $g(X_{\rm M}) = X_\alpha\left[A(X_{\rm M})\cos\theta + B(X_{\rm M})\sin\theta\right]$ and hence

$$\begin{aligned}{\rm Var}(X_{\rm L}(\theta)) &= \frac{1}{2} + \int {\rm d}X_{\rm M} P_i(X_{\rm M}) g(X_{\rm M})^2 - \left[\int {\rm d}X_{\rm M} P_i(X_{\rm M}) g(X_{\rm M})\right]^2 \\ &= \frac{1}{2} + {\rm Var}(X_{\rm M}) \\ &\geq \frac{1}{2} \end{aligned} \tag{15.56}$$

as the variance of the function $g(X_{\rm M})$ must be greater than or equal to zero.

In Figs. 15.9 and 15.10 the Wigner function $W_{\rm L}$ and the function ${\rm Var}(X_{\rm L}(\theta))$ are plotted. Here, I choose $\bar{\Delta} = -0.5$, $X_\alpha = 10$, $\sigma^2 = 100$, and μ and θ are varied. Although the unitary ${\rm e}^{{\rm i}\varphi(X_{\rm M})n_{\rm L}}$ can be utilized to achieve mechanical squeezing, both deterministically and non-deterministically[4], it is seen here that the protocol detailed above cannot generate optical squeezing due to the adiabatic elimination of the cavity mode.

[4]Note that this chapter covers non-deterministic pulsed squeezing, whereas in Chapter 13 measurement-outcome dependent squeezing was investigated.

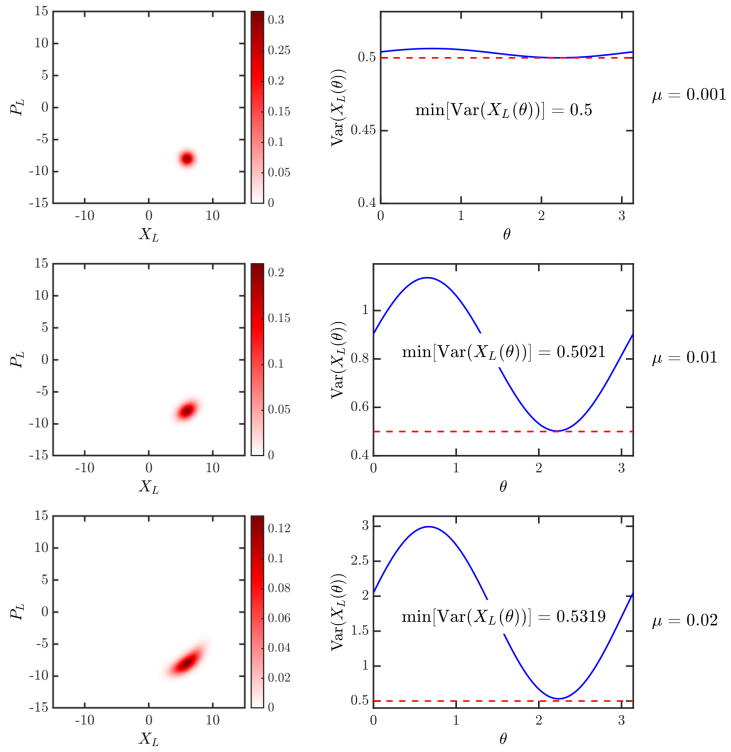


Figure 15.9: **Optical state after the non-linear cavity enhanced optomechanical unitary.** Left: Wigner functions $W_{\mathrm{L}}(X_{\mathrm{L}}, P_{\mathrm{L}})$. Right: $\mathrm{Var}(X_{\mathrm{L}}(\theta))$ versus θ. Here, $\bar{\Delta} = -0.5$, $X_\alpha = 10$, $\sigma^2 = 100$ and $\mu = 0.001$, 0.01, or 0.02. Here, no squeezing is observed.

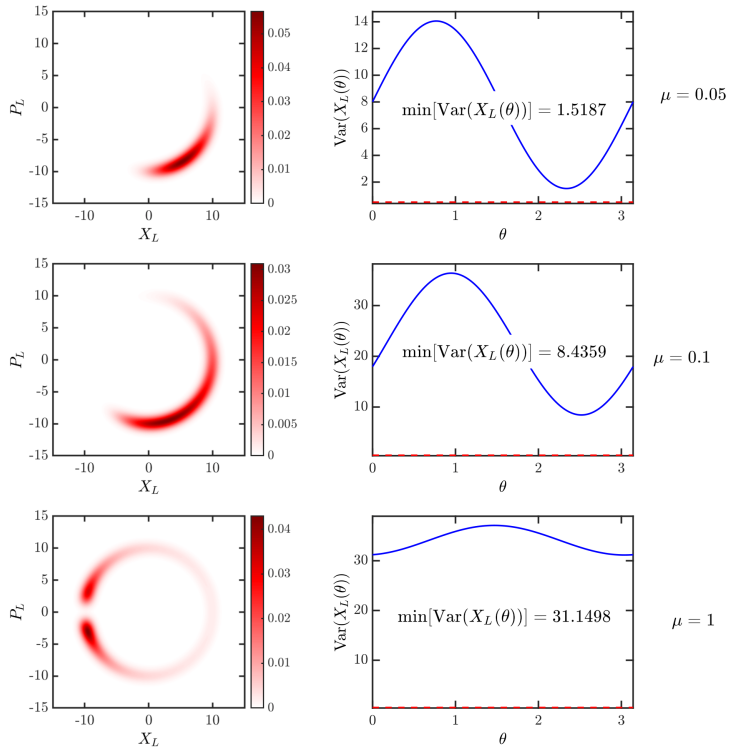


Figure 15.10: **Optical state after the non-linear cavity enhanced optomechanical unitary.** Left: Wigner functions $W_{\mathrm{L}}(X_{\mathrm{L}}, P_{\mathrm{L}})$. Right: $\mathrm{Var}(X_{\mathrm{L}}(\theta))$ versus θ. Here, $\bar{\Delta} = -0.5$, $X_\alpha = 10$, $\sigma^2 = 100$ and $\mu = 0.05$, 0.1, or 1. Here, no squeezing is observed.

Although optical quadrature squeezing is not possible in the adiabatic regime, the optical state still contains interesting phase-space features. Noting that the mechanical state is useful for sensing quadrature displacements along the squeezed quadrature, and due to asymmetric phase distributions in Figs. 15.9 and 15.10, the optical state may be useful for sensing rotations in optical phase space. This difference in the utility of the states for sensing purposes is apparent from the inherent asymmetry of the radiation-pressure interaction $a^\dagger a X_{\mathrm{M}}$ between the optical and mechanical mode.

15.6 Conclusions and outlook

Here, I have motivated and introduced our deterministic mechanical squeezing protocol that exploits the nonlinearities of cavity optomechanics. The squeezing mechanism can be understood as a light-induced shearing of the mechanical mode, which is capable of realizing quantum squeezing of the mechanical oscillator via the generation of X_{M}-P_{M} correlations. I have shown how a short-pulsed Gaussian approximation to the squeezing mechanism agrees well with the exact description given by the nonlinear cavity-enhanced ME. Moreover, I have described how a two-pulse sequence may be used to cancel classical back action to prepare quantum squeezed states at the origin of mechanical phase space. Although the experiment of Ref. [12] operates in the regime where the thermal noise dominates over the quantum back action noise, we have also discussed how squeezing below quantum ground state width is possible as the initial thermal noise tends to zero.

Furthermore, the exact ME can go beyond the short-pulsed-Gaussian approximation to (i) include the effects of finite mechanical evolution and dissipation and (ii) operate at even larger optomechanical coupling strengths, which can induce mechanical non-Gaussianity. Finally, by studying the optical Wigner function, I have provided an outlook towards the interesting phase-space features of the optical mode after the nonlinear cavity-enhanced interaction.

Thesis conclusion

In this thesis I have detailed the work done during my PhD in the Quantum Measurement Lab. In Part I, I reviewed the required background theory including core concepts from quantum optics, quantum open systems, Gaussian continuous-variable theory, and quantum measurement theory. Finally, I provided an overview of cavity quantum optomechanics in Chapter 6. Here, I stressed the limitations of the linearized approximation to motivate the nonlinear regime, which is now being observed by a growing number of experiments.

In Part II, I discussed several theoretical proposals and experiments for quantum state engineering in optomechanics. Chapters 7 and 8 focused on our proposals for creating nonclassical and entangled mechanical states via the radiation-pressure interaction. Following this, in Chapters 9 and 10, I discussed the underlying theory of the experiments performed in our group that utilize Brillouin optomechanics. Here, single-photon detection was used to generate non-Gaussian mechanical states and zero-photon detection was used to cool a mechanical resonator beyond the capabilities of standard laser cooling.

Finally in Part III, I discussed our framework for nonlinear cavity quantum optomechanics that includes the nonlinearities of the radiation-pressure interaction, couplings up to arbitrary order in position, and the nonlinear response of the cavity. In Chapter 11, I introduced the unitaries that describe the nonlinear optomechanical interaction in the adiabatic regime. Chapter 12 then focused on the construction of a measurement operator and a stochastic master equation, which were used to describe our general-dyne scheme for pulsed and continuous position measurements in Chapters 13 and 14, respectively. Lastly, in Chapter 15, I discussed the theory behind the experiment performed by our collaborators at AMOLF with an outlook towards achieving mechanical squeezing below the quantum ground state.

At the time of writing, I am preparing two manuscripts for publication that build upon the results of this thesis [10, 13]. Firstly, in Ref. [10], we develop the results of Ref. [6] by introducing a statistical framework for finding optimal negative-partial-transpose-based entanglement criteria. Secondly, building on our framework for nonlinear cavity quantum optomechanics [7], we have made the first prediction of deterministic mechanical Wigner negativity in the unresolved-sideband regime in Ref. [13]. Future work in this direction will include quantum sensing with nonlinear optomechanics and exploring the border between quantum mechanics and gravity.

Appendix A

Useful formulae in quantum optics

Dyson series solution for the unitary time-evolution operator:

$$U(t,t_0) = \mathcal{T}\exp\left[-\frac{\mathrm{i}}{\hbar}\int_{t_0}^{t} H(t')\mathrm{d}t'\right] \tag{A.1}$$

$$= \sum_{n=0}^{\infty} U_n(t_n,t_0), \tag{A.2}$$

with

$$U_n(t_n,t_0) = \frac{(-\mathrm{i}/\hbar)^n}{n!}\int_{t_0}^{t}\mathrm{d}t_1\int_{t_0}^{t}\mathrm{d}t_n\ldots\int_{t_0}^{t}\mathrm{d}t_n\mathcal{T}\left[H(t_1)H(t_2)\ldots H(t_n)\right], \tag{A.3}$$

where the time-ordering operator $\mathcal{T}$ orders the Hamiltonians[1] such that

$$\mathcal{T}\left[H(t_1)H(t_2)\right] = H(t_1)H(t_2)\theta(t_1-t_2) + H(t_2)H(t_1)\theta(t_2-t_1). \tag{A.4}$$

Note this implies

$$U_n(t_n,t_0) = \left(-\frac{\mathrm{i}}{\hbar}\right)^n\int_{t_0}^{t}\mathrm{d}t_1\int_{t_0}^{t_1}\mathrm{d}t_n\ldots\int_{t_0}^{t}\mathrm{d}t_{n-1}H(t_1)H(t_2)\ldots H(t_n), \tag{A.5}$$

for $t_1 > t_2 > \ldots t_n$.
Overlap between a coherent state $|\alpha\rangle$, $\alpha = (X_\alpha + \mathrm{i}P_\alpha)/\sqrt{2}$ and the quadrature

[1] If instead, one considers the time ordering of fermionic operators, one must carefully consider the sign associated with each operator permutation. However, the Hamiltonians of fermionic fields only contain an even number of operators, so we need not worry here.

basis states:

$$\langle X|\alpha\rangle = \frac{1}{\pi^{\frac{1}{4}}}\exp\left(-\frac{1}{2}(X-X_\alpha)^2+\mathrm{i}P_\alpha X-\frac{\mathrm{i}}{2}X_\alpha P_\alpha\right), \quad (A.6)$$

$$\langle P|\alpha\rangle = \frac{1}{\pi^{\frac{1}{4}}}\exp\left(-\frac{1}{2}(P-P_\alpha)^2-\mathrm{i}X_\alpha P+\frac{\mathrm{i}}{2}X_\alpha P_\alpha\right), \quad (A.7)$$

$$\begin{aligned}\langle X_\theta|\alpha\rangle = \frac{1}{\pi^{\frac{1}{4}}}\exp\Bigg(&-\frac{1}{2}(X_\theta-X_\alpha\cos\theta-P_\alpha\sin\theta)^2\\&+\mathrm{i}(P_\alpha\cos\theta-X_\alpha\sin\theta)X_\theta\\&-\frac{\mathrm{i}}{2}(X_\alpha\cos\theta+P_\alpha\sin\theta)(P_\alpha\cos\theta-X_\alpha\sin\theta)\Bigg),\end{aligned} \quad (A.8)$$

where the rotated quadrature X_θ is given by $X_\theta = X\cos\theta + P\sin\theta$.
Baker-Campbell-Hausdorff (BCH) formula:

$$\mathrm{e}^A\mathrm{e}^B = \exp\left(A+B+\frac{1}{2}[A,B]+\frac{1}{12}[A,[A,B]]-\frac{1}{12}[B,[A,B]]+\ldots\right). \quad (A.9)$$

Zassenhaus formula:

$$\mathrm{e}^{A+B} = \mathrm{e}^A\mathrm{e}^B\mathrm{e}^{-\frac{1}{2}[A,B]}\mathrm{e}^{\frac{1}{6}([A,[A,B]]+2[B,[A,B]])}\ldots \quad (A.10)$$

Hadamard lemma:

$$\mathrm{e}^A B\mathrm{e}^{-A} = B+[A,B]+\frac{1}{2!}[A,[A,B]]+\ldots+\frac{1}{n!}[A,[A,\ldots,[A,B]\ldots]]+\ldots \quad (A.11)$$

Normal-ordering of the exponential:

$$:\mathrm{e}^{\lambda a^\dagger a}: = \sum_{k=0}^{\infty}\frac{\lambda^k}{k!}a^{\dagger k}a^k \quad (A.12)$$

$$= (1+\lambda)^{a^\dagger a}. \quad (A.13)$$

Reordering functions of annihilation and creation operators:

$$\mathrm{e}^{\lambda a^\dagger a}f(a)\mathrm{e}^{-\lambda a^\dagger a} = f(a\mathrm{e}^{-\lambda}), \quad (A.14)$$

$$\mathrm{e}^{\lambda a^\dagger a}f(a^\dagger)\mathrm{e}^{-\lambda a^\dagger a} = f(a^\dagger\mathrm{e}^{\lambda}), \quad (A.15)$$

$$\mathrm{e}^{\lambda a^\dagger}f(a) = f(a-\lambda)\mathrm{e}^{\lambda a^\dagger}, \quad (A.16)$$

$$\mathrm{e}^{\lambda a}f(a^\dagger) = f(a^\dagger+\lambda)\mathrm{e}^{\lambda a}. \quad (A.17)$$

For a function f of the two conjugate variables X and P, which satisfy $[X,P]=\mathrm{i}$:

$$[f(X,P),X] = -\mathrm{i}\frac{\partial f}{\partial P}, \quad (A.18)$$

$$[f(X,P),P] = +\mathrm{i}\frac{\partial f}{\partial X}. \quad (A.19)$$

Appendix B

Fourier transforms

Fourier transform of $f(x)$:

$$\tilde{f}(k) \quad = \quad \mathcal{F}\left[f(x)\right] = \frac{1}{\sqrt{2\pi}} \int_{-\infty}^{\infty} f(x) \mathrm{e}^{-\mathrm{i}kx} \mathrm{d}x. \tag{B.1}$$

Inverse Fourier transform:

$$f(x) \quad = \quad \mathcal{F}^{-1}\left[\tilde{f}(k)\right] = \frac{1}{\sqrt{2\pi}} \int_{-\infty}^{\infty} \tilde{f}(k) \mathrm{e}^{+\mathrm{i}kx} \mathrm{d}k. \tag{B.2}$$

Paserval's identity:

$$\int_{-\infty}^{\infty} |f(x)|^2 \mathrm{d}x = \int_{-\infty}^{\infty} |\tilde{f}(k)|^2 \mathrm{d}k. \tag{B.3}$$

Convolution theorem:

$$\mathcal{F}[f * g(x)] = \sqrt{2\pi} \tilde{f}(k) \tilde{g}(k). \tag{B.4}$$

Derivative:

$$\mathcal{F}[f'(x)] = \mathrm{i}k \tilde{f}(k). \tag{B.5}$$

Gaussian:

$$g(x) \quad = \quad \frac{1}{\sqrt{2\pi\sigma^2}} \exp\left(-\frac{x^2}{2\sigma^2}\right), \tag{B.6}$$

$$\tilde{g}(k) \quad = \quad \sqrt{2\pi} \exp\left(-\frac{1}{2}k^2\sigma^2\right). \tag{B.7}$$

Dirac-delta function:

$$\mathcal{F}\left[\delta(x - x_0)\right] \quad = \quad \frac{1}{\sqrt{2\pi}} \mathrm{e}^{-\mathrm{i}kx_0}. \tag{B.8}$$

Appendix C

Useful sums and integrals

Geometric sums

One can differentiate the infinite geometric sum

$$\sum_{m=0}^{\infty} x^m = \frac{1}{1-x}, \quad \text{for } |x| < 1, \tag{C.1}$$

n times to get

$$\sum_{m=0}^{\infty} \frac{m!}{(m-n)!} x^{m-n} = \frac{n!}{(1-x)^{n+1}}. \tag{C.2}$$

Gaussian integrals

The Gaussian integral in one-dimension is given by

$$\int_{-\infty}^{+\infty} \mathrm{d}x \ \mathrm{e}^{-\alpha(x-\beta)^2} = \sqrt{\frac{\pi}{\alpha}}, \tag{C.3}$$

where $\alpha > 0$.
Extra useful one-dimensional integrals:

$$\int_{-\infty}^{+\infty} \mathrm{d}x \ x\mathrm{e}^{-\alpha(x-\beta)^2} = \beta\sqrt{\frac{\pi}{\alpha}}, \tag{C.4}$$

$$\int_{-\infty}^{+\infty} \mathrm{d}x \ x^2\mathrm{e}^{-\alpha(x-\beta)^2} = \frac{1+2\alpha\beta^2}{2}\sqrt{\frac{\pi}{\alpha^3}}, \tag{C.5}$$

$$\int_{-\infty}^{+\infty} \mathrm{d}x \ x^n\mathrm{e}^{-\alpha x^2} = \frac{1}{2}\left(1+(-1)^n\right)\alpha^{-\frac{1+n}{2}}\Gamma\left[\frac{n+1}{2}\right], \tag{C.6}$$

where $\alpha > 0$, n is a positive integer, and Γ is the gamma function. For $n = 2m$, the last integral has the simple form

$$\int_{-\infty}^{+\infty} \mathrm{d}x \ x^{2m}\mathrm{e}^{-\alpha x^2} = \sqrt{\pi}\alpha^{-\frac{1+2m}{2}}\frac{(2m)!}{4^m m!}. \tag{C.7}$$

The Gaussian integral in n-dimensions is given by

$$\int_{-\infty}^{+\infty} \mathrm{d}^n x \; \mathrm{e}^{-\frac{1}{2}(\mathbf{x}-\mathbf{b})^{\mathrm{T}} A(\mathbf{x}-\mathbf{b})} = \sqrt{\frac{(2\pi)^n}{\det(A)}}, \tag{C.8}$$

where A is a symmetric matrix with all positive eigenvalues.

Appendix D

Objective collapse models

Here, I provide a brief introduction to objective collapse models, which were the subject of investigation in our work of Ref. [5]. Specifically, Ref. [5] asks "Can the displacemon device be used to test objective collapse models?"

Collectively, objective collapse models are equations that modify the standard von-Neumann evolution of Eq. (1.8) to include an inherent dynamical collapse of the quantum wavefunction, without the explicit need for measurement from an observer [160]. Mathematically, objective collapse models may be derived by introducing position measurements to the von-Neumann evolution, which occur randomly, or at some rate, throughout the state's evolution [406]. Crucially, to recover the equations that describe objective collapse one must demand that the measurement records of these spontaneous measurements are fundamentally inaccessible. This corresponds to setting the measurement efficiency η_n in the general SME of Eq. (5.7) to zero. Operationally, this may seem similar to the derivation of the Lindblad master equation of Eq. (3.1) which describes open system dynamics. However unlike open system dynamics, objective collapse models do not correspond to tracing out environmental degrees of freedom that are—in principle but not in practice—accessible. But instead from a quantum measurement theory perspective, objective collapse models may be thought as a fundamental modification to quantum theory due to, potentially, inaccessible degrees of freedom. Nevertheless, they do predict an additional heating rate of quantum systems on top of conventional dissipation mechanisms [159].

Experiments that test for the presence of such a heating rate from the collapse noise are known as *non-interferometric* experiments, while experiments that directly probe the effect of spontaneous collapse mechanisms on quantum superposition states are known as *interferometric* experiments. While non-interferometric tests currently exclude a larger area of parameter space for different collapse models, interferometric tests provide a more direct test of objective collapse as the heating rate will depend on the statistical properties of collapse noise, whereas the reduction of quantum interference is unambiguous [407].

The lack of energy conservation is a problem in objective collapse theories.

The collapse noise leads to a heating mechanism, which is in most theories unbounded. However, this may be resolved by postulating a finite temperature the collapse noise thermalizes the system to. The models are known as *dissipative collapse models* [408]. Although, collapse models often have the disadvantage of lack of motivation and derivation from first principles, they have the distinct advantage of being experimentally testable theories. Therefore, from the point of view of experiment, objective collapse models can be viewed as a possible phenomenological description of nature, which do not yet invoke the underlying physical mechanisms that would allow one to derive such equations from first principles.

Historically, the first objective collapse theory to be developed was the GRW theory in 1986, named after its authors Ghirardi, Rimini, and Weber [156], which built on the earlier work of Philip Pearle [409]. Here, the typical von-Neumann evolution is interrupted by spontaneous Gaussian position measurements of width r. These measurements act on the individual constituent particles of the quantum state, and occur randomly at a rate λ following Poissonian statistics. Again the outcome of these measurements is considered to be fundamentally inaccessible, and importantly the collapse mechanism amplifies with the total number of constituents. Hence, providing a possible explanation for the lack of quantum superposition states at the macroscopic scale through one dynamical equation.

However, for the purposes of this thesis I choose to provide only a brief summary of two collapse theories: (1) continuous spontaneous localization (CSL) which is a continuous limit of GRW theory, where the collapse mechanism and the von-Neumann evolution are now combined into one equation, and (2) Diósi-Penrose (DP) collapse, which postulates that the origin of collapse is due to the fundamental incompatibility between quantum mechanics and gravity.

D.1 Continuous spontaneous localization

CSL is characterized by two parameters, the localization length scale r_{C} and the collapse rate λ_{C}. In this model, continuous weak Gaussian position measurements are made on all the constituent particles of an object at a rate λ_{C}. The localization length r_{C} describes the characteristic width of these Gaussian measurements.

The Lindblad equation describing CSL collapse is [160, 410]

$$\dot{\rho}(t) = -\frac{\mathrm{i}}{\hbar}[H,\rho(t)] - \frac{\lambda_{\mathrm{C}}}{2\pi^{3/2}r_{\mathrm{C}}^3 m_0^2}\int \mathrm{d}^3\mathbf{r}\,[M(\mathbf{r}),[M(\mathbf{r}),\rho(t)]]\,, \quad \text{(D.1)}$$

$$M(\mathbf{r}) = \sum_n m_n \exp\left(-\frac{(\mathbf{r}-\mathbf{r}_n)^2}{2r_{\mathrm{C}}^2}\right) \quad \text{(D.2)}$$

Here, $m_0 = 1.67\times10^{-27}\,\mathrm{kg}$ is the nucleon mass and $M(\mathbf{r})$ is the Gaussian-averaged mass density operator, which is a sum over all constituent particles, each of mass m_n with position operator $\mathbf{r}_n$. Note $M(\mathbf{r})$ is localized at each

particle position with a width determined by the length $r_{\rm C}$. Hence, it is seen that the Lindblad term in CSL describes weak Gaussian position measurements at each particle site at a rate $\lambda_{\rm C}$. Furthermore, the sum is in principle taken over all constituent protons, neutrons, and electrons. However, due to the double commutator in Eq. (D.1) electron-nucleon and electron-electron cross terms scale as $m_{\rm e}/m_0$ and $(m_{\rm e}/m_0)^2$, respectively, where $m_{\rm e} = 9.11 \times 10^{-31}\,{\rm kg}$. As $m_{\rm e}/m_0 \approx 5 \times 10^{-4}$, the contribution of electrons to CSL collapse can safely be ignored [411].

Defining the CSL parameters $r_{\rm C}$ and $\lambda_{\rm C}$ with respect to the spontaneous localizations of constituent nucleons, and not any larger constituent masses, allows for fair and direct comparisons to be made between different experiments. In particular, this enables one to combine $\lambda_{\rm C}$-$r_{\rm C}$ exclusion plots from many different experiments [407, 412].

D.1.1 CSL collapse rate of an extended body

I now present a derivation of the CSL collapse rate for an extended body, which takes a particularly useful and simple form. This derivation follows Ref. [413], and is based on three assumptions: (i) a rigid body, (ii) a continuous mass distribution, and (iii) small oscillations or superposition size. I now discuss these assumptions in turn.

(i) *Rigid body.*—Using the Fourier transform of a Gaussian from Appendix B gives

$$\exp\left(-\frac{(\mathbf{r}-\mathbf{r}_n)^2}{2r_{\rm C}^2}\right) = \frac{r_{\rm C}^3}{(2\pi)^{3/2}}\int_{-\infty}^{\infty}\exp\left(-\frac{1}{2}\mathbf{k}^2 r_{\rm C}^2 + {\rm i}\mathbf{k}\cdot(\mathbf{r}-\mathbf{r}_n)\right){\rm d}^3\mathbf{k}. \quad \text{(D.3)}$$

Then writing the position operators $\mathbf{r}_n$ as the sum of a centre of mass position operator $\mathbf{R}$ and a relative position operator $\mathbf{r}_n^{\rm rel}$ gives $\mathbf{r}_n = \mathbf{R} + \mathbf{r}_n^{\rm rel}$. For a rigid body, the centre of mass position is treated as an operator and the relative position as a classical variable $\mathbf{q}_n = \langle \mathbf{r}_n^{\rm rel}\rangle$, which is valid if $\langle \mathbf{r}_n^{\rm rel} - \mathbf{q}_n\rangle \ll r_{\rm C}$. The quantum uncertainty in the position of each particle is therefore completely encoded in the centre of mass coordinate, while the position of each particle within the structures is scanned by a classical vector. Hence, inserting $\mathbf{r}_n = \mathbf{R} + \mathbf{q}_n$ into Eq. (D.3), $M(\mathbf{r})$ becomes

$$M(\mathbf{r}) = r_{\rm C}^3\int_{-\infty}^{\infty}\exp\left(-\frac{1}{2}\mathbf{k}^2 r_{\rm C}^2 + {\rm i}\mathbf{k}\cdot(\mathbf{r}-\mathbf{R})\right)\tilde{\varrho}(\mathbf{k}){\rm d}^3\mathbf{k}, \quad \text{(D.4)}$$

$$\tilde{\varrho}(\mathbf{k}) = \frac{1}{(2\pi)^{3/2}}\sum_n m_n {\rm e}^{-{\rm i}\mathbf{k}\cdot\mathbf{q}_n}, \quad \text{(D.5)}$$

where $\tilde{\varrho}(\mathbf{k})$ is proportional the Fourier transform of the mass density $\varrho(\mathbf{r}) = \sum_n m_n\delta(\mathbf{r}-\mathbf{q}_n)$. Here, the Fourier transform convention of Appendix B is

used. Then inserting Eq. (D.4) into Eq. (D.1) gives

$$\begin{aligned}\dot{\rho}(t) &= -\frac{\mathrm{i}}{\hbar}[H,\rho(t)] \\ &\quad + \frac{8\pi^{3/2}\lambda_{\mathrm{C}} r_{\mathrm{C}}^3}{m_0^2}\int \mathrm{d}^3\mathbf{k}\mathrm{e}^{-\mathbf{k}^2 r_{\mathrm{C}}^2}|\tilde{\varrho}(\mathbf{k})|^2\left(\mathrm{e}^{\mathrm{i}\mathbf{k}\cdot\mathbf{R}}\rho\mathrm{e}^{-\mathrm{i}\mathbf{k}\cdot\mathbf{R}}-\rho\right), \end{aligned} \tag{D.6}$$

where $\tilde{\varrho}^*(\mathbf{k}) = \tilde{\varrho}(-\mathbf{k})$ was used.

(ii) *Continuous mass distribution.*—Treating the object as a continuous mass distribution is valid when the average interatomic spacing a is such that $a \lesssim \sqrt{2}r_{\mathrm{C}}$ as shown in Ref. [414]. This condition may be understood as the mass density operator of Eq. (D.2), which is localized at each particle site, now leads to an effectively continuous mass distribution $\langle\mathbf{r}|\, M(\mathbf{r})\,|\mathbf{r}\rangle$. Hence, one may treat $\varrho(\tilde{\mathbf{k}})$ as a continuous function

$$\tilde{\varrho}(\mathbf{k}) = \frac{1}{(2\pi)^{3/2}}\int \mathrm{d}^3\mathbf{q}\varrho(\mathbf{q})\mathrm{e}^{-\mathrm{i}\mathbf{k}\cdot\mathbf{q}} \tag{D.7}$$

when $a \lesssim \sqrt{2}r_{\mathrm{C}}$ is met.

(iii) *Small oscillations or superposition size.*—Finally, the oscillations of the rigid body are assumed to be confined along one dimension, say x, such that $\mathbf{k}\cdot\mathbf{R} = k_x x$. If the amplitude of these oscillations, or size of the quantum superposition, Δx obeys $\Delta x \ll r_{\mathrm{C}}$ then the exponentials in Eq. (D.4) may be expanded to second order in $k_x x$ to give

$$\dot{\rho}(t) = -\frac{\mathrm{i}}{\hbar}[H + H_{\mathrm{C}},\rho(t)] - D_{\mathrm{CSL}}[x,[x,\rho(t)]], \tag{D.8}$$

$$H_{\mathrm{C}}/\hbar = \frac{-8\pi^{3/2}\lambda_{\mathrm{C}} r_{\mathrm{C}}^3}{m_0^2}\int \mathrm{d}^3\mathbf{k}\mathrm{e}^{-\mathbf{k}^2 r_{\mathrm{C}}^2} k_x|\tilde{\varrho}(\mathbf{k})|^2\, x, \tag{D.9}$$

$$D_{\mathrm{CSL}} = \frac{4\pi^{3/2}\lambda_{\mathrm{C}} r_{\mathrm{C}}^3}{m_0^2}\int \mathrm{d}^3\mathbf{k}\mathrm{e}^{-\mathbf{k}^2 r_{\mathrm{C}}^2} k_x^2|\tilde{\varrho}(\mathbf{k})|^2. \tag{D.10}$$

The last term in Eq. (D.8) predicts momentum diffusion due to CSL. This may be investigated by studying the associated heating rate in non-interferometric experiments or by measuring the decay of quantum interference fringes in interferometric tests. In either case, to be able to test for CSL, one requires that the CSL momentum diffusion rate is greater than the thermal diffusion: $D_{\mathrm{CSL}}x_0^2 > D_{\mathrm{TH}}$. Note the zero point fluctuation is for dimensional consistency between the two rates[1].

A cuboid.—As and example, consider a specific case of a cuboid of total mass M and mass density

$$\varrho(\mathbf{q}) = \frac{M}{L_x L_y L_z}\begin{cases}1 & \text{for } |x|<L_x/2,\ |y|<L_y/2, \text{ and } |z|<L_z/2,\\ 0 & \text{otherwise}\end{cases} \tag{D.11}$$

[1] In Eq. (D.8) the position operator has dimensions, while in Eq. (3.4) the position operator is dimensionless.

Taking the Fourier transform of the mass density the gives

$$\tilde{\varrho}(\mathbf{k}) = \frac{M}{L_x L_y L_z}\left(\frac{2}{\pi}\right)^{3/2}\frac{\sin\left(k_x L_x/2\right)\sin\left(k_y L_y/2\right)\sin\left(k_z L_z/2\right)}{k_x k_y k_z}. \quad \text{(D.12)}$$

Inserting into Eq. (D.10) then gives

$$D_{\mathrm{CSL}} = \lambda_{\mathrm{C}} N_{\mathrm{TOT}}^2 g(L_y) g(L_z)\left(1-\mathrm{e}^{-L_x^2/4r_{\mathrm{C}}^2}\right)\frac{1}{L_x^2}, \quad \text{(D.13)}$$

$$g(z) = \frac{4r_{\mathrm{C}}^2}{z^2}\left[\mathrm{e}^{-z^2/4r_{\mathrm{C}}^2} - 1 + \frac{\sqrt{\pi}}{2}\frac{z}{r_{\mathrm{C}}}\,\mathrm{erf}\left(\frac{z}{2r_{\mathrm{C}}}\right)\right], \quad \text{(D.14)}$$

where the total number of nucleons is given by $N_{\mathrm{TOT}} = M/m_0$. Note that the results presented here agree with that of Ref. [414] and disagrees by a factor of 2 with the derivation in Ref. [413]. In Ref. [5], we modelled an aluminium mechanical resonator as a cuboid to study the effects of CSL collapse within the "displacemon" electromechanical device [14].

D.2 Diósi-Penrose collapse

In Ref. [157], Penrose proposed his interpretation of the measurement problem[2], namely that the incompatibility of quantum mechanics and general relativity leads to collapse of the wave function. A massive superposition of an object in two positions implies a superposition of two spacetimes, which is incompatible with the principle of general covariance in general relativity [415]. Penrose conjectures that this incompatibility of the two theories cause the superposition to become unstable and decay over some timescale t_{DP}. Importantly, this timescale scales inversely with the gravitational self energy E_{G} between the two mass distributions in each branch of the superposition, and hence more massive superpositions will decay faster. Furthermore, in Ref. [416] Howl, Penrose, and Fuentes detail how t_{DP} maybe be derived be applying the equivalence principle to the massive object in a quantum superposition. Here, by considering a freely falling massive superposition and applying the equivalence principle to analyze the problem in the freely falling reference frame, a non-trivial phase difference is derived between the two branches of the wavefunction. This non-trivial phase is not present when the problem is analyzed in the lab frame and so the equivalence principle is at odds with the quantum superposition principle. This non-trivial phase implies that the two branches of the superposition now begin to inhibit different Hilbert spaces and therefore cannot be in a quantum superposition [416].

Independently, Diósi derived a gravity-induced dynamical equation [158], which predicts the same collapse timescale t_{DP} and hence the theory is sometimes referred to as Diósi-Penrose collapse. However, Penrose's theory does not predict such an equation. Experiments that suggest Diósi-Penrose theory could be

[2] In short the measurement problem is "how and why do wavefunctions collapse?".

ruled out soon assume a dynamical equation as suggested by Diósi, and further assume the noise in Diósi's model is white up to x-ray frequencies [417] or rely on Diósi's model to observe heating rates [418, 419]. Even more challenging interferometric experiments—such as the Marshall–Simon–Penrose–Bouwmeester mirror-superposition proposal [95]—may be needed to unambiguously test Penrose's ideas.

D.2.1 Collapse time of an extended body

To summarize the results, the gravitational self energy between the two mass distributions in each branch of the superposition is given by

$$E_{\mathrm{G}} = \frac{1}{2} G \iint \frac{[\varrho(\mathbf{q}) - \varrho'(\mathbf{q})][\varrho(\mathbf{q}') - \varrho'(\mathbf{q}')]}{|\mathbf{q} - \mathbf{q}'|} \, d^3\mathbf{q} \, d^3\mathbf{q}', \tag{D.15}$$

where $\varrho(\mathbf{q})$ and $\varrho'(\mathbf{q})$ are the mass densities corresponding to each branch. Here, E_{G} is proportional to the integral of the non-trivial phase difference between the two branches of the quantum superposition and therefore quantifies the incompatibility of the equivalence principle with quantum superposition. As E_{G} is an energy quantity, one may associate some characteristic timescale of the gravity-induced collapse via the Heisenberg uncertainty principle

$$t_{\mathrm{DP}} = \frac{\hbar}{E_{\mathrm{G}}}. \tag{D.16}$$

As an example, one may consider a sphere of radius σ and mass m_a in a superposition of size $\Delta x > 2\sigma$. Eq. (D.15) therefore gives [420]

$$E_{\mathrm{G}}^{(1)} = G m_a^2 \left(\frac{6}{5\sigma} - \frac{1}{\Delta x} \right). \tag{D.17}$$

The atoms in an extended body may be modelled as a collection of many of these hard spheres. Therefore, if the interatomic spacing a is much greater than size of the superposition Δx, the major contribution to the total gravitational self energy E_{G} is the sum of the individual self energies of each nuclei[3]:

$$E_{\mathrm{G}} \approx \sum_i E_{\mathrm{G}}^{(1)}(\Delta x_i). \tag{D.18}$$

Here, x_i refers to the position coordinate of each atom. Treating the extended body as a rigid body, as in the previous section, implies that $\Delta x_i \approx \Delta x$, where x is now the centre of mass coordinate. Here, the differences in the relative coordinate between the two mass densities of each branch are ignored. For the case of a doubly clamped vibrating nanobeam [5], this is valid is the length of the beam is much greater than its width. Hence, the gravitational self energy

[3] As in the previous section, the contribution from the electrons is neglected.

$E_{\rm G}$ of an extended body may be approximated as[4]

$$E_{\rm G} = GMm_a^2 \left(\frac{6}{5\sigma} - \frac{1}{\Delta x} \right), \tag{D.19}$$

where M is the total mass and $m_{\rm a}$ is the nuclear mass.

Note that Eq. (D.19) is independent of the shape of the total object, but rather just depends on the total number of nuclei M/m_a. This is in contrast to the results in the previous section for the CSL rate of an extended body. The relevant length scale for the CSL model is the localization length scale $r_{\rm C}$, which is typically assumed to be much larger than the relevant length scale in Diósi-Penrose theory σ. In this section, the *gravitational radius* σ is assumed to be the nuclear radius, however in Ref. [5] we also consider alternative candidates for σ, including the zero-point amplitude of the extended body.

[4] Ref. [5] uses the root-mean-square displacement to quantify the size of the superposition, hence there are several factors of 2 difference with the results presented here.

Appendix E

An adiabatic cavity

E.1 Relation between the input and cavity amplitudes in linear optomechanics

In linearized optomechanics and for a large optical drive $|\alpha_{\rm in}| \gg 1$, the Heisenberg-Langevin equation for the intracavity field (see Eq. (6.14) or Eq. (6.80)) can be split up into a part describing the large intracavity field α_c and a part describing quantum fluctuations. In this regime, the large intracavity mean field amplitude obeys

$$\dot{\alpha_c} = +\mathrm{i}\sqrt{2}g_0\alpha_c X_{\rm M} - \kappa\alpha_c + \sqrt{2\kappa}\alpha_{\rm in} \tag{E.1}$$

Then for small optical rotations $\mu^2\sigma^2 \sim 2g_0^2\left\langle X_{\rm M}^2\right\rangle/\kappa^2 \ll 1$ the equation for this large amplitude is well approximated by

$$\dot{\alpha_{\rm c}} = -\kappa\alpha_{\rm c} + \sqrt{2\kappa}\alpha_{\rm in} \tag{E.2}$$

with steady state (adiabatic) solution $\kappa|\alpha_{\rm c}|^2 = 2|\alpha_{\rm in}|^2$.

E.2 The linearized measurement rate

With $k = |\alpha_{\rm in}|^2/2$, the previous section implies $k = \dfrac{\kappa|\alpha_{\rm c}|^2}{4}$. Using $\mu = \sqrt{8}g_0/\kappa$ and $g = |\alpha_{\rm c}|g_0$, one arrives at an expression for $k_{\rm L}$ which is *only* true in the linearized regime of optomechanics

$$k_{\rm L} = \mu^2 k = \frac{2g^2}{\kappa}. \tag{E.3}$$

Note that some authors include an additional factor of 2 in their definition of $k_{\rm L}$ by defining κ as an intensity quantity and if one also includes optical loss in the definition, this rate becomes $k_{\rm L} = 2\eta g^2/\kappa$.

E.3 Adiabatic elimination outside the unresolved sideband regime

In the linearized regime of optomechanics, the evolution of the cavity field over the time interval $t - \tau \to t$ is given by

$$a(t) = a(t-\tau)\mathrm{e}^{-(\kappa - \mathrm{i}\Delta)\tau} + \int_{t-\tau}^{t} \mathrm{d}t' \left[\sqrt{2\kappa}a_{\mathrm{in}}(t') + \mathrm{i}\sqrt{2}g\tilde{X}_{\mathrm{M}}(t')\right] \mathrm{e}^{-[\kappa - \mathrm{i}\Delta](t-t')}. \tag{E.4}$$

Here, we are working in the same rotating frame as Section 11.1.2 and Eq. (E.4) may be inferred from Eq.(11.39) by making the linearized approximation and identifying $g = g_0\alpha_{\mathrm{c}}$. As in Section 11.1.2, the first term on the right-hand side is approximately zero if $\kappa\tau \gg 1$. Also, the $a_{\mathrm{in}}(t')$ term may be pulled out of the integral and evaluated at $t' = t$ if $\tau_{\mathrm{in}} \gg \kappa^{-1}$. However, in the resolved sideband regime of optomechanics $\omega_{\mathrm{M}} \gg \kappa$, $\tilde{X}_{\mathrm{M}}(t')$ varies too quickly to be pulled out of the integral, which precludes the adiabatic approximation.

Nevertheless, to achieve adiabatic elimination of the cavity mode $\dot{a} \approx 0$ in the resolved sideband regime, one may demand that

$$|\sqrt{2\kappa}\,\langle a_{\mathrm{in}}(t')\rangle\,| \gg |\mathrm{i}\sqrt{2}g\left\langle \tilde{X}_{\mathrm{M}}(t')\right\rangle| \tag{E.5}$$

is satisfied within the integrand of Eq. (E.4), which, by using $\kappa|\alpha_{\mathrm{c}}|^2 = 2|\alpha_{\mathrm{in}}|^2$, implies $\mu\sigma \ll 1$. Thus, the cavity mode may be adiabatically eliminated in the resolved sideband regime within the linearized approximation.

Appendix F

Details on growing mechanical cats

F.1 δ of the Schrödinger cat state

The negativity in $W_{\rm SCS}$ is due to the oscillating cosine term in Eq. (7.11). For well-separated Schrödinger cat states where $N\mu \gg 1$, such that the overlap of the interference term with the population terms can be ignored, to calculate the value of $\delta_{\rm SCS}$ it is sufficient to consider only this term. From Eq. (7.11) it is clear that any overlap of the interference term with the population terms will lead to a reduction in $\delta_{\rm SCS}$. The quantity

$$E = -2\frac{\mathcal{N}_{\rm SCS}}{(1+2\bar{n})\pi}\int_{-\infty}^{+\infty}\int_{-\infty}^{+\infty}{\rm d}X_{\rm M}{\rm d}P_{\rm M}\cos(N\mu X_{\rm M})\exp\Big(\frac{-X_{\rm M}^2-(P_{\rm M}-N\mu/2)^2}{1+2\bar{n}}\Big) \tag{F.1}$$

gives total volume introduced by the interference term. Note that $E<0$ because the minimum of the interference term occurs at $X_{\rm M}=0$, $P_{\rm M}=N\mu/2$ and away from this point the Wigner function is modulated by a decaying Gaussian envelope. E may be decomposed as $E=\delta^{+}-\delta_{\rm SCS}$. Here, δ^{+} is the total positive volume and $\delta_{\rm SCS}$ is the non-classicality measure of interest in the limit $N\mu\gg 1$. One may also consider the quantity J

$$J = 2\frac{\mathcal{N}_{\rm SCS}}{(1+2\bar{n})\pi}\int_{-\infty}^{+\infty}\int_{-\infty}^{+\infty}{\rm d}X_{\rm M}{\rm d}P_{\rm M}|\cos(N\mu X_{\rm M})|\exp\Big(\frac{-X_{\rm M}^2-(P_{\rm M}-N\mu/2)^2}{1+2\bar{n}}\Big), \tag{F.2}$$

which may be rewritten as $I=\delta^{+}+\delta_{\rm SCS}$. This therefore leads to the expression $\delta_{\rm SCS}=\frac{1}{2}(J-E)$. E is readily calculated using basic Gaussian integration, and hence one obtains $E=-\exp\big[-N^2\mu^2(1+2\bar{n})/4\big]/\{1-\exp\big[-N^2\mu^2(1+2\bar{n})/4\big]\}$. However, the absolute sign in Eq. (F.2) makes the evaluation of J more involved.

Introducing the change of variable $\lambda=1/[N^2\mu^2(1+2\bar{n})]$ and $x=N\mu X_{\rm M}$

allows one to write

$$J = \frac{2\mathcal{N}_{\mathrm{SCS}}}{N\mu\sqrt{(1+2\bar{n})\pi}} I, \tag{F.3}$$

with

$$\begin{aligned} I &= \int_{-\infty}^{+\infty} \mathrm{e}^{-\lambda x^2} |\cos(x)| \mathrm{d}x \\ &= \sum_{n=-\infty}^{\infty} \int_{-n\pi}^{(n+1)\pi} \mathrm{e}^{-\lambda x^2} |\cos(x)| \mathrm{d}x. \end{aligned} \tag{F.4}$$

By introducing the change of variables $t = x - n\pi$, I becomes

$$\begin{aligned} I &= \textstyle\sum_{n=-\infty}^{\infty} \int_0^{\pi} \mathrm{e}^{-\lambda(t+n\pi)^2} |\cos(t)| \mathrm{d}t \\ &= \textstyle\sum_{n=-\infty}^{\infty} \left[\int_0^{\pi/2} \mathrm{e}^{-\lambda(t+n\pi)^2} \cos(t) \mathrm{d}t - \int_{\pi/2}^{\pi} \mathrm{e}^{-\lambda(t+n\pi)^2} \cos(t) \mathrm{d}t \right]. \end{aligned}$$

Then in the second integral of Eq. (F.5) I let $t \to t - \pi$, which allows I to be written as

$$I = \sum_{n=-\infty}^{\infty} \int_0^{\pi/2} \left(\mathrm{e}^{-\lambda(t+n\pi)^2} + \mathrm{e}^{-\lambda((n+1)\pi - t)^2} \right) \cos(t) \mathrm{d}t. \tag{F.5}$$

The Poisson summation formula which relates the infinite sum over inverse Fourier components,

$$\sum_{n=-\infty}^{n=\infty} a(n) = \sum_{k=-\infty}^{k=\infty} \tilde{a}(k), \tag{F.6}$$

may be used by assigning

$$a(n) = \int_0^{\pi/2} \left(\mathrm{e}^{-\lambda(t+n\pi)^2} + \mathrm{e}^{-\lambda((n+1)\pi - t)^2} \right) \cos(t) \mathrm{d}t. \tag{F.7}$$

$\tilde{a}(k)$ is then calculated by Fourier transform,

$$\begin{aligned} \tilde{a}(k) &= \textstyle\int_{-\infty}^{+\infty} \mathrm{e}^{-2\pi \mathrm{i} k s} a(s) \mathrm{d}s \\ &= \textstyle\int_0^{\pi/2} \int_{-\infty}^{+\infty} \mathrm{e}^{-2\pi \mathrm{i} k s} \left(\mathrm{e}^{-\lambda(t+n\pi)^2} + \mathrm{e}^{-\lambda((n+1)\pi - t)^2} \right) \cos(t) \mathrm{d}t \mathrm{d}s \\ &= \textstyle\frac{2}{\sqrt{\lambda\pi}} \mathrm{e}^{-k^2/\lambda} \frac{(-1)^k}{1+(-1)^k 2k}. \end{aligned} \tag{F.8}$$

By putting Eqs (F.5)–(F.8) together, the value of I is found to be

$$I = \sum_{k=-\infty}^{k=\infty} \frac{2}{\sqrt{\lambda\pi}} \mathrm{e}^{-k^2/\lambda} \frac{(-1)^k}{1+(-1)^k 2k}. \tag{F.9}$$

The total negative volume of the Wigner function $\delta_{\rm SCS}$ in the limit $N\mu \gg 1$ is then given by

$$\delta_{\rm SCS} = \frac{1}{2}\Big\{\frac{4\mathcal{N}_{\rm SCS}}{\pi}\sum_{k=-\infty}^{k=\infty} \mathrm{e}^{-k^2N^2\mu^2(1+2\bar{n})}\frac{(-1)^k}{1+(-1)^k 2k} + \frac{\mathrm{e}^{-N^2\mu^2(1+2\bar{n})/4}}{[1-\mathrm{e}^{-N^2\mu^2(1+2\bar{n})/4}]}\Big\}. \tag{F.10}$$

As $N\mu \to \infty$, Eq. (F.10) tends to $1/\pi$ even in the case that the mechanical mode has a non-zero initial thermal occupation. Hence, by dropping the requirement that $N\mu \gg 1$, one arrives at the result $0 \leq \delta_{\rm SCS} < 1/\pi$ valid for all finite N, μ and $\bar{n}$. Numerical results show that the introduction of thermal decoherence at each step in the protocol leads to a depletion in δ that cannot be compensated for by an increase in cat state separation.

F.2 Arbitrary input pulse

An arbitrary input pulse $|\psi\rangle$ with temporal envelope $f(t)$ is defined as

$$|\psi\rangle = \int \mathrm{d}t f(t)\,|\psi\rangle_t\,, \tag{F.11}$$

i.e. the state has a probability to be located at some specific time within the optical pulse. Here, one has

$$|\psi\rangle = \sum_n c_n\,|n\rangle\,, \tag{F.12}$$

$$|\psi\rangle_t = \sum_n c_n\,|n\rangle_t\,, \tag{F.13}$$

$$1 = \sum_n |c_n|^2, \tag{F.14}$$

where $|n\rangle_t$ are the temporal number states from Section 7.6.2, which satisfy ${}_t\langle n|m\rangle_{t'} = \delta_{n,m}\delta(t-t')$.

The correlation function $\left\langle a_{\rm in}^\dagger(t')a_{\rm in}(t'')\right\rangle$ with respect to the state $|\psi\rangle$ is then

$$\left\langle a_{\rm in}^\dagger(t')a_{\rm in}(t'')\right\rangle = \int \mathrm{d}t_1 \int \mathrm{d}t_2 f^*(t_1)f(t_2)\ {}_{t_1}\langle\psi|\,a_{\rm in}^\dagger(t')a_{\rm in}(t'')\,|\psi\rangle_{t_2}\,. \tag{F.15}$$

I first focus on the matrix element:

$$\begin{aligned} {}_{t_1}\langle\psi|\,a_{\rm in}^\dagger(t')a_{\rm in}(t'')\,|\psi\rangle_{t_2} &= \sum_n\sum_m c_n^*c_m\ {}_{t_1}\langle n|\,a_{\rm in}^\dagger(t')a_{\rm in}(t'')\,|m\rangle_{t_2} \\ &= \sum_n\sum_m c_n^*c_m\sqrt{nm}\delta_{n,m}\delta(t_1-t')\delta(t_2-t''). \end{aligned}$$

Therefore, one has

$$\begin{aligned} \left\langle a_{\rm in}^\dagger(t')a_{\rm in}(t'')\right\rangle &= f^*(t')f(t'')\sum_n n|c_n|^2 \\ &= f^*(t')f(t'')\,\langle n_{\rm L}\rangle \end{aligned} \tag{F.16}$$

and so the result

$$\mu = \sqrt{8} g_0 \kappa \int_{-\infty}^{+\infty} \mathrm{d}t \mathrm{e}^{-2\kappa t} \int_{-\infty}^{t} \mathrm{d}t' \int_{-\infty}^{t} \mathrm{d}t'' \mathrm{e}^{\kappa t'} \mathrm{e}^{\kappa t''} f^*(t') f(t''), \tag{F.17}$$

from Section 7.6.2 is valid for any optical input pulse.

Appendix G

Details on generating and verifying mechanical entanglement

G.1 Verification procedure and inverse maps

G.1.1 Outline of the verification procedure

The covariance matrix $\sigma(t)$ of the entangled state after a time t since entanglement generation is given by

$$\sigma(t) = G^{1/2}\sigma(0)G^{1/2} + (\mathbb{1} - G)\sigma_{\text{ENV}}, \tag{G.1}$$

and the reconstructed covariance matrix σ_{VER} is defined so that in the absence of loss $\sigma_{\text{VER}} = \sigma(0)$. Here, I work in a rotating frame at the mechanical frequency only for computational convenience—and hence I don't consider free mechanical evolution in $\sigma(t)$. I now give two examples of elements defined for σ_{VER} in the optical-mechanical entanglement scheme. The elements of σ_{VER} in the mechanical entanglement protocols are defined in precisely the same way.

$B_{\text{VER},12}$ and $C_{\text{VER},11}$ in the optical-mechanical entanglement scheme— From Eq. (8.21), one has that

$$B_{\text{VER},12} = \frac{1}{2\chi^2}\left[\text{Var}(P_{\text{V}}(\frac{\pi}{4})) - \text{Var}(P_{\text{V}}(\frac{3\pi}{4}))\right], \tag{G.2}$$

and by using $P_{\text{V}}(\theta) = P_{\text{IN}} + \chi X_{\text{M}}(\theta)$ one finds that, in the absence of decoherence,

$$\begin{aligned} B_{\text{VER},12} &= \frac{1}{2\chi^2}[\text{Var}(P_{\text{IN}} + \frac{\chi}{\sqrt{2}}(X_{\text{M}} + P_{\text{M}})) - \text{Var}(P_{\text{IN}} + \frac{\chi}{\sqrt{2}}(X_{\text{M}} - P_{\text{M}}))] \\ &= \frac{1}{2}\langle\{X_{\text{M}}, P_{\text{M}}\}\rangle - \langle X_{\text{M}}\rangle\langle P_{\text{M}}\rangle \\ &= B_{12}(0). \end{aligned} \tag{G.3}$$

Similarly, from Eq. (8.22) one has that

$$C_{\mathrm{VER},11} = \frac{1}{2\chi}\left[\mathrm{Var}(P_{\mathrm{V}}''(2\pi)) - \mathrm{Var}(X_{\mathrm{L}}''(2\pi))\right]. \tag{G.4}$$

$P_{\mathrm{V}}''(\theta)$ and $X_{\mathrm{L}}''(\theta)$ are given by $P_{\mathrm{V}}''(\theta) = \frac{1}{\sqrt{2}}(P_{\mathrm{V}}(\theta) + X_{\mathrm{L}})$ and $X_{\mathrm{L}}''(\theta) = \frac{1}{\sqrt{2}}(X_{\mathrm{L}} - P_{\mathrm{V}}(\theta))$, respectively. Therefore, one has that

$$\begin{aligned} C_{\mathrm{VER},11} &= \frac{1}{4\chi}\left[\mathrm{Var}(P_{\mathrm{V}}(2\pi) + X_{\mathrm{L}}) - \mathrm{Var}(X_{\mathrm{L}} - P_{\mathrm{V}}(2\pi))\right] \\ &= \frac{1}{2}\left\langle\{X_{\mathrm{L}}, X_{\mathrm{M}}\}\right\rangle - \left\langle X_{\mathrm{L}}\right\rangle\left\langle X_{\mathrm{M}}\right\rangle \\ &= C_{11}(0). \end{aligned} \tag{G.5}$$

However, the reconstruction process will be imperfect due to decoherence processes and as such $\sigma_{\mathrm{VER}} \neq \sigma(0)$. A *conservative in time* approach is therefore taken to ensure that entanglement is not overestimated and a *conservative in time and noise* approach is also taken when $\mathrm{Var}(P_{\mathrm{IN}})$ is unknown and cannot be subtracted.

To describe the effect of decoherence in the reconstruction process and address the fact that all the matrix elements of σ_{VER} are accessed at different times, I use the elements of $\sigma(t)$ to calculate those of σ_{VER}. Describing the elements of σ_{VER} using those of $\sigma(t)$ is slightly more complicated when the elements of σ_{VER} depend on two different mechanical phase-space angles θ—and therefore two different times $t = \theta/\omega_{\mathrm{M}}$, as illustrated in the calculation of $B_{\mathrm{VER},12}$ below.

$B_{\mathrm{VER},22}$, an element that depends on one time— The $B_{\mathrm{VER},22}$ element is given by

$$\begin{aligned} B_{\mathrm{VER},22} &= \frac{1}{\chi^2}\left[\mathrm{Var}(P_{\mathrm{V}}(\frac{\pi}{2})) - \mathrm{Var}(P_{\mathrm{IN}})\right] \\ &= \begin{cases} B_{22}(\frac{\pi}{2}) & \text{conservative in time} \\ B_{22}(\frac{\pi}{2}) + \frac{1}{2\chi^2} & \text{conservative in time and noise.} \end{cases} \end{aligned} \tag{G.6}$$

The conservative in time and noise approach corresponds to not subtracting $\mathrm{Var}(P_{\mathrm{IN}})$ and here I assume that vacuum noise contaminates $B_{\mathrm{VER},22}$.

$B_{\mathrm{VER},12}$, an element that depends on two times— As above

$$\begin{aligned} B_{\mathrm{VER},12} &= \frac{1}{2\chi^2}\left[\mathrm{Var}(P_{\mathrm{V}}(\frac{\pi}{4})) - \mathrm{Var}(P_{\mathrm{V}}(\frac{3\pi}{4}))\right] \\ &= \frac{1}{4}\left[B_{11}(\frac{\pi}{4}) - B_{11}(\frac{3\pi}{4}) + B_{22}(\frac{\pi}{4}) - B_{22}(\frac{3\pi}{4}) + 2B_{12}(\frac{\pi}{4}) + 2B_{12}(\frac{3\pi}{4})\right]. \end{aligned} \tag{G.7}$$

In the absence of decoherence, $\sigma(0) \equiv \sigma(t)$ and so $B_{\mathrm{VER},12} = B_{12}(0)$.

G.1.2 Including optical loss in $\sigma_{\mathbf{ver}}$

If optical losses are included in the verification stage, the formulas for σ_{VER} are modified. To derive these new forms for σ_{VER}, one assumes that the variance

of each loss mode is equal to that of P_{IN} and at each loss channel an optical quadrature Q transforms according to

$$Q \to \sqrt{\eta}Q + \sqrt{1-\eta}Q_{\text{VAC}}, \tag{G.8}$$

where Q_{VAC} is the environmental quadrature for a given channel and $\text{Var}(Q_{\text{VAC}}) = \text{Var}(P_{\text{IN}})$. Below I present how the formulas for σ_{VER} are modified in each entanglement scheme.

Optical-mechanical entanglement scheme.— By including optical losses in the verification stage, the A_{VER} block is modified as follows:

$$A_{\text{VER}} \to \frac{1}{\eta}\begin{pmatrix} \text{Var}(X_{\text{L}}) - (1-\eta)\text{Var}(P_{\text{IN}}) & \frac{1}{2}[\text{Var}(P_{\text{L}}(\frac{3\pi}{4})) - \text{Var}(P_{\text{L}}(\frac{\pi}{4}))] \\ \frac{1}{2}[\text{Var}(P_{\text{L}}(\frac{3\pi}{4})) - \text{Var}(P_{\text{L}}(\frac{\pi}{4}))] & \text{Var}(P_{\text{L}}) - (1-\eta)\text{Var}(P_{\text{IN}}) \end{pmatrix}.$$

The B_{VER} and C_{VER} blocks rescale according to $B_{\text{VER}} \to B_{\text{VER}}/\eta$, and $C_{\text{VER}} \to C_{\text{VER}}/\eta$.

Interferometric mechanical entanglement scheme.— In this scheme, all the elements of the reconstructed covariance matrix rescale in the same way $\sigma_{\text{VER}} \to \sigma_{\text{VER}}/\eta$.

Non-interferometric mechanical entanglement scheme.— Here, the A_{VER} and B_{VER} blocks are modified in the same way $A_{\text{VER}} \to A_{\text{VER}}/\eta$ and $B_{\text{VER}} \to B_{\text{VER}}/\eta$. While C_{VER} is modified to $C_{\text{VER}} \to C_{\text{VER}}/\eta^2$.

Assuming that η is a well-known quantity, none of the results in the reconstruction stage are affected.

G.2 Single mode Gaussian state of fixed purity in a phase-insensitive decoherence channel

Consider the covariance matrix

$$\sigma = \begin{pmatrix} a\text{e}^{2r} & 0 \\ 0 & b\text{e}^{-2r} \end{pmatrix}, \tag{G.9}$$

which characterizes a general single mode Gaussian state of fixed purity $\mu(\sigma) = 1/\sqrt{4\text{Det}\sigma} = 1/\sqrt{4ab}$ up to a local rotation. After the state passes through a phase-insensitive decoherence channel $\mathcal{E}_{\text{G}}$, with $G = \eta\mathbb{1}_2$ and σ_{env} corresponding to a thermal state with occupation $\bar{N}$, the covariance matrix is given by

$$\sigma' = \eta\begin{pmatrix} a\text{e}^{2r} + \delta & 0 \\ 0 & b\text{e}^{-2r} + \delta \end{pmatrix}. \tag{G.10}$$

Here, $\delta = \frac{(1-\eta)(1+2\bar{N})}{2\eta} > 0$. Maximizing $\mu(\sigma')$ with respect to r gives $\text{e}^{2r} = \sqrt{b/a}$ and hence the input state σ which maximizes the output purity from the channel is $\sigma = \sqrt{ab}\mathbb{1}_2$.

Likewise, the von-Neumann entropy of the output state [50] is given by

$$s_{\text{V}}(\sigma') = (\nu + \frac{1}{2})\log_2\left(\nu + \frac{1}{2}\right) - (\nu - \frac{1}{2})\log_2\left(\nu - \frac{1}{2}\right) \tag{G.11}$$

where ν is the symplectic eigenvalue of σ'—given by

$$\nu = \eta\sqrt{(a\mathrm{e}^{2r}+\delta)(b\mathrm{e}^{-2r}+\delta)}. \tag{G.12}$$

The output entropy is minimized with $\mathrm{e}^{2r} = \sqrt{b/a}$, which again leads to a symmetric input state.

G.3 Avoiding non-monotonic behaviour

As mentioned in Section 8.3, when the squeezing operation can be applied before the optical decoherence channel at the cavity output, the non-monotonic behaviour in logarithmic negativity in the optical-mechanical and interferometric entanglement schemes is avoided. This is because the entangled state is protected from loss of information to the environment before it enters the decoherence channels. In this case, as the optical loss channels are now consecutive, and occur after the optical squeezing operations, they may be combined into a single loss channel with efficiency $\eta = \eta_{\mathrm{CAV}}\eta_{\mathrm{DET}}$. Below, I present a brief study of how optical squeezers are used in the optical-mechanical entanglement scheme to avoid non-monotonic behaviour in this case.

The PPT entanglement criterion reads

$$\tilde{\nu}_- = \begin{cases} \geq \frac{1}{2} & \text{separable} \\ < \frac{1}{2} & \text{entangled,} \end{cases} \tag{G.13}$$

and can be rewritten as

$$\Lambda = \begin{cases} \geq 0 & \text{separable} \\ < 0 & \text{entangled} \end{cases}. \tag{G.14}$$

Here,

$$\Lambda = 4\mathrm{Det}\sigma - \tilde{\Delta} + \frac{1}{4} \tag{G.15}$$

and σ refers to the optomechanical state formed by Eq. (8.23) when the order of the U_{SQ} and $\mathcal{E}_{\eta_{\mathrm{CAV}}}$ operations is swapped. One may expand Λ in the parameter χ to study the PPT criterion in the limit $\chi \to \infty$. For brevity, this expansion is not reported here, but I find that, with an ansatz for the optical squeezing parameter of the form $r = \ln\left(1 + c\chi^2\right)$, it is possible to ensure that $\lim_{\chi\to\infty}\Lambda < 0$ if $V_{\mathrm{P}} < f(c, \bar{N}, \eta, \mathrm{e}^{\gamma t})$. Here, f is a function of the system parameters and represents the minimal cooling requirement to observe entanglement in the large χ limit—hence avoiding non-monotonic behaviour. Maximising the upper bound over all c gives the cooling requirement for entanglement to persist as $\chi \to \infty$

$$V_{\mathrm{P}} < \frac{2\left[f_1(\eta, \mathrm{e}^{\gamma t}, \bar{N}) + f_2(\eta, \mathrm{e}^{\gamma t}, \bar{N})\right]}{\mathrm{e}^{-\gamma t}(1+2\bar{N})(f_3(\eta, \mathrm{e}^{\gamma t}, \bar{N}))}, \tag{G.16}$$

$$
\begin{aligned}
f_1(\eta, \mathrm{e}^{\gamma t}, \bar{N}) &= \bar{N}(1+\bar{N})[\mathrm{e}^{-4\gamma t} - (3-\eta)\mathrm{e}^{-3\gamma t} + 3(1-\eta)\mathrm{e}^{-2\gamma t} + (3\eta - 1)\mathrm{e}^{-\gamma t} - \eta], \\
f_2(\eta, \mathrm{e}^{\gamma t}, \bar{N}) &= -\mathrm{e}^{-3\gamma t} + (1-\eta)\mathrm{e}^{-2\gamma t} + \mathrm{e}^{-\gamma t}\eta, \\
f_3(\eta, \mathrm{e}^{\gamma t}, \bar{N}) &= \mathrm{e}^{-3\gamma t} - (2-\eta)\mathrm{e}^{-2\gamma t} + (1-2\eta)\mathrm{e}^{-\gamma t} + \eta.
\end{aligned}
$$

The c which maxmizes f is given by

$$
c = (1+2\bar{N})\frac{1-\mathrm{e}^{-\gamma t}}{1+\mathrm{e}^{-\gamma t}}. \tag{G.17}
$$

For a genuine mechanical covariance matrix one also requires $V_{\mathrm{P}} > 0$. When decoherence processes dominate, f becomes negative and it is no longer possible to avoid separability in the large χ limit. Note that this cooling condition does not depend on the position variance of the mechanical precooled state V_{X}. This is because the optomechanical unitary generates phase-space displacements in an orthogonal direction to the position quadrature.

G.4 Kraus operator approach

In this appendix, I derive the Kraus operators that describe the entanglement protocols of Sections 8.3 and 8.4. This Kraus operator representation allows one to further understand the dependence of logarithmic negativity on homodyne measurement angles, and the balance between unitary and positive operations in the generation of entanglement.

As this approach will be completely equivalent to the symplectic formalism outlined previously, and so as not to obscure the key elements of this discussion, I neglect the effects of optical loss and mechanical decoherence. However, if one wishes, these deleterious effects may be included: each optical or mechanical loss channel introduces another Hilbert space one would need to consider when calculating the Kraus operator, and hence introduces an index to the Kraus operator indicating the number of photons or phonons which leak to the environment. A sum over all possible photon and phonon numbers detected by the environment would then be performed to describe the lossy Kraus operation. In what follows I take the amplitude of the coherent pulse to be real without loss of generality, $\alpha = X_\alpha/\sqrt{2} \in \mathbb{R}$.

G.4.1 Optical-mechanical and the precooling stage

The Kraus operator corresponding to the optical-mechanical entanglement protocol is given simply by

$$
\Upsilon(X_{\mathrm{L}}, X_{\mathrm{M}}) = U_{\mathrm{SQ}}(r)\mathrm{e}^{\mathrm{i}\chi X_{\mathrm{L}} X_{\mathrm{M}}}. \tag{G.18}
$$

The two mode unitary $\mathrm{e}^{\mathrm{i}\chi X_{\mathrm{L}} X_{\mathrm{M}}}$ entangles the optical and mechanical states, while the optical squeezer protects the state from optical loss and mechanical decoherence.

$\Upsilon(X_{\rm L}, X_{\rm M})$ is completely unitary, which reflects the continuous behaviour of the entanglement montone with respect to the system parameters, such as interaction strength χ and optical efficiency η.

The Kraus operator $\Upsilon(X_{\rm M}, \varphi)$ describing the precooling stage results from a single optomechanical interaction, where the input light is in the state $|\alpha\rangle$, followed by optical squeezing and homodyne detection at angle φ. Hence,

$$\begin{aligned}\Upsilon(X_{\rm M}, \varphi) &= \langle X_{\rm L}(\varphi)|\, U_{\rm SQ}(r) \mathrm{e}^{\mathrm{i}\chi X_{\rm L} X_{\rm M}}\, |\alpha\rangle \\ &= \mathrm{e}^{\mathrm{i}\chi X_\alpha X_{\rm M}/2}\, \langle X_{\rm L}(\varphi)|\, U_{\rm SQ}(r) \left|(X_\alpha + \mathrm{i}\chi X_{\rm M})/\sqrt{2}\right\rangle . \end{aligned} \tag{G.19}$$

Therefore,

$$\begin{aligned}\Upsilon(X_{\rm M}, \varphi) &= (\Gamma_{\rm R}/\pi)^{1/4} \exp\{-\Gamma(X_{\rm L}(\varphi) - X_0)^2/2\} \\ &\exp\{\mathrm{i}P_0 X_{\rm L}(\varphi)\} \exp\{-\mathrm{i}X_0 P_0/2\} \exp\{\mathrm{i}\chi X_\alpha X_{\rm M}/2\}. \end{aligned} \tag{G.20}$$

Here,

$$X_0 = \mathrm{e}^r X_\alpha \cos\varphi + \mathrm{e}^{-r}\chi X_{\rm M} \sin\varphi, \tag{G.21}$$

$$P_0 = \mathrm{e}^{-r}\chi X_{\rm M} \cos\varphi - \mathrm{e}^r X_\alpha \sin\varphi, \tag{G.22}$$

$$\Gamma(\varphi) = \Gamma_{\rm R}(\varphi) + \mathrm{i}\Gamma_{\rm I}(\varphi), \tag{G.23}$$

$$\Gamma_{\rm R}(\varphi) = \frac{1}{\cosh 2r + \cos 2\varphi \sinh 2r}, \tag{G.24}$$

$$\Gamma_{\rm I}(\varphi) = \frac{2\sin 2\varphi \sinh 2r}{\cosh 2r + \cos 2\varphi \sinh 2r}. \tag{G.25}$$

The optimal homodyne angle to precool the mechanical mode via measurement is $\varphi = \pi/2$. This is because the mechanical position quadrature is imprinted on the optical phase quadrature of light. In this case the Kraus operator is

$$\Upsilon(X_{\rm M}, \pi/2) = (\mathrm{e}^{2r}/\pi)^{1/4} \exp\{-\mathrm{e}^{2r}(P_{\rm L} - \mathrm{e}^{-r}\chi X_{\rm M})^2/2 - \mathrm{i}\mathrm{e}^r X_\alpha P_{\rm L}\}. \tag{G.26}$$

The action of the Kraus operator on the mechanical mode is written as $\Upsilon \circ \rho$. Applying the Kraus operator m times produces the state $\Upsilon^m \circ \rho$, where

$$\begin{aligned}[\Upsilon(X_{\rm M}, \varphi)]^m &= (\Gamma_{\rm R}/\pi)^{m/4} \exp\{-\Gamma(\sqrt{m}X_{\rm L}(\varphi) - \sqrt{m}X_0)^2/2\} \\ &\exp\{\mathrm{i}mP_0 X_{\rm L}(\varphi)\} \exp\{-\mathrm{i}mX_0 P_0/2\} \exp\{\mathrm{i}m\chi X_\alpha X_{\rm M}/2\}. \end{aligned} \tag{G.27}$$

This operation is equivalent to a single application of the Kraus operator but with rescalings $\chi \to \sqrt{m}\chi$, $\alpha \to \sqrt{m}\alpha$, and $X_{\rm L}(\varphi) \to \sqrt{m}X_{\rm L}(\varphi)$. Hence, increasing the number of pulsed optomechanical interactions by a factor m is equivalent to a single pulsed interaction with m-times more photons.

G.4.2 Interferometric mechanical entanglement

The Kraus operator which acts on the initially separable state of the two mechanical oscillators, corresponding to Eq. (8.24), is

$$\Upsilon(X_{\mathrm{M1}}, X_{\mathrm{M2}}, \varphi, \psi) = \langle X_{\mathrm{L1}}(\varphi)| \langle X_{\mathrm{L2}}(\psi)| U_{\mathrm{BS}} U_{\mathrm{SQ}}^{\otimes 2} \mathrm{e}^{\mathrm{i}\chi X_{\mathrm{L2}} X_{\mathrm{M2}}} \mathrm{e}^{\mathrm{i}\chi X_{\mathrm{L1}} X_{\mathrm{M1}}} U_{\mathrm{BS}} \left|\sqrt{2}\alpha\right\rangle |0\rangle \tag{G.28}$$

Up to irrelevant phase terms, the Kraus operator is therefore given by

$$\begin{aligned}\Upsilon(X_{\mathrm{M1}}, X_{\mathrm{M2}}, \varphi, \psi) = (\Gamma_{\mathrm{R}}(\varphi)\Gamma_{\mathrm{R}}(\psi)/\pi^2)^{1/4} \exp\{-\Gamma(\varphi)(X_{\mathrm{L1}}(\varphi) - X_1)^2/2\} \exp\{\mathrm{i}P_1 X_{\mathrm{L1}}(\varphi)\} \\ \exp\{-\mathrm{i}X_1 P_1/2\} \exp\{-\Gamma(\psi)(X_{\mathrm{L2}}(\psi) - X_2)^2/2\} \exp\{\mathrm{i}P_2 X_{\mathrm{L2}}(\psi)\} \exp\{-\mathrm{i}X_2 P_2/2\},\end{aligned} \tag{G.29}$$

where Γ is defined as above, while

$$X_1 = \mathrm{e}^{-r}\chi(X_{\mathrm{M1}} + X_{\mathrm{M2}}) \sin\varphi/\sqrt{2}, \tag{G.30}$$

$$P_1 = \mathrm{e}^{-r}\chi(X_{\mathrm{M1}} + X_{\mathrm{M2}}) \cos\varphi/\sqrt{2}, \tag{G.31}$$

$$X_2 = -\sqrt{2}\mathrm{e}^{r} X_\alpha \cos\psi - \mathrm{e}^{-r}\chi(X_{\mathrm{M1}} - X_{\mathrm{M2}}) \sin\psi/\sqrt{2}, \tag{G.32}$$

$$P_2 = \sqrt{2}\mathrm{e}^{r} X_\alpha \sin\psi - \mathrm{e}^{-r}\chi(X_{\mathrm{M1}} - X_{\mathrm{M2}}) \cos\psi/\sqrt{2}. \tag{G.33}$$

In this case, the polar decomposition of the Kraus operator is given by $\Upsilon(X_{\mathrm{M1}}, X_{\mathrm{M2}}, \varphi, \psi) = U(X_{\mathrm{M1}}, X_{\mathrm{M2}}, \varphi, \psi)P(X_{\mathrm{M1}}, X_{\mathrm{M2}}, \varphi, \psi)$, with positive operator

$$\begin{aligned}P(X_{\mathrm{M1}}, X_{\mathrm{M2}}, \varphi, \psi) = (\Gamma_{\mathrm{R}}(\varphi)\Gamma_{\mathrm{R}}(\psi)/\pi^2)^{1/4} \exp\{-\Gamma_{\mathrm{R}}(\varphi)(X_{\mathrm{L1}}(\varphi) - X_1)^2/2\} \\ \exp\{-\Gamma_{\mathrm{R}}(\psi)(X_{\mathrm{L2}}(\psi) - X_2)^2/2\},\end{aligned} \tag{G.34}$$

and effective unitary operator

$$\begin{aligned}U(X_{\mathrm{M1}}, X_{\mathrm{M2}}, \varphi, \psi) = (\Gamma_{\mathrm{R}}(\varphi)\Gamma_{\mathrm{R}}(\psi)/\pi^2)^{1/4} \exp\{-\mathrm{i}\Gamma_{\mathrm{I}}(\varphi)(X_{\mathrm{L1}}(\varphi) - X_1)^2/2\} \exp\{\mathrm{i}P_1 X_{\mathrm{L1}}(\varphi)\} \\ \exp\{-\mathrm{i}X_1 P_1/2\} \exp\{-\mathrm{i}\Gamma_{\mathrm{I}}(\psi)(X_{\mathrm{L2}}(\psi) - X_2)^2/2\} \exp\{\mathrm{i}P_2 X_{\mathrm{L2}}(\psi)\} \exp\{-\mathrm{i}X_2 P_2/2\},\end{aligned} \tag{G.35}$$

which also depends on the homodyne measurement outcomes. The parts of these operators which depend on the square of the mechanical EPR quadratures may induce entanglement as they contain terms proportional to the product $X_{\mathrm{M1}}X_{\mathrm{M2}}$. I call these parts P_{ENT} and U_{ENT}, respectively, and they are given by

$$\begin{aligned}P_{\mathrm{ENT}} = (\Gamma_{\mathrm{R}}(\varphi)\Gamma_{\mathrm{R}}(\psi)/\pi^2)^{1/4} \exp\{-\Gamma_{\mathrm{R}}(\varphi)\mathrm{e}^{-2r}\chi^2(X_{\mathrm{M1}} + X_{\mathrm{M2}})^2 \sin^2\varphi/4\} \\ \exp\{-\Gamma_{\mathrm{R}}(\psi)\mathrm{e}^{-2r}\chi^2(X_{\mathrm{M1}} - X_{\mathrm{M2}})^2 \sin^2\psi/4\},\end{aligned} \tag{G.36}$$

and

$$\begin{aligned}U_{\mathrm{ENT}} = (\Gamma_{\mathrm{R}}(\varphi)\Gamma_{\mathrm{R}}(\psi)/\pi^2)^{1/4} \exp\{-\mathrm{i}\Gamma_{\mathrm{I}}(\varphi)\mathrm{e}^{-2r}\chi^2(X_{\mathrm{M1}} + X_{\mathrm{M2}})^2 \sin^2\varphi/4\} \\ \exp\{-\mathrm{i}\Gamma_{\mathrm{I}}(\psi)\mathrm{e}^{-2r}\chi^2(X_{\mathrm{M1}} - X_{\mathrm{M2}})^2 \sin^2\psi/4\} \exp\{-\mathrm{i}\mathrm{e}^{-2r}\chi^2(X_{\mathrm{M1}} + X_{\mathrm{M2}})^2 \sin\varphi\cos\varphi/4\} \\ \exp\{-\mathrm{i}\mathrm{e}^{-2r}\chi^2(X_{\mathrm{M1}} - X_{\mathrm{M2}})^2 \sin\psi\cos\psi/4\}\end{aligned} \tag{G.37}$$

The homodyne configurations $(\varphi, \psi) = (0, \pi/2)$ and $(\varphi, \psi) = (\pi/2, 0)$ therefore corresponds to Bayesian inference of the mechanical EPR quadratures $(X_{\text{M1}} + X_{\text{M2}})$ and $(X_{\text{M1}} - X_{\text{M2}})$, respectively. To see this explicitly, consider the case when $(\varphi, \psi) = (0, \pi/2)$, then one has that

$$\begin{aligned} P_{\text{ENT}} &= \exp\{-\chi^2 (X_{\text{M1}} - X_{\text{M2}})^2/4\}, \\ U_{\text{ENT}} &= \mathbb{1}. \end{aligned} \tag{G.38}$$

Hence, the total operation $\Upsilon(X_{\text{M1}}, X_{\text{M2}}, \theta, \phi)$ corresponds to Bayesian inference up to local unitaries.

Whilst at $(\varphi, \psi) = (\pi/4, 3\pi/4)$ and $(\varphi, \psi) = (3\pi/4, \pi/4)$ the measurement induces a two-mode entangling unitary operation and the positive operator P_{ENT} does not lead to any entanglement generation. From a Bayesian perspective, this operation amounts to unitarily evolving the prior towards a more entangled state. Taking $(\varphi, \psi) = (\pi/4, 3\pi/4)$, one has that

$$\begin{aligned} P_{\text{ENT}} &= \exp\{-\mathrm{e}^{-2r} \chi^2 (X_{\text{M1}}^2 + X_{\text{M2}}^2)/4 \cosh 2r\}, \\ U_{\text{ENT}} &= \exp\{-\mathrm{i}\mathrm{e}^{-2r} \chi^2 (1 + 2\tanh 2r) X_{\text{M1}} X_{\text{M2}}/2\}. \end{aligned} \tag{G.39}$$

Fig. G.1 shows the balance between Bayesian inference and unitary action with and without the use of optical squeezers. These contour plots for the logarithmic negativity, show that there is a continuum of optimal homodyne configurations, regardless of whether or not optical squeezers are implemented. The configurations $(\varphi, \psi) = (0, \pi/2)$ and $(\varphi, \psi) = (\pi/2, 0)$ chosen above correspond to just two of these optimal choices.

When optical squeezers are not used the contour plot is more heavily weighted around the set of points $(\varphi, \psi) = \{(0, \pi/2), (\pi/2, 0), (\pi, \pi/2), (\pi/2, \pi)\}$, which corresponds to maximizing the contribution of P_{ENT}, as compared to the regions surrounding $(\varphi, \psi) = \{(0, \pi/2), (3\pi/4, \pi/4)\}$, which corresponds to maximizing the entangling effect of U_{ENT}. This observation demonstrates that Bayesian inference of the mechanical EPR quadratures is the more effective way to create mechanical entanglement from the optical-mechanical entanglement. This is because, without the use of squeezers, the optical subspace is asymmetric with more information about the mechanical position quadratures encoded in the phase quadratures of the optical modes.

It is interesting to note that when the optimal choice of optical squeezers is utilized, the contour plot shows a more equal balance between the effects of P_{ENT} and U_{ENT}. With the best choice of homodyne angles corresponding to approximately $\psi = \varphi - \pi/2$ and $\psi = \varphi + \pi/2$. Optical squeezers bring the optical modes to a more symmetric state, and hence the contour plot is less heavily weighted to areas that correspond to a combination of a phase and an amplitude quadrature measurement. No entanglement can be generated when $\varphi = \psi$ as this allows one to gain knowledge of X_{M1} and X_{M2} separately.

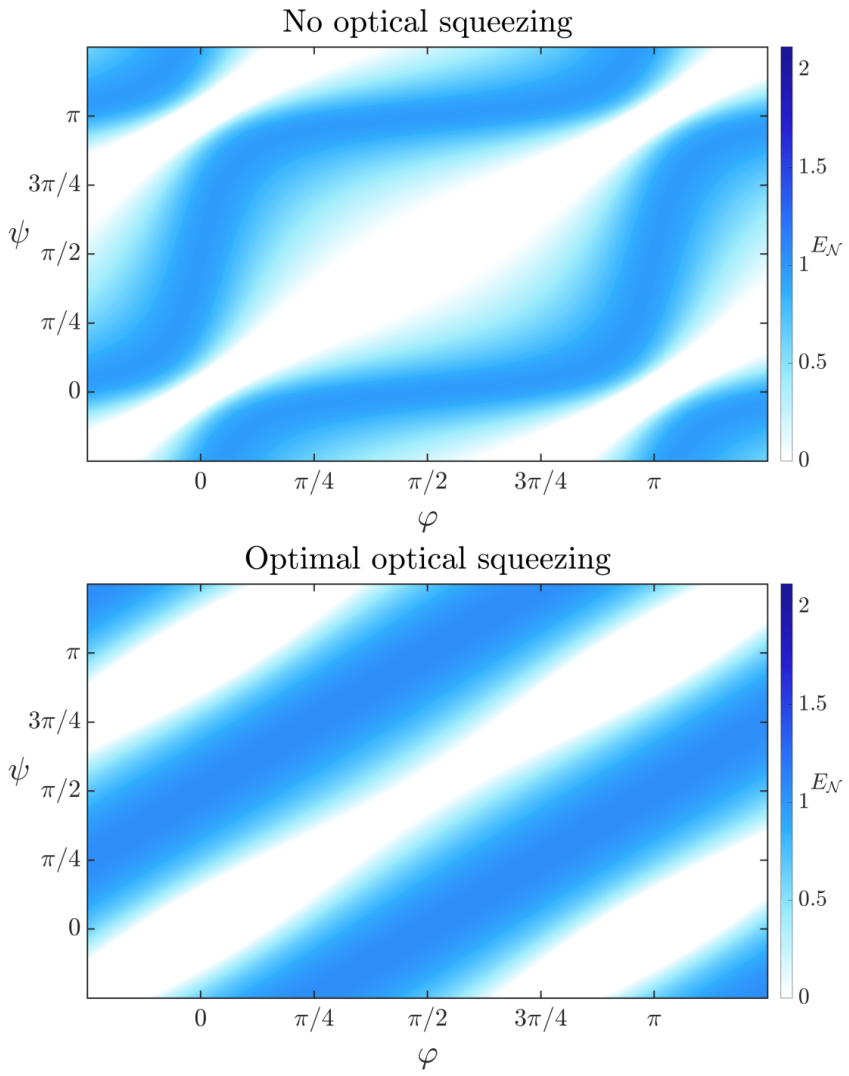


Figure G.1: **Dependence of the logarithmic negativity, with and without optical squeezing, as a function of the optical homodyne angles φ and ψ in the interferometric scheme.** Here, $E_{\mathcal{N}}$ is plotted after the mechanical modes have rotated and decohered through a quarter of a period since entanglement generation. The contour plot with no optical squeezing has $\chi = 2.97$, while the plot with optimal optical squeezing has $r = 0.57$ and $\chi = 3.15$. These values are the same as those obtained from Fig. 8.4, which maximize the logarithmic negativity. Without optical squeezing, the logarithmic negativity reaches a maximum of $E_{\mathcal{N}} = 0.98$, while with optimal optical squeezing, $E_{\mathcal{N}} = 1.07$ is reached. There are a continuum of maximum in the region $\varphi = [0, \pi)$ and $\psi = [0, \pi)$, and I plot an extra $\pi/4$ outside this range to demonstrate the oscillatory nature more clearly.

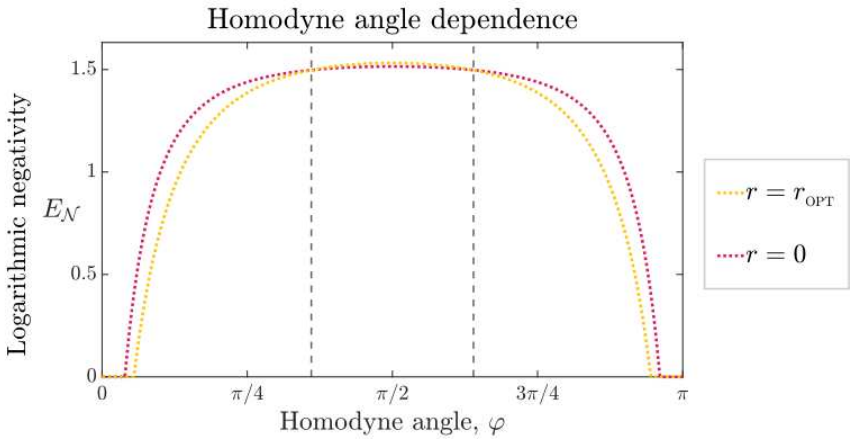


Figure G.2: **Dependence of the logarithmic negativity, with and without optical squeezing, as a function of the optical homodyne angle φ in the non-interferometric scheme.** Here, $E_{\mathcal{N}}$ is plotted after the mechanical modes have rotated and decohered through a quarter of a period since entanglement generation. When $r = 0$ I set $\chi = 3.00$, and when the squeezing parameter is set to be optimal, $r_{\mathrm{OPT}} = 0.15$, I set $\chi = 2.97$. These correspond to the values that maximize logarithmic negativity, found in Fig. 8.6. The two curves intersect at $\varphi = 1.13$ and $\varphi = 2.01$, showing that there is a region around $\varphi = \pi/2$ where squeezing is beneficial to entanglement generation.

G.4.3 Non-interferometric mechanical entanglement

The Kraus operator that acts on the initial separable mechanical state, corresponding to Eq. 8.29, is given by

$$\Upsilon(X_{\mathrm{M1}}, X_{\mathrm{M2}}, \varphi) = \langle X_{\mathrm{L}}(\varphi)|\, U_{\mathrm{SQ}} \mathrm{e}^{\mathrm{i}\chi X_{\mathrm{L}} X_{\mathrm{M2}}} U_{\mathrm{SQ}} \mathrm{e}^{\mathrm{i}\chi X_{\mathrm{L}} X_{\mathrm{M1}}} |\alpha\rangle \tag{G.40}$$

Up to irrelevant local unitaries, the Kraus operator may be expressed as

$$\begin{aligned}\Upsilon(X_{\mathrm{M1}}, X_{\mathrm{M2}}, \varphi) = (\Gamma_{\mathrm{R}}/\pi)^{1/4} \exp\{-\Gamma(X_{\mathrm{L}}(\varphi) - X_0)^2/2\} \\ \exp\{\mathrm{i}P_0 X_{\mathrm{L}}(\varphi)\} \exp\{-\mathrm{i}X_0 P_0/2\}.\end{aligned} \tag{G.41}$$

Here,

$$X_0 = \mathrm{e}^{2r} X_\alpha \cos\varphi + \chi(\mathrm{e}^{-2r} X_{\mathrm{M1}} + \mathrm{e}^{-r} X_{\mathrm{M2}}) \sin\varphi, \tag{G.42}$$

$$P_0 = \chi(\mathrm{e}^{-2r} X_{\mathrm{M1}} + \mathrm{e}^{-r} X_{\mathrm{M2}}) \cos\varphi - \mathrm{e}^{2r} X_\alpha \sin\varphi, \tag{G.43}$$

$$\Gamma(\varphi) = \Gamma_{\mathrm{R}}(\varphi) + \mathrm{i}\Gamma_{\mathrm{I}}(\varphi), \tag{G.44}$$

$$\Gamma_{\mathrm{R}}(\varphi) = \frac{1}{\cosh 4r + \cos 2\varphi \sinh 4r}, \tag{G.45}$$

$$\Gamma_{\mathrm{I}}(\varphi) = \frac{2 \sin 2\varphi \sinh 4r}{\cosh 4r + \cos 2\varphi \sinh 4r}. \tag{G.46}$$

The operator $\Upsilon(X_{\mathrm{M1}}, X_{\mathrm{M2}}, \varphi)$ for the non-interferometric scheme admits a similar polar decomposition as the operator for the interferometric scheme. However, from Fig. G.2 it may be seen that regardless of whether or not optical squeezers are used, there only exists one angle φ that corresponds to maximum entanglement. This occurs at $\varphi = \pi/2$ and corresponds to Bayesian inference of the EPR quadrature. The region between $\varphi = 1.13$ and $\varphi = 2.01$ is the region where the use of optical squeezers leads to an increase in logarithmic negativity.

G.5 The functions J_a, J_b, and J_c

The functions J_a, J_b, and J_c are given by

$$
\begin{aligned}
J_a &= \Big\{ \mathrm{e}^{8r}(1-\eta_{\mathrm{DET}})^2 + 2\mathrm{e}^{6r}\eta_{\mathrm{DET}}(1-\eta_{\mathrm{DET}})(1-\eta_{\mathrm{CAV}}^2+2V_{\mathrm{X}}\eta_{\mathrm{CAV}}^3\chi^2) \\
&+ \mathrm{e}^{4r}\eta_{\mathrm{DET}}\left\{\eta_{\mathrm{DET}}+\eta_{\mathrm{CAV}}^2\left[2-(4-\eta_{\mathrm{CAV}}^2)\eta_{\mathrm{DET}}+2V_{\mathrm{X}}\eta_{\mathrm{CAV}}(1+(1-2\eta_{\mathrm{CAV}}^2)\eta_{\mathrm{DET}})\chi^2+4V_{\mathrm{X}}^2\eta_{\mathrm{CAV}}^4\eta_{\mathrm{DET}}\chi^4\right]\right\} \\
&+ \mathrm{e}^{2r}\eta_{\mathrm{CAV}}^2\eta_{\mathrm{DET}}^2\left\{2+\eta_{\mathrm{CAV}}[2V_{\mathrm{X}}\chi^2-2\eta_{\mathrm{CAV}}(1-V_{\mathrm{X}}\eta_{\mathrm{CAV}}\chi^2(1+2V_{\mathrm{X}}\eta_{\mathrm{CAV}}\chi^2))]\right\} \\
&+ \eta_{\mathrm{CAV}}^4\eta_{\mathrm{DET}}^2[1+2V_{\mathrm{X}}\eta_{\mathrm{CAV}}\chi^2]\Big\} \Big/ \Big\{ \mathrm{e}^{8r}(1-\eta_{\mathrm{DET}})^2 \\
&+ 2\mathrm{e}^{6r}\eta_{\mathrm{DET}}(1-\eta_{\mathrm{DET}})(1-\eta_{\mathrm{CAV}}^2+2V_{\mathrm{X}}\eta_{\mathrm{CAV}}^3\chi^2) \\
&+ \mathrm{e}^{4r}\eta_{\mathrm{DET}}\left\{\eta_{\mathrm{DET}}+\eta_{\mathrm{CAV}}^2\left[2+4V_{\mathrm{X}}\eta_{\mathrm{CAV}}\chi^2-\eta_{\mathrm{DET}}(4-\eta_{\mathrm{CAV}}^2(1-4V_{\mathrm{X}}\chi^2(1-V_{\mathrm{X}}\eta_{\mathrm{CAV}}\chi^2)))\right]\right\} \\
&+ \mathrm{e}^{2r}\eta_{\mathrm{CAV}}^2\eta_{\mathrm{DET}}^2\left[2-2\eta_{\mathrm{CAV}}^2+4V_{\mathrm{X}}\eta_{\mathrm{CAV}}\chi^2+8V_{\mathrm{X}}^2\eta_{\mathrm{CAV}}^4\chi^4\right] \\
&+ \eta_{\mathrm{CAV}}^4\eta_{\mathrm{DET}}^2[1+4V_{\mathrm{X}}\eta_{\mathrm{CAV}}\chi^2(1+V_{\mathrm{X}}\eta_{\mathrm{CAV}}\chi^2)]\Big\},
\end{aligned}
$$

$$
\begin{aligned}
J_b &= \Big\{ \mathrm{e}^{8r}(1-\eta_{\mathrm{DET}})^2 + 2\mathrm{e}^{6r}\eta_{\mathrm{DET}}(1-\eta_{\mathrm{DET}})(1-\eta_{\mathrm{CAV}}^2+V_{\mathrm{X}}\eta_{\mathrm{CAV}}^3) \\
&+ \mathrm{e}^{4r}\eta_{\mathrm{DET}}\left\{\eta_{\mathrm{DET}}+\eta_{\mathrm{CAV}}^2\left[2-(4-\eta_{\mathrm{CAV}}^2)\eta_{\mathrm{DET}}+2V_{\mathrm{X}}\eta_{\mathrm{CAV}}(2-(1+\eta_{\mathrm{CAV}}^2)\eta_{\mathrm{DET}})\chi^2\right]\right\} \\
&+ \mathrm{e}^{2r}\eta_{\mathrm{CAV}}^2\eta_{\mathrm{DET}}^2\left\{2+\eta_{\mathrm{CAV}}\left[4V_{\mathrm{X}}\chi^2-2\eta_{\mathrm{CAV}}(1+V_{\mathrm{X}}\eta_{\mathrm{CAV}}\chi^2(1-2V_{\mathrm{X}}\eta_{\mathrm{CAV}}\chi^2))\right]\right\} \\
&+ \eta_{\mathrm{CAV}}^4\eta_{\mathrm{DET}}^2\left[1+4V_{\mathrm{X}}\eta_{\mathrm{CAV}}\chi^2(1+V_{\mathrm{X}}\eta_{\mathrm{CAV}}\chi^2)\right]\Big\} \Big/ \Big\{ \mathrm{e}^{8r}(1-\eta_{\mathrm{DET}})^2 \\
&+ 2\mathrm{e}^{6r}\eta_{\mathrm{DET}}(1-\eta_{\mathrm{DET}})(1-\eta_{\mathrm{CAV}}^2+2V_{\mathrm{X}}\eta_{\mathrm{CAV}}^3) \\
&+ \mathrm{e}^{4r}\eta_{\mathrm{DET}}\left\{\eta_{\mathrm{DET}}+\eta_{\mathrm{CAV}}^2\left[2+4V_{\mathrm{X}}\eta_{\mathrm{CAV}}\chi^2-\eta_{\mathrm{DET}}(4-\eta_{\mathrm{CAV}}^2(1-4V_{\mathrm{X}}\eta_{\mathrm{CAV}}\chi^2(1-V_{\mathrm{X}}\eta_{\mathrm{CAV}}\chi^2)))\right]\right\} \\
&+ \mathrm{e}^{2r}\eta_{\mathrm{CAV}}^2\eta_{\mathrm{DET}}^2\left[2-2\eta_{\mathrm{CAV}}^2+4V_{\mathrm{X}}\eta_{\mathrm{CAV}}\chi^2+8V_{\mathrm{X}}^2\eta_{\mathrm{CAV}}^4\chi^4\right] \\
&+ \eta_{\mathrm{CAV}}^4\eta_{\mathrm{DET}}^2\left[1+4V_{\mathrm{X}}\eta_{\mathrm{CAV}}\chi^2(1+V_{\mathrm{X}}\eta_{\mathrm{CAV}}\chi^2)\right]\Big\},
\end{aligned}
$$

$$
J_c = \frac{4}{\mathrm{e}^{5r}(1-\eta_{\mathrm{DET}})+\mathrm{e}^{3r}\eta_{\mathrm{DET}}\left[1-\eta_{\mathrm{CAV}}^2(1-2V_{\mathrm{X}}\eta_{\mathrm{CAV}}\chi^2)\right]+\mathrm{e}^{r}\eta_{\mathrm{CAV}}^2\eta_{\mathrm{DET}}(1+2V_{\mathrm{X}}\eta_{\mathrm{CAV}}\chi^2)}.
$$

For $r=0$, these functions simplify to the form

$$
\begin{aligned}
J_a &= \frac{1}{2}\left[1+\frac{1+4V_{\mathrm{X}}\eta_{\mathrm{CAV}}^3\eta_{\mathrm{DET}}\chi^2}{1+8V_{\mathrm{X}}\eta_{\mathrm{CAV}}^3\eta_{\mathrm{DET}}\chi^2(1+2V_{\mathrm{X}}\eta_{\mathrm{CAV}}^3\eta_{\mathrm{DET}}\chi^2)}\right] \\
J_b &= \frac{1}{2}\left[1+\frac{1+4V_{\mathrm{X}}\eta_{\mathrm{CAV}}^3\eta_{\mathrm{DET}}\chi^2}{1+8V_{\mathrm{X}}\eta_{\mathrm{CAV}}^3\eta_{\mathrm{DET}}\chi^2(1+2V_{\mathrm{X}}\eta_{\mathrm{CAV}}^3\eta_{\mathrm{DET}}\chi^2)}\right] \\
J_c &= \frac{4}{1+4V_{\mathrm{X}}\eta_{\mathrm{CAV}}^3\eta_{\mathrm{DET}}\chi^2}.
\end{aligned}
$$

Appendix H

Proof of Kraus map completeness

Using Eq. (10.29) one has that

$$\sum_{m=0}^{\infty} \Upsilon_m^\dagger \Upsilon_m \;=\; T^{\hat{n}_1} \left(\sum_{m=0}^{\infty} \frac{1}{m!} \left(\frac{|R|^2}{|T|^2} \right)^m (a_1^\dagger)^m a_1^m \right) T^{\hat{n}_1}. \tag{H.1}$$

From Appendix A, I then use

$$\begin{aligned} :\mathrm{e}^{\lambda a^\dagger a}: \;&=\; \sum_{m=0}^{\infty} \frac{\lambda^m}{m!} (a^\dagger)^m a^m \\ &=\; (1+\lambda)^{a^\dagger a} \\ &=\; \mathrm{e}^{\ln(1+\lambda) a^\dagger a}, \end{aligned} \tag{H.2}$$

with $\lambda = (|R|^2/|T|^2)$ to arrive at the statement of the Kraus map's completeness:

$$\begin{aligned} \sum_{m=0}^{\infty} \Upsilon_m^\dagger \Upsilon_m \;&=\; T^{\hat{n}_1} \mathrm{e}^{\ln(1+\lambda)\hat{n}_1} T^{\hat{n}_1} \\ &=\; \left(\mathrm{e}^{\ln(T)+\ln(T)+\ln(1+\lambda)} \right)^{\hat{n}_1} \\ &=\; \left(\mathrm{e}^{\ln\left(|T|^2+|R^2|\right)} \right)^{\hat{n}_1} = \mathbb{1}. \end{aligned} \tag{H.3}$$

Here, I have used $|T|^2 + |R|^2 = 1$, $T \in \mathbb{R}$, and $\ln(1) = 0$.

Appendix I

Full Gaussian approximation to the pulsed position measurement

Here, I consider the full Gaussian approximation to the measurement map of Eq. (13.3). I would like to remind the reader that here I consider a nonlinear cavity-enhanced pulsed optomechanical interaction with linear position coupling, which means the unitary is $\mathrm{e}^{\mathrm{i}\varphi(X_{\mathrm{M}})n_{\mathrm{L}}}$ with $\varphi(X_{\mathrm{M}}) = \arg(f)$ and

$$f = \frac{1 + \mathrm{i}\left(\frac{\mu}{2}X_{\mathrm{M}} + \frac{\Delta}{\kappa}\right)}{1 - \mathrm{i}\left(\frac{\mu}{2}X_{\mathrm{M}} + \frac{\Delta}{\kappa}\right)}. \tag{I.1}$$

Furthermore, I consider a resonant input pulse $\Delta = 0$. In this case, the A and B functions are given by

$$A(X_{\mathrm{M}}) = \frac{1 - \left(\frac{\mu}{2}X_{\mathrm{M}}\right)^2}{1 + \left(\frac{\mu}{2}X_{\mathrm{M}}\right)^2}, \tag{I.2}$$

$$B(X_{\mathrm{M}}) = \frac{\mu X_{\mathrm{M}}}{1 + \left(\frac{\mu}{2}X_{\mathrm{M}}\right)^2}. \tag{I.3}$$

I.1 Polar decomposition and cavity coordinates

First, consider the polar decomposition[1] of the measurement operator $\Upsilon = \frac{1}{\sqrt{\pi}} PU$, which is

$$\begin{aligned}
\Upsilon &= \frac{1}{\sqrt{\pi}} \exp\Big[-\frac{1}{2}\left(X_{\rm L} - aA(x)\right)^2 - \frac{1}{2}\left(P_{\rm L} - B(x)\right)^2 \\
&\quad -\mathrm{i}bP_{\rm L}A(x) + \mathrm{i}aX_{\rm L}B(x) + \frac{\mathrm{i}}{2}(b^2-a^2)A(x)B(x)\Big], \qquad \text{(I.4)} \\
P &= \exp\Big[-\frac{1}{2}\left(X_{\rm L} - aA(x)\right)^2 - \frac{1}{2}\left(P_{\rm L} - B(x)\right)^2 \Big], \qquad \text{(I.5)} \\
U &= \exp\Big[-\mathrm{i}bP_{\rm L}A(x) + \mathrm{i}aX_{\rm L}B(x) + \frac{\mathrm{i}}{2}(b^2-a^2)A(x)B(x)\Big], \qquad \text{(I.6)}
\end{aligned}$$

where

$$\begin{aligned}
a &= \sqrt{1-\zeta^2}X_\alpha, \qquad \text{(I.7)} \\
b &= \zeta X_\alpha, \qquad \text{(I.8)} \\
x &= \mu X_{\rm M}. \qquad \text{(I.9)}
\end{aligned}$$

The general-dyne coordinates (z, δ) are related to the measurement space variables $(X_{\rm L}, P_{\rm L})$ via

$$\begin{aligned}
A(z) &= \frac{4-z^2}{4+z^2}, \qquad \text{(I.10)} \\
B(y) &\quad \frac{4z}{4+z^2}, \qquad \text{(I.11)} \\
X_{\rm L} &= aA(z) + \delta\cos\psi, \qquad \text{(I.12)} \\
P_{\rm L} &= bB(z) + \delta\sin\psi, \qquad \text{(I.13)} \\
\sin(\psi) &= \frac{aB}{\sqrt{b^2A^2 + a^2B^2}}, \qquad \text{(I.14)} \\
\cos(\psi) &= \frac{bA}{\sqrt{b^2A^2 + a^2B^2}}. \qquad \text{(I.15)}
\end{aligned}$$

Now one may expand P and U to second order in δx by using $x = z + \delta x$. In the torrent of algebra that ensues it is useful to know that $aB(z)\cos\psi - bA(z)\sin\psi = 0$.

Gaussian approximation: Positive part

After said torrent of algebra, one arrives at

$$\begin{aligned}
P &= \exp\left[-\frac{1}{2}\delta^2 - \frac{1}{2}\beta(x-z)^2\right], \qquad \text{(I.16)} \\
\beta &= \frac{16}{(4+z^2)^2}\left[a^2B^2 + b^2A^2 + \delta\frac{ab}{\sqrt{a^2B^2 + b^2A^2}}\right], \qquad \text{(I.17)}
\end{aligned}$$

[1] I use U here to represent the unitary part of Υ in the polar decomposition, not to be confused with the nonlinear cavity-enhanced optomechanical unitary $\mathrm{e}^{\mathrm{i}\varphi(X_{\rm M})n_{\rm L}}$.

for the positive part of Υ in the Gaussian approximation. Here, $A = A(z)$ and $B = B(z)$.

Gaussian approximation: Unitary Part

Likewise the unitary part in the Gaussian approximation is

$$U = \exp\left[\mathrm{i}\Omega + \mathrm{i}\Psi(x-z) + \mathrm{i}\Phi(x-z)^2\right], \tag{I.18}$$

$$\Omega = \frac{1}{2}AB(a^2-b^2), \tag{I.19}$$

$$\Psi = \frac{2X_\alpha^2}{4+z^2} + \delta\frac{4ab}{(4+z^2)\sqrt{b^2A^2+a^2B^2}}, \tag{I.20}$$

$$\Phi = -\frac{1}{2}X_\alpha^2\frac{B}{4+z^2} + \frac{8(a^2-b^2)}{(4+z^2)^2}AB - \delta\frac{abB}{(4+z^2)\sqrt{b^2A^2+a^2B^2}}, \tag{I.21}$$

where again $A = A(z)$ and $B = B(z)$.

I.2 Full covariance matrix transformation in Gaussian approximation

I will now find the Gaussian transformation for the first moments vector and the covariance matrix.

Unitary symplectic

The Schrödinger picture transformation for the state ρ is $U\rho U^\dagger$, while the Heisenberg transformation for an operator A is $U^\dagger AU$. Hence, one needs to find $U^\dagger X_{\mathrm{M}} U$ and $U^\dagger P_{\mathrm{M}} U$. One can do so using the Hadamard lemma, which gives,

$$U^\dagger X_{\mathrm{M}} U = X_{\mathrm{M}}, \tag{I.22}$$

$$U^\dagger P_{\mathrm{M}} U = P_{\mathrm{M}} + \mu\Psi - 2\mu\Phi y + 2\mu^2\Phi X_{\mathrm{M}}. \tag{I.23}$$

I then write the transformation due to the unitary U as a symplectic transformation:

$$\begin{pmatrix} X_{\mathrm{M}} \\ P_{\mathrm{M}} \end{pmatrix} \rightarrow S_U \begin{pmatrix} X_{\mathrm{M}} \\ P_{\mathrm{M}} \end{pmatrix} + d_U, \tag{I.24}$$

$$S_U = \begin{pmatrix} 1 & 0 \\ 2\mu^2\Phi & 1 \end{pmatrix} \quad ; \quad d_U = \begin{pmatrix} 0 \\ \mu\Psi - 2\mu\Phi z \end{pmatrix}. \tag{I.25}$$

Action of P

A Gaussian state ρ_G is completely described by the first moments vector $\langle \mathbf{X} \rangle$ and covariance matrix σ:

$$\langle \mathbf{X} \rangle = \begin{pmatrix} X_G \\ P_G \end{pmatrix} \; ; \quad \sigma = \begin{pmatrix} \sigma_X & \sigma_{XP} \\ \sigma_{XP} & \sigma_P \end{pmatrix}. \tag{I.26}$$

The determinant of σ is $d = \sigma_X\sigma_P - \sigma_{XP}^2$ and the Wigner function of the Gaussian state is[2]

$$W_G(X,P) = \frac{1}{2\pi\sqrt{d}}\exp\left\{-\frac{1}{2}(\mathbf{X}-\langle\mathbf{X}\rangle)\sigma^{-1}(\mathbf{X}-\langle\mathbf{X}\rangle)\right\}$$
$$= \frac{1}{2\pi\sqrt{d}}\exp\left\{-\frac{1}{2d}\left[\sigma_P(X-X_G)^2 - 2\sigma_{XP}(X-X_G)(P-P_G)+\sigma_X(P-P_G)^2\right]\right\}. \tag{I.27}$$

Using the inverse transform, this allows you to find

$$\left\langle X-\frac{u}{2}\right|\rho_G\left|X+\frac{u}{2}\right\rangle = \frac{1}{\sqrt{2\pi\sigma_X}}\exp\left\{-\frac{d}{2\sigma_X}u^2 - \frac{1}{2\sigma_X}(X-X_G)^2 - \mathrm{i}P_G u - \mathrm{i}\frac{\sigma_{XP}}{\sigma_X}(X-X_G)u\right\}. \tag{I.28}$$

In the Gaussian approximation then

$$\rho_{OUT} = \frac{\hat{P}(X_{\rm M})\rho_G\hat{P}(X_{\rm M})}{\mathrm{tr}\left\{\hat{P}^2(X_{\rm M})\rho_G\right\}} \tag{I.29}$$

is Gaussian too. The Wigner function of ρ_{OUT} is then given by

$$W_{OUT}(X,P) = \mathcal{N}\int \mathrm{e}^{\mathrm{i}Pu}P(X-\frac{u}{2})P(X+\frac{u}{2})\left\langle X-\frac{u}{2}\right|\rho_G\left|X+\frac{u}{2}\right\rangle\,\mathrm{d}u \tag{I.30}$$

$$= \frac{1}{2\pi\sqrt{D}}\exp\left\{-\frac{1}{2}(\mathbf{X}-\langle\mathbf{X}'\rangle)\Sigma^{-1}(\mathbf{X}-\langle\mathbf{X}'\rangle)\right\} \tag{I.31}$$

$$= \frac{1}{2\pi\sqrt{D}}\exp\left\{-\frac{1}{2D}\left[\Sigma_P(X-X'_G)^2 - 2\Sigma_{XP}(X-X'_G)(P-P'_G)+\Sigma_X(P-P'_G)^2\right]\right\},$$

with $\mathcal{N}$ being the normalization and

$$P(X\pm\frac{u}{2}) = \exp\left\{-\frac{\delta^2}{2}-\frac{\beta}{2}(\mu X\pm\mu\frac{u}{2}-z)^2\right\}, \tag{I.32}$$

$$\langle\mathbf{X}'\rangle = \begin{pmatrix}X'_G\\P'_G\end{pmatrix}\;;\quad \Sigma = \begin{pmatrix}\Sigma_X & \Sigma_{XP}\\ \Sigma_{XP} & \Sigma_P\end{pmatrix}, \tag{I.33}$$

$$D = \Sigma_X\Sigma_P - \Sigma_{XP}^2. \tag{I.34}$$

Without loss of generality, one can set $\langle\mathbf{X}\rangle = \mathbf{0}$, by displacing the initial

[2]The subscripts on $X_{\rm M}$ and $P_{\rm M}$ are dropped for convenience.

Gaussian state appropriately. Using Eq. (I.30), one finds that

$$\begin{aligned} W_{OUT}(X,P) &\propto \exp\{-\mathcal{A}X^2 - \mathcal{B}P^2 + 2\mathcal{C}XP + XX_0\} \qquad \text{(I.35)} \\ &= \exp\left\{ -\frac{1}{2D}\left[\Sigma_P X^2 - 2\Sigma_{XP}XP + \Sigma_X X^2 \right.\right. \\ &+ \left.\left. X(-2\Sigma_P X'_G + 2\Sigma_{XP}P'_G) + P(-2\Sigma_X P'_G + 2\Sigma_{XP}X'_G)\right]\right\} \\ \mathcal{A} &= \frac{1}{2D}\Sigma_P = \frac{(2d+\beta\mu^2\sigma_X)(1+2\beta\mu^2\sigma_X)+2\sigma_{XP}^2}{2\sigma_X(2d+\beta\mu^2\sigma_X)} \qquad \text{(I.36)} \\ \mathcal{B} &= \frac{1}{2D}\Sigma_X = \frac{\sigma_X}{2d+\beta\mu^2\sigma_X}, \qquad \text{(I.37)} \\ \mathcal{C} &= \frac{1}{2D}\Sigma_{XP} = \frac{\sigma_{XP}}{2d+\beta\mu^2\sigma_X}, \qquad \text{(I.38)} \\ D &= \frac{1}{4(\mathcal{A}\mathcal{B}-\mathcal{C}^2)} = \frac{2d+\beta\mu^2\sigma_X}{2(1+2\beta\mu^2\sigma_X)}, \qquad \text{(I.39)} \\ X_0 &= 2\mu\beta z = \frac{X'_G}{\Sigma_X}, \qquad \text{(I.40)} \\ P'_G &= \frac{\Sigma_{XP}}{\Sigma_X}X'_G. \qquad \text{(I.41)} \end{aligned}$$

All this implies that for an initial Gaussian state ρ_G with first moments vector $\langle \mathbf{X} \rangle$ and covariance matrix σ

$$\langle \mathbf{X} \rangle = \begin{pmatrix} 0 \\ 0 \end{pmatrix} \; ; \quad \sigma = \begin{pmatrix} \sigma_X & \sigma_{XP} \\ \sigma_{XP} & \sigma_P \end{pmatrix}. \qquad \text{(I.42)}$$

The operation

$$\begin{aligned} \rho_{OUT} &= \frac{\hat{P}(X_{\rm M})\rho_G\hat{P}(X_{\rm M})}{\mathrm{tr}\left\{\hat{P}^2(X_{\rm M})\rho_G\right\}}, \qquad \text{(I.43)} \\ P(X_{\rm M}) &= \exp\left\{-\frac{\delta^2}{2} - \frac{\beta}{2}(x-z)^2\right\}, \qquad \text{(I.44)} \end{aligned}$$

produces a Gaussian state ρ_{OUT} with first moments vector $\langle \mathbf{X}' \rangle$ and covariance

matrix Σ;

$$\langle \mathbf{X}' \rangle = \begin{pmatrix} X'_G \\ P'_G \end{pmatrix} \quad ; \quad \Sigma = \begin{pmatrix} \Sigma_X & \Sigma_{XP} \\ \Sigma_{XP} & \Sigma_P \end{pmatrix}, \tag{I.45}$$

$$\Sigma_X = \frac{\sigma_X}{1 + 2\beta\mu^2\sigma_X}, \tag{I.46}$$

$$\Sigma_{XP} = \frac{\sigma_{XP}}{1 + 2\beta\mu^2\sigma_X}, \tag{I.47}$$

$$\Sigma_P = \sigma_P + \frac{1}{2}\beta\mu^2 \left(1 - \frac{4\sigma_{XP}^2}{1 + 2\beta\mu^2\sigma_X}\right), \tag{I.48}$$

$$X'_G = \frac{2\beta\mu\sigma_X z}{1 + 2\beta\mu^2\sigma_X}, \tag{I.49}$$

$$P'_G = \frac{2\beta\mu\sigma_{XP} z}{1 + 2\beta\mu^2\sigma_X}. \tag{I.50}$$

Action of full Υ

Combining the maps for the unitary operator U and the positive operator P gives the full Gaussian transformation induced by Υ. For an initial Gaussian state ρ_G with first moments vector $\langle \mathbf{X} \rangle$ and covariance matrix σ

$$\langle \mathbf{X} \rangle = \begin{pmatrix} X_G \\ P_G \end{pmatrix} \; ; \quad \sigma = \begin{pmatrix} \sigma_X & \sigma_{XP} \\ \sigma_{XP} & \sigma_P \end{pmatrix}. \tag{I.51}$$

The operation

$$\rho_{OUT} = \frac{\Upsilon(X_{\text{M}})\rho_G\Upsilon^\dagger(X_{\text{M}})}{\text{tr}\{\Upsilon^\dagger(X_{\text{M}})\Upsilon(X_{\text{M}})\rho_G\}}, \tag{I.52}$$

$$\Upsilon(X_{\text{M}}) = \frac{1}{\sqrt{\pi}} P(X_{\text{M}})U(X_{\text{M}}) = \frac{1}{\sqrt{\pi}} U(X_{\text{M}})P(X_{\text{M}}), \tag{I.53}$$

produces a Gaussian state ρ_{OUT} with first moments vector $\langle \mathbf{X}' \rangle$ and covariance matrix Σ;

$$\langle \mathbf{X}' \rangle = \begin{pmatrix} X'_G \\ P'_G \end{pmatrix} \quad ; \quad \Sigma = \begin{pmatrix} \Sigma_X & \Sigma_{XP} \\ \Sigma_{XP} & \Sigma_P \end{pmatrix}, \tag{I.54}$$

$$\Sigma_X = \frac{\sigma_X}{1 + 2\beta\mu^2\sigma_X}, \tag{I.55}$$

$$\Sigma_{XP} = \frac{\sigma_{XP} + 2\mu^2\Phi\sigma_X}{1 + 2\beta\mu^2\sigma_X}, \tag{I.56}$$

$$\begin{aligned} \Sigma_P &= \sigma_P + 4\mu^2\Phi(\sigma_{XP} + \mu^2\Phi\sigma_X) \\ &+ \frac{1}{2}\beta\mu^2 \left(1 - \frac{4(\sigma_{XP} + 2\mu^2\Phi\sigma_X)^2}{1 + 2\beta\mu^2\sigma_X}\right), \end{aligned} \tag{I.57}$$

$$X'_G = \frac{2\beta\mu\sigma_X z}{1 + 2\beta\mu^2\sigma_X}, \tag{I.58}$$

$$P'_G = \mu\Psi - 2\mu\Phi z + \frac{2\beta\mu(\sigma_{XP} + 2\mu^2\Phi\sigma_X)z}{1 + 2\beta\mu^2\sigma_X}. \tag{I.59}$$

Appendix J

Details on continuous position measurement

J.1 Linearized continuous position measurements: Riccati equations

In the linearized regime $\mu\sigma \ll 1$, the displacement vector $\mathbf{d}$ may be simply transformed away. This is because the small optical rotations are approximated by small phase shifts, so one never runs into the nonlinear response of the cavity that becomes apparent at larger values of $\mu\sigma$. Defining the vector $\mathbf{r} = (X_{\mathrm{M}}, P_{\mathrm{M}})^{\mathrm{T}}$ I rewrite the free Hamiltonian as

$$H = \frac{1}{2}\mathbf{r}^T R \mathbf{r}, \tag{J.1}$$

$$R = \omega_{\mathrm{M}} \mathbb{1}, \tag{J.2}$$

$$\Omega = \begin{pmatrix} 0 & 1 \\ -1 & 0 \end{pmatrix}. \tag{J.3}$$

To arrive at the linearized regime from the stochastic Gaussian regime, I approximate the measurement output operator in Eq. (14.11) by $c_{\mathrm{L}} = \sqrt{2k_{\mathrm{L}}} X_{\mathrm{M}}$. This amounts to (i) ignoring the stochastic term $\sqrt{2k} f(\langle X_{\mathrm{M}} \rangle)$, and (ii) approximating

$$\left[1 - \mathrm{i}\left(\frac{\mu}{2}\langle X_{\mathrm{M}}\rangle + \frac{\Delta}{\kappa}\right)\right]^2 \approx 1. \tag{J.4}$$

Furthermore, I do not expand about X_{M} at each time step, so there is no concept of Y_{M}.

The measurement output operators for the general-dyne detection scheme

may then be written as the vector $\mathbf{c} = C\mathbf{r}$ with

$$C = \begin{pmatrix} C_{11} & 0 \\ C_{21} & 0 \end{pmatrix}, \tag{J.5}$$

$$C_{11} = \mathrm{i}\sqrt{2k_{\mathrm{L}}(1-\zeta^2)}, \tag{J.6}$$

$$C_{21} = \sqrt{2k_{\mathrm{L}}\zeta^2}. \tag{J.7}$$

$$\tag{J.8}$$

Here, mechanical interactions with the environment for simplicity have been ignored for simplicity. However, to include these interactions one should also include C_{31} and C_{32} in the C matrix. Inserting this form of C into the Riccati matrix equation of Eq. (14.30), one sees that the evolution of the covariance matrix elements is purely deterministic. Setting $\dot{V} = 0$, then leads to the steady state solutions shown in Section 14.2.2.

In the linearized regime, mechanical information is only encoded on the P_{L} quadrature of light and so one should set $\zeta = 1$. Furthermore, as the dynamics is Markovian, one may see that the steady state solutions of Section 14.2.2 do not depend on the initial conditions. Finally, note that in the limit $k_{\mathrm{L}}/\omega_{\mathrm{M}} \to 0$, $V_{XP}^{ss} \to 0$ and V_X^{ss} and V_P^{ss} are indeterminate. This is because the dynamics are no longer Markovian as the covariance matrix should simply freely evolve about its initial conditions. Therefore, when no measurement is made $k_{\mathrm{L}}/\omega_{\mathrm{M}} = 0$, or indeed $\eta = 0$, Eqs (14.8), (14.9), and (14.10) don't strictly hold.

J.2 Gallery of results for the stochastic Gaussian regime simulations

Here I simulate the SDEs of Eqs (14.29) and (14.30) over 100 mechanical periods and 100 stochastic trajectories. I fix $R = \mu^2 k/\omega_{\mathrm{M}} = 2$, $\omega_{\mathrm{M}}/2\pi = 10\,\mathrm{MHz}$, $\mu = 0.05$, $X_\alpha/\sqrt{2} = 10$, $\zeta = 1/\sqrt{2}$, and vary η, γ, and T. Furthermore, I consider an initial mechanical state at effective temperature $T_i = 100\,\mathrm{mK}$, which may be out of equilibrium with the higher temperature bath at T. Interestingly, Fig. J.7 shows that when $\eta = 0.5$, $\gamma = 100\,\mathrm{Hz}$, and $T = 4\,\mathrm{K}$, drive locking allows the mean of the minimum value of V_X to drop below 1/2.

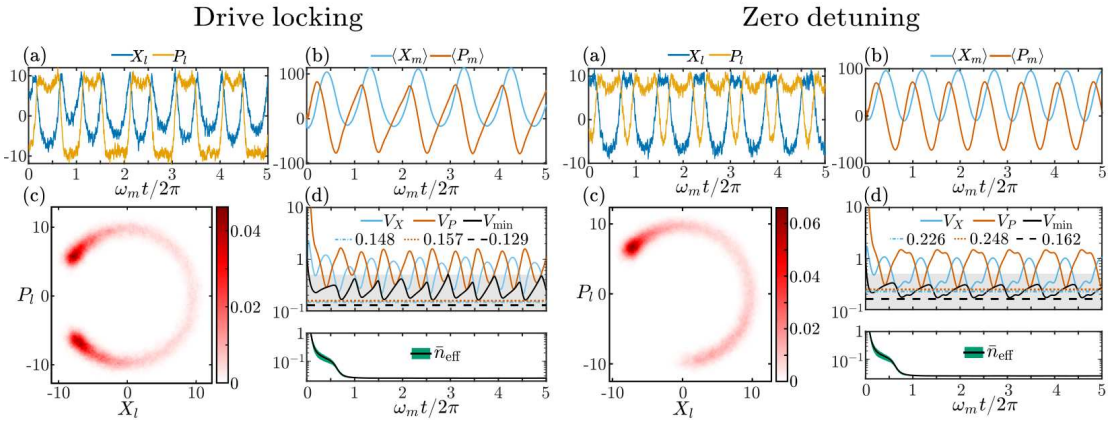


Figure J.1: **Set 1:** $\eta = 0.95$, $\gamma = 1\,\text{Hz}$, $T = 100\,\text{mK}$.

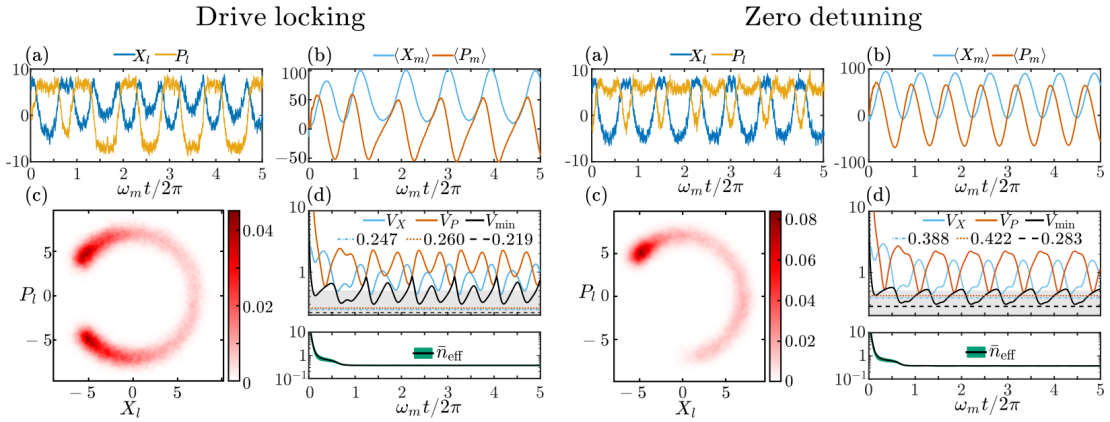


Figure J.2: **Set 2:** $\eta = 0.5$, $\gamma = 1\,\text{Hz}$, $T = 4\,\text{K}$.

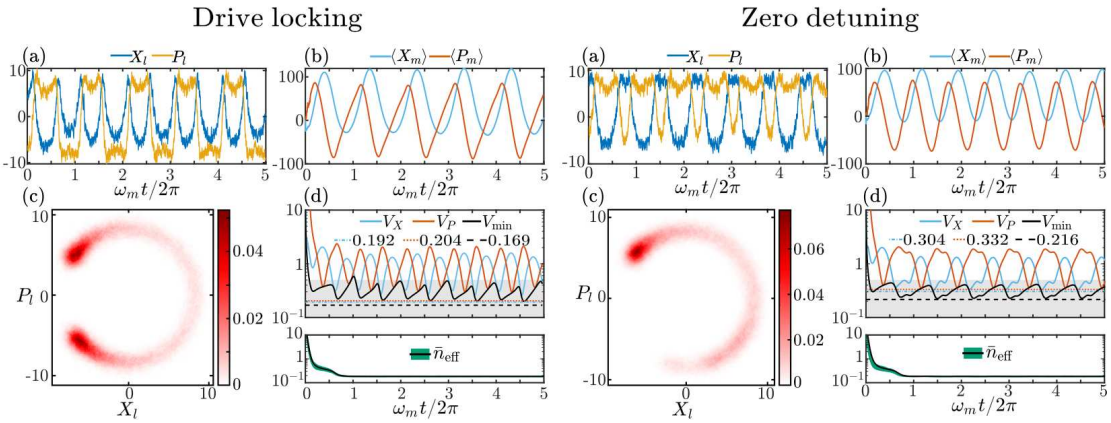


Figure J.3: **Set 3:** $\eta = 0.7$, $\gamma = 1\,\text{Hz}$, $T = 4\,\text{K}$.

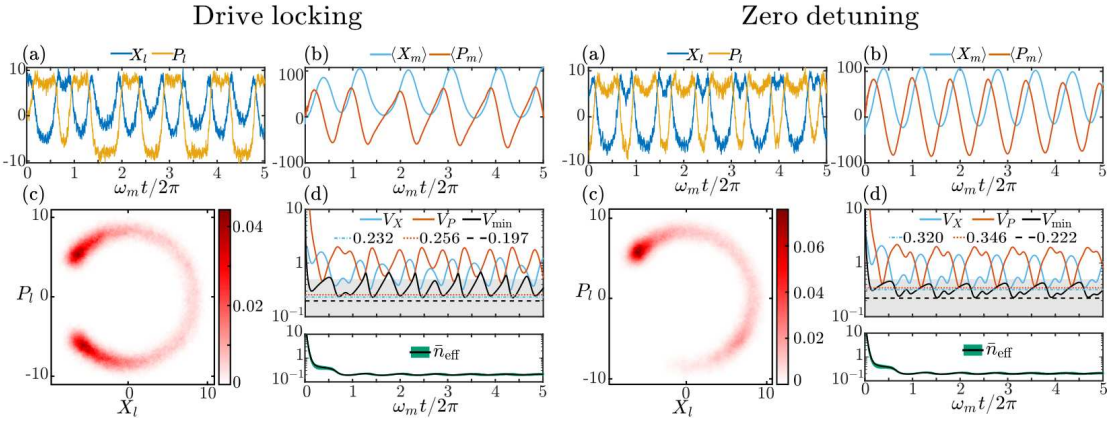


Figure J.4: **Set 4:** $\eta = 0.7$, $\gamma = 10\,\text{Hz}$, $T = 4\,\text{K}$.

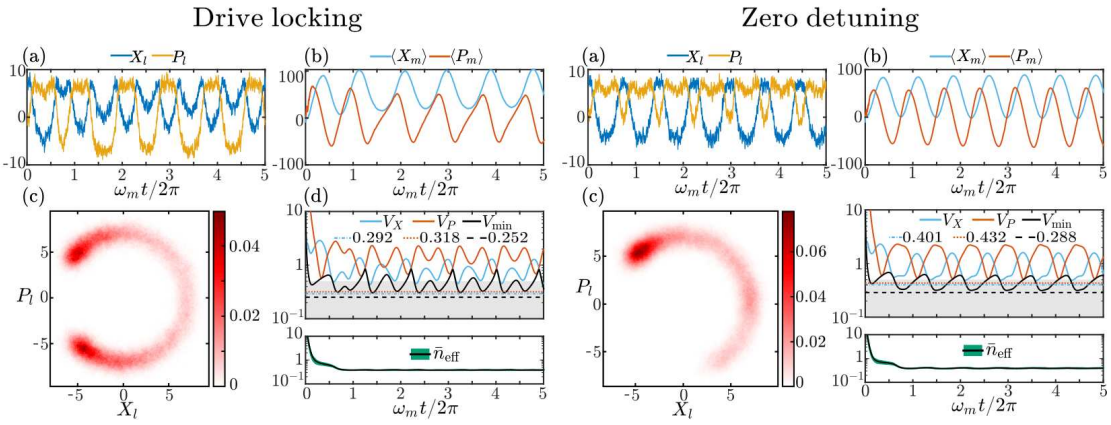


Figure J.5: **Set 5:** $\eta = 0.5$, $\gamma = 10\,\text{Hz}$, $T = 4\,\text{K}$.

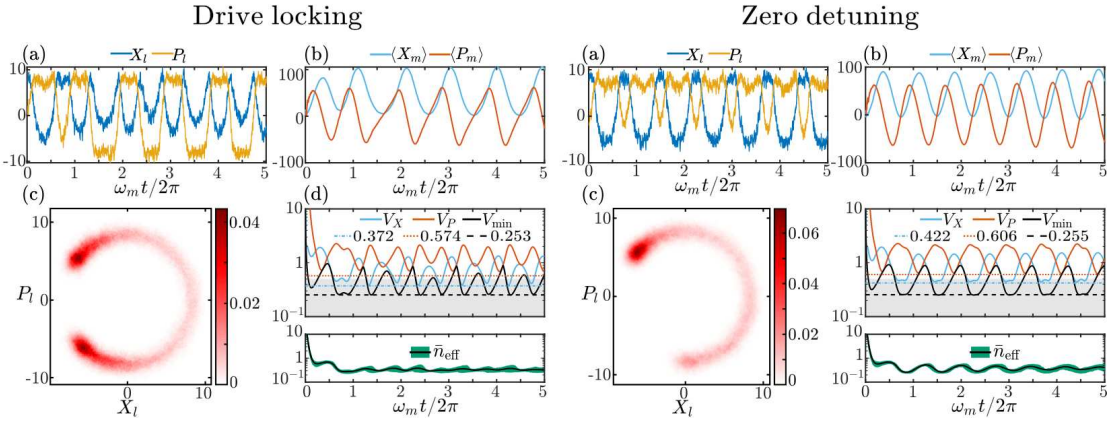


Figure J.6: **Set 6:** $\eta = 0.7$, $\gamma = 100\,\text{Hz}$, $T = 4\,\text{K}$.

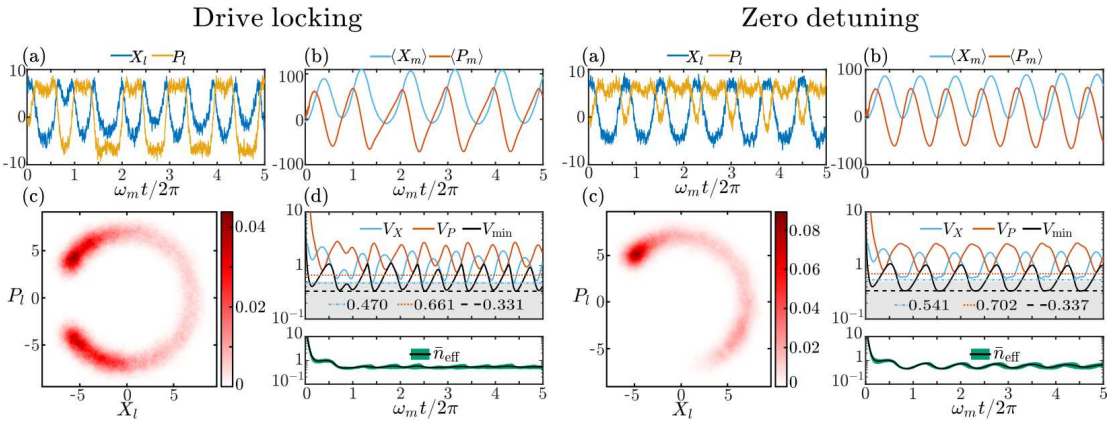


Figure J.7: **Set 7:** $\eta = 0.5$, $\gamma = 100\,\mathrm{Hz}$, $T = 4\,\mathrm{K}$.

Bibliography

[1] J. Clarke and M. R. Vanner, Quantum Science and Technology **4**, 014003 (2019).

[2] J. Clarke, P. Sahium, K. E. Khosla, I. Pikovski, M. S. Kim, and M. R. Vanner, New Journal of Physics **22**, 063001 (2020).

[3] P. Neveu, J. Clarke, M. R. Vanner, and E. Verhagen, New Journal of Physics **23**, 023026 (2021).

[4] G. Enzian, L. Freisem, J. J. Price, A. Ø. Svela, J. Clarke, B. Shajilal, J. Janousek, B. C. Buchler, P. K. Lam, and M. R. Vanner, Physical Review Letters **127**, 243601 (2021).

[5] L. A. Kanari-Naish, J. Clarke, M. R. Vanner, and E. A. Laird, AVS Quantum Science **3**, 045603 (2021).

[6] L. A. Kanari-Naish, J. Clarke, S. Qvarfort, and M. R. Vanner, Quantum Science and Technology **7**, 035012 (2022).

[7] J. Clarke, P. Neveu, K. E. Khosla, E. Verhagen, and M. R. Vanner, Physical Review Letters **131**, 053601 (2023).

[8] J. Clarke, E. A. Cryer-Jenkins, A. Gupta, K. D. Major, J. Zhang, G. Enzian, M. Szczykulska, A. C. Leung, H. Rathee, A. Ø. Svela, et al., Physical Review A **111**, 023516 (2025).

[9] E. A. Cryer-Jenkins, K. D. Major, J. Clarke, G. Enzian, M. Szczykulska, J. Zhang, A. Gupta, A. C. Leung, H. Rathee, A. Ø. Svela, et al., Physical Review Letters **134**, 073601 (2025).

[10] L. A. Kanari-Naish, J. Clarke, S. Qvarfort, and M. R. Vanner, arXiv:2502.19624 (2025).

[11] J. Clarke, in *Quantum Sensing, Imaging, and Precision Metrology III* (SPIE, 2025), vol. 13392, p. 147.

[12] P. Neveu, J. Clarke, M. R. Vanner, and E. Verhagen (In preparation).

[13] J. Clarke, P. Neveu, E. Verhagen, and M. R. Vanner (In preparation).

[14] K. E. Khosla, M. R. Vanner, N. Ares, and E. A. Laird, Physical Review X **8**, 021052 (2018).

[15] S. Barnett and P. M. Radmore, *Methods in theoretical quantum optics* (Oxford University Press, 2002).

[16] C. Gerry, P. Knight, and P. L. Knight, *Introductory quantum optics* (Cambridge University Press, 2005).

[17] D. F. Walls and G. J. Milburn, *Quantum optics* (Springer Science & Business Media, 2007).

[18] U. Leonhardt, *Essential quantum optics: from quantum measurements to black holes* (Cambridge University Press, 2010).

[19] P. Meystre, *Quantum Optics: Taming the Quantum* (Springer Nature, 2021).

[20] A. Einstein, B. Podolsky, and N. Rosen, Physical Review **47**, 777 (1935).

[21] E. Schrödinger, Naturwissenschaften **23**, 844 (1935).

[22] B. Yurke, S. L. McCall, and J. R. Klauder, Physical Review A **33**, 4033 (1986).

[23] M. Dakna, L. Knöll, and D.-G. Welsch, Optics Communications **145**, 309 (1998).

[24] E. P. Wigner, in *Part I: Physical Chemistry. Part II: Solid State Physics* (Springer, 1997), pp. 110–120.

[25] K. Husimi, Proceedings of the Physico-Mathematical Society of Japan. 3rd Series **22**, 264 (1940).

[26] E. Sudarshan, Physical Review Letters **10**, 277 (1963).

[27] R. J. Glauber, Physical Review **131**, 2766 (1963).

[28] K. E. Cahill and R. J. Glauber, Physical Review **177**, 1882 (1969).

[29] H.-P. Breuer, E.-M. Laine, J. Piilo, and B. Vacchini, Reviews of Modern Physics **88**, 021002 (2016).

[30] D. Manzano, AIP Advances **10**, 025106 (2020).

[31] W. E. Lamb Jr and R. C. Retherford, Physical Review **72**, 241 (1947).

[32] C. Gardiner, P. Zoller, and P. Zoller, *Quantum noise: a handbook of Markovian and non-Markovian quantum stochastic methods with applications to quantum optics* (Springer Science & Business Media, 2004).

[33] T. W. Marshall, Proceedings of the Royal Society of London. Series A. Mathematical and Physical Sciences **276**, 475 (1963).

[34] T. H. Boyer, American Journal of Physics **79**, 1163 (2011).

[35] L. Novotny, M. Frimmer, A. Militaru, A. Norrman, O. Romero-Isart, and P. Maurer, Physical Review A **106**, 043511 (2022).

[36] A. O. Caldeira and A. J. Leggett, Physica A: Statistical mechanics and its Applications **121**, 587 (1983).

[37] S. Gao, Physical Review Letters **79**, 3101 (1997).

[38] A. Lampo, S. H. Lim, J. Wehr, P. Massignan, and M. Lewenstein, Physical Review A **94**, 042123 (2016).

[39] M. A. Schlosshauer, *Decoherence: and the quantum-to-classical transition* (Springer Science & Business Media, 2007).

[40] K. Jacobs, Europhysics Letters **85**, 40002 (2009).

[41] M. Schlosshauer, Physics Reports **831**, 1 (2019).

[42] H.-P. Breuer, F. Petruccione, et al., *The theory of open quantum systems* (Oxford University Press on Demand, 2002).

[43] C. W. Gardiner and M. J. Collett, Physical Review A **31**, 3761 (1985).

[44] W. P. Bowen and G. J. Milburn, *Quantum optomechanics* (CRC press, 2015).

[45] M. Aspelmeyer, T. J. Kippenberg, and F. Marquardt, Reviews of Modern Physics **86**, 1391 (2014).

[46] C. L. Degen, F. Reinhard, and P. Cappellaro, Reviews of Modern Physics **89**, 035002 (2017).

[47] C. Weedbrook, S. Pirandola, R. García-Patrón, N. J. Cerf, T. C. Ralph, J. H. Shapiro, and S. Lloyd, Reviews of Modern Physics **84**, 621 (2012).

[48] A. Serafini, *Quantum continuous variables: a primer of theoretical methods* (CRC press, 2017).

[49] R. Simon, N. Mukunda, and B. Dutta, Physical Review A **49**, 1567 (1994).

[50] S. Olivares, The European Physical Journal Special Topics **203**, 3 (2012).

[51] J. Eisert, S. Scheel, and M. B. Plenio, Physical Review Letters **89**, 137903 (2002).

[52] R. Penrose, in *Mathematical proceedings of the Cambridge philosophical society* (Cambridge University Press, 1955), vol. 51, pp. 406–413.

[53] A. Ferraro, S. Olivares, and M. G. Paris, arXiv preprint quant-ph/0503237 (2005).

[54] A. Peres, Physical Review Letters **77**, 1413 (1996).

[55] M. Horodecki, P. Horodecki, and R. Horodecki, Physics Letters A **283**, 1 (2001).

[56] R. Simon, Physical Review Letters **84**, 2726 (2000).

[57] R. F. Werner and M. M. Wolf, Physical Review Letters **86**, 3658 (2001).

[58] J. Lee, M. Kim, Y. Park, and S. Lee, Journal of Modern Optics **47**, 2151 (2000).

[59] K. Audenaert, M. B. Plenio, and J. Eisert, Physical Review Letters **90**, 027901 (2003).

[60] G. Vidal and R. F. Werner, Physical Review A **65**, 032314 (2002).

[61] E. Shchukin and W. Vogel, Physical Review Letters **95**, 230502 (2005).

[62] K. Jacobs, *Quantum measurement theory and its applications* (Cambridge University Press, 2014).

[63] H. M. Wiseman and G. J. Milburn, *Quantum measurement and control* (Cambridge University Press, 2009).

[64] M. A. Nielsen and I. Chuang, *Quantum computation and quantum information* (American Association of Physics Teachers, 2002).

[65] M. G. Genoni, S. Mancini, and A. Serafini, Russian Journal of Mathematical Physics **21**, 329 (2014).

[66] M. G. Genoni, L. Lami, and A. Serafini, Contemporary Physics **57**, 331 (2016).

[67] C. M. Caves and G. J. Milburn, Physical Review A **36**, 5543 (1987).

[68] A. A. Clerk, M. H. Devoret, S. M. Girvin, F. Marquardt, and R. J. Schoelkopf, Reviews of Modern Physics **82**, 1155 (2010).

[69] S. L. Adler, Physics Letters A **265**, 58 (2000).

[70] H. M. Wiseman and L. Diósi, Chemical Physics **268**, 91 (2001).

[71] K. Jacobs and D. A. Steck, Contemporary Physics **47**, 279 (2006).

[72] M. C. Hunter, in *Beyond Mimesis and Convention* (Springer, 2010), pp. 193–219.

[73] C. Baxter and R. Loudon, Journal of Modern Optics **57**, 830 (2010).

[74] T. P. Purdy, D. Brooks, T. Botter, N. Brahms, Z.-Y. Ma, and D. M. Stamper-Kurn, Physical Review Letters **105**, 133602 (2010).

[75] M. H. Schleier-Smith, I. D. Leroux, H. Zhang, M. A. Van Camp, and V. Vuletić, Physical Review Letters **107**, 143005 (2011).

[76] T. Rocheleau, T. Ndukum, C. Macklin, J. Hertzberg, A. Clerk, and K. Schwab, Nature **463**, 72 (2010).

[77] J. D. Teufel, T. Donner, D. Li, J. W. Harlow, M. Allman, K. Cicak, A. J. Sirois, J. D. Whittaker, K. W. Lehnert, and R. W. Simmonds, Nature **475**, 359 (2011).

[78] J. Thompson, B. Zwickl, A. Jayich, F. Marquardt, S. Girvin, and J. Harris, Nature **452**, 72 (2008).

[79] I. Favero, S. Stapfner, D. Hunger, P. Paulitschke, J. Reichel, H. Lorenz, E. M. Weig, and K. Karrai, Optics Express **17**, 12813 (2009).

[80] M. Eichenfield, R. Camacho, J. Chan, K. J. Vahala, and O. Painter, Nature **459**, 550 (2009).

[81] J. Riedrich-Möller, L. Kipfstuhl, C. Hepp, E. Neu, C. Pauly, F. Mücklich, A. Baur, M. Wandt, S. Wolff, M. Fischer, et al., Nature Nanotechnology **7**, 69 (2012).

[82] G. Anetsberger, O. Arcizet, Q. P. Unterreithmeier, R. Rivière, A. Schliesser, E. M. Weig, J. P. Kotthaus, and T. J. Kippenberg, Nature Physics **5**, 909 (2009).

[83] P. H. Kim, C. Doolin, B. D. Hauer, A. J. MacDonald, M. R. Freeman, P. E. Barclay, and J. P. Davis, Applied Physics Letters **102**, 053102 (2013).

[84] A. Abramovici, W. E. Althouse, R. W. Drever, Y. Gürsel, S. Kawamura, F. J. Raab, D. Shoemaker, L. Sievers, R. E. Spero, K. S. Thorne, et al., Science **256**, 325 (1992).

[85] B. P. Abbott, R. Abbott, T. D. Abbott, M. R. Abernathy, F. Acernese, K. Ackley, C. Adams, T. Adams, P. Addesso, R. X. Adhikari, et al., Physical Review Letters **116**, 061102 (2016).

[86] M. Metcalfe, Applied Physics Reviews **1**, 031105 (2014).

[87] S. Barzanjeh, A. Xuereb, S. Gröblacher, M. Paternostro, C. A. Regal, and E. M. Weig, Nature Physics **18**, 15–24 (2021).

[88] G. Ranjit, M. Cunningham, K. Casey, and A. A. Geraci, Physical Review A **93**, 053801 (2016).

[89] W. Zhao, S.-D. Zhang, A. Miranowicz, and H. Jing, Science China Physics, Mechanics & Astronomy **63**, 1 (2020).

[90] N. Lauk, N. Sinclair, S. Barzanjeh, J. P. Covey, M. Saffman, M. Spiropulu, and C. Simon, Quantum Science and Technology **5**, 020501 (2020).

[91] N. J. Lambert, A. Rueda, F. Sedlmeir, and H. G. Schwefel, Advanced Quantum Technologies **3**, 1900077 (2020).

[92] S. Bose, K. Jacobs, and P. Knight, Physical Review A **56**, 4175 (1997).

[93] F. Khalili, S. Danilishin, H. Miao, H. Müller-Ebhardt, H. Yang, and Y. Chen, Physical Review Letters **105**, 070403 (2010).

[94] L. Garziano, R. Stassi, V. Macrí, S. Savasta, and O. Di Stefano, Physical Review A **91**, 023809 (2015).

[95] W. Marshall, C. Simon, R. Penrose, and D. Bouwmeester, Physical Review Letters **91**, 130401 (2003).

[96] H. Miao, *Exploring macroscopic quantum mechanics in optomechanical devices* (Springer Science & Business Media, 2012).

[97] C. Law, Physical Review A **51**, 2537 (1995).

[98] A. Pace, M. Collett, and D. Walls, Physical Review A **47**, 3173 (1993).

[99] G. J. Milburn and M. J. Woolley, Acta Physica Slovaca **61**, 483 (2011).

[100] F. Elste, S. M. Girvin, and A. A. Clerk, Physical Review Letters **102**, 207209 (2009).

[101] A. Xuereb, R. Schnabel, and K. Hammerer, Physical Review Letters **107**, 213604 (2011).

[102] P. Meystre, Annalen der Physik **525**, 215 (2013).

[103] C. Law, Physical Review A **49**, 433 (1994).

[104] A. Jayich, J. Sankey, B. Zwickl, C. Yang, J. Thompson, S. Girvin, A. Clerk, F. Marquardt, and J. Harris, New Journal of Physics **10**, 095008 (2008).

[105] J.-Q. Liao and F. Nori, Scientific Reports **4**, 1 (2014).

[106] S. Butera and R. Passante, Physical Review Letters **111**, 060403 (2013).

[107] K. Sala and T. Tufarelli, Scientific Reports **8**, 1 (2018).

[108] C. Doolin, B. Hauer, P. Kim, A. MacDonald, H. Ramp, and J. Davis, Physical Review A **89**, 053838 (2014).

[109] M. Poot and H. S. van der Zant, Physics Reports **511**, 273 (2012).

[110] K. W. Murch, K. L. Moore, S. Gupta, and D. M. Stamper-Kurn, Nature Physics **4**, 561 (2008).

[111] P. Forn-Díaz, L. Lamata, E. Rico, J. Kono, and E. Solano, Reviews of Modern Physics **91**, 025005 (2019).

[112] D. J. Wilson, V. Sudhir, N. Piro, R. Schilling, A. Ghadimi, and T. J. Kippenberg, Nature **524**, 325 (2015).

[113] M. Rossi, D. Mason, J. Chen, Y. Tsaturyan, and A. Schliesser, Nature **563**, 53 (2018).

[114] J. T. Muhonen, G. R. La Gala, R. Leijssen, and E. Verhagen, Physical Review Letters **123**, 113601 (2019).

[115] K. Børkje, Physical Review A **101**, 053833 (2020).

[116] A. Rimberg, M. Blencowe, A. Armour, and P. Nation, New Journal of Physics **16**, 055008 (2014).

[117] I. Iorsh, A. Poshakinskiy, and A. Poddubny, Physical Review Letters **125**, 183601 (2020).

[118] A. Nunnenkamp, K. Børkje, and S. M. Girvin, Physical Review Letters **107**, 063602 (2011).

[119] P. Rabl, Physical Review Letters **107**, 063601 (2011).

[120] D. Hu, S.-Y. Huang, J.-Q. Liao, L. Tian, and H.-S. Goan, Physical Review A **91**, 013812 (2015).

[121] A. F. Kockum, A. Miranowicz, S. De Liberato, S. Savasta, and F. Nori, Nature Reviews Physics **1**, 19 (2019).

[122] S. Gröblacher, K. Hammerer, M. R. Vanner, and M. Aspelmeyer, Nature **460**, 724 (2009).

[123] J. D. Teufel, D. Li, M. Allman, K. Cicak, A. Sirois, J. Whittaker, and R. Simmonds, Nature **471**, 204 (2011).

[124] G. Enzian, M. Szczykulska, J. Silver, L. Del Bino, S. Zhang, I. A. Walmsley, P. Del'Haye, and M. R. Vanner, Optica **6**, 7 (2019).

[125] J. M. Dobrindt, I. Wilson-Rae, and T. J. Kippenberg, Physical Review Letters **101**, 263602 (2008).

[126] E. Verhagen, S. Deléglise, S. Weis, A. Schliesser, and T. J. Kippenberg, Nature **482**, 63 (2012).

[127] A. Ranfagni, P. Vezio, M. Calamai, A. Chowdhury, F. Marino, and F. Marin, Nature Physics **17**, 1120 (2021).

[128] F. Benz, M. K. Schmidt, A. Dreismann, R. Chikkaraddy, Y. Zhang, A. Demetriadou, C. Carnegie, H. Ohadi, B. De Nijs, R. Esteban, et al., Science **354**, 726 (2016).

[129] Y.-D. Wang and A. A. Clerk, Physical Review Letters **108**, 153603 (2012).

[130] S. G. Hofer, W. Wieczorek, M. Aspelmeyer, and K. Hammerer, Physical Review A **84**, 052327 (2011).

[131] F. Brennecke, S. Ritter, T. Donner, and T. Esslinger, Science **322**, 235 (2008).

[132] G. A. Brawley, M. R. Vanner, P. E. Larsen, S. Schmid, A. Boisen, and W. P. Bowen, Nature Communications **7**, 10988 (2016).

[133] R. Leijssen, G. R. La Gala, L. Freisem, J. T. Muhonen, and E. Verhagen, Nature Communications **8**, 16024 (2017).

[134] S. A. Fedorov, A. Beccari, A. Arabmoheghi, D. J. Wilson, N. J. Engelsen, and T. J. Kippenberg, Optica **7**, 1609 (2020).

[135] C. M. Pluchar, A. R. Agrawal, and D. J. Wilson, Optica **10**, 1543 (2023).

[136] A. Schliesser, R. Rivière, G. Anetsberger, O. Arcizet, and T. J. Kippenberg, Nature Physics **4**, 415 (2008).

[137] K. Vahala, M. Herrmann, S. Knünz, V. Batteiger, G. Saathoff, T. Hänsch, and T. Udem, Nature Physics **5**, 682 (2009).

[138] A. C. Doherty and K. Jacobs, Physical Review A **60**, 2700 (1999).

[139] M. R. Vanner, I. Pikovski, G. D. Cole, M. Kim, Č. Brukner, K. Hammerer, G. J. Milburn, and M. Aspelmeyer, Proceedings of the National Academy of Sciences **108**, 16182 (2011).

[140] M. R. Vanner, J. Hofer, G. D. Cole, and M. Aspelmeyer, Nature Communications **4**, 1 (2013).

[141] A. Dorsel, J. D. McCullen, P. Meystre, E. Vignes, and H. Walther, Physical Review Letters **51**, 1550 (1983).

[142] V. B. Braginskii, Y. I. Vorontsov, and F. Y. Khalili, JETP Letters **27** (1978).

[143] V. B. Braginsky, Y. I. Vorontsov, and K. S. Thorne, Science **209**, 547 (1980).

[144] V. B. Braginsky and F. Y. Khalili, *Quantum measurement* (Cambridge University Press, 1995).

[145] I. Pikovski, M. R. Vanner, M. Aspelmeyer, M. Kim, and Č. Brukner, Nature Physics **8**, 393 (2012).

[146] J. S. Bennett, K. Khosla, L. S. Madsen, M. R. Vanner, H. Rubinsztein-Dunlop, and W. P. Bowen, New Journal of Physics **18**, 053030 (2016).

[147] K. E. Khosla, M. R. Vanner, W. P. Bowen, and G. J. Milburn, New Journal of Physics **15**, 043025 (2013).

[148] M. Brunelli, D. Malz, A. Schliesser, and A. Nunnenkamp, Physical Review Research **2**, 023241 (2020).

[149] M. Aspelmeyer, T. J. Kippenberg, and F. Marquardt, *Cavity optomechanics: nano-and micromechanical resonators interacting with light* (Springer, 2014).

[150] A. C. Doherty, A. Szorkovszky, G. Harris, and W. Bowen, Philosophical Transactions of the Royal Society A: Mathematical, Physical and Engineering Sciences **370**, 5338 (2012).

[151] K. E. Khosla, Ph.D. thesis, University of Queensland (2019).

[152] R. Almog, S. Zaitsev, O. Shtempluck, and E. Buks, Physical Review Letters **98**, 078103 (2007).

[153] X.-Y. Lü, J.-Q. Liao, L. Tian, and F. Nori, Physical Review A **91**, 013834 (2015).

[154] R. Meucci, S. Euzzor, E. Pugliese, S. Zambrano, M. R. Gallas, and J. A. Gallas, Physical Review Letters **116**, 044101 (2016).

[155] M. Ringbauer, T. J. Weinhold, L. Howard, A. White, and M. Vanner, New Journal of Physics **20**, 053042 (2018).

[156] G. C. Ghirardi, A. Rimini, and T. Weber, Physical Review D **34**, 470 (1986).

[157] R. Penrose, General Relativity and Gravitation **28**, 581 (1996).

[158] L. Diósi, Physical Review A **40**, 1165 (1989).

[159] M. Bahrami, M. Paternostro, A. Bassi, and H. Ulbricht, Physical Review Letters **112**, 210404 (2014).

[160] A. Bassi, K. Lochan, S. Satin, T. P. Singh, and H. Ulbricht, Reviews of Modern Physics **85**, 471 (2013).

[161] S. Bose, K. Jacobs, and P. L. Knight, Physical Review A **59**, 3204 (1999).

[162] J. D. Bekenstein, Physical Review D **86**, 124040 (2012).

[163] P. Bosso, S. Das, I. Pikovski, and M. R. Vanner, Physical Review A **96**, 023849 (2017).

[164] S. Bose, A. Mazumdar, G. W. Morley, H. Ulbricht, M. Toroš, M. Paternostro, A. A. Geraci, P. F. Barker, M. Kim, and G. Milburn, Physical Review Letters **119**, 240401 (2017).

[165] C. Marletto and V. Vedral, Physical Review Letters **119**, 240402 (2017).

[166] H. Miao, D. Martynov, H. Yang, and A. Datta, Physical Review A **101**, 063804 (2020).

[167] P. Haslinger, N. Dörre, P. Geyer, J. Rodewald, S. Nimmrichter, and M. Arndt, Nature Physics **9**, 144 (2013).

[168] J. Clarke and F. K. Wilhelm, Nature **453**, 1031 (2008).

[169] M. H. Devoret and R. J. Schoelkopf, Science **339**, 1169 (2013).

[170] T. Berrada, S. van Frank, R. Bücker, T. Schumm, J.-F. Schaff, and J. Schmiedmayer, Nature Communications **4**, 1 (2013).

[171] A. Armour, M. Blencowe, and K. C. Schwab, Physical Review Letters **88**, 148301 (2002).

[172] U. Akram, N. Kiesel, M. Aspelmeyer, and G. J. Milburn, New Journal of Physics **12**, 083030 (2010).

[173] P. Marek and R. Filip, Physical Review A **81**, 042325 (2010).

[174] C. Lei, A. Weinstein, J. Suh, E. Wollman, A. Kronwald, F. Marquardt, A. Clerk, and K. Schwab, Physical Review Letters **117**, 100801 (2016).

[175] O. Romero-Isart, A. C. Pflanzer, F. Blaser, R. Kaltenbaek, N. Kiesel, M. Aspelmeyer, and J. I. Cirac, Physical Review Letters **107**, 020405 (2011).

[176] M. R. Vanner, Physical Review X **1**, 021011 (2011).

[177] K. C. Lee, B. J. Sussman, M. R. Sprague, P. Michelberger, K. F. Reim, J. Nunn, N. K. Langford, P. Bustard, D. Jaksch, and I. A. Walmsley, Nature Photonics **6**, 41 (2012).

[178] M. R. Vanner, M. Aspelmeyer, and M. S. Kim, Physical Review Letters **110**, 010504 (2013).

[179] R. Riedinger, S. Hong, R. A. Norte, J. A. Slater, J. Shang, A. G. Krause, V. Anant, M. Aspelmeyer, and S. Gröblacher, Nature **530**, 313 (2016).

[180] G. Enzian, J. J. Price, L. Freisem, J. Nunn, J. Janousek, B. C. Buchler, P. K. Lam, and M. R. Vanner, Physical Review Letters **126**, 033601 (2021).

[181] R. N. Patel, T. P. McKenna, Z. Wang, J. D. Witmer, W. Jiang, R. Van Laer, C. J. Sarabalis, and A. H. Safavi-Naeini, Physical Review Letters **127**, 133602 (2021).

[182] T. Milburn, M. Kim, and M. Vanner, Physical Review A **93**, 053818 (2016).

[183] U. B. Hoff, J. Kollath-Bönig, J. S. Neergaard-Nielsen, and U. L. Andersen, Physical Review Letters **117**, 143601 (2016).

[184] R. W. Andrews, R. W. Peterson, T. P. Purdy, K. Cicak, R. W. Simmonds, C. A. Regal, and K. W. Lehnert, Nature Physics **10**, 321 (2014).

[185] L. Tian, Annalen der Physik **527**, 1 (2015).

[186] K. Xia, M. R. Vanner, and J. Twamley, Scientific Reports **4**, 5571 (2014).

[187] D. Rugar, R. Budakian, H. Mamin, and B. Chui, Nature **430**, 329 (2004).

[188] M. Hosseini, G. Guccione, H. J. Slatyer, B. C. Buchler, and P. K. Lam, Nature Communications **5**, 4663 (2014).

[189] K. Stannigel, P. Komar, S. Habraken, S. Bennett, M. D. Lukin, P. Zoller, and P. Rabl, Physical Review Letters **109**, 013603 (2012).

[190] F. Fröwis, P. Sekatski, W. Dür, N. Gisin, and N. Sangouard, Reviews of Modern Physics **90**, 025004 (2018).

[191] C.-W. Lee and H. Jeong, Physical Review Letters **106**, 220401 (2011).

[192] D. Petz and C. Ghinea, in *Quantum probability and related topics* (World Scientific, 2011), pp. 261–281.

[193] F. Fröwis and W. Dür, New Journal of Physics **14**, 093039 (2012).

[194] E. Oudot, P. Sekatski, F. Fröwis, N. Gisin, and N. Sangouard, JOSA B **32**, 2190 (2015).

[195] V. Giovannetti, S. Lloyd, and L. Maccone, Nature Photonics **5**, 222 (2011).

[196] M. Tsang, New Journal of Physics **15**, 073005 (2013).

[197] R. Demkowicz-Dobrzański, M. Jarzyna, and J. Kołodyński, Progress in Optics **60**, 345 (2015).

[198] S. L. Braunstein and C. M. Caves, Physical Review Letters **72**, 3439 (1994).

[199] W. J. Munro, K. Nemoto, G. J. Milburn, and S. L. Braunstein, Physical Review A **66**, 023819 (2002).

[200] D. R. Arvidsson-Shukur, N. Yunger Halpern, H. V. Lepage, A. A. Lasek, C. H. Barnes, and S. Lloyd, Nature Communications **11**, 3775 (2020).

[201] N. B. Lupu-Gladstein, B. Y. Yilmaz, D. R. Arvidsson-Shukur, A. Brodutch, A. O. Pang, A. M. Steinberg, and N. Y. Halpern, Physical Review Letters **128**, 220504 (2022).

[202] M. Reck, A. Zeilinger, H. J. Bernstein, and P. Bertani, Physical Review Letters **73**, 58 (1994).

[203] C. Gerry and P. Knight, American Journal of Physics **65**, 964 (1997).

[204] W. H. Zurek, Nature **412**, 712 (2001).

[205] L. A. Howard, T. J. Weinhold, F. Shahandeh, J. Combes, M. R. Vanner, A. G. White, and M. Ringbauer, Physical Review Letters **123**, 020402 (2019).

[206] M. D. Eisaman, J. Fan, A. Migdall, and S. V. Polyakov, Review of Scientific Instruments **82**, 071101 (2011).

[207] N. Somaschi, V. Giesz, L. De Santis, J. Loredo, M. P. Almeida, G. Hornecker, S. L. Portalupi, T. Grange, C. Anton, J. Demory, et al., Nature Photonics **10**, 340 (2016).

[208] J. Stachurski, S. Tamariz, G. Callsen, R. Butté, and N. Grandjean, Light: Science & Applications **11**, 1 (2022).

[209] A. Kuhn, M. Hennrich, and G. Rempe, Physical Review Letters **89**, 067901 (2002).

[210] B. Pepper, R. Ghobadi, E. Jeffrey, C. Simon, and D. Bouwmeester, Physical Review Letters **109**, 023601 (2012).

[211] Z. H. Musslimani, S. L. Braunstein, A. Mann, and M. Revzen, Physical Review A **51**, 4967 (1995).

[212] A. Kenfack and K. Życzkowski, Journal of Optics B: Quantum and Semiclassical Optics **6**, 396 (2004).

[213] S. Luo, Letters in Mathematical Physics **53**, 243 (2000).

[214] B. Yadin and V. Vedral, Physical Review A **93**, 022122 (2016).

[215] O. Arcizet, V. Jacques, A. Siria, P. Poncharal, P. Vincent, and S. Seidelin, Nature Physics **7**, 879 (2011).

[216] Z.-q. Yin, T. Li, X. Zhang, and L. Duan, Physical Review A **88**, 033614 (2013).

[217] C. Regal and K. Lehnert, in *Journal of Physics: Conference Series* (IOP Publishing, 2011), vol. 264, p. 012025.

[218] F. Lecocq, J. D. Teufel, J. Aumentado, and R. W. Simmonds, Nature Physics **11**, 635 (2015).

[219] T. Bera, S. Majumder, S. K. Sahu, and V. Singh, Communications Physics **4**, 1 (2021).

[220] A. Heidmann, R. Horowicz, S. Reynaud, E. Giacobino, C. Fabre, and G. Camy, Physical Review Letters **59**, 2555 (1987).

[221] A. Furusawa, J. L. Sørensen, S. L. Braunstein, C. A. Fuchs, H. J. Kimble, and E. S. Polzik, Science **282**, 706 (1998).

[222] S. L. Braunstein and P. Van Loock, Reviews of Modern Physics **77**, 513 (2005).

[223] S. J. Freedman and J. F. Clauser, Physical Review Letters **28**, 938 (1972).

[224] A. Aspect, P. Grangier, and G. Roger, Physical Review Letters **47**, 460 (1981).

[225] P. Walther, J.-W. Pan, M. Aspelmeyer, R. Ursin, S. Gasparoni, and A. Zeilinger, Nature **429**, 158 (2004).

[226] M. W. Mitchell, J. S. Lundeen, and A. M. Steinberg, Nature **429**, 161 (2004).

[227] B. Julsgaard, A. Kozhekin, and E. S. Polzik, Nature **413**, 400 (2001).

[228] C.-W. Chou, J. Laurat, H. Deng, K. S. Choi, H. De Riedmatten, D. Felinto, and H. J. Kimble, Science **316**, 1316 (2007).

[229] J. Hofmann, M. Krug, N. Ortegel, L. Gérard, M. Weber, W. Rosenfeld, and H. Weinfurter, Science **337**, 72 (2012).

[230] H. Bernien, B. Hensen, W. Pfaff, G. Koolstra, M. S. Blok, L. Robledo, T. H. Taminiau, M. Markham, D. J. Twitchen, L. Childress, et al., Nature **497**, 86 (2013).

[231] S. Qvarfort, Ph.D. thesis, University College London (2020).

[232] N. Gisin, G. Ribordy, W. Tittel, and H. Zbinden, Reviews of Modern Physics **74**, 145 (2002).

[233] J. S. Bell, Physics Physique Fizika **1**, 195 (1964).

[234] J. D. Jost, J. Home, J. M. Amini, D. Hanneke, R. Ozeri, C. Langer, J. J. Bollinger, D. Leibfried, and D. J. Wineland, Nature **459**, 683 (2009).

[235] A. Parkins and H. Kimble, Journal of Optics B: Quantum and Semiclassical Optics **1**, 496 (1999).

[236] J. Zhang, K. Peng, and S. L. Braunstein, Physical Review A **68**, 013808 (2003).

[237] M. S. Kim, W. Son, V. Bužek, and P. L. Knight, Physical Review A **65**, 032323 (2002).

[238] D. Vitali, S. Gigan, A. Ferreira, H. Böhm, P. Tombesi, A. Guerreiro, V. Vedral, A. Zeilinger, and M. Aspelmeyer, Physical Review Letters **98**, 030405 (2007).

[239] M. Paternostro, D. Vitali, S. Gigan, M. Kim, C. Brukner, J. Eisert, and M. Aspelmeyer, Physical Review Letters **99**, 250401 (2007).

[240] A. A. Rakhubovsky and R. Filip, Physical Review A **91**, 062317 (2015).

[241] Q. Lin and B. He, Optics Express **23**, 24497 (2015).

[242] S. Mancini, V. Giovannetti, D. Vitali, and P. Tombesi, Physical Review Letters **88**, 120401 (2002).

[243] M. J. Hartmann and M. B. Plenio, Physical Review Letters **101**, 200503 (2008).

[244] M. Pinard, A. Dantan, D. Vitali, O. Arcizet, T. Briant, and A. Heidmann, EPL (Europhysics Letters) **72**, 747 (2005).

[245] S. Huang and G. Agarwal, New Journal of Physics **11**, 103044 (2009).

[246] S. Qvarfort, S. Bose, and A. Serafini, Journal of Physics B: Atomic, Molecular and Optical Physics **53**, 235501 (2020).

[247] J. Poyatos, J. I. Cirac, and P. Zoller, Physical Review Letters **77**, 4728 (1996).

[248] M. Woolley and A. Clerk, Physical Review A **89**, 063805 (2014).

[249] M. Brunelli, D. Malz, and A. Nunnenkamp, Physical Review Letters **123**, 093602 (2019).

[250] S. Pirandola, D. Vitali, P. Tombesi, and S. Lloyd, Physical Review Letters **97**, 150403 (2006).

[251] N. Vostrosablin, A. A. Rakhubovsky, and R. Filip, Physical Review A **94**, 063801 (2016).

[252] G. Vacanti, M. Paternostro, G. M. Palma, and V. Vedral, New Journal of Physics **10**, 095014 (2008).

[253] K. Børkje, A. Nunnenkamp, and S. Girvin, Physical Review Letters **107**, 123601 (2011).

[254] T. A. Palomaki, J. D. Teufel, R. W. Simmonds, and K. W. Lehnert, Science **342**, 710 (2013).

[255] L.-M. Duan, G. Giedke, J. I. Cirac, and P. Zoller, Physical Review Letters **84**, 2722 (2000).

[256] K. C. Lee, M. R. Sprague, B. J. Sussman, J. Nunn, N. K. Langford, X. M. Jin, T. Champion, P. Michelberger, K. F. Reim, D. England, et al., Science **334**, 1253 (2011).

[257] R. Riedinger, A. Wallucks, I. Marinković, C. Löschnauer, M. Aspelmeyer, S. Hong, and S. Gröblacher, Nature **556**, 473 (2018).

[258] L.-M. Duan, M. D. Lukin, J. I. Cirac, and P. Zoller, Nature **414**, 413 (2001).

[259] K. S. Choi, H. Deng, J. Laurat, and H. Kimble, Nature **452**, 67 (2008).

[260] C. F. Ockeloen-Korppi, E. Damskägg, J. M. Pirkkalainen, M. Asjad, A. A. Clerk, F. Massel, M. J. Woolley, and M. A. Sillanpää, Nature **556**, 478 (2018).

[261] L. Mercier de Lépinay, C. F. Ockeloen-Korppi, M. J. Woolley, and M. A. Sillanpää, Science **372**, 625 (2021).

[262] S. Kotler, G. A. Peterson, E. Shojaee, F. Lecocq, K. Cicak, A. Kwiatkowski, S. Geller, S. Glancy, E. Knill, R. W. Simmonds, et al., Science **372**, 622 (2021).

[263] P. Sekatski, M. Aspelmeyer, and N. Sangouard, Physical Review Letters **112**, 080502 (2014).

[264] L. F. Buchmann, L. Zhang, A. Chiruvelli, and P. Meystre, Physical Review Letters **108**, 210403 (2012).

[265] R. Leijssen and E. Verhagen, Scientific Reports **5**, 15974 (2015).

[266] G. La Gala, J. P. Mathew, P. Neveu, and E. Verhagen, Journal of Physics D: Applied Physics **55**, 225101 (2022).

[267] S. M. Meenehan, J. D. Cohen, G. S. MacCabe, F. Marsili, M. D. Shaw, and O. Painter, Physical Review X **5**, 041002 (2015).

[268] Q. Zheng, Y. Yao, and Y. Li, Physical Review A **93**, 013848 (2016).

[269] N. Vostrosablin, A. A. Rakhubovsky, U. B. Hoff, U. L. Andersen, and R. Filip, New Journal of Physics **20**, 083042 (2018).

[270] V. Montenegro, A. Ferraro, and S. Bose, Physical Review A **100**, 042310 (2019).

[271] W. H. Furry, Physical Review **49**, 393 (1936).

[272] S. Kiesewetter, R. Teh, P. Drummond, and M. Reid, Physical Review Letters **119**, 023601 (2017).

[273] F. Armata, L. Latmiral, I. Pikovski, M. R. Vanner, Č. Brukner, and M. Kim, Physical Review A **93**, 063862 (2016).

[274] A. S. Holevo and R. F. Werner, Physical Review A **63**, 032312 (2001).

[275] A. Ferraro, S. Olivares, and M. G. A. Paris, arXiv quant-ph/0503237 (2005).

[276] L. Mišta Jr and R. Filip, Physical Review A **71**, 032342 (2005).

[277] R. Filip, Physical Review A **78**, 012329 (2008).

[278] A. Serafini, S. De Siena, F. Illuminati, and M. G. A. Paris, Journal of Optics B: Quantum and Semiclassical Optics **6**, S591 (2004).

[279] R. Filip, Physical Review A **87**, 042308 (2013).

[280] R. A. Brewster, T. B. Pittman, and J. D. Franson, Physical Review A **98**, 033818 (2018).

[281] H. Le Jeannic, A. Cavaillès, K. Huang, R. Filip, and J. Laurat, Physical Review Letters **120**, 073603 (2018).

[282] V. Giovannetti, S. Guha, S. Lloyd, L. Maccone, and J. H. Shapiro, Physical Review A **70**, 032315 (2004).

[283] A. Mari, V. Giovannetti, and A. S. Holevo, Nature Communications **5**, 3826 (2014).

[284] R. E. Slusher, P. Grangier, A. LaPorta, B. Yurke, and M. Potasek, Physical Review Letters **59**, 2566 (1987).

[285] A. Ourjoumtsev, R. Tualle-Brouri, J. Laurat, and P. Grangier, Science **312**, 83 (2006).

[286] Y. Miwa, J.-i. Yoshikawa, N. Iwata, M. Endo, P. Marek, R. Filip, P. van Loock, and A. Furusawa, Physical Review Letters **113**, 013601 (2014).

[287] C. H. Bennett, D. P. DiVincenzo, J. A. Smolin, and W. K. Wootters, Physical Review A **54**, 3824 (1996).

[288] G. Giedke, M. M. Wolf, O. Krüger, R. F. Werner, and J. I. Cirac, Physical Review Letters **91**, 107901 (2003).

[289] A. Shkarin, N. Flowers-Jacobs, S. Hoch, A. Kashkanova, C. Deutsch, J. Reichel, and J. Harris, Physical Review Letters **112**, 013602 (2014).

[290] P. Piergentili, L. Catalini, M. Bawaj, S. Zippilli, N. Malossi, R. Natali, D. Vitali, and G. Di Giuseppe, New Journal of Physics **20**, 083024 (2018).

[291] C. Gärtner, J. P. Moura, W. Haaxman, R. A. Norte, and S. Gröblacher, Nano Letters **18**, 7171 (2018).

[292] J. P. Mathew, J. d. Pino, and E. Verhagen, Nature Nanotechnology **15**, 198 (2020).

[293] U. Akram, W. P. Bowen, and G. J. Milburn, New Journal of Physics **15**, 093007 (2013).

[294] B. Xiong, X. Li, S.-L. Chao, Z. Yang, W.-Z. Zhang, and L. Zhou, Optics Express **27**, 13547 (2019).

[295] M. G. Genoni, M. G. Paris, and K. Banaszek, Physical Review A **78**, 060303 (2008).

[296] M. G. Genoni and M. G. Paris, Physical Review A **82**, 052341 (2010).

[297] P. Marian, I. Ghiu, and T. A. Marian, Physical Review A **88**, 012316 (2013).

[298] S. Walborn, B. Taketani, A. Salles, F. Toscano, and R. de Matos Filho, Physical Review Letters **103**, 160505 (2009).

[299] E. Shchukin, T. Richter, and W. Vogel, Physical Review A **71**, 011802 (2005).

[300] D. Zhang, D. Barral, Y. Cai, Y. Zhang, M. Xiao, and K. Bencheikh, Physical Review Letters **127**, 150502 (2021).

[301] C. Ottaviani, C. Lupo, A. Ferraro, M. Paternostro, and S. Pirandola, Physical Review A **99**, 030301 (2019).

[302] M. Dakna, T. Anhut, T. Opatrnỳ, L. Knöll, and D.-G. Welsch, Physical Review A **55**, 3184 (1997).

[303] J. Wenger, R. Tualle-Brouri, and P. Grangier, Physical Review Letters **92**, 153601 (2004).

[304] J. S. Neergaard-Nielsen, B. M. Nielsen, C. Hettich, K. Mølmer, and E. S. Polzik, Physical Review Letters **97**, 083604 (2006).

[305] G. Agarwal and K. Tara, Physical Review A **43**, 492 (1991).

[306] A. Zavatta, S. Viciani, and M. Bellini, Science **306**, 660 (2004).

[307] A. Zavatta, V. Parigi, and M. Bellini, Physical Review A **75**, 052106 (2007).

[308] V. Parigi, A. Zavatta, M. Kim, and M. Bellini, Science **317**, 1890 (2007).

[309] M. S. Kim, H. Jeong, A. Zavatta, V. Parigi, and M. Bellini, Physical Review Letters **101**, 260401 (2008).

[310] A. Zavatta, V. Parigi, M. Kim, H. Jeong, and M. Bellini, Physical Review Letters **103**, 140406 (2009).

[311] P. Kok, W. J. Munro, K. Nemoto, T. C. Ralph, J. P. Dowling, and G. J. Milburn, Reviews of Modern Physics **79**, 135 (2007).

[312] J. L. O'brien, A. Furusawa, and J. Vučković, Nature Photonics **3**, 687 (2009).

[313] A. I. Lvovsky and M. G. Raymer, Reviews of Modern Physics **81**, 299 (2009).

[314] T. J. Dunn, I. A. Walmsley, and S. Mukamel, Physical Review Letters **74**, 884 (1995).

[315] E. Skovsen, H. Stapelfeldt, S. Juhl, and K. Mølmer, Physical Review Letters **91**, 090406 (2003).

[316] Y. Chu, P. Kharel, W. H. Renninger, L. D. Burkhart, L. Frunzio, P. T. Rakich, and R. J. Schoelkopf, Science **358**, 199 (2017).

[317] Y. Chu, P. Kharel, T. Yoon, L. Frunzio, P. T. Rakich, and R. J. Schoelkopf, Nature **563**, 666 (2018).

[318] K. J. Satzinger, Y. Zhong, H.-S. Chang, G. A. Peairs, A. Bienfait, M.-H. Chou, A. Cleland, C. R. Conner, É. Dumur, J. Grebel, et al., Nature **563**, 661 (2018).

[319] M. Tomes, F. Marquardt, G. Bahl, and T. Carmon, Physical Review A **84**, 063806 (2011).

[320] G. Bahl, M. Tomes, F. Marquardt, and T. Carmon, Nature Physics **8**, 203 (2012).

[321] C.-H. Dong, Z. Shen, C.-L. Zou, Y.-L. Zhang, W. Fu, and G.-C. Guo, Nature Communications **6**, 1 (2015).

[322] L. Brillouin, in *Annales de physique* (1922), vol. 9, pp. 88–122.

[323] L. I. Mandelstam, Zhurnal Russii Fizicheskoi Khimii Ova **58**, 146 (1926).

[324] G. P. A. Enzian, Ph.D. thesis, University of Oxford (2020).

[325] J. J. Price, Ph.D. thesis, Imperial College London (2022).

[326] A. Ø. Svela, Ph.D. thesis, Imperial College London (2022).

[327] B. J. Eggleton, C. G. Poulton, P. T. Rakich, M. Steel, G. Bahl, et al., Nature Photonics **13**, 664 (2019).

[328] J. Sipe and M. Steel, New Journal of Physics **18**, 045004 (2016).

[329] R. Van Laer, R. Baets, and D. Van Thourhout, Physical Review A **93**, 053828 (2016).

[330] S. M. Barnett, G. Ferenczi, C. R. Gilson, and F. C. Speirits, Physical Review A **98**, 013809 (2018).

[331] U. Leonhardt, *Measuring the quantum state of light* (Cambridge University Press, 1997).

[332] U. Leonhardt and H. Paul, Physical Review A **48**, 4598 (1993).

[333] C. Gagatsos, J. Fiurášek, A. Zavatta, M. Bellini, and N. Cerf, Physical Review A **89**, 062311 (2014).

[334] M. Mičuda, I. Straka, M. Miková, M. Dušek, N. J. Cerf, J. Fiurášek, and M. Ježek, Physical Review Letters **109**, 180503 (2012).

[335] R. Brewster, I. Nodurft, T. Pittman, and J. Franson, Physical Review A **96**, 042307 (2017).

[336] C. Nunn, J. Franson, and T. Pittman, Physical Review A **104**, 033717 (2021).

[337] C. Nunn, J. Franson, and T. Pittman, Physical Review A **105**, 033702 (2022).

[338] A. Beige, D. Braun, B. Tregenna, and P. L. Knight, Physical Review Letters **85**, 1762 (2000).

[339] A. Beige, D. Braun, and P. L. Knight, New Journal of Physics **2**, 22 (2000).

[340] J. Clausen, M. Dakna, L. Knöll, and D. Welsch, Journal of Optics B: Quantum and Semiclassical Optics **1**, 332 (1999).

[341] B. Misra and E. G. Sudarshan, Journal of Mathematical Physics **18**, 756 (1977).

[342] K. Kraus, Foundations of Physics **11**, 547 (1981).

[343] X. Gu, A. F. Kockum, A. Miranowicz, Y.-x. Liu, and F. Nori, Physics Reports **718**, 1 (2017).

[344] J. Millen, T. S. Monteiro, R. Pettit, and A. N. Vamivakas, Reports on Progress in Physics **83**, 026401 (2020).

[345] D. M. Stamper-Kurn, in *Cavity optomechanics* (Springer, 2014), pp. 283–325.

[346] A. G. Krause, J. T. Hill, M. Ludwig, A. H. Safavi-Naeini, J. Chan, F. Marquardt, and O. Painter, Physical Review Letters **115**, 233601 (2015).

[347] H. M. Wiseman and G. J. Milburn, Physical Review A **47**, 642 (1993).

[348] H. Kaviani, C. Healey, M. Wu, R. Ghobadi, A. Hryciw, and P. E. Barclay, Optica **2**, 271 (2015).

[349] P. Fonseca, E. Aranas, J. Millen, T. Monteiro, and P. Barker, Physical Review Letters **117**, 173602 (2016).

[350] M. Karuza, M. Galassi, C. Biancofiore, C. Molinelli, R. Natali, P. Tombesi, G. Di Giuseppe, and D. Vitali, Journal of Optics **15**, 025704 (2012).

[351] D. Cattiaux, X. Zhou, S. Kumar, I. Golokolenov, R. Gazizulin, A. Luck, L. M. de Lépinay, M. Sillanpää, A. Armour, A. Fefferman, et al., Physical Review Research **2**, 033480 (2020).

[352] J. C. Sankey, C. Yang, B. M. Zwickl, A. M. Jayich, and J. G. Harris, Nature Physics **6**, 707 (2010).

[353] J. N. Westwood-Bachman, T. Firdous, A. E. Kobryn, M. Belov, and W. K. Hiebert, Physical Review A **105**, 053517 (2022).

[354] G. Longo, L. Alonso-Sarduy, L. M. Rio, A. Bizzini, A. Trampuz, J. Notz, G. Dietler, and S. Kasas, Nature Nanotechnology **8**, 522 (2013).

[355] A. G. Krause, M. Winger, T. D. Blasius, Q. Lin, and O. Painter, Nature Photonics **6**, 768 (2012).

[356] F. Guzmán Cervantes, L. Kumanchik, J. Pratt, and J. M. Taylor, Applied Physics Letters **104**, 221111 (2014).

[357] S. Forstner, E. Sheridan, J. Knittel, C. L. Humphreys, G. A. Brawley, H. Rubinsztein-Dunlop, and W. P. Bowen, Advanced Materials **26**, 6348 (2014).

[358] B.-B. Li, J. Bilek, U. B. Hoff, L. S. Madsen, S. Forstner, V. Prakash, C. Schäfermeier, T. Gehring, W. P. Bowen, and U. L. Andersen, Optica **5**, 850 (2018).

[359] J. Chaste, A. Eichler, J. Moser, G. Ceballos, R. Rurali, and A. Bachtold, Nature Nanotechnology **7**, 301 (2012).

[360] S. Liu, B. Liu, J. Wang, T. Sun, and W.-X. Yang, Physical Review A **99**, 033822 (2019).

[361] J. Moser, J. Güttinger, A. Eichler, M. J. Esplandiu, D. Liu, M. Dykman, and A. Bachtold, Nature Nanotechnology **8**, 493 (2013).

[362] D. C. Moore and A. A. Geraci, Quantum Science and Technology **6**, 014008 (2021).

[363] D. Carney, S. Ghosh, G. Krnjaic, and J. M. Taylor, Physical Review D **102**, 072003 (2020).

[364] D. Carney, G. Krnjaic, D. C. Moore, C. A. Regal, G. Afek, S. Bhave, B. Brubaker, T. Corbitt, J. Cripe, N. Crisosto, et al., Quantum Science and Technology **6**, 024002 (2021).

[365] A. A. Geraci, S. J. Smullin, D. M. Weld, J. Chiaverini, and A. Kapitulnik, Physical Review D **78**, 022002 (2008).

[366] S. Qvarfort, D. Rätzel, and S. Stopyra, New Journal of Physics **24**, 033009 (2022).

[367] S. L. Danilishin and F. Y. Khalili, Living Reviews in Relativity **15**, 1 (2012).

[368] C. M. Caves, Physical Review D **23**, 1693 (1981).

[369] T. P. Purdy, R. W. Peterson, and C. Regal, Science **339**, 801 (2013).

[370] A. A. Clerk, F. Marquardt, and K. Jacobs, New Journal Physics **10**, 095010 (2008).

[371] J. Hertzberg, T. Rocheleau, T. Ndukum, M. Savva, A. A. Clerk, and K. Schwab, Nature Physics **6**, 213 (2010).

[372] J. Suh, A. Weinstein, C. Lei, E. Wollman, S. Steinke, P. Meystre, A. A. Clerk, and K. Schwab, Science **344**, 1262 (2014).

[373] S. Mancini, D. Vitali, and P. Tombesi, Physical Review Letters **80**, 688 (1998).

[374] P.-F. Cohadon, A. Heidmann, and M. Pinard, Physical Review Letters **83**, 3174 (1999).

[375] S. Vyatchanin and E. Zubova, Physical Letters A **201**, 269 (1995).

[376] D. Mason, J. Chen, M. Rossi, Y. Tsaturyan, and A. Schliesser, Nature Physics **15**, 745 (2019).

[377] T. K. Paraïso, M. Kalaee, L. Zang, H. Pfeifer, F. Marquardt, and O. Painter, Physical Review X **5**, 041024 (2015).

[378] T. Kippenberg, H. Rokhsari, T. Carmon, A. Scherer, and K. Vahala, Physical Review Letters **95**, 033901 (2005).

[379] I. S. Grudinin, H. Lee, O. Painter, and K. J. Vahala, Physical Review Letters **104**, 083901 (2010).

[380] T. Carmon, H. Rokhsari, L. Yang, T. J. Kippenberg, and K. J. Vahala, Physical Review Letters **94**, 223902 (2005).

[381] T. Carmon, M. Cross, and K. J. Vahala, Physical Review Letters **98**, 167203 (2007).

[382] D. W. Brooks, T. Botter, S. Schreppler, T. P. Purdy, N. Brahms, and D. M. Stamper-Kurn, Nature **488**, 476 (2012).

[383] A. Kronwald and F. Marquardt, Physical Review Letters **111**, 133601 (2013).

[384] K. Børkje, A. Nunnenkamp, J. Teufel, and S. Girvin, Physical Review Letters **111**, 053603 (2013).

[385] M.-A. Lemonde, N. Didier, and A. A. Clerk, Physical Review Letters **111**, 053602 (2013).

[386] R. Huang, A. Miranowicz, J.-Q. Liao, F. Nori, and H. Jing, Physical Review Letters **121**, 153601 (2018).

[387] G. de Moraes Neto and V. Montenegro, Physics Letters A **438**, 128101 (2022).

[388] M. Rossi, D. Mason, J. Chen, and A. Schliesser, Physical Review Letters **123**, 163601 (2019).

[389] J. Zhang and K. Mølmer, Physical Review A **96**, 062131 (2017).

[390] K. Jacobs, *Stochastic processes for physicists: understanding noisy systems* (Cambridge University Press, 2010).

[391] A. I. Lvovsky, Photonics: Scientific Foundations, Technology and Applications **1**, 121 (2015).

[392] G. S. Agarwal and S. A. Kumar, Physical Review Letters **67**, 3665 (1991).

[393] J. Janszky and P. Adam, Physical Review A **46**, 6091 (1992).

[394] D. Rugar and P. Grütter, Physical Review Letters **67**, 699 (1991).

[395] G. Milburn and D. Walls, Optics Communications **39**, 401 (1981).

[396] A. Chowdhury, P. Vezio, M. Bonaldi, A. Borrielli, F. Marino, B. Morana, G. Prodi, P. M. Sarro, E. Serra, and F. Marin, Physical Review Letters **124**, 023601 (2020).

[397] A. Kronwald, F. Marquardt, and A. A. Clerk, Physical Review A **88**, 063833 (2013).

[398] E. E. Wollman, C. Lei, A. Weinstein, J. Suh, A. Kronwald, F. Marquardt, A. A. Clerk, and K. Schwab, Science **349**, 952 (2015).

[399] K. Jähne, C. Genes, K. Hammerer, M. Wallquist, E. Polzik, and P. Zoller, Physical Review A **79**, 063819 (2009).

[400] K. Kustura, C. Gonzalez-Ballestero, A. de los Ríos Sommer, N. Meyer, R. Quidant, and O. Romero-Isart, Physical Review Letters **128**, 143601 (2022).

[401] J. S. Bennett and W. P. Bowen, New Journal of Physics **20**, 113016 (2018).

[402] M. Asjad, G. Agarwal, M. Kim, P. Tombesi, G. Di Giuseppe, and D. Vitali, Physical Review A **89**, 023849 (2014).

[403] A. Setter, J. Vovrosh, and H. Ulbricht, Applied Physics Letters **115**, 153106 (2019).

[404] J. R. Johansson, P. D. Nation, and F. Nori, Computer Physics Communications **183**, 1760 (2012).

[405] T. P. Purdy, P.-L. Yu, R. W. Peterson, N. S. Kampel, and C. A. Regal, Physical Review X **3**, 031012 (2013).

[406] L. Diósi, arXiv:1710.02814 (2017).

[407] V. Allori, A. Bassi, D. Dürr, and N. Zanghi, *Do Wave Functions Jump?: Perspectives of the Work of GianCarlo Ghirardi*, vol. 198 (Springer Nature, 2020).

[408] A. Smirne and A. Bassi, Scientific Reports **5**, 1 (2015).

[409] P. Pearle, Physical Review D **13**, 857 (1976).

[410] G. C. Ghirardi, P. Pearle, and A. Rimini, Physical Review A **42**, 78 (1990).

[411] S. Belli, R. Bonsignori, G. D'Auria, L. Fant, M. Martini, S. Peirone, S. Donadi, and A. Bassi, Physical Review A **94**, 012108 (2016).

[412] A. Vinante, M. Carlesso, A. Bassi, A. Chiasera, S. Varas, P. Falferi, B. Margesin, R. Mezzena, and H. Ulbricht, Physical Review Letters **125**, 100404 (2020).

[413] S. Nimmrichter, K. Hornberger, and K. Hammerer, Physical Review Letters **113**, 020405 (2014).

[414] L. Ferialdi and A. Bassi, Physical Review A **102**, 042213 (2020).

[415] R. Penrose, Foundations of Physics **44**, 557 (2014).

[416] R. Howl, R. Penrose, and I. Fuentes, New Journal of Physics **21**, 043047 (2019).

[417] S. Donadi, K. Piscicchia, C. Curceanu, L. Diósi, M. Laubenstein, and A. Bassi, Nature Physics **17**, 74 (2021).

[418] L. Diósi, New Journal of Physics **16**, 105006 (2014).

[419] A. Vinante and H. Ulbricht, AVS Quantum Science **3**, 045602 (2021).

[420] D. Kleckner, I. Pikovski, E. Jeffrey, L. Ament, E. Eliel, J. Van Den Brink, and D. Bouwmeester, New Journal of Physics **10**, 095020 (2008).